116

FIFTH CANADIAN/AMERICAN CONFERENCE ON HYDROGEOLOGY

Banff, Alberta, Canada **September, 1990**

Jointly Organized By

Alberta Research Council

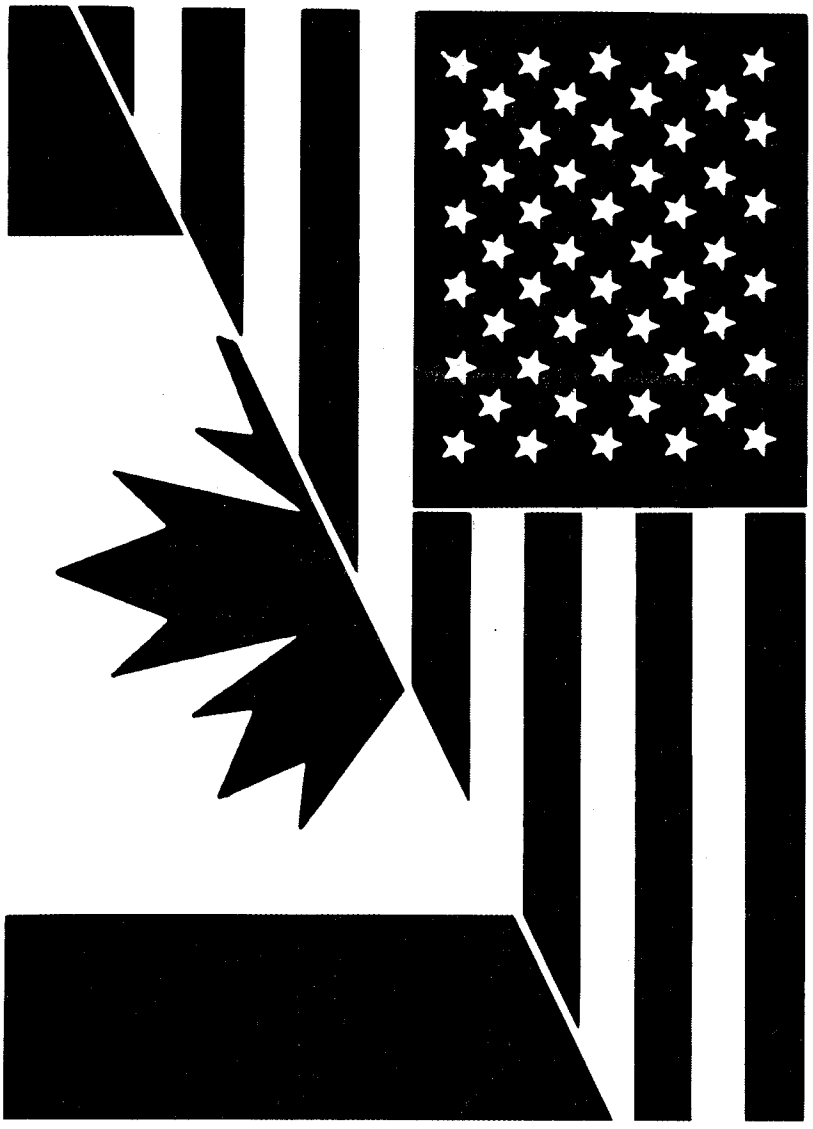

National Water Well Association

PROCEEDINGS

Edited by: **Stefan Bachu**
(Alberta Research Council, Edmonton, Alberta, Canada)

Published by: **National Water Well Association**

Proceedings Fifth Canadian/American Conference on Hydrogeology

Parameter Identification and Estimation for Aquifer and Reservoir Characterization

Calgary, Alberta, Canada
September 18-20, 1990

Edited by

Stefan Bachu
Alberta Research Council
Edmonton, Alberta, Canada

Published by

National Water Well Association
Dublin, Ohio, USA

Preface

This volume contains the Proceedings of the Fifth Canadian/American Conference on Hydrogeology, held in Calgary, Alberta, September 18-20, 1990, on the subject of "Parameter Identification and Estimation for Aquifer and Reservoir Characterization".

The present conference format started with the anonymous donation of $5000 to the Alberta Research Council under the condition that the money be spent to encourage the development of the discipline of geochemistry. After the success of the first Applied Geochemistry Workshop, Banff, June 1-3, 1982, it was decided to enlarge the scope and broaden the area of these meetings, and to bring together scientists and practitioners from both sides of the Canada/USA border. Thus, the idea of a series of Canadian/American Conferences on Hydrogeology was born. The conferences were sponsored jointly by the Alberta Research Council and the National Water Well Association. Since then, the Alberta Research Council has been responsible for program development, running the conferences, and the scientific editing of the proceedings, while the National Water Well Association has handled the advertising and publication of the proceedings volume.

The Canadian/American Conferences on Hydrogeology comprise invited speakers for subjects relevant to the conference theme, and a suite of unsolicited papers which are grouped into broad sections corresponding to the main subjects covered by the invited specialists. The first conference (June 22-26, 1984) dealt with "Practical Applications of Ground Water Geochemistry". The subject of the second conference (June 25-29, 1985) was "Hazardous Wastes in Ground Water: A Soluble Dilemma". After the third conference (June 22-26. 1986) on the subject of "Hydrogeology of Sedimentary Basins: Application to Exploration and Exploitation", it is now apparent that, from the point of view of organization and participation, it would be better to hold the conferences biannually rather than annually. Hence, the fourth conference on "Fluid Flow, Heat Transfer and Mass Transport in Fractured Rocks" was held June 21-24, 1988, and the present one, the fifth, was held in 1990.

The subject of this conference was chosen because of the increasing importance of proper aquifer and reservoir characterization in the use of exploration, exploitation and protection methods and techniques for water and energy resources. It became widely accepted that natural earth materials are intrinsically heterogeneous in terms of their properties, and that the issue of homogeneity is rather a question of scale. Aquifer and reservoir characterization is the process of identifying and quantitatively assigning properties, recognizing both hard and soft information and at the same time taking into account uncertainties related to the data capture, distribution and representativeness. This is an area of currently active research in both the hydrogeological and reservoir engineering communities, and one of the goals of this conference was to bridge the communication gap between the two. This goal was attained, as attested by the subject of the papers and the interests of the participants at the conference. The wide spectrum of subjects, and the theoretical and more applied papers presented, indicate also the timeliness of the conference.

It is hoped that the present volume will be of interest and help to other researchers and workers in this very challenging field.

All manuscripts submitted were subject to peer review, as well as scrutiny by the editor. I would particularly like to acknowledge the following who acted as scientific reviewers and provided many additional valuable comments for the benefit of the authors and the editors:

F. Agterberg
M.P. Anderson
S. Bachu
J. Bahr
R.E. Crowder
D. Cuthiell
A. Desbarats
R. Dimitrakopoulos
I. Ershaghi
A. Freeze
G.S. Fraser
J. Gale
S.P. Garabedian
O. Guven
D. Hackbarth
J. Heller
M.J. Hendry
B. Hitchon
A. Journel
B.L.N. Kennett
P. Kitanidis
J.W. Kramers
L. Lake
J. Long
R.L. Naff
D.W. Oldenberg
F. Phillips
E. Poeter
N. Scheier
R. Stein
H.L. Vacher
G. vander Kamp
A. Vonhof
K.J. Weber
R. Wong
L.P. Yuan

This conference would not have taken place without the encouragement and close cooperation of the Alberta Research Council and the National Water Well Association, and I duly acknowledge their efforts in once more supporting this international venture. Logistical organization for the conference and the smooth running of manuscript processing were due to the outstanding efforts of Kathie Skogg (Alberta Research Council) to whom the editor expresses his deep appreciation. Finally, the continued cooperative efforts of Dr. Jay Lehr, Executive Director of the National Water Well Association, who has given enthusiastic encouragement and the commitment of his organization, are most gratefully recognized.

Stefan Bachu
Editor
Fifth Canadian/American
Conference on Hydrogeology

Table of Contents

The role of geology in parameter estimation
John L. Wilson and Fred M. Phillips 1
Aquifer heterogeneity -- a geological perspective
Mary P. Anderson. 3
Using a sedimentary depositional model to simulate heterogeneity in glaciofluvial sediments
E.K. Webb and M.P. Anderson 23
Hydraulic conductivity predicted as a function of grain size, sorting and porosity for dune, washover and foreshore depositional environments on a barrier island, Florida, USA
Rick J. Stebnisky and H. Leonard Vacher 42
Impacts on geological structure on transport: creating a data base
Timothy D. Scheibe and David L. Freyberg 56
Reservoir characterization case study: sandy facies
John Kramers, Li-Ping Yuan, Stefan Bachu and David Cuthiell 72
Reservoir characterization case study: bimodally heterogeneous facies
Stefan Bachu, David Cuthiell, John Kramers and Li-Ping Yuan 87
Use of detailed sedimentological information for the assessment of pumping and tracer tests in a shallow fluvial aquifer
J.C. Herweijer and S.C. Young 101
Geostatistical evaluation of a three-dimensional hydraulic conductivity field in an alluvial terrace aquifer
Steven C. Young, Joost Herweijer and Dudley J. Benton 116
Stochastic characterization of subsurface flows
Lynn W. Gelhar 138
Spatial averaging of transmissivity
Alexandre J. Desbarats 139
Identification of effective conductivity tensor in randomly heterogeneous and stratified aquifers
Rachid Ababou 155
Kriging application to estimate groundwater and top of aquifer elevations for eastern Arizona
Jeff Riddle 158
Multiple indicator conditional stochastic simulation of a section of the unconfined aquifer, Hanford Site, Washington, USA
Eileen Poeter and Peter Townsend. 159
Investigation of the spatial correlation of saturated hydraulic conductivities from a vertical wall of a trench
Elizabeth A. Jabobson. 189
Stochastic modelling of contaminant movement in ground water
Kevin K. Wolka and T. Al Austin 199

Determination of scales of porosity variability through the use of image analysis
Lisa D. Shepherd, Jean M. Bahr and Gerilynn R. Moline 201
A multivariate statistical method for using geophysical log data to delineate hydrostratigraphy and estimate hydraulic parameters: St. Peter Sandstone, Michigan Basin
Gerilynn R. Moline, Jean M. Bahr and Lisa D. Shepherd 214
Regionalized classification: ideas and applications
Geoffrey C. Bohling, Jan Harff and John C. Davis 229
State-of-the-art borehole geophysics applied to hydrogeology
Elliot N. Yearsley and Robert E. Crowder 243
Aquifer parameters defined by borehole geophysics
Bruce Manchon 260
Quantification of ionic and hydrocarbon-type contaminants with geophysical resistivity surveys and drill hole sample data
Joe O. Davis 261
The inversion of E-SCAN resistivity data in the solution of ground water contamination and enhanced oil recovery problems
P.R. McGillivray and D.W. Oldenburg 262
A conceptual framework for the geostatistical approach to the inverse problem
Peter K. Kitanidis 275
Optimization methods in inverse solution of ground water flow systems
Jiannan Xiang and Derek Elsworth 276
Inverse modelling in the frequency domain: the example of estimating transmissivity from observations of the combined solid earth tide and atmospheric pressure influence
Robert W. Ritzi, Jr. 289
Modelling a multi-unit aquifer system with uncertain aquifer geometry
Malcolm Reeves and Rebecca Yost Grambo 305
Assessment of the rational set of field tests in heterogeneous aquifers on imitation models
V.A. Mironenko 321
New approaches to the simulation of field-scale solute transport in fractured rocks
Leslie Smith, Tom Clemo and Mark D. Robertson 329
Controls on porosity and permeability in fracture-flow/conduit-flow rocks of the Knox Group, southern Appalachian Fold-and-Thrust Belt, USA
James C. Redwine, Richard R. Parizek and Fred J. Molz 343
Characterization and modelling of ground water flow in a heterogeneous aquifer system to evaluate contaminant migration
Fred G. Baker and Hannah F. Pavlik 344
A percolation model for hydraulic conductivity in porous media
B. Berkowitz and I. Balberg 362
Computed effect of heterogeneity on well-to-well tracer results
Saleem G. Ghori and John P. Heller 371
Simulating fluid flow through a geologically realistic permeable medium
Larry W. Lake 385

Visualization of flow and transport in heterogeneous media
John L. Wilson. 386
The impact on large scale heterogeneities on hydrocarbon recoveries
Sait Kocberber and R. Eugene Collins 387
Estimation of reservoir parameters in heterogeneous gas storage reservoirs under aquifer support I.
I. Ershaghi, H. Calisgan, J. Chang and Y. Shikari 394
Regional characterization of variable-density fluid flow in sedimentary basins: implications of model interpretation
Rainer K. Senger 415
Use of noble gases to determine boundary conditions in ground water and petroleum system models
Emanuel Mazor and Adi Bosch 435
Boundary conditions needed for ground water modelling, derived from isotopic, chemical and physical measurements: Mediterranean-Dead Sea transect
Emanuel Mazor and Levy Kroitoru 443
Hydraulic evidence of Wisconsinan-aged open fractures in a deep clayey till
David G. Thomson and John A. Cherry. 453

The role of geology in parameter estimation

by John L. Wilson and Fred M. Phillips

Abstract

Parameter values assigned to simulation models are presumably related to the actual property distributions of real aquifers and reservoirs. These property distributions are themselves a function of the geological depositional environment and subsequent diagenesis. Historically this has been recognized by modellers only when dealing with relatively large-scale geological features. For example, in hydrology aquifers and aquitards are recognized, and codes are often designed around such layered features, as in the popular Modflow code. Reservoir engineers typically subdivide reservoirs into a layercake structure, emulating an easily recognized stratigraphic succession that is typically simulated using block finite differences. Fractures, if they occur, are assumed to follow the same orthogonal pattern. These standard hydrologic and reservoir conceptualizations are easy to visualize, program, and parameterize. One need only assign property values to each layer. If desired, various zones may be designated within each layer to provide for any 'necessary' lateral trends in property values. There is little formalism in picking a zoning pattern, one simply tries different and somehow reasonable patterns until 'satisfied'. Yet within each of these layers and arbitrary zones there is additional property variability. As is now recognized, this smaller spatial scale of variation has important influences on pollutant modelling transport in hydrology and the performance of oil recovery efforts in reservoirs. There are many ongoing studies to incorporate this variability into the models, and to parameterize it.

One approach to this issue employs geostatistical models (e.g. variograms) of the parameter space. These geostatistical models are used to interpolate sparse and uncertain, but correlated measurements via kriging or co-kriging. The kriged fields and their covariances may in turn be used as prior information in history matching exercises, to provide unique and stable inverse solutions. The parameters of the geostatistical models may themselves be the object of these estimation approaches, but in almost every case the geostatistical model is assumed to be known, or drawn from a small family of possible models. One might ask if the geological world is appropriately described by these geostatistical models?

The real issue is that it is typical to abandon most of our general and site-specific geological knowledge once we have selected a conceptual model and begun the parameter estimation process, even when using geostatistics. In this paper the use of subjective geological information in the construction and parameterization of appropriate geostatistical models is explored. In particular, the relation between measurable hydrologic quantities, such as permeability, and observable geological features are investigated. If there is a strong correlation between the two, then subjective geological knowledge can be used to extend significantly, the data sets used in parameter estimation.

John L. Wilson is Professor of Hydrology and Director of the Hydrology Program at the New Mexico Institute of Mining and Technology. (Department of Geoscience, Socorro, New Mexico

87801, USA). His present research interests include the fundamental fluid mechanics of porous media flow and transport, primarily using flow visualization tools.

Fred M. Phillips is Associate Professor of Hydrology at the New Mexico Institute of Mining and Technology (Department of Geoscience, Socorro, New Mexico 87801, USA). His research spans a variety of areas, including geological controls on permeability distribution in sediments, radiometric dating of ground water, isotopic tracing of ground water recharge processes in desert soils, reconstruction of fluctuations in the water balance over the Quaternary, and dating of landforms using cosmogenic nuclide accumulation.

Aquifer Heterogeneity-- A Geological Perspective

by Mary P. Anderson

Abstract

Efforts to quantify heterogeneity in aquifers involve assumptions about the variability inherent in geological materials. Delving into the geological literature for help in quantifying heterogeneity is both enlightening and frustrating. Conceptual models of the distribution of sediments and sedimentary rocks in specific geological environments, so-called facies models, provide information about regional sequences of deposits. The literature also contains detailed descriptions of site-specific deposits at the scale of an outcrop. The petroleum literature contributes information at the core scale, including discussions about the permeability of small-scale sedimentary structures such as cross-bedding.

Hydrogeological problems, however, are most often at a regional scale or somewhere between the regional scale and the scale of an outcrop. There is very little information in the sedimentological literature of the kind needed to quantify heterogeneity at this scale. In part this is due to fundamental philosophical differences in the use of facies models in sedimentology and the needs of hydrogeologists. Nevertheless, there are at least three insights from the sedimentological literature that may be helpful in quantifying heterogeneity in aquifers: 1) There are predictable sequences of deposits at a regional scale; 2) Geological units identified at a local scale may provide a way of classifying heterogeneity; 3) Interconnection of geological units is an important feature of heterogeneity. Numerical experiments involving particle tracking demostrate that interconnected units of high hydraulic conductivity cause preferential flow and funneling or channeling of contaminants. An example is presented in this paper. Such behavior cannot be described by a Fickian model of dispersion with standard dispersivities. The task of quantifying preferential flow is the most challenging problem facing those interested in aquifer heterogeneity.

Introduction

It seems surprising that scientists interested in describing geological deposits, subsurface reservoirs, and ecosystems are only now coming to grips with a fundamental characteristic inherent in all such systems, namely heterogeneity. Careful, detailed descriptions at the local scale are now accompanied by a desire to relate these observations to the "big picture". The application of increasingly sophisticated field techniques, including remote sensing, geophysical methods and other types of electronic monitoring, has made it easier to obtain field measurements. At the same time, the development of small powerful computers has made it easier to analyze large numbers of data. But methodologies for extrapolating detailed data sets to a larger frame of reference have not yet been perfected.

Geologists have always been interested in the spatial and temporal variability in the rock record. Although geology has traditionally been a qualitative science, recent literature (e.g. Cross, 1990) suggests that a new quantitative approach, dubbed quantitative dynamic stratigraphy (QDS), may provide a better way of describing geological heterogeneity. The term QDS refers to stratigraphic analysis using quantitative techniques including physically based sedimentation models that simulate the deposition of sediments through geological time. This type of model was introduced into the ground-water literature by Price (1974). The development of these models signals a shift away from the conceptual models that had previously been used to depict a representative succession of deposits for a particular depositional environment. Conceptual models of the relation of geological deposits typically take the form of a block diagram and stratigraphic column (Figure 1) showing the spatial relations of geological units of similar characteristics, known as facies. Hence, the relations depicted in Figure 1 are termed a facies model. Facies models can be developed on at least two scales: a local scale (Figure 1A) and a regional scale (Figure 1B).

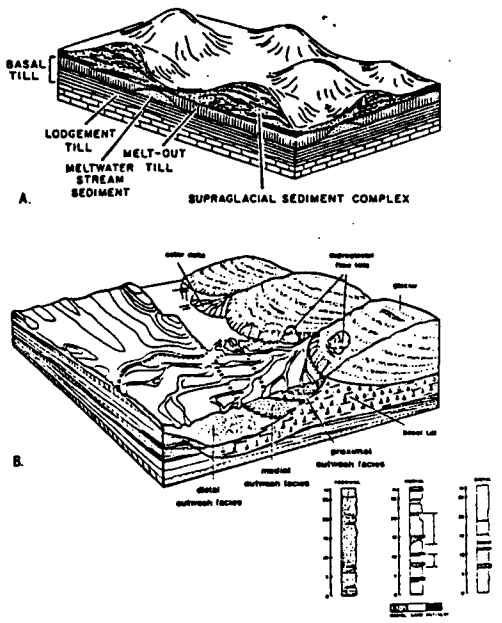

Figure 1. Conceptual models of geological facies (Anderson, 1989).
A) Till facies at a local scale showing basal till overlain by supraglacial sediment. The basal till consists of lodgement till overlain by melt-out till, which contains meltwater stream sediment that may form a preferential flow path.
B) Outwash succession shown at a regional scale. The proximal, medial and distal outwash facies assemblages are shown proceeding from the ice margin. A facies assemblage consists of a distinctive suite of facies.

Walker (1984) identified four functions of a facies model: 1) to form a norm for purposes of comparison; 2) to provide a framework for future observations; 3) to help predict facies occurrences in new geological situations where field information is

limited; and 4) to help interpret the processes operating in a particular system. Facies models have been used most successfully when fulfilling functions 1,2 and 4. It is the third function, however, that appeals most to hydrogeologists who would like to quantify aquifer heterogeneity at specific sites where geological field information is limited or even lacking.

Although theoretically possible, using facies models for prediction is in fact difficult. The fundamental rationale behind a facies model is the belief that there are facies transitions that occur more commonly than would be expected if the process of deposition were random. The facies model captures these trends. Even if this supposition is true, the chief difficulty with facies models is that the ideal summary of a geological environment is unlikely to be found in any given field situation. The dilemma was best articulated by Smith (1985): "The facies assemblage as depicted was in fact not actually seen in outcrop and could be thought of as the most representative depositional sequence that would have resulted had nature cooperated to its fullest. It never does, and therein lies a large part of the problem..." Hence, a facies model is not very helpful in predicting the precise location of units of high permeability, for example, although a facies model may indicate the likelihood that such units exist somewhere in the deposit. It is hoped that physically based sedimentation models will provide better ways of describing both the generic features of facies as well as specific deposits. If it is demonstrated that computer simulations can accurately represent facies distributions, these models will have applications in economic geology, in surface water hydrology to simulate sedimentation in rivers and coastal environments, and in petroleum geology and hydrogeology to describe subsurface reservoirs.

Natural scientists interested in ecosystems are also struggling with spatial heterogeneity. The National Science Foundation through its Long Term Ecological Research (LTER) program, and the US Geological Survey through its recently initiated program on Water, Energy, and Biogeochemical Budgets (WEBB), are wrestling with the need to investigate regional systems that incorporate some critical scale of site heterogeneity. Eventually such hydrological descriptions may interface with global climate models to address the potential effects of global climate change on water resources.

Geologists and ecologists deal with both spatial and temporal scales. Theoretically, spatial variability is more easily studied because changes in space are apparent at any given moment in time. Temporal variablity is difficult to study because one must wait for change to occur. And in the case of geological change, the relevant time scales exceed a human life time. The need to study long periods of time is, of course, what distinguishes geology from other sciences; geologists have developed ways of studying geological time by analyzing the rock record. In QDS, the problem is complicated by the need to consider several different time scales, from the time required to deposit grains of sand (seconds) to the time required to form a sandstone (hundreds to thousands of years).

Ecologists also deal with time scales ranging from what Magnuson (1990) has called the "invisible present" to millennia (Figure 2). Long-term trends are invisible in the one-year time frame traditionally used to study ecosystems (or hydrological systems). Conclusions about trends drawn from such short-term records can be misleading or wrong.

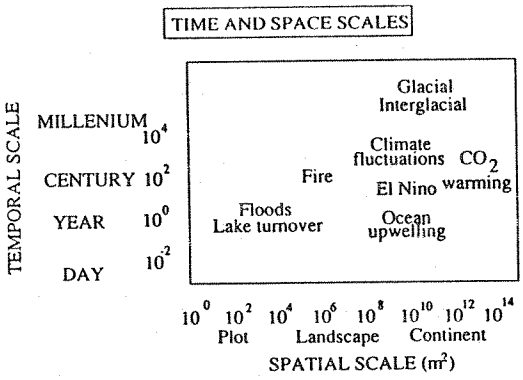

Figure 2. Spatial and temporal scales of concern to ecologists (modified from Franklin et al. 1990).

While hydrogeologists as well as petroleum geologists are indirectly interested in temporal variability, attention is naturally focused on the spatial variability that currently exists. In both of these fields there is a need to quantify geological information for input to computer models that simulate the movement of fluids and contaminants in the subsurface. Proceedings from two recent conferences (Lake and Carroll, 1986; Tillman and Weber, 1987) suggest that petroleum geologists currently face problems similar to those confronted by hydrogeologists. Petroleum geologists, however, have the advantage in that in addition to outcrop studies, they typically have access to large numbers of cores that allow detailed stratigraphic correlation and analysis of geological units. This allows for the possibility of detailed geological characterization in reservoir simulations (Jones et al., 1984).

In ground-water work, most efforts to analyze aquifer heterogeneity have involved stochastic models that require the assumption of stationarity. In this framework, spatial variability is assumed to be spatially periodic so that mean or effective aquifer parameters can be defined using the statistical moments of the relevant random variable, e.g. the mean, the variance and the covariance of the hydraulic conductivity field. This viewpoint incorporates the notion that there are discrete natural units within a random field. Another viewpoint assumes continuous or evolving heterogeneity, often described by a fractal model. Neuman (1990) demonstrated that a fractal model appears to explain heterogeneity in aquifers, as measured by dispersivity values. Geological facies mapped at the scale of an outcrop and facies assemblages in regional facies models (Figure 1B) involve discrete natural units. It may be the fractal model of Neuman (1990) applies between these two extremes, i.e. within facies assemblages defined at the regional scale (Figure 3).

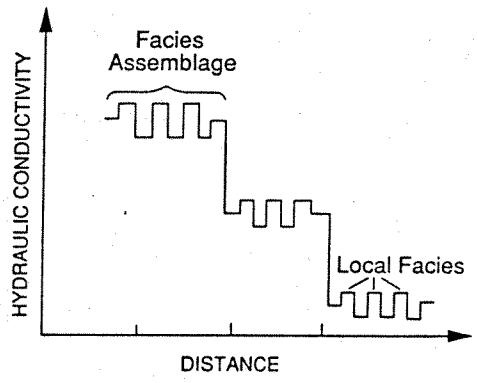

Figure 3. Scales of heterogeneity showing discrete natural units (facies) at the local and regional level. The Neuman (1990) fractal model may apply within regionally defined facies assemblages.

As ground-water scientists and engineers seriously begin to attack the issue of heterogeneity, we must ask: "What can we learn from the geological literature?".

Gems(?) from the Geological Literature

We will consider two types of geological literature-- the sedimentological literature and the more applied literature of petroleum geology.

It is difficult to extract information from the sedimentological literature that is directly useful to hydrogeologists because geological information is qualitative, while hydrogeology requires quantitative descriptions of aquifer characteristics. It could be argued that qualitative description is an inherent and essential feature of geological description because there is more variablity in geological systems than in other types of natural systems. One can expect a certain type of plant or animal to occur in essentially the same form in more than one locality. Hence, it is possible to develop precise classification systems for plant and animal species. In geology too, we can expect rock types to occur in more than one locality but the possible variations of a general rock type like sandstone are so large that cumbersome qualifiers are needed to give a precise description of a specific rock. Facies classification schemes also require qualifiers such as "sand, medium to very coarse, may be pebbly with solitary (alpha) or grouped (omikron) planar crossbeds, indicative of linguoid, transverse bars, sand waves (lower flow regime)" (Miall, 1978). A seemingly unambiguous quantitative descriptor like grain size cannot capture differences in genesis and hence becomes ambiguous when used in geological classification. For example, similar coarsening-upward profiles of a sediment may indicate deposition in an alluvial fan, delta, barrier island, or submarine fan. Attempts to develop a standard terminology for alluvial facies (Miall, 1978) and glacial facies (Eyles et al., 1983) have met with mixed reactions. Dreimanis (1984) called the classification of glacial deposits of Eyles et al. (1983) "too elementary to be useful" because the number of qualifiers used was too small. Similarly, Kemmis and Hallberg (1984) stressed that genetic classification of glacial deposits must be based on multiple criteria and criticized Eyles et al. (1983) for not including fabric and deformation structures in their classification scheme.

Hence, we find that much of the sedimentological literature consists of detailed descriptions of facies at specific locations, with each researcher using a different classification system. Such a description forms a site-specific conceptual model of a particular depositional system. Sedimentologists would like to be able to use a generic facies model as a guide to their site-specific model. They compare their detailed site-specific information against the trends predicted by a generic facies model which represents the ideal for the relevant environment. In this way they can identify and/or verify the processes that formed their deposit. Hydrogeologists, on the other hand, would like to use a generic model to extrapolate sketchy field data.

A good example of the approach of sedimentologists toward facies models is given by Fraser and Cobb (1982) who studied a large outwash complex in Illinois. Facies assemblages were identified, following the accepted generic facies model for outwash (Figure 1B). Each facies assemblage was described in qualitative terms and by grain size. Representative outcrops of each facies assemblage were mapped in detail (Figure 4).

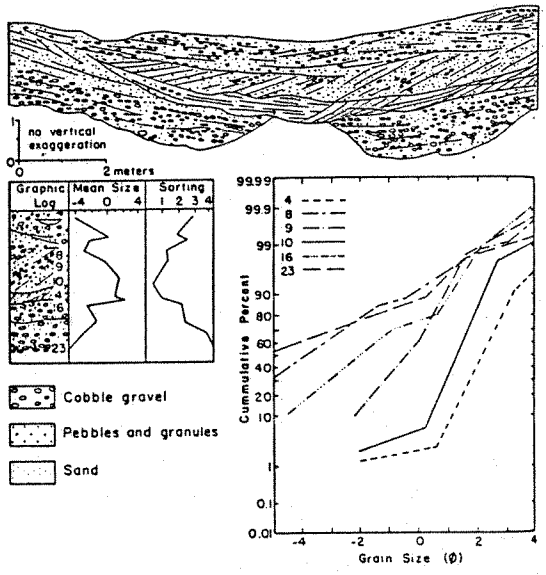

Figure 4. Detailed map of a representative outcrop in the proximal assemblage of an outwash succession together with grain size information (Fraser and Cobb, 1982).

Based on these observations, details of the processes responsible for forming the deposits were deduced. The general features of the outwash facies mapped by Fraser and Cobb (1982) have also been observed in outwash in Wisconsin (Webb and Anderson, 1991) suggesting that there are points in common among generically defined facies in different geographic locations.

The sedimentological literature describing fluvial systems is voluminous. The most enticing of these studies from a hydrogeological point of view include the work of Miall (1985) on architectural element analysis. Miall (1985) described eight geometrically and lithologically distinct deposits or elements typically found in fluvial

systems (Figure 5A). An element consists of a suite of facies that are associated with a specific depositional process. Elements combine to form different types of fluvial environments (Figure 5B).

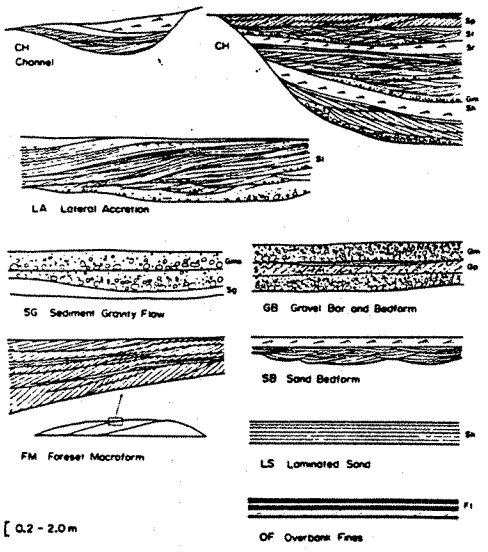

A.

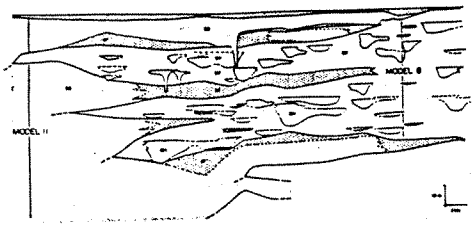

B.

Figure 5. Architectural elements for alluvial systems.
A) Individual architectural elements (Miall, 1985).
B) Grouping of elements in a deposit in Pakistan to form two river types: model 8, which indicates a low-sinuosity river with linquoid bars and "Platte-type macroforms", and model 11, which indicates a distal braidplain, typically ephemeral (Miall, 1988).

This approach offers a start toward a systematic classification of heterogeneity in fluvial systems at a scale consistent with scales of interest in contaminant hydrogeology. Other papers of interest include those dealing with interconnection of sand units (Allen, 1978; Bridge and Leeder, 1979; Glezen and Lerche, 1985). Interconnected units in aquifers may form preferential paths for contaminant movement.

Thus we find that the sedimentological literature contains information at three scales: generic facies models are constructed at a regional scale and site-specific facies models are developed at the scale of an outcrop, while architectural elements offer an intermediate scale of analysis. The petroleum geological literature has contributed information at yet another scale-- the core scale. The need for quantitative geological input to reservoir simulation models motivated petroleum geologists and engineers to attempt to quantify heterogeneity in terms of permeability and grain size. For example, Pryor (1973) defined permeability and porosity patterns in sands, but as Miall (1988) observed, few reservoir studies in the petroleum literature use this information. Weber (1986) presented formulae to quantify the variablity in cross-bedded fluvial and aeolian sands (Figure 6) but such fine detail among sands is probably unimportant in most hydrogeological investigations.

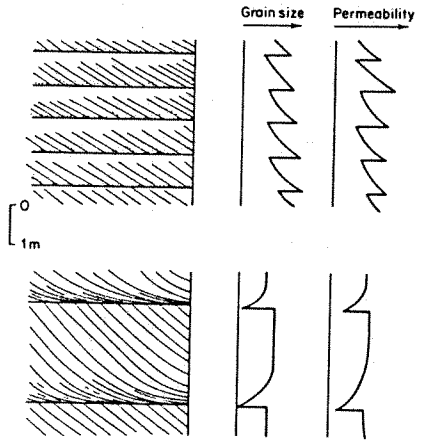

Figure 6. Cross-bedding with inferred variations in grain-size and permeability (Selley, 1986).

Instead, it is likely that interconnected paths of high hydraulic conductivity, which form preferential flow paths, are the most important type of heterogeneity in aquifers. Dual permeability systems in the form of interconnected sandstones separated by shale are also of special interest to petroleum geologists (Weber, 1986; Geehan et al., 1986) because shale distribution is an important geological control on reservoir performance.

Out of the geological literature, then, three concepts emerge that have immediate relevance to aquifer heterogeneity.

1. There are predictable regional successions of deposits that can be deduced from the study of depositional systems. The belief that such successions are related to the processes operative in a particular depositional environment is the basis of regional conceptual models of geological facies.
2. Detailed mapping of facies and architectural elements at the scale of an outcrop may provide a way of describing geological heterogeneity for numerical simulation of flow and contaminant transport.
3. Interconnection of geological units (e.g. sands) is an important feature of geological heterogeneity.

Cross Over to the Hydrogeological Literature

Heterogeneities have always troubled hydrogeologists. Meinzer (1932) observed that: "The most formidable difficulties result from the complexity of the texture of water-bearing formations, which make it hard to get reliable figures for their two properties of chief significance--specific yield and permeability." The problem of heterogeneity was temporarily solved by Theis (1935) who developed a technique for obtaining average values for these two aquifer properties by analyzing drawdown data from a pumping test. From then on, quantitative analysis in ground-water hydrology used the paradigm of the equivalent homogeneous porous medium whereby a heterogeneous aquifer is represented by a homogeneous aquifer with average properties that mimic the effects of heterogeneity. The solution of Theis (1935) to the heterogeneity dilemma proved useful for solving the flow problems that pre-occupied ground-water hydrologists for the next 40 years.

Theis (1967) concluded from experiments performed by Skibitzke and Robinson (1963), that the

equivalent porous medium approach would not work for contaminant transport investigations: "The type of aquifer study in which our homogeneous model of ground water flow is most grossly inadequate is that dealing with transport phenomena" (Theis, 1967). He went on to say that reliance upon the equivalent homogeneous porous medium approach "will mislead us if we apply it to problems of transport, in which we are concerned with the actual detailed movment of the water" and called for the development of "a new conceptual model, containing the known heterogeneities of the natural aquifer". The inadequacy of the equivalent homogeneous porous medium assumption was not widely recognized until almost 10 years later with the pioneering work of Freeze (1975) who questioned the validity of using average or effective parameters in modeling ground-water flow and who introduced stochastic simulation to the ground-water literature.

Effective Parameters

It is clear that measurement of bulk average parameters, such as is done in a pumping test, cannot capture the heterogeneity that is important in contaminant investigations. It is also clear that there is a lack of information in the geological literature at the scale of interest relevant to most practical problems in contaminant hydrogeology. Generic facies models are typically formulated at regional scales-- the scale of a river basin, an alluvial fan or a delta, for example, while detailed geological studies are typically conducted at the scale of an outcrop. Problems of contaminant hydrogeology are generally somewhere between the regional scale and the outcrop scale. While summaries of hydrogeological characteristics gleaned from the geological literature (Anderson, 1989; Bradbury and Muldoon, 1989; Sharp, 1989; Stephenson et al., 1989) will be useful, attempts to quantify heterogeneity must include detailed site-specific hydrogeological descriptions of the type pioneered by Smith (1981). Recently, Davis et al. (1990) used Miall's architectural elements during detailed mapping of an alluvial aquifer. Site-specific geological descriptions are also being compiled in conjunction with long term tracer tests at the Borden site (Sudicky, 1986), Cape Cod site (Hess, 1990; Wolf and Celia, 1989), MADE site (EPRI, 1989; Waldrop et al., 1989), and Chalk River (Moltyaner and Killey, 1988).

However, it is as yet unclear how best to treat such geological detail in analyses of flow and contaminant transport. Frind et al. (1988) introduced micro-scale modeling of heterogeneities of the order of centimeters using million-node simulations. However, for practical application such computer intensive simulations will seldom be possible. Traditional ground-water modeling assumes that it is possible to scale up by defining effective parameters that simulate the average effect of small "unknowable" heterogeneities. This is also the approach traditionally used in reservoir simulation (Lasseter et al., 1986, Bachu and Cuthiell, 1990). A number of researchers have used stochastic analysis to define effective parameters that consider the variation in hydraulic conductivity about the mean as well as the structure of the hydraulic conductivity field.

The existence of an effective hydraulic conductivity has been questioned by numerous researchers including Smith and Freeze (1979), El-Kadi and Brutsaert (1985), and Gomez-Hernandez and Gorelick (1989), all of whom based their conclusions on the results of Monte Carlo simulations. Williams (1988) questioned the concept on geological grounds. While an effective hydraulic conductivity may exist for some special combinations of hydrogeological conditions, it seems that the concept is not generally applicable. From the geological point of view, doubts about the validity of a stochastic description of heterogeneity center around the usual assumption of stationarity, which requires the existence of a uniform mean hydraulic conductivity or ensemble average for the system being modeled. The assumption of stationarity may be appropriate at the scale of a locally defined facies because a facies is a geological unit of similar physical characteristics. At a regional scale, however, facies models predict the existence of definable patterns in geological characteristics (Figure 1B) making the assumption of stationarity inappropriate at this scale. Neuman's (1990) fractal model may describe effective heterogeneity within regionally defined facies assemblages (Figure 3). It seems that in order to utilize effective parameters on a local scale, however, one must first identify facies distributions and then obtain enough hydrogeological information at the scale of the facies to calculate effective values for hydrogeologic parameters.

Davis et al. (1990) described the start of this process at a field site in New Mexico. They mapped, in detail, the sedimentology of portions of an alluvial aquifer using the architectural elements and facies nomenclature of Miall. They also measured in situ permeability using an air minipermeameter (Goggin et al., 1988). If such measurements could be linked to Miall's generic classification, it would be possible to report permeabilities in terms of his facies. Such information may be transferable to other sites.

Preferential Flow Paths-Overview

Another unresolved issue is how to treat interconnected units that may form preferential flow paths. While field studies documenting the occurrence of connected paths of high conductivity are few, geological facies models suggest that paths of high hydraulic conductivity commonly occur in many sedimentary environments (Figure 1A). There is no question that interconnected units of high hydraulic conductivity are important in describing contaminant movement. When referring to the assumption of a statistically homogeneous medium commonly used in stochastic simulation, Williams (1988) observed that: "hydrogeologists have not demonstrated that the ensemble average (or any other average) of any hydraulic property is necessarily the critical element of interest in the theory of groundwater flow and transport...", while the "identification of the so-called fastest path is critical. It is unreasonable to bury the identification of the fastest path in statistical parameters of the total rock population." Along these same lines, Fogg (1986) noted that: "One or two well-connected sands among a system of otherwise disconnected sands can completely alter a velocity field." Winograd and Pearson (1976) and

Osiensky et al. (1984) noted the same phenomenon, and Gelhar (1986) pointed out the need to evaluate the influence of "unmodeled heterogeneity" on the predictions of analytical stochastic models.

A few investigators have explicitly addressed the importance of preferential flow in ground-water systems. Following the lead from the petroleum literature, some ivestigators (Johnson and Dreiss, 1989; Bachu and Cuthiell, 1990; Desbarats, 1990) studied dual permeability systems in which sandstone bodies form interconnected units of high permeability. Silliman and Wright (1988) used Monte Carlo analysis to investigate the importance of paths of high hydraulic conductivity within low conductivity media. They found that for the cases they examined, there was at least one path crossing the three-dimensional grid along which the hydraulic conductivity was greater than the effective conductivity of the medium. The implication is that contaminants would preferentially follow the path of high hydraulic conductivity. Desbarats (1990) used a geostatistical description of a dual permeability sand/shale system combined with particle tracking to study preferential flow. He found that some of his systems exhibited pronounced channeling of particles and bimodal breakthrough curves.

Preferential Flow Paths-An Example

Results from a particle tracking simulation of a regional system are presented next in order to illustrate the way in which contaminants are funneled through units of high hydraulic conductivity. A hypothetical outwash sequence was generated and represented by a 24 x 20 cell grid with four layers. Each layer was 2 m thick except for the top layer which was 4 m thick (Figure 7). The areal dimensions of the outwash were 3 km x 5 km, represented by nodal spacings of 125 m and 250 m, respectively. Each cell was assumed to be isotropic with respect to hydraulic conductivity.

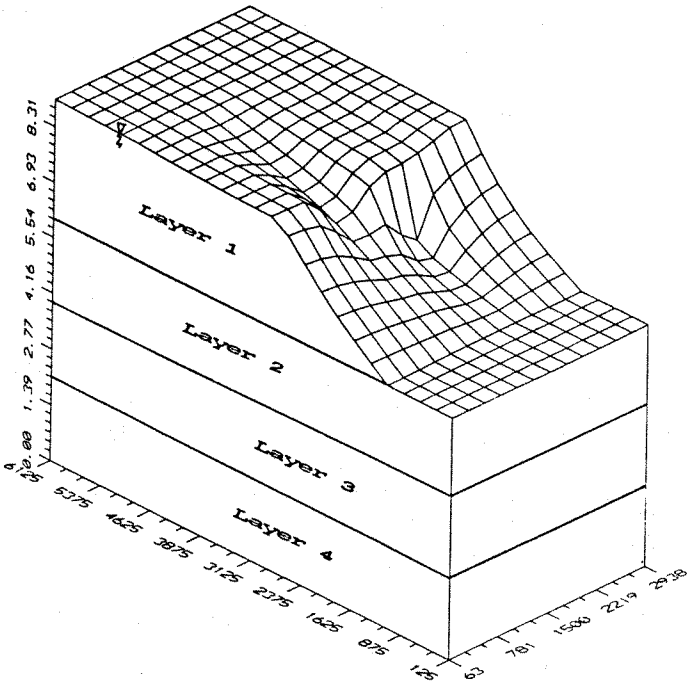

Figure 7. Geometry of the system used in the particle tracking experiments. The configuration of the water for the heterogeneous facies simulation of Figure 8B is shown. Elevations and distances are in meters.

The regional facies model for outwash calls for three facies assemblages: the proximal, medial and distal facies assemblages (Figure 1B). Two patterns of lithologies were used in the particle tracking simulations. Figure 8A shows a pattern in which each of the three facies assemblages is homogeneous; in Figure 8B each assemblage is heterogeneous.

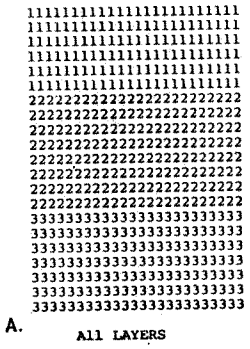

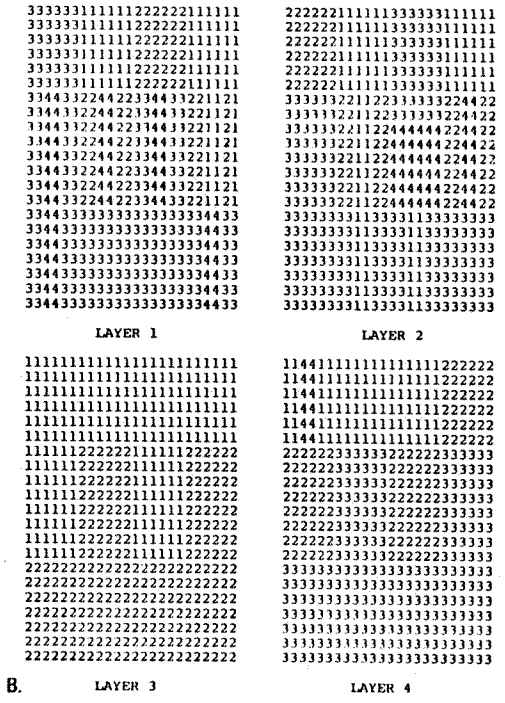

Figure 8. Lithologies used in the particle tracking simulations. Three facies assemblages are shown: the proximal, medial and distal facies assemblages. Hydraulic conductivity values for each lithology code are:

Lithology Code	Hydraulic Conductivity (m/s)
1	10^{-2}
2	10^{-4}
3	10^{-6}
4	10^{-8}

A) Homogeneous facies. Each facies assemblage is homogeneous. All layers have the same distribution of lithologies.
B) Heterogeneous facies. Each facies assemblage is heterogeneous, both areally and vertically.

Hydraulic conductivities were assigned to each lithology code to allow a two-order-of-magnitude constrast between successive lithologies. Constant head boundaries were specified at either end of the model to create a horizontal hydraulic gradient of 6×10^{-4} m/m across the length of the model. The flow model (MODFLOW, McDonald and Harbaugh, 1988) treated the upper layer as unconfined and calculated the configuration of the water table during the simulation. The bottom and the sides of the model were assumed to be no flow boundaries. The water-table configuration for each sediment distribution is shown in Figure 9.

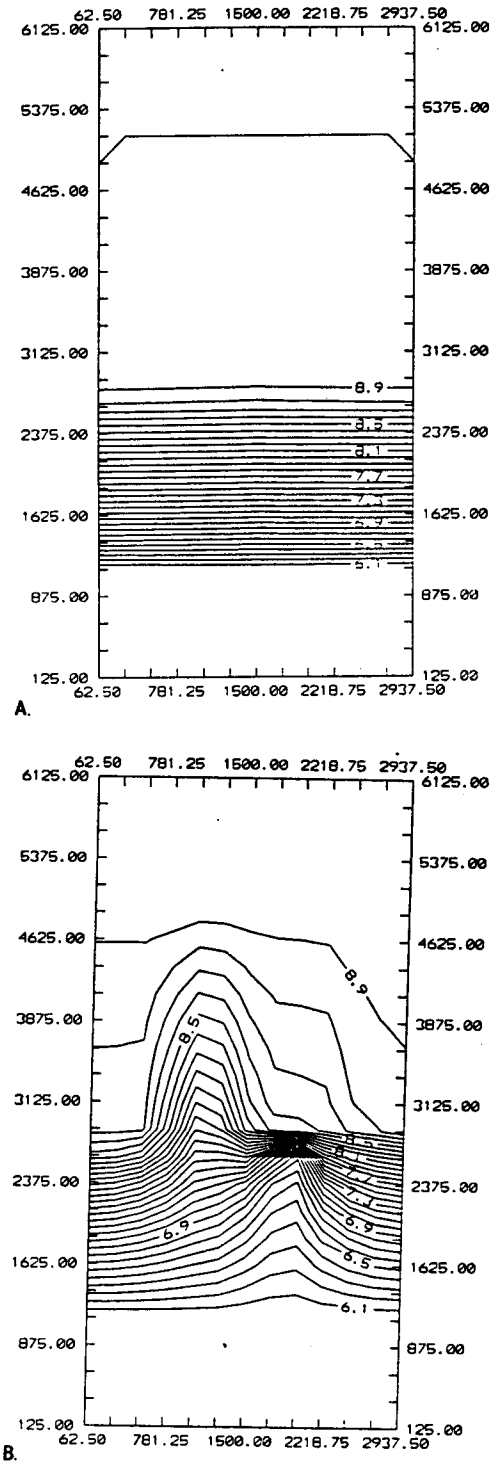

Figure 9. Water-table contour maps. Elevations are in meters above the datum shown in Figure 7.
A) Homogeneous facies simulation.
B) Heterogeneous facies simulation.

Particles were placed at the up-gradient end of the system in layer 1, 1 m below the water table. One particle was placed in each of the 24 nodal blocks across the inflow end of the model. Particles were tracked using the code PATH3D (Zheng, 1989). In the homogeneous facies simulation, particles followed straight-line flow paths as projected onto a horizontal plane. In the heterogeneous facies model, however, particles were funneled through units of high hydraulic conductivity as shown in Figure 10.

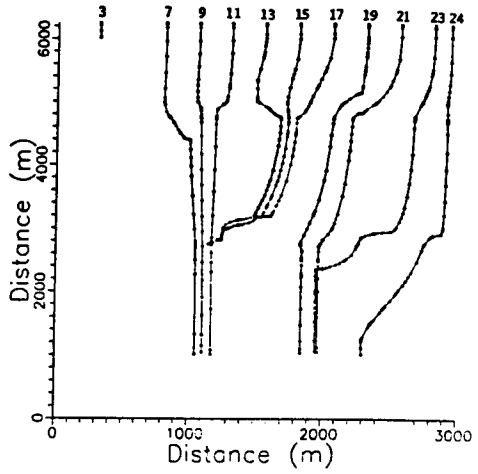

Figure 10. Paths of selected particles as projected onto a horizontal plane. Numbers identify the particle and indicate its starting position.

The eleven particle paths shown were selected to delineate the preferential flow paths. Particles 1-6 were slowed down by the presence of a unit of low hydraulic conductivity in the proximal facies and travelled only ~ 200 m in the time allowed for the particle tracking simulation ($1x10^7$ d). Particles 13-18 discharged at the water table after traveling about 3500 m through the

proximal and medial facies. The rest of the particles, which were uniformly distributed at the beginning of the simulation, were funneled along preferential flow paths and are arranged in two clusters at the outflow boundary: particles 7-12 and particles 19-24.

The funneling effect is also evident in the distribution of discharge at the outflow face. A total of 72 cells form the outflow face (the top layer is dry at the outflow end). The 12 particles that reached the discharge boundary in the heterogeneous facies model exited through 9 cells that carried 66% of the total outflow. The 9 cells occupy only 12.5% of the area of the outflow face. In the homogeneous facies simulation, contaminants exited through cells that occupied 33% of the outflow face and carried 33% of the flow. The channeling of contaminants in the system with preferential flow paths cannot be described by dispersion parameters which assume that contaminants will disperse as they move downgradient. In other words, a Fickian model of dispersion is inappropriate in such systems (also see Desbarats, 1990).

The arrival times of particles at the discharge location is often of interest in contaminant investigations (Nelson, 1978). In the homogeneous facies simulation, all 24 particles arrived at the discharge location in about $9x10^6$ d. Arrival times and locations for the 12 particles that reached the discharge boundary in the heterogeneous simulation are illustrated in Figure 11.

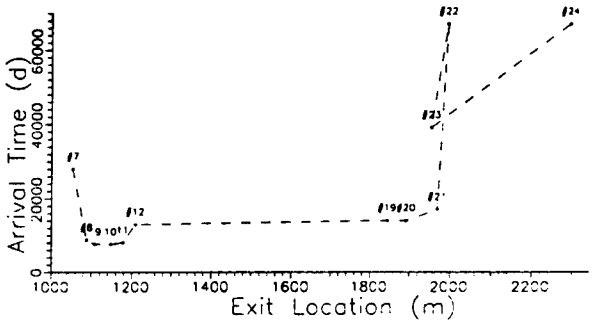

Figure 11. Arrival times of particles at the discharge location.

Particles arrived in two groups: a fast group arrived in < 20,000 d and a slow group arrived after ~ 30,000 d. The travel times are long because the outflow face is at the end of a regional system, 5 km in length. From Figure 10 it is clear that the same effect would be observed after a travel distance of > 1500 m, that is, as particles travel through the medial facies (Figure 8B). Desbarats (1990) also noted biomodal breakthrough curves for his system, which was of the order of several hundreds of meters in length.

Vertical gradients, although small, were large enough to cause vertical movement of the particles along paths of high hydraulic conductivity. The paths of selected particles are shown in Figure 12. The width of the paths shown in Figure 12 is a measure of the transverse dispersion that would be experienced by a solute following that pathway.

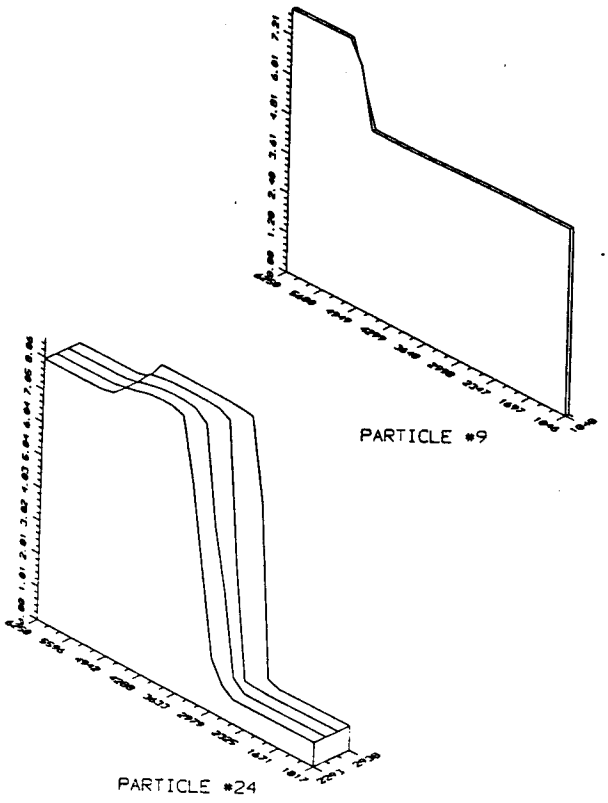

Figure 12. Paths of selected particles as projected onto a vertical plane.

The geometic mean of all hydraulic conductivities for both the heterogeneous and homogeneous facies models is 1.0 m/s. While definition of a meaningful effective hydraulic conductivity is still a matter of debate, the similarity of means suggests that the effective hydraulic conductivity for the two models might be similar. Yet, the volumetric flow rates through the systems are strikingly different-- 3.6 m^3/d for the homgeneous facies model and 661 m^3/d for the heterogeneous facies model. It seems that in the heterogeneous facies model, water is preferentially drawn through paths of high hydraulic conductivity in response to the applied gradient.

Results of this simulation suggest that preferential flow paths, when present, control the discharge location and arrival time of contaminants. When paths of high hydraulic conductivity are present, the implications for solute transport predictions are obvious. In this study hydraulic conductivity contrasts of only two orders of magnitude were sufficient to produce channeling. In the system studied by Desbarats (1990) a contrast of 10^4 was required. While it is clear that preferential flow is important, ways of locating preferential flow paths in the field and ways of quantifying these special kinds of heterogeneities for numerical modeling are lacking.

Summary and Conclusions

Many researchers from different fields have recently identified heterogeneity in natural systems as a high priority focus of research. Hydrogeologists looking to the geological literature for help in quantifying aquifer heterogeneity find that: 1) conceptual models of geological facies indicate that there are predictable successions of deposits at the regional scale; 2) local mapping of geological facies using systems such as architectural element analysis may be helpful in defining units within a heterogeneous aquifer for quantitative purposes such as numerical modeling; 3) interconnection of units of high hydraulic conductivity is an important feature of heterogeneity.

It may be that detailed geological mapping is required to define the hydraulic conductivity distribution in order to solve contaminant transport problems at certain local scales. At other scales lumped measures of heterogeneity, such as effective parameters and scaling rules (Neuman,

1990), may be adequate. However, when interconnected units of high hydraulic conductivity form preferential flow paths at either a local scale (Debarats, 1990) or a regional scale (Anderson, 1989; Fogg, 1986; Winograd and Pearson, 1976), lumped parameters will not correctly describe flow or contaminant movement. When permeability contrasts are sufficient, preferential flow paths may cause channeling or funneling of flow. Such flow does not obey a Fickian model, making it impossible to use the standard advection-dispersion equation with effective dispersivity values. We must conclude that the task of quantifying preferential flow paths is the greatest challenge facing researchers studying aquifer heterogeneity.

Acknowledgements:

This material is based upon work supported by the National Science Foundation under Grant No. ECE-8420864.

Mary P. Anderson received a BA in geology from SUNY-Buffalo and a PhD in hydrology from Stanford University. She has been a professor at the University of Wisconsin-Madison (Department of Geology and Geophysics, 1215 W. Dayton St., Madison, Wisconsin 53706) since 1975, where she is also affiliated with the Institute of Environmental Studies, the Water Resource Management Program and the Center for Limnology. She is the coauthor of a popular textbook on ground water modeling and is currently writing a second book on applicaton of ground water models. Dr. Anderson has served on numerous national committees and published more than fifty research papers.

References

Allen, J.R.L. 1978. Studies in fluviatile sedimentation: An exploratory quantitative model for the architecture of avulsion-controlled alluvial suites. Sediment. Geol., v. 21, pp. 129-147.

Anderson, M.P. 1990. Hydrogeologic facies models to delineate large-scale spatial trends in glacial and glaciofluvial sediments. Geol. Soc. Am. Bull., v. 101, pp. 501-511.

Bachu, S. and D. Cuthiell. 1990. Effects of core-scale heterogeneity on steady state and transient fluid flow in porous media: numerical analysis. Water Resour. Res., v. 26, pp. 863-874.

Bradbury, K.R. and M.A. Muldoon. 1989. Hydraulic conductivity determinations in unlithified glacial and fluvial materials. Standard Tech. Publ. 1053, Am. Soc. for Testing and Materials, Philadelphia, PA, pp. 138-151.

Bridge, J.S. and M.R. Leeder. 1979. A simulation model of alluvial stratigraphy. Sedimentology, v. 26, pp. 617-644.

Cross, T.A. (ed.). 1990. Quantitative Dynamic Stratigraphy. Prentice Hall.

Davis, J.M., R.C. Lohmann, S.J. Colarullo and F.M. Phillips. 1990. Alluvial aquifer heterogeneities in the Rio Grande Valley: Implications for ground water contamination. Technical Completion Report, New Mexico Water Resources Research Institute.

Desbarats, A.J. 1990. Macrodispersion in sand-shale sequences. Water Resour. Res., v. 26, pp. 153-164.

Dreimanis, A. 1984. Discussion of Eyles et al. (1983). Sedimentology, v. 31, pp. 885-886.

El-Kadi, A.I. and W. Brutsaert. 1985. Applicability of effective parameters for unsteady flow in nonuniform aquifers. Water Resour. Res., v. 21, pp. 183-198.

EPRI (Electric Power Research Institute). 1989. MADE: Reinjection to include reactive tracers. Land and Water Quality News, v. 4, no. 2, p. 7.

Eyles, N., C.H. Eyles and A.D. Miall. 1983. Lithofacies types and vertical profile models: an alternative approach to the description and environmental interpretation of glacial diamict and diamictite sequences. Sedimentology, v. 30, pp. 393-410.

Fogg, G.E. 1986. Groundwater flow and sand body interconncectedness in a thick, multiple-aquifer system. Water Resour. Res., v. 22, pp. 679-694.

Fraser, G.S. and J.C. Cobb. 1982. Late Wisconsinan proglacial sedimentation along the West Chicago Moraine in northeastern Illinois. J. Sediment. Petrol., v. 52, pp. 473-491.

Franklin, J.F., C.S. Bledsoe and J.T. Callahan. 1990. Contributions of the long-term ecological research program. BioScience, v. 40, pp. 509-523.

Freeze, R.A. 1975. A stochastic conceptual analysis of one-dimensional groundwater flow in non-uniform homgeneous media. Water Resour. Res., v. 11, pp. 725-741.

Frind, E.O., E.A. Sudicky and S.L. Schellenberg. 1988. Micro-scale modelling in the study of plume evolution in heterogeneous media. In Groundwater Flow and Quality Modelling, (E. Custodio et al., eds.), pp. 439-461.

Geehan, G.W., T.F. Lawton, S. Sakurai, H. Klob, T.R. Clifton, K.F. Inman and K.E. Nitzberg. 1986. Geologic prediction of shale continuit, Prudhoe Bay Field. In Reservoir Characterization, (L.W. Lake and H.B. Carroll, Jr., eds.), Academic Press, pp. 63-82.

Gelhar, L.W. 1986. Stochastic subsurface hydrology from theory to applications. Water Resour. Res., v. 22, pp. 135S-145S.

Glezen, W.H. and I. Lerche. 1985. A model of regional fluid flow: Sand concentration factors and effective lateral and vertical permeabilities. Math. Geol., v. 17, pp. 297-315.

Gomez-Hernandez, J.J. and S.M. Gorelick. 1989. Effective groundwater model parameter values: influence of spatial variability of hydraulic conductivity, leakance and recharge. Water Resour. Res., v. 25, pp. 405-420.

Googin, D.J., R. Thrasher and L.W. Lake. 1988. A theoretical and experimental analysis of minipermeameter response including gas slippage and high velocity flow effects. In Situ, v. 12, pp. 79-116.

Hess, K.M. 1990. Spatial structure in a glacial outwash, sand and gravel aquifer, Cape Cod, Massachusetts, EOS, April 24, p. 509.

Johnson, N.M. and S.J. Dreiss. 1989. Hydrostratigraphic interpretation using indicator geostatistics. Water Resour. Res., v. 25, pp. 2501-2510.

Jones, J.R., Jr., A.J. Scott and L.W. Lake. 1984. Reservoir characterization for numerical simulation of Mesaverde meanderbelt sandstone, northwestern Colorado. Soc. Petrol. Eng., SPE 13052, 14 pp.

Kemmis, T.J. and G.R. Hallberg. 1984. Discussion of Eyles et al. (1983). Sedimentology, v. 31, pp. 886-890.

Lake, L.W. and H.B. Carroll, Jr. (eds.) 1986. Reservoir Characterization. Academic Press.

Lasseter, T.J., J.R. Waggoner and L.W. Lake. 1986. Reservoir heterogeneitites and their influence on ultimate recovery. In Reservoir Characterization (L.W. Lake and H.B. Carroll, Jr., eds.) Academic Press, pp. 545-559.

McDonald M.G. and A.W. Harbaugh. 1988. A modular three-dimensional finite-difference ground-water flow model. U.S. Geol. Sur., TWI 06-A1.

Magnuson, J.J. 1990. Long-term ecological research and the invisible present. BioScience, v. 40, pp. 495-501.

Meinzer, O.E. 1932. Outline of methods for estimating ground-water supplies. Water Supply, Paper 638C, U.S. Geol. Sur., 162 pp.

Miall, A.D. 1978. Lithofacies types and vertical profile models in braided river deposits: a summary. In Fluvial Sedimentology, (A.D. Miall, ed.), Can. Soc. Petrol. Geol. Mem. 5, pp. 597-604.

Miall, A.D. 1985. Architectural-element analysis: A new method of facies analysis applied to fluvial deposits. Earth Sci. Rev., v. 22, pp. 261-308.

Miall, A.D. 1988. Reservoir heterogeneities in fluvial sandstones: Lessons from outcrop studies. Bull. Am. Assoc. Petrol. Geol., v. 72, pp. 682-697.

Moltyaner, G.L. and R.W.D. Killey. 1988. The Twin Lake tracer tests: longitudinal dispersion. Water Resour. Res., v. 24, pp. 1613-1627.

Nelson, R.W. 1978. Evaluating the environmental consequences of groundwater contamination, 2. Obtaining location/arrival time and location/outflow quantity distributions for steady flow systems. Water Resour. Res., v. 14, pp. 416-428.

Neuman, S.P. 1990. Universal scaling of hydraulic conductivites and dispersivities in geologic media. Water Resour. Res., v. 26, pp. 1749-1758.

Osiensky, J. L., G.V. Winter and R.E. Williams. 1984. Monitoring and mathematical modeling of contaminated ground-water plumes in fluvial environments. Ground Water, v. 22), pp. 298-306.

Price, W.E. 1974. Simulation of alluvial fan deposition by a random walk model. Water Resour. Res., v. 10, pp. 263-274.

Pryor, W.A. 1973. Permeability-porosity patterns and variations in some Holocene sand bodies. Bull. Am. Assoc. Petrol. Geol., v. 57, pp. 162-189.

Selley, R.C. 1988. Applied Sedimentology. Academic Press.

Sharp, J. 1989. Alluvial aquifers along major rivers. Geol. Soc. Am., Decade of North American Geology, v. O-2, Ch. 35, pp. 273-282.

Silliman, S.E. and A.L. Wright. 1988. Stochastic analysis of paths of high hydraulic conductivity in porous media, Water Resour. Res., v. 24, pp. 1901-1910.

Skibitzke, H.E. and G.M. Robinson, 1963. Dispersion in groundwater flowing through heterogeneous materials. U.S. Geol. Surv. Prof. Paper 386-B.

Smith, L. 1981. Spatial variability of flow parameters in a stratified sand. Math. Geol., v. 13, pp. 1-21.

Smith, L. and R.A. Freeze. 1979. Stochastic analysis of steady state groundwater flow in a bounded domain: 2. Two-dimensional simulations. Water Resour. Res., v. 15, pp. 1543-1559.

Smith, N.D. 1985. Proglacial fluvial environment. In Galcial Sedimentary Environments, (G.M. Ashley, J. Shaw and N.D. Smith, eds.), Soc. of Paleont. Mineral., Short Course no. 16, pp. 85-134.

Stephenson, D.A., A.H. Fleming and D.A. Mickelson. 1989. The hydrogeology of glacial deposits. Geol. Soc. Amer., Decade of North American Geology, v. O-2, Ch. 35, pp. 301-314.

Sudicky, A.E. 1986. Natural gradient experiment on solute transport in a sand aquifer: Spatial variation of hydraulic conductivity and its role in the dispersion process. Water Resour. Res., v. 22, pp. 2069-2082.

Theis, C.V. 1935. The relation between the lowering of the piezometric surface and the rate and duration of discharge of a well using groundwater storage. Trans. Am. Geophys. Union, v. 2, pp. 519-524.

Theis, C.V. 1967. Aquifers and models. In Proceedings of the Symposium on Groundwater Hydrology (M.A. Marino, ed.), American Water Resources Association, pp. 138-148.

Tillman, R.W. and K.J. Weber (eds.) 1987. Reservoir Sedimentology. Society of Economic Paleontologists and Mineralogists Spec. Publ. 40.

Waldrop, W.R., J.M. Boggs and S.C. Young. 1989. A field experiment to define transport and dispersion in a heterogeneous aquifer. EOS, v. 70, p. 340.

Walker, R.G. 1984. Facies, facies sequences and facies models. In Facies Models, 2nd ed., R.G. Walker (ed.), Geoscience Canada, Reprint Ser. 1, pp. 1-9.

Webb, E. and M.P. Anderson. 1991. Using a sedimentary depositional model to simulate heterogeneity in glaciofluvial sediments. In Parameter Identification and Estimation for Aquifer and Reservoir Characterization. National Water Well Association, Dublin, Ohio, this volume.

Weber, R.J. 1986. How heterogeneity affects oil recovery. In Reservoir Characterization (L.W. Lake and H.B. Carroll, Jr., eds.), Academic Press, pp. 487-544.

Williams, R.E. 1988. Comment on "Statistical theory of groundwater flow and transport: Pore to laboratory, laboratory to formation, and formation to regional scale. Water Resour. Res., v. 24, pp. 1197-1200.

Winograd, I.J. and F.J. Pearson, Jr. 1976. Major carbon 14 anomaly in a regional carbonate aquifer: Possible evidence for megascale channeling, south central Great Basin. Water Resour. Res., v. 12, pp. 1125-1143.

Wolf, S.H. and M.A. Celia. 1989. Spatial variability of hydraulic conductivity in a sand and gravel aquifer. EOS, v. 69, p. 367.

Zheng, C. 1989. PATH3D: A groundwater path and travel-time simulator. Version 2.0 User's Manual. S.S. Papadopulos and Assoc., Inc.

Using a Sedimentary Depositional Model to Simulate Heterogeneity in Glaciofluvial Sediments

by E.K.Webb and M.P.Anderson

Abstract

Glaciofluvial deposits usually consist of several depositional facies, each of which has different physical characteristics, depositional structures and hydraulic properties. Therefore, it is unlikely that the property of stationarity (a constant mean hydraulic conductivity and a mono-modal probability distribution) holds for an entire glaciofluvial succession. The process of dividing an outwash succession into geological facies presumably identifies units of material with similar physical characteristics. Therefore, hydraulic conductivity, or other hydraulic characteristics, may exhibit the property of stationarity at the scale of a single facies unit.

It is proposed that patterns of geological facies determined by field observation can be quantified by mathematical simulation of sediment deposition. Subsequently, the simulated sediment distributions can be used to define the distribution of hydrogeological parameters and locate possible "fastest paths" for contaminant movement. To test this hypothesis, a hypothetical glacial outwash deposit, based on geological facies descriptions contained in the literature, was simulated using a sedimentary depositional model, SEDSIM, to produce a three-dimensional description of sediment grain-size distributions. Grain-size distributions were then used to estimate the spatial distribution of hydraulic conductivity. Subsequently, a finite-difference model was used to simulate ground-water flow through the hypothetical glacial outwash deposit. This represents a first step in describing the spatial heterogeneity of hydrogeological characteristics for glaciofluvial and other braided stream environments.

Background

Accurate tracking of contaminants in the subsurface depends on a detailed understanding of spatial heterogeneities. Determining the distribution of hydraulic properties, however, can be enormously time consuming or impossible depending on the geological environment. For this reason collecting the geological detail necessary for adequate predictions of fluid velocity fields is a major research problem. Ways to approach this problem include detailed field description, mathematical descriptions of geological heterogeneity, and geological facies models.

One can attempt to develop deterministic models of a given area based on detailed field mapping at several scales (Molz et al., 1983). For example, Lake (1990) and others made more than 10,000 hydraulic conductivity measurements using a mini air-permeameter (Goggin et al., 1988; Chandler et al., 1989) on an eolian sandstone outcrop hundreds of meters in length. Lewis and Lowden (1990) coupled photo-mosaics with detailed permeability measurements to produce lateral permeability profiles for a shallow-marine sand body of approximately the same size. Kung (1990) traced preferential flow paths in

the vadose zone by observing the residue of red dye over a 3.0 m x 3.6 m plot in increments as small as 10 cm. Irrespective of the method, deterministic, observation-oriented studies require enormous effort. Geophysical methods have also been used to produce detailed maps of spatial heterogeneity. Two developments in this area include measuring the coupled fluid and electric current flows in porous media (Haupt and Martin, 1990; Sill, 1983; Ishido and Mizutani, 1981) and cross-hole tomography (Long et al., 1989). These offer a non-destructive means of measuring in situ properties, but are usually hindered by inadequate ground truth. With both direct observation and geophysical approaches, a conversion is often required to transfer the estimated value from the scale of measurement to the scale of interest.

Mathematical approximations can be used to estimate hydraulic properties using limited site-specific data or information about the general geological environment. Mathematical treatment includes statistical methods such as indicator variograms (Johnson and Dreiss, 1989); cross semivariograms (Istok et al., 1988); conservation scaling (Shouse and Sisson, 1990); empirical Bayes regionalization (Butcher and Medina, 1990); intrinsic random functions of order k (Dimitrakopoulos, 1990a; Dimitrakopoulos, 1990b); pseudo functions (Lake, 1990), and geostatistical analysis of unsaturated material properties (Greenholtz et al., 1988). These methods generally represent extrapolations of an existing data set based on assumptions of randomness or quantifiable trends. Therefore, their accuracy is dependent on the detail of the initial data, similar to deterministic models. Other mathematical descriptions include viewing geological materials as self similar following a fractal model (Menduni, 1990; Wheatcraft and Tyler, 1988; Hewett, 1986), or spatially periodic and stationary under a stochastic model (Dagan, 1987; Vomvoris and Gelhar, 1987). At certain scales either of these methods may be valid, but fractal models may be limited to discrete size intervals (Anderson, 1991a) and the assumption of stationarity may not be valid for regional scales. There are, therefore, certain length scales and/or entire environments to which these models may not apply.

A third approach, the use of geological facies models to guide either sampling or modeling, has been proposed by Anderson (1987, 1989) and Fraser and Bleuer (1987). Facies models have been described for several environments including glacial and glaciofluvial systems (Eyles et al., 1983; Ashley et al., 1985; Fraser and Cobb, 1982). A successful facies model as applied to hydrogeological investigations must " characterize spatial trends in hydraulic conductivity, ... predict geometry of hydrogeological facies from limited field data, ... describe horizontal trends in hydraulic conductivity and establish a method for calculating the anisotropy in hydraulic conductivity for each facies" (Anderson, 1989). Defining the areal distribution of storativity and porosity could also be included in this list. Davis et al. (1990) have had some success in correlating

hydrogeological parameters with suites of facies known as architectural elements (Miall, 1985).

Finally, process simulation models can be used to estimate the geometry and distribution of spatial heterogeneities. By this approach geological processes can be simulated using theoretical or empirical laws. However, unlike groundwater flow models, there are no simple analytical solutions with which to compare these simulations. Therefore, well defined and well understood site-specific data must be used to validate the combination of theory, assumptions, and mathematical methods used in such models. Once this step has been accomplished, it may be possible to use these codes with more limited field data. Most process simulation models are designed to reproduce narrowly defined geological environments. Early models described deltaic sedimentation (Bonham-Carter and Sutherland, 1968), deposition rates for alluvial fan successions (Price, 1973), and floodplain migration (Bridge and Leeder, 1979). More recently, Juergens (1990), and Juergens and Small (1990) described a model that simulates the aggradation of a meandering river channel. Other models are more general, being based on theoretical laws of fluid motion and empirical equations describing erosion and deposition. One of these, SEDSIM by Tetzlaff and Harbaugh (1989), has been used to simulate several rather diverse geological environments including: modern and ancient braided stream deposits (Scott, 1986); submarine deltaic successions (Tetzlaff and Harbaugh, 1989); modern deltas (Koltermann and Gorelick, 1990); and glacial outwash successions (Webb and Anderson, 1990).

Geological facies models can indicate the trends in hydrogeological parameters but do not quantify them. Process simulation models may offer a method for quantifying the distribution of sediment properties described qualitatively in facies models.

Objectives

It is proposed that patterns of geological facies determined by field observation can be quantified by mathematical simulation of sediment deposition. Subsequently, the simulated sediment distributions can be used to define the distribution of hydrogeological parameters and locate possible "fast paths" for contaminant movement.

For this study, SEDSIM (Tetzlaff and Harbaugh, 1989), was used to simulate a glaciofluvial outwash succession. The model was calibrated to qualitative facies descriptions and limited grain-size data reported by Cobb and Fraser (1981) and Fraser and Cobb (1982). The resulting estimates of grain-size distribution were converted to estimates of hydraulic conductivity using the method of Hazen (Freeze and Cherry, 1979). The distribution of hydraulic conductivity was then used to construct a two-dimensional, areal ground-water flow model using MODFLOW (McDonald and Harbaugh, 1988). Finally, a particle tracking code, PATH3D (Zheng, 1989) was linked to the ground-water flow code to trace the movement of water particles.

Glaciofluvial Sediments

Glacial meltwater carries large quantities of sediment away from the ice margin. The coarser material is usually deposited in alluvial fans or plains and is commonly referred to as glacial outwash or sandur (sand plains, Smith, 1985). The lateral extent of these outwash deposits is a function of water volume and lateral boundaries. Where the melt water is confined to narrow valleys, outwash may extend 50 km in length, as in the valley of the Wisconsin River, Wisconsin. As meltwater moves across broad, flat, alluvial fans, is spreads out increasing surface shear which reduces flow velocity. As the energy of the water dissipates, coarse sediment is rapidly deposited. The coalescence of several braided stream successions form alluvial plains, analogous to bajada of the Basin and Range Region of the western U.S.A. However, outwash successions are unique among alluvial deposits due to "fluctuating ice margins, buried and transported ice blocks, and highly seasonal and weather-dependent discharge variations" (Smith, 1985).

Suspended sediment loads have been measured in the range of grams per liter, but due to the difficulty in observation, bedload is less well defined (Smith, 1985). Both suspended and bedload sediment discharge are believed to vary exponentially with discharge rate (Kang, 1981; Hammer and Smith, 1983). Bedload is a major component of total transport and may exceed 50% (Church, 1972; Hammer and Smith, 1983; Smith, 1985).

Both the geomorphology and sediment characteristics (facies assemblages) can be divided into zones related to distance from the ice margin. Here, the terminology of Fraser and Cobb (1982) is adopted for the description of deposits in the various facies assemblages.

The marginal zone or assemblage is closest to the ice margin. Its width depends on fluctuations of the ice margin. Deposits consist of 1. muddy cobble gravels; 2. laminated muds; 3. cross-bedded sand and gravel; and 4. massive cobble gravels. This zone is characterized by higher relief and topographic gradient, a lack of erosional features, mud flows and other mass movement, a small percentage of washed, bedded material, and extensive lateral compressive and vertical load deformation (Figure 1A). This succession is not dominated by water-lain deposits and therefore cannot be modeled by SEDSIM.

The next two facies assemblages away from the ice margin are the proximal and medial zones, respectively. The boundary between the proximal and marginal zones occurs where washed sediments begin to dominate in the proximal zone. Differentiating between proximal and medial deposits depends on distinctions in texture and bedding styles, but the two are closely related genetically (Cobb and Fraser, 1981). Generally, the proximal assemblage is dominated by very coarse sediments in irregular and discontinuous strata defined as 1. crudely bedded cobble gravel, 2. cross-bedded sand, and 3. ripple-laminated sands and silts (Figure 1B) (Fraser and Cobb, 1982). Coarse cobble gravels are the dominant feature, indicating

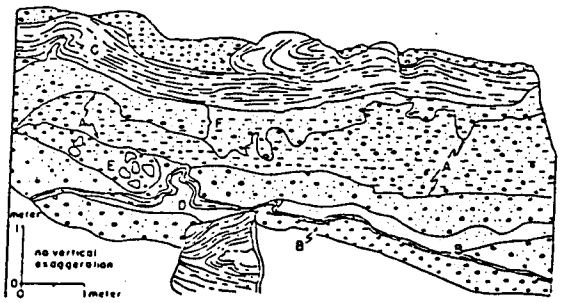

A

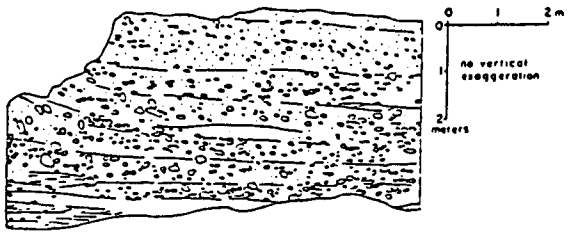

B

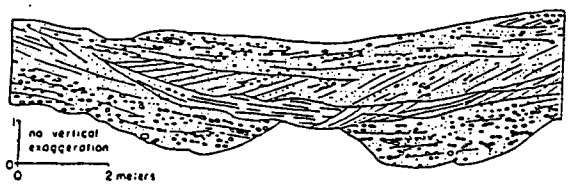

C

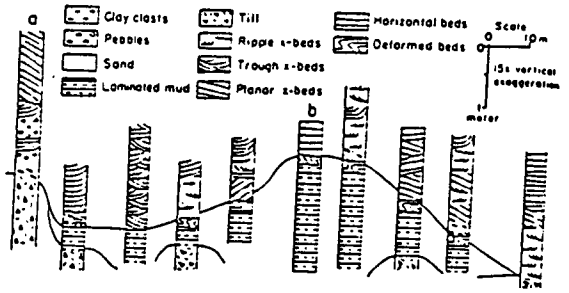

D

Figure 1. Facies assemblages described by Fraser and Cobb (1982). A. Marginal assemblage; B. Proximal assemblage; C. Medial assemblage; D. Distal assemblage.

rapid deposition from bedload commonly in the form of longitudinal bars. The medial assemblage consists of "finer-grained and better sorted (material with) the sand-to-gravel ratio ... higher and the gravel fraction ... finer-grained ... with trough and planar cross beds comprising 80% of the stratification" (Figure 1C) (Fraser and Cobb, 1982). Facies in this assemblage include 1. cross-laminated sand and fine gravel, 2. crudely bedded gravel, and 3. ripple-laminated sands and silts. The distal assemblage consists of parallel-laminated muds and fine-grained cross-bedded sands in equal amounts, with a some ripple-bedded sand and silt (Figure 1D) which were probably deposited in a ponded environment. A similar succession of deposits is described for Glacial Lake Wisconsin by Clayton and Attig (1989) and Brownell (1986).

The proximal, medial, and distal assemblages are dominated by water-lain sediments, and therefore can be simulated using SEDSIM. A calibration standard was developed from statistical analysis of grain-size data reported in Fraser and Cobb (1982) and Cobb and Fraser (1981). Figure 2A-D shows the distribution of bulk gravel, sand, silt, and clay percentages for the four assemblages which were used as the calibration standard in our application of SEDSIM. Notice, that between the marginal and proximal assemblages, the initiation of water-dominated transport removes the silt and clay fraction and increases the percent gravel. From the proximal to the distal assemblage, gravel percent decreases and sand percent increases. Finally, silt and clay become significant again in

the distal facies and gravel is no longer present.

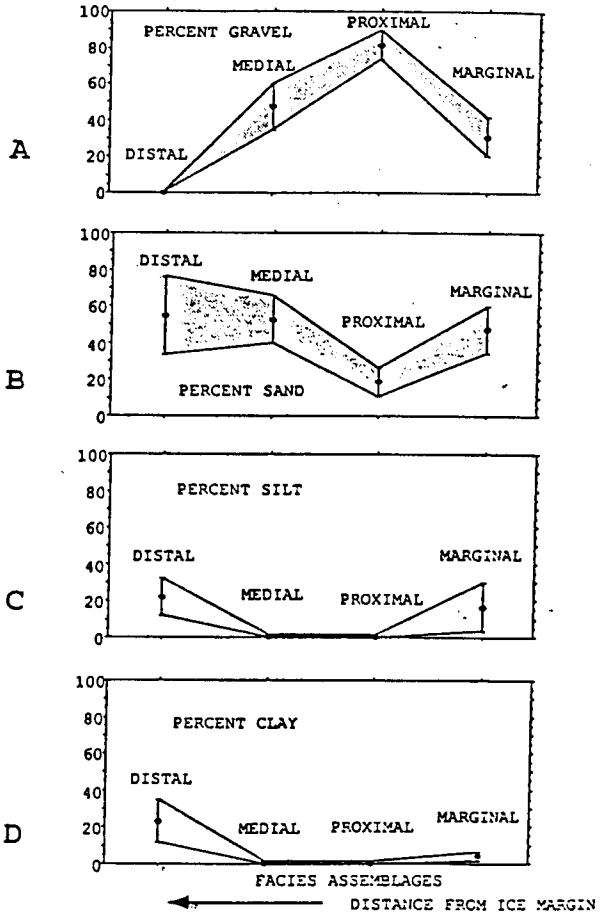

Figure 2. Observed values of percent gravel, sand, silt, and clay in each of four facies assemblages from Fraser and Cobb (1982), Cobb and Fraser (1981). A. Percent gravel; B. Percent sand; C. Percent silt; D. Percent clay.

Figure 3A-D shows histograms of the mean grain size for each assemblage. These histograms are based on limited data, but seem to indicate compound distributions.

No statistical tests were performed to substantiate this speculation. Figure 3A, which represents the marginal assemblage, indicates a bimodal distribution. This observation corresponds to the expected presence of generally fine-grained material (muddy cobble gravel, laminated mud) as well as coarser sediments (cross-bedded sand and gravel, massive cobble gravel). Figure 3B and 3C, show a continuum between coarse- and fine-grained sediments, indicative of sorting. Figure 3D, which represents grain sizes in the distal facies, shows a bimodal (or even tri-modal) distribution that may correspond to the three facies types, namely laminated mud, cross-bedded fine sand, and ripple-bedded sand and silt.

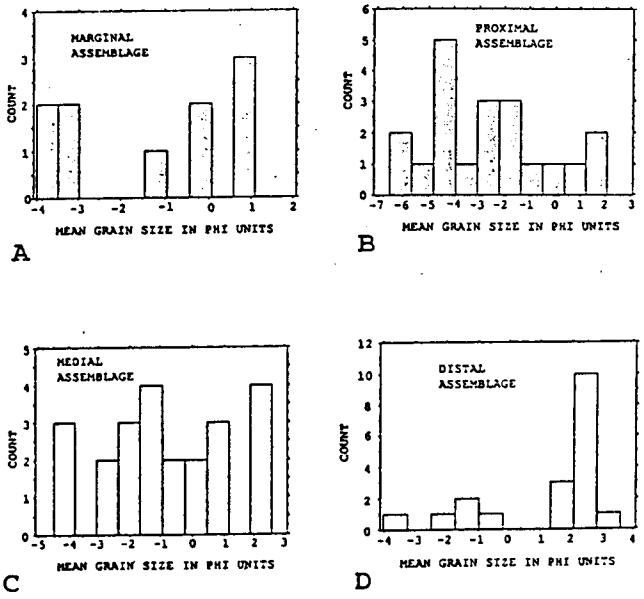

Figure 3. The distribution of mean grain sizes for the marginal, proximal, medial and distal assemblages from Fraser and Cobb (1982), Cobb and Fraser (1981). A. Marginal assemblage; B. Proximal assemblage; C. Medial assemblage; D. Distal assemblage.

SEDSIM: A Process Simulation Model

SEDSIM (Tetzlaff and Harbaugh, 1989) is a deterministic, three-dimensional, dynamic, process-simulation computer code that describes the flow of water over a sediment surface. Fluid motion is describe by the Navier-Stokes equation. Modified versions of formulas by Kalinske (1947) and Laursen (1958) are used to describe the transport of a mixture of different sediment grain sizes.

Like other deterministic models, SEDSIM produces a unique set of output for each array of input parameters. However, comparison of model output may indicate chaotic behavior because small differences in input parameters can cause dramatically different output. The SEDSIM code operates in three-dimensional space, allowing packets of water to move across an irregular topographic surface. At specified intervals, the energy regime is evaluated for each water element and erosion or deposition occurs. To simplify the flow equations, a constant vertical velocity is assumed for each fluid element. This simplification eliminates the formation of bedforms dependent on a changing vertical velocity profile. It also limits SEDSIM output to estimates of bulk (spatially averaged) sediment properties. As a result, the two-dimensional cross sections of sediment deposits may not be correct at small scales. For this reason, we focus on the areal distribution of sediments.

Input requirements of SEDSIM include initial conditions, boundary conditions, and parameters controlling run time. Input files include the following parameters: number of grid nodes and their dimensions; starting topography; the density and mean grain size for four sediment types; the location, flow rate, total sediment load, and the percentage of each of the four sediment types for each water source; the distribution of sediment types beneath the initial topography; total time of flow; and several factors that allow erosion and deposition to be estimated for a short time and then extrapolated over longer periods to reduce computer effort. Several parameters, one of which is the Mannings roughness coefficient, are fixed at pre-determined constant values within the code. The inflexibility caused by pre-setting these values is a weakness identified by Gorelick and Koltermann (pers. comm., 1991) and should be corrected in future versions of the code.

The code produces an estimate of the three-dimensional distribution of up to four specified grain types, changes in topography, and the status of water elements within the grid boundary. Sophisticated graphical output to display sediment accretion is available for use with work stations operating on Silicon Graphics UNIX.

Limitations

Several important limiting assumptions are inherent in the version of SEDSIM that we used. These assumptions were required to reduce computational requirements. First, assuming a constant vertical velocity

profile restricts the ability of the model to simulate sedimentary structures. Consequently, the model has limited vertical and horizontal resolution, and produces only estimates of the bulk sediment grain-size distribution. Therefore, the minimum size of model cells must be large enough to encompass several of these bedforms. Similarly, the thickness of simulated sediment deposits is controlled by the time-step specified for model output. Longer times, produce thicker successive layers. These layers must also encompass several bedforms in order to average sediment properties.

Second, SEDSIM allows the division of sediment grain sizes into only four sediment types. These are defined by mean grain diameter and density. Model output is reported in terms of the thickness of these four sediment divisions. Limiting the grain size continuum to only four types restricts resolution of the cumulative grain-size curve.

Third, as the energy regime of each fluid element is evaluated for erosion or deposition, depth of flow is determined by dividing the volume of the fluid element by the area of a grid cell. In other words, each cell containing a fluid element is considered to be submerged, and erosion or deposition occurs uniformly over the cell. For subaqueous environments such as river deltas, cell size is unimportant. However, for sub-areal environments, the cell width chosen should be controlled by the average channel width. For example, to simulate a meandering river, the cell size should be no larger than the width of the channel and ideally only a fraction of the width.

Finally, current versions of SEDSIM assume a constant flow rate. Few geological processes occur at a constant rate. For instance, most sediment transport by glacial meltwater occurs only during two to three months of summer, with diurnal variations and storm events. In our simulations only the annual summer flood was deemed significant, and smaller scale variation was ignored.

These four assumptions place different and somewhat conflicting limitations on the use of SEDSIM. For example, the minimum grid size and minimum time step length imposed by the lack of a vertical velocity profile must be balanced against the maximum cell size defined by channel width in sub-areal environments.

To circumvent these restrictions, a regional depositional system was simulated, using large grid cells (200 m x 200 m). At this scale, the localized influence of bedforms is negligible and model estimates of grain size represent bulk averages. For the braided stream environment, it was assumed that most sediment transport occurs during three months in the summer, so that 1 year of model time represents 4 years of summer floods. Thus 50 model years represent 200 actual years, the total length of the simulation. During flooding the outwash plain is submerged by meltwater so that a single fluid element in the simulation represents the movement of water in many small, interconnected channels. The code was not modified to allow more than four sediment types, although this could be done for future

simulations. Because, the shape of the cumulative grain-size curve was used to help predict hydraulic conductivity, the lower limit of hydraulic conductivity is a function of the grain size chosen for the finest of the four sediment types.

Model Input

The SEDSIM code was used to simulate a 4000 m x 4000 m area divided into 20 rows and 20 columns. The initial topography was specified as a planar surface with a 1% dip to the west representing a lake bed which underlies the outwash described by Fraser and Cobb (1982). Subsequent simulation of deposition produced irregular topography on this original planar surface. Nineteen fluid sources were specified along the eastern edge. This simulates a set of distributed melt water sources and ignores the possible occurrence of catastrophic discharge through tunnel channels (jokulhlaups). The discharge for each source was set at 30 m^3/s (total discharge 570 m^3/s) an approximation from valley glaciers (Church and Gilbert, 1975). Initial velocities were set at 0.5 m/s toward the west with minor perturbations of 0.001 m/s to the north/south. This is a conservative estimate, velocities may be much greater in the proximal and medial zones. Total sediment load, including suspended and bed load, was set at 2.8 kg/m^3 divided into the four sediment types with the following distribution: 10%, 25%, 15%, 50%, from largest to smallest grain size. Initial source sediment loads correspond to the percentage of gravel, sand, silt and clay in local glacial till. The model was run to simulate the three months of summer flood then was dormant for the remaining nine months of the year. A single simulation was extrapolated to represent 10 years of sediment accumulation. Twenty simulations were run to produce a total simulation time of 200 years.

The four sediment types were defined as 8 mm (gravel), 1 mm (coarse sand), 0.25 mm (fine sand), and 0.06 mm (silt-clay) with constant density of 2650 kg/m^3. Definition of the four sediment types controls the resolution of the cumulative grain-size curve for the simulated deposits. For instance gravel in glacial outwash ranges from 2 mm up to the size of cobbles (64 mm - 256 mm) and boulders (> 256 mm). If we had chosen the grain size representing gravel to be 100 mm and the next smaller sediment type to be 1 mm (very coarse sand), the model would predict that all deposition of the first sediment type occurs at the glacial margin, when in fact, material coarser than 1 mm may be transported a great distance from the ice margin. As a consequence of choosing 8 mm for the largest grain size, we can trace the transport of gravel to the proximal and medial zones which would be expected in the field, but the model also underestimates the percent gravel near the glacial margin.

SEDSIM Results

SEDSIM estimates the thickness of each sediment type deposited over each cell for each time step, along with estimates of the final surface elevation. Simulated deposits ranged from 0 to 12 m in thickness for the 200-year simulation. These high rates of

deposition were documented in studies of the depositional history of northern Illinois (Cobb and Fraser, 1981). The initial model input was formulated so that each east-west row of cells began with identical surface topography, fluid sources (+/- minor perturbations) and sediment types. SEDSIM tended to be chaotic, in that small differences in input parameters gave very different results. Consequently, we could calibrate the model to only one set of input parameters; attempts to test the sensitivity of the calibrated model to variations in parameter values produced an uncalibrated model.

Because we were unable to produce a suite of calibrated models for statistical analysis, the sediments deposited in each row of the model (excluding the two outside rows) were considered to represent separate realizations of the same flow system. We justify this approach by noting that we are not trying to reproduce an exact field location, but to simulate a realistic hypothetical case. Therefore, the bulk grain-size estimates for all cells in a column were treated as belonging to the same underlying distribution. This allows an estimate of the mean and the 95% confidence interval of grain sizes in each column to represent the variability in a single calibrated simulation. The distribution of percent of each sediment type was estimated and matched with those observed by Fraser and Cobb (1982).

Figures 4A-C show the simulated results compared with observed values for three grain types of gravel, sand, and fines (silt and clay). In each diagram the stippled area indicates the 95% confidence interval of grain sizes estimated by Fraser and Cobb (1982). Simulated values of percent sand (Figure 4B) show a nearly perfect match with observed values. Simulated gravel percent (Figure 4A) is much lower in the proximal succession, and too high for the distal succession, but general trends are similar to observed values. Fines (Figure 4C) match well in all but the distal assemblage. A possible explanation lies in having fixed values for transport parameters and roughness coefficient over the entire length of the simulation (Gorelick and Koltermann, 1991, per. comm.).

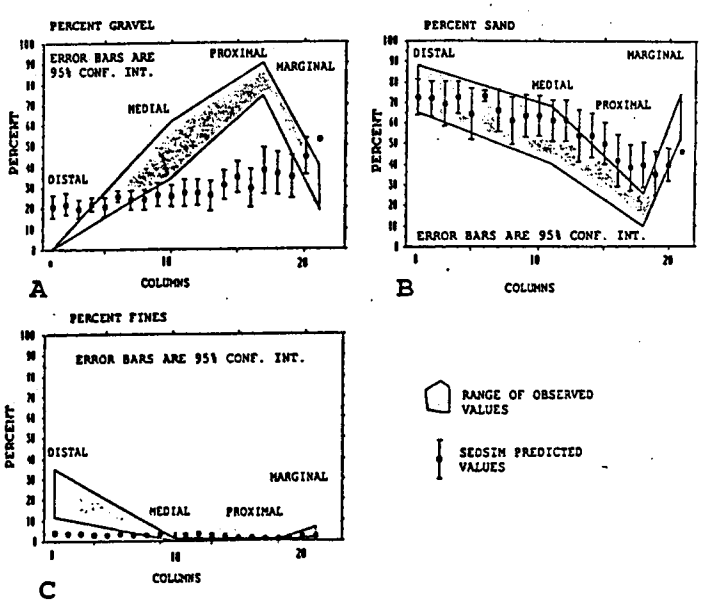

Figure 4. Percent gravel, sand, and fines, used as calibration standards for SEDSIM. Shaded areas indicate observed values. Error bars are 95% confidence intervals about the mean model estimates. A. Percent gravel; B. Percent sand; C. Percent fines.

It is likely that the low gravel percent estimated by SEDSIM is a function of the grain size chosen for the coarsest sediment type. The estimates of transport of 8 mm size particles or less may be correct; and the difference between SEDSIM estimates and the observed values may represent material coarser than 8 mm. Because the sand fraction is the dominant constituent in all but the proximal assemblage, it was treated as the most significant calibration target. The relatively small percentage of fines makes it difficult to identify variations or trends. However, it appears that the relative percentage of fines increased from approximately zero in the proximal zone to 5% in column 20 (marginal zone). The estimated sediment distributions of both gravel and fines do not match observed values for the distal assemblage. However, for the proximal and medial assemblages, grain-size estimates are considered appropriate.

In Wisconsin, the transition between the medial and distal zones occurs between 10 and 50 km from the ice margin, or where outwash streams emptied into proglacial lakes. To reduce computational requirements the model did not simulate the distal zone in our application. In future work it would be desirable to increase the number of sediment types handled by SEDSIM and extend the length of the model grid to improve estimates of the coarser and finer sediment grain-size fractions.

Ground-Water Flow Model

Sediment grain-size estimates, from SEDSIM, were translated to estimates of hydraulic conductivity using a method after Hazen (Freeze and Cherry, 1979) where

$$K = A\, d_{10}$$

K	Hydraulic conductivity
A	Proportionality constant, equal to 1 for K in cm/s and d_{10} in mm.
d_{10}	Characteristic measure of grain size. Defined to be the grain size where 10 % of a sample by weight is finer.

This simple transformation was used to produce relative estimates of hydraulic conductivity allowing the identification of paths of higher conductivity. More complex approximation techniques are available, but the limited resolution of the cumulative grain-size curve produced from four or fewer than four points taken from the four grain size types makes estimation of grain sorting difficult or impossible. Therefore, the simplest estimation technique was chosen. Conductivity estimates by this method should not be considered absolute. However, in applying this model to a specific site, it may be possible to determine the localized relation between conductivity and grain-size distribution. The resulting areal distribution of hydraulic conductivity is displayed in Figure 5. Two regions of higher hydraulic conductivity are evident along rows 5-8 and 12-15. Other model realizations produced from 1 to 6 such channels. The number of

channels appears to be a function of the number of sources, their spatial density, and variations of velocity.

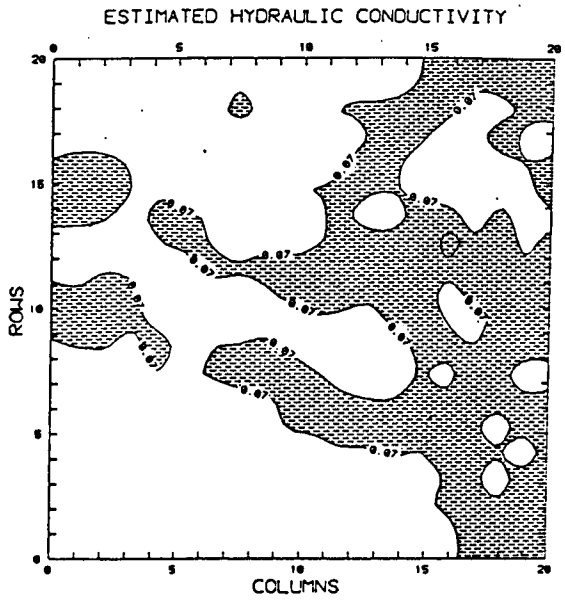

Figure 5. Map of the areal distribution of hydraulic conductivity in cm/s. Hatched areas indicate areas of high conductivity.

The values of hydraulic conductivity were evaluated statistically as components of a single underlying distribution. Figures 6A,B display a histogram and box plot of all conductivity values. Generally, the distribution appears to be unimodal with some skew toward lower conductivities. A large spike of low conductivities is located at -2.4 in log K units. This is explained by the fact that as the percent of fines increases, resolution in determining the d_{10} grain size is lost.

As a result, the minimum estimate of hydraulic conductivity becomes a function of the diameter of the smallest sediment type.

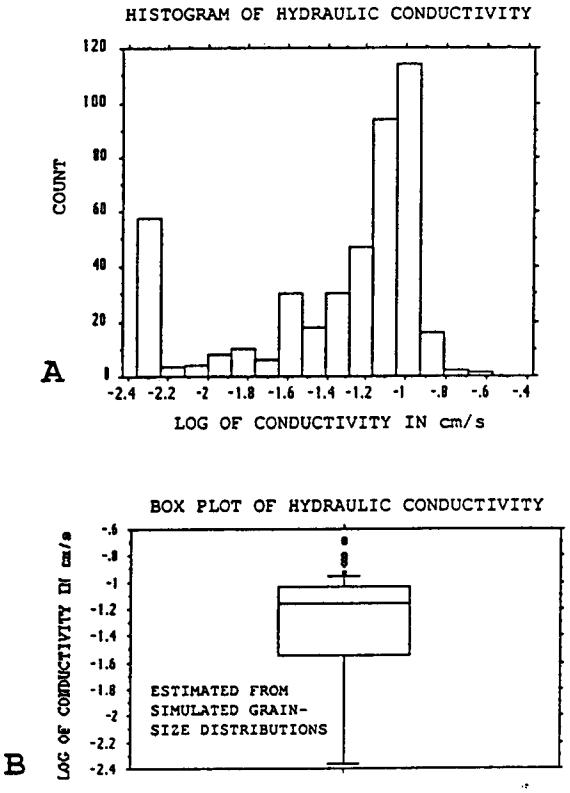

Figure 6. Histogram and box plot of the hydraulic conductivity in Log K units estimated from SEDSIM grain-size distributions.

The overall geometric mean of hydraulic conductivity is 4.1×10^{-2} cm/s with a range from 4.4×10^{-3} to 2.1×10^{-1} cm/s. Figure 7 shows the mean and range of conductivities for each column. Both values decrease with distance from the glacial margin.

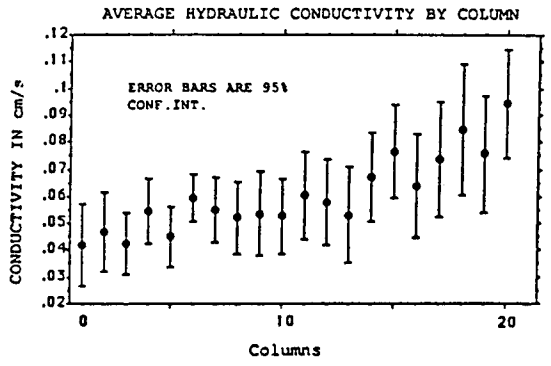

Figure 7. Trends in hydraulic conductivity with distance for the glacial margin estimated from SEDSIM sediment grain-size data.

The ground-water flow code MODFLOW (McDonald and Harbaugh, 1988) was used to simulate a simple ground-water flow system. An areal discretization, similar to that employed for SEDSIM, was used to divide an area of 4000 m x 4000 m into 200 m x 200 m cells, producing 20 rows and 20 columns (Figure 8). Conductivity estimates derived from the SEDSIM output were assigned to cells in the flow model. The system was treated as confined, with constant cell thickness of 10 m. Constant head boundaries were set to 48 m along the eastern edge and 10 m along the western edge, thereby establishing a fixed regional hydraulic gradient. Thus, local variations in hydraulic gradient are the result of the conductivity distribution. Although SEDSIM produces a three-dimensional approximation of sedimentary characteristics, the vertical profiles are not accurate because the model assumes a constant vertical velocity profile. For this reason, one layer of the simulated sediment deposit was translated into a two-dimensional areal distribution of hydraulic conductivity and assigned an arbitrary constant thickness of 10 m for input into the ground-water flow simulations. A uniform hydraulic gradient was specified across the system to induce ground water to flow from the proximal to the medial facies assemblage. This flow orientation is realistic for outwash deposits in Wisconsin. We did not consider the effects that unconfined flow or recharge might have on the system because we wanted to isolate the effects on the flow field caused by heterogeneities.

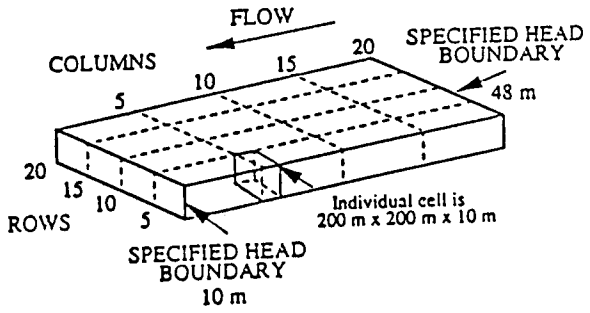

Figure 8. Schematic diagram showing the hypothetical confined aquifer simulated by MODFLOW.

The results from a steady-state simulation showing the areal distribution of hydraulic head are (Figures 9 A,B). The troughs in the potentiometric surface evident in Figure 9B correspond to the regions of higher hydraulic conductivity shown in Figure 5.

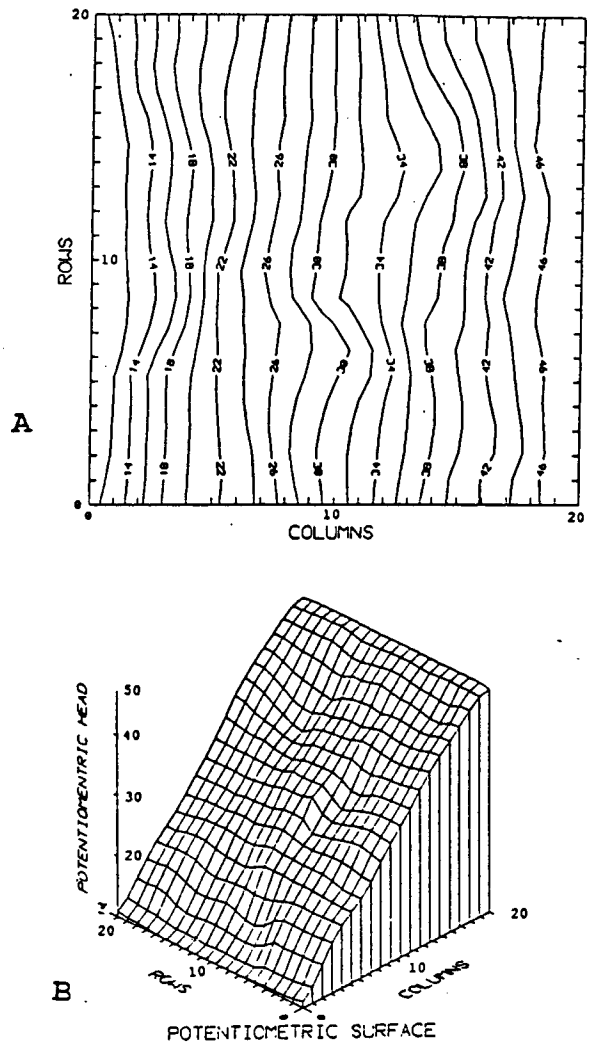

Figure 9. Areal distribution of hydraulic head in meters. Flow is from right to left. A. Contours of heads; B. Potentiometric surface.

Particle Tracking

The program, PATH3D (Zheng, 1989) was used to trace water particles through the constructed flow system. The code links directly with MODFLOW, using some of its input packages. Two functions are performed by PATH3D. First, it determines the velocity field based on hydraulic conductivities and the applied hydraulic head. Second, the location and velocity of particles is recorded for a specified period of time.

Input to PATH3D, in addition to the input files for MODFLOW, include the number of particles, the time frame of particle movement, several iteration and output control parameters, estimates of porosity, along with the initial x, y and z locations for each particle. In this study, the simulation was of the release of 100 particles from the eastern boundary of the model at increments of 40 m. A constant effective porosity of 15% was assumed as a constant over the model area.

Figure 10 shows the paths taken for a select number of particles. An average particle velocity of 2.7 x 10^{-3} cm/s would be expected, given a constant hydraulic gradient of 0.01, effective porosity of 0.15, and the geometric average of hydraulic conductivity estimated from grain sizes (4.1 x 10^{-2} cm/s). However, for the 100 particles tracked, the average particle velocity was 30% higher or 3.5 x 10^{-3} cm/s with a range of 1.7 x 10^{-4} to 7.4 x 10^{-3} cm/s. More than 60% of the particles moved with a faster-than-average velocity by following the paths of high conductivity.

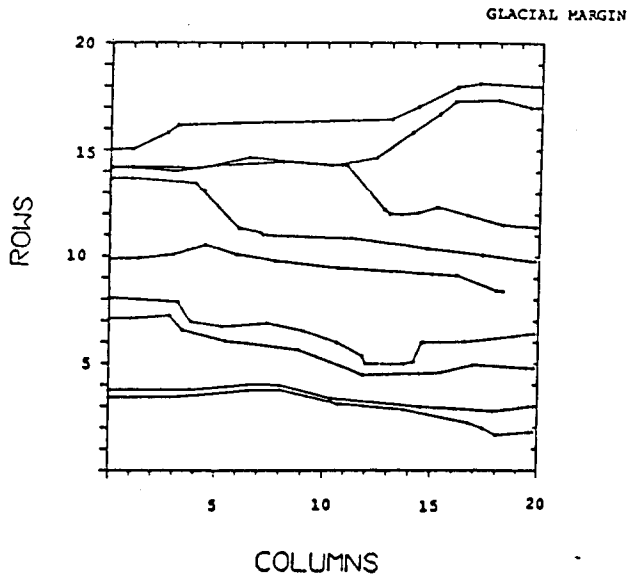

Figure 10. Paths of selected particles indicating convergence and channeling caused by areas of high hydraulic conductivity. Flow is from right to left.

Conclusions

Our work shows that a process simulation model can produce a gross representation of the regional distribution of sediment grain sizes expected in the braided stream environment of northern Illinois, but the simulation is subject to numerous limitations and assumptions. Grain size information was converted to estimates of hydraulic conductivity and used to simulate groundwater flow through the constructed aquifer. Simulations of flow with particle tracking indicate that paths of higher hydraulic conductivity can be expected at the regional scale in this outwash environment. These regions of higher hydraulic conductivity, if present, would channel flow and contaminants. Similar channeling effects were reported by Desbarats (1990) and Anderson (1991b).

Our simulation results point to several limitations of SEDSIM for simulation of fluvial environments. The minimum cell size and consequently the spatial resolution in the grain-size distribution are limited by the assumption of a constant velocity profile. Description of the grain-size continuum by only four sediment types reduces the accuracy in estimates of characteristic grain-sizes such as d_{10}. As a result, estimates of hydraulic conductivity are directly related to the grain diameter chosen for the smallest sediment type. In a fluvial environment maximum cell size can be no larger than the total channel width. Finally, the version of the model we used was unable to handle variations in discharge rate.

Acknowledgements

This work was partially funded by the Water Resources Center of the University of Wisconsin - Madison. The research was performed while Mr. Webb was under appointment to the Environmental Restoration and Waste Management Fellowship program administered by Oak Ridge Associated Universities for the U.S. Department of Energy, while at the University of Wisconsin - Madison.

We thank Dr. John Harbaugh and his students who supplied the process simulation code, SEDSIM, for our use. We also thank the reviewers of an earlier version of this paper.

Erik K. Webb is a Ph.D. candidate and Mary P. Anderson is a Professor of Hydrogeology. Both are in the Department of Geology and Geophysics at the University of Wisconsin-Madison (1215 W. Dayton St., Madison, WI, 53706).

References

Anderson, M.P. 1987. Treatment of heterogeneities in groundwater flow modeling. In Solving Ground Water Problems with Models, (ed. B.J. Graves) National Water Well Association, Dublin, Ohio, p. 444-463.

Anderson, M.P. 1989. Hydrogeologic facies models to delineate large-scale spatial trends in glacial and glaciofluvial sediments, Geol. Soc. Am., v. 101, pp. 501-511.

Anderson, M.P. 1991a. Comment on "Universal scaling of hydraulic conductivities and dispersivities in geologic media" by S.P. Neuman, Water Resour. Res., in press.

Anderson, M.P. 1991b. Aquifer heterogeneity-- A geological perspective, In: Parameter Identification and Estimation for Aquifer and Reservoir Characterization, (ed. B. Hitchon) Assoc. of Ground-Water Scientists and Engineers (this volume).

Ashley, G.M., J. Shaw and N.D. Smith. 1985. Glacial Sedimentary Environments. Soc. Econ. Paleont. and Mineral. Short Course no. 16.

Bonham-Carter, C.G. and A.J. Sutherland. 1968. Mathematical model and FORTRAN IV program for computer simulation of deltaic sedimentation. Kansas State Computer Center, Pub. 25.

Bridge, J.S. and M.R. Leeder. 1979. A simulation model of alluvial stratigraphy. Sedimentology, v. 26, pp. 617-644.

Brownell, J.R. 1986. Stratigraphy of unlithified deposits in the central sand plain of Wisconsin. M.S. Thesis, University of Wisconsin - Madison.

Butcher, J.B. and M.A. Medina, Jr. 1990. Empirical Bayes regionalization for characterization of media heterogeneity. EOS Trans. Am. Geophys. Union, v. 71(17), p. 519.

Chandler, M.A., D.J. Goggin and L.W. Lake. 1989. A mechanical field permeameter for making rapid non-destructive, permeability measurements. Sediment. Petrol. v. 59, pp. 613-635.

Church, M. and R. Gilbert. 1975. Proglacial fluvial and lacustrine environments. In Glaciofluvial and Glaciolacustrine Sedimentation. (eds. A.V. Joplin and B.C. McDonald). Soc. Econ. Paleont. and Mineral. Spec. Pub. 23. pp. 22-100.

Church, M. 1972. Baffin Island sandurs: a study of Arctic fluvial processes. Geol. Surv. Can. Bull. 216.

Clayton, L. and J.W. Attig. 1989. Glacial Lake Wisconsin. Geol. Soc. Am. Mem. 173.

Cobb, J.C. and G.S. Fraser. 1981. Application of sedimentology to development of sand and gravel resources in McHenry and Kane Counties, northeastern Illinois. Ill. State Geol. Sur. Illinois Mineral Notes 82.

Dagan, G. 1987. Theory of solute transport by groundwater. Ann. Rev. of Fluid Mech. v. 19, pp. 183-215.

Davis, J.M., R.C. Lohmann, S.J. Colarullo and F.M. Phillips. 1990. Alluvial aquifer heterogeneities in the Rio Grande Valley: Implications for ground-water contamination, Tech. Completion Rept. New Mexico Water Resources Research Institute, July, 1990.

Desbarats, A.J. 1990. Macrodispersion in sand-shale sequence. Water Resour. Res. v. 26, pp. 153-164.

Dimitrakopoulos, R. 1990a. Permeability characterization at the Crystal Viking field, Alberta. EOS Trans. Am. Geophys. Union. v. 71, p. 511.

Dimitrakopoulos, R. 1990b. Conditional simulation of intrinsic random functions of order k^1. Math. Geol. v. 22, pp. 361-380.

Eyles, N., C.H. Eyles and A.D. Miall. 1983. Lithofacies types and vertical profile models: an alternative approach to the description and environmental interpretation of glacial diamict and diamictite sequences. Sedimentology, v. 30, pp. 393-410.

Fraser, G.S. and J.C. Cobb. 1982. Late Wisconsinan proglacial sedimentation along the West Chicago Moraine in northeastern Illinois. J. Sediment. Petrol. v. 52, pp. 473-491.

Fraser, G.S. and N.K. Bleuer. 1987. Use of facies models as predictive tools to locate and characterize aquifers in glacial terrains. In: Proceedings of the NWWA Focus Conference on Midwestern Ground Water Issues, National Water Well Association, Dublin, Ohio, pp. 123-143.

Freeze, R.A. and J.A. Cherry. 1979. Groundwater, Prentice Hall, Inc.

Goggin, D.J., R.L. Thrasher and L.W. Lake. 1988. A theoretical and experimental analysis of minipermeameter response including gas slippage and high velocity flow effects. In Situ, v. 12, pp. 79-116.

Greenholtz, D.E., T.C.J. Yeh, M.S.B. Nash and P.J. Wierenga. 1988. Geostatistical analysis of soil hydrologic properties in a field plot. J. Contaminant Hydrol. v. 3, pp. 227-250.

Hammer, K.M. and N.D. Smith. 1983. Sediment production and transport in a proglacial stream: Hilda Glacier, Alberta, Canada. Boreas, v. 12, pp. 91-106.

Haupt, R.W. and R.J. Martin. 1990. Determining the spatial distribution of permeability from coupled fluid and electric current flows. EOS Trans. Am. Geophy. Union, v. 71, p. 508.

Hewett, T.A. 1986. Fractal distributions of reservoir heterogeneity and their influence on fluid transport. Soc. Petrol. Eng. Paper no. 15286.

Ishido, T. and H. Mizutani. 1981. Experimental and theoretical basis of electrokinetic phenomena in rock-water systems and its application to geophysics. J. Geophys. Res., v. 86, pp. 1763-1775.

Istok, J.D., R.M. Cooper and A.L. Flint. 1988. Three-dimensional, cross-semivariogram calculations for hydrogeological data. Ground Water, v. 26, pp. 638-646.

Johnson, N.M. and S.J. Dreiss. 1989. Hydrostratigraphic interpretation using indicator geostatistics. Water Resour. Res., v. 25, pp. 2501-2510.

Jopling, A.V. 1975. Early studies in stratified drift, In Glaciofluvial and Glaciolacustrine Sedimentation (eds. A.V. Jopling and B.C. McDonald), Soc. Econ. Paleont. and Mineral., Special Pub. 23., pp. 4-21.

Juergens, L.J. 1990. A model of channel deposition and resulting interconnectedness and dispersion. M.S. Thesis. Carnegie Mellon Univ.

Juergens, L.J. and M.J. Small. 1990. A model of channel deposition and resulting interconnectedness and dispersion. EOS Trans. Am. Geophys. Union, v. 71, p. 511.

Kalinske, A.A. 1947. Movement of sediment as bed load in rivers. Trans. Am. Geophy. Union v. 28, p. 615.

Kang, S. 1981. Sediment transport in a small glacial stream: Hilda Creek, Alberta. Unpublished M.S. Thesis, University of Illinois at Chicago.

Koltermann, C.E. and S.M. Gorelick, 1990. Geologic modelling of heterogeneity in alluvial fan deposits influenced by paleoclimatic variability. EOS Trans. Am. Geophys. Union, v. 71, p. 508.

Kung, K-J.S. 1990. Preferential flow in a sandy vadose zone: 1. field observation. Geoderma, v. 46, pp. 51-58.

Lake, L.W. 1990. Simulating fluid flow through a geologically realistic permeable medium. EOS Trans. Am. Geophys. Union, v. 71, p. 508.

Laursen, E.M. 1958. The total sediment load in streams. Proc. Am. Soc. Civil Eng., v. 84, pp. 1530-1531.

Lewis, J.J.M. and B.W. Lowden, 1990. A quantification through minipermeametry of permeability heterogeneity in a tidally dominated, shallow marine sand-body. EOS Trans. Am. Geophys. Union, v. 71, pp. 508-509.

Long, J.C.S., K. Hestir, K.Karasaki, A. Davey, J.Peterson, J. Kemeny and M. Landsfeld. 1989. Fluid flow in fractured rock: theory and application, In Transport Processes in Porous Media. (eds. J. Bear, and M.Y. Corapcioglu). Kluwer Academic Publishers, Netherlands.

McDonald, M.G. and A.W. Harbaugh. 1988. A modular three-dimensional finite-difference ground-water flow model. U.S. Geol. Surv. Tech. Water-Resour. Invest., Bk. 6, Chap. A1.

Menduni, G. 1990. Geometric characterization of porous media heterogeneity by fractal approach. EOS Trans. Am. Geophys. Union, v. 71, p. 512.

Miall, A.D. 1985. Architectural-element analysis: A new method of facies analysis applied to fluvial deposits. Earth Sci. Rev., v. 22, pp. 261-308.

Molz, F.J., O. Guven and J.G. Melville. 1983. An examination of scale-dependent dispersion coefficients. Ground Water, v. 21, pp. 714-725.

Neumann, S.P. 1990. Universal scaling of hydraulic conductivities and dispersivity in geologic media. Water Resour. Res., v. 26, pp. 1749-1758.

Price, R.J. 1973. Glacial and Fluvioglacial Landforms. Hafner Publishing Co.

Scott, N. 1986. Modern vs. ancient braided stream deposits: a comparison between simulated sedimentary deposits and the Ivishak Formation of the Prudhoe Bay Field, Alaska. M.S. Thesis, Department of Applied Earth Sciences, Stanford University.

Shouse, P.J. and J.B. Sisson. 1990. Estimating unsaturated hydraulic conductivity for a layered soil using conservation scaling. EOS Trans. Am. Geophys. Union., v. 71, p. 519.

Sill, W.R. 1983. Self-potential modeling from primary flows. Geophysics, v. 48, pp. 76-86.

Smith, N.D. 1985. Proglacial fluvial environment, In Glacial Sedimentary Environments. (eds. G.M. Ashley, J. Shaw and N.D. Smith). Soc. Econ. Paleontol. and Mineral. Short Course no. 16, pp. 85-134.

Tetzlaff, D.M. and J.W. Harbaugh. 1989. Simulating Clastic Sedimentation, Van Nostrand Reinhold.

Vomvoris, E.G. and L.W. Gelhar. 1987. Stochastic prediction of dispersive contaminant transport. Project Summary, EPA/600/S2-86/117.

Webb, E.K. and M.P. Anderson. 1990. Simulating Spatial Heterogeneity in Glaciofluvial sediments using a sedimentary depositional model. EOS Trans. Am. Geophys. Union, v. 71, p. 518.

Wheatcraft, S.W. and S.W. Tyler. 1988. An explanation of scale-dependent dispersivity in heterogeneous aquifers using concepts of fractal geometry. Water Resour. Res., v. 24, pp. 566-578.

Zheng, C. 1989. PATH3D Version 2.0 User's Manual, S.S. Papadopulos and Associates, Inc.

Hydraulic Conductivity Predicted as a Function of Grain Size, Sorting and Porosity for Dune, Washover and Foreshore Depositional Environments on a Barrier Island, Florida, U.S.A.

by Rick J. Stebnisky and H. Leonard Vacher

Abstract

Permeameter analysis of 90 undisturbed, triaxially oriented sediment cores indicates that sediments recently deposited on Anclote Key, a west-central Florida barrier island, are heterogeneous and isotropic with respect to hydraulic conductivity (K). Statistical analyses show that factors affecting K are complex and interrelated. Mean grain size is the only variable consistently affecting K for all three depositional environments (dune, washover and foreshore) and the total data set. Overall, statistical correlations suggest that K increases with mean grain size, porosity, improved sorting, and as skewness becomes more positive. For any single variable, these correlations generally are weak and account for only a small percentage of the variance. Hydraulic conductivity, therefore, seems to be best described by a multivariate function.

The Kozeny-Carman equation was modified to incorporate a grain-sorting factor patterned after the Krumbien-Monk equation. For the fine-grained, very well-sorted sands of this study, the modified equation predicts K values that average only 1% lower than permeameter measurements of K for the 7 data groups, and 1% higher than permeameter measurements of K when considering each of the 30 triaxial samples. These data indicate that K values for any given sample can be predicted to within ± 30% of its measured value, with 95% confidence, by:

$$K = [450\, d_m^{\,2}]\, [n^3/(1-n)^2]\, [e^{-S\phi}]$$

where K is hydraulic conductivity (cm/s); d_m is mean grain diameter (cm); n is porosity (fraction); and S_ϕ is the phi sorting coefficient. This empirical relation expresses K as a product of a size-shape factor, a porosity factor, and a sorting factor.

This equation is suggested for purposes of estimating hydraulic conductivity for unconsolidated sands from beach-related environments. Values for the necessary variables can be obtained easily and inexpensively by routine laboratory analysis of sediments.

Introduction

Knowledge of how grain texture affects the variability of hydraulic conductivity (K) can be useful in predicting flow phenomena. If textural parameters can be related to specific depositional environments, then trends in K may be inferred from studies of depositional geometries and paleoenvironments of the sediments under consideration. Accordingly, the purpose of this study is to quantify the effects of a variety of textual parameters on K for recently deposited, unconsolidated sediments of volumetrically important depositional environments of a barrier island. The three environments are the foreshore, dune and washover environments; the barrier island is Ancote Key, Pinellas and Pasco Counties, Florida. A more thorough treatment of this work is provided by Stebnisky (1987).

Previous Work

Publications regarding the effects of grain texture on K (or permeability, k) of artificially packed sands and ideal particle masses began to appear in the mid-1930's. The classic and detailed paper by Fraser (1935) laid the ground-work for this field of study. His experiment varied grain size and sorting to determine the effects of each upon k and porosity (n). He found that k increased with grain size increase and with a decrease in sorting. Krumbien and Monk (1942) manipulated a constant porosity of 40% and derived a formula for k as a function of grain size and sorting, where k varies as the square of the mean grain size diameter, and inversely as the log of the standard deviation (sorting). Masch and Denny (1966) documented a similar relation and also found that the effect of sorting on k decreases as the mean grain size decreases. Beard and Weyl (1973) indicated that k varies directly with mean grain size and degree of sorting. The relation between k and sorting reported by Beard and Weyl (1973) contradicts the results of Fraser (1935), as do the results of Krumbien and Monk (1942).

Bedinger (1961) found a linear relation between log k and median grain size diameter; in contrast, Smith (1981) indicated that k seems to vary with the 16th percentile grain size.

In a study relating k to angularity of artificial, unconsolidated sands, Tickell and Hiatt (1938) proposed that k reaches a minimum at a roundness number (the area of the grain divided by the area of the smallest circumscribing circle) of 0.75, and increases sharply as the roundness number deviates from that value in either direction.

Little work has been done to determine relations between sedimentary parameters and hydraulic conductivity in recent, undisturbed sediments of specific depositional environments. Byers and Stephens (1983) studied fluvial sediments and found that the strongest correlation between hydraulic conductivity (K) and grain-size parameters is between the log of K and the 10th-percentile grain size. Pryor (1973) focused on recently deposited sediments of specific depositional environments. He related trends in grain size and sorting to trends in k and n. The three environments Pryor studied (dunes, beaches and rivers) showed an increase in k as grain size increased. However, as sorting increased, k increased in the river bar deposits and decreased in the beach and dune deposits. Pryor attributed this inconsistency to the different styles of packing associated with the various environments, although he had no quantitative data on packing.

Study Area

The study area for this investigation is Anclote Key, the northernmost barrier of the west-central Florida chain of barrier islands (Figure 1). Anclote Key is virtually unaltered by man due to its status as a state wildlife refuge and lack of a causeway connecting it to the mainland. Kuhn (1983) and Davis and Kuhn (1985) describe the stratigraphy of Anclote Key and interpreted its geological evolution as recorded in sediment cores. They identify eleven depositional environments on and around the island. Of these, the most prevalent in the subsurface are washovers, dunes and beaches. It seems, therefore, that the sediments of these three environments would have a major control on the distribution of K in this barrier island.

Field Methods

A stratified sampling plan was used in the summer of 1985 to sample recently

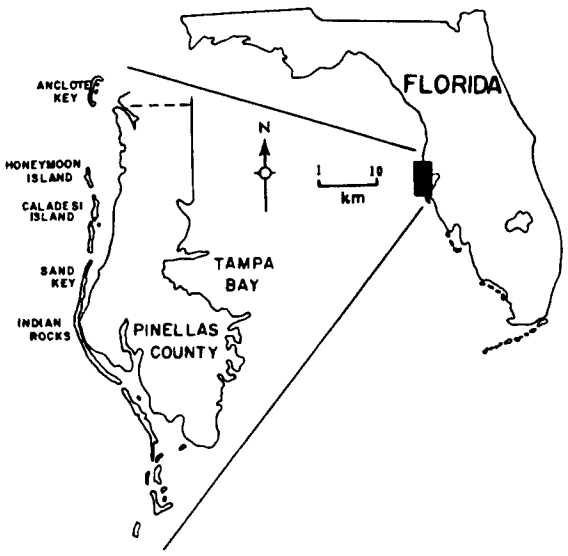

Figure 1. Map showing location of Anclote Key and the west-central Florida barrier-island chain (from Davis and Kuhn, 1985).

deposited sediments from foreshore, dune and washover environments. The samples were undisturbed, oriented cores taken from shallow trenches excavated in the sediments. Samples were collected at an approximate depth of 10 cm. A 5-point sample grid was randomly established in each of the 3 environments. Sample points were spaced 3 m apart in a 5-point cross pattern (Figure 2). Each triaxial sample consisted of 3 oriented cores which were taken at each of the 5 sample points within the grids. Orientation designations are: "x", horizontal and parallel to the Gulfshore; "y", horizontal and normal to the Gulfshore; and "z", vertical. All core lengths and diameters where 8.7 cm and 4.8 cm, respectively.

In addition, 5 random triaxial samples were taken outside the grid in each of the 3 environments; therefore, a total of 10 triaxial samples (30 oriented cores) was taken from each of the three environments. A grand total of 30 triaxial samples (90 oriented cores) was obtained. Sample locations are shown in Figure 2.

Laboratory Methods

Core sediments were analyzed for K, n and grain-size parameters. Ninety sediment cores were analyzed for K and n. Further, K was measured using SOIL TEST® K-605 constant-head permeameters with custom-made permeameter chambers. Porosity was determined on the same 90 sediment cores from the water-saturated and dry sample masses.

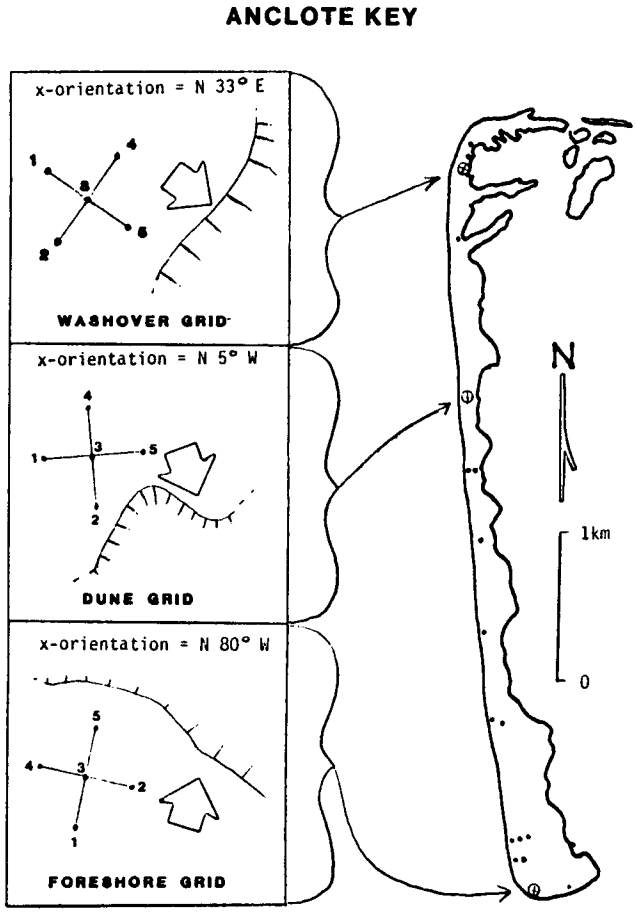

Figure 2. Sample location map on Anclote Key (right), and spatial arrangements of grids (left). Sample points (1-5) are spaced at 3 m centers. Arrows indicate dominant transport directions at time of sampling. Hatch marks represent sediment slipface surfaces.

Table 1

Foreshore: analytical results for hydraulic conductivity (K), porosity (n), mean grain size (X_ϕ), sorting (S_ϕ), and skewness (Sk)

Sample		Orientation	K (x 10^{-2} cm/s)	n (%)	X_ϕ	S_ϕ	Sk
	F-1	x	2.1	43	2.7	.64	-.48
		y	1.3	40	2.7	.64	-.48
		z	0.96	39	2.7	.64	-.48
	F-2	x	1.1	38	2.4	.59	-.32
		y	1.6	38	2.4	.59	-.32
		z	1.0	39	2.4	.59	-.32
G	F-3	x	1.6	37	2.3	.56	-.29
R		y	1.5	38	2.3	.56	-.29
I		z	1.3	39	2.3	.56	-.29
D	F-4	x	1.5	39	2.2	.63	-.23
		y	1.6	37	2.2	.63	-.23
		z	1.2	38	2.2	.63	-.23
	F-5	x	1.3	39	2.6	.38	-.13
		y	1.5	39	2.6	.38	-.13
		z	0.98	39	2.6	.38	-.13
	F-6	x	1.4	38	2.6	.31	+.07
		y	1.3	38	2.6	.31	+.07
		z	1.2	39	2.6	.31	+.07
	F-7	x		36	2.6	.33	+.06
R		y	1.6	37	2.6	.33	+.06
A		z	1.2	36	2.6	.33	+.06
N	F-8	x	1.0	42	2.8	.30	-.02
D		y	0.73	38	2.8	.30	-.02
O		z	1.0	38	2.8	.30	-.02
M	F-9	x	0.82	36	2.8	.28	-.01
		y	0.91	39	2.8	.28	-.01
		z	1.2	39	2.8	.28	-.01
	F-10	x	1.1	38	2.6	.37	-.11
		y	1.2	38	2.6	.37	-.11
		z	0.98	38	2.6	.37	-.11

Grain-size analysis was conducted on 30 samples using an Allen-Bradley SONIC SIFTER®. Each of these samples was a composite of the 3 oriented cores at a single sample point. Approximately 10 g of sediment were sieved for 10 min at 1/4-phi intervals. Probability paper plots of cumulative percentages were used with formulas of Folk (1968) to calculate graphic mean (X_ϕ), inclusive graphic standard deviation (phi sorting coefficient, S_ϕ), and inclusive graphic skewness (Sk).

Results of Laboratory Analyses

Results of analyses for K, n, X_ϕ, S_ϕ and Sk for the foreshore, dune and washover environments are listed in Tables 1, 2 and 3, respectively. Mean values and the standard error of the mean for the 5 parameters for each depositional environment and for the total data set are summarized in Table 4. The standard error of the mean is a measure of variance weighted to sample size, thus allowing comparison of variances between sample groups of different sizes.

Qualitatively, the between-environment variations in the measured properties can be summarized in terms of rankings of the various means. Washovers have the highest n, largest X_ϕ and least Sk. Washovers and dunes are tied for the highest K and best S_ϕ. Dunes have the most positive Sk and are tied with foreshores for lowest n and smallest X_ϕ. Extremes in the foreshore are: lowest K, poorest S_ϕ and most

Table 2

Dune: analytical results for hydraulic conductivity (K), porosity (n), mean grain size (X_ϕ), sorting (S_ϕ), and skewness (Sk)

Sample		Orientation	K (x 10^{-2} cm/s)	n (%)	X_ϕ	S_ϕ	Sk
	D-1	x	1.8	39	2.6	.27	+.06
		y	1.6	38	2.6	.27	+.06
		z	1.7	39	2.6	.27	+.06
	D-2	x	1.8	40	2.5	.25	+.30
		y	1.7	38	2.5	.25	+.30
		z	1.6	39	2.5	.25	+.30
G	D-3	x	2.0	39	2.5	.29	+.06
R		y	2.4	38	2.5	.29	+.06
I		z	1.7	38	2.5	.29	+.06
D	D-4	x	1.8	36	2.5	.24	+.28
		y	2.0	39	2.5	.24	+.28
		z	1.7	38	2.5	.24	+.28
	D-5	x	2.1	38	2.5	.23	+.24
		y	2.6	37	2.5	.23	+.24
		z	1.7	37	2.5	.23	+.24
	D-6	x	2.2	36	2.5	.28	+.18
		y	1.8	38	2.5	.28	+.18
		z	1.8	38	2.5	.28	+.18
	D-7	x	1.6	38	2.6	.26	+.05
R		y		40	2.6	.26	+.05
A		z	1.5	38	2.6	.26	+.05
N	D-8	x	1.2	38	2.5	.33	+.06
D		y	1.2	36	2.5	.33	+.06
O		z	1.1	37	2.5	.33	+.06
M	D-9	x	0.82	38	2.7	.27	+.04
		y	1.1	38	2.7	.27	+.04
		z	1.3	37	2.7	.27	+.04
	D-10	x	1.3	40	2.7	.26	+.06
		y	1.2	41	2.7	.26	+.06
		z	1.2	40	2.7	.26	+.06

Table 3

Washover: analytical results for hydraulic conductivity (K), porosity (n), mean grain size (X_ϕ), sorting (S_ϕ), and skewness (Sk)

	Sample	Orientation	K ($\times 10^{-2}$ cm/s)	n (%)	X_ϕ	S_ϕ	Sk
	W-1	x	1.9	39	2.5	.27	+.11
		y	1.6	40	2.5	.27	+.11
		z	1.5	41	2.5	.27	+.11
	W-2	x	1.8	40	2.6	.26	+.18
		y	1.5	40	2.6	.26	+.18
		z	2.0	39	2.6	.26	+.18
G	W-3	x	1.3	40	2.5	.29	-.01
R		y	1.9	40	2.5	.29	-.01
I		z	1.5	39	2.5	.29	-.01
D	W-4	x	1.6	44	2.5	.27	+.09
		y	1.8	39	2.5	.27	+.09
		z	1.4	40	2.5	.27	+.09
	W-5	x	1.6	40	2.6	.29	+.05
		y	1.7	41	2.6	.29	+.05
		z	1.6	41	2.6	.29	+.05
	W-6	x	2.0	39	2.5	.26	+.11
		y	1.4	40	2.5	.26	+.11
		z	1.9	39	2.5	.26	+.11
	W-7	x	1.9	40	2.5	.28	+.01
R		y	2.3	40	2.5	.28	+.01
A		z	1.5	44	2.5	.28	+.01
N	W-8	x		48	2.5	.27	+.15
D		y	1.6	40	2.5	.27	+.15
O		z	1.8	44	2.5	.27	+.15
M	W-9	x	1.7	41	2.5	.29	+.09
		y	2.1	43	2.5	.29	+.09
		z	1.5	41	2.5	.29	+.09
	W-10	x	1.0	36	2.6	.27	+.28
		y	1.0	35	2.6	.27	+.28
		z	0.89	39	2.6	.27	+.28

negative Sk. Between-environment rankings for the standard error of the means follow similar trends as those of the means, except that foreshore sediments are most variable in X_ϕ.

The averages of the cumulative grain-size distributions for each environment are shown in Figure 3. The three environments demonstrate nearly identical grain-size distributions. The only noteworthy difference is the presence of some coarse, sand-sized material in the foreshore and X_ϕ lack of the same in washovers and dunes.

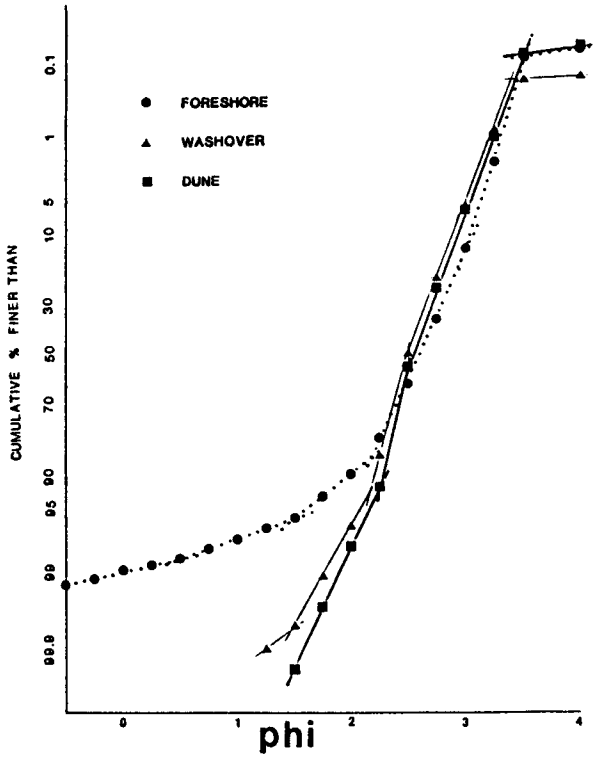

Figure 3. Averaged cumulative grain-size curves for foreshore, washover and dune environments.

Table 4

Summary of means ($\bar{x}$) and standard error of the means (s_x) of all variables for each depositional environment and for the total data set

Parameter		Total	Foreshore	Dune	Washover
K(cm/s)	$\bar{x}$	0.015	0.012	0.016	0.016
	s_x	0.00042	0.00056	0.00075	0.00060
n (%)	$\bar{x}$	39.	38.	38.	40.
	s_x	0.21	0.28	0.22	0.42
X_ϕ	$\bar{x}$	2.6	2.6	2.6	2.5
	s_x	0.012	0.032	0.013	0.0077
S_ϕ	$\bar{x}$	0.33	0.44	0.27	0.27
	s_x	0.012	0.026	0.0048	0.0020
Sk	$\bar{x}$	+0.032	-0.14	+0.13	+0.11
	s_x	0.018	0.031	0.018	0.015

Note: K is hydraulic conductivity, n is porosity, X_ϕ is mean grain size, S_ϕ is sorting, Sk is skewness.

Statistical Analyses, Results and Discussion

The K data were organized into two types of "groups" for purposes of statistical analysis: oriented-data groups and pooled-data groups. Oriented-data groups each contain data representing a specific core orientation ("x", "y", or "z"). Pooled-data groups lump all three core orientations ("x", "y", and "z"). The 7 data groups of this study are: the total data set (a pooled-data group), the data sets for each of the 3 environments (3 pooled-data groups), and the data sets for each of the 3 orientations (3 oriented-data groups).

To compare means between various groups of interest using t tests, one must satisfy assumptions of random sampling, normally-distributed data, and equal variances. Accordingly, statistical analyses conducted on K data include Chi-square tests for normalcy, F tests for variance equality, and t tests to compare the means. In addition, correlation coefficients between all the variables were calculated for each of the 7 groups. The significance level for these analyses is 95% (P=95%), unless otherwise noted.

Chi-square (X^2) Tests

Chi-squared tests to determine if the populations being tested are normally distributed (Naiman et al., 1977) were performed on four pooled-data groups: all cores, all foreshore cores, all dune cores, and all washover cores. Results are summarized in Table 5. All 4 groups are normally distributed.

Values for K may vary in nature by ~13 orders of magnitude and are generally thought to be lognormally distributed (Freeze and Cherry, 1979). However, minimal variability in K apparently allows the data to fit a normal distribution, as is the case here.

Values for K in this study varied by a factor of < 3. Smith (1981) showed that his K data set also fitted a normal distribution, even though the data had a range ~6 times greater than the range of this data set.

Table 5

Summary results of Chi-square tests for normalcy

Test Conditions: one-tail, P = 95%

Test Hypotheses:
H_0: K data are normally distributed
H_1: K data are not normally distributed

Group	d.f.	X_c^2	X^2	Decision
all cores	7	14	4.2	f
all foreshores cores	5	11	5.8	f
all dune cores	6	13	9.7	f
all washover cores	5	11	7.7	f

Note: d.f = degrees of freedom
X^2 = calculated value
X_c^2 = critical value
f = fail to reject H_0

F tests

The F test (Naiman et al., 1977) to compare the variances of two distributions assumes random sampling and normal distributions. Results of F tests between the 3 environments, and between the 3 orientations are summarized in Table 6. There are no significant differences in variance between any combination of environments or between any combination of orientations.

t tests

The t test (Naiman et al., 1977) to compare the means of distributions assumes random sampling, normally distributed data, and equal variances. These requirements are satisfied by this data set. Results of t tests between the 3 environ-

Table 6

Results of F tests comparing variances of hydraulic conductivities between environments and between orientations

Test Conditions: two-tail, P = 95%

Test Hypotheses: H_O: $s_1^2 = s_2^2$, H_1: $s_1^2 \neq s_2^2$

Category	Group Pair Relations*	F_c	F	Decision
Between Environments	Foreshore = Dune	2.07	1.84	f
	Foreshore = Washover	2.07	1.16	f
	Dune = Washover	2.07	1.59	f
Between Orientations	"x" = "y"	2.07	1.20	f
	"x" = "z"	2.07	1.59	f
	"y" = "z"	2.07	1.90	f

Note: * symbols (=, <, and >) indicate variance rankings, F = calculated value, F_c = critical value, f= fail to reject H_O

ments and between the 3 orientations are summarized in Table 7. Both dunes and washovers show significantly higher mean K values than the foreshore. Dunes and washovers are approximately equal. There are no significant differences in mean K values between any combination of orientations. The Anclote sands are thus characterized as heterogeneous and isotropic. While these differences are statistically significant, their practical implications are limited.

Table 7

Results of t tests comparing means of hydraulic conductivities between environments and between orientations

Test Conditions: two-tail, P = 95%

Test Hypotheses: H_O: $u_1 = u_2$, H_1: $u_1 \neq u_2$

Category	Group Pair Relations*	$(\pm)t_c$	t	Decision
Between Environments	Foreshore < Dune	2.00	-4.12	R
	Foreshore < Washover	2.00	-4.55	R
	Dune = Washover	2.00	.15	f
Between Orientations	"x" = "y"	2.00	-.11	f
	"x" = "z"	2.00	1.64	f
	"y" = "z"	2.00	1.68	f

Note: * symbols (=, <, and >) rank the means, t = calculated value, t_c = critical value, f = fail to reject H_O, R = reject H_O

The overall ratio of horizontal to vertical hydraulic conductivity (K_h/K_v) is 1.12. That ratio is greatest in foreshores (1.20) and least in washovers (1.07). These isotropic conditions can be largely attributed to the limited range in grain size and mineralogy of the source area, and the resultant lack of well-pronounced stratification that would likely occur if widely divergent grain sizes and mineralogies were available.

Foreshore sands commonly have nearly horizontal, finely laminated, residual deposits of heavy minerals (Davis, 1985). Such laminations may have some minimizing effect on K_v. This phenomenon may also contribute to the overall low K values in the foreshore.

Factors Affecting Hydraulic Conductivity

The Pearson product-moment correlation coefficient (r) is used to evaluate the strength of linear relations between pairs of variables (Upchurch, in press). Significant correlations between variables for each of the 7 data groups are summarized in Table 8, together with the percent of variance accounted for (r^2) by each correlation. Significant correlations between variables for the total data set, and for each of the 3 environments are illustrated in Figure 4. The following sections detail and discuss these correlations.

Porosity

For the total set of cores, there is a positive correlation between K and n (Figure 4); however, the regression accounts for < 5% of the variance. There is not a statistically significant correlation between K and n in any of the specific depositional environments. Thus n, in itself, appears to have very little effect on the K of Anclote sands.

Table 8

Summary of significant (P = 95%) correlations between hydraulic conductivity (K), porosity (n), mean grain size (X_φ), sorting (S_φ) and skewness (Sk) for the 7 data groups

Group	Significant Correlations	r^2	Group	Significant Correlations	r^2
Total	K + n	.05	Dunes	*K - X_φ	.42
	*K - X_φ	.14		K - S_φ	.19
	K - S_φ	.05		*K + Sk	.28
	*K + Sk	.10		n + X_φ	.14
	*S_φ - X_φ	.17		*X_φ - Sk	.48
	*S_φ - Sk	.79		*S_φ - Sk	.40
"x" orientation	K - X_φ	.15	Washovers	K - X_φ	.14
	X_φ - S_φ	.17		*K - Sk	.25
	*S_φ - Sk	.79		*S_φ - Sk	.53
"y" orientation	*K - X_φ	.27	Foreshores	K - X_φ	.14
	X_φ - S_φ	.17		K + S_φ	.20
	*S_φ - Sk	.79		n - Sk	.20
				*X_φ - S_φ	.49
"z" orientation	*K - S_φ	.27			
	*K + Sk	.32			
	X_φ - S_φ	.17			
	*S_φ - Sk	.79			

Notes: Positive (+) or negative (-) correlations are indicated between variables.
r^2 indicates the percent of variance accounted for by the given correlation.
* indicates correlation with P = 99%.

According to Gaither (1953), n of modern sands is affected by mode of deposition, sorting, grain size, and grain shape. Sand deposited in water should have a higher n than sand deposited subaerially because of the greater buoyancy of water (Gaither, 1953). Also, n increases with rate of deposition because sediments are unable to assume their most stable position when rapidly buried.

For the Anclote sands, n is probably most affected by mode and rate of deposition. Washovers on Anclote Key have a mean n 2% greater than foreshore or dunes (Table 4). The n of washover is twice as variable as that of dunes. The rapid rate of deposition of the Anclote washovers is probably the principal reason for their variable and elevated values of n. These washovers were deposited in a matter of days by Hurricane Elena in late August, 1985. Lower n values for dune and foreshore sediments are interpreted to result from subaerial deposition and slower deposition rates, respectively.

Grain-Size Parameters

Mean (X_φ)

Every sample taken on Anclote Key has a X_φ within the fine-sand class of Folk (1968). Most samples fall toward the middle of that class.

Relations between grain size and K are well documented in the literature. If all other factors are held constant, K should increase as grain size increases (Fraser, 1935; Krumbien and Monk, 1942; Masch and Denny, 1966; Beard and Weyl, 1973; Pryor, 1973; Smith, 1981; Byers and Stephens, 1983; Trommer, 1987).

This expected relation is suggested by the significant negative correlation between K and X_φ for the total data set, each of the 3 environments, and for "x" and "y" orientations. The relation is inverse because X_φ is expressed in phi. The correlation between K and X_φ is consistently stronger than that between K and any other variable in this study; however, the correlation accounts for only 14 % of the variance for the total data set. Only in the "z" group is the correlation between X_φ and K not significant. In this group, Sk and S_φ appear more important and may be the result of horizontally laminated fines that would tend to retard vertical fluid flow without contributing substantially to the the X_φ statistic.

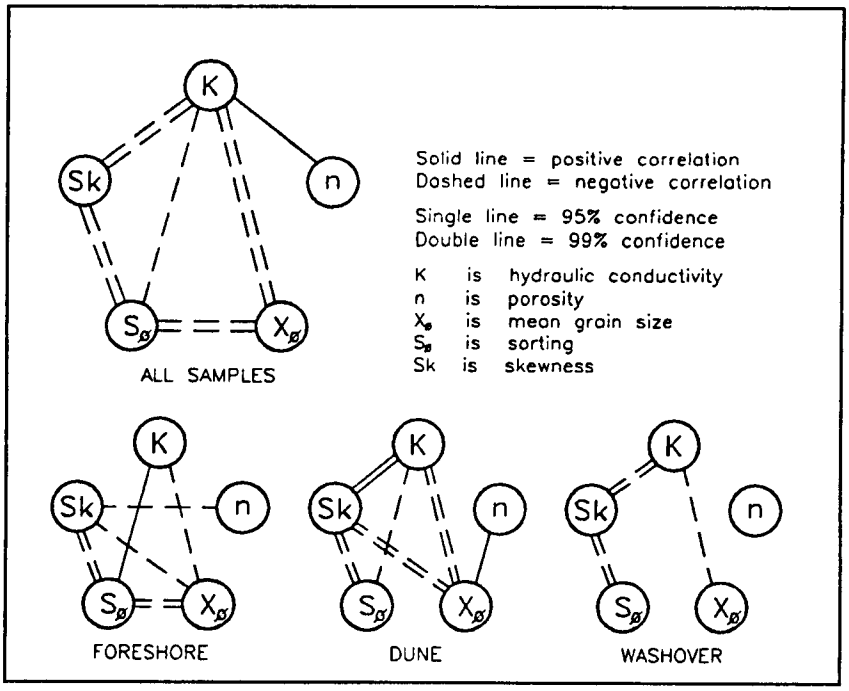

Figure 4. Significant correlations between variables for all samples and each depositional environment.

Skewness (Sk)

On Anclote Key, Sk varies between depositional environments. Dune and washover sediments are positively skewed (a fine tail), and foreshore sediments are negatively skewed. Overall, if sediments from the 3 environments are combined, the grain-size distribution is nearly symmetrical.

Foreshore sediments typically show negative skewness due to fines being removed by wave energy or due to the addition of coarse clastics (Davis, 1985). Dune sediments typically show positive skewness due to the upper grain-size limit of eolian transport, with no corresponding lower limit.

The relation between K and Sk also varies between depositional environments (Figure 4). For dunes and the entire data set, there is a very weak positive correlation between K and Sk (K increasing as Sk becomes more positive). For washovers, there is a very weak negative correlation (K increasing as Sk becomes less positive). There is no significant correlation between K and Sk in the foreshore samples. Correlations between K and Sk account for only small percentages of the variances.

Masch and Denny (1966) found K to increase with positive skewness for sediments of various median grain sizes; the effects diminish with finer grain-

sizes. They concluded that positive skewness reflects excess coarse material, which would result in large flow paths and higher permeability.

Sorting (S_φ)

Overall, the sands on Anclote Key are very well sorted according to the classification of Folk (1968). Sediment is well sorted in the foreshore environment and very well sorted in dunes and washovers.

The relation between sediment sorting and K is variable (Figure 4). Where correlation between S_φ and K is significant, it accounts for no more than 27% of the variance.

Variable results regarding the nature of the correlation between K and S_φ are reported in other studies. For example, Krumbien and Monk (1942), Masch and Denny (1966) and Beard and Weyl (1973) all found that K increased as sorting improved in their samples. In contrast, Pryor (1973) found that K decreased somewhat as sorting improved for his beach and dunes samples (and the opposite for his river samples), and Byers and Stephens (1983) found no correlation.

Predictive Relations Between K and Measured Parameters

In this study, only a small percentage of the variance of K is accounted for by the correlations between K and the other variables considered individually. Therefore, K would seem to be best predicted by a multivariate function.

According to the Kozeny-Carman equation, which is possibly the best-known predictive equation for K (Bear, 1972; Freeze and Cherry, 1979),

$$K = (1.02 \times 10^{-5})\, c\, n^3 / M^2, \qquad (1)$$

where K is in cm/s; M is specific surface (cm^{-1}); c is a numerical coefficient (Kozeny' constant); and 1.02×10^{-5} converts k to K for water at 20°C.

According to Carman (1937, 1938, 1956), a value of 0.2 for c fits well with empirical data. Bear (1972) presents a form of the Kozeny-Carman equation in which M has been removed; the equation is written in terms of a mean grain diameter, d_m. The derivation follows from the fact that, for spheres of constant diameter (d), the specific surface of a unit volume of solid (M_s) follows the relation $M_s = 6/d$. Then, according to Bear (1972) and for $c = 0.2$, the Kozeny-Carman equation becomes:

$$K = [d_m^2/0.0018]\, [n^3/(1-n)^2] \qquad (2)$$

where d_m is in centimeters. This equation holds for the idealized case of spheres with constant diameter (i.e. perfect sorting). For the 7 data groups in this study, this grain-size form of the Kozeny-Carman equation (eqn 2) gives calculated-to-measured K ratios ranging from 1.4 to 1.9; the average is 1.7.

In their study of unconsolidated sands, Krumbien and Monk (1942) proposed that permeability varies with the negative exponential of the logarithmic sorting values. This, together with the tendency toward negative correlation between K and S_φ in the Anclote sands,

suggests that K may be more accurately predicted by taking into account the effect of sorting. An empirical relation that fits the Anclote data well is:

$$K = [450\ d_m^2]\ [n^3/(1-n)^2]\ [e^{-S\phi}] \qquad (3)$$

where d_m is in cm. In this equation, the Kozeny constant (c), which Carman used to adjust for grain shape, has been changed from 0.2 to 0.16 to shift the range of calculated values toward their measured values of this study. The sorting factor serves to limit the range of calculated-to-measured ratios. Thus overall, this empirical relation expresses K as a product of a size-shape factor, a porosity factor, and a sorting factor.

For the 7 data groups in this study, eqn (3) gives calculated-to-measured K ratios ranging from 0.86 to 1.17, and averaging 0.99. To further evaluate eqn (3), K was calculated using averaged parameter values for each of the 30 Anclote samples. These calculations result in calculated-to-measured K ratios ranging from 0.71 to 1.44, with a mean of 1.01 and standard deviation of 0.18. These data indicate that eqn (3) can predict K values to within ±30% of their measured values, with 95% confidence. These data are illustrated in Figure 5.

This modified form of the Kozeny-Carman eqn (3), which includes a sorting factor, is suggested for purposes of predicting hydraulic conductivity for unconsolidated sands from beach-related environments. Values for the necessary variables can be obtained easily and inexpensively by routine laboratory analysis of sediments.

Conclusions

Sediments currently being deposited on Anclote Key are heterogeneous and isotropic. Dunes and washovers each have mean K values that are 33% higher than the foreshore sediments. These differences are statistically significant, yet, the degree of heterogeneity is of limited practical importance.

Values for K in this study fit a normal distribution, although K is generally thought to be a lognormal property. It seems that this normal distribution can be attributed to the small range in these data.

Factors affecting K are complex and interrelated. Statistically significant correlations are very weak and fail to indicate bivariate relations between variables. For every environment studied and the total data set, there is a weak correlation suggesting that K may increase with mean grain size. Because no individual variable demonstrates a correlation that accounts for a reasonable percentage of the variance, K is best described by a multivariate function.

The Kozeny-Carman equation was modified in this study to incorporate a sorting factor. When mean parameter values for each of the 7 major data groups in study are inserted into a grain-size version of this equation, resultant K values average only 1% lower than their measured values. When parameter values for each of the 30 samples are inserted, resultant K values average only 1% higher than

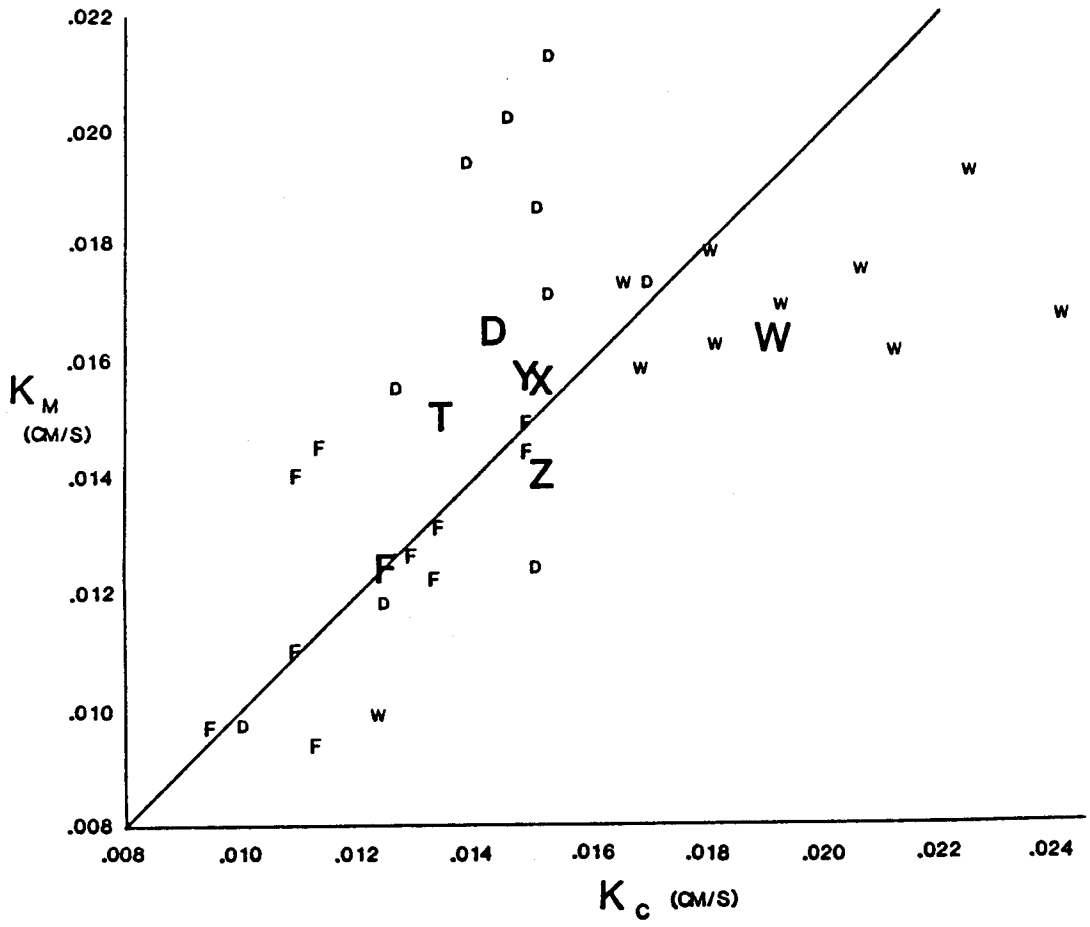

Figure 5. Graph of measured K (K_m) vs calculated K (K_c) using a modification of the Kozeny-Carman eqn (3) that includes a sorting factor. The smaller letters represent the 30 individual samples from dunes (D), washovers (W), and the foreshore (F). The larger letters represent the 7 major data groups: the total sample set (T), all dune samples (D), all washover samples (W), all foreshore samples (F), all "x" cores (X), all "y" cores (Y), and all "z" cores (Z). The solid line represents the 1:1 correlation line.

their measured values. For any given sample, the modified equation proved capable of predicting K values to within ±30% of their measured values, with 95% confidence. This equation, which includes a grain-size-shape factor, a porosity factor, and a sorting factor, appears to be an accurate description of the effects of texture on the K of Anclote sands.

Acknowledgments

We gratefully thank J.B. Butler and Associates, Inc. for enthusiastically supporting the production of this report.

Biographical Sketch

Rick Stebnisky is the Senior Hydrogeologist at J.B. Butler Associates, Inc. (P. O. Box 23526, Tampa, Florida, 33623 U.S.A.), an environmental

consulting firm. He has designed, executed and managed a variety of hydrogeological investigations primarily concerning water resources development and related impacts, and groundwater and soil contamination and remediation. He received a B.S. in Geology from Edinboro University of Pennsylvania (1983) and a M.S. in Geology from the University of South Florida, Tampa (1987). His primary research interest is in evaluation of aquifer characteristics and water resources of islands and coastal environments.

Len Vacher is Associate Professor of Geology at the University of South Florida (4202 Fowler Avenue, Tampa, Florida 33620 U.S.A.). He received a B.S. in Geology from the University of Washington and M.S. and Ph.D. in Geology from Northwestern University, and came to Florida after nine years at Washington State University. His research interests involve mainly Pleistocene sea-level history, hydrology of ocean islands, and meteoric digenesis of carbonates. He and his students work mainly in the Florida Keys, Bahamas, and Bermuda.

References

Bear, J. 1972. Dynamics of Fluids in Porous Media. Elsevier.

Beard, D. C. and P. K. Weyl. 1973. Influence of texture on porosity and permeability of unconsolidated sand. Bull Am. Assoc. Petrol. Geol., v. 57, pp. 344-369.

Bedinger, M. S. 1961. Relation between median grain size and permeability in the Arkansas River Valley. U. S. Geol. Surv. Prof. Paper 292, pp. 1-31.

Byers, E. and D. B. Stephens. 1983. Statistical and stochastic analyses of hydraulic conductivity and particle-size in a fluvial sand. Soil Sci. Soc. Am. J., v. 47, pp. 1072-1080.

Carman, P. C. 1937. Fluid flow through a granular bed. Trans. Inst. Chem. Eng. London, v. 15, pp. 150-156.

Carman, P. C. 1938. Determination of the specific surface of powders I. J. Soc. Chem. Indus., v. 57, pp. 225-235.

Carman, P. C. 1956. Flow of Gases through Porous Media. Butterworths.

Davis, R. A. and B. J. Kuhn. 1985. Origin and development of Anclote Key, west-peninsular Florida. Marine Geol., v. 63, pp. 153-171.

Davis, R. A. 1985. Beach and Nearshore Zone. In Coastal Sedimentary Environments (ed. R.A. Davis). 2nd Edn. Spring-Verlag.

Folk, R. L. 1968. Petrology of Sedimentary Rocks. Hemphill's, Austin, Texas.

Fraser, H. J. 1935. Experimental study on the porosity and permeability of clastic sediments. J. Geol., v. 43, pp. 910-1010.

Freeze, R. A. and J. A. Cherry. 1979. Groundwater. Prentice-Hall, Inc.

Gaither, A. 1953. A study of porosity and grain relationships in experimental sands. J. Sediments Petrol., v. 23, pp. 180-195.

Krumbien, W. C. and G. D. Monk. 1942. Permeability as a function of the size parameters of unconsolidated sand. Petrol. Tech., AIME Tech. Pub. 1492, v. 5, pp. 1-11.

Kuhn, B. J. 1983. Stratigraphy and geologic evolution of Anclote Key, Pinellas county, Florida. MS thesis, University of South Florida.

Masch, F. D. and F. D. Denny. 1966. Grain size distribution and its effect on the permeability of unconsolidated sands. Water Resour. Res., v. 2, pp. 665-677.

Naiman, A., R. Rosenfeld and G. Zirkel. 1977. Understanding Statistics. McGraw-Hill, Inc.

Pryor, W. A. 1973. Permeability-porosity patterns and variations in some Holocene sand bodies. Bull. Am. Assoc. Petrol. Geol., v. 57, pp. 162-189.

Smith, L. 1981. Spatial variability of flow parameters in a stratified sand. Math. Geol., v. 13, pp. 1-21.

Stebnisky, R. J. 1987. Hydraulic conductivity as a function of depositional environments on a barrier island, Anclote Key, Pinellas and Pasco Counties, Florida. MS thesis, University of South Florida.

Tickell, F. G. and W. N. Hiatt. 1938. Effect of angularity on porosity and permeability of unconsolidated sands. Bull. Am. Assoc. Petrol. Geol., v. 22, pp. 1272-1274.

Trommer, J. 1987. Sedimentologic properties controlling hydraulic conductivity of beach sediment. MS thesis, University of South Florida.

Upchurch, S. B. (in press). Statistical Analysis for Hydrogeologists and Hydrologists. Springer-Verlag.

Impacts of Geological Structure on Transport: Creating a Data Base

by Timothy D.Scheibe and David L. Freyberg

Abstract

Understanding the relations among sediment or rock hydraulic properties at various spatial locations (referred to as "spatial structure"), and the effect of such structure on flow and transport processes, is a key problem in hydrogeology. Knowledge of spatial structure offers one approach to characterization of a particular porous sediment or rock body given limited measurements. However, the spatial structure of natural rocks and sediments is extremely complex, and cannot be completely described. Therefore, models of spatial structure commonly assume that this complexity can be represented by at most a few basic characteristics of the structure, usually defined at relatively large scales. The impacts of such assumptions on predictions of subsurface flow and transport are not well understood, nor is it clear how the modeled characteristics of structure relate to the structural character actually exhibited by geological media.

The body of observations which has been accumulated by investigators in geological fields of study represents a wealth of information regarding the types of patterns which occur in natural sediments. Here, some of this information has been applied, in conjunction with quantitative measurements, to develop a parameter field, fully characterized at a fine scale in three dimensions, which can be assumed to be a realistic example of a natural sediment. Characterization of the spatial structure of this "numerical aquifer", and evaluation of its impacts on model predictions, is under way.

Introduction

A great deal of research attention has been devoted to quantifying the impacts of spatial structuring of subsurface hydraulic properties on transport and flow processes. Recently, there has been an increase in general awareness of the need to more carefully consider the nature of geological structure in various environments when formulating quantitative predictive models.

In the initial parts of this paper, one approach to study of this problem and some accompanying issues are discussed. A three-stage plan of study is outlined. The remainder of the paper focuses on methods and results of the first stage of study, in which a hypothetical but geologically realistic "numerical aquifer" has been created as the basis for the remaining stages of the study.

Problem Statement

There is growing evidence that for many problems in a wide variety of different geological environments groundwater solute transport is dominated by the spatial variability of the velocity field. For example, it has been observed in several field studies (e.g. Sudicky and Cherry, 1979; Pickens and Grisak, 1981;Freyberg, 1986) that the magnitude of spreading of solutes is orders of magnitude greater than that explainable by pore-scale diffusion and microdispersion alone. In particular, the spreading, mixing, and apparent dilution of solute plumes may often be attributed primarily to the convective heterogeneity found in almost all groundwater environments. The principal physical property giving rise to this heterogeneity is the permeability (hydraulic conductivity). Because of its relatively small magnitude, porosity variability is much less important in controlling velocity variability (Freeze, 1975). Many studies and data

collection efforts have demonstrated that permeability variability is extraordinarily complex and that it is clearly linked to the geological environment (e.g. Pryor, 1973; Stalkup, 1986; Szpakiewicz *et al.*, 1987). Depositional processes and environment, parent material, mineralogy, weathering and other post-depositional processes, all contribute to the observed patterns and scales of spatial variability of permeability. Unfortunately, because collecting detailed permeability data is expensive and usually destructive of the flow domain, our knowledge of particular permeability fields will usually be quite limited and uncertain. Efficient use of our understanding of geological environments and processes is therefore an essential tool in reducing uncertainty and in improving our ability to predict transport adequately.

However, direct application of geological understanding to subsurface transport prediction is difficult, at best. The primary goal of geologists in formulating descriptions of spatial patterns of sediment properties (often referred to as "facies models") is to enable the inference of ancient depositional environments from observed patterns. The goal of hydrologists is the reverse; i.e., to infer patterns of properties given some knowledge of depositional environment (and perhaps limited observations). Because of this contrast in goals, facies models are often not directly applicable to hydrogeologic problems (Anderson, 1989). In formulation of a facies model, many specific examples (with their complex variations) are sifted and assimilated into a generalized description, useful for the geologists' goals. While knowledge of large scale trends and generalizations can be useful in hydrologic applications (Fraser and Bleuer, 1987; Anderson, 1989), variations from the generalized model may be equally or more important for site-specific prediction (depending on their scale and nature).

These problems raise the question of whether there exists some descriptor which is useful in enabling application of geological insight to prediction of site-specific patterns of hydrologic properties, and which may provide a framework for the study of impacts of natural variability on groundwater model predictions. Spatial structure models, defined as the quantitative relationships among hydraulic properties as a function of spatial location, may serve in this capacity. Spatial structure provides a potential link between qualitative generalizations and quantitative specifications in that terms such as "shape", "connectedness", "texture", and "scale" (as well as more explicitly geological terms such as "stratification") can be given mathematical meaning. Structural models can provide for site-specific application in so far as they remain flexible through the site-specific estimation of structural model parameter values. Further flexibility for site-specific application can be attained by formulation of models within a probabilistic framework, such that the potential for local variations from a generalized model can be explored and quantified. Finally, since spatial structure models allow analysis (and control in synthetic simulation) of the character of spatial patterns, they provide a powerful framework for study of the impact of the character of natural patterns on prediction of transport behavior.

Of course, the use of models of spatial structure in hydrogeology is not new. But such use has historically been limited to a small number of structural models, typically selected on the basis of simplifying assumptions and analysis of limited data rather than on the ability to represent important aspects of geological structure. For example, a number of investigators have demonstrated the role of the mean and covariance of the log-permeability field in controlling ensemble mean concentrations under uniform mean head gradients (Dagan,1982; Gelhar and Axness, 1983; Neuman *et al* ., 1987), but little is known about whether these popular descriptors are adequate in characterizing the structure of aquifer deposits when attempting to design and predict the consequences of, say, a remedial action in a particular aquifer. In general, it is not yet clearly understood which aspects of natural spatial structure play an important role in controlling transport behavior in particular problems. There is significant uncertainty about the need to identify and represent different characteristics of spatial structure in various geological environments, and about the minimum scale

of geological variability that must be explicitly represented to predict transport adequately.

Fortunately, the study of spatial structure is by no means limited to the narrow class of models commonly used in hydrogeologic studies. Investigators in the growing field of pattern recognition and machine vision have explored a wide variety of ways in which to represent complex spatial patterns using parsimonious models. They have shown quite convincingly that the class of patterns which is well represented visually by second-order stochastic models is limited to what are referred to as "microtextures"; that is, textures with a fine grain and little or no geometric structure at medium to large scales (Haralick, 1978; Garber and Sawchuck, 1981; Gagalowicz and Tournier-Lasserve, 1986). Many other approaches to characterization of spatial structure (specifically visual patterns) have been outlined in this body of literature, some of which do not rely on the assumptions of second-order stationarity and are well-suited for characterization of patterns with a variety of types of structure at multiple scales.

Study Objective

The broad objective of the study of spatial structure of natural sediments, as discussed above, is the development of quantitative statements of the nature of spatial structure which will be useful in strengthening model predictions of subsurface transport behavior. Such statements should be formulated both in terms of "typical" patterns and of site-specific variations from those norms, with regard to general classes of soil, sediment, or rock. Since there is a wide diversity of structural character in natural materials, and since the site-specific variability is not well described or understood yet, this objective is far beyond the scope of a single research project.

A more feasible current objective, but one which is consistent with the broad objective above, is to begin to evaluate the impact of the character and scale of spatial structuring of sediment properties on site-specific prediction of subsurface flow and transport. This is the objective of the current study.

The specific goal is to identify and propose appropriate methods for quantification of those elements of the spatial structure of permeability that are in some sense important to transport prediction. Throughout, the impacts of artificial assumptions about geological structure and environment are minimized. The context of this study is the set of transport prediction problems arising in the detection, analysis, and remediation of contamination at individual Superfund or RCRA sites. Thus, the focus is on near-surface environments, relatively small scales (meters to a few kilometers), and problems for which mass transfer and local chemical and biochemical reactions may be important.

Project Description

To attempt to meet these goals, a study was initiated having three basic components:

1) *Develop a detailed data base describing the three-dimensional spatial variability of permeability in a "case-study" geological environment.* Because part of the objective is to explore minimum scales of variability, while avoiding untested assumptions about the importance or unimportance of any particular scale of variability, this data base must necessarily be extraordinarily detailed. However, because permeability measurement data bases do not exist characterizing three-dimensional permeability variability over an aquifer segment on the scale of, say, small laboratory core samples, and because developing such a data base would be enormously expensive, the data base was constructed from available quantitative and qualitative information to be as plausible as possible and as consistent as possible with geological understanding down to the scale of multiple cross-strata. To meet the study goals, it is important that the "numerical aquifer" be constructed without resorting to "non-geological" assumptions about,

say, the stationarity, variance, or two-point correlation structure of the field.

2) *Thoroughly characterize the spatial structure of the "numerical aquifer"*. The objective is to explore the spatial structure of the permeability field, both to compare with common assumptions and models (stationary mean and variance, exponential covariance, etc.), and to identify structural components that may have a significant impact on transport. Measures may be exhaustive (using all data points), or may be sampled (using selected data points). Aggregated and filtered data can also be examined. Quality of fit to existing models of variability is of interest and value. While geostatistical models are important, less-conventional models drawn from the pattern recognition and image analysis literatures can also be used to identify and evaluate structural components other than those normally considered.

3) *Test the relationship between geological structure and transport prediction.* The importance of geological structure depends upon the particular transport problem at hand. Thus, it is necessary to go beyond geometric and statistical characterization to determine those aspects of the geometric and statistical structure of a geological deposit that influence transport. Sensitivity to spatial structure may be systematically explored at increasing spatial scales by removing selected features of the spatial structure. For example, aggregation and filtering are two straightforward techniques for removing structure, which may be applied either to units of the numerical aquifer itself or to deterministic or stochastic models of units of the aquifer.

In the following paragraphs the first phase of the investigation is described: the construction of a high-density, geologically plausible permeability field for an aquifer in unconsolidated point bar sediments. After a more detailed discussion of the criteria used to develop the numerical aquifer, a description of the data and methods which were used to construct the data base is given. Included are several graphical images revealing some features of the resulting permeability field. A brief discussion of the next phase of the study concludes the paper.

A Numerical Aquifer

As noted above, the motivation for this study is primarily the problem of predicting transport in shallow deposits over relatively short distances. Because the objective is to investigate minimum scales of variability and structure which must be considered for successful site-specific prediction, three-dimensional arrays of measured permeability data would be ideal. Some detailed permeability studies using air-minipermeameters have been initiated (e.g. Goggin *et al.*, 1986; Jones *et al.*, 1987; Phillips *et al.*, 1990), but these studies have been primarily in consolidated formations with limited three-dimensional exposure. Unfortunately, to date no unconsolidated aquifer deposit has been quantitatively characterized in three dimensions at a sufficiently fine scale. This leads to the uncomfortable necessity of making assumptions regarding the very thing being studied. However, there is such a wide gap between the scale and character of spatial structure represented by current models of variability and that of natural geological materials that significant advances in understanding can be made by developing a closer, if imperfect, representation of natural structure based on defensible assumptions. For example, Cole and Foote (1987) used land surface elevation data as a model database to represent parameter variation in porous media. While it is clear that topography and permeability are not truly analogous, these authors were able to study the impact of certain aspects of spatial structure not considered in previous models and known to exist in natural porous media.

Criteria

A numerical aquifer was created, based upon geologically-based geometric descriptions of a specific sediment body in combination with available quantitative data

for that body. Two main criteria were applied in order to obtain a database which, although not real, does exhibit characteristics of real structure which were observed at the specific site, and which are not considered in conventional models.

The first criterion was that the numerical aquifer should conform to what is known about the particular deposit it purports to represent, in terms of both available quantitative data and qualitative insights gained through sedimentological study. In particular, it was necessary to avoid simple statistical inferences from widely-spaced measured data that do not explicitly account for geological observations and controls exerted by physical depositional processes.

Second, those models of spatial structure which do explicitly account for geological controls on parameters typically do so at a scale which ignores several levels of highly organized but complex structure, the importance of which is not well understood. Although previous workers have been able to make some statements about minimum resolution scales required, these have been based on assumptions regarding the nature of spatial structure. The second criterion, then, was to attempt to resolve these structures.

Basis

The geometric description of the numerical aquifer was developed primarily on the basis of two specific field studies performed on point bar sediments in the Wabash River (USA) by Pryor (1973) and Jackson (1976). These sediments were selected as the initial basis for the study for several reasons:

- Detailed information regarding the structure of these specific deposits was available, in terms of the qualitative nature of stratification, detailed sketches, and quantitative measurements of permeability.

- These deposits contain a variety of different structural elements and scales, including thin planar beds of low conductivity, trough-shaped elongate (sinuous) beds, angled crossbeds, and fan-shaped avalanche beds. This allows the comparison of these various elements in terms of their impact on transport prediction, and encourages diverse approaches to quantitative modeling of spatial structure.

- The scale at which the deposits are described is quite small, allowing detailed study of the impact of various scale averaging assumptions. Understanding of flow and transport character at this scale provides a necessary building block for study at larger (perhaps more practically important) scales without introducing arbitrary assumptions.

Note that this choice was not made with the intent of obtaining a description which is typical or representative of point bar deposits in general. In fact, these particular sediments exhibit significant variation from the typical (facies) model of point bar deposition, as might be expected for any particular example of a general sediment type. As discussed above, however, the goal is to examine the impact of the character of spatial structure on site-specific transport prediction, rather than to make general statements regarding typical flow and transport behavior in point bar deposits. Nonetheless, the elements of structure which exist in this particular deposit (cross-bedding, fan-shaped beds, elongated beds, and vertical and horizontal trends in permeability) exist in other sedimentary deposits as well; thus the study of their relative importance has general value despite the site-specificity of the absolute results. Furthermore, some other specific examples of point bars may be expected to exhibit similar character of variations from the general facies model because of the similarity of depositional processes (e.g. Nanson, 1980).

Depositional Model

Figure 1, modified from Pryor (1973), is a schematic representation of a block of Wabash River point bar sediments. Three major types of depositional sub-units are labeled. The sequence of sedimentation indicated for this particular depositional system is aggradation of the point bar bank slope by accretion of scroll bars, followed by a period of dune migration and reworking of upper sediments (formation of trough sets), followed finally by nearly continuous sub-aerial exposure during which the point bar is inactive and a fine-grained layer (mud drape) forms by deposition during large flood events. The cycle is repeated at a higher level when a new stream meander passes the location.

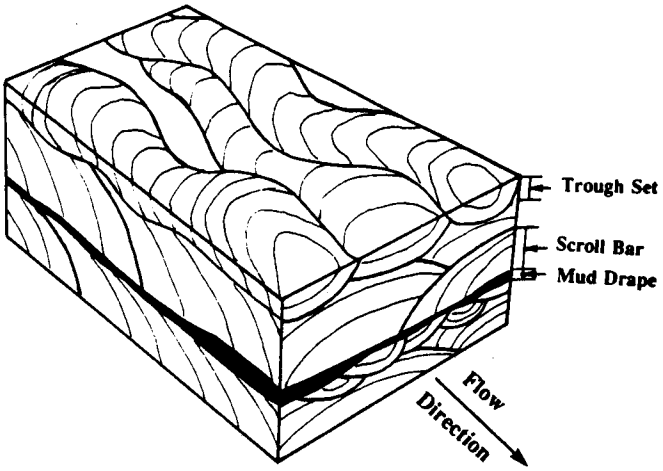

Figure 1. Schematic diagram of Wabash River point bar stratification, after Pryor (1973).

Scroll Bars

Scroll bars, or "sand-scale fronts" in the terminology of Pryor (1973), are elongate, large-scale bedform features of inner banks of gently curved river meanders. They can be up to hundreds of meters long, and up to 200 cm high. Crestlines are oriented approximately parallel to the main river channel and slightly curved to conform to the shape of the point bar. The upper surface of a scroll bar is concave downward, with a steeper slope on the bankward side. The depositional process is non-erosive; the bottom of the bar conforms to the underlying topography. Internal stratification is complex, consisting primarily of local, fan-shaped, avalanche sets. Planar reactivation beds which dip toward the bank and have greater lateral extent also occur. Observed in a section perpendicular to the bar axis, the strata appear tabular to slightly concave-downward; in a section parallel to the bar axis, avalanche fan sets, each concave downward in form, intermesh with planar reactivation beds to create a complex pattern.

Trough Sets

Trough sets are depositional features which result from migration of sub-aqueous dune bedforms (also known as megaripples). Dunes are much smaller features than scroll bars, with short crestlines and heights ranging from 5-120 cm (more frequently at the lower end of this range). Resulting cross-strata appear concave-upward (or trough-shaped) in section perpendicular to flow, thus the term "trough" cross-bedding (or "festoon" cross-bedding). In a section parallel to flow, the strata appear tabular or slightly S-shaped. Trough sets have erosional bases, and are superimposed on larger bedforms such as scroll bars. In plan view, trough sets are slightly sinuous and appear in interwoven groups (see Figure 1).

Mud Drapes

These beds consist of fine-grained sediments (muddy silts) deposited on top of an inactive point bar during receding flood conditions. The beds are sub-horizontal and laterally extensive, with small but variable thickness.

Digital Model

The process used to obtain a digital representation of the numerical aquifer is described in the following paragraphs:

For representation of scroll bars and trough sets, three-dimensional geometric forms have been selected to define the

boundaries of the smallest sedimentation units to be explicitly characterized. At this small scale, two types of elemental forms are defined, elementary rhythm units (Basumallick, 1966) and interbeds. Elementary rhythm units (more completely defined below) are groups of cross-laminae which are characterized by a regular cyclic variation in median grain size, and interpreted as being created during a time period over which the local depositional process is consistent but cyclically variable. Interbeds are relatively thin laminae which are to be interpreted as forming during a local hiatus or transition in the process of elementary unit deposition; these are slightly finer grained, deposited from near-bed suspended load rather than by avalanching of bedload. The geometric forms used to represent units within scroll bars vary from those of trough sets, in accordance with the depositional model for (and observed geometries of) each. The internal structure of each scroll bar or trough set to be represented is constructed by superposition of the elemental forms (interbeds and elementary rhythm units). External boundaries of scroll bars and trough sets have also been assigned specific geometric shapes, representative of the geometries of each as described in the previous section. Once the overall shape and internal structure of a particular scroll bar or trough set has been defined geometrically, a uniform fine grid is overlaid. Geometric boundaries enclosing the centerpoint of each grid block define the sediment type at that coordinate location, allowing assignment of a sediment classification to the grid block.

The process used to represent the mud drape is somewhat different. Because the drape was observed to be laterally extensive and smoothly varying in thickness, and exhibits little or no internal structure, a smooth and continuous drape was constructed for the numerical aquifer by simply interpolating from a coarse grid of thicknesses chosen to reproduce the mean thickness and qualitative variation in thickness shown in diagrams in Pryor (1973) and others. Figure 2 shows the resulting contour map of drape thicknesses. Quantitative justification for the assumption of continuity of the drape at the study scale is available (e.g. Geehan *et al.*, 1986, Figure 11). However, because the mud drape units were not studied in much detail by Pryor (1973) or Jackson (1976), the method used to interpolate smooth thicknesses (and permeabilities as described in the following section) relied on inherently non-geological assumptions. Because of the potentially great impact such low-permeability, highly connected units may have on fluid flow patterns, the impact of these assumptions will be tested during later stages of the study.

Once each scroll bar, trough set, and mud drape is in digital form at the same discretization scale and within the same coordinate framework, it is a straightforward task to combine them to form the digital representation of the overall sediment body.

Assumptions introduced at this stage of representation relate to the scale of characterization, continuity of individual units, and imposition of irregularity (randomness) upon the geometric structure.

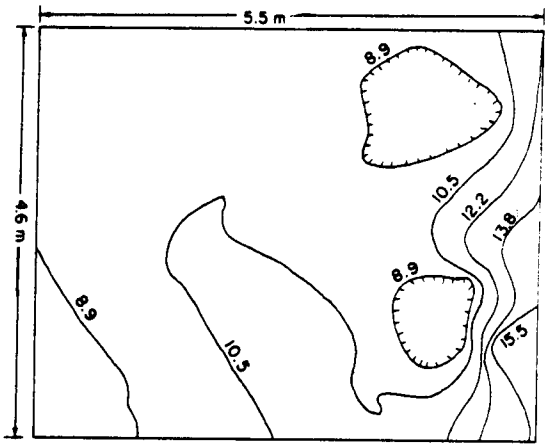

Figure 2. Contour map of mud drape thicknesses (cm).

Scale of Characterization

Basumallick (1966) performed a field study of point bar sediments at a very small scale. Lacquer peels were made in the field, then individual laminae (of the order of millimeters in thickness) were sawed out and grain size analyses performed. He observed the occurrence of groups of adjacent laminae within which a cyclic and quite regular

pattern of variation was present. Figure 3 shows two examples of median grain size variation from one lamination to the next within a single group.

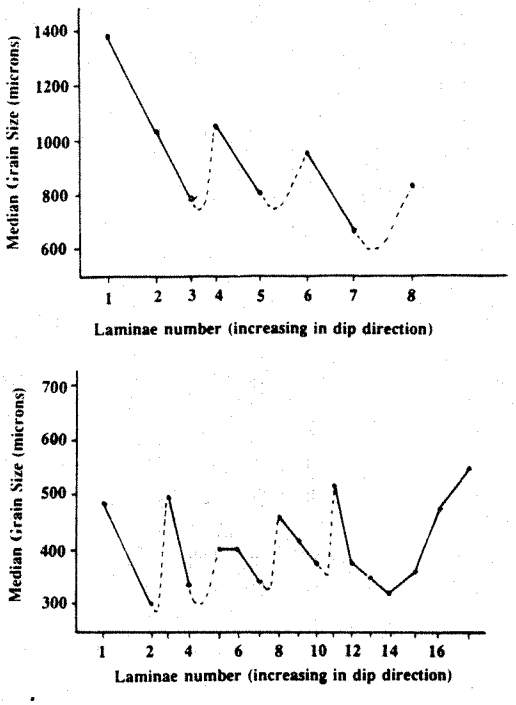

Figure 3. Variation of median grain size in successive laminae within a point bar cross-stratified unit, from Basumallick (1966).

These groups of laminae were termed "elementary rhythm units", and Basumallick (1966) proposed a hierarchy of scales based on them: Trough sets and avalanche fan sets, referred to as "ripple bodies" and "delta lobes", were observed to consist of a number of distinguishable elementary rhythm units; in turn, "cross-stratified units", corresponding to scroll bars or groups of trough sets, were composed of several ripple bodies or delta lobes. To take the hierarchy a step further, a morphological unit (i.e. a point bar) is composed of several cross-stratified units. This hierarchy of scales of structured variation, relating terms used by Basumallick (1966) to terms used here, is summarized in Table 1.

Table 1

Hierarchy of sedimentation scale proposed by Basumallick (1966), and corresponding geometric elements used in simulation

Basumallick Unit Type	Corresponding Geometric Element	Relative Scale
Cross-Lamination	———	Smallest
Elementary Rythym Unit	Fan or Trough Crossbed	↕
Ripple Body/Delta Lobe	Trough Set/Avalanche Bed Set	↕
Cross-Stratified Unit	Scroll Bar/Group of Trough Sets	↕
———	Point Bar	Largest

This hierarchical structure forms the basis for the choice of a lower limit for the representation of explicit geometric structure. The geometry was characterized down to the scale of the elementary rhythm unit, neglecting the variability between individual cross-laminae within an elementary rhythm unit.

Bed Continuity

Bed continuity is clearly one aspect of spatial structure which may be important to flow and transport. Therefore, assumptions about bed continuity must be approached with caution. While there are relatively few data describing continuity, two observations are helpful: First of all, the process of deposition of thin units (i.e. interbeds, see Figure 4) can be inferred to produce beds of increasing thickness and continuity in the downward direction, as dip angles become less steep. Secondly, elementary rhythm units generally do not lose continuity. It was assumed that elementary rhythm unit geometries within scroll bars and trough sets are continuous. Further, the scale of digitization (pixel size) was selected such that continuity was lost only for very thin (interbed) units, and that loss tended to occur only where the units were steeply angled (see Figure 4).

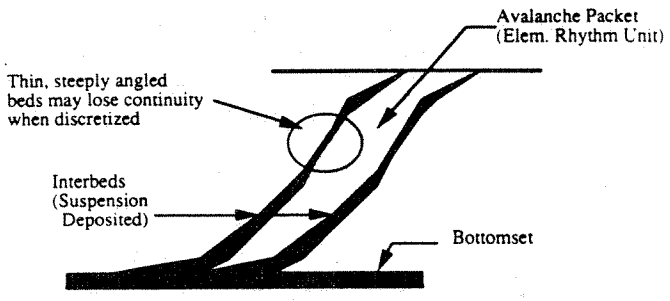

Figure 4. Schematic sketch showing terminology used for small-scale stratification units.

Irregularity

Available information indicates that the individual beds of which the numerical aquifer is composed have variable thickness, orientation, and shape. However, no quantitative geometric data were available. Therefore, as an initial approximation, parameters of the geometric model such as angles and lengths were generated from low-variance normal distributions so that the resulting images qualitatively match field sketches such as that shown in Figure 5, taken from Pryor (1973).

Permeability Assignment

The model used to assign sediment classifications (depositional unit types) to grid blocks at a fine scale has been discussed. The final step in generation of the parameter field was to assign permeability values to each grid location according to some relation between sediment classification and permeability. Here again the study suffered from a lack of observed data. Therefore, permeabilities were assigned on the basis of:

- Available quantitative measurements (Basumallick, 1966; Weber *et al.*, 1972; Pryor, 1973; Weber, 1982).
- Qualitative and quantitative descriptions of overall trends (Basumallick, 1966; Jopling, 1967; Pryor, 1973).

It has already been noted that geometric variations at scales smaller than the "elementary rhythm unit" are not explicitly characterized. Similarly, permeability values were assigned to be constant within these units, except for the imposition of a trend of increasing permeability downward along the unit. This trend is inferred from the documented increasing median grain size along the unit.

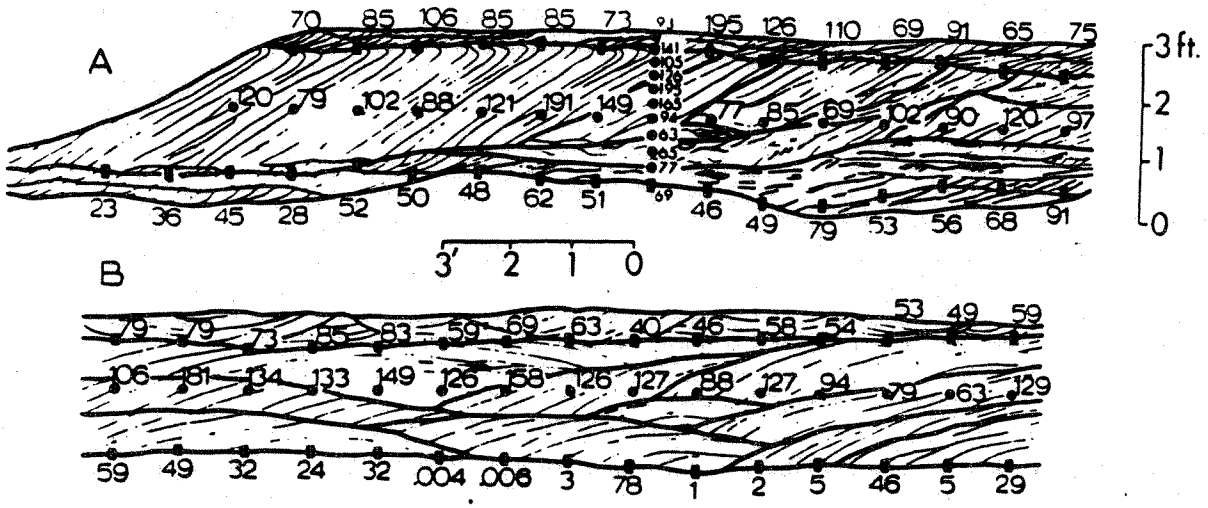

Figure 5. Sketch of point bar stratification observed in trenches, with measured permeabilities (Darcys) from Pryor (1973). Section A is parallel to flow direction; section B is perpendicular.

some variations were modeled. The only variation imposed at the bed scale was assignment of one permeability for elementary units and another for interbeds, reflective of the weak variation in mean grain size in adjacent elementary units within a particular ripple lobe or delta body (Basumallick, 1966). Variability at the larger bed set scale (i.e. trough set or avalanche fan set scale) was represented by low-variance normal distributions derived from a combination of quantitative measurements and field drawings at the Wabash River sites, and substantiated by other quantitative studies in similar sediments. Pryor (1973) reported results of some measurements made on samples taken from trench walls; Figure 6 shows a histogram of these data.

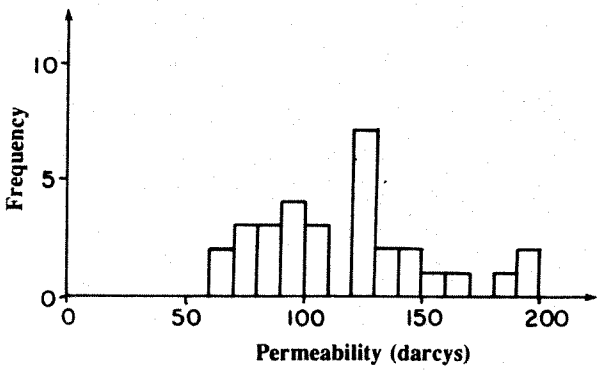

Figure 6. Histogram of permeability data measured by Pryor (1973).

The sample scale was such that it encompassed multiple laminae, and was thus representative of the average permeability of either an elementary unit or an interbed, depending on the location of the sample. Sample spacing was large enough that adjacent samples were in different bed sets, so that the variability represented is that of the bed set scale. Although the number of data was too small to make definitive statistical statements, the histogram lends qualitative support to the concept (based on the depositional model) of a frequency distribution with two closely spaced modes, or more precisely, two overlapping low-variance distributions corresponding to elementary rhythm unit and interbed permeabilities. Using this concept, the mean value and variance reported by Pryor (1973), supported by data from Weber (1982), was distributed among three sources of variation: 1. A distribution of permeabilities for elementary units, 2. a distribution for interbeds, and 3. superimposed trends. By this approach, and based upon the volumetric fraction of each sediment type, a mean value and variance of elementary unit permeability, a mean and variance of interbed permeability, and a trend slope were calculated. A linear form was assumed for the trend, with a magnitude accounting for 30% of the total variance. Finally, the thin units which form the lower external boundaries of trough sets (called bottomsets) were given permeability values which were lower than those of the overlying crossbeds by factors of 2 to 4, depending on the size of the trough set unit; this assignment is based on data reported by Weber *et al* . (1972).

Assignment of permeability values to mud drape sediments was based on a similar process to that used to assign drape thicknesses. The mean and variance of a low-variance normal distribution were estimated from available data (Pryor, 1973), and sample values from this distribution were smoothly interpolated over the drape volume.

Sample Images

Using the above methodology a complete description of a realistic sediment body analogous to that shown schematically in Figure 1 was constructed. The discretization grid for assigning permeability contains 1440 x 1200 x 480 (nearly 900 million) cubic elements, 3.8 mm on each side. Several individual cross-sections through the sediment body were generated in each of the three principal orientations; these have been used for some preliminary two-dimensional structural analysis and for visual verification.

Figure 7A shows a cross-section through the entire sediment body, with gray scale values representing permeability. Because it may be difficult for the reader to resolve individual scroll bars and trough units, a tracing of the boundaries of these

units is given as Figure 7B. Figures 8 and 9 are enlarged views of an individual scroll bar and trough set cross-section, respectively, and show the internal detail of each.

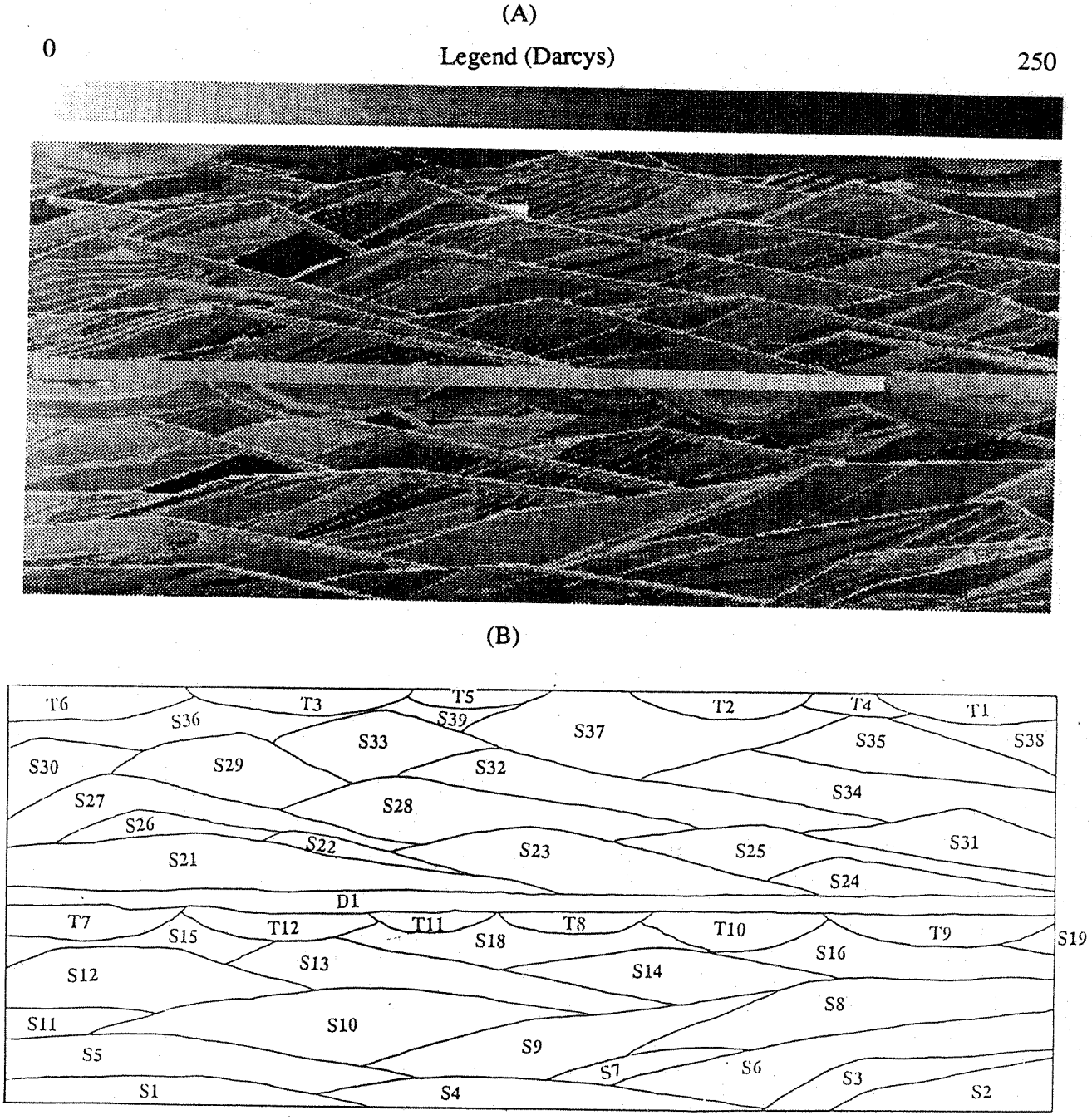

Figure 7. Permeability field of a cross section, perpendicular to flow direction, through the simulated sediment body: A. Grey scale map; B. Tracing of outllines of depositional units (S=scroll bar, T=trough set, D=mud drape).

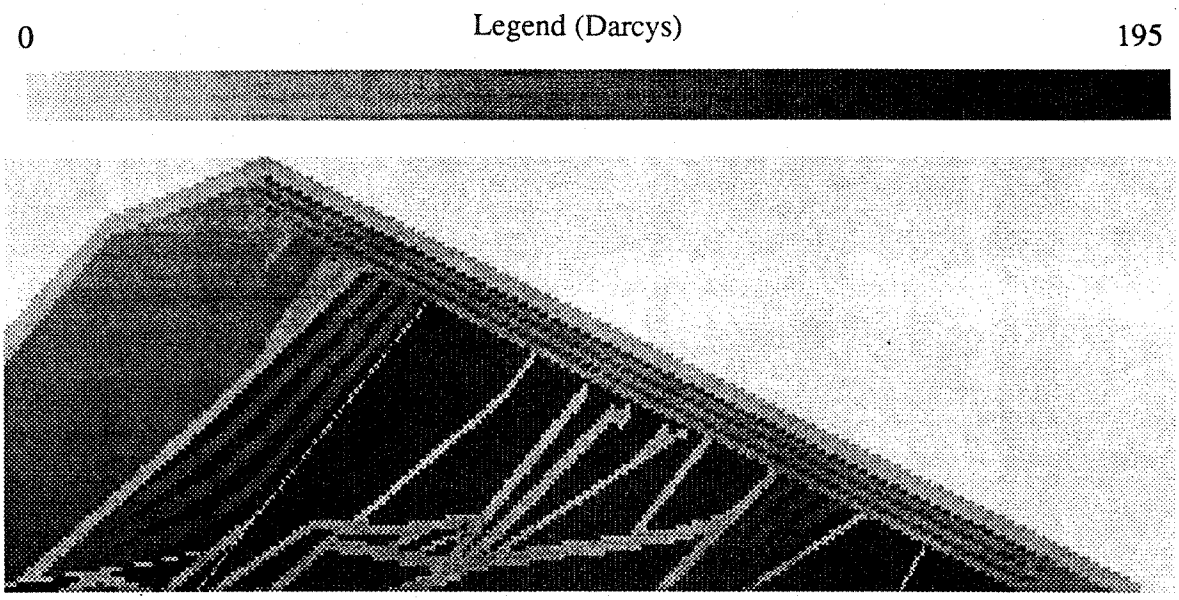

Figure 8. Permeability field of a cross section through an individual scroll bar (S13 in Figure 7B). Vertical exaggeration = 2.67.

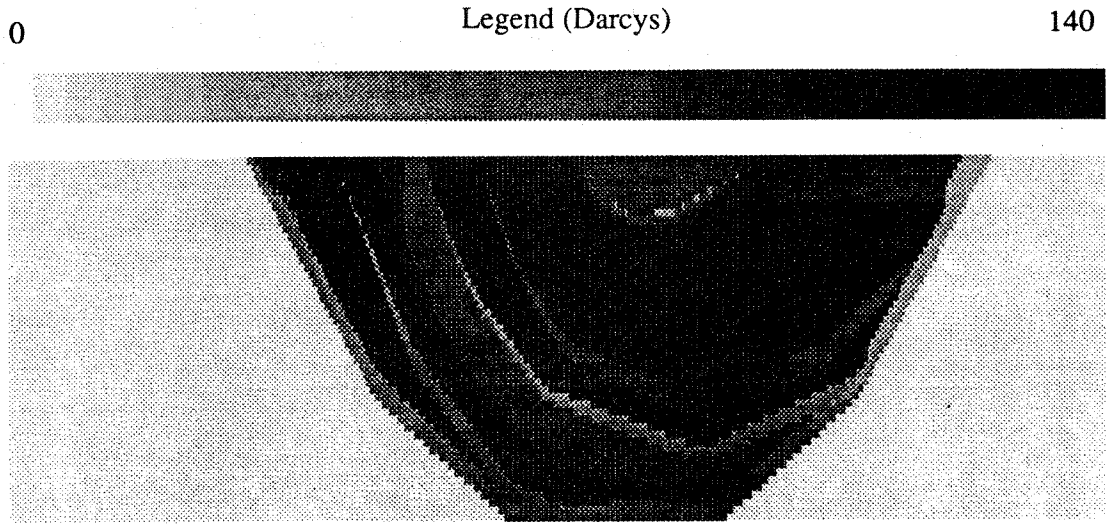

Figure 9. Permeability field of a cross section through an individual trough set (T12 in Figure 7B). Vertical exaggeration = 3.0.

Planned Study and Analysis

The numerical aquifer which has been developed holds promise for study in several important areas. Three such areas of study are outlined below, with specific examples.

First, the validity of assumptions used in conventional models of spatial structure can be assessed. Because complete knowledge of the parameter space is available, spatial moment functions (usually assumed to equal ensemble moment functions via the ergodic hypothesis) can be computed without sampling error. Assumptions of second-order stationarity and isotropy of the spatial distribution, as well as goodness-of-fit to commonly used moment function models (e.g. exponential covariance) can be assessed. Plots of spatial moment functions can be examined visually for evidence of nested scales of variability.

Second, several alternative means of representing the spatial structure of the numerical aquifer can be explored. Examples include shape-oriented analyses (Pavlidis, 1978; Leu and Wee, 1985), methods which quantify connectedness of flow paths (Ronse and Devijver, 1984; Journel and Alabert, 1988), higher-order statistical analyses (Gagalowicz and Tournier-Lasserve, 1986), and structural approaches to texture analysis (Garber and Sawchuck, 1981). Consideration of alternative approaches to structural characterization is aimed at determining those aspects of spatial structure emphasized or best characterized by each model, and at determining which models are best suited to visual representation of the structure of the numerical database.

The most important question to be addressed through analysis and study of the numerical database is: Which aspects and scales of spatial structure, among those exhibited in the study aquifer, are most critical to good prediction of site-specific transport behavior? This question will be addressed through a sequence of comparative modeling studies. Having explored a variety of spatial structure models, the particular aspects of structure well represented by each model will be known. Therefore, it will be possible to systematically modify the parameter space (i.e. filter out particular aspects of the structure) and compare the resulting model predictions. In addition, various upscaling (or effective parameter) approaches can be applied to assess the impacts of structural assumptions required in each upscaling approach, and to determine whether there is some minimum scale of heterogeneity which must be characterized to obtain a good prediction. Finally, since there is no single predictive measure of transport behavior, it will be of interest to explore several different measures (for example, breakthrough curves at selected points as well as spatial moments of contaminant plumes).

Summary

Increased reliability of subsurface transport prediction models requires greater understanding of the character and impacts of spatial structure in geological media.

One approach to gaining such understanding is the application of geological information (field observations and understanding of depositional mechanisms) to develop realistic representations of natural sediment bodies. While finely detailed quantitative measurements of actual sediments are lacking, this approach nevertheless allows characterization at a much finer scale, and with fewer "non-geological" assumptions, than has previously been attempted.

This approach was used to define the detailed permeability structure of a coarse-grained point bar deposit. It is believed that this "numerical aquifer" contains realistic elements of geological structure, and therefore is a valuable resource for the study of spatial structure and its impacts on transport prediction.

As the next stage of our study, we plan detailed characterization of the spatial structure of the numerical aquifer, using both conventional and alternate models, with the following goals:

1. to compare the structure of the numerical aquifer to that represented by models commonly assumed for parameter estimation procedures in subsurface flow and transport modeling,

2. to explore alternative ways of representing the structure of the numerical aquifer using non-conventional models, and

3. to evaluate the impact of assumptions required in formulation of various models of spatial structure upon prediction of flow and transport.

Timothy D. Scheibe received a B.S. degree in geological engineering from Washington State University in 1984, and an M.S. degree in civil engineering from the University of Washington in 1987. He is currently a research assistant pursuing a Ph.D in civil engineering at Stanford University (Department of Civil Engineering, Stanford University, Stanford, CA 94305-4020), where his research interests are in the area of characterization of geological variability and its impacts on subsurface flow and transport.

David L. Freyberg is Associate Professor of Civil Engineering and Associate Dean of Engineering for Undergraduate Education at Stanford University (Department of Civil Engineering, Stanford University, Stanford, CA 94305-4020). After receiving A.B. and B.E. degrees from Dartmouth College in 1972, he spent three years in consulting practice in Boston, Massachusetts. In 1977, he received an M.S. degree from Stanford University. He completed his Ph.D. at Stanford in 1981 and has been on the faculty since then. In addition to his responsibilities as Associate Dean, he is the leader of the Water Resources Program in the Department of Civil Engineering. His research interests center on transport in the subsurface, with a particular emphasis on understanding and modeling the effects of spatial variability and parameter uncertainty on transport prediction and model validation. He is a recipient of a 1985 Presidential Young Investigator Award.

References

Anderson, M. P. 1989. Hydrogeologic facies models to delineate large-scale spatial trends in glacial and glaciofluvial sediments. Geol. Soc. of Am. Bull., v. 101, pp. 501-511.

Basumallick, S. 1966. Size differentiation in a cross-stratified unit. Sedimentology, v. 6, pp. 35-68.

Cole, C. P. and H. P. Foote. 1987. Use of a multigrid technique to study effects of limited sampling of heterogeneity on transport prediction. *In* Solving Groundwater Problems with Models, Nat. Well Water Assoc., pp. 355-380.

Dagan, G. 1982. Stochastic modeling of groundwater flow by unconditional and conditional probabilities. 2. The solute transport. Water Resour. Res., v. 18, pp. 835-848.

Fraser, G. S. and N. K. Bleuer. 1987. Use of facies models as predictive tools to locate and characterize aquifers in glacial terrains. Proc. of the NWWA Focus Conf. on Midwestern Ground Water Issues, Nat. Well Water Assoc., pp. 123-143.

Freeze, R. A. 1975. A stochastic-conceptual analysis of one-dimensional groundwater flow in nonuniform heterogeneous porous media. Water Resour. Res., v. 11, pp. 725-741.

Freyberg, D. L. 1986. A natural gradient experiment on solute transport in a sand aquifer: 2. Spatial moments and the advection and dispersion of nonreactive tracers. Water Resour. Res., v. 22, pp. 2031-2046.

Gagalowicz, A. and C. Tournier-Lasserve. 1986. Third-order model for nonhomogeneous natural textures. Proc. 8th Inter. Conf. on Pattern Recognition, 409-411, 1986.

Garber, D. D. and A. A. Sawchuck. 1981. Computational models for texture analysis and synthesis. Proc. of SPIE - The Inter. Soc. for Optical Engin., v. 281, p. 254-72.

Geehan, G. W., T. F. Lawton, S. Sakurai, H. Klob, T. R. Clifton, K. F. Inman and K. E. Nitzberg. 1986. Geologic prediction of shale continuity: Prudhoe Bay field. *In* Reservoir Characterization (eds. L. W. Lake and H. B. Carroll, Jr.), Academic Press, pp. 63-82.

Gelhar, L. W. and C. L. Axness. 1983. Three-dimensional stochastic analysis of macro-dispersion in aquifers. Water Resour. Res., v. 19, pp. 161-180.

Goggin, D. J., M. A. Chandler, G. A. Kocurek and L. W. Lake. 1986. Patterns of permeability in eolian deposits. Soc. Petrol. Engin. Paper 14893 presented at the 1986 SPE/DOE Enhanced Oil Recovery Symp., pp. 181-198.

Haralick, R. M. 1978. Statistical and structural approaches to texture. Proc. 4th Inter. Joint Conf. on Pattern Recognition, pp. 45-69.

Jackson, R. G. II. 1976. Largescale ripples of the lower Wabash River. Sedimentology, v. 23, pp. 593-623.

Jones, J. R., A. J. Scott, and L. W. Lake. 1987. The geologic aspects of reservoir characterization for numerical simulation: Mesaverde meanderbelt sandstone, northwestern Colorado. Soc. Petrol. Engin. Formation Evaluation, v. 2, pp. 97-107.

Jopling, A. V. 1967. Origin of laminae deposited by the movement of ripples along a stream bed: A laboratory study. J. Geol., v. 75, pp. 287-305.

Journel, A.G. and F. Alabert. 1988. Focusing on spatial connectivity of extreme-valued attributes: Stochastic indicator models of reservoir heterogeneities. Soc. Petrol. Engin. Paper 18324 presented at the 63rd Ann. Tech. Conf. and Exhib., Houston, Texas, Oct. 2-5, 1988.

Leu, J. G. and W. G. Wee. 1985. Detecting the spatial structure of natural textures based on shape analysis. Computer Vision Graphics and Image Processing, v. 31, pp. 67-88.

Nanson, G. C. 1980. Point bar and floodplain formation of the meandering Beatton River, northeastern British Columbia, Canada. Sedimentology, v. 27, pp. 3-30.

Neuman, S. P., C. L. Winter and C. M. Newman. 1987. Stochastic theory of field-scale Fickian dispersion in anisotropic porous media. Water Resour. Res., v. 23, pp. 453-466.

Pavlidis, T. 1978. A review of algorithms for shape analysis. Computer Graphics and Image Processing, v. 7, pp. 243-258.

Phillips, F. M., J. M. Davis, A. L. Gutjahr and D. W. Love. 1990. A quantitative geological study of heterogeneity, Sierra Ladrones Formation, Central New Mexico (abstract). Eos, v. 71, p. 509.

Pickens, J. F. and G. E. Grisak. 1981. Scale-dependent dispersion in a stratified granular aquifer. Water Resour. Res., v. 17, pp. 1191-1211.

Pryor, W. A. 1973. Permeability-porosity patterns and variations in some Holocene sand bodies. Am. Assoc. Petrol. Geol. Bull., v. 57, pp. 162-189.

Ronse, C. and P. A. Devijver. 1984. Connected components in binary images: The detection problem. New York: Wiley, 165 pp.

Stalkup, F. I. 1986. Permeability variations observed at the faces of crossbedded sandstone outcrops. *In* Reservoir Characterization (eds. L. W. Lake and H. B. Carroll, Jr.), Academic Press, pp. 141-179.

Szpakiewicz, M., K. McGee and B. Sharma. 1987. Geologic problems related to characterization of clastic reservoirs for EOR. Soc. Petrol. Engin. Formation Evaluation, v. 2, pp. 449-460.

Sudicky, E. A. and J. A. Cherry. 1979. Field observations of tracer dispersion under natural flow conditions in an unconfined sandy aquifer. Water Poll. Res. in Canada, v. 14, pp. 1-17.

Weber, K. J., R. Eijpe, D. Leijnse and C. Moens. 1972. Permeability distribution in a Holocene distributary channel-fill near Leerdam (The Netherlands). Geol. en Mijnbouw, v. 51, pp. 53-62.

Weber, K. J. 1982. Influences of common sedimentary structures on fluid flow in reservoir models. J. Petrol. Tech., v. 34, pp. 665-672.

Reservoir Characterization Case Study: Sandy Facies

by John Kramers, Li-Ping Yuan, Stefan Bachu and David Cuthiell

Abstract

The Provost Upper Mannville B Pool in east central Alberta is contained in McLaren Formation sands of Lower Cretaceous age. The reservoir provides an ideal case study for developing reservoir characterization techniques because several scales of heterogeneity are present and because there is a high density of wells, with excellent core and a suite of modern geophysical well logs. The reservoir is up to 35 m thick, and original oil-in-place has been estimated at 34.2 x 10^6 m^3 of 13^o API oil. Wells in the reservoir have primary production and several EOR projects are or have been active in the pool.

The reservoir sands were deposited in fluvial environments in a valley fill setting. They consist of an overall fining upward sequence and can be divided into a lower blocky channel lithofacies, making up most of the reservoir, grading up through a transition zone lithofacies into a channel margin lithofacies. This in turn is overlain by overbank and abandonment lithofacies. Within the blocky channel and transition zone lithofacies there is a shale clast lithofacies, comprised of extremely heterogeneous zones of shale breccia in a sand matrix. The reservoir can be divided into two main portions, a relatively "uniform" sandy part and a heterogeneous portion comprised of shale clast breccia. Petrophysical properties, such as permeability, can be estimated for each of these using different techniques. Four flow units were recognized in the sandy portion of the reservoir based on lithology, porosity and permeability measurements, and supported by results from pore-type definition using petrographic image analysis techniques. These are: the water-saturated blocky channel sands, the oil-saturated blocky channel sands, the transition zone sands, and the channel margin sands. The flow units were characterized using statistical averaging of core analysis data on a well and pool wide basis. This characterization for each of the flow units produces information at the scale required for numerical process simulation and basin modelling.

Introduction

The oil sands and heavy oil deposits of Western Canada with resources of 471.6 x 10^9 m^3 bitumen (Outtrim and Evans, 1978; MacCallum and McCrossan, 1979; Wilson and Bennet, 1985) are North America's largest petroleum energy resources. However, only a small portion (~ 5%) is recoverable by surface mining methods, the remainder must be recovered by *in situ* techniques. These oil sands and heavy oil reservoirs are heterogeneous and complex, and similar to enhanced recovery of conventional oil reservoirs, requires an integrated team with expertise in geology, petrophysics, reservoir engineering and numerical modelling to develop recovery strategies for individual reservoirs based on an understanding and characterization of the reservoir. With this in mind, the Alberta Geological Survey, through its Joint Oil Sands Geology Program with the Alberta Oil Sands Technology and Research Authority (AOSTRA) and the Alberta Department of Energy, initiated a project with the objective to develop and evaluate techniques for the detailed characterization of oil sands and heavy oil reservoirs for use in numerical process simulations.

This paper reports on studies carried out for the sandy portions of the Provost Upper Mannville B Pool, which has been characterized from the pore scale to the reservoir flow unit scale using a variety of techniques ranging from petrographic image analysis to statistical

methods. Characterization of the more heterogeneous portions of the reservoir was carried out using numerical modelling of fluid flow through two-dimensional domains based on images of actual core-size regions, and then scaling these results up to the reservoir scale. These results have been reported by Bachu and Cuthiell (1990), Bachu et al. (1991), and Cuthiell et al. (1990). The combination of these approaches in one multidisciplinary project has provided a comprehensive quantitative characterization of all the reservoir flow units, suitable for numerical simulation studies.

The Provost Upper Mannville B Pool was chosen for study because of: 1. it's limited stratigraphic and areal extent; 2. good data control (logs and core); 3. a variety of reservoir conditions (such as bottom water, gas cap and permeability barriers); and 4. because several EOR projects are, or have been active in the pool. In addition, data on its reservoir properties, useful for numerical process simulation, are available in the public domain through a series of Petroleum Recovery Institute reports (Collins, 1977; Collins and Pilles, 1981; Hayashitani and Davis, 1981), and papers by Nazarko (1983) and Salahub and Mudie (1990) describing several pilot projects in the reservoir.

Reservoir Geology

The Provost Upper Mannville B Pool is located in east-central Alberta, Canada near the Alberta-Saskatchewan border, and occupies most of the northern half of Tp 36 and the western half of Tp 37, R 1 W4 Mer (Figure 1). The reservoir is located in McLaren Formation channel sands of Upper Mannville (Lower Cretaceous) age (Figure 2), at a depth of ~725 m KB. The Alberta Energy Resources Conservation Board has estimated original oil in place at 34.2 x 10^6 m^3 of 13° API oil. The reservoir is long and narrow, ~ 1.5 km wide by 15 km long, and up to 35 m thick, with an average net pay of 10-12 m. It is underlain by shales and silts of the Waseca Formation and capped by the upper McLaren Formation shales and the overlying Colony Formation.

The mixed marine and continental sand/shale succession of the Lower Cretaceous

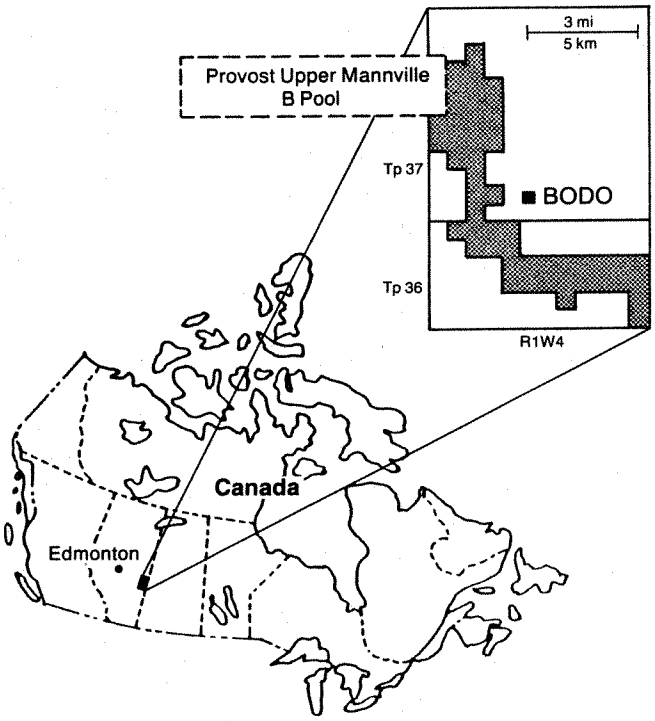

Figure 1. Location of the Provost Upper Mannville B Pool.

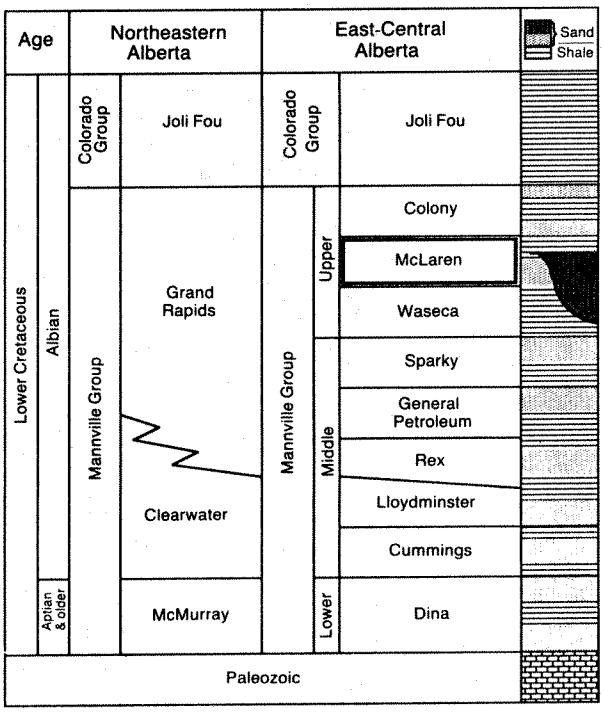

Figure 2. Lower Cretaceous stratigraphy in northeastern and east-central Alberta.

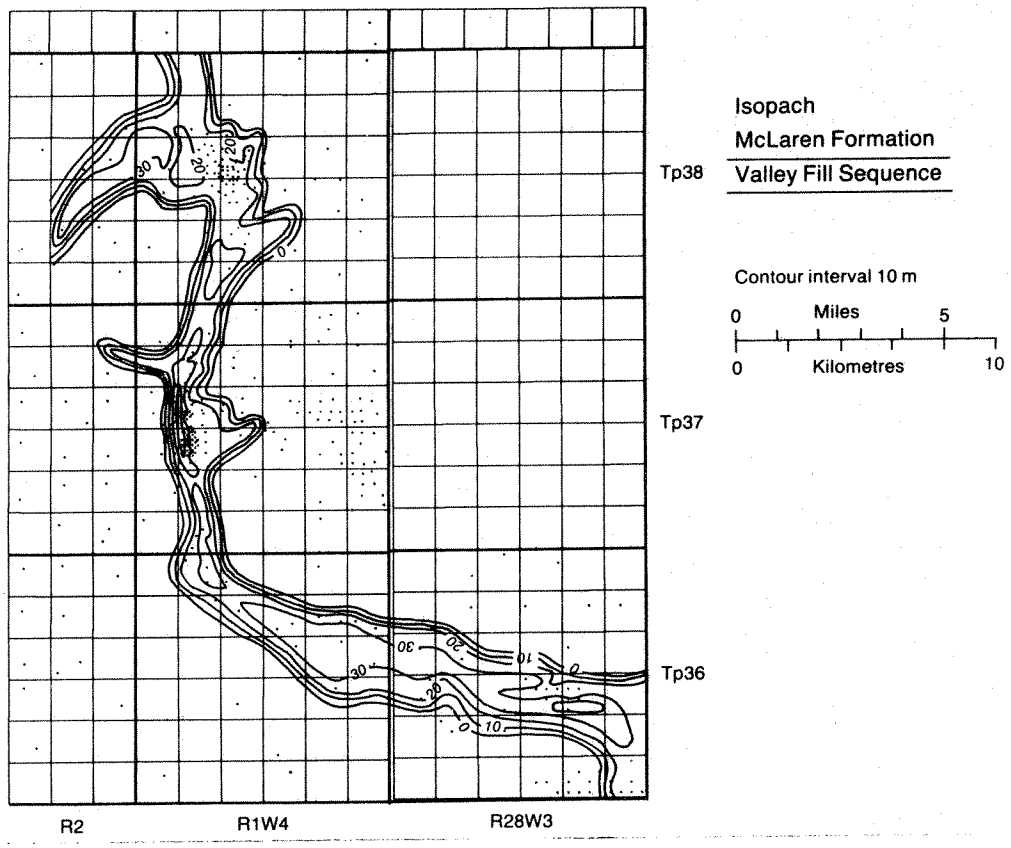

Figure 3. Isopach of McLaren Formation valley fill sequence.

Mannville Group (Figure 2) unconformably overlies Paleozoic carbonate rocks and in turn is unconformably overlain by the marine Joli Fou shales of the Colorado Group. The McLaren Formation along with the overlying Colony and underlying Waseca Formations makes up the Upper Mannville Group. The regional setting of the Mannville Group in Alberta has been discussed by numerous authors. The most recent detailed treatment is provided by Jackson (1984), in a series of paleogeographic maps covering selected time intervals through the Mannville Group. Gross (1980, 1981a, b) has considered the Provost Upper Mannville B Pool.

A number of depositional cycles are recognized within the Mannville Group. Sheet sands, consisting of one or more coarsening upward shale to sand sequences can be correlated over large areas using a combination of geophysical well logs and cores. A number of thick, linear-trending sand bodies, generally considered to be of channel origin by most authors, cut through these regional sand cycles. In the Provost area, following depostion of the shallow marine and nearshore regional McLaren Formation sediments, there was a lowering of relative sea level which resulted in the cutting of a valley system. The extent of this valley is shown in Figure 3. As base level rose again, due to a rise in relative sea level, this valley was aggraded and the valley fill sediments were deposited. The sequence of lithologies and sedimentary structures indicates a sandy, fluvial system origin for the valley fill sediments. A modern example of similar depositional conditions is found in the sandy braided river deposits of the South Saskatchewan River in central Saskatchewan (Cant and Walker, 1978).

Lithofacies

The McLaren Formation in the Provost area can be subdivided into a regional McLaren and a

McLaren valley fill sequence. Figure 3, an isopach of the valley fill sequence, shows the location of the McLaren valley. Figure 4 is a west-to-east stratigraphic cross section showing the geometry of the valley fill, which can be subdivided into six distinct lithofacies, recognizable on geophysical well logs and in cores. Figure 5 shows the gamma ray and resistivity logs for a typical well, with lithology, lithofacies, and oil saturation. Because the Provost Upper Mannville B Pool reservoir is contained within four of the valley fill lithofacies (the blocky channel, transition zone, shale clast, and channel margin lithofacies, in ascending order), only these lithofacies will be considered further. A detailed description of all the lithofacies has been presented by Kramers et al. (1989).

Blocky Channel Lithofacies

The blocky channel lithofacies forms the main part of the reservoir. It consists of trough and planar cross bedded, well sorted, quartz-rich sands. Grain size varies from medium grained at the base to fine-to medium-grained near the top. This is the thickest of all lithofacies, up to 20-25 m, and is interpreted as having been deposited in the main part of the channel complex that occupied the McLaren valley.

Transition Zone Lithofacies

This lithofacies overlies and is transitional with the underlying blocky channel lithofacies and grades upward into the overlying channel margin lithofacies. It represents the fining upward from the blocky channel sands to the finer grained channel margin sands. Grain size ranges from fine-to medium-grained to very fine-grained at the top. Sedimentary structures vary from cross bedding at the base to laminations, ripple laminations, ripples and climbing ripples near the top. The thickness is highly variable, but can be up to 5 m.

Channel Margin Lithofacies

The channel margin lithofacies is the uppermost sandy facies. Grain size varies from fine- to very fine-grained at the base to silty at the top. At the transitional base the sand is relatively clean, but quickly becomes argillaceous and has interbedded shale and silty shale beds near the top. Thickness varies from 1 to 5 m. Deposition of this facies is interpreted as having occurred in the margins of the channel complex, on the edge of and on top of point bars.

Shale Clast Lithofacies

The shale clast lithofacies occurs within the blocky channel and transition zone lithofacies and could be considered a subfacies. It consists of shale, silty shale or carbonaceous siltstone clasts in a matrix of fine- to medium-grained heavy oil sands. The clasts vary in size from several millimetres to decimetres. Shapes vary from equant to flat, and from well rounded to very angular. Density of clasts varies from an occasional clast to as high as 70% in core cross section.

Gross thickness of the shale clast lithofacies is up to 14 m, with the thickest continuous zone being 3 m. Lateral continuity of intervals with shale clast zones is predicted to be of the order of tens to hundreds of metres. Figure 6 shows the areas within the reservoir where shale clast zones have been identified from cores and geophysical well logs. The shale clast lithofacies is interpreted as having been deposited in the main part of the channel complex with the clasts coming from erosion of the channel cutbank. Shale clast zones are not unique to the Provost Upper Mannville B Pool, and can occur in any reservoir of channel origin.

The Reservoir

The Provost Upper Mannville B reservoir is contained entirely within the blocky channel, transition zone, shale clast and channel margin lithofacies of the McLaren valley fill sequence. Figure 7 is an isopach of these four lithofacies and is equivalent to the gross reservoir thickness. From this figure it can be seen that the maximum reservoir thickness of 35 m occurs in Sec 17 to 20, in Tp 37, R 1 W4 Mer. As shown in Figure 8, maximum net pay varies from 13 m in the southern portion of the pool to 26.5 m in the northern portion of the pool.

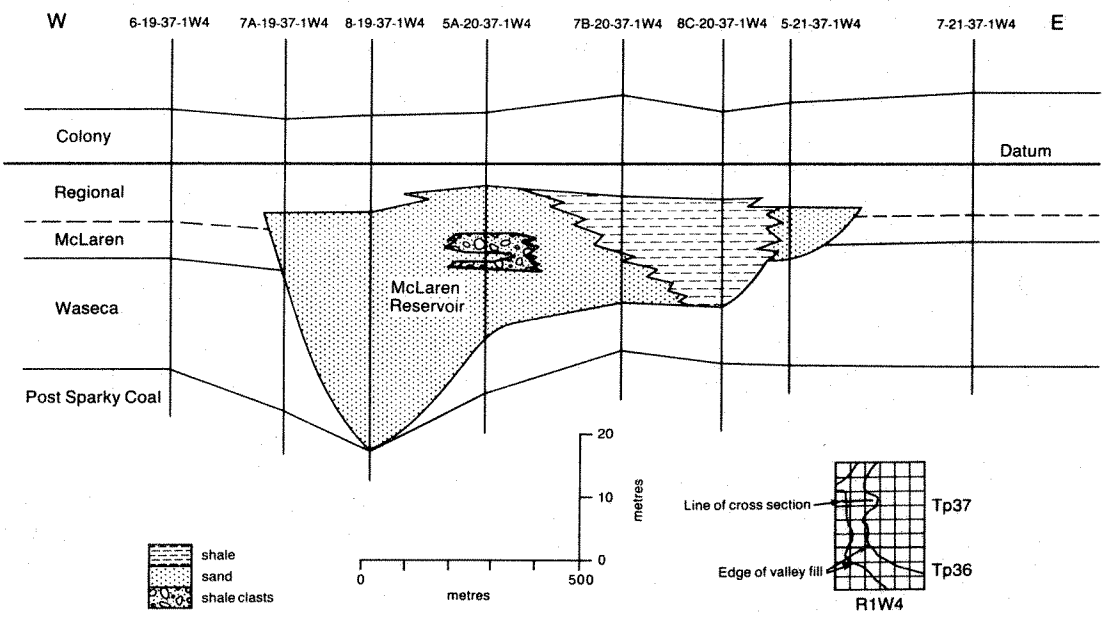

Figure 4. West to east stratigraphic cross section through the Provost Upper Mannville B Pool.

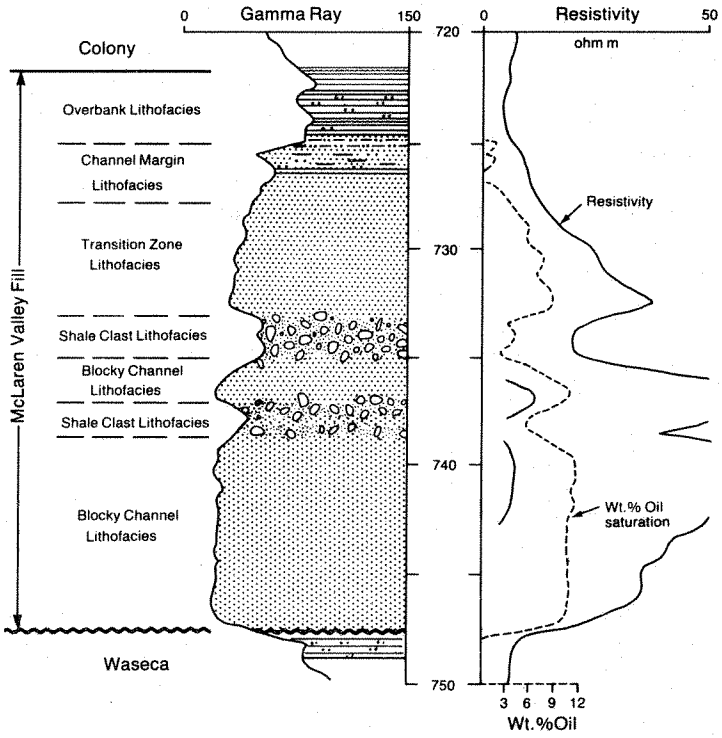

Figure 5. Typical well log from the Provost Upper Mannville B Pool showing four of the five lithofacies of the McLaren valley fill sequence.

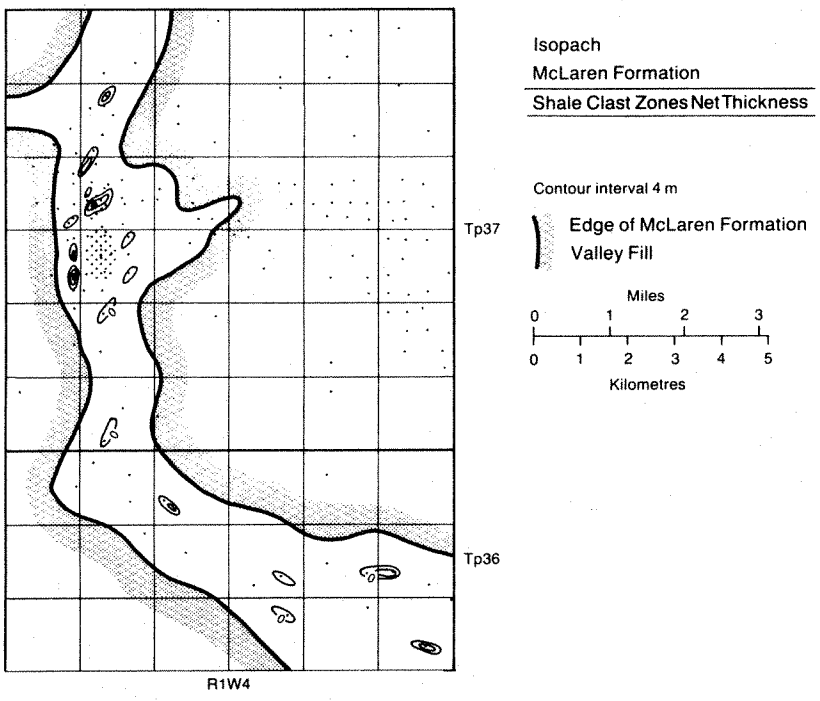

Figure 6. Isopach of the net thickness of the shale clast zones.

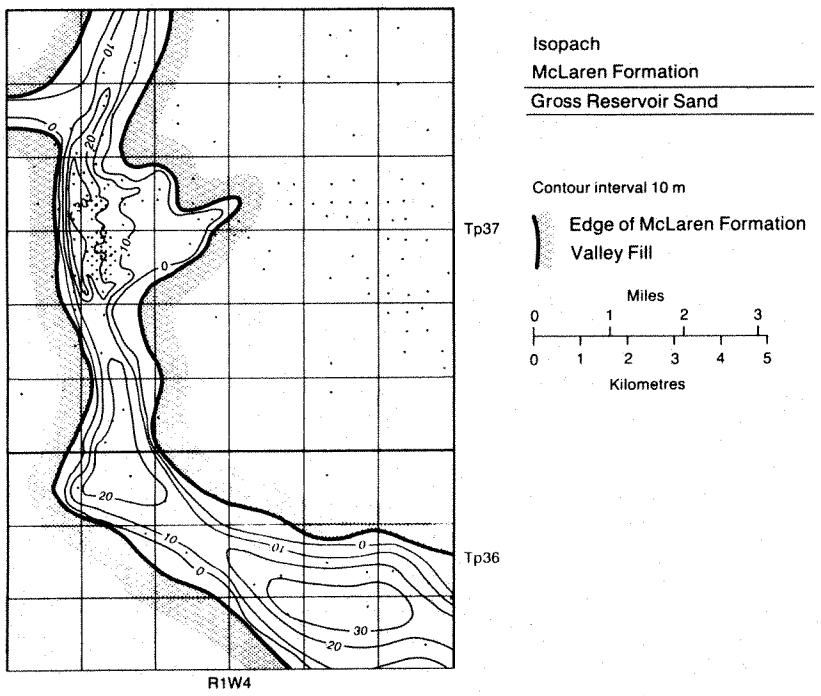

Figure 7. Isopach of the gross thickness of reservoir sands.

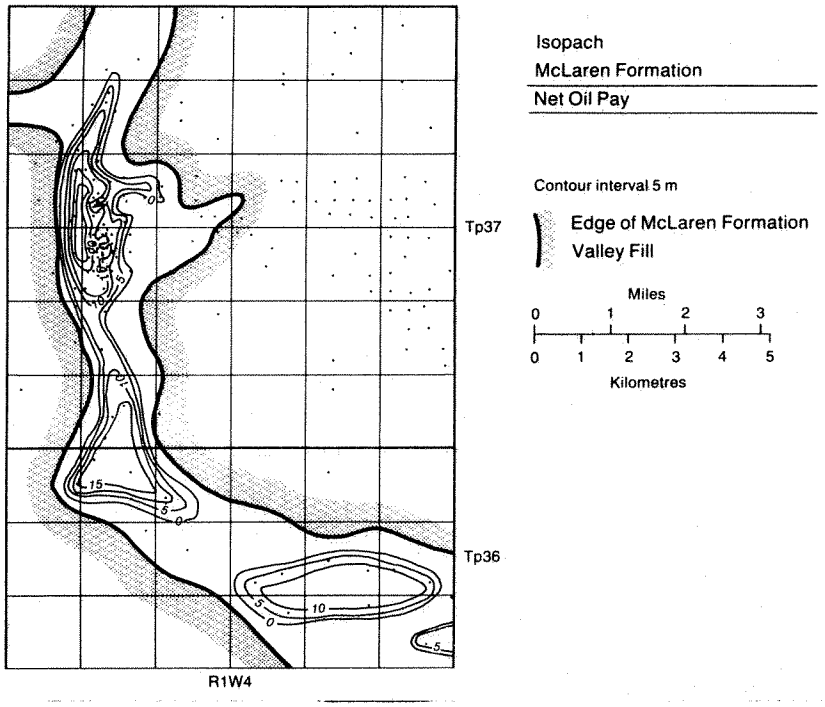

Figure 8. Isopach of net oil pay.

Where underlying water occurs there is usually a transition to the water zone, varying from1.5-4 m. Small gas pockets occur in structurally high areas.

Characterizing reservoir properties for process simulations involves scaling-up from core and well log-derived values to the flow unit or reservoir grid block scale. On the basis of lithology and internal heterogeneity, the Provost Upper Mannville B Pool reservoir can be divided into two parts: the "relatively uniform" sandy portions; and the heterogeneous shale clast zones. Different techniques were used to characterize the reservoir properties for these two subdivisions, with an emphasis being placed on absolute permeability. The characterization of the heterogeneous shale clast zones is reported by Bachu and Cuthiell (1990), Bachu et al. (1991) and Cuthiell et al. (1990).

Sandy Facies Characterization

The sandy facies of the Provost Upper Mannville B Pool compromises the blocky channel, transition zone, and channel margin lithofacies. These three lithofacies represent a natural gradational sequence from the main channel complex, to the margins of the channel, to the point bar, respectively. In general, porosities in the blocky channel lithofacies average close to 30% with maximum oil saturation near 80%. In the transition and channel margin lithofacies, both porosity and oil saturation decrease upward as a result of the fining upward trend in the reservoir lithology. Horizontal air permeabilities of 5×10^{-12} m^2 (5 Darcies) have been measured in fresh core samples from the blocky channel lithofacies. They decrease to the 10^{-15} m^2 (hundreds of millidarcies) range near the top of the channel margin lithofacies. Because of this gradational variability, the sandy facies cannot be characterized as a single flow unit. Rather, it has to be divided into a number of units, based on flow characteristics. A combination of techniques was used to delineate the flow units and to characterize the absolute permeability of the Provost Upper Mannville B Pool sandy facies.

Pore System Analysis

Petrographic image analysis (Ehrlich et al., 1984; Ehrlich and Davis, 1989; Yuan, 1990) was used to characterize the pore systems of the sandy facies. Representative core plug samples were taken from each of the sandy lithofacies. Sixteen thin section images from each core plug were digitized as binary images representing pores and grains. An erosion-dilation image processing technique was applied to each image to produce generalized pore size distributions. The measurements were averaged for each thin section. The size distributions for all the core plug samples were then analyzed using an unmixing algorithm (Full et al., 1981, 1984) to represent each sample as being composed of fractions of a number of end member pore systems. In order to evaluate pore connectedness, pore areas were divided into smooth and rough components. For each connected pore area, the smooth component is defined as the area of the largest inscribed circle, and the rough component is defined as the remaining pore area. A connectivity indicator was then defined as the ratio of the rough area to the total pore area. A value of zero corresponds to isolated circular pores and as the indicator approaches unity, the pore area typically consists of highly connected pores. Yuan (1990) discusses the methodology and theory of the petrographic image analysis technique, and the details of how it was applied to the Provost Upper Mannville B Pool sandy facies. Only the results of the petrographic image analysis are reported here.

A quantitative relation between measured permeability values and image data can be established by regression analysis (Kramers et al., 1991). This can be used to predict the permeability of samples for which no measurements are available. Horizontal permeability values were correlated with pore size and pore connectivity indicator (Figure 9). Vertically oriented thin sections through horizontal core plugs were used, because laminae in the core plug are best sampled by a vertical thin section. The following relation (R^2 = 0.86) was found:

$$k = 0.00647\ p^2 + 32.2\ c - 23.0$$

where k is permeability in darcies (1 darcy = 10^{-12} m^2), p is the average pore radius in μm, and c is the connectivity indicator.

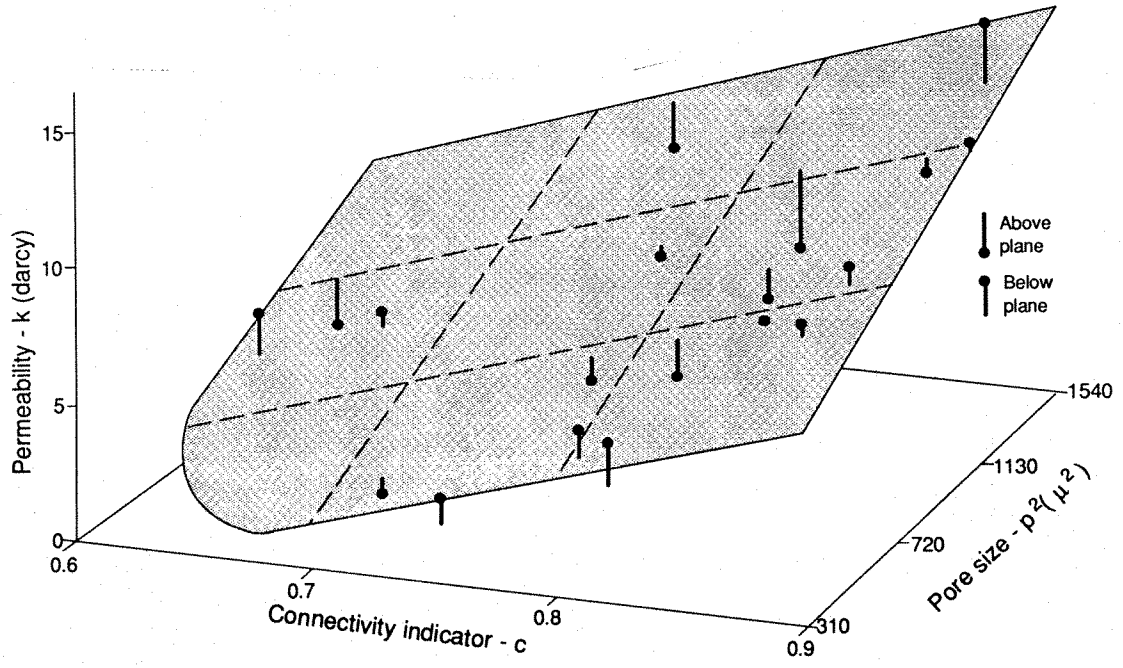

Figure 9. Regression relation between pore size, connectivity indicator and permeability. The filled circles are the data projected onto the regression surface and the vertical lines indicate the distance between the data point and their projection.

The unmixing procedure (Full et al., 1981, 1984) used to identify the pore systems includes a Q-mode factor analysis with an iterative process to represent each sample as being composed of several end members. The number of end members is chosen in such a way that most of the variance of the size distributions are explained. Four end member pore systems were identified for the Provost Upper Mannville B Pool reservoir and the pore images in Figure 10 represent the closest real image examples of these four hypothetical end members. In general, end member 1 represents large, highly connected pores; end member 2 represents medium size and highly connected pores; end member 3 is composed of medium-large but poorly connected pores; and end member 4 represents small and poorly connected pores.

The fractional end member amounts in each sample have been plotted within a tetrahedron (Figure 11) to show the relation between end member pore types and reservoir lithofacies. End member 1 is present in significant amounts in the oil-saturated blocky channel sands, end member 2 is found in large amounts in the transition zone sands, end member 3 is closely associated with the water-saturated blocky channel sands, and end member 4 is typical of the channel margin sands. The trend from end member 1 through end member 2 to end member 4 is closely related to the fining upward sequence found in the reservoir. The poorly connected pore networks found in end member 3 sands, typical of the water-saturated blocky channel sands, is the result of a different diagenetic history of these sands compared to the other sands. After oil invaded the reservoir, formation water was still able to access those sands in the underlying water leg, thus allowing diagenetic processes to continue; whereas in the oil-saturated portion of the reservoir diagenetic processes either ceased or were severely inhibited.

Linking the reservoir pore systems and lithofacies has allowed for a qualitative extension of flow parameters to areas of the reservoir where only geological information is available. In addition, it also provides a methodology to predict absolute permeability values for samples where no measurements are available.

Definition of Flow Units

Within the sandy facies of the Provost Upper Mannville B Pool there is a large body of petrophysical data measured from cores. It consists of interval measurements of fluid saturations and porosity, and discrete point (plug) measurements of permeability. These data need to be scaled up from the core scale to the flow unit or grid block scale to be useful in numerical reservoir models used in simulations of recovery processes.

Most wells show a definite variability of permeability with depth, in which permeability is relatively constant in the main portion of the reservoir (the blocky channel lithofacies), and then decreases toward the top of the reservoir through the transition zone and channel margin lithofacies. This variability is most clearly shown by wells in the currently active steam pilot (Figure 12). Not shown in Figure 12, because these wells do not have a water leg, is a lower permeability in the water-saturated blocky channel sands than in the overlying oil-saturated blocky channel sands. This overall trend of decreasing permeability toward the upper portions of the reservoir and lower permeability in the water-saturated sands is what one would expect, based on the geological nature of the reservoir. The overall fining upward cycle inherited from the depositional environment is the controlling factor for permeability variability within the reservoir, except for the diagenetic overprint in the water-saturated sands.

The scaling up of core analysis measurements in individual wells to a characteristic value for flow units or grid blocks on a reservoir scale requires a sequential process (Cushman, 1984). Data density is different in the vertical than in the horizontal direction, i.e. plug measurements are centimeters apart in the same well, but tens to hundreds of meters between wells. Thus, the first step is to scale the core analysis measurements to flow units on a well-by-well basis. The next step is to scale up these values to flow units on a reservoir scale.

Based on lithology, fluid saturations, porosity and permeability measurements, and supported by the pore system analysis, the sandy reservoir facies have been divided into

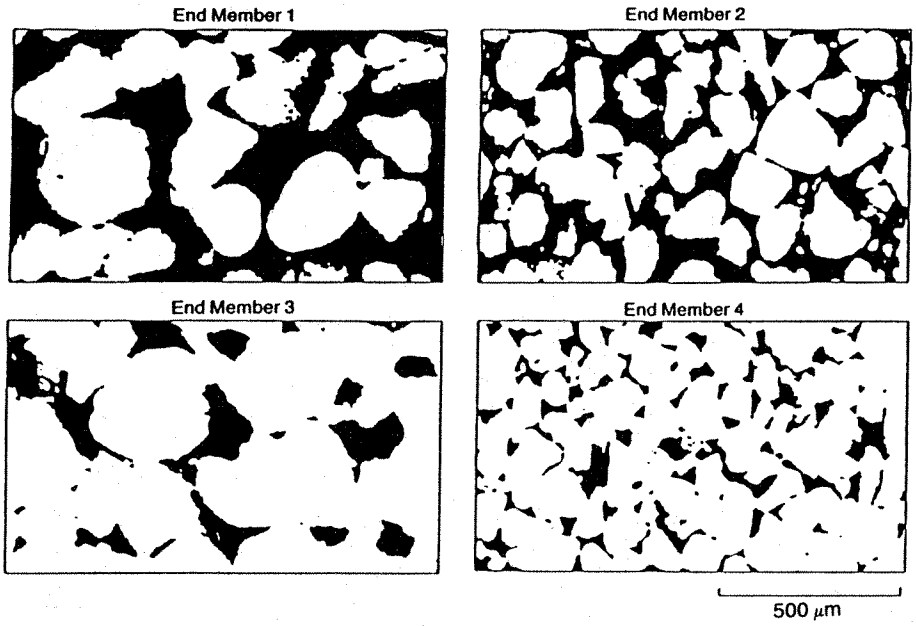

Figure 10. Characteristic pore system end members for the Provost Upper Mannville B Pool.

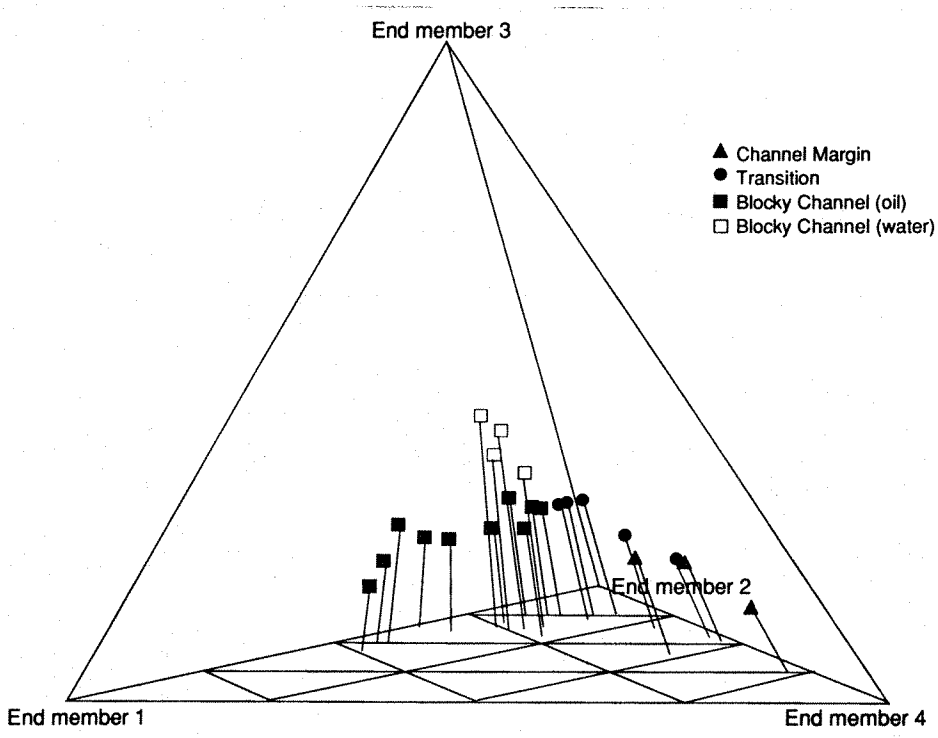

Figure 11. Plot of sample pore system end member composition and lithofacies.

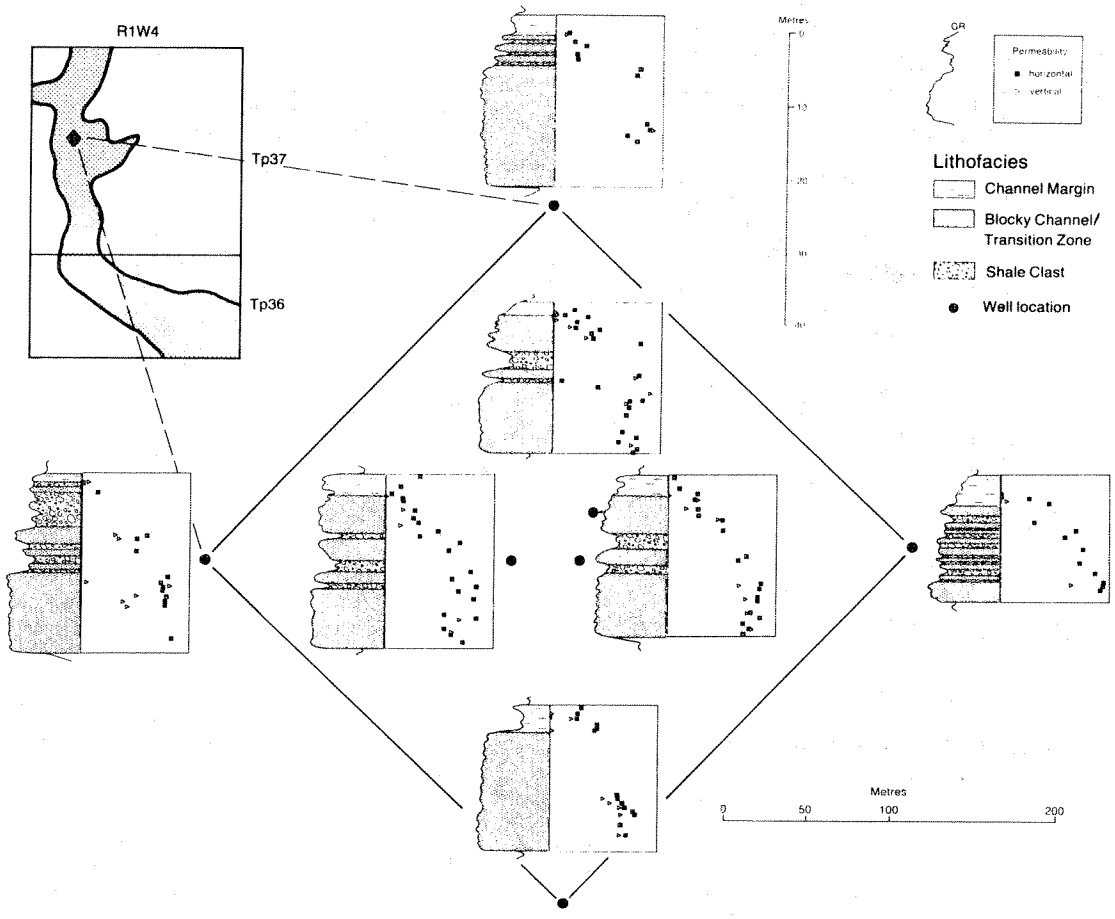

Figure 12. Permeability trends for wells from the active steam pilot in the Provost Upper Mannville B Pool.

four flow units. In ascending order, these are: the water-saturated blocky channel sands; the oil-saturated blocky channel sands; the transition zone sands; and the channel margin sands. Figure 13 presents the results of the first step for an example well: subdivision of the reservoir into flow units and quantification of permeability values for each flow unit in the well. The permeability values in the blocky channel and channel margin flow units vary within a relatively narrow range and show no significant variability with depth. The permeability in the transition zone flow unit exhibits a gradual decrease from the blocky channel to the channel margin sands (Figure 13). Thus, for the blocky channel and channel margin flow units, the effective permeability values for individual wells were calculated as the geometric average of the individual core plug values (Weber and van Geuns, 1989). Calculation of the well-effective permeability values for the transition zone flow unit took the almost linear trend in permeability variation into account by calculating the integrated average of this variation. The characteristic porosity for each flow unit on a per well basis was calculated as the weighted arithmetic average of the individual interval measurements.

Effective permeability and porosity values at the well scale represent local conditions, whereas the entire reservoir represents a larger scale. The average thickness of the flow units is on the order of 10 m or less, while their areal extent is on the order of 10^2-10^3m. Thus, it is appropriate to use the 'shallow water' approximation by which hydraulic conductivity (directly related to

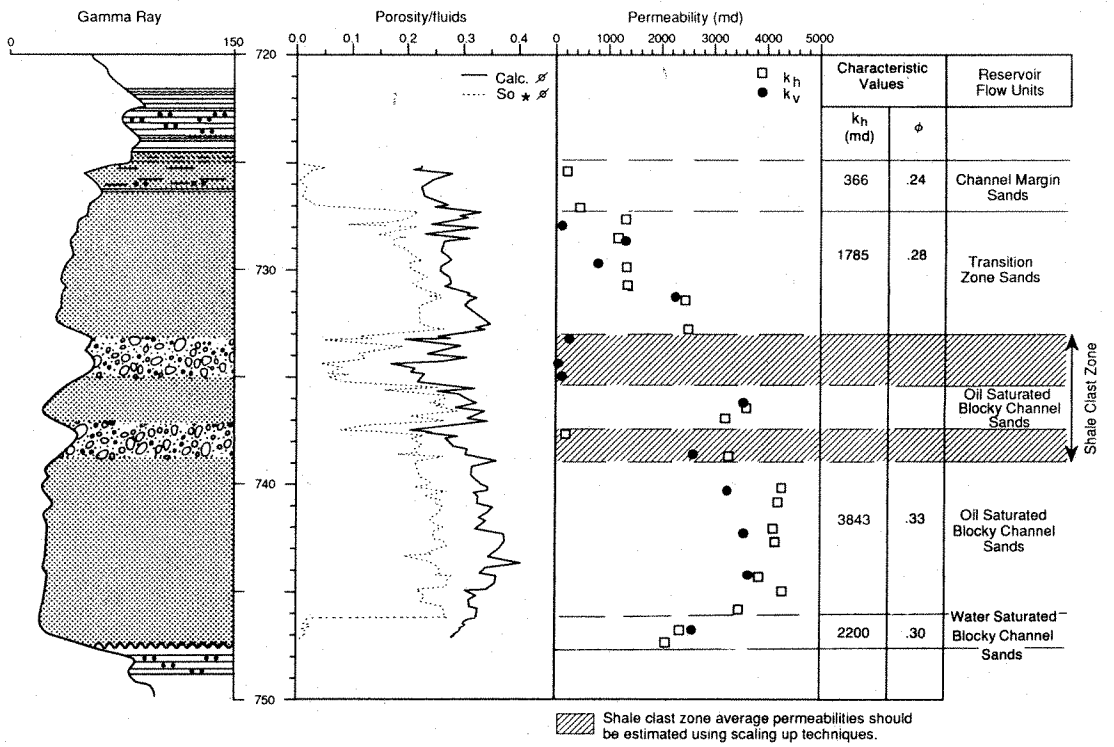

Figure 13. Sandy facies flow units and their characteristic permeability values for the central well in the steam pilot.

permeability) is averaged over the thickness of the flow unit and becomes transmissivity (T) (Dagan, 1989). This is represented as a point value in a horizontal system of coordinates. Transmissivity values were calculated for each flow unit at every well location. The actual number of points (wells with core data) are 15, 18, 21 and 2 for the channel margin, transition zone, oil-saturated blocky channel and water-saturated blocky channel flow units, respectively. No trend is present in the areal transmissivity distributions, thus the effective or characteristic transmissivity value was calculated as the geometric average of the respective frequency distribution. In the absence of any trend, the effective porosity at the flow unit scale was taken as the arithmetic average of the well values. Based on well density and lithological and fluid saturation considerations, only the cored wells in the northern portion of the Provost Upper Mannville B Pool (Sec 17-20, Tp 37, R 1 W4 Mer, Figure 8) were included in this step of the scaling-up process. Table 1 presents the resulting characteristic values at the reservoir scale. These effective values are dependent on the flow conditions (Dagan, 1989), which in this case are assumed to be steady and uniform. In addition to the sandy facies flow units, the shale clast zones also represent distinct flow units, but of a much smaller areal extent. The scaling up of their properties is discussed by Bachu et al. (1991), Bachu and Cuthiell (1990), and Cuthiell et al. (1991).

For single-well numerical simulation of recovery processes, the first scaling-up step is probably sufficient to assign characteristic permeability and porosity values to the simulator grid blocks. If a recovery process is to be simulated for a specific area of the reservoir, then the entire scaling-up process should be applied to every well in that portion of the reservoir and interwell prediction techniques (Haldorsen and Damsleth, 1990) should be used to assign values to the non-well simulator blocks. The subject of interwell variability of reservoir properties is a separate area of research, and was not addressed in this study. The reservoir-scale effective values of transmissivity and porosity can be used directly in regional scale modelling.

Table 1

Reservoir-scale characteristic values of porosity and transmissivity for the sandy flow units, northern portion of the Provost Upper Mannville B Pool.

Flow Unit	Number of Wells	Porosity		Transmissivity (10^{-4} m^2/sec)	
		Characteristic Value	Variance	Characteristic Value	Variance (ln T)
Channel Margin Sands	15	0.255	1.1×10^{-3}	0.095	0.706
Transition Zone Sands	18	0.306	7.0×10^{-4}	0.514	0.285
Oil-saturated Blocky Channel Sands	21	0.342	4.0×10^{-4}	4.200	0.177
Water-saturated Blocky Channel Sands	2	0.246	-	0.250	-

Conclusions

Using the Provost Upper Mannville B heavy oil pool in east-central Alberta as a case study, a multidisciplinary approach to reservoir characterization has shown that:

1. Based on lithological characteristics and internal heterogeneity, the Provost Upper Mannville B Pool reservoir can be divided into two parts, a relatively "uniform" sandy portion, and a heterogeneous portion composed of shale clast breccia zones. Different characterization techniques are required for the characterization of these dissimilar portions of the reservoir.

2. At the pore scale, the sandy portion of the reservoir was characterized using petrographic image analysis. As a result, four end member pore systems were identified. A regressive relation between pore system characteristics and permeability was developed that can be used to predict permeability values where no measurements were taken.

3. At the reservoir scale, flow units were defined based on lithological character, fluid saturations, porosity and permeability measurements, and the results of the pore system analysis. The sandy portion of the reservoir can be divided into four flow units: the water-saturated blocky channel sands; the oil-saturated blocky channel sands; the transition zone sands; and the channel margin sands. Characteristic permeability and porosity values were calculated for each flow unit at the well scale and then scaled up to reservoir scale transmissivity and porosity values. The shale clast zones represent a fifth flow unit.

Acknowledgements

The authors thank the Alberta Research Council, The Alberta Oil Sands Technology and Research Authority, and the Alberta Department of Energy for financially sponsoring this research program and for allowing the publication of these results. We also thank our colleagues at the Alberta Geological Survey for their comments and suggestions as the project evolved and specifically Joe Olic, Campbell Kidston, Max Baaske, Ed Hasiuk and Kathy Hamilton for technical support, as well as the staff of the Graphic Services Department of the Alberta Research Council for drafting the figures.

John Kramers received his BSc and MSc in geology from The University of Alberta and his PhD in geology from Rensselaer Polytechnic Institute. He is currently a senior research officer with the Alberta Geological Survey, Alberta Research Council (P.O. Box 8330, Station F Edmonton, Alberta, Canada T6H 5X2) and project leader for the Reservoir Analysis Project. His current research interests include quantitative reservoir description and characterization.

Li-Ping Yuan received his BSc in geology from the National Taiwan University in 1978, his MSc in geological sciences from the University of Illinois and his PhD in geology from the University of South Carolina in 1987. He is currently an assistant research officer with the Alberta Geological Survey, Alberta Research Council (P.O. Box 8330, Station F Edmonton, Alberta, Canada T6H 5X2). His current research interests include image analysis of pore systems and computer applications in geology.

Stefan Bachu has an engineering degree in hydraulics and a PhD in transport processes from Technion-Israel Institute of Technology. He is presently Head of the Petroleum Geology and Basin Analysis Section of the Alberta Geological Survey (P.O. Box 8330, Station F Edmonton, Alberta, Canada T6H 5X2). His main areas of interest are hydrogeological and geothermal processes in sedimentary basins, and scaling-up of rock and fluid properties from core (lab) to basin scale.

David Cuthiell is a member of the Mathematical Modelling Group in the Oil Sands and Hydrocarbon Recovery Department at the Alberta Research Council (P.O. Box 8330, Station F Edmonton, Alberta, Canada T6H 5X2). Dave received his PhD in physics from Cornell University in 1977. He has been with the Alberta Research Council since 1981; his current major interests are the modelling of geological heterogeneity for purposes of reservoir simulation and recovery mechanisms in steam-based enhanced oil recovery.

References

Bachu, S. and D.L. Cuthiell. 1990. Effects of core scale heterogeneity on steady state and transient fluid flow in porous media; Numerical analysis. Water Resour. Res., v 26, pp. 863-874.

Bachu, S., D.L. Cuthiell, J.W. Kramers and L-P. Yuan. 1991. Reservoir characterization case study; bimodally heterogeneous facies. In Parameter Identification and Estimation for Aquifer and Reservoir Characterization (ed. S. Bachu), Proc. 5th Canadian/American Conference on Hydrogeology. National Water Well Association, Dublin, Ohio (this volume).

Cant, D.J. and R.G. Walker. 1978. Fluvial processes and facies sequences in the sandy braided South Saskatchewan River, Canada. Sedimentology, v. 25, pp. 625-648.

Collins, H.N. 1977. Properties of unconsolidated sands, log-core study of Bodo Upper Mannville 'B' Pool. Petroleum Recovery Institute, Interim Rep. IR-4.

Collins, H.N. and D. Pilles. 1981. Reconciliation of porosity interpretations in McLaren Sands using functional analysis. Petroleum Recovery Institute, Rept. 1981-11.

Cushman, J.H. 1984. On unifying the concepts of scale, instrumentation and stochastics in the development of multiphase transport theory. Water Resour. Res., v. 20, pp. 1668-1676.

Cuthiell, D.L., S. Bachu, J.W. Kramers and L-P. Yuan. 1991. Characterizing shale clast

heterogeneities and their effect on fluid flow. In Proceedings Second International Reservoir Characterization Technical Conference, National Institute for Petroleum and Energy Research, Bartlesville, OK, USA (*in press*).

Dagan, G. 1989. Flow and Transport in Porous Formations. Springer Verlag.

Ehrlich, R., S.K. Kennedy, S.J. Crabtree and R.L. Cannon. 1984. Petrographic image analysis 1. Analysis of reservoir pore complexes. J. Sediment. Petrol., v. 54, pp. 1365-1378.

Ehrlich, R. and D.K. Davis. 1989. Image analysis of pore geometry, relationship to reservoir engineering and modelling. SPE Paper 19054.

Full, W.E., R. Ehrlich and S.K. Kennedy. 1984. Optimal configuration and information content of sets of frequency distributions. J. Sediment. Petrol. v. 54, pp. 117-126.

Full, W.E., R. Ehrlich and J.E. Klovan. 1981. EXTENDED QMODEL - Objective definitions of external end members in the analysis of mixtures. Math. Geol.,v. 13, pp. 331-344.

Gross, A.A. 1981a. Some aspects of geological contribution to EOR - Comparison of the geometry of three Mannville Sand reservoirs. CIM Paper 81-32-15.

Gross, A.A. 1981b. A geological study of three Mannville Sand reservoirs - Chauvin South (Sparky A and B), Provost (Upper Mannville B) Bodo, David (Lloydminster A). Petroleum Recovery Institute Rept. 1981-5.

Gross, A.A. 1980. Mannville channels in east-central Alberta: In Lloydminster and Beyond, Geology of Mannville Hydrocarbon Reservoirs, (eds. L.S. Beck, J.E. Christopher and D.M. Kent). Saskatchewan Geological Society Spec. Pub. No. 5, pp. 33-63.

Haldorsen, H.H. and E. Damsleth. 1990. Stochastic modeling. J. Petrol. Tech., v. 42, pp. 404-412.

Hayashitani, M. and W. Davis. 1981. Provost Upper Mannville B Pool. Petroleum Recovery Institute Rept. 1981-7.

Jackson, P.C. 1984. Paleogeography of the Lower Cretaceous Mannville Group of Western Canada. In Elmworth - Case study of a Deep Basin gas field. (ed. J.A. Masters). Am. Assoc. Petrol. Geol. Mem. 38, pp. 49-77.

Kramers, J.W., S. Bachu, D.L. Cuthiell and L-P. Yuan. 1991. Reservoir characterization - a case study: the Provost Upper Mannville B Pool. Project Technical Report to AOSTRA and Alberta Department of Energy.

Kramers, J.W., S. Bachu, D.L. Cuthiell, M.P. Prentice and L-P. Yuan 1989. A multidisciplinary approach to reservoir characterization: the Provost Upper Mannville B Pool. J. Can. Petrol. Tech. v. 28, pp. 48-58.

MacCallum, G.T. and R.G. McCrossan. 1979. The Lloydminster oil play in Alberta (abs.). Can. Soc. of Petrol. Geol. Reservoir, v. 6, pp. 1-2.

Nazarko, T.W. 1983. Review of Bodo fireflood pilot project. Fourth Annual Advances in Petroleum Technology Conference, AOSTRA/ Canadian Petroleum Association, Calgary.

Outtrim, C.P. and R.G. Evans. 1978. Alberta's oil sands reserves and their evaluation. In The Oil Sands of Canada-Venezuela (eds. D.A. Redford and A.G. Winestock). CIM Spec. Vol. 17, pp. 36-66.

Salahub, D.W. and D.W. Mudie. 1990. Bodo; steaming into the nineties. Oil Sands 2000, Energy-Environment-Enterprise, AOSTRA Annual Meeting, Edmonton.

Weber, K.J. and L.C. van Geuns. 1989. Framework for constructing clastic reservoir simulation models. SPE Paper 19582.

Wilson, M.A. and R.W. Bennett. 1985. Evaluation of Saskatchewan's heavy oil reserves. Saskatchewan Energy and Mines, Saskatchewan Geol. Surv. Open File Rept.

Yuan, L-P. 1990. Pore image characterization and its relationship to permeability. Society of Core Analysts Paper 9002, Annual Technical Conference, Dallas, Tx, Aug. 14-16, 1990.

Reservoir Characterization Case Study: Bimodally Heterogeneous Facies

by Stefan Bachu, David Cuthiell, John Kramers and Li-Ping Yuan

Abstract

Heterogeneity is present in geological structures at all scales, and its distribution and characteristics have an impact on fluid flow and transport processes. The rocks need to be characterized by their effective properties at the scale of interest, but in most instances information or data are available at a smaller scale. In these cases, there is need for a scaling-up of rock property data, based on the particular characteristics of the heterogeneous porous medium. Shale clasts or quartzite pebbles randomly distributed in a sand matrix constitute a particular type of stochastic heterogeneity, and have a bimodal distribution and a binary character with regard to hydraulic conductivity (permeability). Two-dimensional numerical simulations based on actual core data, and physical fluid flow experiments were used to study the core-scale effects of this type of heterogeneity. The results show that the effective hydraulic conductivity depends primarily on the heterogeneity fraction and on the conductivity contrast between heterogeneity and the embedding matrix, a dependence which can be described by a generalized weighted mean model. Another important factor is the connectedness of the more permeable component. The effective conductivity has a second order dependence on such heterogeneity characteristics as shape, aspect ratio, orientation and distribution within the porous matrix. Depending on these characteristics, the bounds of effective values for hydraulic conductivity can be narrowed further from the extreme bounds expressed by the arithmetic and harmonic averages.

Introduction

Understanding of fluid flow and transport processes in aquifers and hydrocarbon reservoirs is essential to successful and environmentally safe exploitation of water and energy resources. To this end, the study and characterization of aquifer or reservoir variability is very important, and has attracted the attention of various researchers. The issue of spatial variability is intrinsically linked with the scale at which the flow processes take place or are studied. Very few geological structures are homogeneous, and the flow processes of interest usually take place in heterogeneous regions of much larger extent than the heterogeneity scale. In this case, the main objective is to define and quantify the effective properties of the flow domain at the large scale based on knowledge of property variability at the smaller scale, such that the large-scale flow and transport equations are satisfied. The variations associated with heterogeneity are smoothed out, and the large-scale equations become similar to those describing the behaviour of an equivalent homogeneous porous medium. The scaling-up from the heterogeneity scale to the domain scale must retain the main characteristics of the heterogeneous medium, neglecting at the same time the particular details. Different methods, broadly classified as direct and indirect, have been used to arrive at effective or equivalent property values for heterogeneous systems. A general overview of these methods can be found in Bachu and Cuthiell (1990).

A particular type of heterogeneity is represented by the two-component system. In such systems, the variability of

the given property within any individual component is much smaller than the contrast in property values between the two components. By neglecting the small range variability of a property for each individual component, bimodal heterogeneity distributions become binary. This type of heterogeneity is present at all scales (e.g. the fluid-solid at the pore scale, pebbles in a sandy aquifer at the local scale, or shale lenses in sandstones at the regional scale).

There are cases of aquifers and reservoirs where various types of heterogeneity are present, and each one has to be dealt with in a different way. Such a reservoir is the Provost Upper Mannville B Pool in Alberta, Canada, which contains both sandy and binary facies. The sandy parts of the reservoir have been characterized at all scales (from pore to facies) using a variety of techniques (Kramers et al., 1991). The characterization of the binary facies, which consists of shale clasts embedded in a sand matrix, is reported in this paper using an indirect method with the aim of defining the effective hydraulic conductivity of such core-scale heterogeneity in a quasi-empirical way. The indirect method is based on knowledge of the heterogeneity distribution at the smaller scale, and of the behaviour of the flow variables at the larger scale. The ultimate goal is to characterize the heterogeneous binary facies at the scale needed in reservoir process simulations. Because this scale is several orders of magnitude greater than the heterogeneity scale, a sequential scaling-up approach is needed (Cushman, 1984; Lassetter, Waggoner and Lake, 1986). In the first step, the shale-clast heterogeneity is replaced at the layer scale by core-scale regions each characterized by an effective permeability. In the next step, the variability in core-region permeability is replaced by a layer-scale effective permeability. Finally, the various shale-clast layers in the reservoir are similar with shale lenses, and can be treated in various ways in process simulations (Haldorsen and Damsleth, 1990).

Previous papers on the particular subject of shale clasts presented general reservoir characteristics (Kramers et al., 1989) and a detailed statistical characterization of the shale clasts (Cuthiell et al., 1991), together with the scaling-up approach. This paper reports further results obtained in the first step of the scaling-up process. Numerical simulations of fluid flow were performed for two-dimensional images of actual heterogeneous core from three wells in the reservoir. Given the lack of knowledge about the three-dimensional characteristics of the shale clasts, physical experiments were used to study the fluid flow through systems consisting of pebbles embedded in sand. It was found that the generalized weighted mean model (Korvin, 1982) offers a good representation of the effect of heterogeneity on the effective hydraulic conductivity of such binary heterogeneous systems.

Source Of Data

The Mannville Group (Lower Cretaceous) in Alberta, Canada, is characterized by repeated alternations of thin marine and non-marine deposits. Deep channels occur at all levels within this succession. The infill of the channels varies substantially, from clean sand to conglomerate to shale and silt. The Provost Upper Mannville B Pool in east-central Alberta can be subdivided into two parts: a "relatively uniform" sandy part, and the binary, heterogeneous, shale clast zones. A detailed description of the reservoir and a characterization of the sandy facies can be found in Kramers et al., (1989, 1991). The shale clast zones have lateral continuity of the order of 10^1 - 10^2 m as correlated between wells, with a continuous thickness of up to 3 m. The permeability contrast between the sand matrix and the shale clasts is of the order of 10^3. About 7000 clasts in 20 m of core from three wells were digitized, producing several megabytes of

data describing two-dimensional clast outlines located in the core system of coordinates. Figure 1 shows the image of a core segment containing shale clasts.

The two-dimensional clast outlines are in fact polygons whose characteristics can be easily calculated. The following parameters were calculated for each individual clast: area, orientation (defined as the direction of the principal axis of inertia), length and width (defined as the dimensions of the minimum enclosing rectangle oriented in the principal direction), aspect ratio (defined as width-to-length ratio), and shape factor (defined as the ratio of clast area to the product of width and length). The characteristics of the clasts and the shale-fraction distribution were treated separately for the three wells. Figure 2 presents frequency distributions for some of the clast characteristics, a more detailed analysis can be found in Cuthiell et al., (1989). The clasts vary in size (length) from < 1 cm to ~ 10 cm with a mode ~ 5 mm. They are predominantly flat in shape, with some being angular and others well rounded. Their orientation is mostly subhorizontal, although a significant number of clasts are oriented at 30° to the horizontal, and a few up to 90°. The aspect ratio of the clasts varies between 0.1 and 1, with an average of 0.45. Finally, most of the clasts are small (50% of them have a cross-sectional area < 0.1 cm^2), although there are a few very large ones (area > 10 cm^2).

Analysis of Flow Effects

Because of their large number and relatively small size, the shale clasts or pebbles cannot be directly incorporated into studies of fluid flow in aquifers and reservoirs. Therefore, it is important to determine effective values for flow parameters characterizing the clast zone at larger scales. At the core scale one has to deal with a random distribution of binary values for hydraulic conductivity. In the

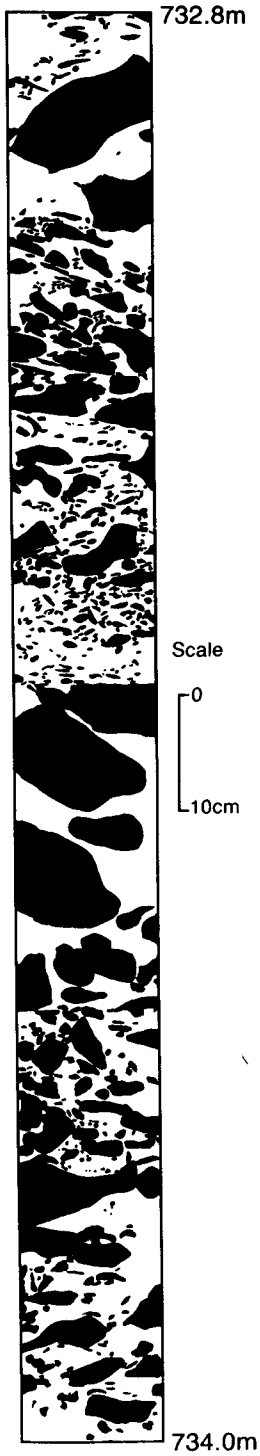

Figure 1. Binary image of a core portion from a shale clast layer (the clasts are dark, the embedding sand matrix is light).

averaging method (Hassanizadeh and Gray, 1979), the heterogeneity characteristic dimension must be much smaller than the characteristic dimension of the Representative Elementary Volume (Quintard and Whitaker, 1987) over which the averaging takes place. Because this condition is not satisfied in the case at hand, the method is not applicable. Neither can statistical methods be applied, because the ergodic condition is not met and because the domain for which data are available is actually bounded. Closed expressions derived from the self-consistent method, which assumes circular shapes, are not applicable because of the irregular shape and distribution of the clasts. Only the indirect method allows the computation of the effective conductivity for this type of heterogeneity.

The modelling of fluid flow through a heterogeneous core region is viewed here as a measuring instrument according to the relativist concept (Baveye and Sposito, 1984). Therefore, the effective core-scale values are defined operationally in terms of the characteristics of the region being modelled rather than by any REV. The steady-state effective values K_{ef} of the hydraulic conductivity for the core region as a whole can then be calculated from Darcy's law applied at the core scale (Dagan, 1982):

$$< q > = - K_{ef} \nabla < \phi > \qquad (1)$$

where q is specific discharge, K is hydraulic conductivity, ϕ is the hydraulic potential driving the flow, and the angle brackets denote mean value over the entire flow domain. Given the direct relation between permeability and hydraulic conductivity, the physically or computationally measured changes in effective hydraulic conductivity are equivalent to identical changes in permeability.

Numerical simulations of two-dimensional fluid flow were carried out for actual core-scale regions a few centimeters in

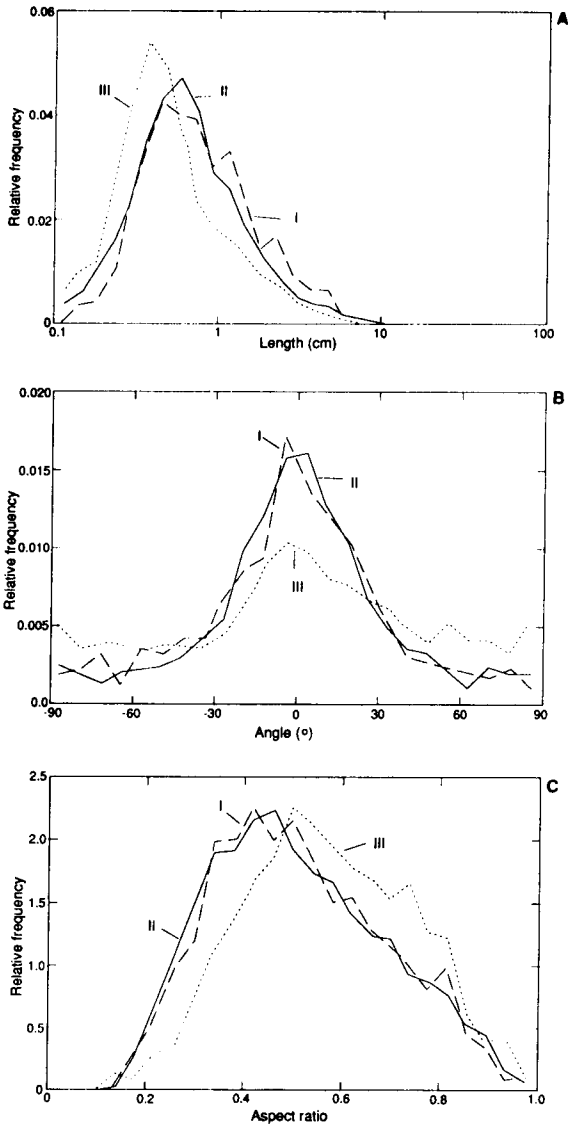

Figure 2. Frequency distributions for clast parameters in three wells (I, II and III) in the Provost Upper Mannville B Pool reservoir: A. length; B. aspect ratio; and C.orientation.

size, taking into account the individual position and geometry of the clasts. Initial simulations of vertical and horizontal flow were performed assuming homogeneous hydraulic conductivity for each region, to validate the numerical model. The computed fluxes agreed to within 0.3% of the calculated theoretical values. Sixteen representative core-scale regions were identified in the 20 m of digitized core in such a way as to cover a wide spectrum of shale clast fraction without having a single large clast accounting for most of the heterogeneity or obstructing the entire core cross-section. The binary images of the sixteen core regions are presented in Figure 3 together with the corresponding shale clast fractions f. In this study of stochastic heterogeneity based on measured data, the physical dimension (core diameter) of the sampling device and the deterministic character of the very large clasts excluded the analysis of core regions with a shale fraction > 50%. Although the results to be presented subsequently cannot be generalized in the sense of Monte Carlo simulations (e.g. Warren and Price, 1961; Desbarats, 1987; Deutsch, 1989), it is felt that the conclusions are representative for the effects of this type of heterogeneity on fluid flow.

In the context of this paper, heterogeneity is defined as that component of the medium formed of bodies (clasts or pebbles) which are not connected, even if occasionally some of them are touching. The other component, embedding the heterogeneity and forming a continuous flow path, is called the matrix. The following conductivity ratios (K_{het}/K_{mat}, the subscripts het and mat stand for heterogeneity and matrix, respectively) were considered in simulations: 0.5, 0.33, 0.2, 0.1, 0.02, 10^{-2}, 10^{-3}, 10^{-4} and 10^{-5}. Because the predominant orientation of the clasts is subhorizontal, the principal directions of the core-scale effective conductivity tensor are expected to be vertical and horizontal. With this assumption, vertical and horizontal effective hydraulic conductivities were calculated for each core region and the entire spectrum of conductivity ratios K_{het}/K_{mat} by imposing appropriate boundary conditions in the flow simulations. The hydraulic head at two opposite sides of a rectangular core region were maintained at uniform and constant but different values, while the other two sides are no flow boundaries. The results are presented in dimensionless form as the ratio K_{ef}/K_{mat} of the effective (or equivalent) core-scale hydraulic conductivity to the matrix conductivity, function of the conductivity ratio K_{het}/K_{mat} and heterogeneity fraction f.

Figure 4 presents the reduction in effective hydraulic conductivity as a function of heterogeneity fraction f, for a conductivity contrast $K_{het}/K_{mat} = 0.001$. The following generalized weighted mean model (Korvin, 1982):

$$K_{ef} = \left[f K_{het}^{\omega} + (1 - f) K_{mat}^{\omega} \right]^{1/\omega} \qquad (2)$$

was fitted by least squares to the calculated values and used to extrapolate past f = 0.50. In the above relation, ω is a power value to be found by regression analysis, bounded by the values -1 and +1 which correspond to the harmonic and arithmetic averages, respectively. The geometric average is retrieved for $\omega = 0$. The generalized weighted mean is a single-parameter model equivalent to resistor models comprised of conductive elements in series and in parallel.

Despite the assumption of individual homogeneity and isotropy of the two components, the effective conductivity clearly exhibits a tensorial character, with the vertical component smaller than the horizontal one for all heterogeneity fractions. This result is similar to results reported for impervious shale lenses (Desbarats, 1987; Deutsch, 1989) and

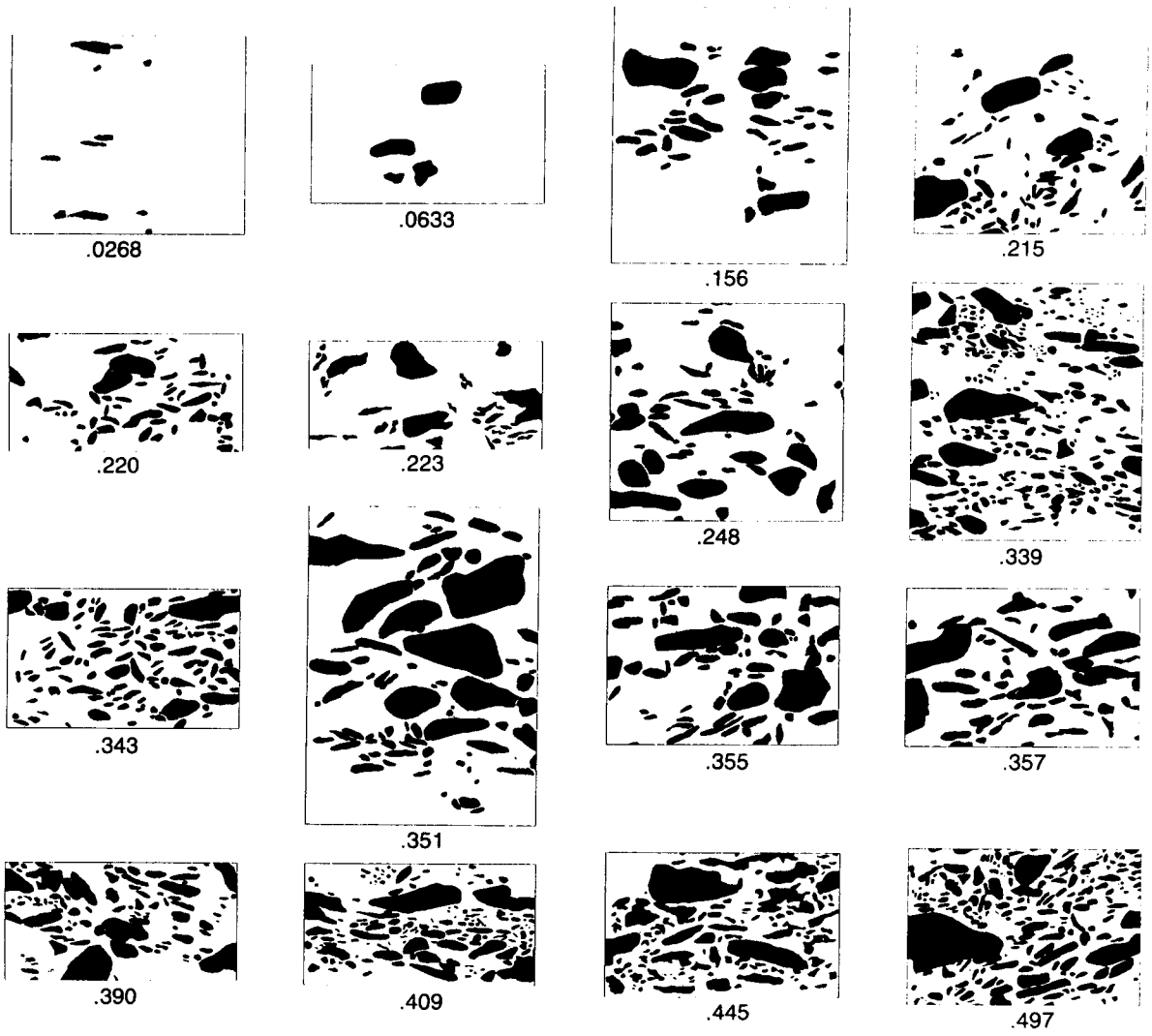

Figure 3. Binary images of the core-scale regions for which numerical fluid flow simulations were performed. The corresponding heterogeneity fraction is indicated below each one. Each core is approximately 11 cm in width.

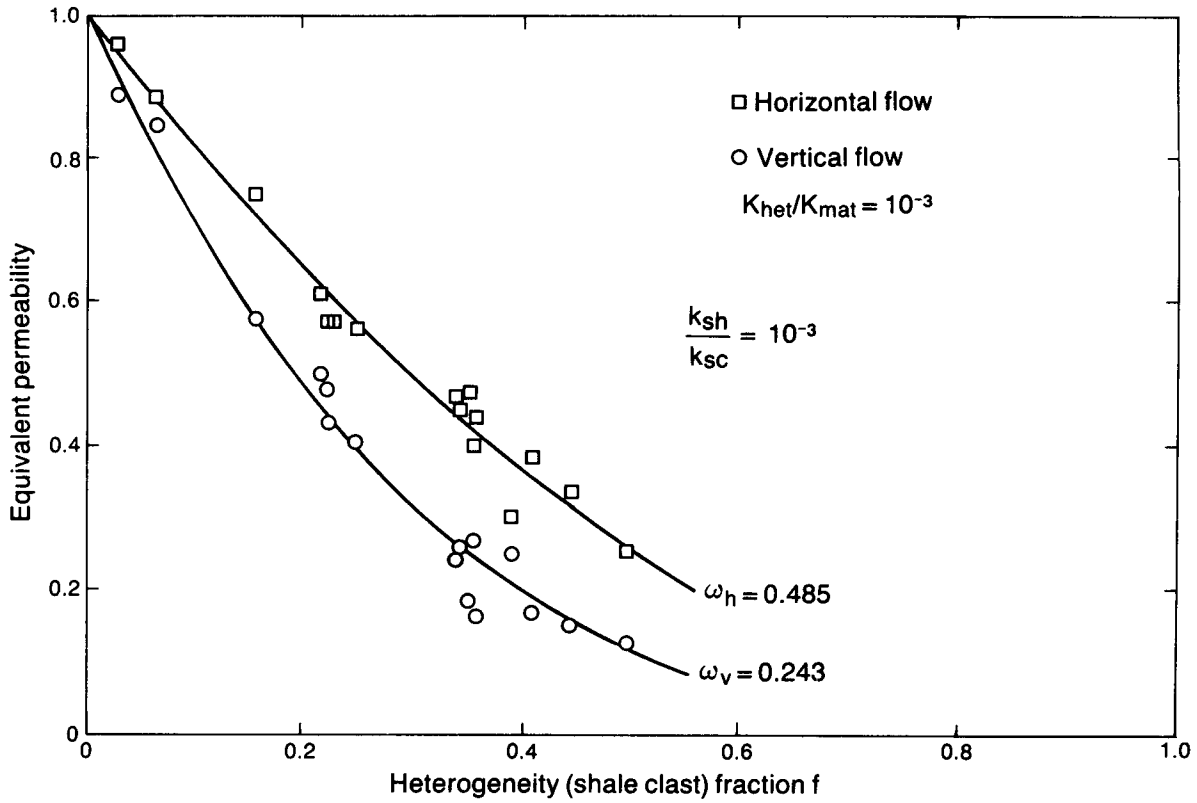

Figure 4. Variation of effective hydraulic conductivity (K_{ef}/K_{mat}) as a function of heterogeneity fraction f for two-dimensional core-scale regions. The generalized weighted mean model is fitted to the data.

confirms the theoretical conclusion reached by Quintard and Whitaker (1987) regarding the large-scale conductivity tensor. The large-scale anisotropy is due to, and controlled by, the shape and distribution of heterogeneities. Further examination of Figures 3 and 4 shows that the effect of heterogeneity on fluid flow (effective hydraulic conductivity) is not the same for different core regions, even if the heterogeneity contrast and fraction are the same. The obvious reason is that there are differences in other characteristics of the clast distributions, such as size, aspect ratio, shape and orientation. However, these have a secondary effect. Simulations for the entire spectrum of conductivity contrasts K_{het}/K_{mat} (Bachu and Cuthiell, 1990) have shown that for the same heterogeneity fraction f, the reduction in the effective permeability has an asymptotic behaviour for $K_{het}/K_{mat} < 0.01$. The presence of heterogeneities has a greater impact for large conductivity contrasts in terms of both anisotropy and reduction of effective conductivity; nevertheless, their effect is significant for low contrasts ($K_{het}/K_{mat} > 0.01$) as well, and should not be neglected.

The results presented in Figure 4 assume that the heterogeneity is less conductive than the embedding matrix, which is the case of shale clasts or pebbles in sand, or shale lenses in sandstone. At other scales, the opposite situation may occur, when the heterogeneity is more conductive than the matrix (e.g. sand bodies in shales). Korvin (1982) has shown that the generalized weighted mean of the ωth order expressed by relation (2) is the only possible functional form for the pro-

perty of a composite material consisting of two phases, provided that is unambiguously determined by the volume fractions and the individual properties of the two phases, and that a certain set of physically plausible conditions are met. In particular, the conditions of reflexivity, idempotency and bi-symmetry imply interchangeability of the two components (Korvin, 1982). Accordingly, the change in the effective hydraulic conductivity should present a certain symmetry if the heterogeneity and matrix hydraulic conductivities are interchanged in the sixteen core regions being studied, this interchange being equivalent to $f > 0.5$ and $f < 0.5$ for the same geometry. However, the numerical simulations have shown that this is not the case. For the same clast distributions (Figure 3) and heterogeneity contrasts of 10^{-3} (sand matrix) and 10^{3} (shale matrix), respectively, the corresponding values of the power ω in the generalized weighted mean model (2) are $\omega_h = 0.486$ and $\omega_v = 0.243$ for connected sand, and $\omega_h = -0.215$ and $\omega_v = -0.470$ for connected shale (the subscripts h and v stand for horizontal and vertical flow, respectively). The ω values and particularly their sign show that the effective hydraulic conductivity for this type of heterogeneity has values above or below the geometric average ($\omega = 0$) of the conductivity values of the two components, depending on the connectedness of the most conductive component. The above results show that the generalized weighted mean model of the ωth order, while generally adequate, is not sufficient to capture, in a quantitative way, all the dependencies of the effective hydraulic conductivity on various characteristics of a binary heterogeneous porous medium.

The dependence of the effective hydraulic conductivity K_{ef} on the conductivity contrast between the two individual components and on matrix connectedness is best summarized by the variation of the power exponent ω of the generalized weighted mean (relation 2) as a function of the conductivity ratio K_{het}/K_{mat} (Figure 5).

The values of ω for each conductivity ratio and flow direction were obtained by least squares fit of the functional (relation 2) to the calculated effective conductivity values. While admitting that the position and shape of the two curves will probably change for different distributions of heterogeneity size, aspect ratio, shape and orientation, it is believed that the main features of the variation of the power exponent ω remain the same. This is because the effective conductivity is dependent mainly on the heterogeneity fraction f and on the conductivity ratio K_{het}/K_{mat}, and has only a second order dependence on other heterogeneity characteristics. The primary dependence of K_{ef} on K_{het}/K_{mat} and f is strongly implied by the monotonic behaviour of the power ω as a function of K_{het}/K_{mat}, and by the fact that the effective hydraulic conductivity satisfies all the conditions defined by Korvin (1982), except bi-symmetry. Accordingly, the results presented so far for heterogeneities with relatively large aspect ratios ($0.1 <$ width/length < 1) suggest that the bounds of the effective conductivity K_{ef} can be restricted to:

$$
\begin{cases}
K_H < K_{ef,h},\ K_{ef,v} < K_G & \text{for } K_{het}/K_{mat} \geq 10^2 \\
K_H < \min(K_{ef,h},\ K_{ef,v}) < K_G & \\
K_G < \max(K_{ef,h},\ K_{ef,v}) < K_A & \text{for } 10^{-2} < K_{het}/K_{mat} < 10^2 \\
K_G < \max(K_{ef,h},\ K_{ef,v}) < K_A & \text{for } K_{het}/K_{mat} \leq 10^{-2}
\end{cases}
\qquad (3)
$$

where $K_{ef,h}$ and $K_{ef,v}$ are the horizontal and vertical components of the effective conductivity tensor, and the subscripts H, G and A stand for harmonic, geometric and arithmetic averages, respectively. If the main directions of anisotropy are other than

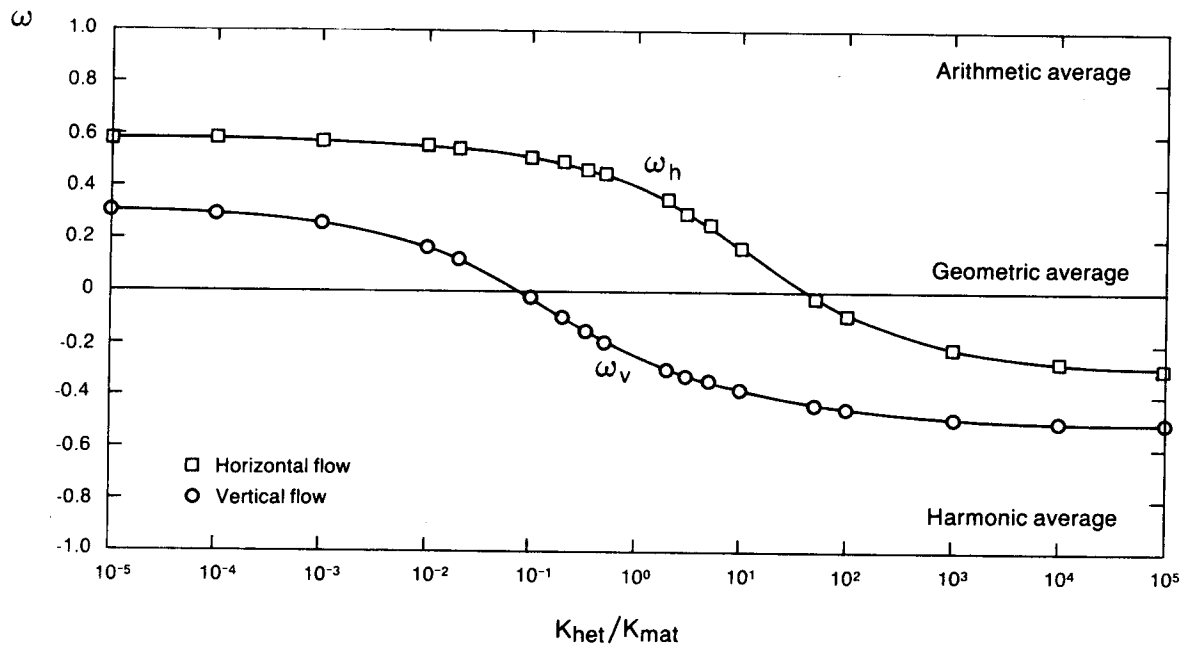

Figure 5. Variation of the power ω of the generalized weighted mean model as a function of the heterogeneity-to-matrix contrast in hydraulic conductivity K_{het}/K_{mat}.

horizontal and vertical, then the respective components should be used in relations (3). The bounds 10^{-2} and 10^{2} for conductivity ratio K_{het}/K_{mat} in relations (3) are somewhat empirical, but their choice is supported by the fact that the behaviour of the effective conductivity as a function of the conductivity ratio becomes asymptotic around these values (Bachu and Cuthiell, 1990). The practical application of these results to any case for which the conductivity contrast K_{het}/K_{mat} and the heterogeneity fraction f are known, consists in estimating the power averages ω_h and ω_v from Figure 5 for use in the generalized weighted mean model (2) for the calculation of the horizontal and vertical components of the effective conductivity.

The numerical simulations and the analysis carried out so far for a binary heterogeneous porous medium consisting of irregularly sized, shaped and distributed heterogeneities in an isotropic porous matrix show that the effective hydraulic conductivity depends primarily on the heterogeneity fraction, the conductivity contrast and the connectedness of the more permeable component. The dependence on the heterogeneity fraction and the conductivity contrast can be expressed in a semi-empirical way by the generalized weighted mean model. Other characteristics like heterogeneity size, aspect ratio, shape, and orientation, have a secondary effect, not yet quantified.

Three-Dimensional Effects

The results of the numerical simulations presented in the previous part of this paper, although based on cross-sections of actual heterogeneous core regions, are limited by the two-dimensionality of the data and of the flow analysis. It is well recognized, and mathematically proved for other types of statistical heterogeneity, that the effective hydraulic conductivity in a three-dimensional system is higher than in a two-dimensional system with the same statistical characteristics (Dagan, 1982; Gelhar and Axness, 1983). Quantitative evaluation of the effect of shale clasts on fluid flow in a three dimensional system is difficult because: 1) large enough portions of shale-clast regions are not available from core or outcrop for laboratory study; 2) the three-dimensional geometries and characteristics of the clasts are not known; and 3) in core, the shale clasts are set in an unconsolidated sand saturated with bituminous heavy oil, which inhibits the flow of fluids through the sand matrix. To that one must add the very large amount of computer resources needed for three-dimensional numerical simulations. For these reasons it was considered that the most effective alternative was to perform flow experiments using an analogue system that simulates a shale-clast region, in order to evaluate the three-dimensional effects of this type of heterogeneity.

The physical flow experiments were carried out for cubic blocks (20 cm on each side) composed of impermeable quartzite pebbles distributed in a 10/20 frac-sand matrix. In designing the experiments, the following considerations were taken into account: 1) the size and distribution of the pebbles should be appropriate compared to the respective volume of porous medium; 2) the statistical properties of the pebbles have to be similar to those of the real shale clasts; 3) the permeability contrast between the pebbles and sand should be several orders of magnitude; 4) both horizontal and vertical fluid flow have to be simulated for each sample; and 5) the pebble distribution has to cover the same range of heterogeneity fraction as the actual core regions used in two-dimensional numerical simulations. Figure 6 shows a diagrammatic cross-section of the constant-head permeameter used in the experiments. The quartzite pebbles range in size from 1.25 to 7.6 cm, with a higher aspect ratio and a more rounded shape than the shale clasts. For a given volumetric fraction, the pebbles were placed randomly in the sand matrix with a subhorizontal orientation. The mixture of sand and "pebble clasts" was then heated in an oven at 140°C for 10 h in order to cure the epoxy coated sand. The result was an artificially cemented block of binary heterogeneous porous medium. The block could then be placed in the permeameter in any of three orientations, in order to run the flow of water in the horizontal and vertical directions. The effective hydraulic conductivity for each block and flow direction was calculated using relation (1) after measuring the flow rate at steady state for a constant drop in hydraulic head.

Two blocks were prepared containing no pebbles, in order to determine the hydraulic conductivity of the sand component. The hydraulic conductivity for these sand blocks and all flow directions ranges from 4.42×10^{-3} to 4.57×10^{-3} m/s, with a mean of 4.51×10^{-3} m/s and standard deviation of 0.04×10^{-3} m/s. The corresponding average permeability is 5.25×10^{-10} m^2 (532 Darcies). Four other blocks were prepared with pebble fractions of 10%, 20%, 30% and 40%. The reduction in effective hydraulic conductivity for the blocks with pebbles is presented in Figure 7 as a function of heterogeneity (pebble) fraction, with the corresponding generalized weighted mean model (2) fitted to the data. The reduction in hydraulic conductivity was obtained as the ratio between the hydraulic conductivity of the heterogeneous block and the average value for sand.

The values of the parameter ω obtained

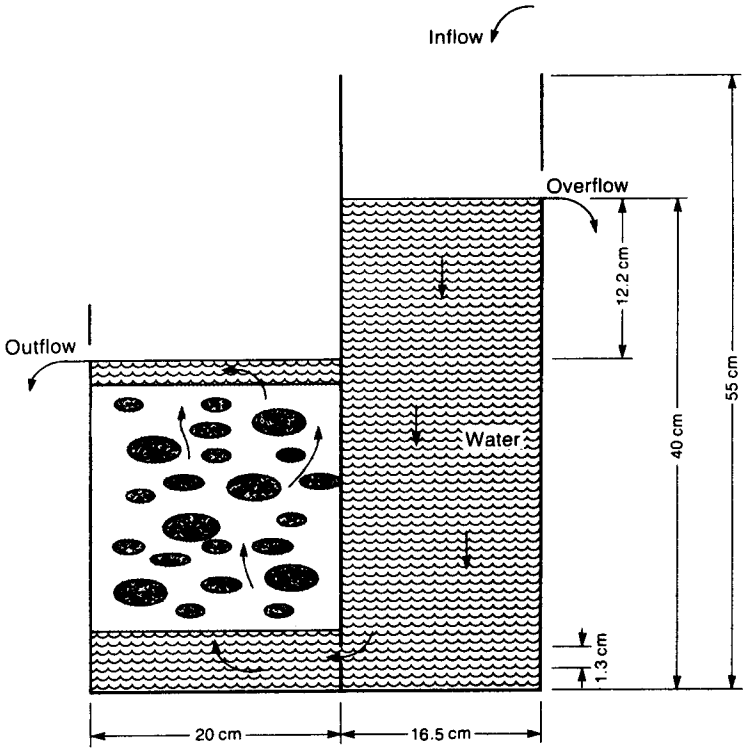

Figure 6. Diagrammatic cross-section of the constant-head permeameter used in three-dimensional physical experiments.

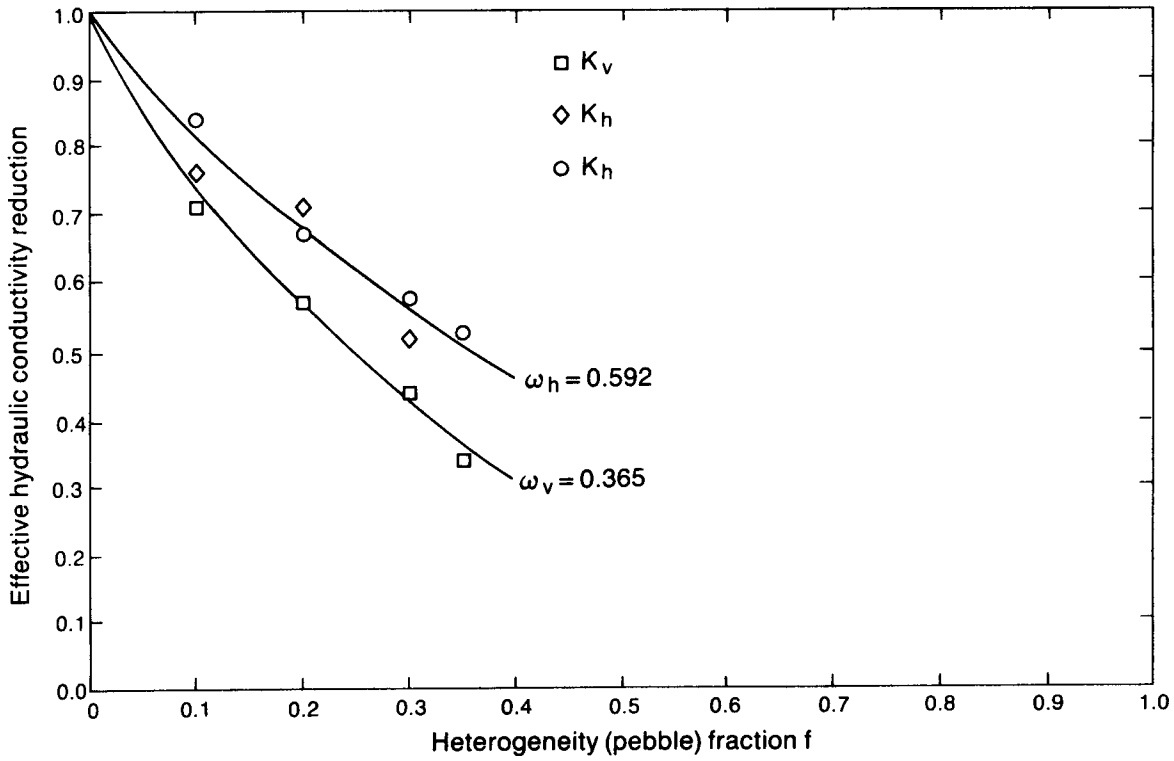

Figure 7. Variation of effective hydraulic conductivity (K_{ef}/K_{mat}) as a function of heterogeneity fraction f for cubes of sand containing pebbles. The two types of horizontal permeability measurements correspond to the two horizontal flow directions. The generalized weighted mean model is fitted to the data.

for the three-dimensional physical experiments (ω_h = 0.592 and ω_v = 0.365) are higher than those obtained from the two-dimensional numerical simulations of shale clasts (ω_h = 0.486 and ω_v = 0.243), as expected. The reason is a combination of dimensionality and differences in heterogeneity characteristics (e.g. the quartzite pebbles have a higher aspect ratio and are more rounded than the shale clasts, favouring fluid flow). The results show that the effect of this type of heterogeneity on fluid flow is also significant in three dimensions. Because the shale clasts and the quartzite pebbles have close, but different, statistical characteristics, a direct comparison of two-dimensional vs three-dimensional effects is not possible with the mixture of results obtained so far. For this reason, it is intended to carry out two-dimensional numerical simulations of flow through many cross sections of the blocks used in the physical experiments. Then, two- and three-dimensional effects can be related directly for the same statistical characteristics of heterogeneity.

Conclusions

The effect of a particular type of stochastic heterogeneity on the hydraulic conductivity of sediments was studied using an inverse approach based on numerical simulations and physical experiments. The heterogeneity consists of bodies of one lithology embedded in a matrix of a different lithology, with a strong contrast in hydraulic conductivity between the two, resulting in a bimodal and binary character. The two-dimensional numerical simulations were based on the heterogeneity distribution in sixteen actual core-scale regions containing shale clasts embedded in a sand matrix. The three-dimensional fluid flow experiments were performed for cubes of sand containing quartzite pebbles, set in a constant head permeameter. Appropriately set boundary conditions drove vertical or horizontal flow through the region being modelled. The effective conductivity of the heterogeneous region was calculated as the ratio between the mean flux and the mean gradient driving the flow.

The results of the modelling show that:

1. The effective conductivity of binary systems consisting of irregularly shaped and sized heterogeneities randomly distributed in a homogeneous and isotropic matrix has a first order dependence on the heterogeneity fraction and conductivity contrast, a dependence which can be described by a generalized weighted mean model.
2. For structures containing stochastic heterogeneities with a large aspect ratio (> 0.1) and large conductivity contrasts, the bounds of both horizontal and vertical components of the effective hydraulic conductivity can be narrowed to the geometric average and either the arithmetic or the harmonic average, depending on the connectedness of the more permeable component.
3. The effective conductivity has a second-order dependence on the shape, aspect ratio, orientation and distribution of heterogeneities in the matrix.
4. The presence of stochastic heterogeneities in a homogeneous and isotropic matrix creates anisotropy at larger scales, which for sedimentary rocks usually means a larger horizontal than vertical effective conductivity.

Future studies are needed to relate two- to three-dimensional flow effects, and to quantify the importance and role of secondary factors such as heterogeneity size, aspect ratio, shape and orientation, on the effective value of hydraulic conductivity of bimodally/binary heterogeneous porous media.

Acknowledgements

The work presented is part of a Reservoir Analysis Project equally funded by the Alberta Research Council, the Alberta Oil Sands Technology and Research Authority, and the Alberta Department of Energy, whose support is gratefully acknowledged. Thanks are due to J. Olic, M. Baaske and Mrs. M. Booth for valuable technical and clerical support.

Biographic Sketches

Stefan Bachu has an engineering degree in hydraulics and a PhD in transport processes from the Technion-Israel Institute of Technology. He is presently Head of the Petroleum Geology and Basin analysis Section of the Alberta Geological Survey (Alberta Research Council, P.O. Box 8330, Postal Station F, Edmonton, Alberta, T6H 5X2, Canada). His main areas of interest are hydrogeological and geothermal processes in sedimentary basins, and scaling-up of rock and fluid properties from core (lab) to basin scale.

Dave Cuthiell is a member of the Mathematical Modelling Group in the Oil Sands and Hydrocarbon Recovery Department of the Alberta Research Council (Alberta Research Council, P.O. Box 8330, Postal Station F, Edmonton, Alberta, T6H 5X2, Canada). Dave received his PhD in physics from Cornell University in 1977. He has been with the Alberta Research Council since 1981; his current major interests are the modelling of geological heterogeneity for purposes of reservoir simulation and recovery mechanisms in steam-based enhanced oil recovery.

John Kramers earned his BSc and MSc in geology from The University of Alberta and his PhD in geology from Rensselaer Polytechnic Institute. He is currently a senior research officer with the Alberta Geological Survey (Alberta Research Council, P.O. Box 8330, Postal Station F, Edmonton, Alberta, T6H 5X2, Canada) and project leader for the Reservoir Analysis Project. His current research interests include quantitative reservoir description and characterization.

Li-Ping Yuan earned his BSc in geology from the National Taiwan University in 1978, his MSc in geological sciences from the University of Illinois and his PhD in geology from the University of South Carolina in 1987. He is currently an assistant research officer with the Alberta Geological Survey (Alberta Research Council, P.O. Box 8330, Postal Station F, Edmonton, Alberta, T6H 5X2, Canada). His current research interests include image analysis of pore systems and computer applications in geology.

References

Bachu, S. and D. Cuthiell. 1990. Effects of core-scale heterogeneity on steady-state and transient fluid flow in porous media: numerical analysis. Water Resour. Res., v. 26, pp. 863-874.

Baveye, P. and G. Sposito. 1984. The operational significance of the continuum hypothesis in the theory of water movement through soils and aquifers. Water Resour. Res., v. 20, pp. 521-530.

Cushman, J.H. On unifying the concepts of scale, instrumentation and stochastics in the development of multiphase transport theory. Water Resour. Res., v. 20, pp. 1668-1676.

Cuthiell, D.L., S. Bachu, J.W. Kramers and L.P. Yuan. 1991. Characterizing shale clast heterogeneities and their effect on fluid flow. In Proc. Second Internat. Reservoir Characterization Conf., (L.W. Lake, H.B. Carroll Jr. and T.C. Wesson eds.), Academic Press, Orlando, pp. 226-250.

Dagan, G. 1982. Analysis of flow through

heterogeneous random aquifers, 2. Unsteady flow in confined formations. Water Resour. Res., v. 18, pp. 1571-1585.

Desbarats, A.J. 1987. Numerical estimation of effective permeability in sand-shale formations. Water Resour. Res., v. 23, pp. 273-286.

Deutsch, C. 1989. Calculating effective absolute permeability in sandstone-/shale sequences. SPE Formation Evaluation, v. 4, pp. 343-348.

Gelhar, L.W. and C.L. Axness. 1983. Three-dimensional stochastic analysis of macrodispersion in aquifers. Water Resour. Res., v. 19, pp. 161-180.

Haldorsen, H.H. and E. Damsleth. 1990. Stochastic modeling. J. Petrol. Tech., v. 42, pp. 404-412.

Hassanizadeh, M. and W.G. Gray. General conservation equations for multiphase systems, 1, Averaging procedure. Adv. Water Resour. v. 2, pp. 131-144.

Korvin, G. 1982. Axiomatic characterization of the general mixture rule. Geoexploration, v. 19, pp. 267-276.

Kramers, J.W., S. Bachu, D.L. Cuthiell, M.E. Prentice and L.P. Yuan. 1989. A multidisciplinary approach to reservoir characterization: the Provost Upper Mannville B Pool. J. Can. Petrol. Tech., v. 28, pp. 48-58.

Kramers, J.W., L.P. Yuan, S. Bachu and D. Cuthiell. 1991. Reservoir characterization case study: sandy facies. In Parameter Identification and Estimation for Aquifer and Reservoir Characterization (ed. S. Bachu), Proc. 5th Canadian/American Conference on Hydrogeology. National Water Well Association, Dublin, Ohio, (this volume).

Lasseter, T.J., J.R. Waggoner and L.W. Lake. 1986. Reservoir heterogeneities and their influence on ultimate recovery. In Reservoir Characterization (eds. L.W. Lake and H.B. Carroll Jr.), Academic Press, pp. 545-559.

Quintard, M. and S. Whitaker. 1987. Ecoulement monophasique en milieu poreux: effet des heterogeneities locales. J. Mecanique Theorique et Applique, v. 6, pp. 691-726.

Use of Detailed Sedimentological Information for the Assessment of Pumping and Tracer Tests in a Shallow Fluvial Aquifer

by J.C. Herweijer and S.C. Young

Abstract

Methods were investigated to provide a practical link between traditional engineering measurement tools such as pumping tests, and geological information about aquifer heterogeneity. A field experiment was conducted in a strongly heterogeneous unconfined aquifer, involving an extensive program of aquifer and tracer tests. As was expected, the heterogeneity is reflected in the test results. The sedimentological data available for the 1-ha test site indicate the existence of high hydraulic conductivity lenses that are elongated in a SW to NE direction. The storage coefficients, as interpreted from the pumping test, show a strong dependence on the flow pattern induced by pumping and the inter-connectivity of high hydraulic conductivity lenses between pumping and observation wells. The tracer tests show that the lenses are the main conduit for the injected solutes and confirm the validity of using the storage coefficient to indicate connections between wells.

Introduction

Many practicing hydrogeologists intuitively realize that sedimentary heterogeneity can dramatically influence the pathway of contaminant movement in sandy aquifers. Sedimentological models, describing the depositional history of the sands, are available, but lack the quantitative information necessary for a proper description of groundwater flow. Pumping tests, the main tool used to quantify flow parameters, are considered inappropriate to deal with heterogeneity, because they are based on ideal models that typically assume radial symmetry, isotropy and infinite aquifers. A detailed field experiment was conducted with the aim to develop tools for integrating qualitative sedimentological information with pumping-test data to predict solute-transport behavior. The field experiment was conducted by the Tennessee Valley Authority (TVA), contracted to the U.S. Air Force. A 1-ha test site was selected and equipped with a network of 37 fully penetrating wells. The overall objective of the ongoing project is to investigate aquifer characterization methods in order to improve techniques for contaminant recovery from shallow aquifers.

In a typical heterogeneous sandy aquifer, the pattern of high and low hydraulic conductivity zones defines a lenticular network which govern fluid movement. A sedimentological model provides a qualitative framework for description of this network. Pumping tests offer the opportunity for quantification of hydraulic parameters. However, highly idealized conceptual models underlie all curve fitting procedures. Thus, heterogeneity is generally neglected. The curve matching results in average aquifer properties, which in general are suitable for describing flow problems, but insufficient for an accurate prediction of solute transport. The deviations from the theoretical curves, observed on the field curves, and the inconsistent results from different observation wells, add to the uncertainty in the averaged properties. Part of this uncertainty

could be resolved by introducing extra fitting parameters and mathematically more complex solutions than the Theis solution, such as delayed yield models. In many instances, better curve fits are possible; however, they are still based on an over-simplified model. The apparent increase in accuracy may be deceiving.

This paper presents a field procedure which links the description of the sedimentary architecture of a heterogeneous aquifer with the non-uniform flow patterns. The results from the field experiment show that pumping tests yield information for the quantitative assessment of lenticular structures connecting the wells. The tests involved are conventional multi-well pumping tests. Simple Theis curve fits are used to obtain early time storage coefficients for each observation well. This allows mapping of the non-uniform hydraulic disturbance propagating through the aquifer in response to the pumping stress. The results of the tracer tests confirm that the method can predict solute-transport pathways from well to well.

Location and Hydrogeological Conditions

The project test site (Figure 1) occupies 1 ha of the 25 ha of TVA's Columbus Groundwater Research Test Site on Columbus Air Force Base (CAFB), Mississippi. The site is located 6 km east of the Tombigbee River and 2.5 km south of the Buttahatchee River. The aquifer is composed of 11 m of Pleistocene and Holocene fluvial deposits primarily consisting of irregular lenses of poorly-sorted to well-sorted sandy-gravel and gravelly-sand.

Groundwater levels across the Columbus Research Test Site have been monitored since 1985. The water table fluctuates from 2 to 3 m below ground surface. The water-table gradient ranges from 0.02 (low water

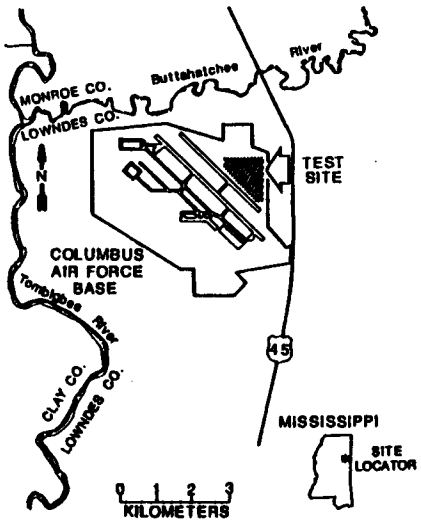

Figure 1. Location map.

table) to 0.05 (high water table). Strong vertical hydraulic gradients, which are related to the presence of heterogeneities, have been observed in several locations at the site. Rainfall at the test site averages 144 cm annually.

Well Network and Field Experiments

The network of 37 wells installed at the test site was designed using a geostatistical optimization technique (Herweijer and Young, 1990; Warrick and Myers, 1987; Olea, 1984). This optimization balanced several conflicting objectives: 1. availability of information on all scales from 1 to 50 m to determine the spatial structure (variogram); 2. sufficient coverage to interpolate correctly areal data; and 3. a radial distribution of observation wells around the central Well 5 for conducting aquifer tests. The well network is shown in Figure 2 (inter-well distances range from 2 to 75 m).

The aquifer testing program included several large-scale and small-scale pumping tests. The large-scale tests, lasting 6 days, involved pumping of a central well while monitoring water levels at distances of 4 to 30 m. The small-scale tests, lasting 2 hr, involved

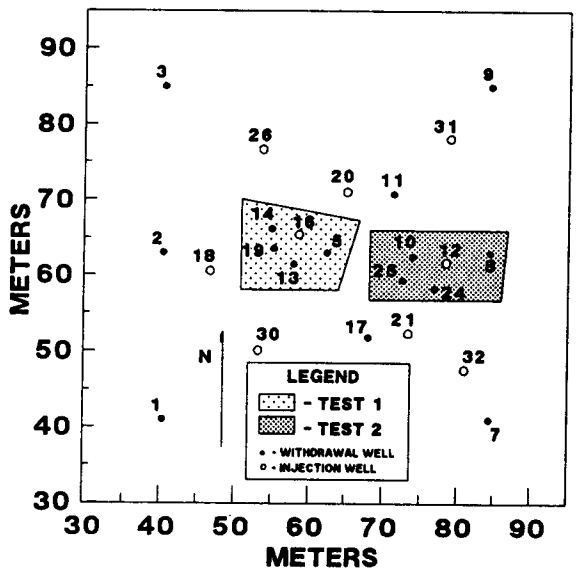

Figure 2. Well Network at the Test Site.

well clusters consisting of one pumping well and several observation wells within a radius of 6 m. This program was aimed at investigating the sensitivity of the calculated hydraulic conductivities and storage coefficients to different lenticular structures connecting the pumping and observation wells.

A series of tracer tests was then conducted to investigate in greater detail flow patterns between wells. These consisted of: 1. two three-dimensional tests injecting tracer in one well and withdrawing from four closely spaced (3 to 8 m) wells; 2. seven tests utilizing injection-withdrawal well pairs 8 to 20 m apart; and 3. a large-scale three-dimensional test injecting in the central well and withdrawing from four wells located at 35 m.

Additionally, single-well pumping tests were conducted in each well within the network. During these tests, borehole flowmeter measurements were made at 0.3-m intervals using a highly sensitive electromagnetic device (Young and Pearson, 1990). A profile of the hydraulic conductivity in the borehole was obtained by proportioning the total estimated transmissivity using flow rates in each layer (see e.g. Molz et al., 1989). The borehole flowmeter results thus provide basic information on the hydraulic conductivity of the different strata, serving as an indicator of heterogeneity.

This data set, reported by Young (1990a,b), provides hydraulic conductivity values representing a range from small-scale heterogeneities to large-scale average aquifer properties. It provides quantitative hydraulic data in conjunction with the three-dimensional geometric data resulting from the sedimentological model discussed in the next section. The tracer tests serve as a benchmark to assess the impact of this approach on the solute transport behavior.

Sedimentological Model of the Test Site

The test site is located in an alluvial valley of the Tombigbee River. The valley is filled with coarse-grained, gravelly, fluvial sands that were deposited during the Pleistocene and Holocene. Aerial photographs clearly show deposits of a former river meander. The test site lies on the inner edge of this channel, the pointbar. The upper 3 m of the aquifer are exposed in gravel pits near the site and are described by Rehfeldt et al. (1989) as a heterogeneous architecture of sand and gravel lenses ranging in length from 1 m to 8 m.

Muto and Gunn (1986) present a comprehensive description of the depositional history of the entire Tombigbee Valley. They based their interpretation on numerous field data including trenches, core holes and aerial photographs. According to this work, braided streams dominated the area during the Pleistocene. Larger meandering streams developed during the end of the Pleistocene, occasionally cutting deeply into the older deposits.

Depositional models for the sands at the test site were evaluated in order to characterize the occurrence and

dimensions of gravel lenses and clay drapes. Given the regional model of Muto and Gunn (1986) and the more localized data, two depositional models will be emphasized: deposition on the pointbar of a meandering stream, and braided stream deposition.

Pointbar Deposition

Classically, a well established model exists for the sedimentation of sands on the pointbar (the inner meander bend). The grain size of the deposited sands trends from medium coarse to very fine at a distance from the channel. Due to outward channel migration, a typical vertical sequence at a specific location shows a fining upward trend, with clay drapes occurring in the top half of the sequence. An extensive review of pointbar deposition is provided by Reading (1986).

The grain size of the gravelly sands at the test site, of which the upper half evidently were deposited on a pointbar, is coarser than would be predicted by the classical pointbar model. The observed abrupt changes in the vertical sequence and the absence of the typical fining upward trend, point to more catastrophic depositional events. Such events result in an uneven sand distribution and more chaotic occurrence of gravel lenses and clay drapes (Collinson and Thompson, 1989).

Figure 3 shows a cross section (A) and an aerial view (B) of two modern pointbars of the Amite River in Louisiana that have been described by McGowen and Garner (1971). The cross section shows a three tier system: channel floor, lower pointbar and upper pointbar. At low water stage only the channel and a small part of the lower pointbar is active and under water. In compliance with the classical pointbar model, coarse sand is deposited in the channel and finer sand is deposited on the part of the lower pointbar which is active.

During the infrequent high water (flood) stage, the entire pointbar becomes active. Small chute channels suddenly break through the upper pointbar as catastrophic events, depositing very coarse gravelly material as chute bars, shown in the left of Figure 3B. When the flood recedes, the chute channels are abandoned and, from the stagnant water in these chute channels, a clay drape is deposited.

The dimensions of chutes are given by McGowen and Garner (1971) as follows: depth 1.2 to 1.5 m; width 5 to 7 m; length 30 to 150 m. Levey (1978), who investigated similar sediments from the Upper Congaree River in South Carolina, indicates the following dimensions for chute channels: depth 0.3 to 1 m; width 3 m; and for chute bars: width 2 to 8 m; length 10 m to 100 m. It is clear that on the scale of the project test site, these deposits are major heterogeneities with a large potential impact on groundwater flow and contaminant transport.

Braided River Deposits

The lower half of the aquifer is better represented by a braided stream model. This model implies an irregular pattern of coarse gravelly lenses deposited as braid bars at high flow stage, alternating with finer sediments, deposited in the channels at low flow stage. Detailed studies of braided stream deposits are less common than those of pointbars (Reineck and Sing, 1986). Levey (1978) points out the similarities between chute channel and bar deposition on the upper pointbar, and braided stream deposition. This supports the gradual transition at the test site from coarse grained pointbar sediments to braided stream sediments.

The rapidly changing bar and channel patterns result in units which are laterally smaller than the chute channels and chute bars discussed earlier. As a result, groundwater flow and contaminant transport will be less

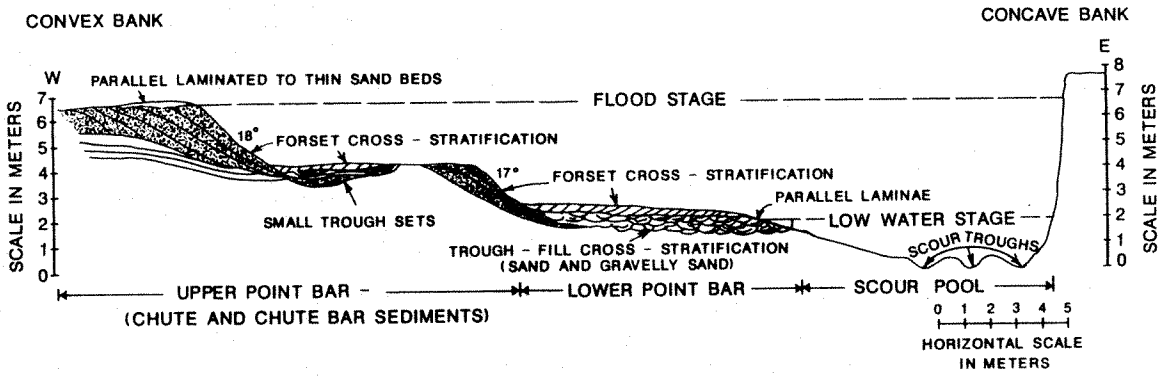

Figure 3A. Cross Section of the Modern Amite River as Observed by McGowen and Garner (1971).

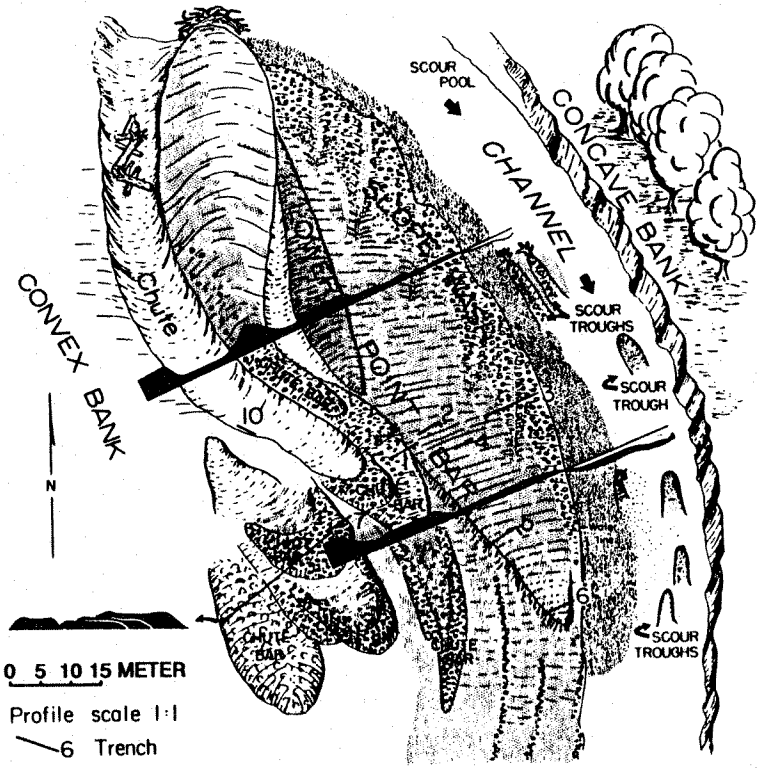

Figure 3B. Lateral View of the Modern Amite River as Observed by McGowen and Garner (1971).

impacted by these heterogeneities.

Implications for a Heterogeneous Aquifer Model

The coarse-grained pointbar depositional model for the upper part of the aquifer implies a trend from coarse gravelly sediments in the NW, in the vicinity of the former channel, to slightly finer material in the center and SE area of the site. However, elongated coarse-gravel lenses do occur in the center and SE of the site in the form of chute channels and chute bars. From the meander direction it can be inferred that these lenses are oriented SW to NE. The sedimentological model predicts that the lenses are longer than 10 m, and 2 to 7 m wide. The lenses can be capped and tailed (to the NE) by thin clays.

Because the position of the bars and channels is less stable than in meandering river deposits, the braided stream model for the lower half of the aquifer predicts a more regular structure of alternating gravelly lenses (braid bars) and clay/silt infills of the braided channels. These lenses should be laterally less extensive than in the upper part of the aquifer.

Pumping Tests

Figure 4 shows the drawdown curves that were observed for one of the large-scale pumping tests. The fact that the aquifer is unconfined and some of the curves are slightly S-shaped, suggests that the delayed yield concept could be applicable. However, the irregular shape of the curves and the differences between curves at the same radial distance from the pumping well point to the presence of heterogeneity. Therefore the data assessment should incorporate the sedimentological knowledge about the presence of high hydraulic conductivity lenses, rather than focussing on the fitting of a theoretical curve based on an idealized homogeneous model. The next sections discuss how the heterogeneous lenticular structure interferes with the classical delayed yield concept.

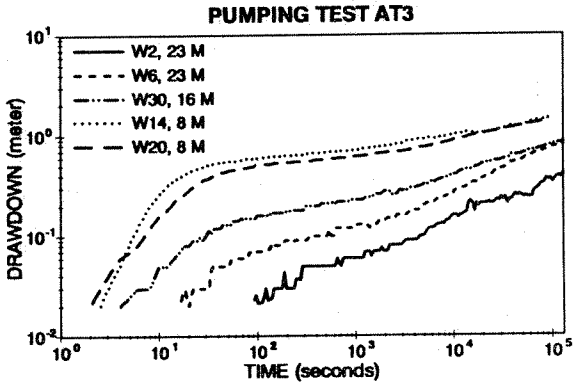

Figure 4. Drawdown Curves Observed for Long Duration Pumping Test.

Delayed Yield

During the pumping of an unconfined aquifer, water is first released from elastic storage and, after a delay, water is released from a second storage. This delayed yield phenomenon has been extensively described (e.g. Neuman, 1979). The second storage, the specific yield, is considered to be the drainable pore volume of the aquifer between the original water table and the water table at steady-state pumping. Steady-state vertical flow occurs only during late pumping and only then is this second storage fully drained. The drawdown curve is typically S-shaped, with the horizontal segment representing the transitional phase between the flow regimes.

For homogeneous unconfined aquifers, Streltsova (1972) and Neuman (1972) presented a well defined

physical concept to describe delayed yield. The approximation of Streltsova (1972) implies that the unconfined aquifer can be simulated by an aquitard overlying a confined aquifer. The aquitard has zero transmissivity and a storage coefficient equal to the specific yield. The vertical resistance of the aquitard is smaller, by a factor of three, than the vertical resistance of the aquifer. The solution of Neuman (1972) is more complex: the vertical resistance of the aquitard varies as a function of the distance to the pumping well. The latter corrects for the fact that the vertical trajectory varies at different distances from the pumping well. The solution of Neuman (1975) describes the anisotropic case. Type curves are provided to determine the horizontal and vertical hydraulic conductivity of the aquifer, the latter mainly based on the platform part of the S-shaped curve.

Pumping an Aquifer with a Lenticular Architecture

Obviously, individual drawdown curves could be fitted using theoretical curves generated using one of the above described analytical solutions for delayed yield. As a result of heterogeneity, different observation wells would give different values for transmissivity, elastic storage, specific yield, and vertical hydraulic conductivity. However, these results do not address the important issue of high hydraulic conductivity lenses connecting wells, as outlined by the sedimentological analysis. A more correct interpretation of the observed drawdowns in different wells requires that the flow field in a heterogeneous aquifer be considered. Figure 5 shows an example of a lenticular heterogeneous aquifer. Fully screened wells penetrate lenses of very high hydraulic conductivity (K1, e.g. a chute channel) and moderately high hydraulic conductivity (K2, e.g. a chute bar deposit). Both hydraulic conductivities K1 and K2 are high relative to K3 (e.g. medium-fine pointbar deposits).

When pumping Well B (Figure 5), most of the water will be drawn out of the high hydraulic conductivity (K1) lenses. Nearly instantaneous drawdown will be observed in Well A, which is connected to Well B by one of these lenses, because water is released from elastic storage in the lens.

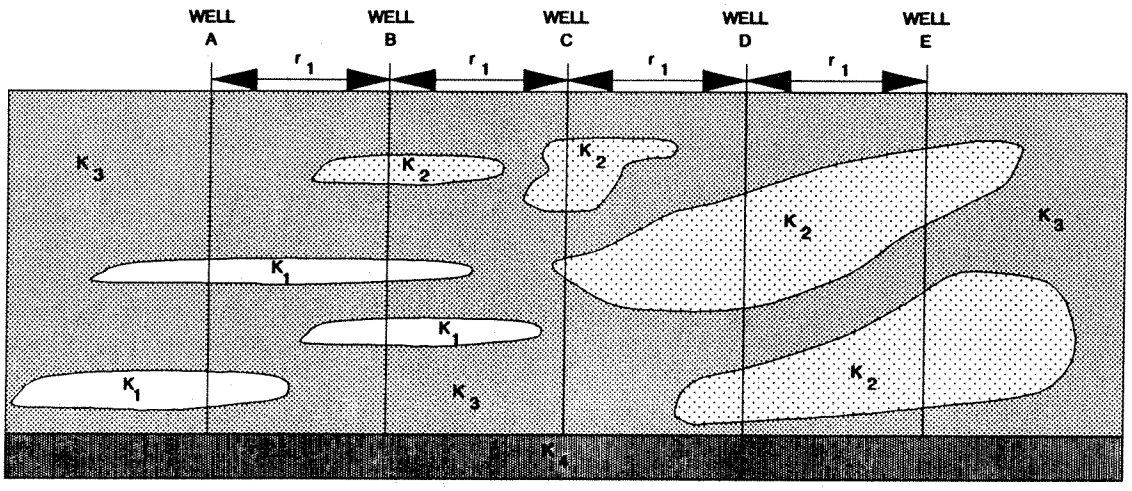

Figure 5. Fictitious Crossection of a Schematic Lenticular Aquifer.

A storage coefficient based on analyzing the early part of the curve is on the order of 10^{-5} (the elastic storage coefficient). After a delay, a hydraulic gradient will be established, resulting in vertical and lateral flow toward the lens as the rest of the aquifer is drained during late time. A storage coefficient based on analyzing the late time part of the drawdown curve is approximately 10^{-1} and represents the specific yield. The overall drawdown curve will show the transition phase, comparable to the S-shaped delayed yield curve.

Well C, at the same distance from Well B as Well A, is not connected by a lens to Well B. Thus the water level in Well C does not respond to pumping of Well B as quickly as in Well A. However, because a lens connected to the pumping Well B is rather close, the quick water level response through this lens can still be felt in Well C. Therefore analyzing the early part of the curve gives a storage coefficient greater than the elastic storage coefficient but smaller than the specific yield.

Wells D and E are at a large distance from the pumping well. Even lenses of considerable size do not connect them to the pumping Well B. Thus, no rapid response is observed in Wells D and E. Therefore, analyzing the early part of the drawdown curve gives a storage coefficient on the order of the specific yield.

The transition between release of water from elastic storage and the release from the drainable pore volume is a function of the connection between the pumping and observation well. Given the irregular pattern of connecting lenses and hydraulic conductivities, this transition will vary between different well pairs and not always be sharp. As a result, the observed drawdown curves are not perfectly S-shaped (Figure 4), especially for wells at a relatively large distance. They show a cascade of transitional phases, reflecting a structure of multiple lenses connecting the pumping and observation wells.

Interpretation of the Field Data

A simple approach for curve analysis was chosen to analyze the transitional flow field resulting from the heterogeneous architecture. Drawdown curves were fitted, based on the Theis formula including Jacob's correction for the transmissivity decrease when pumping an unconfined aquifer. Different portions of the curve were analyzed to deal with the flow field changing over time. Figure 6 shows the results of fitting portions of the curve (the first 2000, 10000, 50000, 100000, and 250000 s).

The transmissivity values cover a normal range for the average aquifer material when the drawdown curves are analyzed for time > 10000 s. The storage coefficient ranges from 10^{-2} , which is a 'normal' value for an unconfined aquifer (specific yield), to 10^{-5} which is more typical for a confined aquifer. All values in the 10^{-5} range were obtained when fitting the

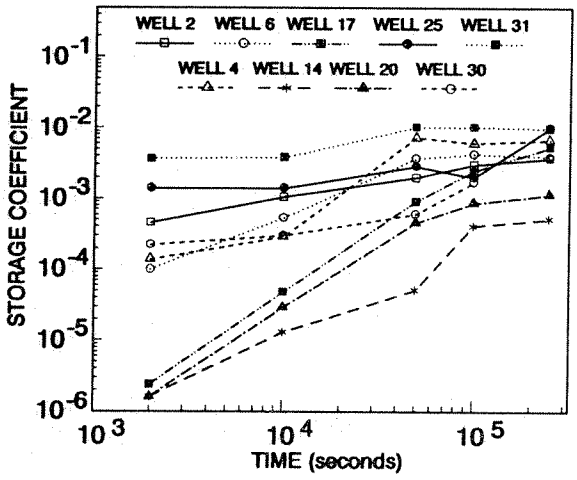

Figure 6. Storage Coefficient vs. Period of Analysis.

drawdown curve for the first 10000 s. Wells 14, 17 and 20, for which these low storage coefficients were obtained, are interpreted to be connected by a high hydraulic conductivity lens to the pumping Well 5. The other wells have less permeable connections to the pumping Well 5.

Figure 7 shows the distance between the pumping well and monitor well vs the storage coefficient. All existing drawdown curves, from the large- and small-scale test, were used. For the longer tests, the first 10000 s of the drawdown curve were analyzed; the small-scale tests lasted 7000 s.

The diagonal line in Figure 7 represents, at each distance, the maximum 'delayed yield' effect of the lenticular aquifer architecture. For distances > 20 m the storage coefficient is > 10^{-3}. This indicates that high hydraulic conductivity lenses having a length > 20 m do not exist between any of the well pairs. The vertical line in Figure 7 shows that, for a distance of 4 m, the whole range of values (10^{-2} to 10^{-5}) is found for the storage coefficient. This indicates that some of the well pairs that are 4 m apart are connected by a high hydraulic conductivity lens, while others are connected by a lens having only a moderate hydraulic conductivity, or are not connected at all.

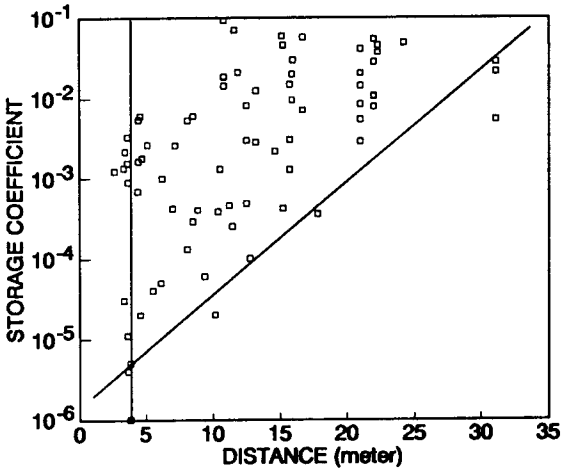

Figure 7. Storage Coefficient vs. Distance.

This picture of connections between wells matches well with the sedimentological model. The coarse-grained chute channels and chute bars form the high hydraulic conductivity connections between the wells. Their width is restricted to about 7 m; the length is considerably longer (10 to 100 m). However, the different coarse-grained depositional events alternated with clay drapes make it unlikely that wells > 20 m apart are connected by one continuous high hydraulic conductivity lens.

Conclusion of the Aquifer Test Analysis

The presented procedure shows that the combination of sedimentological data and the analysis of early time drawdown identifies important connections within the lenticular network of the heterogeneous aquifer. The storage coefficient obtained from analyzing the early time part of the drawdown curve is a good indicator for high hydraulic conductivity connections between the pumping and observation well. The late time part of the curve yields an effective aquifer transmissivity.

This approach makes it unnecessary to fit type curves which represent the more complex delayed-yield model. Better fits may result, but the lateral heterogeneity could be masked in the extra parameters which are determined. The lenticular structure of the aquifer incorporated in the presented analysis is derived from the sedimentological model. The coarse lenses consist of chute channels, chute bars, and braid bars. The drawdown analysis allows benchmarking of these lenses which serve as high hydraulic conductivity connections between wells.

Tracer Tests

To validate the results from the aquifer test analysis, a series of tracer tests were carried out at the test site using a Br tracer. The tracer test results are also envisaged as a data set for the testing of techniques for calibration of three-dimensional solute transport models in strongly heterogeneous aquifers. In total, 10 tracer tests were carried out on scales ranging from 3 to 100 m.

The next sections present Tracer Tests 1 and 2, involving clusters of closely drilled wells (4-6 m) for which pumping tests had been conducted (locations are shown in Figure 2). Water was injected in one well and withdrawn in 4 equal portions from the observation wells. Tracer injection started when the drawdowns reached steady-state. Tracer breakthrough was measured using multi-level samplers located at 1.5-m intervals.

Tracer Test 1

Tracer was injected in Well 16 and breakthroughs were observed in Wells 5, 13, 14 and 19. Figure 8 shows the borehole flowmeter profiles observed during the tracer test and during previous single-well tests. Lenses at two levels (56 m MSL and 59-60 m MSL) can be readily correlated between all the wells except Well 5. Table 1 summarizes data collected during the tracer test. Hydraulic conductivities were calculated from the tracer-breakthrough time, and borehole flowmeter observations made during the previous single-well tests. The storage coefficients were obtained from analyzing a small-scale pumping test conducted at Well 16.

Breakthrough occurred within 100 min in all wells except Well 5. This fits well with the good correlation of the borehole flowmeter profiles (Figure 8). The small (10^{-5}) confined storage coefficients support the conclusion that Wells 13, 14, 16 and 19 are connected by high hydraulic conductivity lenses.

The hydraulic conductivities, calculated from peak breakthrough of the tracer, fit well with the values observed independently using the borehole flowmeter during a single-well test. The tracer hydraulic conductivity should be compared to the average of the borehole flowmeter conductivities of the tracer injection and observation well. The tracer hydraulic conductivity is biased towards the lower of the two borehole flowmeter conductivities.

Tracer Test 2

Tracer was injected in Well 12 and breakthrough was observed in Wells 8, 10, 24 and 25. Figure 9 shows the borehole flowmeter profiles observed during the tracer test and during previous single-well tests. Table 1 shows data collected during the tracer test. Lenses occurring at 59-60 m MSL cannot be correlated between the wells as easily as in the previous example. The storage coefficients were obtained from the analysis of a small-scale pumping test conducted at Well 12.

Compared to Tracer Test 1, breakthrough takes significantly more time for nearly the same distance between injection and observation well. The vertical borehole flowmeter profiles (Figure 9) indicate large contrasts in hydraulic conductivity. However, these contrasts do not line up on the same horizontal level as nicely as shown for Tracer Test 1 (Figure 8). In contrast to Tracer Test 1, lenses do not connect the injection and observation wells of Tracer Test 2. This is reflected in the storage coefficients obtained from the pumping test analysis, which are one order of magnitude greater than those observed for the wells of Tracer Test 1.

The storage coefficients also allow the comparison of connections between the injection well and different observation wells of this tracer test. Obviously Wells 8 and 24 are less

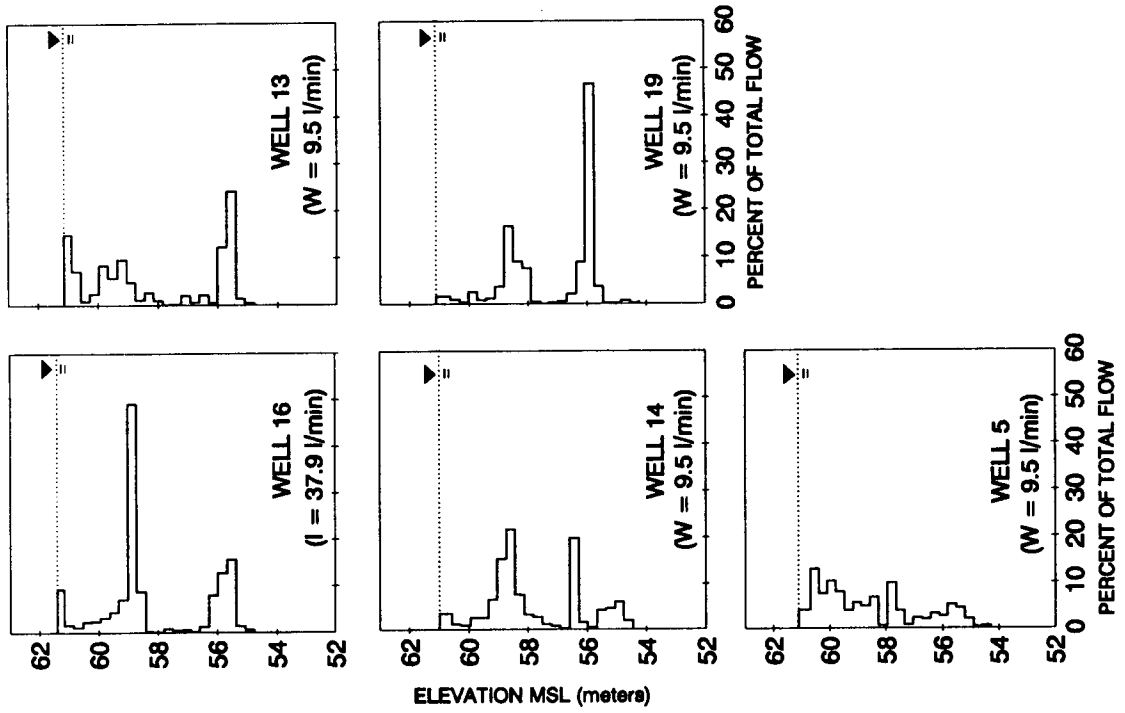

Figure 8. Vertical Borehole Flowmeter Profiles, Tracer Test 1.

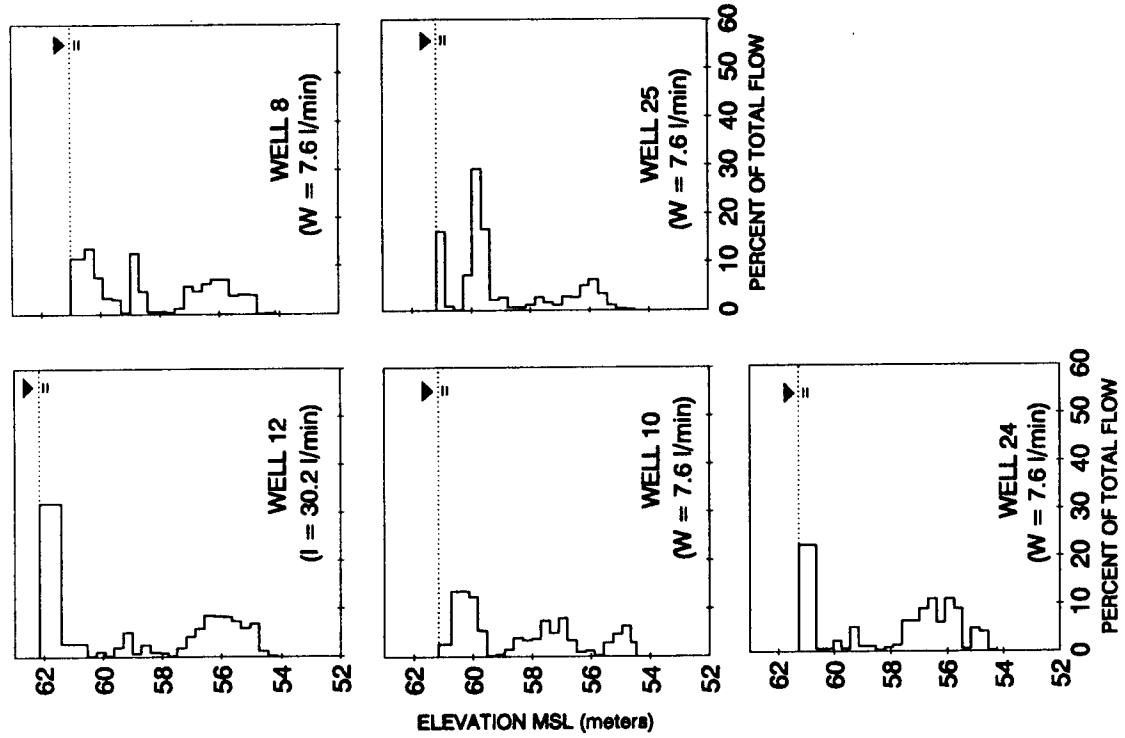

Figure 9. Vertical Borehole Flometer Profiles, Tracer Test 2

Table 1

Breakthrough Results of Tracer Test 1 and Tracer Test 2

Obs. Well	Dist. m	Depth m MSL	Azimuth	Time min	Flux mg/s	K TR[1] cm/s	K BHF[2] cm/s	K BHF[3]	S SCPT[4]
Tracer Test 1, 1750 l tracer (800 mg/l Br) injected in well 16 at a rate of 38 l/min									
19	4.2	58.5	250 W	<60	>400	>0.58	1.60	1.50	4.0×10^{-6}
19	4.2	56.1	250 W	<60	>200	>0.58	1.70	0.40	
14	4.1	58.7	290 W	80	1200	0.24	0.36	1.50	1.1×10^{-5}
14	4.1	56.3	290 W	<48	>400	<0.40	0.12	0.40	
13	4.4	59.6	185 S	96	140	0.40	0.38	1.50	1.0×10^{-6}
13	4.4	59.6	185 S	96	100	0.40	0.61	0.40	
5	5.3	60.7	110 E	213	75	0.23	0.26	1.50	2.0×10^{-5}
5	5.3	59.5	110 E	306	25	0.16	0.26	1.50	
5	5.3	55.8	110 E	171	10	0.28	0.12	0.40	
Tracer Test 2, 4000 l tracer (800 mg/l Br) injected in well 12 at a rate of 31 l/min									
25	6.1	60.6	250 W	144	600	0.14	0.20	0.43	5.0×10^{-5}
24[5]	3.6	57.0	195 S	969	450	0.008	0.007	0.022	1.6×10^{-3}
10	4.4	60.2	280 W	<174	1400	<0.043	0.27	0.43	6.8×10^{-4}
8	6.3	59.9	80 E	504	450	0.036	0.009	0.43	1.0×10^{-3}

[1] TR from tracer test using peak travel time, hydraulic gradient and effective porosity (n=0.3)

[2] BHF from borehole flowmeter observations in observation well

[3] BHF from borehole flowmeter observations in injection well

[4] S SCPT storage coefficient from small-scale aquifer test pumping the injection well

[5] No multi-level sampler at 61.0 m MSL was available, although water influx at this level was recorded

connected to Well 12, resulting in breakthrough times 3 to 5 times larger compared to Wells 10 and 25. Well 25 can be classified as well connected, based on both storage coefficient and breakthrough time. For Well 10, the storage coefficient and peak breakthrough time slightly contradict each other; the storage coefficient is too high for the relatively fast breakthrough.

Because the borehole flowmeter profiles of the injection observation pairs do not match, the hydraulic conductivities are difficult to compare with the results of the tracer test. Only for Well 25, which is well connected to the injection well, all three hydraulic conductivity values match. For the other pairs, the tracer test hydraulic conductivity values compared best with the lowest value of the borehole flowmeter conductivity determined for the observation and injection well.

Conclusions

The integration of the sedimentological model and pumping test analysis allowed the assessment of the lenticular structure of a heterogeneous aquifer, and the classification of its hydraulic behavior. It explains problems in curve fitting and inconsistent results from different observation wells when analyzing well tests with analytical models based on assumed homogeneity. Rather than focussing on improving curve fits, a procedure was chosen to use anomalous values for the storage coefficient as an indicator for high hydraulic conductivity connections between wells. In doing so, the flow properties of a lenticular network as predicted by the sedimentological model can be benchmarked in a semi-quantitative manner. This procedure involves conventional multi-well pumping tests and the Theis curve-fit method for determination of the early time storage coefficient. This procedure offers a rather straightforward method for characterization of strongly heterogeneous aquifers.

This approach performs well in relating results of aquifer tests and tracer tests in an unconfined aquifer. Using the lenticular model, the tracer results of two small-scale clusters of 1 injection to 4 withdrawal wells were explained in terms of three-dimensional connections by high hydraulic conductivity lenses. The identified connections match well with the trend observed for the storage coefficient calculated from two small-scale aquifer tests carried out for these clusters. These storage coefficients range from 10^{-3} - 10^{-6}. The lower values indicate high hydraulic conductivity lenses connecting the pumping well and the observation well. The higher values indicate the absence of such connections. Independently, the geological correlation of the vertical borehole flowmeter profiles also confirms the difference in connections between wells for the two well-clusters analyzed.

The presented results address mainly one scale of heterogeneity, the 10 m scale, which is relevant given the site dimensions. This is also the typical scale relevant to many groundwater-contamination cases. The tracer test results emphasize that the lenses are the main conduits for solute transport during pumping. For heterogeneous flow patterns, probably sedimentary discontinuities (e.g. clay drapes, temporarily exposed surfaces between the flow deposited sands and gravels) are as equally important as the hydraulic conductivity contrasts.

A three-dimensional groundwater flow and transport model needs to integrate all this knowledge and uncertainty (e.g. Begg et al., 1989). Future research will address simulation of the aquifer tests to validate the hydraulic performance of such a model in a more direct relation to heterogeneity. The site-wide large-scale tracer test, which was conducted, could then be used to test whether this approach will result in a better calibrated solute transport model.

Acknowledgements

The work was funded by the United States Air Force Engineering And Services Center, Tyndall AFB, Florida.

Joost C. Herweijer received his M.S. in Hydrogeology and Geophysics from the Free University of Amsterdam (Netherlands). His academic interests are the characterization of heterogeneous aquifers and application of solute transport models. After graduation (1983) he worked for two years as a data processing consultant, mainly in petroleum engineering projects. Subsequently, he joined Royal Dutch Shell as a research petroleum

geologist, working on probabilistic facies modelling and sedimentological application of high resolution geophysical (dipmeter) well logs. Since October 1988 he has been employed with GeoTrans Inc (3300 Mitchell Lane, Suite 250, Boulder, CO 80301, USA), working on a variety of research and operational projects in the field of groundwater remediation.

Steven C. Young received his B.A. in Environmental Sciences from the University of Virginia and his M.S. in Civil Engineering from Stanford University. During the last seven years, he has worked with the Tennessee Valley Authority (TVA Engineering Laboratory, 129 Pine Road, Norris, TN 37828, USA) to improve methods for characterizing the hydraulic properties of aquifers and for applying computer models to solve groundwater problems. His research experience includes the design and analysis of aquifer pump tests, artificial and natural gradient three-dimensional tracer tests, borehole flowmeter tests, small-scale evaporation experiments, water budget measurements of ash landfills, and studies to evaluate the EPRI FASTCHEM model.

References

Begg, S.H., R.R. Carter and P. Dranfield. 1989. Assigning effective values to simulator gridblock parameters for heterogeneous reservoirs. Soc. Petrol. Eng., Res. Eng., Nov. 1989

Collinson, J.D. and D.B. Thompson. 1989. Sedimentary Structures. Unwin Hyman, p. 16.

Herweijer J.C. and S.C. Young. 1990. Three-dimensional characterization of hydraulic conductivity in heterogeneous sands using pump tests and well tests on different scales. Poster Paper presented at ModelCARE90, 3-6 Sept. 1990, The Hague, Netherlands.

Levey, R.A. 1978. Bed-form distribution and internal stratification of coarse grained pointbars, Upper Congaree River, S.C. In: Fluvial Sedimentology (ed. A.D. Miall), Canadian Society of Petroleum Geologists, pp. 105-127.

Molz, F.J., R.H. Morin, A.E. Hess, J.G. Melville and O. Guven. 1989. The impeller meter for measuring aquifer permeability variations: Evaluation and comparison with other tests. Water Resour. Res., v. 25, pp. 1677-1683.

Muto, G.R. and J. Gunn. 1986. A study of late Quaternary environments and early man, phase I final report, project narrative and appendices A-D. U.S. Army Corps of Engineers, Mobile and Nashville Districts.

McGowen J.H. and L.E. Garner. 1971. Physiographic features and stratification types of coarse grained pointbars: Modern and ancient examples. Sedimentology, v. 14, pp. 77-111.

Neuman, S.P. 1972. Theory of flow in Unconfined Aquifers Considered Delayed Response of the Water Table. Water Resour. Res., v. 8, pp. 1031-1045.

Neuman, S.P. 1975. Analysis of pumping test data from anisotropic unconfined aquifers considering delayed gravity response. Water Resour. Res., v. 11, pp. 329-342.

Neuman, S.P. 1979. Perspective on delayed yield. Water Resour. Res., v. 15, pp. 899-445.

Olea, R.A. 1984. Systematic sampling of spatial functions, Kansas Geol. Surv., Series on Spatial Analysis, no. 7.

Reading, H.G. 1986. Sedimentary Facies and Environments. Blackwell, pp. 36-37.

Rehfeldt, K.R., L.W. Gelhar, J.B. Southard and A.M. Dasinger. 1989. Estimates of macro-dispersivity based on analyses of hydraulic conductivity variability at the MADE site. Interim Report

EN-6405, Electric Power Research Institute.
Reineck, H.E. and I.B. Sing. 1986. Depositional Sedimentary Environments. Springer-Verlag, pp. 274-284.
Streltsova, T.D. 1972. Unsteady radial flow in an unconfined aquifer. Water Resour. Res., v. 8, pp. 1059-1066.
Warrick, A.W. and D.E. Myers. 1987. Optimization of sampling locations for variogram calculations. Water Resour. Res., v. 23, pp. 496-500.
Young, S.C. 1990a. A site characterization methodology for aquifers in support of bioreclamation activities. Vol I. Well network design, well equations, and aquifer multi- and single-well tests. U.S. Air Force Engineering and Services Center, Tyndall AFB, FL (Report in review).
Young, S.C. 1990b. A site characterization methodology for aquifers in support of bioreclamation activities. Vol II. Borehole flowmeter technique, tracer tests, geostatistics, and geology. U.S. Air Force Engineering and Services Center, Tyndall AFB, FL (Report in review).
Young, S.C. and H.S. Pearson, 1990. Application of an electromagnetic borehole flowmeter to predict three-dimensional solute transport in a heterogeneous aquifer. Proc. 83rd Ann. Mtg. Air and Water Managment Assoc., Paper 90-8.3.

Geostatistical Evaluation of a Three-Dimensional Hydraulic Conductivity Field in an Alluvial Terrace Aquifer

by Steven C. Young, Joost Herweijer, and Dudley J. Benton

Abstract

Extensive borehole flowmeter tests were performed at 37 fully screened wells on 1 ha of an alluvial terrace aquifer to characterize the three-dimensional hydraulic conductivity field. At each well location, approximately 24 hydraulic conductivity measurements were taken at 0.3 m vertical intervals. These hydraulic conductivity measurements indicate that the arithmetic mean, geometric mean, and the variance of the natural logarithm of the hydraulic conductivity field is 0.26 cm/s, 0.032 cm/s, and 4.7, respectively. A data analysis shows that the hydraulic conductivity field is not log-normally distributed and has definite trends. These trends are supported by the location of a former river meander in a 1956 aerial photograph of the site. Prior to the borehole flowmeter tests, the well locations were optimized with respect to a computer-aided geostatistical analysis. In order to apply geostatistics, the original data set was detrended using several different polynomial equations. The different residual data sets were analyzed with respect to their statistical properties. Although the analyses showed very different results for the residual data sets, no criteria could be established to determine which data set was the most appropriate for geostatistical analyses. The results show that in some heterogeneous aquifers, a significant obstacle to geostatistics is detrending the data. As a result, a considerable amount of uncertainty will accompany geostatistical analyses of these aquifers.

Introduction

Within the last decade considerable progress has been made in developing stochastic theories/models for problems related to solute transport in groundwater. Many of the stochastic theories assume an intrinsic stationarity hypothesis to extract/simulate attributes of the hydraulic conductivity data. Intrinsic stationarity, in this case, means that the first two moments (i.e. the mean and the variance) of the probability density function for the hydraulic conductivity field are invariant with respect to translation through space. For convenience, stochastic theories will henceforth refer to those theories that assume intrinsic stationarity as defined above.

One of the assumptions in developing and applying the stochastic theories is that heterogeneity becomes homogeneous or spatially periodic at some scale, so that the random variable used to represent the hydraulic conductivity exhibits intrinsic stationarity. For those aquifers in which the scale of the heterogeneities is large compared to the scale of the problem, the assumption is made that the stochastic theory can be applied after detrending the field and creating a set of residuals that is stationary. To date, very little work has been published that

evaluates and/or demonstrates the utility/optimality of these stochastic theories in heterogeneous aquifers.

This paper examines some of the potential problems associated with performing geostatistical and trend analysis on 881 hydraulic conductivity values taken at a 1-ha test site in an 11 m thick alluvial terrace aquifer. These problems include determining whether a nonstationarity exists, a method for detrending, and the extent to which the data should be detrended. The results of this exercise show that considerable uncertainty may accompany the application of stochastic theories to heterogeneous materials.

Description of the Test Site

The United States Air Force (USAF) test site occupies ~ 1 ha of the Columbus Groundwater Research Test Site of the TVA on Columbus Air Force Base (CAFB), Mississippi. The site is ~ 6 km east of the Tombigbee River and 2.5 km south of the Buttahatchee River, and lies above the 100-a flood plain of both rivers. The unconfined terrace aquifer is composed of ~ 11 m of Pleistocene and Holocene fluvial deposits primarily consisting of irregular lenses of poorly-sorted to well-sorted sandy-gravel and gravelly-sand. Quaternary deposits unconformably overlie the Cretaceous age Eutaw Formation that consists primarily of marine clay and silt.

Groundwater levels across the Columbus Research Test Site have been monitored since 1985 using single and multistaged monitor wells. Seasonally, the phreatic surface fluctuates 2 to 3 m. The horizontal hydraulic gradient varies from ~ 0.02 (low water table) to 0.05 (high water table). Upward and downward vertical gradients, several orders of magnitude higher, have been observed over most of the site. These vertical gradients are related to the spatial variability in the hydraulic conductivity field and produce complex groundwater flow patterns.

Design of the Well Network

An initial point of concern was the design of an optimal well network. Different conflicting needs must be satisfied. Information on the spatial variability must be obtained on all scales, ranging from very short ranges (1 m) to the scale of the test site (100 m). However, to obtain sufficient areal coverage for mapping, an evenly spaced network is optimal. Formulated in geostatistical terms: a variogram, representing the spatial structure, requires a certain number of closely spaced wells, and kriging (mapping) requires sufficient coverage over the whole area of evenly spaced wells.

Warrick and Myers (1987) presented a procedure to optimize a well network for empirical determination of a variogram, and Olea (1984) outlined criteria for selecting an optimal sampling network for kriging. Based on the guidelines provided by these authors a computer code (WELPLAN) was developed to generate and analyze well networks. The program receives as input the number of existing wells, the number of new wells to improve the data set for kriging, and the number of wells to improve the data set for variogram determination. Additionally, the boundaries of the well network can be specified as a polygon and building sites can be excluded.

Figure 1 graphically illustrates the distribution of the number of

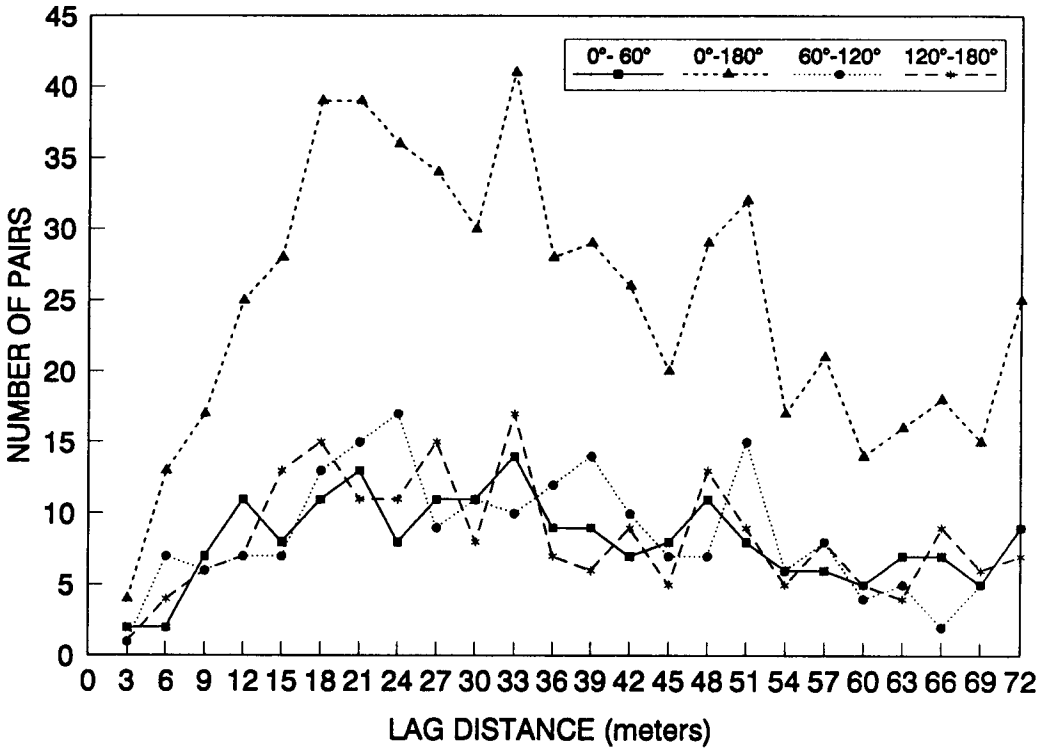

Figure 1. Number of well pairs for each lag distance.

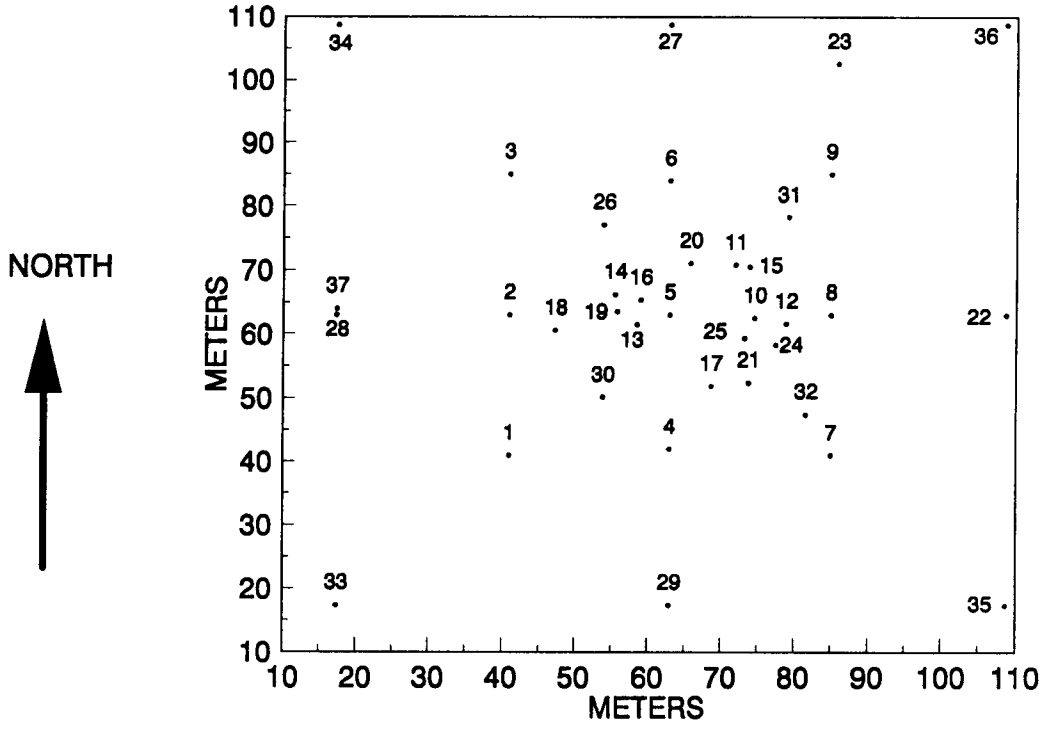

Figure 2. Well network at Columbus Air Force Base Test Site.

well pairs as a function of lag distances and the azimuth of the connecting vector. Figure 2 illustrates the selected optimal well network. Because the wells were not installed at the same time, the WELPLAN program was run several times, using existing wells as fixed input. The first 17 wells were selected to provide uniform well coverage suitable for kriging and conducting a large-scale 5-well recirculating tracer test. The next 10 wells were selected to improve the optimization of the variogram.

The Hydraulic Conductivity Field

A depth profile of the hydraulic conductivity, representative for a local area around a wellbore, can be obtained during a single well test by using a borehole flowmeter to measure the contributions of the different layers to the total rate withdrawn or injected. The concept of the borehole flowmeter is illustrated in Figure 3. Basically, the method involves achieving a "steady-state" drawdown in the well and measuring the vertical flow inside the well at designated depths. By successively differencing the incremental flow measurements, the amount of water leaving or entering a length of screen is calculated.

The analysis of the borehole flowmeter data consists of three steps. The first step is determining the ratio of the hydraulic conductivity of each layer, K_i, to the depth-averaged hydraulic conductivity value, $\bar{K}$. This ratio is calculated from the borehole flowmeter measurements and equations for well headlosses. The second step is determining the value of the depth-averaged hydraulic conductivity, $\bar{K}$, by applying the Cooper-Jacob straight-line method (Cooper and Jacob, 1946) to the well drawdown response. The third step is determining the hydraulic conductivity of each layer by multiplying the value of K_i by $\bar{K}$. Reports by Young (1990a,b) and Young and Pearson (1990) detail the procedures for the borehole flowmeter method used at CAFB. Molz, et al., (1989) and Rehfeldt, et al., (1989a) provide general information on the technique.

At each of the 37 wells, the borehole flowmeter measurements were made at 0.3-m intervals. Figure 4 provides the calculated hydraulic conductivity profiles at wells 1 through 6 to illustrate the very heterogeneous nature of the aquifer. At a typical well location, the hydraulic conductivity values range over three orders of magnitude. Over distances as short as 0.3 m, order of magnitude changes are common. Figure 5 shows areal cross-sections of depth-averaged hydraulic conductivities over a 2-m aquifer interval.

Table 1 summarizes the statistical properties of 881 hydraulic conductivity measurements. By applying the Kolmorgorov-Smirnov Test (Liffiefors, 1967) both normality and log-normality can be rejected at the 99% confidence limits. One possible criticism of the Kolmorgorov-Smirnov Test results is that the sample points are not random; consequently, a bias may exist in the data set. Because of the rather large 'KS' values in Table 1, most, if not all, of the random sampling taken from the 881 hydraulic conductivity measurements would be neither normally nor log-normally distributed.

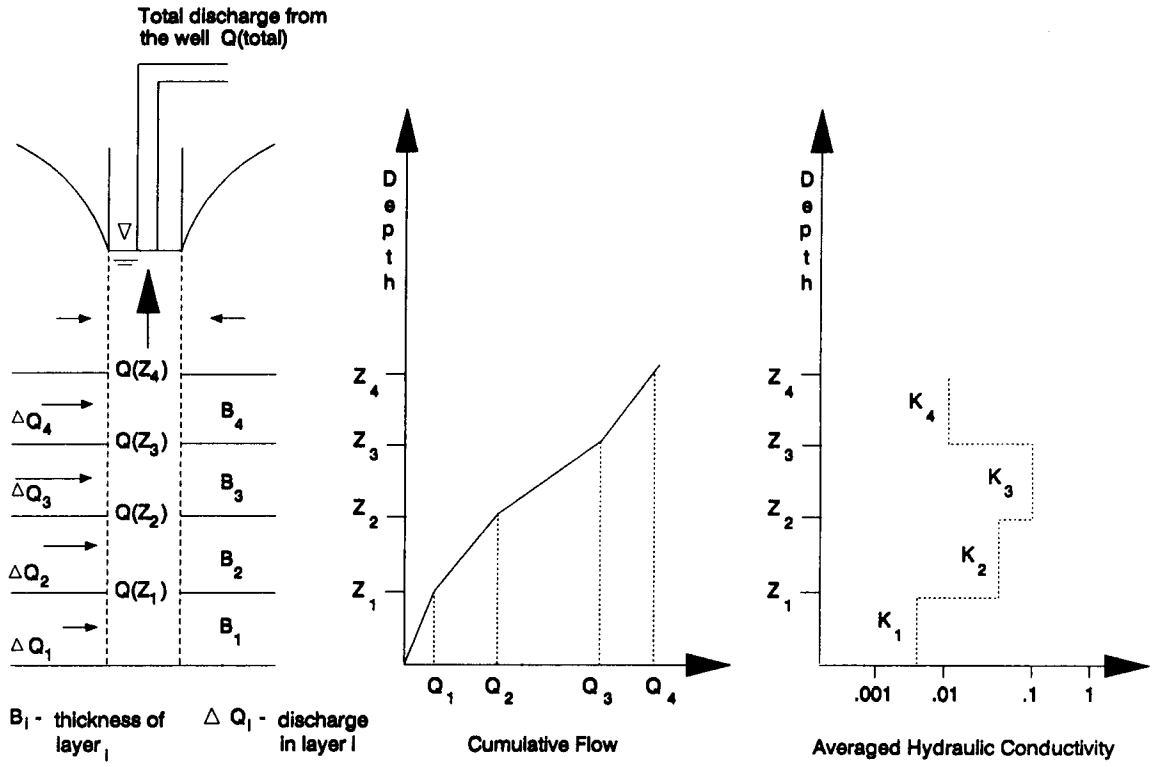

Figure 3. Schematic of relation between flow into a well and hydraulic conductivity.

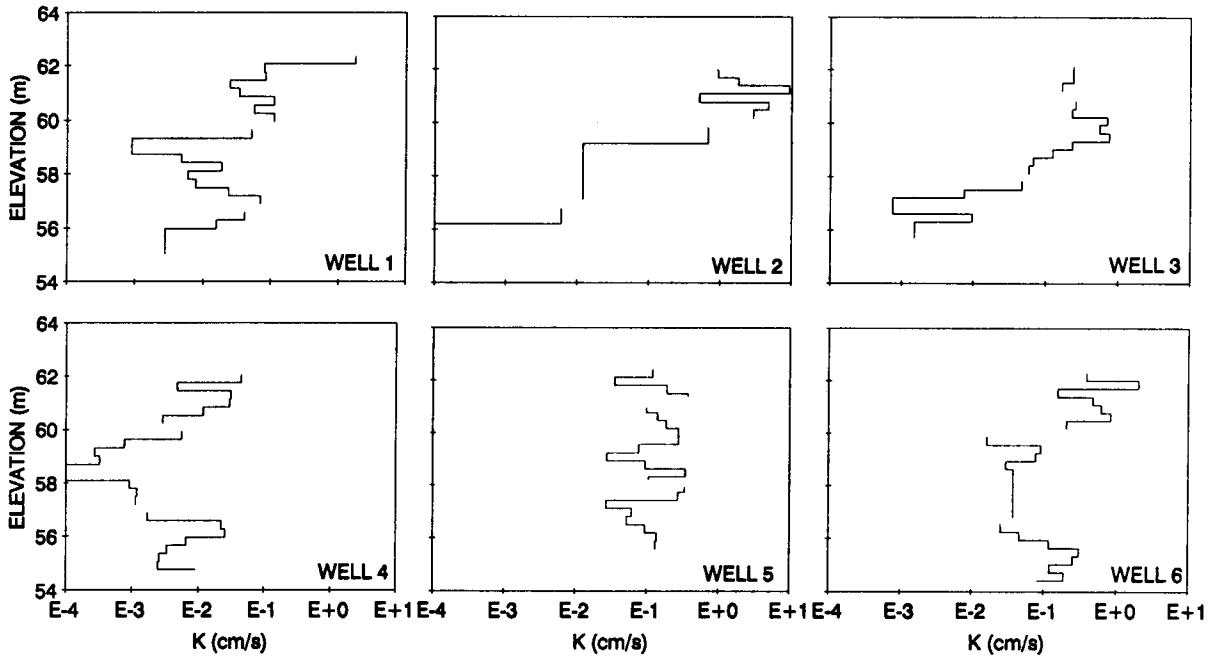

Figure 4. Hydraulic conductivity profiles for wells 1-6.

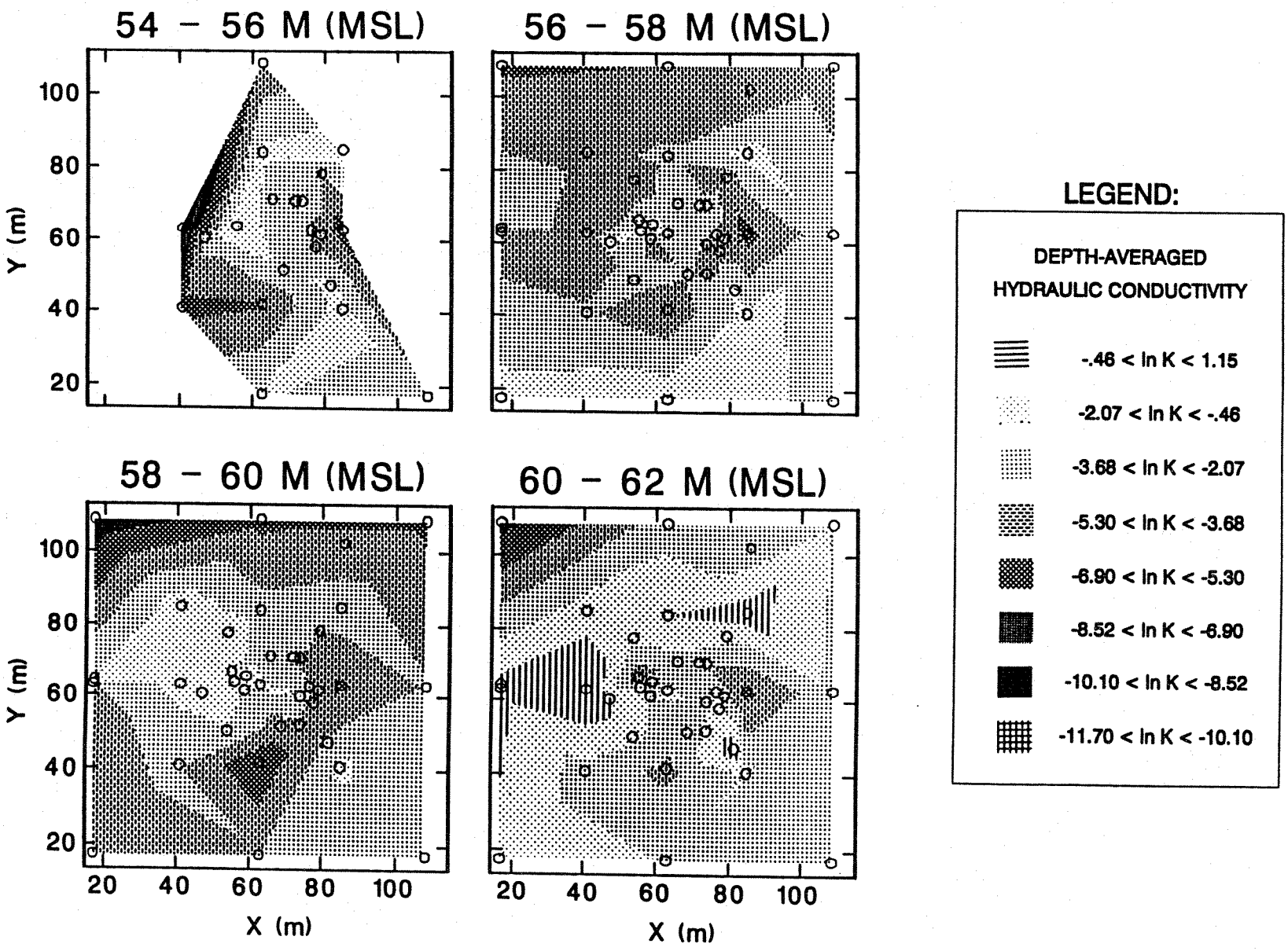

Figure 5. Cross sections of the interpolated three-dimensional hydraulic conductivity field.

Table 1

Arithmetic and Geometric Means for 881 Hydraulic Conductivity Data Points

	Normal	LN
Arithmetic Average (cm/s)	0.261	-3.44
Variance	2.54	4.72
KS	0.483	0.143

KS= value calculated to check for normality based on the Kolmorgorov-Smirnov Test (Liffiefors, 1967). Normality can be rejected at the 95% and/or 99% confidence limits if KS < 0.034 and < 0.030, respectively.

Intrinsic Stationarity

As given by Journal and Huigbregts (1978), the random function Z(x) is assumed to satisfy the intrinsic stationarity hypothesis if:

(i) $E [Z(x+h) - Z(x)] = 0$ for all x and h

(ii) $\gamma (h) = 0.5$ var $[Z(x+h) - Z(x)]$ exists and depends only on h where $\gamma (h)$ denotes the variogram as usual.

In the application of stochastic theories, intrinsic stationarity is neither a feature required to be exhibited by the data nor necessarily an intrinsic property of the field, rather it is the property of the theory.

Because the intrinsic stationarity hypothesis cannot be proven and/or disproven, several researchers, notably Philip and Watson (1986), are critical of stochastic theories. Philip and Watson (1986) argue, "with stochastic models, prediction is qualified by hypothesis. It is not prediction in the sense of deduction, unless the hypothesis is proven." In defense of stochastic theories, geostatisticians, notably Srivastava (1986) and Journal (1986), have responded to the criticism and explain that the intrinsic hypothesis is not a scientific theory and therefore requires no a priori justification, and it can only be refuted a posteriori if proven to be inadequate for the goal at hand.

In the mining industry, the goal at hand is the efficient and accurate prediction of the values of the random variable (e.g., ore grades) at each point in a continuous field. In the groundwater industry, the goal at hand is realistic simulations of solute transport through the random variable (e.g., hydraulic conductivity). To accomplish this goal, not only are the values at each point of interest but also the interconnectivity/continuities among the values. The importance of the interconnectivity/ continuities, though a minor issue related to selecting which regions contain the best ore grades, are a major issue in predicting solute transport through a hydraulic conductivity field.

The simulation of interconnectivity/continuities are controlled by the probabilistic model assumed for the hydraulic conductivity field. As such, geohydrologists should carefully select the best method to transform and/or to detrend the raw data before determining whether, or if, stochastic theories should be applied. Within the literature, a commonly accepted practice is to apply the logarithmic transformation of the hydraulic conductivity data before data analysis. Within the literature, however, there is no commonly accepted practice regarding the removal of a nonstationarity from the data, much less, a commonly accepted method for detecting and defining a nonstationarity.

Trends and Detrending

When referring to nonstationarity, the terms "trend" and "drift" are often used in the groundwater literature. In most instances, as in this case, the term "trend" agrees with its well known usage in the context of trend surface analysis wherein a model like Eq. (1) is used. The term "drift" refers to a trend characterized by a polynominal of zero order.

$$Z(x) = Y(x) + m(x) \qquad (1)$$

The delineation of a trend is accomplished objectively by some type of mathematical function. Within the literature several methods have been proposed for detrending nonstationary fields so that the structure, the variance, and the properties of the stationary portion of the field can be determined. Table 3 lists the methods.

Russo and Jury (1987) have investigated the question of which is the best method for removing the trend and obtaining the correlation length and the variance of the underlying stationary field. In their study, they generated a theoretical two-dimensional stationary field and then tainted the field by adding a deterministic trend. The authors then applied the OLS, IGLS, ML, and RML methods to detrend the data and obtain the variances and correlation lengths listed in Table 4.

Of the six methods shown in Table 3, the OLS method is by far the simplest to implement. A criticism of the OLS method is that the method assumes that all of the residuals are independent and uncorrelated when, in fact, the reason for using the OLS method is to define, better, the correlated

Table 3

Six Methods for Detrending Data (from Rehfeldt, et al., 1989a)

1. Ordinary Least Squares (OLS) to remove the trend and calculate the covariance of the residuals.
2. Iterative Generalized Least Squares (IGLS) to remove the trend and calculate the covariance of the residuals.
3. Maximum Likelihood (ML) to simultaneously estimate the trend and the covariance.
4. Restricted Maximum Likelihood (RML) to estimate the covariance without having to estimate the trend first.
5. Minimum-Variance Unbiased Quadratic Estimation.
6. Generalized Covariances.

Table 4

Summary of Covariance Parameter Estimates for Synthetic Nonstationary Random Fields (from Russo and Jury, 1987)

Linear Trend No. 1 with 72 sampling points

Method	Variance (σ^2)	Correlation Length (λ)
Input	1.0	0.07
OLS	1.267	0.062
ML	1.365	0.174
RML	1.615	0.223

Linear Trend No. 2 with 72 sampling points

	Field 1		Field 2	
Method	Variance (σ^2)	Correlation Length (λ)	Variance (σ^2)	Correlation Length (λ)
Input	1.0	0.07	1.0	0.28
OLS	1.267	0.062	0.703	0.17
IGLS	1.272	0.062	0.728	0.17
ML	1.375	0.174	1.154	0.443
RML	1.614	0.223	2.916	1.414

Non Linear Trend with 288 sampling points

	Field 1		Field 2	
Method	Variance (σ^2)	Correlation Length (λ)	Variance (σ^2)	Correlation Length (λ)
Input	1.00	.07	1.0	0.28
OLS	1.097	0.170	1.006	0.187
IGLS	1.170	1.170	1.209	0.259
RML	5.845	0.989	5.265	1.386

nature among the residuals. However, the results of Russo and Jury (1987) indicate that, even with this potential problem, the OLS method is as good, if not better, than other methods. For the present study, the OLS method was used in conjunction with polynomial expressions of different orders to fit three-dimensional trends through the logarithms of the hydraulic conductivity data.

The results of Jury and Russo (1987) indicate that if the trend is linear and significant, the trend can be easily diagnosed by the variograms. However, when the trend is not strong, or if it is nonlinear, then identifying the presence of a trend from the sample variogram is, for all practical purposes, highly uncertain. An estimate of the importance of this uncertainty is well summarized by

the concluding remarks of Jury and Russo (1987):

"In the case of nonlinear drift the values of λ=0.259 and σ^2=1.209 provided by the IGLS procedure and the values of λ=1.386 and σ^2=5.265 provided by the RML procedure are associated with the values of the Akaike Information Criterion are 185.5 and 185.6, respectively, and hence by the criteria, represent equally valid estimates of the parameters [Original values are λ=0.358 and σ^2=2.9151]. Note however, that the difference between the estimates b=6.6 and 5.4, respectively, of the "slopes" of the variogram, $b=\sqrt{2\ \sigma^2/\lambda}$ in this example are not very large. The parameter b is, as discussed in the work by Russo and Jury (this issue), all that is required for application of conditional probability such as kriging. However, for applications of unconditional probability such a stochastic transport modeling, both λ and σ^2 must be estimated individually. For example, longitudinal macrodispersivity (Gelhar and Axness, 1983) is proportional to the product and λ and σ^2 of the logarithm of the hydraulic conductivity. For the nonlinear drift example above, the two cases with essentially identical values of the AIC have values of the product $(\lambda)(\sigma)^2$ equal to 0.31 and 7.3."

In order to estimate values for λ and σ^2 for the theory of Gelhar and Axness (1983) at the EPRI-MADE site, which is less than 200 meters from the USAF test site, Rehfeldt, et al., (1989b) applied ordinary least squares regression to remove polynomial trends of orders 1, 2, and 3 from a data set of 1242 logarithmic values of hydraulic conductivity. One of the most fundamental questions of this investigation is the definition of what is a trend and what is random. For the stochastic transport theory, Rehfeldt, et al., (1989b) assumed that the variation in the hydraulic conductivity field with scales on the order of the size of the plume are regarded as a trend and variations in hydraulic conductivity with scales on the order of 10% of the plume are treated as random. Based on this premise, Rehfeldt, et al., (1989a) acknowledge that "even within the same aquifer, the definition of what is trend and what is random will change depending on the time and space scales of the problem at hand."

Rehfeldt, et al., (1989b) state "the variograms of the residuals 'look' more like the variogram of stationary random processes, the larger the order of the polynominal, (and that) one would be hard pressed to defend a trend of order 1, 2, or 3 as being the best based on the variograms." In order to select the most appropriate trend, Rehfeldt, et al., (1989b) used information from a natural gradient tracer test and the local geology. In short, they recommend, that the "third order trend surface should be rejected because it is physically inconsistent with the other known information at the EPRI-MADE site. Second order is the highest order trend that is compatible with the other data on site."

Boggs, et al., (1990) reevaluate the detrending of the MADE site after augmenting Rehfeldt's data set by 1114 hydraulic conductivity values, most of which are from locations in the previously untested far-field, which is about 80 to 150 meters downgradient of the tracer injection location. Boggs, et al., (1990) state that "the third-order polynominal trend was judged the best representation of the conductivity drift based on its compatibility with the

groundwater flow field as inferred from observation of the tracer plume during the natural-gradient test." Table 5 shows the significant differences in the variance and the correlation scales from the original data and the residuals created by the third-order detrending.

Inasmuch as Russo and Jury (1987), Rehfeldt, et al., (1989a, b), and Boggs, et al., (1990) illustrate the considerable uncertainty and problems with estimating the covariance parameters in a nonstationarity field, they have understated the problem by implicitly assuming that detrending is best accomplished by only using some type of continuous mathematical function. In reality, heterogeneous aquifers contain geological facies. At the MADE and the USAF site, these facies include chutes, channels, point bars, etc. Each of these facies have different orientations, dimensions, and probability density functions for their hydraulic conductivity field. Some of the inter-facies transitions are gradual, while others are abrupt. Clearly, if such facies are distinguishable, then the approach of representing each of the facies in the aquifer by the same trend and the same covariance parameter is highly questionable.

Facies and Facies Modeling

The term facies can be defined as the combination of the physical, hydrological, and/or mineralogical properties exhibited by a geological formation in a designated volume. With regard to modeling the flow patterns in petroleum reservoirs, numerous articles have advocated the stochastic modeling of facies to generate the architecture of the petroleum reservoir. Haldorsen and Damsleth (1990) and Haldorsen and MacDonald (1987) provide a review of these articles. Stochastic facies models focus on generating synthetic geological architecture and/or hydraulic conductivity fields that are conditioned to observations.

In the stochastic modeling of facies, a point in space belongs to only one of a limited number of classes (or groups), and the model controls how the class values at each point interact. Implicit in these models is that the facies are discrete units and the reservoir construction is driven by a perceived geological dispositional history. For many groundwater problems, facies modeling may not realistically generate spatial variability at the micro-scale. However, facies models and the basis for these models can provide

Table 5

Comparison of Covariance Parameter Estimates for Logarithmic Hydraulic Conductivity Data at the EPRI-MADE Site

	σ^2	λ_h	λ_v
Original Data	4.5	12.0	1.5
Third-Order Residuals	2.8	5.3	0.7

information on: 1) the underlying structure and cause of a nonstationarity at the macro- and possibly the meso-scale, and; 2) insight into the spatial variability in the hydraulic conductivity field for each facies.

The aquifer at the test site is composed of fluvial sediments from the Tombigbee and Buttahatchee Rivers. Aerial photographs of Columbus, Mississippi, and vicinity show outlines of numerous oxbows (Young, 1990a, b). Figure 6 indicates that a former river channel once flowed through both the USAF test site and the EPRI-MADE test site. For Columbus information about geological facies in fluvial environments (Miall, 1977, 1978, 1985; Allen, 1965; Galloway and Hobday, 1985) provide general background information. A detailed assessment of the test site (Herweijer and Young, this issue) indicates a complex depositional history.

The upper half of the aquifer was likely produced by a coarse-grain meandering stream that experienced catastrophic events responsible for the chute bars consisting of very coarse sediment material in the pointbars. The lower half of the aquifer was likely produced by a braided stream that produced regular alternating patterns of coarse-grain lenses (braid bars, and channel deposits at high flow stage) and finer sediments (deposited in the channels at low flow stage) that are laterally and vertically highly discontinuous.

Support for the conceptual model is provided by Muto and Gunn (1986), who present a comprehensive description of the depositional history of the whole Tombigbee Valley, and the high hydraulic conductivity zones in Figure 5. In Figure 5, the band of high hydraulic conductivities from 0.63 to 3.16 cm/s located between 60 and 62 m MSL maps the river channel in Figure 6. In Figure 5, the sinuous pattern of materials with hydraulic conductivities from 0.12 to 0.63 cm/s deposited in a 1-m depression in the Eutaw clay gives the impression of another former stream channel.

Within the test site, several different facies exist. These facies include a coarse-grain meander channel, a coarse-grain point bar, chute bars within the point bar, a cutbank, and a braided channel. Each of these facies is characterized by lenses and clay drapes with different orientations, dimensions and hydraulic properties. The transition between the different facies will be abrupt at some locations but gradual at other locations. In such a heterogeneous aquifer, a stochastic model that assumes intrinsic stationarity is not realistic. Moreover, problems exist with using many types of continuous mathematical functions to detrend because the basic structure of the mathematical function and the hydraulic conductivity field are different.

An understanding of the depositional environment and the facies for a test site is important because it provides insight and direction into how to subdivide and detrend the hydraulic conductivity field. The importance of facies is well illustrated by the trend selected by the third-order trend by Boggs, et al., (1990) for the EPRI-MADE hydraulic conductivity field. The trend shows a zone of high hydraulic conductivity throughout the thickness of the aquifer and aligned longitudinally with the orientation of the MADE

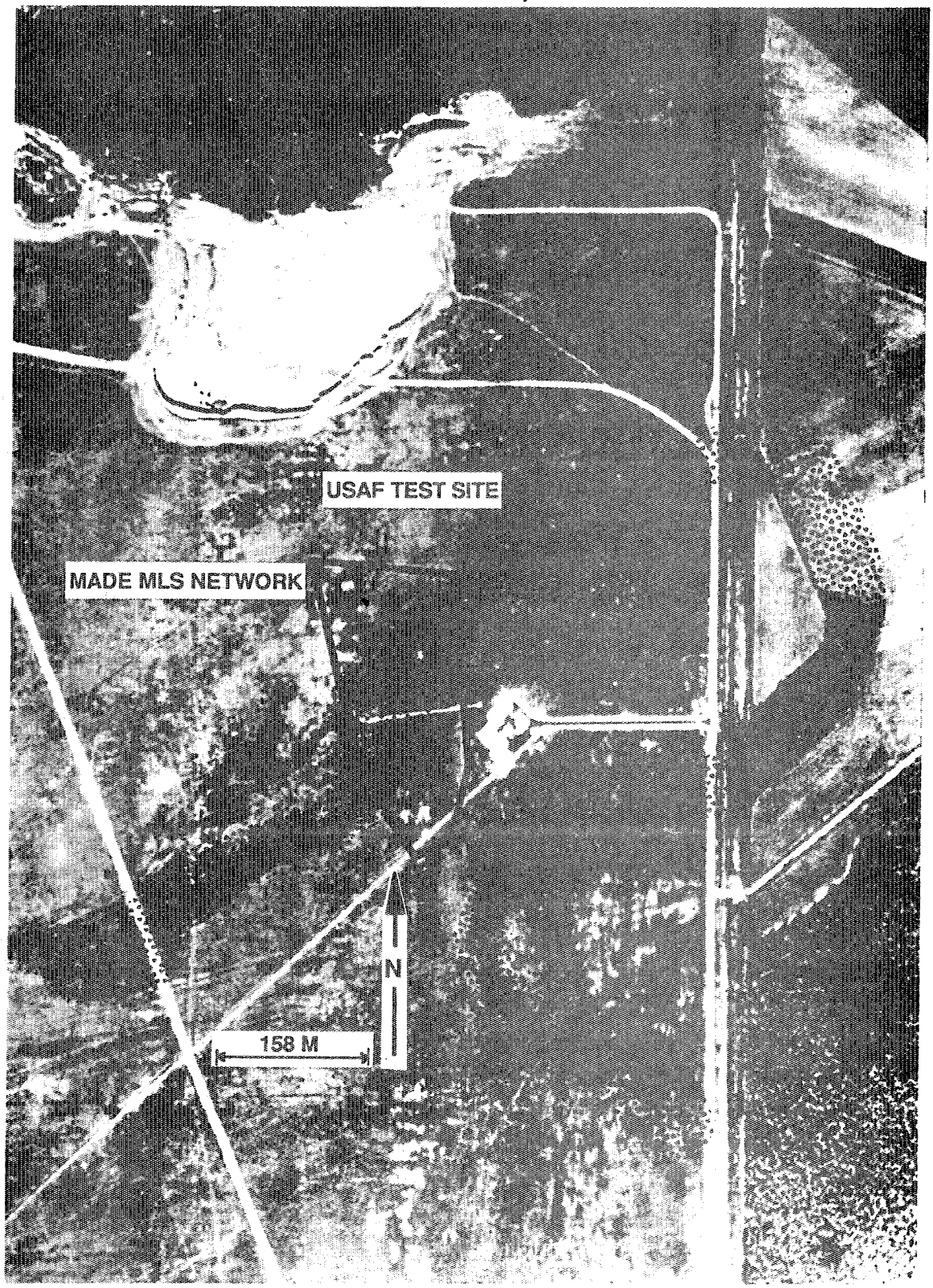

Figure 6. Ox bow at the CAFB Test Site as shown in a 1956 aerial photograph.

sampling network (see Figure 6). The trend starts near the middle of the network where Figure 6 shows the former river channel crossing the network. In short, the trend is inconsistent with the meander, as it is perpendicular to it. This occurred because Boggs, et al., (1990) and Rehfeldt, et al., (1989a): 1) assumed the aquifer was formed by a braided stream; 2) had not seen the former river channel in Figure 6; and, 3) had sparse hydraulic conductivity data in the vicinity of the meander. The inconsistency between the structure in the trend and the structure in the depositional model for the USAF site casts significant uncertainty, in the author's opinion, on the usefulness of variograms for the residuals produced by the third-order polynomial fit at the EPRI-MADE site.

Russo and Jury (1987) indicate that visual inspection of variograms may detect a nonstationary trend when a significant linear trend exists, but will not detect a non-linear trend in the data. Based on these results, one may expect that an investigation into nonstationarity requires more than a visual inspection of the variograms. However, one should recall that Russo and Jury (1987) used only well-behaved trends that affected the complete field. Based on the type of geological facies in fluvial environments, one should expect that the geological facies in the aquifer have significantly different structures in their hydraulic conductivity fields. Hence, a visual inspection of the variograms in the aquifer may indicate whether each region has similar or dissimilar structures. Similar structures would support the intrinsic and stationarity hypothesis; dissimilar structures would support a nonstationary hypothesis.

From the comprehensive borehole flowmeter data set, six smaller data sets were created by partitioning the comprehensive data set into an upper zone and a lower zone, by partitioning the comprehensive data set into an east zone and a west zone, and by partitioning the comprehensive data set into a north zone and a south zone. Table 2 provides a statistical comparison of the first two moments among the data sets.

Figure 7 shows the probability distribution function pdf of Ln(K) for each of the seven data sets. For each of the three-paired sets of hydraulic conductivity data (i.e., north-south), the probability is less than 6% that each of the two data sets was generated by the same pdf based on the Kolmorgorv-Smirnov's limiting distribution (Feller, 1948; Smirnov, 1948). The low percentages support that strict stationarity would be a poor probabilistic model for the hydraulic conductivity field.

Figures 8 and 9 show the vertical and the horizontal variograms calculated for seven data sets. For each variogram, a theoretical exponential variogram was fitted to the data to estimate the correlation length. The vertical and the horizontal variograms for the total region appear well-behaved and do not indicate a nonstationarity. The significant differences in the variograms for the different regions in the aquifer, however, indicate that a nonstationarity exists. Within the variograms for the north, west, and upper regions

TABLE 2

COMPARISON OF THE STATISTICAL PROPERTIES FOR SELECTED DATA FROM THE 881 HYDRAULIC CONDUCTIVITY VALUES

	ALL	TOP	BOTTOM	EAST	WEST	NORTH	SOUTH
NUMBER OF POINTS	881	468	413	433	324	347	367
ARITHMETIC MEAN	0.261	0.416	0.089	0.140	0.480	0.320	0.180
GEOMETRIC MEAN	0.032	0.046	0.021	0.028	0.045	0.038	0.035
HARMONIC MEAN	0.0017	0.0025	0.0012	0.0014	0.0024	0.0057	0.0015
NATURAL VARIANCE	2.540	4.710	0.036	0.120	6.500	5.400	0.310
LOGARITHMIC VARIANCE	4.70	5.10	4.00	3.30	6.04	5.00	3.90

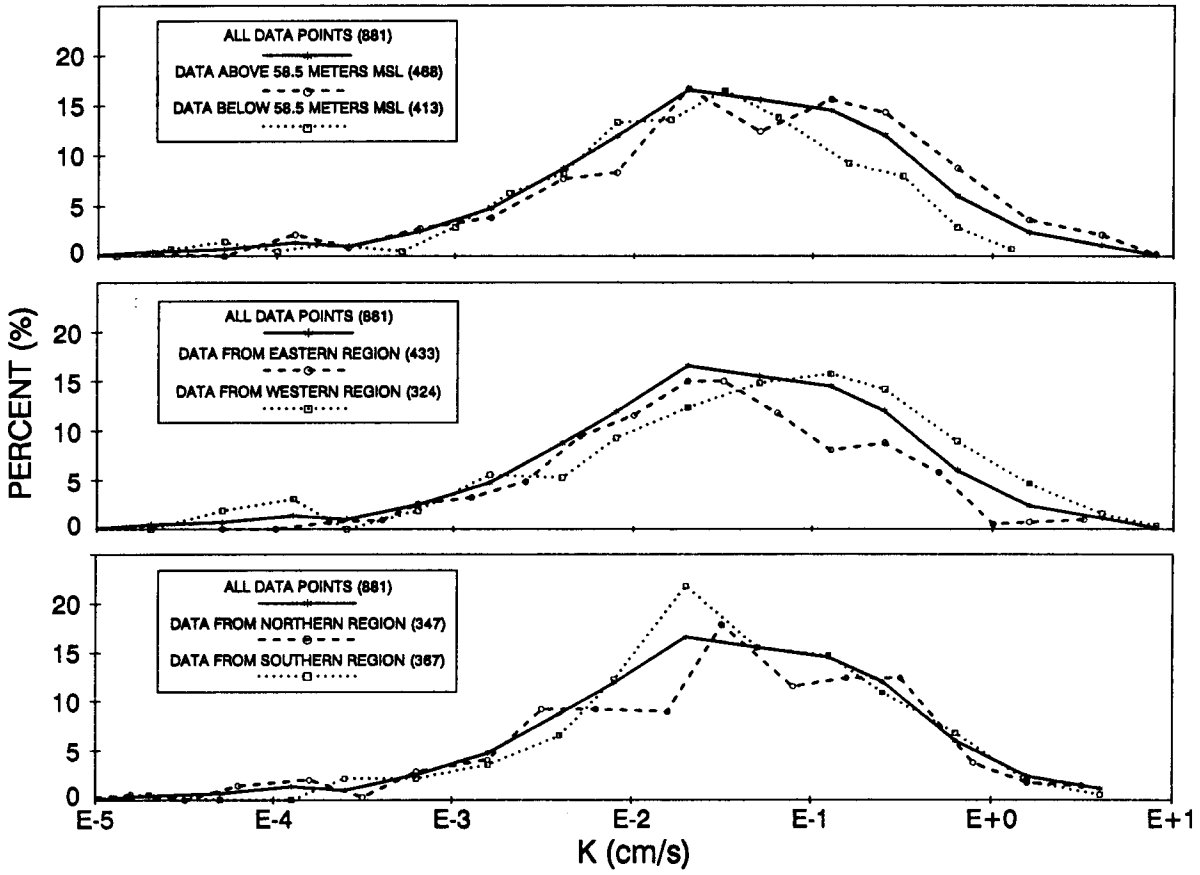

Figure 7. Frequency distribution for different subsets of the hydraulic conductivity data.

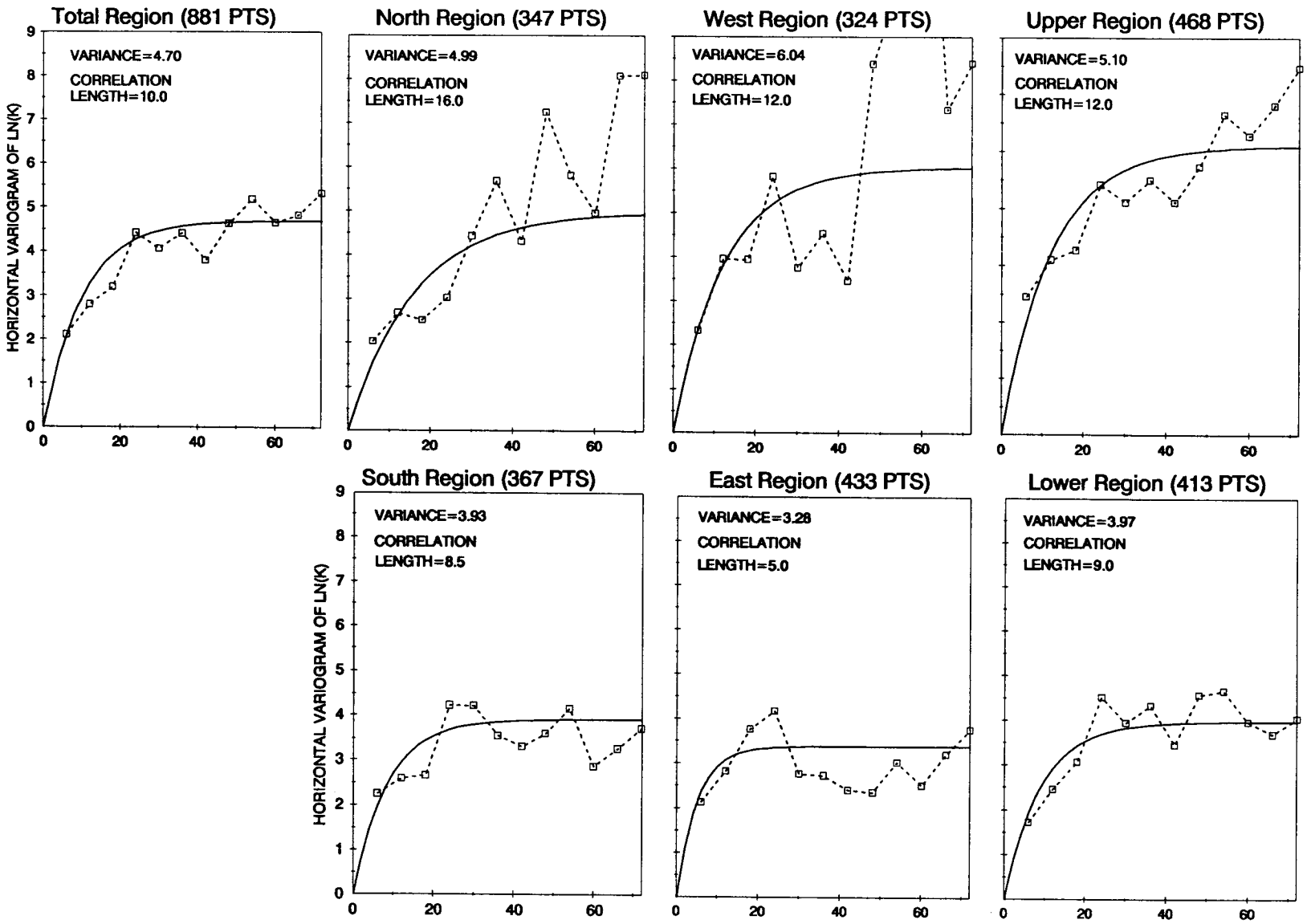

Figure 8. Horizontal variograms for different regions in the test site.

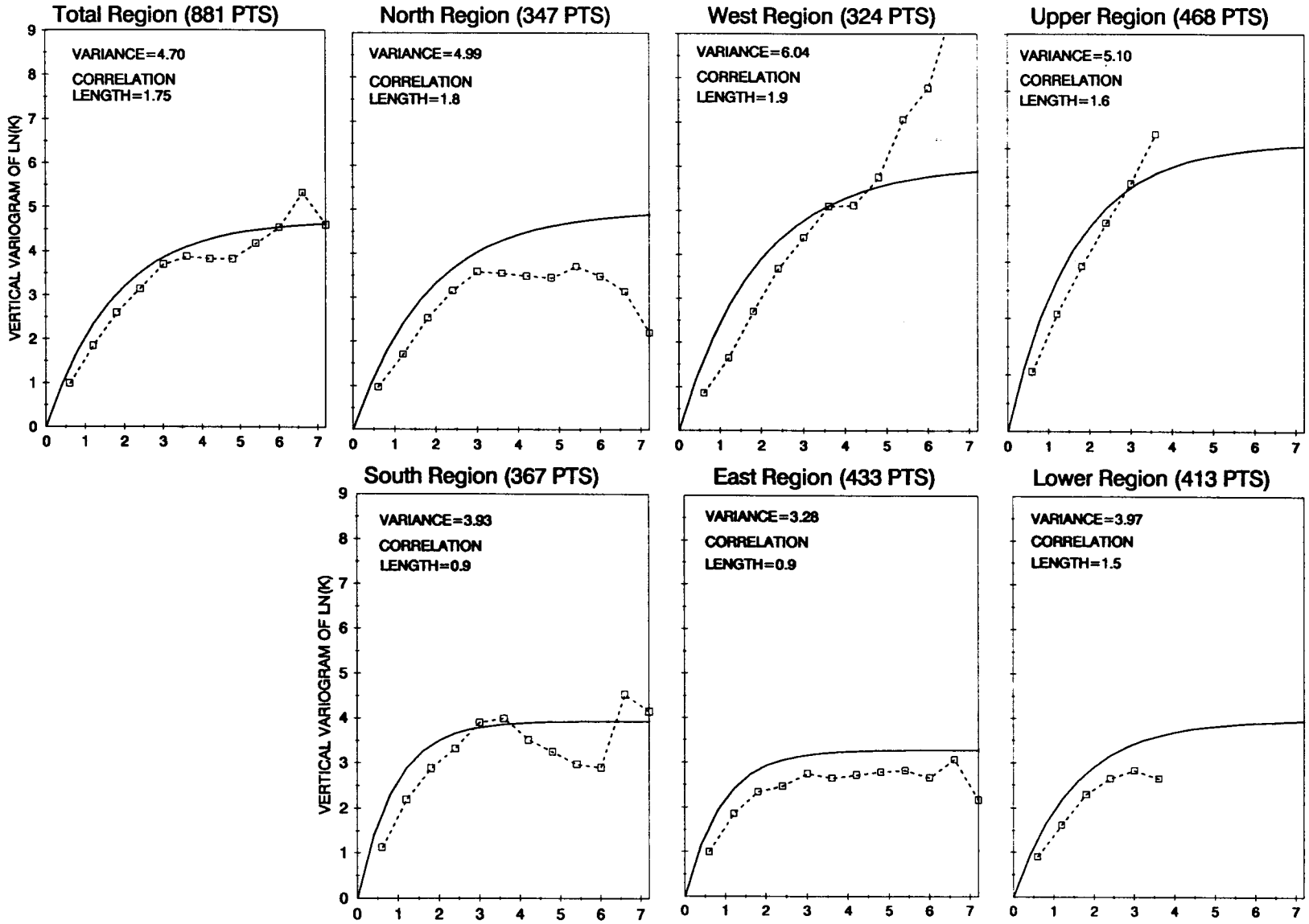

Figure 9. Vertical variograms for the different regions in the test site.

there is evidence of a nonstationarity. The most reasonable explanation for the nonstationarity is different geological facies within the test site.

Detrending with Polynomial Expressions

The global logarithmic hydraulic conductivity field was detrended by polynomial expressions of orders one to six. For each of the six polynomial equations, a set of residuals was calculated by subtracting the value of the trend from the actual hydraulic conductivity value at each measurement location. For each of these sets of residuals, plots similar to Figures 8 and 9 were examined. These figures show gradual changes in the variogram structure and the values of the variance and the correlation lengths.

Figure 10 shows that as one fits higher and higher order polynomials to the data, the residuals show smaller and smaller variance and correlation scales than the detrended data. The effects of detrending are significant; however, there is considerable uncertainty about which polynomial expression best detrends the data. Although the absolute values of the statistical quantities shown in Figure 10 decrease with higher order trends, the relative difference among most of these statistical quantities for each detrending remains similar. This phenomena occurs because the structure of the polynomial expressions and of geological facies, which control the heterogeneity, are different. The trends that make the hydraulic conductivity nonstationary do not extend across the whole test site but are limited to the geological facies that created it. Hence, because the polynomial fits try to fit the same trend through a field, and because the geological facies produce trends that are limited in their influence, polynomial expressions are not well-suited for detrending the hydraulic conductivity field at CAFB.

Conclusions

The results of a geological investigation and a large-scale tracer test indicate that definite trends in the hydraulic conductivity field exist across a 1-ha test site located in fluvial sediments. An analysis of the variograms for different regions of the test site indicates that the logarithmic hydraulic conductivity field is poorly represented by a probalistic model that assumes intrinsic stationarity. Nonstationarity occurs at CAFB because several different geological facies exist within the sediments. Several different polynomial expressions of different orders one to six were used to detrend the hydraulic conductivity field.

Although the effects of detrending had a very large impact on both the variance and the correlation scales of the residuals, no criteria appeared reasonable for determining the point at which optimum detrending had occurred. An examination of the statistical properties of the residuals from different regions show that although the absolute differences in the values had significantly decreased with high-order polynomials, the relative differences remained about the same. It seems that for a

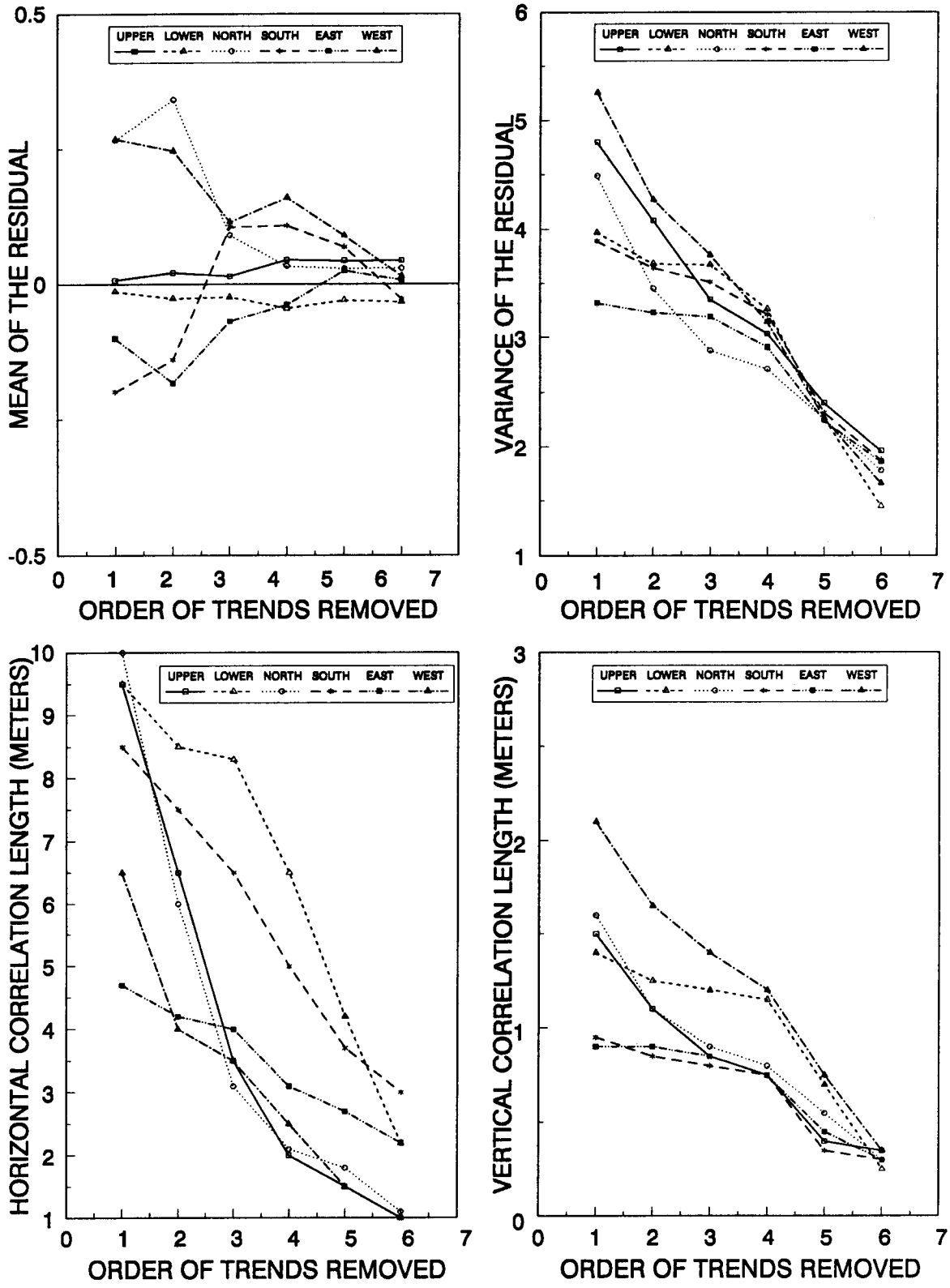

Figure 10. Comparison of the statistical properties of the residual data sets.

the same trend through a whole area whereas the geological facies, which are responsible for the trends in the field, are limited to specific regions.

Partitioning according to geological facies criteria may appear an appealing alternative to mathematical detrending the hydraulic conductivity field of heterogeneous aquifers. However, the following skeptical remarks should be made. Generally the data availability allows, as in our case, to develop a conceptual facies model. Some indications are available where boundaries between facies are, but large uncertainties remain. In our case, for example, the aerial photograph clearly defines a facies boundary at the surface, but how exactly to project this boundary in depth is unknown. The amount of data needed to develop a quantitative facies model to be used for detrending, goes beyond what is generally feasible to collect in the field. And if such an amount of detailed data is available, the question arises whether sometype of a deterministic approach, based on this vast quantity of data, should not be preferred above the stochastic approach.

Acknowledgments

The work was funded by the United States Air Force Engineering and Services Center, Tyndall AFB, Florida.

Biographical Sketch

Steven C. Young received his BA in environmental sciences from the University of Virginia and his MS in civil engineering from Stanford University. During the past seven years, Mr. Young has worked with the Tennessee Valley Authority, (TVA Engineering Laboratory, Norris, Tennessee, 37828, USA) to improve methods for characterizing the hydraulic properties of aquifers and for applying computer models to solve ground water related problems. His research experience includes the design and analysis of aquifer pump tests, artificial and natural gradient three-dimensional tracer tests, borehole flowmeter tests, small- scale evaporation experiments, water budget measurements of ash landfills, and studies to evaluate the EPRI FASTCHEM model.

Joost C. Herweijer received his MS in Hydrogeology and Geophysics from the Free University of Amsterdam. His academic interest are the characterization of heterogeneous aquifers and application of solute transport models. After graduation (1983), he worked two years as a data processing consultant mainly in petroleum engineering projects. He joined Royal Dutch Shell as a research petroleum geologist, working and publishing on probabilistic facies modeling and sedimentological application of high resolution geophysical (dipmeter) well logs. Since October 1988, he has been employed with GeoTrans, Inc., (3300 Mitchell Lane, Suite 250, Boulder, Colorado 80301, USA) and is working on a variety of research and operational projects in the field of ground water remediation.

Dudley J. Benton received his BS in (focusing on fluid mechanics) and BS (focusing on offshore heat exchanger analysis) in ocean engineering from Florida Atlantic University, and a PhD. in mechanical engineering from the University of Tennessee, Knoxville. His areas of interest include heat and mass transfer,

thermodynamics, fluid mechanics, computer programming and numerical mathematics. Dr. Benton has worked with the Tennessee Valley Authority (TVA Engineering Laboratory, Norris, Tennessee 37828, USA) for 9 years.

References

Allen, J.R.L. 1965. A review of the origin and characteristics of recent alluvial sediments. Sedimentology, v. 5, pp. 89-191.

Boggs, J. M., S. C. Young, D. J. Benton and Y. C. Chung. 1990. Hydrogeologic characterization of the MADE site. EPRI Interim Rept. EN-915, Palo Alto, CA.

Cooper, H. H. and C. E. Jacob. 1946. A generalized graphical method for evaluating formation constants and summarizing well-field history. Trans. Am. Geophys. Union, v. 217, pp. 626-534.

Feller, W. 1948. On the Kolmorgorov-Smirnov limit theorems for empirical distributions. Annuals of Math. Stat., v. 19, pp. 177-189.

Galloway, W. E. and D. K. Hobday. 1985. Terrigenous Clastic Depositional Systems. Springer-Verlag.

Gelhar, L. W., and C. L. Axness. 1983. Three-Dimensional Stochastic Analysis of Macrodispersion in Aquifers, Water Resources Research, v. 19, No. 1, pp 161-186.

Haldorsen, H. H., and C. J. MacDonald. 1987. Stochastic Modeling of Underground Reservoir Facies (SMURF). Soc. of Petr. Eng., SPE. 16751, September issue, pp 575-589.

Haldorsen, H. H., and E. Damsleth. 1990. Stochastic Modeling. Soc. of Petr. Eng., SPE. 203321, April issue, pp 404-412.

Journal, A. G. 1986. Geostatistic Models and Tools for the Earth Sciences. Mathematical Geology, Vol. 18, No. 1, pp 119-140.

Journal, A. G. and C. T. Huijbregts, 1978. Mining Geostatistics, London, Academic Press.

Liffiefors, H. W. 1967. On the Kolmorgorov-Smirnov test for normality with the mean and variance unknown. Am. Stat. Assoc. J., pp. 399-402.

Miall, A. D. 1977. A review of the braided river depositional environment. Earth-Sci. Rev., v. 13, pp. 1-62.

Miall, A. D. 1978. Lithofacies types and vertical profile models in braided river deposits. A summary. In A. D. Miall, ed. Fluvial Sedimentology (ed. D. Miall), Can. Soc. of Petrol. Geol. Mem. 5, pp. 597-604.

Miall, A. D. 1985. Architectural-element analysis: A new method of facies analysis applied to fluvial deposits. Earth-Sci. Rev., v. 22, pp. 261-308.

Molz, F. J., R. H. Morin, A. E. Hess, J. G. Melville and O. Guven. 1989. The impeller meter for measuring aquifer permeability variations: evaluation and comparison with other tests. Water Resour. Res., v. 25, pp. 1677-1683.

Muto, G. R. and J. Gunn. 1986. A study of late quaternary environments and early man,

Phase I. Final Report. Project Narrative and Appendices A-D. U.S. Army Corps of Engineers, Mobile and Nashville Districts, Appendix C, Geosciences Documentation.

Olea, R. A. 1984. Systematic Sampling of Spatial Functions. Kansas Geo. Surv., Ser. on Spatial Analysis, No. 7.

Philip, G. M. and D. F. Watson. 1986. Matheronian Geostatistics - Quo Vadis?. Mathematical Geology, Vol. 18, No. 1., pp 93-117.

Rehfeldt, K. R., L. W. Gelhar, J. B. Southard and A. Dasinger. 1989a. Estimates of macrodispersivity based on analyses of Hydraulic conductivity variability at the MADE site. EPRI Interim Rept. EN-405, Palo Alto, CA.

Rehfeldt, K. R., P. Hufschmied, L. W. Gelhar and M. E. Schaefer. 1989b. Measuring hydraulic conductivity with the borehole flowmeter. EPRI Topical Rept. EN-511, Palo Alto, CA.

Russo, D. and W. A. Jury. 1987. A theoretical study of the estimation of the correlation scale in spatially variable fields 2. Nonstationary fields. Water Resour. Res., v. 23, pp. 1269-1279.

Smirnov, N. 1948. Table for estimating the goodness of fit to empirical distributions. Annuals of Math. Stat., v. 19, pp. 279-281.

Srivastava, R. M., 1986. Philip and Watson - Quo Vadunt?. Mathematical Geology, Vol. 18, No. 1, pp 141-146.

Warrick, A. W. and D. E. Myers. 1987. Optimization of sampling locations for variogram calculations. Water Resour. Res., v. 23.

Young, S. C. and H. S. Pearson. 1990. Application of an electromagnetic borehole flowmeter to predict three-dimensional solute transport in a heterogeneous aquifer. 83rd Annual Air and Water Management Association Meeting & Exhibition, Pittsburgh, PA.

Young, S. C. 1990a. A site characterization methodology for aquifers in support of bioreclamation activities, Vol. I: Well network design, well equation, and aquifer multiwell and single-well tests. Report in review. United States Air Force Engineering and Services Center, Tyndall AFB, FL.

Young, S. C. 1990b. A site characterization methodology for aquifers in support of bioreclamation activities, Vol. II: Borehole flowmeter technique, tracer tests, geostatistics, and geology. Report in review. United States Air Force Engineering and Services Center, Tyndall AFB, FL.

Stochastic Characterization of Subsurface Flows

by Lynn W. Gelhar

Abstract

The last decade has seen major developments of stochastic theories which have revolutionized the way in which subsurface flow and transport processes are conceptualized and characterized in naturally heterogeneous media. Experience with large scale numerical simulations and intensively sampled field research sites has confirmed the validity of stochastic theoretical approaches, but the application of the theoretical results to actual field problems has been very limited, largely because of the difficulty of determining the stochastic parameters which characterize spatial variability in natural subsurface material. The focus of this paper is this challenging stochastic characterization problem. First, some key theoretical results are reviewed to emphasize the basic concepts and the role of the important stochastic parameters. Some measurement techniques which have proved useful in characterizing spatial variability of hydraulic conductivity are described briefly, emphasizing, in particular, tools which have potential for routine use in field applications. The results of stochastic characterization at several field research sites indicate that definitive spatial correlation structures can be identified at each individual site. On the other hand, results from a large number of investigations of field heterogeneity, when summarized graphically, appear to indicate a scale dependence of spatial correlation scales. The prospects for improved characterization of heterogeneous subsurface flow systems are discussed with emphasis on the role of large-scale heterogeneity and the use of indirect geological information.

Lynn W. Gelhar is Professor of Civil Engineering at Massachusetts Institute of Technology (Room 48-329, Cambridge, Massachusetts 02139, USA) where he teaches ground water hydrology.

Spatial Averaging of Transmissivity

by Alexandre J. Desbarats

Abstract

Several previous authors have shown that the effective transmissivity of an infinite, statistically isotropic aquifer is given by the ensemble geometric mean of the random transmissivity field when transmissivities are lognormally distributed. Here, an earlier analytical approach of Matheron was modified to show that the effective transmissivity of a finite region, such as represented by a simulator grid block, can be well approximated by the spatial geometric average of point support-scale transmissivities within. This result is strictly valid only for statistically isotropic fields under a uniform mean longitudinal head gradient. The ensemble properties of the block support-scale spatial random function thus defined are shown to depend on the area of spatial averaging and on transmissivity covariance structure. For a second-order stationary and ergodic transmissivity field, the expected block average transmissivity decreases toward the ensemble geometric mean as the averaging area becomes large compared to the correlation range. The validity of spatial geometric averaging was evaluated using a numerical model of steady-state groundwater flow in a simulated heterogeneous transmissivity field discretized on a point support-scale grid. The transmissivity field was generated by an analog method based on digital terrain elevations from the Walker Lake area of Nevada. Log-transmissivities exhibit a bimodal distribution with a variance near 1.0 and an anisotropic covariance structure. Despite these departures from assumed conditions, predicted block-averaged transmissivities were found to be in excellent agreement with true values obtained from the flow simulation. The support-scale dependence of block averaged transmissivities was clearly observed and was well described by theoretical results. Limitations to the applicability of spatial geometric averaging are discussed in light of these results.

Introduction

In the numerical simulation of subsurface fluid flow, heterogeneous aquifers are modeled as discrete arrays of large grid blocks for which representative properties must be determined. The assignment of fluid flow parameters to simulator grid blocks using sample support-scale data from surrounding wells involves the simultaneous yet distinct processes of spatial interpolation and spatial averaging. This paper is concerned with the latter process as it relates to the modeling of transmissivity for two-dimensional flow studies. The problem was approached within the geostatistical framework (Journel and Huijbregts, 1978) where transmissivity is viewed as a stationary and ergodic spatial random

function.

Previous authors (Matheron, 1967; Gutjahr et al., 1978; Dagan, 1979) have shown that the average or effective transmissivity of an infinite, statistically isotropic aquifer is given by the ensemble geometric mean of the random function model, when transmissivities are lognormally distributed. However, this result is not applicable to the determination of effective transmissivity in finite fields such as simulator grid blocks, although it suggests that geometric spatial averaging may serve for this purpose. Using the numerical approach of Warren and Price (1961), Smith and Freeze (1979) and Desbarats and Dimitrakopoulos (1990) observed that this was indeed the case. For statistically isotropic and lognormally distributed values, the effective transmissivity of finite fields was very well approximated by the spatial geometric average of point support-scale transmissivities within.

The objective of this paper is to explain this empirical result in a mathematically rigorous fashion and to examine its implications for geostatistical models of transmissivity. Theoretical results were tested using a numerical model of groundwater flow in the Walker Lake simulated transmissivity field described in Desbarats and Srivastava (1991).

Spatial Averaging Law

This section presents a mathematical justification for spatial geometric averaging based on an earlier derivation of Matheron (1967), reformulated in terms of spatial averages rather than ensemble expectations and introducing explicitly the concept of stream function.

Consider a finite, square, scalar transmissivity field S upon which constant head boundaries ($\phi = cst$) are applied in x and no-flow ($\frac{\partial \phi}{\partial y} = 0$) boundaries are applied in y. Steady, incompressible flow through the field is described by :

$$\frac{\partial}{\partial x}\left(T \frac{\partial \phi}{\partial x}\right) + \frac{\partial}{\partial y}\left(T \frac{\partial \phi}{\partial y}\right) = 0 \qquad (1)$$

Alternatively, two-dimensional steady-state flow without sources or sinks can be described in terms of the stream function Ψ (Bear, 1979 p.167) and hydraulic resistivity $R = T^{-1}$:

$$\frac{\partial}{\partial x}\left(R \frac{\partial \Psi}{\partial x}\right) + \frac{\partial}{\partial y}\left(R \frac{\partial \Psi}{\partial y}\right) = 0 \qquad (2)$$

The no-flow boundaries in y become $\Psi = cst$ boundaries and the constant head boundaries in x become $\frac{\partial \Psi}{\partial x} = 0$ boundaries. Therefore, eqns (1) and (2) have an identical form and identical boundary conditions, rotated 90°. They are linked through the relations (Bear, 1979, p.166) :

$$q_x = -T\frac{\partial \phi}{\partial x} = -\frac{\partial \Psi}{\partial y} \qquad (3)$$

$$q_y = -T\frac{\partial \phi}{\partial y} = \frac{\partial \Psi}{\partial x} \qquad (4)$$

For head as the dependent variable, the effective longitudinal transmissivity of the field can be defined as a ratio of spatial averages (Rubin and Gómez-Hernández, 1989, 1990) :

$$T_e = \frac{\frac{1}{S}\int_S -T\frac{\partial \phi}{\partial x}\, ds}{\frac{1}{S}\int_S \frac{\partial \phi}{\partial x}\, ds} = \frac{\frac{1}{S}\int_S -T\frac{\partial \phi}{\partial x}\, ds}{\frac{1}{S}\int_S R\frac{\partial \Psi}{\partial y}\, ds} \qquad (5)$$

Effective transmissivity is a constitutive variable (Cushman, 1986) and is defined in the

context of a specific flow experiment. Here it is defined for uniform average flow in a finite field.

Similarly, for Ψ as the dependent variable, the effective resistivity of the field can be defined by :

$$R_e = \frac{\frac{1}{S}\int_S -R\frac{\partial \Psi}{\partial y}\,ds}{\frac{1}{S}\int_S \frac{\partial \Psi}{\partial y}\,ds} = \frac{\frac{1}{S}\int_S -R\frac{\partial \Psi}{\partial y}\,ds}{\frac{1}{S}\int_S T\frac{\partial \phi}{\partial x}\,ds} \qquad (6)$$

Therefore,

$$T_e = R_e^{-1} \qquad (7)$$

Consider the transmissivity and resistivity fields scaled by their respective arithmetic spatial averages over S, T_a and R_a. The following assumptions are now made : 1. the scaled fields are statistically isotropic and 2. their multivariate spatial distributions are identical. Assumption 2 is strictly verified only in the case of an infinite and ergodic multivariate lognormal field as considered in the original derivation of Matheron (1967). From the identical form and boundary conditions of eqns (1) and (2), it follows that the functional operator F, by which T_e is derived from the T field, is the same as that by which R_e is derived from the R field. Applying this operator to scaled transmissivity and resistivity fields which verify assumptions 1 and 2, we can write :

$$F(\frac{T}{T_a}) = F(\frac{R}{R_a}) \qquad (8)$$

The scaling factors $1/T_a$ and $1/R_a$ are constant over S and $F(cT) = c\,F(T) = c\,T_e$, therefore :

$$\frac{T_e}{T_a} = \frac{R_e}{R_a} \qquad (9)$$

From eqns (7) and (9), we obtain

$$\frac{T_e}{R_e} = T_e^2 = \frac{T_a}{R_a} \qquad (10)$$

However, from assumption 2, the spatial averages of the logarithm of the scaled fields are equal

$$\frac{1}{S}\int_S \ln(\frac{T}{T_a})ds = \frac{1}{S}\int_S \ln(\frac{R}{R_a})ds \qquad (11)$$

From which it can be shown that

$$\frac{T_a}{R_a} = \exp(2\,\frac{1}{S}\int_S \ln T ds) \qquad (12)$$

Therefore, T_e is given by the spatial geometric average T_S :

$$T_e = T_S = \exp(\frac{1}{S}\int_S \ln T ds) \qquad (13)$$

If the boundary conditions on the transmissivity field are rotated 90°, it follows from symmetry considerations that T_e in the new longitudinal direction is also given by eqn (13). The above derivation could also be repeated considering other (more complicated) boundary conditions ensuring *uniform mean flow* in oblique directions with respect to the field orientation. The result would be the same since eqns (1)-(13) remain valid as does the rotational symmetry in the boundary conditions on ϕ and Ψ. If this rotational symmetry were violated, as in the case of convergent or divergent flow patterns, the above developments no longer would apply. The effective transmissivity tensor of the field S is therefore isotropic for the particular uniform flow conditions assumed in order to calculate T_e through eqn (5). However, it must be emphasized that the boundary conditions applied to S in these developments are not necessarily those experienced when the block is taken in the context of a

much larger surrounding heterogeneous flow field. The apparent transmissivity tensor of the block may then no longer be isotropic or even diagonal (White and Horne, 1987) and depends on the unknown solution to the flow equation over the entire field. Rubin and Gómez-Hernández (1989) address this issue by considering an average of T_e corresponding to different possible sets of local boundary conditions. In fact however, the problem of determining T_e in a finite subregion of a larger flow field is circular unless local boundary conditions are specified. With this caveat, and for the conditions on transmissivity spatial variability required by assumptions 1 and 2 above, eqn (13) provides a non-empirical spatial averaging law for isotropic two-dimensional flow fields analogous to the classic harmonic spatial averaging law for one-dimensional systems.

Geostatistical Model for Block Transmissivity

Following the usual approach of stochastic subsurface hydrology, $Y(x)$, the log-transmissivity at a point x, is modeled as a stationary and ergodic spatial random function. The first and second order moments of $Y(x)$ are defined as :

$$E[Y(x)] = \alpha \quad (14)$$

$$Cov[Y(x), Y(x+h)] = \sigma(h) \quad (15)$$

$$Var[Y(x)] = \sigma^2 \quad (16)$$

The geometric spatial averaging law allows the definition of a block support-scale spatial random function $T_S = \exp(Y_S)$ where the moments of Y_S are given by :

$$E[Y_S] = E[\frac{1}{S}\int_S Y(x)dx] = \alpha$$

$$Var[Y_S] = \frac{1}{S^2}\int_S\int_S \sigma(x-y)\,dx\,dy = \bar{\sigma}(S,S) \quad (17)$$

Thus, assuming $Y(x)$ is multivariate normal, it follows from the properties of the log-normal distribution (Aitchison and Brown, 1957) that the mean and variance of T_S are given by (Desbarats and Dimitrakopoulos, 1990) :

$$E[T_S] = E[e^{Y_S}] = T_G\, e^{\bar{\sigma}(S,S)/2}$$

$$Var[T_S] = E[T_S]^2\,(e^{\bar{\sigma}(S,S)} - 1) \quad (18)$$

where $T_G = e^{\alpha}$ is the ensemble geometric mean. It can be shown (using second-order expansions of e^x) that these relations also hold as good approximations if the normality assumption is relaxed and σ^2 is not too large.

The most interesting feature of eqn (18) is the dependence of the moments of T_S on averaging area or support-scale S through the term $\bar{\sigma}(S,S)$ (Desbarats, 1989; Desbarats and Dimitrakopoulos, 1990; Rubin and Gómez-Hernández, 1990). As S increases from a single point to an infinite field, $\bar{\sigma}(S,S)$ goes to zero and the mean of T_S decreases from the expected value of point transmissivities toward the ensemble geometric mean transmissivity T_G. At the same time, the variance of T_S decreases from the variance of point transmissivities toward zero. Thus, the original result of Matheron (1967) appears as a limiting case of eqn (18) for infinite fields. Indeed, for ergodic discharge and head gradient fields, the spatial averages in eqn (5) tend toward expected values yielding the standard definition of T_e in an infinite medium.

If a large heterogeneous transmissivity field D is subdivided into N grid blocks of

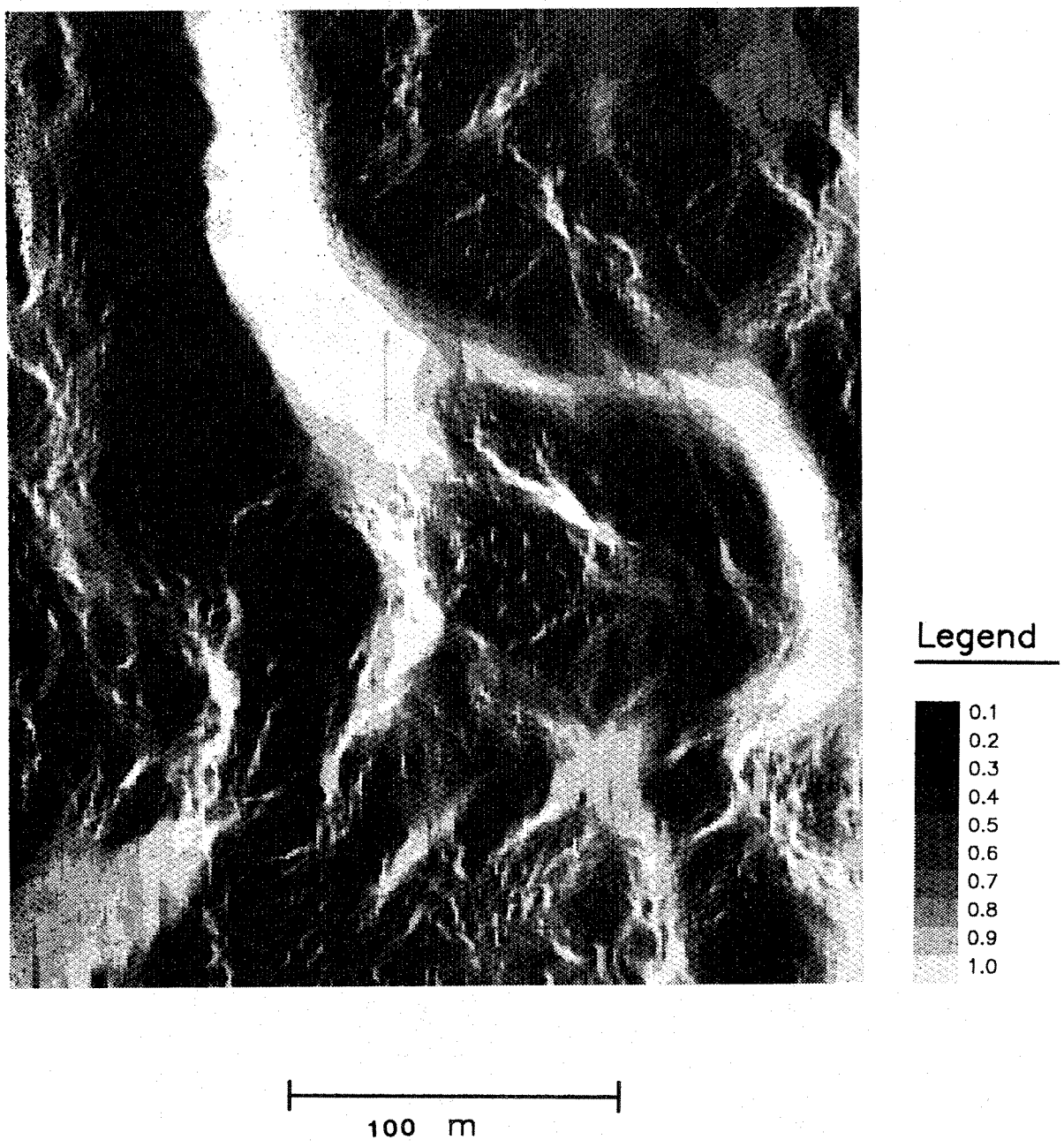

Figure 1: Walker Lake specific discharge field.

area S, then it can easily be shown that the spatial geometric averages over D of point transmissivities $T(x)$ and block transmissivities T_S are both strictly equal to T_G under the ergodic assumption :

$$\exp(\frac{1}{N}\sum_{i=1}^{N} Y_{Si}) = \exp(\frac{1}{D}\int_D Y(x)\,dx) = T_G \qquad (19)$$

However, when steady-state flow is established through the discretized field, the apparent effective transmissivity of the entire field D is equal to T_G only if eqn (13) is valid both at the scale of points within grid blocks S and at the scale of grid blocks within the field D. This point is further discussed in the next section.

Case Study

The geometric spatial averaging law and the support-scale effects are checked using a numerical simulation of groundwater flow in the Walker Lake transmissivity field (Desbarats and Srivastava, 1991). The discrete heterogeneous transmissivity field was generated using an analog simulation method based on digital terrain elevations from the Walker Lake area of Nevada (Isaaks and Srivastava, 1989). The field consists of 78000 transmissivity values on a grid 300 (x) by 260 (y) with unit cell dimensions. Steady-state flow through the field is established by specifying constant head boundaries in x and no-flow boundaries in y. The mean direction of flow is therefore in x, from north to south, under an applied head gradient of 0.01. Figure 1 (from Desbarats and Srivastava, 1991) shows a grey-scale image of the specific discharge field. High velocity flow channels (light colours) meander significantly at the local scale despite the uniform mean head gradient in the north-south direction.

The heterogeneous transmissivity field is characterized by its histogram and spatial covariance function. Figures 1, 2 and 3 show the histograms of $Y(x)$, $T(x)/T_a$ and $R(x)/R_a$, respectively. Summary statistics are given in Table 1. The histograms of $Y(x)$ and $T(x)/T_a$ are bimodal due to a continuous high conductivity channel which cuts across part of the field (Desbarats and Srivastava, 1991). Although their distributions are different, the variances of $T(x)/T_a$ and $R(x)/R_a$ are similar. Figure 4 shows $\sigma(h_x, h_y)$, the spatial covariance function of $Y(x)$ plotted as a function of the lag components h_x and h_y. The spatial covariance structure of $Y(x)$ is anisotropic, with greatest spatial continuity in the direction $N\ 14°\ W$. The integral ranges of correlation are 22.32 m and 17.70 m, in x and y, respectively. The corresponding dimensionless field lengths in these directions are 13.44 and 14.69, respectively (Desbarats and Srivastava, 1991). In summary, the geostatistical characteristics of the transmissivity field differ significantly from those assumed in the derivations presented above.

The heterogeneous flow field was subdivided into 100 blocks of 30 × 26. The spatial geometric average and the true effective transmissivity defined by eqn (5) were calculated for each block. The exercise was repeated for a subdivision of the field into 195 blocks of 20 × 20. Figures 5 and 6 show the plots of T_e versus T_S for the two block sizes considered. The agreement between these values is generally quite good.

The block scale heads corresponding to the above coarse-grid simulations were compared with the spatial arithmetic average of point heads within each block as determined from

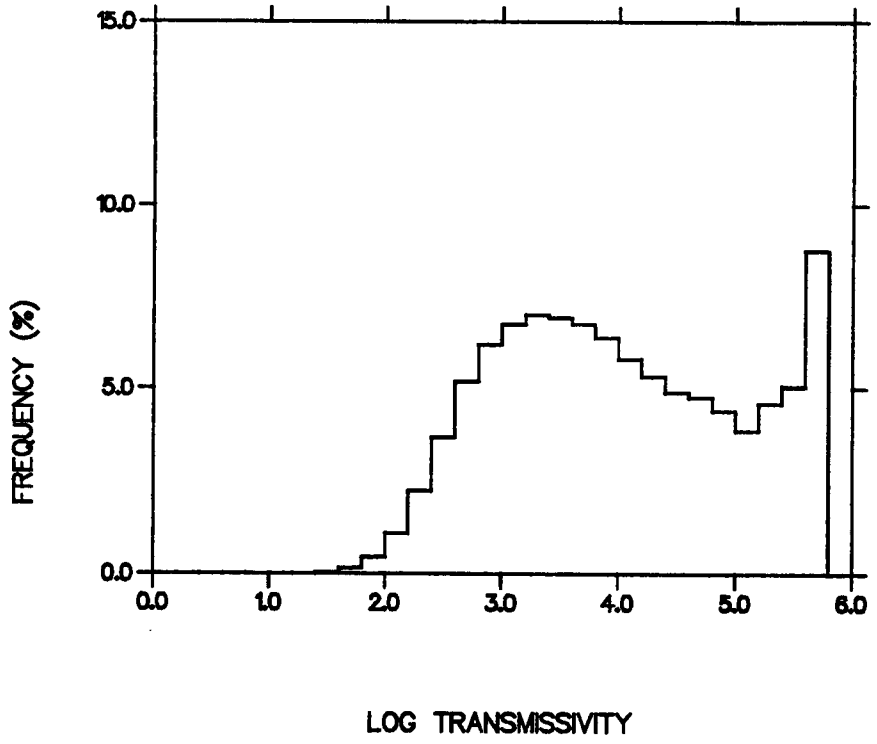

Figure 2: Histogram of log-transmissivity $Y(x)$.

Table 1: Summary statistics.

Variable	mean	variance	skewness
$Y(x)$	4.0082	1.0358	0.0927
$T(x)/T_a$	1.0000	0.9337	1.0195
$R(x)/R_a$	1.0000	0.9129	1.4640

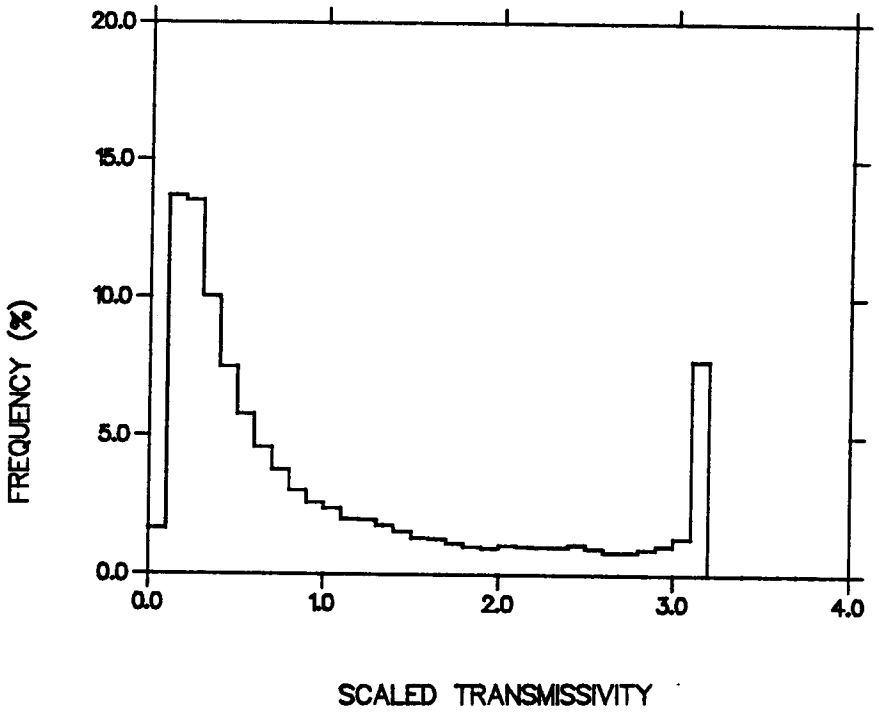

Figure 3: Histogram of scaled transmissivity $T(x)/T_a$.

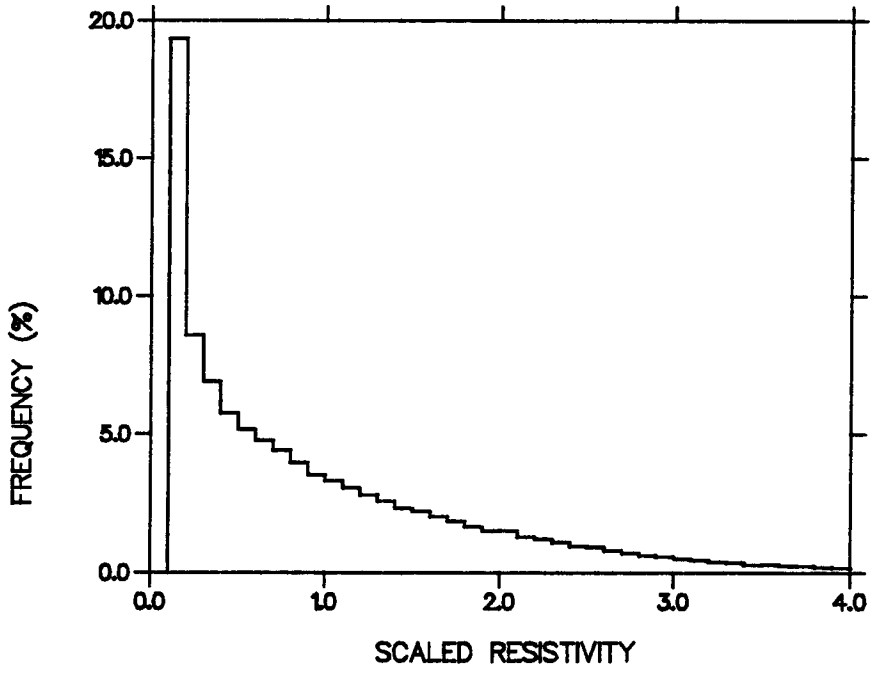

Figure 4: Histogram of scaled resistivity $R(x)/R_a$.

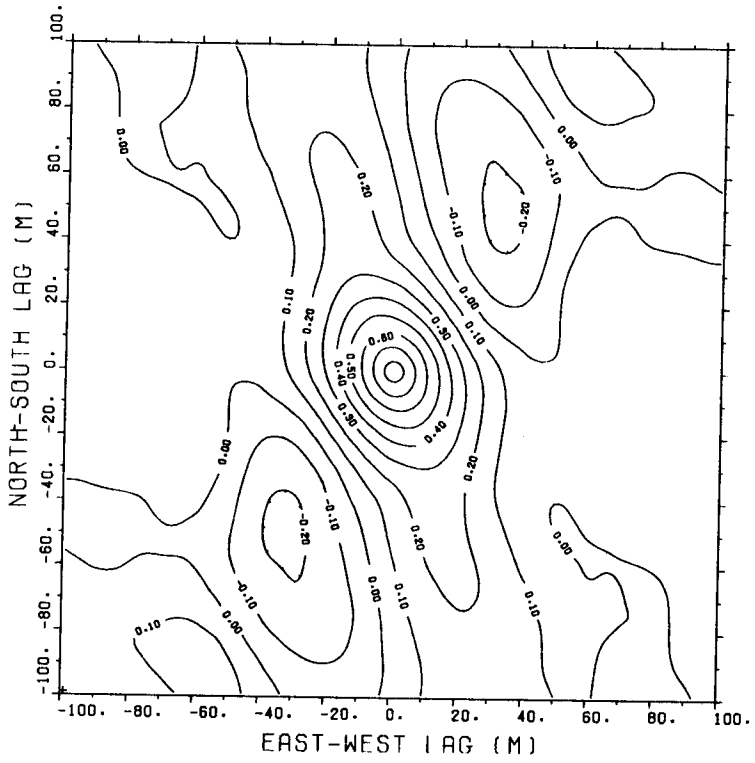

Figure 5: Log-transmissivity spatial covariance $\sigma_Y(h_x, h_y)$.

the exhaustive point scale simulation. Figures 7 and 8 show the agreement between these quantities to be excellent.

The support-scale effects caused by spatial geometric averaging are investigated in Table 2 for a range of block sizes. The second column shows $\bar{\sigma}(S,S)$, the observed variance of the block averages Y_S. The third column shows the expected block transmissivity $E[T_S]$ calculated using $\bar{\sigma}(S,S)$ according to eqn (18). This value is to be compared with the corresponding observed arithmetic average of block transmissivities $\overline{T}_S$. The agreement between columns 3 and 4 is excellent. The theoretical coefficient of variation of T_S, $CV = (\exp(\bar{\sigma}(S,S)) - 1)^{0.5}$, is given in column 5. The observed values are in column 6. The agreement here is only fair because the formula for $Var[T_S]$ is more sensitive to departures of $T(x)$ from lognormality than the one for $E[T_S]$.

For successively coarser grids, the block averaged transmissivities were entered into the flow simulator and the overall effective transmissivity of the field was determined. Results are summarized in Table 3. Column 1 shows $\hat{T}_e$ the observed effective transmissivity for the block discretized field. Column 2 shows T_e the true effective transmissivity, that corresponding to the point (1 x 1) discretization. Column 3 shows the spatial geometric average of block transmissivities T_S over the entire field which, under the ergodic assumption, is equal to T_G, the ensemble geometric mean. Ideally, if spatial geometric averaging were strictly correct, all three columns would be identical. In fact however, the largest relative discrepancy is 4% which is nevertheless a very good agreement.

Discussion

Figures 5 and 6 show that the effective transmissivity of a finite field is well approximated by the spatial geometric average of point support-scale transmissivities within. This encouraging result is somewhat surprising here given the departures of the transmissivity spatial distribution and block boundary conditions from the conditions assumed in the derivation of eqn (13). The transmissivity spatial covariance structure is not isotropic although, at the scale of the averaging area S, the anisotropy is weak. It is conjectured that, in practice, the isotropic assumption can be circumvented by selecting grid block dimensions L_x and L_y such that $L_x/\lambda_x = L_y/\lambda_y$. The univariate distributions of $T(x)/T_a$ and $R(x)/R_a$ are different although their variances are similar. In practice, the latter may be a sufficient condition for the applicability of spatial geometric averaging. This condition is well verified if the transmissivity distribution is multivariate lognormal (Matheron, 1967, 1968). However, it is not verified in the case of high contrast, binary sand-shale permeability distributions where spatial geometric averaging is known to perform poorly in the two-dimensional case (Desbarats, 1987).

The results of Figures 5,6,7 and 8 and Table 3 suggest that spatial geometric averaging of transmissivities does not strongly affect the corresponding spatially averaged fields of the physical variables, discharge and head. In particular, overall mass flux through the field is well conserved. The boundary conditions to which individual grid blocks within the field are subject, do not necessarily ensure the local uniform mean flow assumed in the definition (5) and the derivation of eqn (13). Indeed, the local

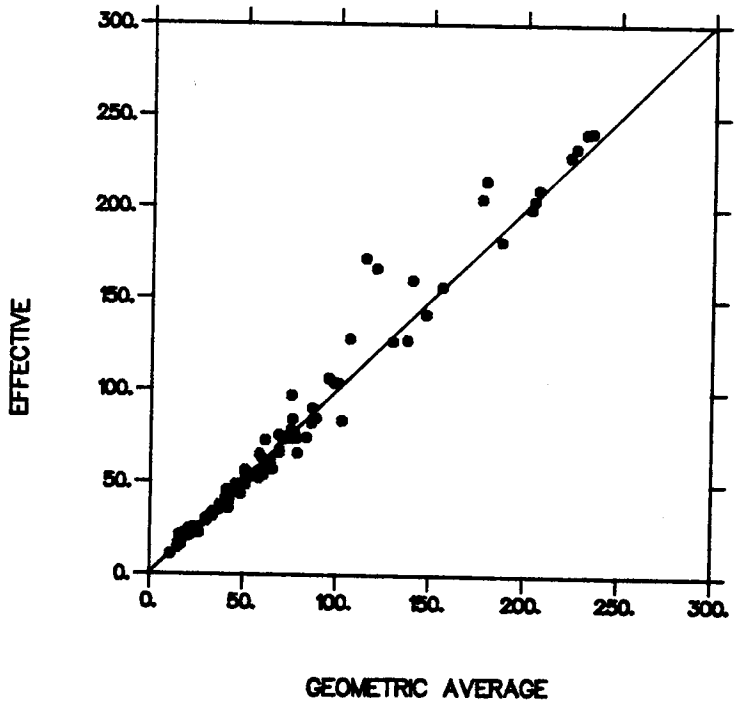

Figure 6: T_e versus T_S for block size 30 x 26.

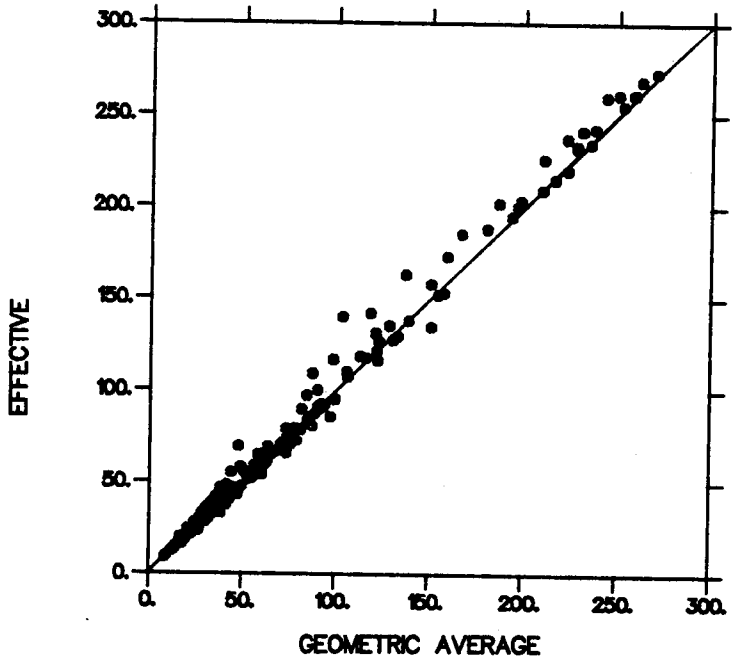

Figure 7: T_e versus T_S for block size 20 x 20.

Table 2: Support-scale effects for block averaged transmissivities.

Block Size (m)	$\bar{\sigma}(S,S)$	$E[T_S]$	$\overline{T}_S$	CV	$\overline{CV}$
1 x 1	1.0358	92.397	89.563	1.3480	0.9663
5 x 5	0.8541	84.374	83.005	1.1615	0.9229
10 x 10	0.7662	80.747	80.041	1.0730	0.8968
20 x 20	0.6296	75.415	75.641	0.9363	0.8526
30 x 26	0.5246	71.558	71.575	0.8305	0.7732
300 x 260	0.0000	55.047	55.047	0.0000	0.0000

Table 3: Effect of block averaging on overall field transmissivity.

Block Size (m)	$\hat{T}_e$	T_e	T_G
1 x 1	55.573	55.573	55.047
5 x 5	55.559	55.573	55.047
10 x 10	54.874	55.573	55.047
20 x 20	53.316	55.573	55.047
30 x 26	53.368	55.573	55.047
300 x 260	55.047	55.573	55.047

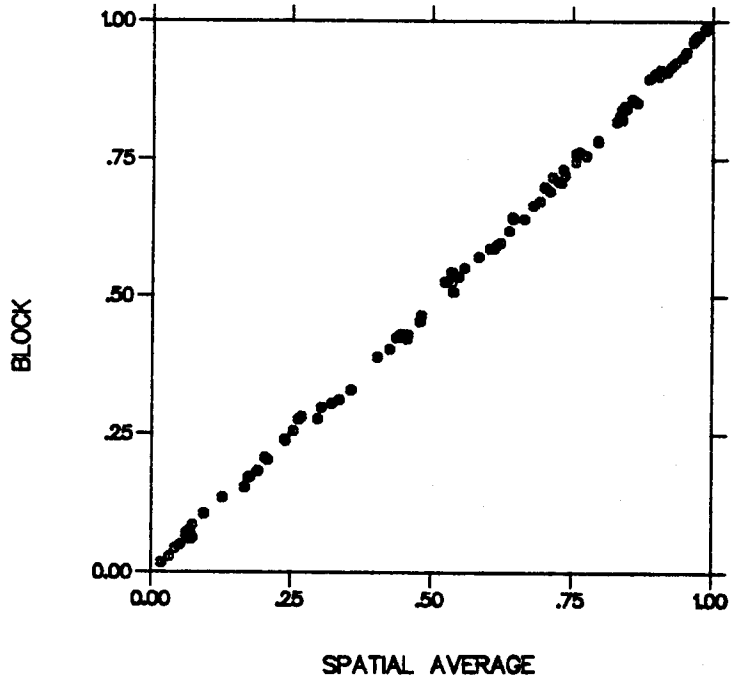

Figure 8: Block head versus spatial average for block size 30 x 26.

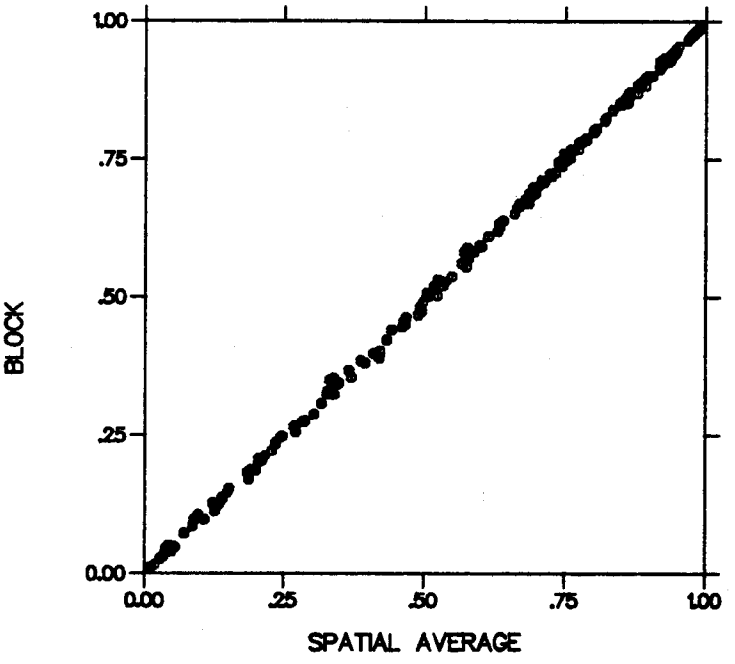

Figure 9: Block head versus spatial average for block size 20 x 20.

variations in flow direction apparent in Figure 1 indicate that these local boundary conditions must vary considerably. However, the sum total of these discrepancies and those due to transmissivity spatial variability noted above, are responsible for the quite tolerable scatter observed in Figures 5 and 6. Therefore, the boundary condition problem inherent in the scaling of constitutive variables such as transmissivity does not appear to invalidate the use of eqn (13) for practical purposes, in the present case. Further investigation of this matter is required.

The results of Table 2 demonstrate the support-scale dependence of the mean and variance of block averaged transmissivities described by eqn (18). These relations are well verified both qualitatively and quantitatively. Although the numerical agreement may vary, the support-scale effects described by eqn (18) remain true regardless of the transmissivity spatial distribution.

Conclusions

Using the analytical approach of Matheron (1967), it is shown that, under certain conditions, geometric spatial averaging gives an excellent approximation of the effective transmissivity of finite heterogeneous flow fields such as simulator grid blocks. The ensemble mean and variance of the block support-scale random function defined by geometric spatial averaging are shown to depend on the size of the averaging area. Numerical results from a flow simulation experiment confirm the analytical results, suggesting that they are fairly insensitive to departures from theoretical models of transmissivity heterogeneity and flow field boundary conditions.

Acknowledgments

The author would like to thank Yoram Rubin and André Journel for their helpful comments. Computing was performed on the CRAY XMP 28 of SUPERNET, the Canadian government supercomputing consortium. Geological Survey of Canada contribution no. 15990.

Alexander Desbarats is a research scientist with the Mathematical Applications in Geology group of the Geological Survey of Canada. He obtained a B.Eng. in geological engineering and a M.A. in applied science (geostatistics) from the Ecole Polytechnique of Montreal in 1980 and 1982, respectively. In 1987 he obtained his Ph.D. from the Department of Applied Earth Sciences of Stanford University. Since July 1987 he has been with the Geological Survey of Canada where he conducts research on fluid flow and solute transport in heterogeneous porous media. (601 Booth st., Ottawa, Ontario, K1A 0E8, CANADA.)

References

Aitchison, J. and J.A.C. Brown. 1957. The Lognormal Distribution. Cambridge University Press.

Bear, J., 1979. Hydraulics of Groundwater. McGraw-Hill.

Cushman, J.H., 1986. On measurement scale and scaling. Water Resour. Res., v.22, pp.129-134.

Dagan, G., 1979. Models of groundwater flow in statistically homogeneous porous formations. Water Resour. Res., v.15, pp.47-63.

Desbarats, A.J., 1987. Numerical estimation of effective permeability in sand-shale sequences. Water Resour. Res., v.23, pp.273-286.

Desbarats, A.J., 1989. Support effects and the spatial averaging of transport properties, Math. Geol., v.21, pp.383-390.

Desbarats, A.J. and R. Dimitrakopoulos. 1990. Geostatistical modeling of transmissivity for two-dimensional reservoir studies. SPE Form. Eval., Dec., pp. 437-443.

Desbarats, A.J. and R.M. Srivastava. 1991. Geostatistical analysis of groundwater flow parameters in a simulated aquifer. Water Resour. Res., (in press).

Gutjahr, A.L., L.W. Gelhar, A.A. Bakr and J.R. MacMillan. 1978. Stochastic analysis of spatial variability in subsurface flows, 2, Evaluation and application. Water Resour. Res., v.14, pp.953-959.

Isaaks, E.H. and R.M. Srivastava. 1989. An Introduction to Applied Geostatistics. Oxford University Press.

Journel, A.G. and C.H. Huijbregts. 1978. Mining Geostatistics. Academic Press.

Matheron G., 1967. Composition des perméabilités en milieux poreux hétérogène : Méthode de Schwydler et règles de pondération. Rev. de l'Inst. Fran. Pet., v.22, pp.443-466.

Matheron G., 1968. Composition des perméabilités en milieux poreux hétérogène : Critique de la règle de pondération géométrique. Rev. de l'Inst. Fran. Pet., v.23, pp.201-218.

Rubin, Y. and J.J. Gómez-Hernández. 1989. Analysis of upscaling and effective properties in disordered media. In Proceedings of the Second International Reservoir Characterization Technical Conference, Sponsored by NIPER/DOE, Dallas TX, June 25-28.

Rubin, Y. and J.J. Gómez-Hernández. 1990. A stochastic approach to the problem of upscaling of transmissivity in disordered media : Theory and unconditional simulations. Water Resour. Res., v.26, pp.691-701.

Smith, L. and R.A. Freeze. 1979. Stochastic analysis of steady-state groundwater flow in a bounded domain 2 : Two-dimensional simulations. Water Resour. Res., v.15, pp.1543-1559.

Warren, J.E. and H.S. Price. 1961. Flow in heterogeneous porous media. SPEJ, v.1, pp.153-169.

White, C.D. and R.N. Horne. 1987. Computing absolute transmissibility in the presence of fine-scale heterogeneity. SPE paper 16011, presented at the 9th SPE Symposium on Reservoir Simulation, San Antonio TX, Feb. 1-4, 1987.

Nomenclature

α : expected value of log-transmissivity $Y(x)$ [dim.].

CV : coefficient of variation of T_S [dim.].

λ : integral range of correlation [L].

L : dimension of averaging area S [L].

$\phi(x)$: head [L].

$\Psi(x)$: stream function [L*L*L/T].

$R(x)$: resistivity $T(x)^{-1}$ [T/L*L].

R_a : arithmetic spatial average of resistivity [T/L*L].

σ^2 : variance of $Y(x)$ [dim.].

$\sigma(h_x, h_y)$: log-transmissivity covariance [dim.].

S : averaging area [L*L].

$T(x)$: transmissivity [L*L/T].

T_a : arithmetic spatial average of transmissivity [L*L/T].

T_e : effective transmissivity [L*L/T].

T_G : ensemble geometric mean transmissivity [L*L/T].

T_S : geometric spatial average transmissivity [L*L/T].

$Y(x)$: log-transmissivity [dim.].

Y_S : arithmetic spatial average of $Y(x)$ over area S [dim.].

Identification of Effective Conductivity Tensor in Randomly Heterogeneous and Stratified Aquifers

by Rachid Ababou

Extended Abstract

The effective macroscale hydraulic conductivity of heterogeneous and stratified geological units can be identified by ad hoc inverse methods, or by more generic, direct methods, such as homogenization. Here, a direct approach is proposed, based on a simple homogenization relation expressing the effective conductivity tensor of randomly heterogeneous flow systems under certain conditions of statistical homogeneity and statistical anisotropy, given the microscale conductivity field $K(x_1,x_2,x_3)$. Imperfectly stratified and anisotropic geological structures are described by means of directional fluctuation scales, while other features, such as degree of variability and bimodality, are conveyed by a probability distribution. The dimensionality of the flow system is also an important factor. The general case of a D-dimensional flow system (D=1,2 or 3) is discussed below.

The proposed homogenization relation expresses the principal components of the D-dimensional effective conductivity tensor by means of a tensorial power-average operator:

$$\hat{K}_{ii} = < K^{p_i} >^{1/p_i} \qquad (i=1,...,D) \qquad (1)$$

where the angular brackets < > designate the operation of averaging. In this equation, the p_i values are directional averaging exponents. They are expressed in terms of the directional fluctuation scales ℓ_i, as follows:

$$p_i = 1 - \frac{2}{D}\frac{\ell_H}{\ell_i} \qquad (i=1,...,D) \qquad (2)$$

where ℓ_H is the D-dimensional harmonic mean fluctuation scale:

$$\ell_H = \left[\frac{1}{D} \sum_{i=1}^{i=D} \ell_i^{-1} \right]^{-1} \qquad (3)$$

Note that the averaging exponents are constrained to lie within the interval [-1,+1], and that they sum up to 2-D. To summarize, eqns 1 to 3 give an analytical relation for the D-dimensional effective conductivity tensor in terms of the single-point probability distribution, the principal directions, and the directional fluctuation scales of the microscale log-conductivity field. Note that the microscale data required for implementation of eqns 1 to 3 are all of a statistical nature. For technical reasons, the statistics of log-conductivity rather than conductivity are preferred.

The power-average effective conductivity tensor (eqns 1 to 3) can be expressed in closed form for several usual types of log-conductivity distributions, such as gaussian and binary. In the case of a "gaussian medium" with normally distributed ℓnK, applying eqns 1 to 3 leads to:

$$\hat{K}_{ii} = K_g \exp\left\{\frac{\sigma_Y^2}{2}\left[1 - \frac{2}{D}\frac{\ell_h}{\ell_i}\right]\right\} \qquad (i=1,...,D) \quad (4)$$

when σ_Y^2 is the log-conductivity variance, and K_g is the geometric mean conductivity. This relation was initially developed by Ababou (1988, v.1, eqn 4.48) in the equivalent form:

$$\hat{K}_{ii} = (K_a)^{\alpha_i} (K_h)^{1-\alpha_i} \qquad (i=1,...,D) \quad (5)$$

where $\alpha_i=(D-\ell_h/\ell_i)/D$, and K_a and K_h represent the arithmetic and harmonic mean conductivities, respectively. Another case of interest is that of a binary medium, made up of a mixture of two distinct conductive phases, α and β, present in the proportions (ρ) and ($1-\rho$), respectively. For instance, phase α could be a sandstone matrix, and phase β a set of shale lenses or shale clast inclusions (Desbarats, 1987; Bachu and Cuthiell, 1990). The conductivity distribution of such a composite medium is of the form:

$$\text{Prob}\{K(x_1,x_2,x_3)=K_\alpha\} = \rho$$
$$\text{Prob}\{K(x_1,x_2,x_3)=K_\beta\} = 1-\rho \quad (6)$$

As before it is assumed as a first approximation that the spatial anisotropy of the random structure can be defined by three fluctuation scales ℓ_1,ℓ_2,ℓ_3. Specializing eqns 1 to 3 for the binary distribution (6) gives:

$$\hat{K}_{ii} = \{\rho K_\alpha^{\,p_i} + (1-\rho)K_\beta^{\,p_i}\}^{1/p_i} \quad (i=1,\ldots,D) \quad (7)$$

with averaging powers (p_i) are as given previously in eqn 2. In the case of a three-dimensional isotropic binary medium, let D=3, and $\ell_1=\ell_2=\ell_3$.This yields $p_i=1/3(i=1,2,3)$ in eqn 7. In the case of a two-dimensional isotropic binary medium, let $\ell_1=\ell_2$ for horizontal isotropy, and D=2 for restriction to two-dimensional space, or equivalently D=3 with $\ell_3 \rightarrow +\infty$ for two-dimensional horizontal flow through a vertically homogeneous medium. Either case yields p_i--0 for i=1 and 2. Inserting this in eqn 7 and using Taylor developments leads to:

$$\hat{K}_{ii} = (K_\alpha)^\rho (K_\beta)^{1-\rho} \quad (i=1 \text{ and } 2) \quad (8)$$

where ρ represents the concentration of phase α, and $1-\rho$ the concentration of phase β.

Although the general form of the effective conductivity model (eqns 1 to 3) remains conjectural at this stage, many specialized forms of this relation appear to be confirmed by other results. The range of validity of the model is being explored in several ways: first, by comparison with exact bounds and with available homogenization solutions in cases of lower dimensionality, statistical isotropy, symmetric distribution, binary distribution, etc., second, by comparison with analytical solutions based on linearized and/or perturbation approximations; and third, by comparison with direct numerical simulations of flow in randomly heterogeneous porous media. The preliminary results of such analyses are encouraging. Some of the relevant effective conductivity results used for comparisons can be found in Ababou (1988), Ababou et al. (1989), Desbarats (1987), Gelhar and Axness (1983), Kohler and Papanicolaou (1982), and Matheron (1967, among others.

Finally, some of the possible applications of the tensorial power-average conductivity model in the area of parameter estimation are indicated. First, the model can be used as a convenient tool for direct identification of the conductivity distribution, principal axes, and fluctuation scales. Unlike other procedures. Further, the model can also be used to estimate geostatistical parameters from large-scale flow tests. To illustrate this second type of application, a parameter identification procedure previously developed for the Oracle fractured granite site by Neuman and Depner (1988) was implemented. Their goal was to estimate the conductivity correlation scales (which play an important role in contaminant macrodispersion) based on a combination of 'microscale' single-hole packer tests and 'macroscale' cross-hole tests. The principal axes of macroscale anisotropy, as inferred from the cross-hole data, appeared to be directly related to the orientations of major fracture sets. Now, given the measured macroscale conductivity tensor and an independent estimate of vertical correlation scale, the remaining correlation scales of the Oracle site can be identified by inverting the effective conductivity model of eqns 1 to 3. Again, this is feasible without recourse to numerical optimization procedures.

Rachid Ababou is currently conducting research on theoretical and computational approaches for modelling

stochastic flow and transport phenomena in highly heterogeneous, three-dimensional conductive media. He received his Dr Ing (honours) in fluid mechanics from the University of Grenoble in 1981 and his PhD in civil engineering from MIT, Cambridge. Dr. Ababou has published a book chapter and several papers in refereed literature. He is currently a senior research scientist with the Center for Nuclear Waste Regulatory Analyses (Southwest Research Institute, Division 20, 6220 Culebra Road, San Antonio, Texas 78228-0510, USA).

References

Ababou, R. 1988. Three-dimensional Flow in Random Porous Media. PhD thesis, Ralph Parsons Laboratory, Massachusetts Institute of Technology.

Ababou, R., D. McLaughlin, L.W. Gelhar and A.F. Tompson. 1989. Numerical simulation of three-dimensional saturated flow in randomly heterogeneous porous media. Transport in Porous Media, v. 4, pp. 549-565.

Bachu, S. and D. Cuthiell. 1990. Effects of core-scale heterogeneity on steady-state and transient fluid flow in porous media: numerical analysis. Water Resour. Res., v. 26, pp. 863-874.

Desbarats, A.J. 1987. Numerical estimation of effective permeability in sand-shale formations. Water Resour. Res., v. 23, pp. 273-286.

Gelhar, L.W. and C.L. Axness. 1983. Three dimensional stochastic analysis of macrodispersion in aquifers. Water Resour. Res., v. 19, pp. 161-180.

Kohler, W. and G.C. Papanicolaou. 1982. Bounds for the effective conductivity of ramdom media. In Macroscopic Properties of Dispordered Media. Lecture Notes in Physics, no. 154, pp. 111-130. Sprintger-Verlag.

Matheron, G. 1967. Elements Pour un Theorie des Mileiux Poreux. Masson et Cie, Paris.

Neuman, S.P. and J.S. Depner. 1988. Use of variable-scale pressure test data to estimate the log hydraulic conductivity covariance and dispersivity of fractured granites near oracle, Arizona. J. Hydrol. v. 102, pp. 475-501.

Kriging Application to Estimate Ground Water and Top of Aquifer Elevations for Eastern Arizona

by Jeff Riddle

Abstract

Ordinary, isotropic and anisotropic block kriging methods have been used to estimate ground water and top-of-aquifer elevations for an 82x74 km (51 x 46 mi) study area in eastern Arizona. These different kriging approaches were compared and it seemed anisotropic kriging was superior only for the top-of-aquifer application. This conclusion was based upon reviewing contours of kriging standard deviation. Cross validation was also reviewed for both kriging applications, and the results showed 85% of kriging estimates were within 30 m (100 ft) of field values for ground water elevations, while 80% of the kriging estimates were within 60 m (200 ft) of field values for top-of-aquifer elevations. These comparative results of cross validation are regarded as good, considering the spread of field data and deviations of 'surface' trends caused by geological deformations in the study area. The worst cross validations were usually located within ~ 3 km (2 mi) perpendicular distance of assumed locations of the axes of synclines and anticlines. In addition to geological deformations, inaccurate recordings of drilling logs, and kriging at data outliers, are suspected as having contributed significantly to the magnitude of difference associated with some cross validations.

Jeff Riddle earned his BS in geology in 1981 from Midwestern State University, Wichita Falls, and his MS in hydrology in 1984 from the University of Arizona, Tucson. He is presently with the Salt River Project (PO Box 52025, Phoenix, Arizona 85072-2025, USA).

Multiple Indicator Conditional Stochastic Simulation of a Section of the Unconfined Aquifer, Hanford Site, Washington, USA

by Eileen Poeter and Peter Townsend

ABSTRACT

Spatial variability of heterogeneities was estimated along a 3.7 km (12,000 ft) cross section in the unconfined aquifer on the Hanford Site, Richland, Washington, USA. A number of equiprobable realizations of heterogeneity for the domain of interest were generated using a multiple indicator conditional simulation technique; emphasis was placed on assessing the continuity of high hydraulic conductivity units. These realizations permit estimation of spatial variability of hydrofacies from limited geologic and hydrologic data. Sedimentary facies with similar hydraulic properties (hydrofacies) were identified based on geologic logs, geophysical logs, and grain size data from borehole samples. Representative hydraulic conductivities (based on field tests and sediment character) were assigned to each facies. Variogram models were used to represent the spatial distribution of each hydrofacies.

Alternative geologic interpretations were considered and different variograms were generated for each: first, the bedrock deformed prior to deposition of sediments and the sediments are flat lying; and second, sediment deposition occurred before or during deformation and/or similar synchronous facies were deposited on a variable topographic surface such that the sedimentary units dip in concert with the dip of the bedrock (thicker in the synclines and thinner over the anticlines). For the dipping scenario (thought to be the more realistic alternative) a shorter variogram range was considered for the gravel and the sand facies which were difficult to model due to the large data spacing.

Numerous, equiprobable realizations were generated for each scenario and analyzed to provide a measure of uncertainty of the distribution of sedimentological units which reflect the distribution of groundwater flow and contaminant transport properties. For horizontal stratigraphy, the simulations indicated there is a 70% chance that lateral continuity of a high hydraulic conductivity facies occurs across the section and a 30% chance that a clay and silt facies severs lateral continuity of high hydraulic conductivity facies. In the simulations of dipping strata, little difference was apparent between simulations generated assuming long and short variogram ranges for gravel and sand facies. Discontinuity throughout the entire section occurred in only 6 to 8% of the simulations generated assuming

dipping strata. Ninety two percent of all the simulations were connected by a combination of gravel, sandy gravel, and sand facies. However, only 9 to 18% of these continuous paths occurred in the shallow zone near the water table which is where the bulk of the contaminants are thought to be concentrated (Gephart et al, 1979). The remainder were continuous deeper in the section which is not monitored for contaminants and may be a pathway for undetected off-site migration.

The equiprobable realizations of aquifer heterogeneity will be used to define the hydrofacies framework of a groundwater flow and contaminant transport model of the cross-section. Results of numerous flow and transport simulations using each realization as the basis for defining aquifer properties will be combined to produce frequency distributions of hydraulic heads, groundwater velocities, and contaminant concentrations as a function of space and time. Such frequency distributions can be used to assess risks and aid management decisions. Ultimately, inverse techniques will be employed to integrate known field conditions in estimates of flow and transport parameters within each stochastic realization, thus further constraining interpretation of the system.

INTRODUCTION

Hydrogeologists at the Hanford Site are concerned about contaminant migration in the vicinity of the study area delineated in Figure 1. Within this area, contaminated springs discharge along the Columbia River. Further, as evidenced by lobes of high tritium concentration, certain sedimentary strata have promoted more rapid contaminant transport than others (Poeter and Gaylord, 1990). Available, though limited, data regarding the contaminant distribution and hydraulic heads in the unconfined aquifer suggest that contaminants remain close to the water table on the Hanford Site (Gephart et al., 1979). However, because of the absence of well-constrained hydrogeologic data, there is concern that contaminants may migrate off-site, beneath the Columbia River.

Poeter and Gaylord (1990) evaluated alternative means to define facies at the Hanford site and found that hydrofacies can be delineated. However, estimations of the interconnectedness of hydrofacies must be undertaken to predict possible paths of contaminant migration because subtle discontinuities in the high hydraulic conductivity units have substantial impact on the migration of contaminants.

The immediate objective of this work was to define sedimentary units with similar hydrological properties (hydrofacies) and estimate their continuity along a 3.7 km (12,000 ft) cross-section (delineated by the line of labeled wells in Figure 1) at the Hanford Site. This cross-section was considered to be representative of other cross-sections which parallel

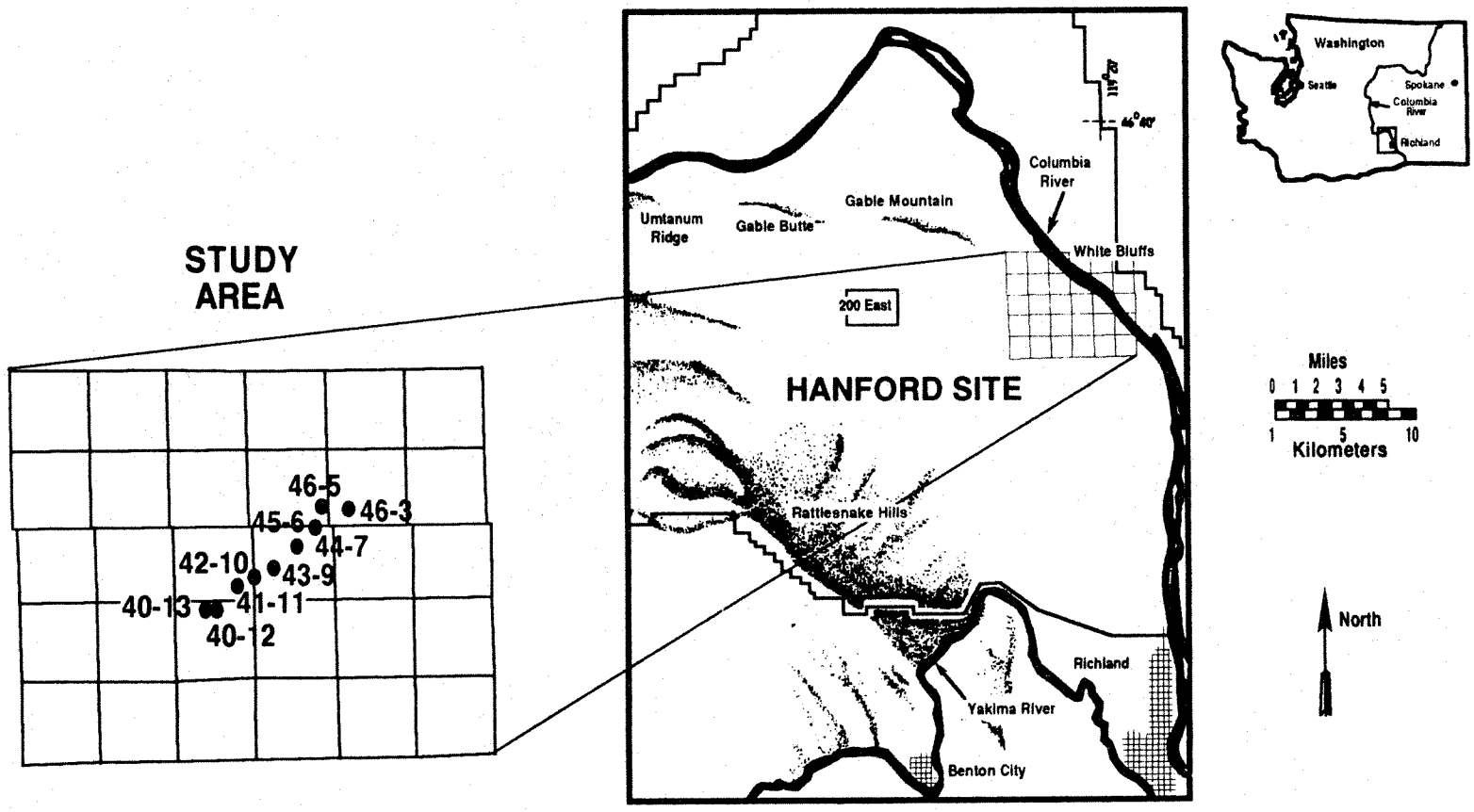

Figure 1. Location of study area on the Hanford Site, Washington, USA.

groundwater flow in the study area.

Prediction of the connectivity of high hydraulic conductivity hydrofacies is vital to evaluating migration rates and dispersal patterns of contaminants in ground water. However, it is not feasible to drill and trace out all hydrofacies of interest. Thus alternative methods for coping with heterogeneity must be sought. One of the most promising of current techniques for delineation of aquifer heterogeneity is conditional multiple indicator stochastic simulation (Journel and Huijbregts, 1978; Journel, 1983; Journel and Alabert, 1988; Fogg, 1986; Dreiss and Johnson, 1988; Gomez-Hernandez and Srivastava, 1990). Stochastic simulations of heterogeneity make it possible to address critical hydraulic and contaminant transport questions that cannot be addressed using standard approaches. Utilization of alternative realizations of aquifer heterogeneity in modeling of contaminant transport allows evaluation of the influence of relatively small discrete features which may control transport. Risk associated with contaminant migration can be assessed using flow and transport models that incorporate the distribution of possible aquifer configurations. Quantified uncertainty associated with the flow system aids decisions regarding the level of financial investment in further characterization and/or remediation.

In the work presented here, the aquifer is represented in only two dimensions. Ultimately, aquifer heterogeneity and its impact on contaminant migration in the area will be evaluated in three dimensions. This preliminary work serves to gather the appropriate tools, establish the methodology, and assess the feasibility of conducting a more extensive three-dimensional analysis.

Advantage of a Stochastic Approach

A stochastic model is a probabilistic approach to quantifying uncertainty associated with available data. Such models can reflect geologic character through use of variograms and address uncertainty by producing different realizations of the spatial distribution of aquifer properties via a random process. The reason for taking a probabilistic approach to characterization of spatial properties of aquifers is the inability of deterministic models to represent complexities in the spatial structure of aquifers. Stochastic approaches produce multiple results based on the statistics of the data. In contrast, deterministic approaches yield only a single result from a data set. Thus, stochastic models can realistically address data uncertainty in the subsurface.

Advantage of a Conditional Simulator

Conditional simulation is illustrated by a one-dimensional hypothetical example shown in Figure 2 which presents two

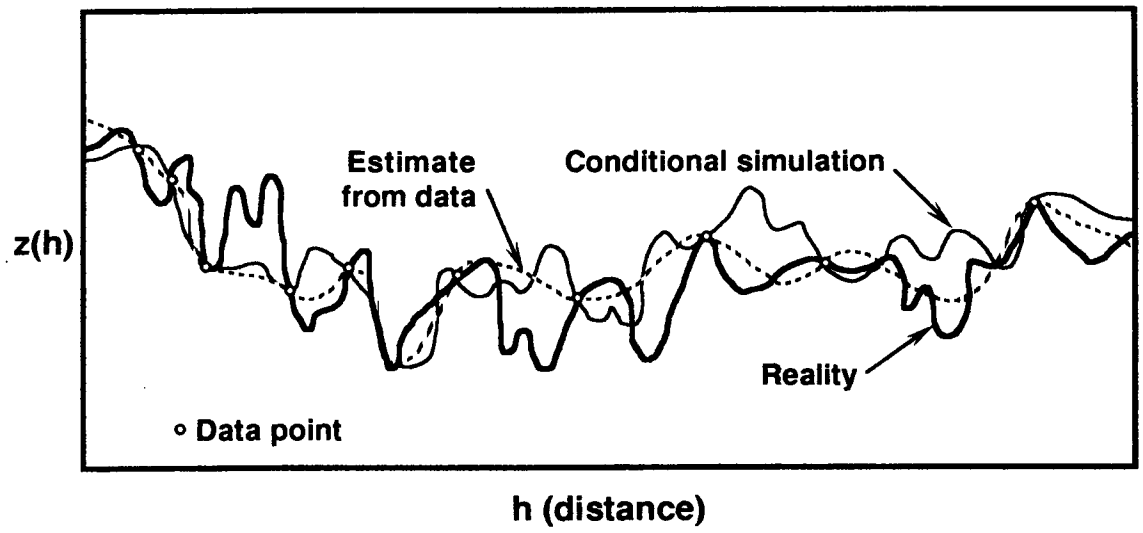

Figure 2. Example of a one-dimensional conditional stochastic simulation (after Journel and Huijbregts, 1978).

interpretations of the distribution of hydraulic conductivity, hydraulic conductivity, along a line. The bold line represents the actual distribution of hydraulic conductivity, the dashed line is a minimum-error-variance linear unbiased estimate (e.g. kriged) of the hydraulic conductivity distribution, and the thin line represents a single realization of the hydraulic conductivity distribution from a conditional stochastic simulation. The minimum-error-variance linear unbiased estimate is smoothed because the data spacing is greater than the scale of variability (Fogg, 1986). The conditional simulation, however, passes through the data points and exhibits similar variability as is observed in the actual field setting (Fogg, 1986), yet each realization honors the available data at each location.

Advantage of the Indicator Approach

Interpolated results of kriging hydraulic conductivity values can be used as input to flow and transport models. Kriging variances can be used to evaluate the uncertainty associated with the distribution of aquifer properties, but cannot be used to assess uncertainty of flow velocities and contaminant concentrations. In addition, the kriged conductivity field will be unrealistically smooth. Smoothed interpretations of the hydrofacies ignore the complex and detailed spatial distributions of the extreme valued units (these include both continuous high hydraulic conductivity units that serve as critical pathways and low hydraulic conductivity units that truncate them and drastically reduce flow velocities). The spatial smoothing of kriging is

confirmed by noting that the resulting distribution of kriged values has a smaller variance and a deficiency of extreme values relative to both the actual data set or an indicator simulation (Journel and Alabert, 1988). When considering contaminant transport in the subsurface, it is essential to estimate the connectivity of extreme valued units. The strength of indicator simulations is their ability to delineate spatial continuity of units with extreme values of hydraulic conductivity.

MULTIPLE INDICATOR STOCHASTIC SIMULATION

Gómez-Hernandez and Srivastava (1990) developed a three-dimensional, multiple indicator, conditional simulation code named ISIM3D which is used in the work presented here. This algorithm allows three-dimensional simulation of known values (hard data) and, after some modification, interpreted values (soft data) in alternative, equiprobable numerical models of aquifer heterogeneity. Soft information consists of both interpretive data (e.g. geological descriptions of environment and history) or "fuzzy" data (e.g. seismic data), complementing the usually sparse, hard-well data (Journel and Alabert, 1988).

Indicators are a transform of the data and represent the probability that a variable will be less than or equal to a specified threshold value; thresholds may be chosen to separate high, intermediate, and low hydraulic conductivity units. The indicator is "on" (has a value of one) if the value is greater than or equal to the threshold, and is "off" (has a value of zero) if the value is less than the threshold. Experimental variograms of indicator functions are extremely robust with regard to extreme-valued hydraulic conductivity units because their estimation does not require the hydraulic conductivity values themselves. Instead, the experimental indicator variogram requires the ranked order of the data relative to the chosen threshold (Journel, 1983).

The multiple indicator conditional stochastic simulator developed by Gómez-Hernandez and Srivastava (1990) operates as follows. First, the facies types are defined and assigned indicator values. Then, a variogram is computed for each indicator in each of the three orthogonal principle directions, with the axes oriented along the principal trends of the geological environment. ISIM3D requires that the variogram model and sill must be the same in each direction for a given indicator but the range may differ. A grid is defined over the domain to be simulated and a random sequence of grid blocks is selected. For each grid block in the sequence, the conditioning data in the search neighborhood are found, a kriging system is set up for each indicator threshold, and these are used to determine the conditional probability distribution function (cpdf) representing the probability that a particular facies occurs at the location. If

the cpdf fails to be a continuously increasing function, an algorithm for correcting order relations is utilized. Once the cpdf is constructed, a random number between zero and one is generated and the associated facies on the cpdf is selected to represent that location for that simulation. This simulated point is then incorporated into the conditioning data set. After all points are simulated, the entire matrix represents one realization of the heterogeneous subsurface and the process is repeated using s different random sequence of grid blocks and new random number seeds to obtain additional simulations.

Evaluation of Simulated Sections

After generating numerous realizations using ISIM3D, the sections were evaluated for hydrofacies connectivity. Continuous paths of one or a combination of facies may be identified. Diagonal connections are not considered to represent continuity of facies because: the grid is assumed to be sufficiently detailed to allow simulation of connected units via horizontal and vertical "stair steps"; and, when the simulations are incorporated into numerical flow and transport codes, computations are made across vertical and horizontal faces, but not on the diagonal.

Location and Geologic Setting of the Simulated Section

The Hanford Site is a U.S. Government facility encompassing approximately 1500 km^2 (570 mi^2) and located in the central and lowest part of the Pasco Basin of south-central Washington, USA (Figure 1). The Pasco Basin, a synclinal trough within the Yakima fold belt, is bounded on three sides by basalt uplifts (DOE, 1988). The Hanford Site is underlain by basalts of the Miocene-age Columbia River Group and by a heterogeneous succession of clastic sediments (Myers et al., 1979; Tallman et al., 1979, 1981; DOE, 1988). The Miocene- to Pliocene-aged Ringold Formation and the late Pleistocene-aged Hanford Formation are the principle sedimentary units comprising the unconfined aquifer. Attempts to characterize heterogeneity of the unconfined aquifer within the framework of standard fluvial models at the scale of interest have been unsuccessful (Poeter and Gaylord, 1990). The complexity of fluvial systems (Miall, 1985, 1987), compounded by the effects of erosion and redeposition by catastrophic Pleistocene-aged flooding (Bretz, 1959; Fecht et al., 1985), limit the application of standard fluvial models at the Hanford Site. Hence the following approach to delineating facies was pursued.

DELINEATION OF HYDROFACIES

Data from nine boreholes were used for simulation of the section (Figure 1). Neutron-neutron, gamma-gamma logs, and descriptive geological logs, were supplemented with grain size data and were used to class

sediments into four categories: 1) clay and silt; 2) sand; 3) sandy gravel; and 4) gravel. The appropriate category for each sample was not always clear so guidelines were established for sediment classification (Table 1). These classifications were applied at 0.3 m (1 ft) intervals for computation of the variograms and at 1.5m (5ft) intervals for the conditional stochastic simulations.

Of the available field scale aquifer tests, only one representative test was identified for each facies. Other tests incorporated more than one facies or exhibited unreliable data. The applicable tests were conducted in the same deposits about 12 miles south of the study area. Based on this limited data, a preliminary value of hydraulic conductivity was assigned to each hydrofacies as follows: Gravel $1.2x10^4$ m/d (40,000 ft/d); Sandy gravel $3x10^3$ m/d (10,000 ft/d); Sand 60 m/d (200 ft/d); Silt 0.2 m/d (0.6 ft/d) (Gaylord and Poeter, 1988). It is unknown whether the hydraulic conductivity value utilized for each facies falls in the high, middle or low portion of the hydraulic conductivity distribution for the facies, so the values must be used with caution.

Hydraulic conductivities were also measured at a small scale using an air permeameter on outcrops of the same deposits approximately 8 miles to the southwest and on core from a hole about 3 miles to the north. Hydraulic conductivities of the clay silt facies ranged from 0.03 to 0.9 m/d (0.1 to 3 ft/d) and the sand facies ranged from 1.2 to 90 m/d (4 to 300 ft/d).

Table 1

Guidelines for Sediment Classification

Sediment Classification	Sediment Description
Gravel	Clean gravel, trace of fine material
Sandy gravel	Gravel and sand, some silt
Sand	Clean sand, trace of silt
Clay and Silt	Silt and clay, some sand and gravel

Coarser grained sediments were not tested with the air permeameter with the exception of a few tests on the matrix of some sandy gravel. Both in outcrop and on the core, hydraulic conductivity of the sand matrix in sandy gravel ranged from 6 to 120 m/d (20 to 400 ft/d). We can only assume that the bulk hydraulic conductivity of these sandy gravels are less than the hydraulic conductivity determined for the matrix because of the impervious nature of the numerous large clasts (estimated at 20-60%). However, the large scale tests, conducted 12 miles south of the study area, indicate hydraulic conductivity two orders of magnitude greater than the matrix hydraulic conductivities as measured by the air permeameter. The

discrepancy between the large and small scale measurements may reflect that sandy gravels in the area where large scale tests were run have a more open or coarser matrix than the sandy gravels tested with the air permeameter. How these different measurements relate to sandy gravel below the study area remains to be determined. For now, it is best to evaluate the study area under two different assumptions: in one case that the sandy gravels are more hydraulically conductive than the sands, and in another case that the sandy gravels have similar hydraulic conductivity as the sands.

SPATIAL DISTRIBUTION OF HYDROFACIES

Each hydrofacies was assigned an indicator and vertical and horizontal variograms were computed for each indicator for both "flat-lying" and "dipping" geological interpretations. Approximately 1600 data points were used in the variogram calculations. Initially, the geostatistical package GEOEAS (Englund and Sparks, 1988) was used to compute experimental variograms and fit variogram models. However, limited array dimensions prevented use of GEOEAS to develop variograms. An alternate variogram code GAMUK (Knudsen et al, 1984), was considered because of its ability to accommodate the entire data set, but was rejected because it did not have modeling capabilities. Finally, experimental variogram data were entered into a spread sheet. This allowed us to experiment with a variety of model types, and incorporate nested structures in the variogram models.

Assumption of Flat-Lying Strata

Variograms were computed for a variety of dip angles and the longest ranges were attained when the variogram was calculated at zero degrees from horizontal which suggested that the strata were nearly flat lying. Later it was decided that the strata had multiple dips that could not be identified by comparing variogram ranges for one dip angle. An approach to simulating the dipping strata is discussed later, but the simulations of flat-lying strata are included for comparison.

Experimental Variograms for Flat Lying Strata

Figure 3 illustrates the experimental vertical variograms (data points), the modeled vertical variograms (solid line), and the variance of the data or sill (dashed line) of the facies developed under the assumption that the strata are flat-lying (i.e. deposited after deformation of the basalt). Actually semi-variograms are calculated; however, for brevity, we refer to them as variograms throughout this document. Parameters of the variogram models, assuming flat-lying units, are presented in Table 2. The variograms are illustrated to 250 feet to focus on the meaningful portion of the data and show detail at smaller spacings. Oscillation of the experimental variograms about

Figure 3. Vertical variograms for assumption of flat-lying strata (50 ft is approximately 15 m).

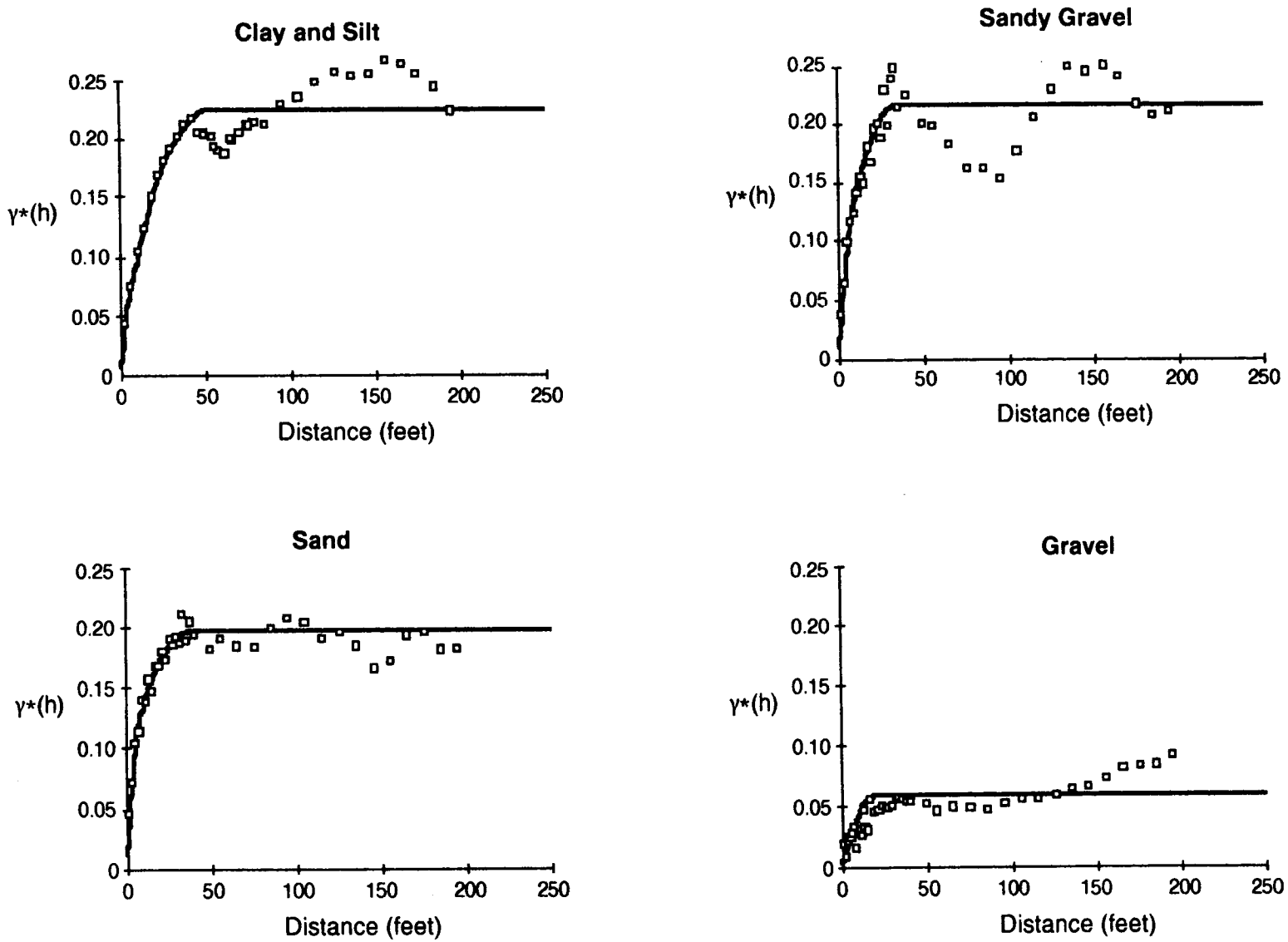

Table 2
Assumed Flat-Lying Stratigraphy
Indicator Variogram Parameters

Hydro-facies	Nugget	Structure	Sill	Range Vertical ~m	Range Vertical ft	Range Horizontal ~m	Range Horizontal ft
Clay and Silt	0.005	spherical	0.026	2	5	30	100
		spherical	0.060	9	29	120	400
		spherical	0.135	17	55	1460	4800
Sand	0.012	spherical	0.066	2	8	60	200
		spherical	0.030	5	18	150	500
		spherical	0.089	12	38	550	1800
Sandy Gravel	0.010	spherical	0.070	3	10	60	200
		spherical	0.060	9	30	150	500
		spherical	0.078	12	38	910	3000
Gravel	0.004	spherical	0.0554	6	19	180	600

the sill is likely a "hole effect" that reflects repetition of the facies. The gravel variograms have low sills because this hydrofacies constitutes less than 10% of the data.

Fewer data pairs were used in the horizontal variogram analysis than in the vertical analysis because of the limited number of boreholes and the large distance between holes. Because these data spacings may be greater than the range of the variograms, the horizontal experimental variograms are less well defined (Figure 4). Additional data between the wells (e.g. additional boreholes or geophysical data) would improve the variograms. In order to model the horizontal experimental variograms, the same nugget value as determined for the vertical variogram of the same facies was used. Use of the same nugget value assumes the variance at small distances is isotropic: Dreiss and Johnson (1988) suggested such an approach. As mentioned earlier, ISIM3D requires that the variogram model and sill have the same value in all directions for a given indicator but that the range can vary with direction. Because the vertical experimental variograms were defined by more closely-spaced data, the variogram models were primarily dictated by the nature of the vertical experimental variograms.

Assumption of Dipping Strata

To accommodate the geological interpretation that assumes the units dip nearly concordantly with the basalt

Figure 4. Horizontal variograms for assumption of flat-lying strata (3000 ft is approximately 915 m).

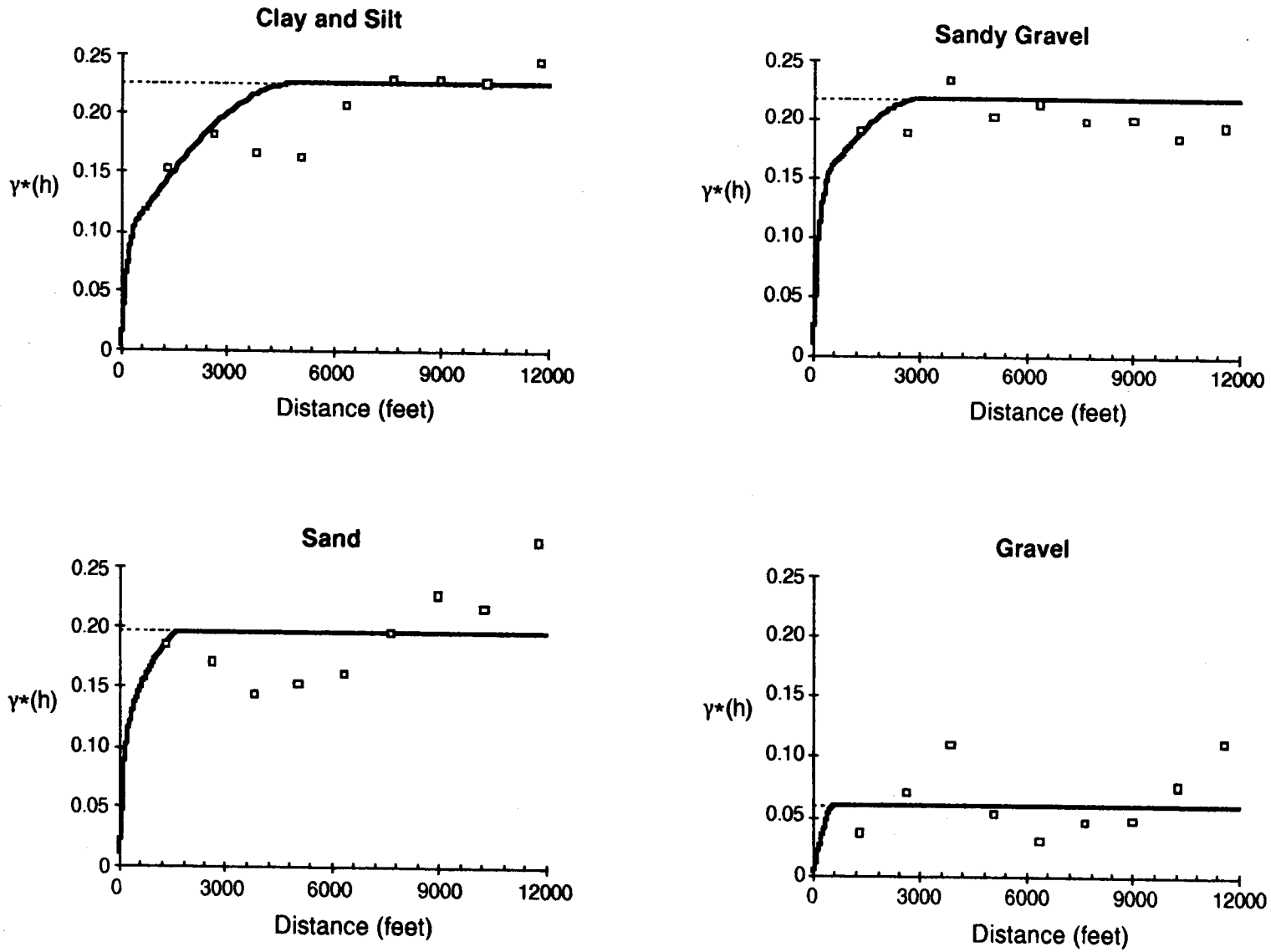

(with the thickest sedimentary accumulations in the synclines) the indicator data were transformed before computing variograms. In short, dimensionless facies thicknesses were determined by normalizing to total thickness. Thus, yielding a total constant thickness of section such that the ground surface was constant (1.0) at the top of the section and the top of basalt was constant (0.0) at the bottom of the section. Once transformed, horizontal and vertical variograms were calculated and simulations were conducted in the transformed geometry. Finally, the simulated units were transformed back to the original coordinate system.

Experimental Variograms for Dipping Strata

Figure 5 illustrates the vertical variograms used when dip of the sedimentary beds is taken into account; parameters of the variogram models for the dipping units are presented in Table 3. In general, the variograms show more correlation, have longer ranges, are better defined before reaching the sill, and are smoother than those developed for the "flat-lying" conceptual geologic model, which suggests that dipping

Table 3
Assumed Dipping Stratigraphy
Indicator Variogram Parameters

Hydro-facies	Nugget	Structure	Sill	Range Vertical		Range Horizontal best estimate		Range Horizontal low connectivity	
				m	ft	m	ft	m	ft
Clay and Silt	0.0	spherical	0.042	3	9	150	500	150	500
		spherical	0.092	12	40	580	1900	580	1900
		spherical	0.081	88	290	1650	5400	1650	5400
Sand	0.0	spherical	0.050	2	8	120	400	120	400
		spherical	0.100	9	30	760	2500	240	800
		spherical	0.042	24	80	1200	3900	1200	3900
Sandy Gravel	0.016	spherical	0.060	8	25	90	300	90	300
		spherical	0.108	12	40	760	2500	760	2500
		spherical	0.042	180	600*	910	3000	910	3000
Gravel	0.0	spherical	0.0100	2	8	30	100	30	100
		spherical	0.0280	12	40	210	700	210	700
		spherical	0.0395	15	50	2130	7000	370	1200

* Large vertical range used to match curve at 60-100 ft section. It must also be noted that the vertical search radius was limited to 295 ft (range of Clay and Silt) in the simulations.

Figure 5. Vertical variograms for assumption of dipping strata (50 ft is approximately 15 m).

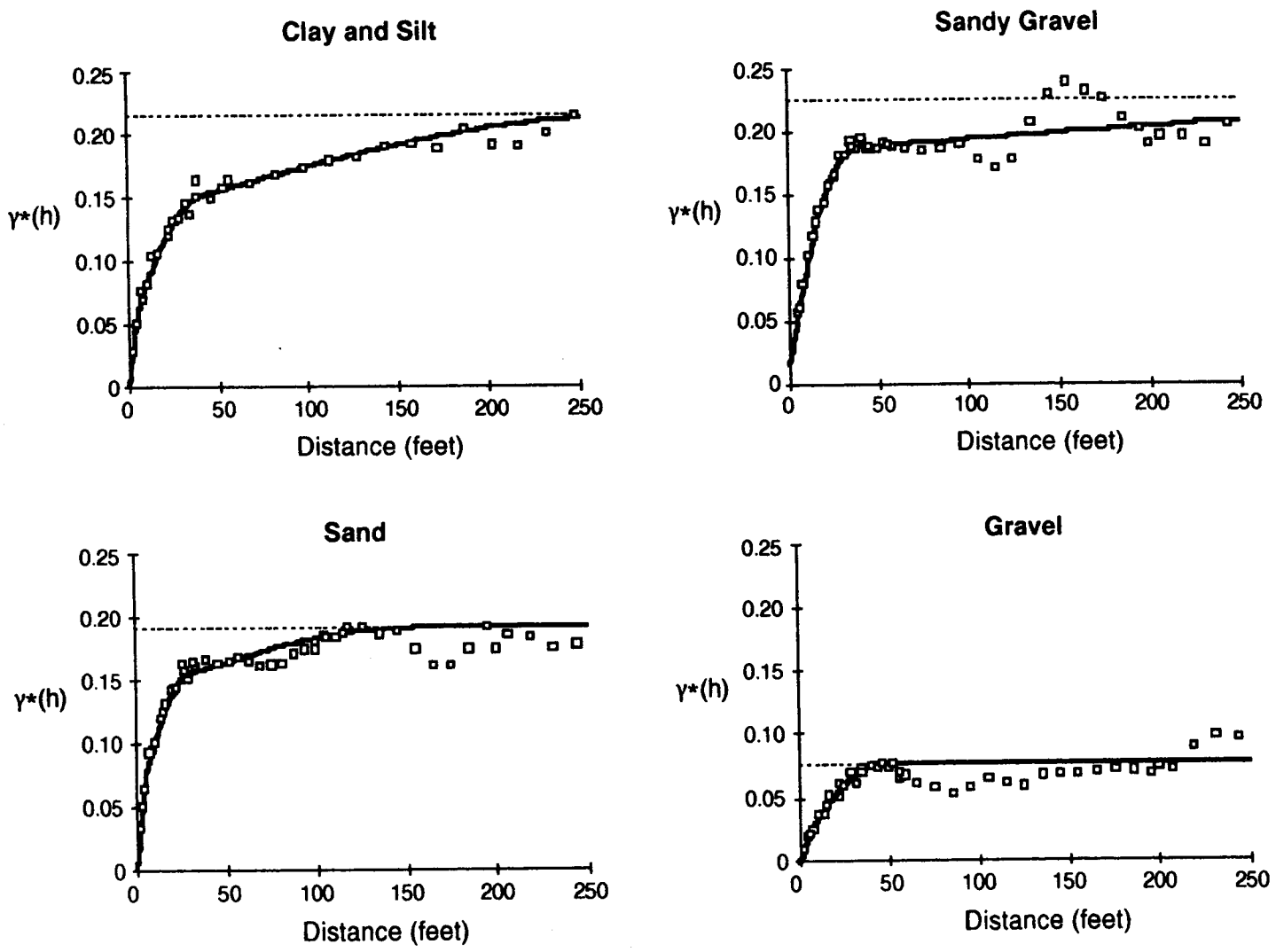

strata are a better conceptual model for the study area.

Because fewer data pairs were used in the horizontal variogram analysis than were used in the vertical variogram analysis, the horizontal variograms are less well defined (Figure 6) yet show better correlation than those for flat-lying strata. The same model, nugget, and sill values determined for the vertical variogram of the same facies were used but a different range was determined from the horizontal experimental variograms.

We believe that the scenario of thinning, dipping beds with the above variograms yields the most realistic simulations of the cross-section given the available data. However, because the horizontal variograms for the dipping strata scenario are ill-defined we conducted a set of simulations with variograms models with shorter ranges for the gravel and sand facies to explore the sensitivity of the results to the character of the variogram. These ranges are also presented in Table 3.

MULTIPLE INDICATOR CONDITIONAL STOCHASTIC SIMULATIONS OF THE HANFORD CROSS-SECTION

One hundred realizations were simulated for each of the three cases to provide the preliminary assessment presented here. Simulations were generated on a 105x120 grid with regular spacing of 1.5 and 30 m (5 and 100 ft) respectively to represent a section up to 160 m (525 ft) deep and 3.7 km (12,000 ft) long. For the cases of dipping strata, the grids were subsequently transformed to their appropriate size based on the thickness of the section.

Character of Simulated Cross-sections

Selected simulated cross-sections for the dipping, "best estimate" variograms are presented in Figure 7. These three simulations represent the end members (with regard to facies continuity) of the simulations including: a cross-section with a continuous high hydraulic conductivity zone near the water table (Figure 7A), a disconnected cross-section (Figure 7B), and a cross-section in which the shallow, highly permeable sediments are truncated and a deep connected path through sandy facies exists (Figure 7C). In Figure 7, the upper boundary of the outlined section corresponds to the ground surface, the lower boundary to basalt, and the sloping line across the middle of the section to the water table; groundwater flows from left to right, and the Columbia River is located in the upper right corner of the section. Continuous high hydraulic conductivity zones near the water table are of concern because it is suspected that contaminants are concentrated there due to the shallow nature of the sources and the upward hydraulic gradient which may prevail in the cross-section which is located in a regional discharge area. Realizations displaying the character of Figure 7C are of concern because of the potential for contaminants to be driven deeper in the cross-section

Figure 6. Horizontal variograms for assumption of dipping strata (3000 ft is approximately 915 m).

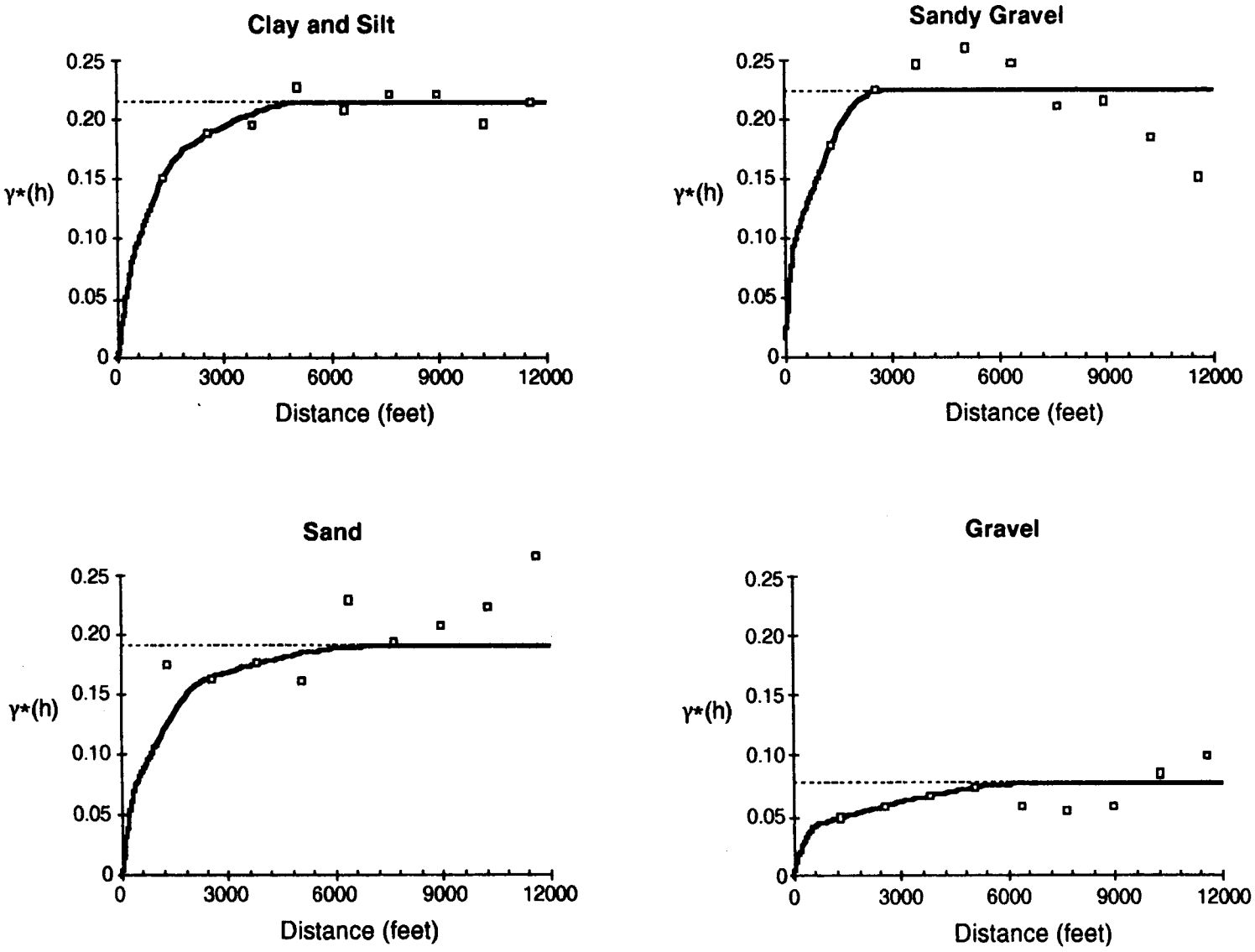

and transported beneath the Columbia River.

Simulations of cross-sections conducted using shorter variogram ranges for the gravel and sand facies are illustrated in Figure 8. As in Figure 7, realizations in Figure 8 represent the end members of the simulations including: a cross-section with a continuous high hydraulic conductivity zone near the water table (Figure 8A), a disconnected cross-section (Figure 8B) and a cross-section in which the shallow highly permeable sediments are truncated and a deep connected path through sandy facies exists (Figure 8C). Cross-sections simulated sections with dipping strata but shorter variogram ranges for the gravel and sand facies have very similar character to those generated with long ranges (compare Figures 7 and 8).

Cross-sections simulated for the flat-lying strata conceptual model have a different appearance (Figure 9). Realizations presented in Figure 9 represent the end members of the simulations including: a cross-section with a continuous high hydraulic conductivity zone near the water table (Figure 9A), a disconnected cross-section (Figure 9B) and a cross-section in which the shallow highly permeable sediments are truncated and a deep connected path through sandy facies exists (Figure 8C).

Influence of Discontinuities in the Critical Path

In order to illustrate the influence of the discontinuities in a section, it is useful to consider the impact of various proportions of facies on the effective hydraulic conductivity along the critical path. The critical path was determined by finding the path of highest hydraulic conductivity that traverses the entire cross-section length regardless of tortuosity (i.e. the path with the most high hydraulic conductivity grid blocks). To accomplish this, first a fully connected gravel path was sought. As none were found in any of the simulated cross-sections, paths including the least amount of sandy gravel to complete the gravel connection were sought. If necessary, some grid blocks of sand were included in the path to connect continuous zones of gravel and sandy gravel, and so on until the path of least resistance that traverses the cross-section was found. Effective hydraulic conductivities along critical paths comprised of a variety of proportions of facies are calculated as the inverse of the sum of the quotients of the fraction of the flow path represented by a hydrofacies and the hydraulic conductivity of that hydrofacies and are presented in Table 4.

The gravel portion of the connected paths was typically 25% of the critical path across the cross-section. Variations in the percent of gravel and sandy gravel yield nearly the same effective hydraulic conductivity (i.e. less than a factor of 2 difference, see Table 4). Addition of 20% sand to such paths decreases the effective hydraulic conductivity by an order of magnitude. The

Figure 7. Examples of multiple indicator conditional stochastic simulations for the deformed geologic conceptual model with the best estimate variograms:

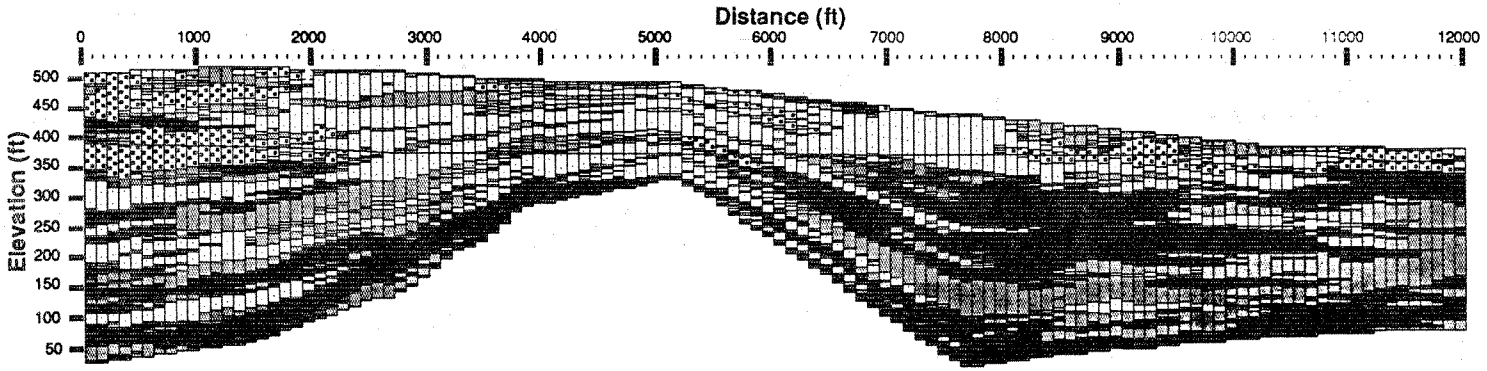

A. a well connected, high hydraulic conductivity facies;

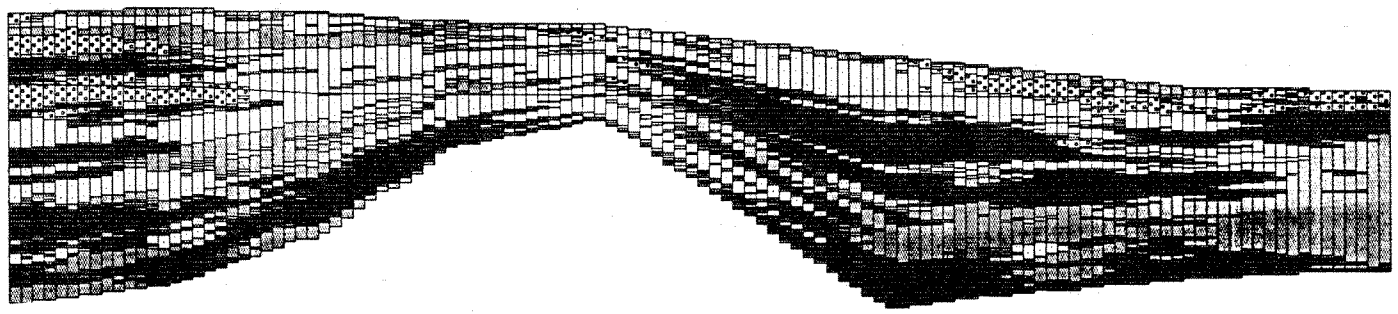

B. a discontinuous high hydraulic conductivity facies;

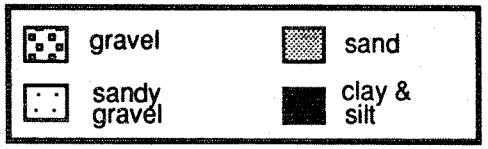

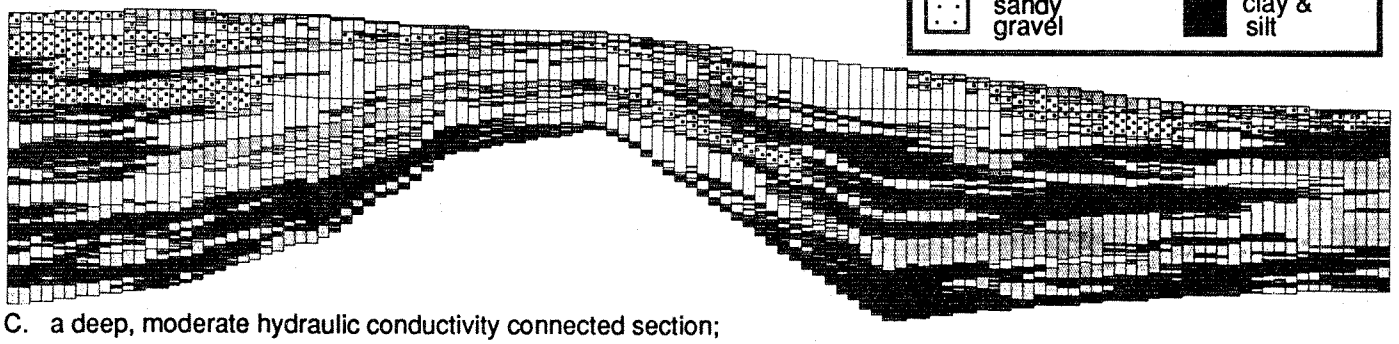

C. a deep, moderate hydraulic conductivity connected section;

Figure 8. Examples of multiple indicator conditional stochastic simulations for the deformed geologic conceptual model with the shorter range gravel and sand facies variograms:

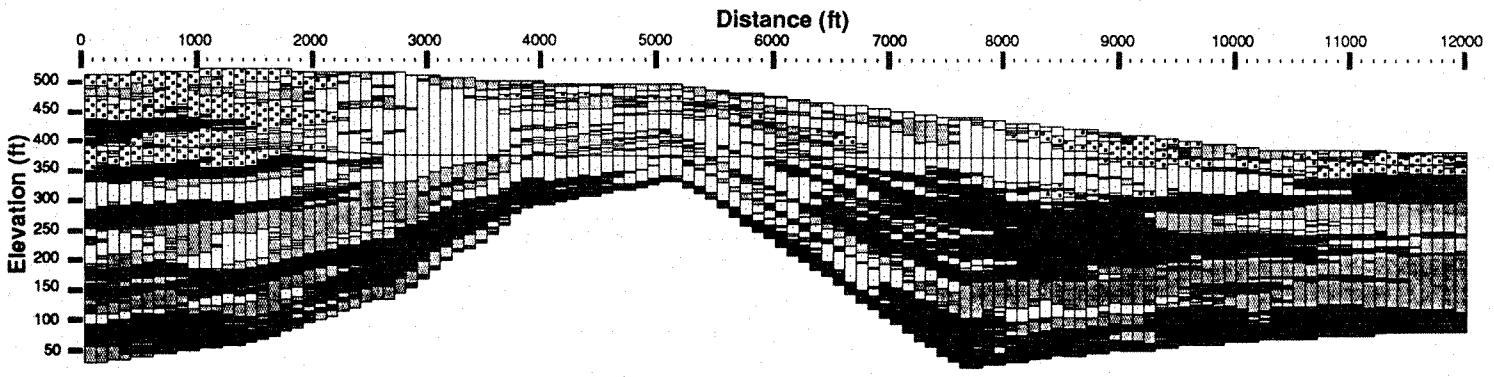

A. a well connected, high hydraulic conductivity facies;

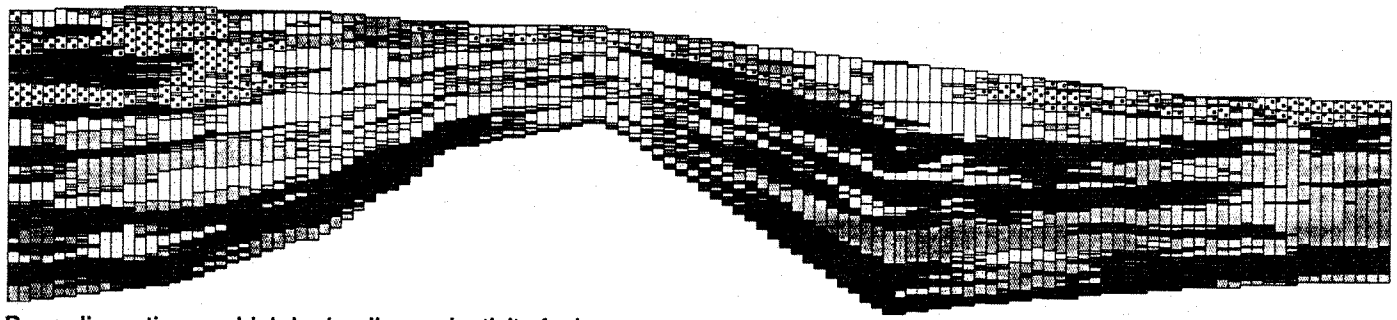

B. a discontinuous high hydraulic conductivity facies;

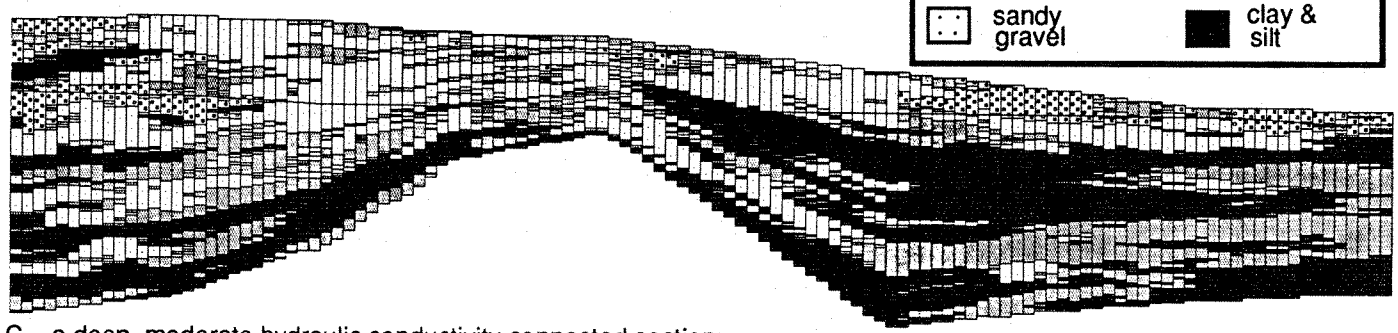

C. a deep, moderate hydraulic conductivity connected section;

Figure 9. Examples of multiple indicator conditional stochastic simulations for the flat stratigraphy geologic model:

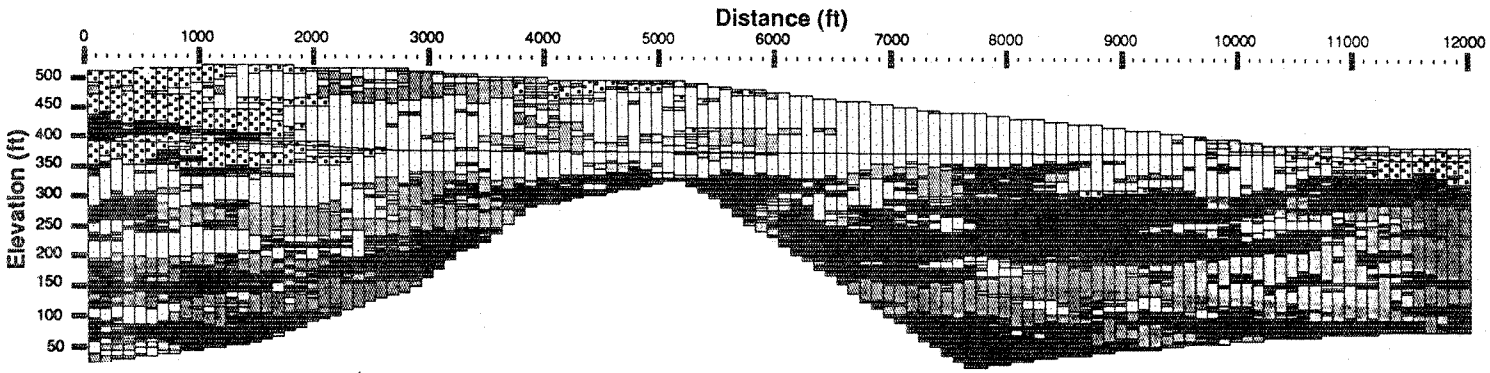

A. a well connected, high hydraulic conductivity facies;

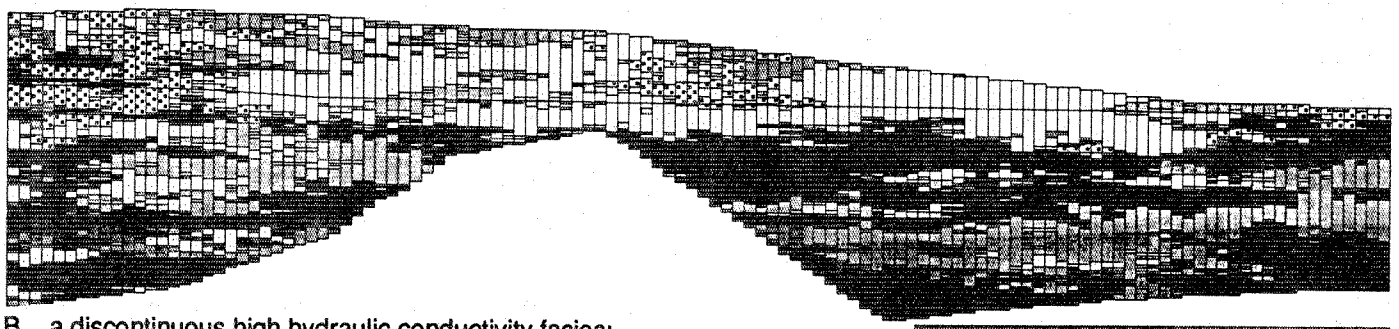

B. a discontinuous high hydraulic conductivity facies;

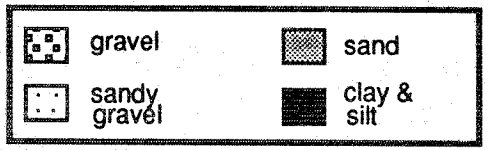

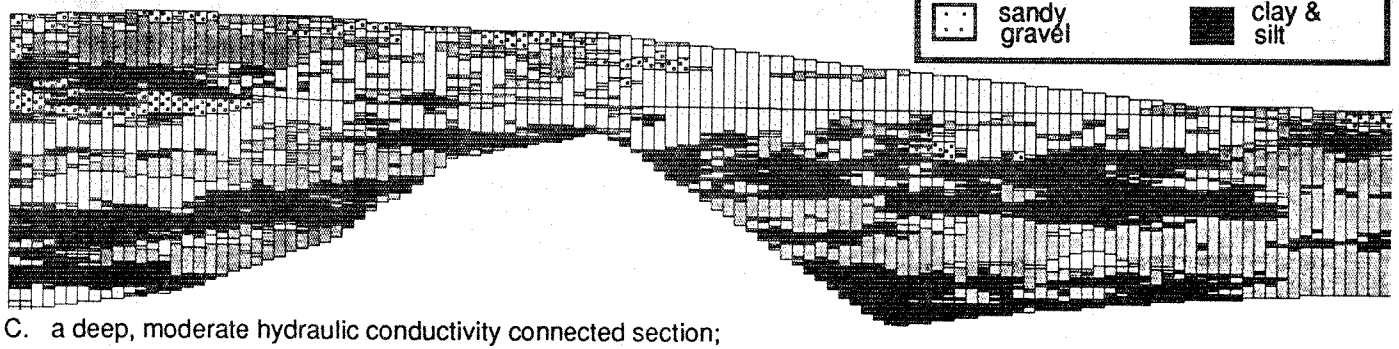

C. a deep, moderate hydraulic conductivity connected section;

Table 4

Effective Hydraulic Conductivity for Selected Proportions of Hydrofacies Along a Critical Path

% gravel	% sandy gravel	% sand	% silt	effective K (m/d)	(ft/day)
50	50	-	-	4,900	16,000
25	75	-	-	3,750	12,300
10	90	-	-	3,300	10,800
25	74	1	-	2,350	7,700
25	71	4	-	1,100	3,600
25	67	8	-	640	2,100
25	50	25	-	235	770
25	25	50	-	120	400
25	74	-	1	18	60
25	54	18	3	6	20
25	71	-	4	5	15
25	67	-	8	2	7
25	65	-	10	2	6

presence of 4% clay and silt facies along the critical path decreases the effective hydraulic conductivity by three orders of magnitude. If it is determined that the sandy gravels are of the same order of magnitude of hydraulic conductivity as the sands as discussed in the section, Delineation of Hydrofacies), cross-sections connected by only sandy gravels and gravel will have the same character as those connected by gravel, sandy gravel and sand facies as listed in Table 4, with an effective hydraulic conductivity dominated by the hydraulic conductivity of the sand facies. In such case, the percent sand traversed across the path will be irrelevant and the only significant feature would be truncation of a section by a silt and clay unit.

It is important to note that these effective hydraulic conductivities are useful in evaluating the nature of groundwater flow through this two-dimensional cross-section because they are the effective property of the critical path and not an effective property of the section as a whole. However, we caution that these reductions in effective hydraulic conductivity were calculated for a two dimensional section. Similar discontinuities would be required in the third dimension to yield such low effective hydraulic conductivity overall. It is likely that the low hydraulic conductivity zones are discontinuous in the third dimension and that contaminants will migrate laterally to circumvent such units. Consequently, effective hydraulic conductivity of critical paths in three-dimensions will be higher than the values presented in Table 4. The ultimate goal is to evaluate conditions in three dimensions.

Continuous units of the highest hydraulic conductivity facies are of greatest interest because they provide a connected zone through which contaminants can migrate rapidly. However, in the case of this simulated cross-section, the gravel unit is non-continuous in every realization. This is reasonable because the gravel facies constitutes only 10% of the data. Therefore, the connectedness of a combination of the sandy gravel and the gravel facies which represents the next highest effective hydraulic conductivity unit. A separate assessment of the connectedness resulting from a combination of gravel, sandy gravel, and sand was also undertaken.

Discontinuous Critical Paths in Simulated Cross-sections

Greater discontinuity was found in simulations based on the assumption of flat-lying units as compared with those generated under the assumption that the units dip. Thirty percent of simulations produced under the assumption of flat-lying strata, were discontinuous (i.e. included silt and clay facies in the critical path). Critical paths in these discontinuous simulations include 0-8% sand and 1-5% clay and silt, averaging 2.5% of each of the two facies. A qualitative assessment of the significance of these percentages on the conductivity of the cross-section can be obtained by referring to Table 4. In contrast, when dipping strata are assumed, only 8% of the simulations which used longer variogram ranges for gravel and sand (our "best estimate" of field conditions) included silt and clay facies in the critical path, whereas 6% of the simulations which used shorter variogram ranges were truncated. Given that 100 realizations were generated for each scenario, the difference between 6 and 8% is of little significance. For the disconnected cross-sections generated using the "best estimate" variograms, the critical path was 2.5 to 9% sand facies and 3 to 6% silt and clay facies by length, averaging 5.5 and 3% each respectively. Although there was no significant difference in the probability of connection, the effective hydraulic conductivity of the critical paths were lower when shorter variogram ranges were used. Disconnected cross-sections generated using the shorter ranges for gravel and sand facies exhibited critical paths with 2 to 10% sand facies and 1 to 9% silt and clay facies by length, averaging 6 and 5% of each facies respectively.

Continuous Critical Paths in Flat-lying Strata

Simulations generated assuming flat-lying strata exhibited a higher probability of a continuous shallow path of high hydraulic conductivity hydrofacies existing near the water table than simulations generated under the dipping strata assumptions. Of all the simulations generated assuming flat-lying strata, 23% of the cross-sections were connected by a continuous path of gravel and sandy gravel and all but one occurred in the shallow zone along the water

table. A total of 63% of the sections were continuous in the second or third highest conductivity facies along a shallow zone near the water table. These shallow paths are composed of 0 to 12.5% sand facies with an average of 4% of their length being a sand facies. Seven percent of the simulations depict deep paths that either start about seventy feet below the water table at the left end of the section or divert downward a few hundreds of feet from the right end of the cross-section to about seventy feet below the water table. These deeper paths are 0 to 12.5% sand (averaging 4%) and are alternatives to shallower paths which traverse from 0 to 7.5% sand and 1 to 5% silt and clay (averaging 2.5 and 2% each respectively).

Continuous Critical Paths in Dipping Strata

Overall continuity (at any depth) throughout the cross-sections via a combination of gravel, sandy gravel, and sand was greater for dipping strata than for flat-lying strata. Ninety-two percent of the simulations generated with "best estimate" variograms and 94% of the simulations using variograms with shorter ranges for gravel and sand facies exhibit critical paths comprised of the the two or three highest hydraulic conductivity facies. However, the likelihood of a shallow interconnected path of high hydraulic conductivity hydrofacies near the water table is smaller when dipping strata are assumed. For the "best estimate" variograms, 9% of the simulations of dipping strata exhibited continuous shallow paths near the water table (composed of an average length of 5% sand) and 83% (composed of an average length of 50% sand) were continuous via a deep path which exits the simulated section approximately 200 feet below the water on the east end. For the case of shorter variogram ranges for gravel and sand facies, 18% (composed of an average length of 5% sand) of the simulations exhibited continuous shallow paths near the water table and 76% (composed of an average length of 50% sand) were continuous via a deep path which exits the simulated section approximately 200 feet below the water table on the east end. In both cases these deeper paths were alternatives to shallower paths consisting of approximately 4% each of sand and clay and silt facies.

Summary of Critical Paths in Simulated Sections

In summary, a flat-lying stratigraphy results in a higher probability of disconnection across the section (30%) as compared with assuming dipping strata (8%) but yields a higher probability of connection along a shallow zone near the water table (i.e. 63% versus 9 to 18%). The effective hydraulic conductivity of the critical path in the disconnected cross-sections are of the same order of magnitude for all cases: averaging 7 m/d (23 ft/d) for the flat-lying strata, 6 m/d (19 ft/d) for the dipping strata using the "best estimate" variograms, and 3 m/d (11 ft/d) for dipping

strata generated using variograms with shorter ranges for gravel and sand facies. Similarly, the shallow connected paths yield the same order of magnitude of effective hydraulic conductivity in all cases, averaging 1100 m/d (3600 ft/d) for flat-lying strata and 950 m/d (3100 ft/d) in both cases for dipping strata regardless of whether the short- or long-range variogram models were employed in the simulation. When the three highest hydraulic conductivity facies were discontinuous in the shallow zone and a deeper path existed, the deeper paths for the flat-lying strata had an effective hydraulic conductivity of approximately 1100 m/d (3600 ft/d) while the shallow disconnected path exhibited an effective hydraulic conductivity of 9 m/d (30 ft/d). In simulations of dipping strata, the deeper paths averaged 120 m/d (400 ft/d) and were alternative routes to shallower paths with effective hydraulic conductivities on the order of 4 m/d (14 ft/d). Again, we emphasize that the effective hydraulic conductivities given here are representative only of two dimensional flow conditions. Total (three-dimensional) effective hydraulic conductivity of the study area will be higher because the low hydraulic conductivity units do not form a continuous barrier between the Hanford Site and the Columbia River. As a result, inhibition of flow in this two-dimensional cross-section will cause flow to be diverted laterally in the third dimension. Such flow patterns are confirmed by the lobate nature of tritium concentration contours in plan view (Poeter and Gaylord, 1990).

Perhaps these probabilities of connectedness along this two-dimensional cross-section reflect similar probabilities of connectedness of facies within other cross-sections which parallel flow in the study area. Most of the wells used to sample groundwater are terminated 1.5 to 4.5 m (5 to 15 ft) below the water table; therefore, data are not available to determine whether the zones of apparently slow contaminant migration illustrated by the lobed shape of the tritium concentration contours reflect differential groundwater velocities or are due to deflection of the plume deeper in the cross-section.

The most prudent way to assess the relative significance of the realizations generated for different assumptions is to conduct flow and transport simulations within the simulated geologic units. Evaluations that explore the sensitivity of streamlines to the imposed gradients will be of particular interest. Flow models could determine the minimum upward gradient required to prevent contaminants from using the alternative, deeper, higher hydraulic conductivity paths. Ultimately, field tests could be designed to measure such a minimum vertical gradient in the field. Flow and transport simulation in the cross-section are the subject of future work.

Locations of Discontinuities in the Critical Paths

Discontinuities in the critical paths occurred primarily at the middle of the cross-section (between wells 43-9 and 44-7) for both flat-lying and dipping strata. This was the largest lateral gap in the field data, so few hard data were available to condition the simulations in this portion of the cross-section, and the data that were available in the shallow portion of wells 43-9 and 44-7 exhibited a greater occurrence of clay and silt facies than most other areas of the simulated section. In simulations produced under the assumption of flat-lying strata, the second most likely area of discontinuity was between wells 46-5 and 46-3. Simulations of dipping strata indicated the second highest probability of disconnection occurs between wells 42-11 and 42-10. Portions of the cross-section which displayed the highest probability of disconnection corresponded with a lower combined probability of occurrence of gravel, sandy gravel, and sand. This high probability of discontinuity is revealed by the lower probability of occurrence of the gravel, sandy gravel, and sand facies in these portions of the cross-section as illustrated in the facies frequency map for dipping strata, using the "best estimate" variograms (Figure 10A). Maps of probability of occurrence for other combined and individual facies are presented as Figures 10B through 10E.

Because of the high probability of discontinuity in this portion of the cross-section, exploration between these wells will probably provide the greatest reduction of uncertainty for the least economic investment. Exploration between wells 41-11 and 42-10, and between 46-5 and 46-3 may also be of value due to the greater probability of discontinuity in these portions of the cross-section. Tests designed to differentiate between flat-lying and dipping geology would reduce the uncertainty substantially by eliminating one of the possible conceptual models. Additional holes could be drilled, but perhaps a more effective and economical approach would be collection of soft data between holes. For example, geophysical data (e.g. from a shallow reflection seismic survey) would reduce the uncertainty of hydrofacies connection in these zones. The potential differentiation and resolution of the facies by the selected technique should be carefully evaluated before undertaking the work. Of course, if the resulting uncertainty of contaminant transport within the range of distributions of hydrofacies interconnectedness predicted by the simulations is sufficiently low to satisfy the risk assessment process for this area, then further testing would not be required.

Comparison of Critical Paths from Simulations and Kriging

Comparing the nature of critical paths as determined by the stochastic simulation and the kriged distribution of the log of hydraulic conductivity (Figure 11)

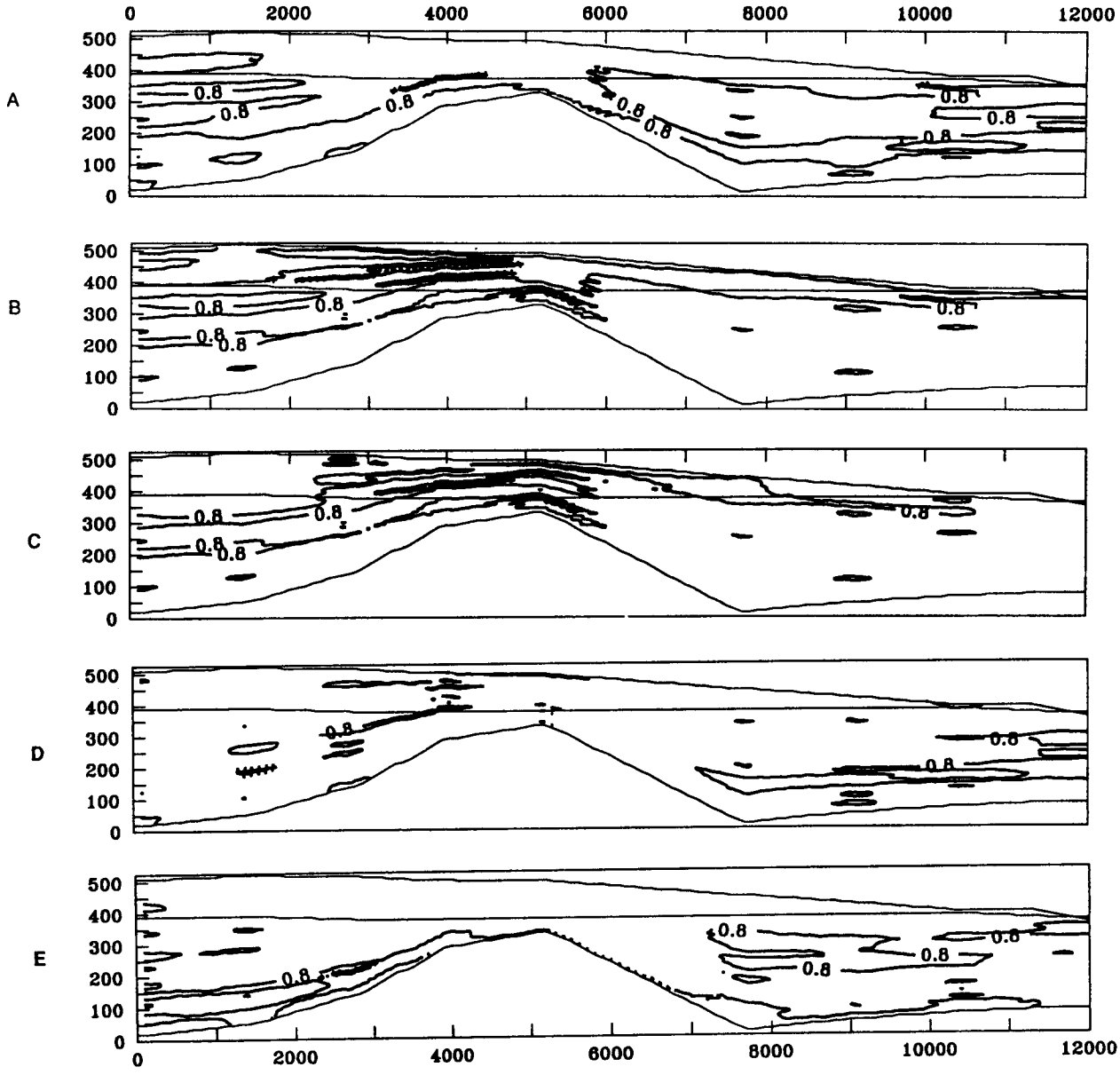

Figure 10. Probability of occurrence of facies for the deformed geologic conceptual model with the best estimate variograms: A. combined gravel, sandy gravel, and sand; B. gravel; C. sandy gravel; D. sand; E. clay-silt (2000 ft is approximately 610 m).

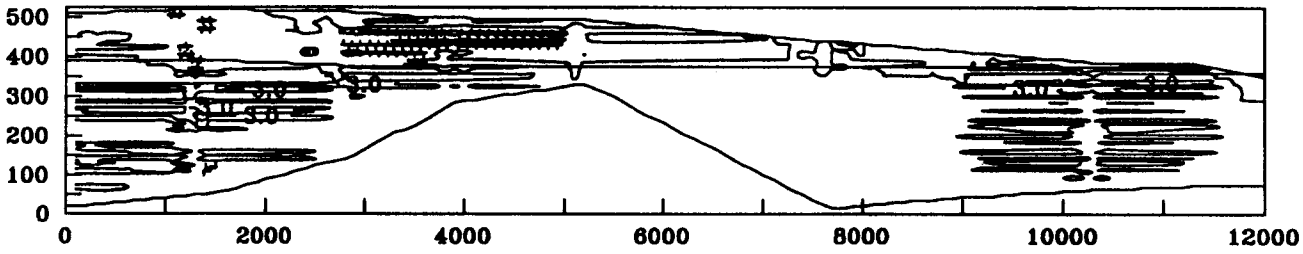

Figure 11. Kriged map of the distribution of log hydraulic conductivity using the hard conditioning data for the stochastic simulations; the only contour shown is 305 m/d (1000 ft/d), (2000 ft is approximately 610 m).

reveals that the kriged version of the data omits the zones of interconnected extremely low and high hydraulic conductivity facies. To krige the data, each indicator was replaced by its associated hydraulic conductivity value and the section was contoured by SURFER (Golden Software). SURFER uses a simple variogram model fit to the data set. The broad range of parameter values, complex nature of the spatial distribution, and the close vertical spacing and large lateral spacing of the data, yield an intricate kriged surface of doubtful utility. The gap near the middle of the section is characterized by hydraulic conductivity in the 30 to 90 m/d (100 to 300 ft/d) range. The highest effective hydraulic conductivity of critical paths crossing this zone was 4000 m/d (13,000 ft/d) and the lowest was 3 m/d (10 ft/d). Use of this kriged parameter distribution for flow and transport simulations ignores the high probability that contaminants may move rapidly in a high hydraulic conductivity connected zone near the water table. It also ignores the possibility of a low hydraulic conductivity barrier to this route and the possible driving of contaminants into a deeper section which may carry contaminants below the river. In essence, a smoothed interpretation leaves the modeler with a cross-section described by moderate effective hydraulic conductivity and a diffuse pathway for contaminants, while indicator simulations provide the opportunity to evaluate thin units of the extreme hydraulic conductivity values.

DISCUSSION

A limited amount of hard data are available to define the subsurface for the purpose of evaluating contaminant transport. Use of multiple indicator conditional stochastic simulation allows probabilistic, discrete simulation of hydrofacies. Although available data did not permit direct assessment of how well the simulations represent the geology, the simulations are consistent with general knowledge of the geology of the site from other borehole data, visual inspection of analogs which crop out on the east side of the Columbia River, and the character of contaminant concentration distributions.

Field tests that will differentiate between flat and dipping stratigraphy would be useful in reducing the uncertainty by eliminating one alternative conceptual model of the study area. These two conceptual geologic models are end members of flat and dipping stratigraphy. The actual condition probably lies between the two conditions.

If this study had been carried out in three dimensions before 1966 (i.e. before high levels of contaminants approached the river), then problematic zones may have been identified and remediation may have been more effective, efficient, and economical. Of course, the techniques applied here were not available at that time, but they can be used to improve our assessment of systems today.

Simulations such as the ones presented here can be used to focus field studies on critical questions regarding the fate of the contaminants that cannot be resolved using currently available data. For example, what is the probability that the shallow, high conductivity zone continuous? Where is the best place to collect additional data that will significantly reduce the uncertainty of connectivity? Does the bulk of the contaminant mass discharge to the springs, or do units of low hydraulic conductivity drive it deeper in the section? Probable risks (given the available data) can be assessed using flow and transport models that incorporate the distribution of possible aquifer configurations. Quantified uncertainty associated with the flow system aids decisions regarding financial investment in further characterization and/or remediation.

ACKNOWLEDGEMENTS

This research was supported by the Pacific Northwest Laboratory, which is operated by Battelle Memorial Institute for the Department of Energy under contract DE-AC06-76RLO 1830. We appreciate the efforts of William Wingle in his assistance with computer software and David Gaylord in his conscientious review.

BIOGRAPHICAL SKETCHES

Eileen Poeter is an Assistant Professor of Geological Engineering at the Colorado School of Mines, Golden, CO, 80401, USA. She received her B.S. degree in Geology from Lehigh University in 1975 and her M.S. and PhD degrees in Engineering (specializing in ground water and geophysics) from Washington State University in 1978 and 1980 respectively. She has worked as a consultant and in academia. Her research is focused on characterization of aquifer heterogeneity as it relates to contaminant transport and site remediation.

Peter Townsend is a Masters Degree candidate at the Colorado School of Mines. He received his B.S. degree in Geological Engineering in 1987 from Washington State University. Peter worked in geotechnical consulting before returning to school to study ground water.

REFERENCES

Bretz, J.H. 1959. Washington's Channeled Scablands. Washington State Department of Natural Resources, Division of Mines and Geology, Bull. 45.

DOE. 1988. Consultation Draft, Site Characterization Plan, Reference Repository Location, Hanford Site, Washington. DOE/RW-0164, U.S. Department of Energy, Office of Civilian Radioactive Waste Management, Washington, D.C.

Dreiss, S.J. and M.J. Johnson. 1988. Geostatistical interpolation of hydrostratigraphy at groundwater contamination sites, U.S. Geol. Surv. Final Tech Rept for Grant No. 14 08 0001-G1311.

Englund, E. and A. Sparks. 1988. GEOEAS (Geostatistical Environmental Assessment software) User's Guide. EPA/600/4-88/033a.

Fecht, K.R., S.P. Reidel and A.M. Tallman. 1985. Paleodrainage of the Columbia River system on the Columbia Plateau of Washington State: A Summary. Rockwell Hanford Operations Rept RHO-BW-SA-31 8P.

Fogg, G.E. Jr. 1986. Stochastic analysis of aquifer interconnectedness, with a test case in the Wilcox Group, East Texas. Doctor of Philosophy, University of Texas at Austin.

Gaylord, D.R. and E.P. Poeter. 1988. Annual report of geologic and geohydrologic site characterization studies during FY88, Hanford Reservation, Washington. Unpublished report submitted to Battelle Pacific Northwest Laboratories.

Gephart, R.A., R.C. Arnett, R.G. Baca, L.S. Leonhart and F.A. Spane Jr. 1979.Hydrologic studies within the Columbia Plateau, Washington: An integration of current knowledge. Rockwell Hanford Operations, RHO-BWI-ST-5.

Golden Software. SURFER Users Manual. Golden, CO.

Gómez-Hernandez, J.J. and R.M. Srivastava. 1990. ISIM3D: An ANSI-C Three dimensional multiple indicator conditional simulation, Computers in Geoscience, Vol.16, No.4, pp. 395-414.

Journel, A.G. 1983. Nonparametric estimation of spatial distributions. Math. Geol. v.15, pp 445-468.

Journel, A.G. and F.G. Alabert. 1988. Focusing on spatial connectivity of extreme-valued attributes: stochastic indicator models of reservoir heterogeneities. SPE Paper No. 18324 presented at the 63rd Annual Technical Conference and Exhibition of the Society of Petroleum Engineers, Houston, TX, October 2-5.

Journel A.G. and CH.J. Huijbregts. 1978. Mining Geostatistics. Academic Press.

Knudsen, H.P., Y.C. Kim, E.Y. Baafi and S.L. Barua. 1984. Software from the

Department of Mining and Geological Engineering, University of Arizona, Tucson, AZ.

Miall, A.D. 1985. Architectural-element analysis: A new method of lithofacies analysis applied to fluvial deposits. Earth Sci Rev, pp. 261-308.

Miall, A.D. 1987. Recent developments in fluvial lithofacies models. In Recent developments in Fluvial Sedimentology, (eds. F.G. Ethridge, R.M. Flores and M.D. Harvey). Soc Econ Geol Mineral Special Pub 39, pp. 1-9.

Myers C.W., S.M. Price, J.A. Caggiono, M.P. Cochran, W.H. Czimer, N.J. Davidson, R.C. Edwards, K.R. Fecht, G.E. Holmes, M.G. Jones, J.R. Kunk, R.D. Landon, R.K. Ledgerwood, J.T. Lillie, P.E. Long, T.H. Mitchell, E.H. Price, S.P. Reidel and Tallman. 1979. Geologic studies of the Columbia Plateau: A Status Report, RHO-BWI-ST-4, Rockwell Hanford Operations, Richland, Washington.

Poeter, E.P. and D.G. Gaylord. 1990. Influence of aquifer heterogeneity on contaminant transport at the Hanford Site. Ground Water, v.28, no.6, pp.900-909.

Tallman, A.M., K.R. Fecht, M.C. Marratt and G.V. Last. 1979. Geology of the Separations Areas, Hanford Site, South-Central Washington. RHO-ST-23, Rockwell Hanford Operations, Richland, WA.

Tallman, A.M., J.T. Lillie and K.R. Fecht. 1981. Suprabasalt Sediments of the Cold Creek Syncline Area, Subsurface Geology of the Cold Creek Syncline. (eds C.W. Meyers and S.M. Price). RHO-BWI-ST-14, Rockwell Hanford Operations, Richland, WA.

Investigation of the Spatial Correlation of Saturated Hydraulic Conductivities From a Vertical Wall of a Trench

by Elizabeth A. Jacobson

Abstract

Stochastic flow and transport theories, such as the theory of Mantoglou and Gelhar, require an estimate of the covariance functions for the hydraulic properties. Estimating a covariance function based on the data for the complete flow region will yield correlation lengths and a variance that are "averaged" values. However, different correlation lengths and variance may be contained in the region of interest, which may influence the comparison of actual field data to the predictions of stochastic flow and transport theories.

A two-dimensional data set of saturated hydraulic conductivity values was obtained from a trench at New Mexico State University, previously reported by Wierenga and his colleagues. The saturated hydraulic conductivity data were measured in-situ using a Guelph permeameter along a vertical wall of the trench, which measured 26.4 m in length and 6.0 m in depth. More than 580 saturated hydraulic conductivity, K_S, values were obtained from nine distinct soil horizons and three vertical transects. The logarithms of the in-situ saturated hydraulic conductivities, ln K_S, were analyzed using directional semivariograms to estimate the variance, the correlation lengths, and the principal directions. The first analysis assumed that the ln K_S data had a constant mean and variance, and horizontal and vertical correlation lengths were estimated based on the entire two-dimensional data set. The second analysis consisted of grouping the ln K_S data from several horizons, or all vertical transects, into separate data sets and estimating the corresponding variance and correlation lengths. Data for different horizons were grouped based on similar means and variances. The estimated horizontal and vertical correlation lengths of 2.5 and 0.5 m, respectively, for the first analysis differed from the values of 2.0 and 0.15 m, respectively, obtained for the second analysis. The variations in vertical correlation lengths will effect the degree of anisotropy $\hat{K}_{22}/\hat{K}_{11}$ as defined by Mantoglou and Gelhar under wetting conditions, where $\hat{K}_{22}$ and $\hat{K}_{11}$ are the effective hydraulic conductivities in the horizontal and vertical directions, respectively.

Introduction

Stochastic flow and transport theories, such as those by Mantoglou and Gelhar (1987a, b, c), have been developed that are based on a statistical representation of the spatial variability of hydraulic properties. The hydraulic properties are generally assumed to be composed of two components, a mean value and deviations from the mean. For example, the natural logarithm of the saturated hydraulic conductivity, K_S, at a point is represented by a mean value, F, and a small-scale fluctuation, f, about the mean (Mantoglou and Gelhar, 1987a, b, c), as follows:

$$\ln K_s = F + f \qquad (1)$$

The statistical characterization of the spatial variability of the hydraulic properties then consists of the mean value, F, and the covariance function based on the fluctuations, f. Information about the mean and covariance function can be obtained from an analysis of field data collected at a specific site.

Field studies are being conducted at the Las Cruces Trench Site in New Mexico (Wierenga et al., 1986, 1989) that will yield data to test flow and transport theories in unsaturated soils. Saturated hydraulic conductivities have been measured along a vertical wall of the trench and represent the two-dimensional data set that is analyzed in this paper. The spatial correlation of the two-dimensional data set is investigated using directional semivariograms to estimate the covariance function, assuming the mean is a constant. A detailed analysis of the spatial correlation of combined portions of the data set is then used to identify regions that contribute to the covariance estimated from the complete two-dimensional analysis. The vertical and horizontal correlation lengths estimated from the complete two-dimensional analysis are different from those

estimated from the detailed analysis of portions of the data set. The implications of the use of the different correlation lengths in the stochastic flow and transport theory of Mantoglou and Gelhar (1987c) are briefly discussed.

Field Saturated Hydraulic Conductivities

Saturated hydraulic conductivities were measured along a vertical wall at the Las Cruces Trench Site (Wierenga et al., 1986, 1989). The saturated hydraulic conductivity data were measured in-situ by the Guelph permeameter method (Reynolds and Elrick, 1985,1986).

Field saturated hydraulic conductivities were measured along nine horizontal layers in the trench and three vertical transects. The nine soil layers were defined based on visual inspection of the morphological horizons on the trench wall. The morphological horizons are shown in Figure 1with the circles representing depth of sampling layers. The alternating patterns in the figure are used to clearly differentiate the nine horizons. A detailed description of the nine layers can be found in Wierenga et al. (1989). For eight of the nine horizons, field saturated hydraulic conductivities were measured along the length of the trench (horizontal) at 0.5-m intervals. In general, a total of 50 measurements were taken from each of the eight soil horizons. To investigate in more detail the horizontal spatial variability of the saturated hydraulic conductivity, measurements were taken at 0.25-m intervals in one soil horizon. Saturated hydraulic conductivities were measured at 48 locations along three vertical transects with a spacing of 0.13 m. A schematic showing the relative locations of the nine horizons and the three vertical transects with the approximate density of the data is presented in Figure 2.

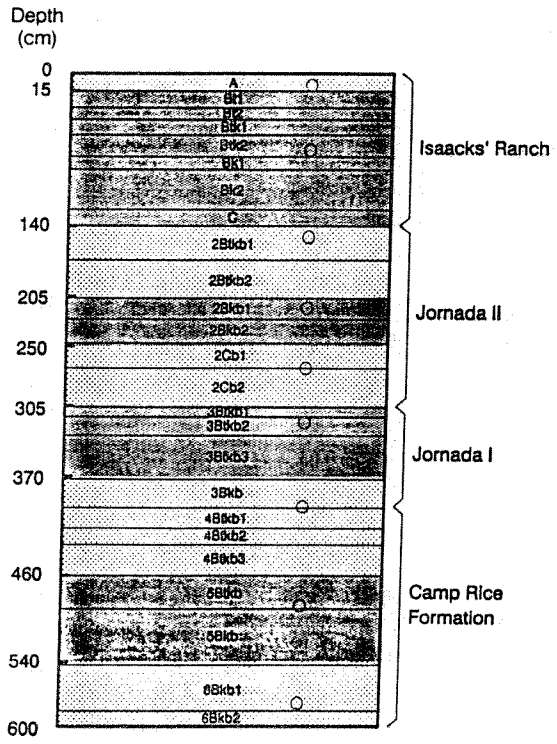

Figure 1. Morphological horizons for vertical wall at Las Cruces trench site (from Wierenga et al., 1989).

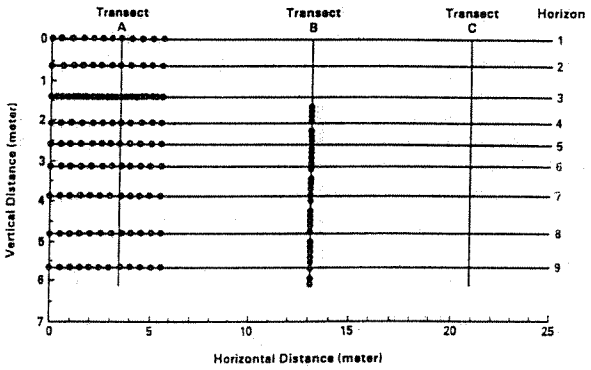

Figure 2. Schematic of trench wall with relative locations of saturated hydraulic conductivity measurements for the nine horizons and three vertical transects.

Transects A and C have the same density of data as shown for transect B. A total of 584 saturated hydraulic conductivities were available for the spatial analysis. This number is less than the total measurement sites because at some locations measurements of saturated hydraulic conductivities were not available.

The statistical characterization of the natural logarithm of the saturated hydraulic conductivity ($\ln K_s$) is needed for the stochastic model developed by Mantoglou and Gelhar (1987a, b, c). Thus, the spatial variability of the $\ln K_s$ will be considered by investigating the $\ln K_s$ two-dimensional data set obtained from the trench measurements. The $\ln K_s$ data versus distance for each of the nine distinct soil horizons are

given in Figure 3, where horizons one to nine correspond to parts (A) to (I), respectively. The ln K_s values for horizons one and two (Figures 3A and B) show random variations about constant mean values. For horizons three and four (Figures 3C and D), the ln K_s data exhibit definite high and low values. The ln K_s data for both horizons five and six (Figures 3E and F) appear to show overall trends, whereas the data for horizons seven, eight and nine (Figures 3G, H and I) appear to be random about lower constant means than for the first two horizons.

The ln K_s data versus distance for the three vertical transects are given in Figure 3, parts (J) to (L). The third vertical transect (Figure 3L) appears to have an overall trend toward lower ln K_s values with depth. The ln K_s values for the first and second transects (Figures 3J and 3K) do not exhibit any apparent trend nor are they clearly random about a constant mean.

Statistical Characterization of ln K_s

Directional semivariograms (Journel and Huijbregts, 1978; David, 1977) can be used to investigate the statistical characteristics of two-dimensional data. Directional sample semivariograms were calculated for the two-dimensional ln K_s data set described in the preceding section. In general, an analysis of these semivariograms indicates if the data are statistically homogeneous, and identifies the principal directions of anisotropy and corresponding correlation lengths.

The ln K_s data from the nine soil horizons, together with the data from the three vertical transects, constitute the two-dimensional data set. Directional sample semivariograms were calculated for four directions with a window of 20° (i.e. a tolerance angle of ±10°) and a distance lag of 50 cm (i.e. a tolerance of ±25 cm). For this analysis, 0° and 90° correspond to the horizontal and vertical directions, respectively. The four directional sample semivariograms are presented in Figures 4A to D. The sample mean of the two-dimensional data set is 5.93 and the sample variance is 1.54.

To estimate a two-dimensional covariance function from the sample semivariograms, the sill must be the same in all directions, and a nugget effect should not depend on direction, however, the correlation lengths may be directionally dependent. The correlation lengths (or range) are observed to be different for the sample semivariograms for the 0° and 90° directions (Figures 4A and C) with the largest correlation length in the horizontal. The correlation lengths for the 45° and 135° directions are not evident from the sample semivariograms (Figures 4B and D). With the longest and shortest correlation lengths observed in the horizontal and vertical directions, respectively, the principal directions of anisotropy have been identified from the sample semivariograms.

The sample semivariogram for the horizontal (0°) direction is the only directional semivariogram that exhibits a distinct sill. A nugget effect is indicated for the sample semivariograms for the 0° and 90° directions, and appears to be of similar magnitude. Based on these observations, a theoretical anisotropic semivariogram with a nugget effect was fitted to the sample semivariograms. Both spherical and exponential theoretical semivariograms were considered; however, the shape of the spherical semivariogram did not fit the sample semivariograms at short separation distances. The exponential theoretical semivariogram reproduced the overall shape of the sample semivariograms for both principal directions. The sample semivariogram for 0° and the theoretical semivariogram (heavy solid line) are presented in Figure 4A. The theoretical semivariogram had a nugget of 0.4, a sill of 1.54, and correlation length of 2.5 m. The correlation length is defined as that distance corresponding to the $1-e^{-1}$ value of the sill not including the nugget. The 1.54 value of the sill was selected by assuming the sample variance was equal to the sill. The nugget value and correlation length were determined by trial and error fitting of the shape of the sample semivariogram at shorter lags.

A two-dimensional anisotropic theoretical semivariogram can only be defined if both the nugget and sill are the same for all directional sample semivariograms; however, the correlation length will depend on direction. Thus, the nugget and sill of the theoretical semivariogram for the 90° direction must be equal to 0.4 and 1.54, respectively. The sample semivariogram for 90° is shown in Figure 4C with the fitted theoretical semivariogram (heavy solid line) that has a correlation length of 0.50 m. Using the estimates of the horizontal and vertical correlation lengths with the sill and nugget values, the theoretical semivariogram for the 45° and 135° directions is

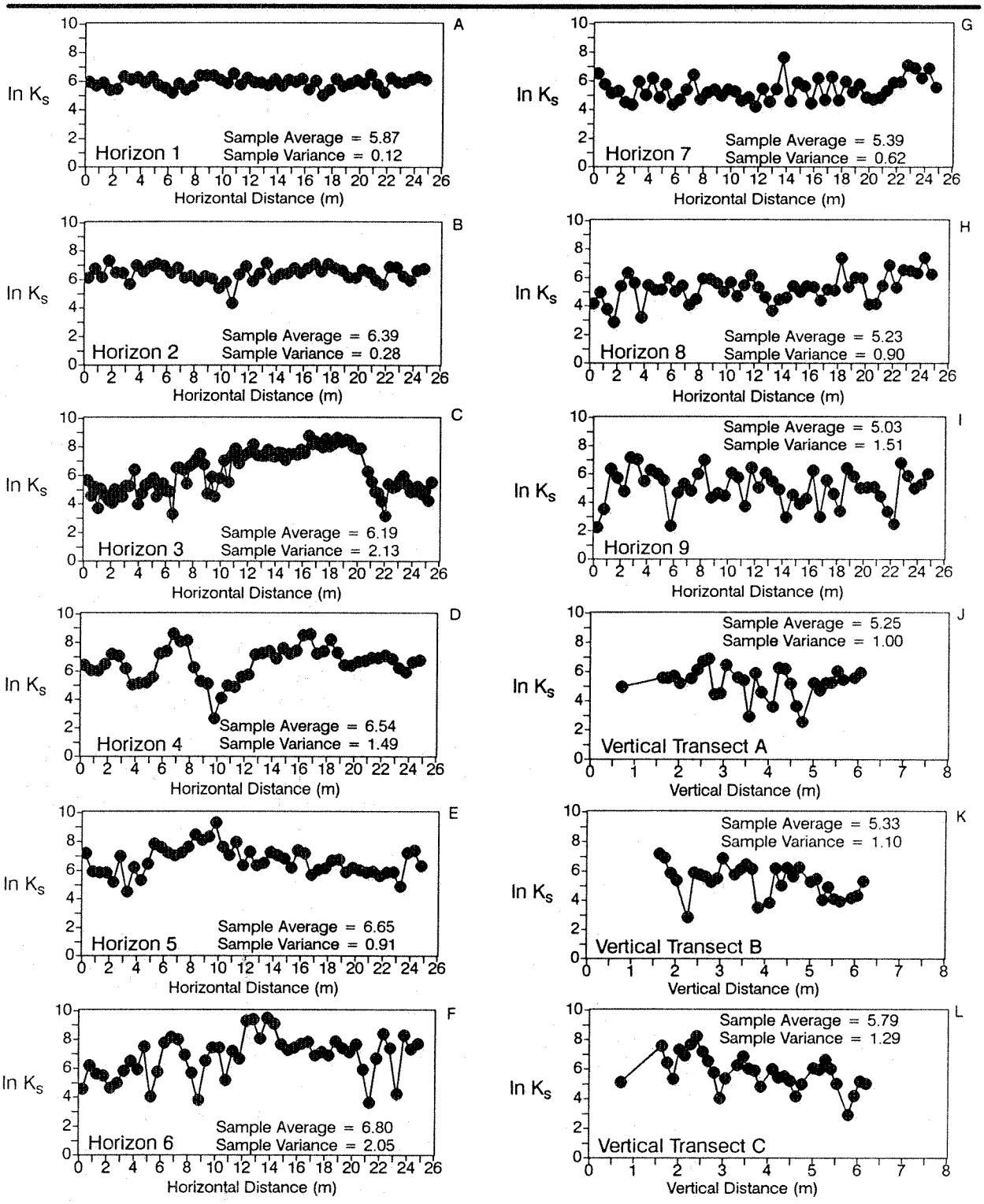

Figure 3. Natural logarithm of saturated hydraulic conductivity vs horizontal distance for nine soil horizons (parts A through I) and natural logarithm of saturated hydraulic conductivity vs depth for three vertical transects (parts J through L). Units of hydraulic conductivity are cm/day.

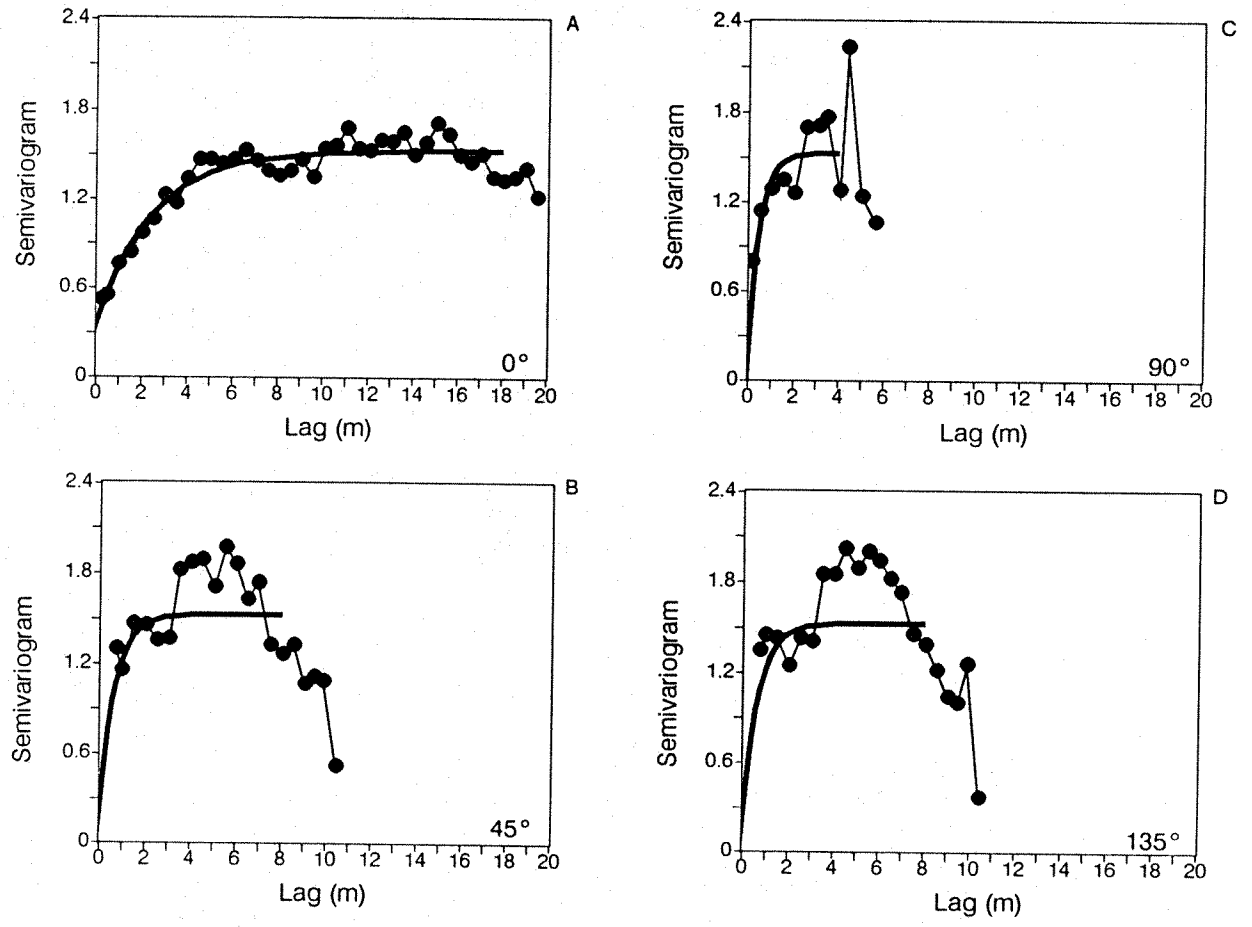

Figure 4. Comparison of theoretical semivariograms to sample semivariograms based on the complete two-dimensional ln K_s data set for directions of 0°, 45°, 90° and 135° (parts A through D, respectively). Heavy solid lines correspond to the theoretical semivariograms.

calculated and plotted in Figures 4B and D, respectively (heavy solid line). In general, the theoretical semivariograms are not representative of the sample semivariograms for these two directions. The theoretical semivariogram for the 0° direction is representative of the sample semivariogram for the direction. However, in the 90° direction, the fit of the theoretical semivariogram to the sample semivariogram is open to interpretation.

In the discussion of the spatial behavior of the ln K_s for specific horizons, it was noted that the ln K_s data in several horizons appeared to be random about a mean value (e.g. horizons 1 and 2, see Figures 3A and B). Thus, the observed correlation based on the two-dimensional analysis may be produced by only a portion of the data. To investigate the spatial correlation of the ln K_s data in more detail, data for different horizons were grouped based on similar means, variances, and spatial proximity. The ln K_s horizon data were grouped into three divisions by combining the data for horizons 1 and 2, horizons 3, 4, 5 and 6, and horizons 7, 8 and 9. The three vertical transects were treated as a separate data set. The horizontal sample semivariograms for the three groups of the horizon data are shown in Figures 5A, B and C. The horizontal sample semivariogram for the combined data for horizons 1 and 2 shows no correlation (Figure 5A). A theoretical semivariogram consisting of a nugget value equal to 0.27 is representative of the sample semivariogram for these data. The

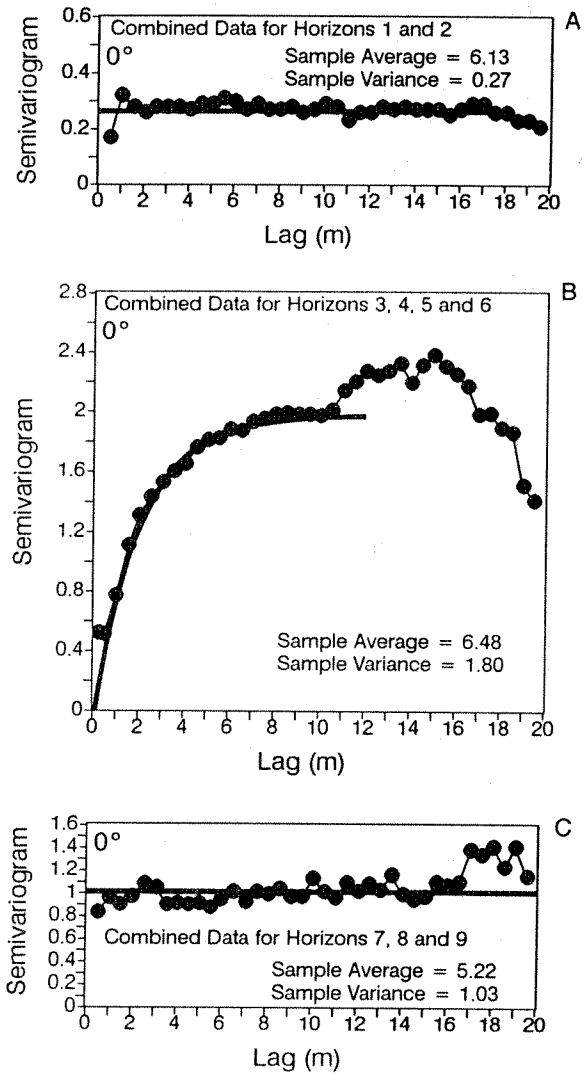

Figure 5. Comparison of theoretical semivariograms to sample semivariograms in the 0° direction for the combined data for horizons 1 and 2, the combined data for horizons 3, 4, 5 and 6 and the combined data for horizons 7, 8 and 9 in parts A, B and C, respectively. Heavy solid lines correspond to the theoretical semivariograms.

horizontal sample semivariogram for the combined data for horizons 3, 4, 5 and 6 indicates a correlation. A theoretical semivariogram with no nugget, correlation length of 2.0 m, and sill equal to 1.98, is representative of the sample semivariogram at shorter lags. The horizontal sample semivariogram for the combined data for horizons 7, 8 and 9, appears to suggest a pure nugget effect of 1.03; however, there may be a slight indication of a trend because the sample semivariogram increases with lag.

The vertical sample semivariogram for the combined data for the three vertical transects is presented in Figure 6A. A theoretical semivariogram with

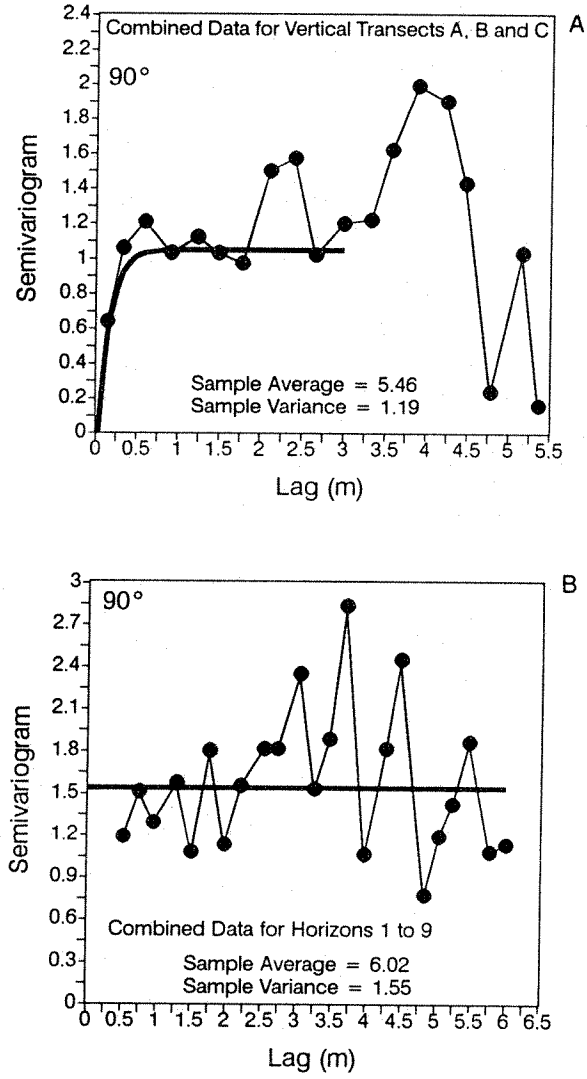

Figure 6. Comparison of theoretical semivariograms to sample semivariograms in the 90° direction for the combined data for vertical transects A, B and C and the combined data for horizons 1 to 9 in parts A and B, respectively. Heavy solid lines correspond to the theoretical semivariograms.

no nugget, a correlation length of 0.15 m, and sill value of 1.06, is representative of the sample semivariogram at shorter lags. The vertical sample semi-

variogram for the combined data from all horizons, excluding the data from the three vertical transects, is given in Figure 6B. This vertical sample semivariogram appears to be uncorrelated and a nugget value of 1.55 is plotted as the heavy solid line in Figure 6B.

Discussion

A comparison of the horizontal theoretical semivariogram obtained from the two-dimensional data analysis (Figure 4A) to the horizontal theoretical semivariograms estimated from the detailed analysis (Figures 5A, B and C) indicates that the correlation observed in the complete two-dimensional data set is primarily from the data from horizons 3, 4, 5 and 6. The data from the other five horizons are generally uncorrelated and contribute to the observed nugget effects in the two-dimensional analysis. It is interesting to note that the correlation length for the two-dimensional analysis is 2.5 m, whereas the correlation length for the combined horizons 3, 4, 5 and 6 is 2.0 m. The longer correlation length for the two-dimensional analysis may reflect the possible trend in the data from horizons 7, 8 and 9 (Figure 5C) as indicated by the slight increase in sample semivariogram with lag.

The vertical theoretical semivariogram obtained from the two-dimensional analysis contained a nugget value and correlation length of 0.5 m (Figure 4C). The vertical theoretical semivariograms estimated from the detailed analysis of the data from the vertical transects had no nugget value and a correlation length of 0.15 m (Figure 6A). The nugget effect observed in the two-dimensional analysis was produced, in part, by the data from the nine horizons as indicated by the nugget effect for the combined data for horizons 1 to 9 (Figure 6B). The correlation length was shorter for the analysis of only the vertical transects because the spacing of the data was 0.13 m and the actual spatial correlation in the horizons was being sampled. In the two-dimensional analysis, the theoretical semivariogram was influenced by the large number of data in each horizon and the vertical spatial separation of the horizons varied from 0.5 m to 0.9 m. The vertical correlation lengths appeared to reflect the vertical spacing of the data used in the analysis.

The results of the two-dimensional analysis and the detailed horizon and transect analysis are summarized in Table 1. The type of observed theoretical semivariogram and the relevant parameters are listed for easy reference.

Implications for Testing Stochastic Theories

The stochastic theory of Mantoglou and Gelhar (1987c) is formulated based on the assumption that the hydraulic properties are each composed of a mean value and small-scale fluctuation. The hydraulic properties are the natural logarithm of the saturated hydraulic conductivity, $\ln K_s$, the pore size distribution, α, and the specific soil moisture capacity, C. As in eqn (1), the hydraulic properties are expressed as:

$$\begin{aligned} \ln K_s &= F + f \\ \alpha &= A + a \\ C &= \Gamma + \gamma \end{aligned} \qquad (2)$$

where F, A and Γ are the mean values of the respec-

Table 1
Summary of Semivariogram Analyses

Analysis	Type of theoretical semivariogram	Semivariogram Parameters			
		Nugget	Sill	Horizontal Correlation length (m)	Vertical Correlation length (m)
Two-Dimensional	Exponential	0.4	1.54	2.5	0.5
Combined horizons 1 and 2	Pure nugget	0.27	–	–	–
Combined horizons 3, 4, 5 and 6	Exponential	0.0	1.98	2.0	–
Combined horizons 7, 8 and 9	Pure nugget	1.03	–	–	–
Combined vertical transects	Exponential	0.0	1.06	–	0.15
Combined horizons 1 to 9	Pure nugget	1.55	–	–	–

tive hydraulic properties and the f, a and γ are the corresponding small-scale fluctuations about the means. The variances of the respective fluctuations are given by σ_f^2, σ_a^2 and σ_γ^2.

Mantoglou and Gelhar (1987c) developed effective anisotropic hydraulic conductivities for transient unsaturated flow and stratified soils. The effective anisotropic hydraulic conductivities were dependent on the statistical parameters of the hydraulic properties as well as the mean flow conditions, such as wetting or drying. The parameter G was used to indicate wetting, drying or steady-state conditions and is defined by:

$$G = e^{-F} e^{-AH} \frac{\partial H}{\partial t} \tag{3}$$

where F and A are defined as previously and H is the mean of the capillary tension head.

Mantoglou and Gelhar (1987c) found that the effective anisotropic hydraulic conductivities calculated based on representative statistical parameters of the various hydraulic properties caused more horizontal spreading of a moisture plume than expected, based on classical theory of distinct layers of stratified sediments. A schematic diagram showing this effect is given in Figure 7. A detailed discussion of this increase in the horizontal spreading is found in Mantoglou and Gelhar (1987c). The degree of anisotropy of the effective hydraulic conductivities was dependent on the mean flow conditions as indicated by the extremes of a parameter G. The degree of anisotropy in effective hydraulic conductivity is defined by $\hat{K}_{22}/\hat{K}_{11}$ where $\hat{K}_{22}$ and $\hat{K}_{11}$ are the effective hydraulic conductivities in the horizontal (i.e. parallel to stratified soils) and vertical (i.e. perpendicular to stratified soils) directions, respectively.

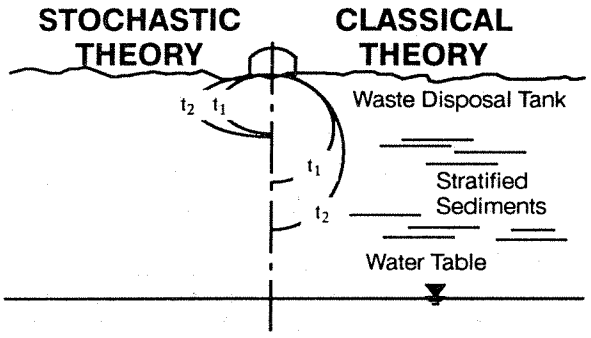

Figure 7. Schematic showing the movement in the unsaturated zone of a moisture plume from a leaking waste storage tank as predicted by the stochastic theory of Mantoglou and Gelhar (1987a, b, c) and a classical deterministic theory. The time t_2 is larger than t_1 and the curves correspond to equal moisture levels (modified from Mantoglou and Gelhar, 1987c, Figure 6).

The asymptotic results found in Mantoglou and Gelhar (1987c) indicate the functional dependence of the degree of anisotropy $\hat{K}_{22}/\hat{K}_{11}$ on the statistical parameters of the hydraulic properties and the mean flow field. For drying, wetting and steady-state conditions, the degree of anisotropy varies as follows:

for $G \to +\infty$ (drying)

$$\frac{\hat{K}_{22}}{\hat{K}_{11}} = 1 \tag{4}$$

for $G \to -\infty$ (wetting)

$$\frac{\hat{K}_{22}}{\hat{K}_{11}} = \exp\left[\frac{\sigma_f^2 + \sigma_a^2 H^2}{A L_1 \lambda_1}\right] \tag{5}$$

and for $G \to 0$ (steady state)

$$\frac{\hat{K}_{22}}{\hat{K}_{11}} = \exp\left[\frac{\sigma_f^2 + \sigma_a^2 H^2}{1 + A L_1 \lambda_1}\right] \tag{6}$$

where λ_1 is the correlation length perpendicular to the stratification (i.e. vertical correlation length for the trench experiment) and $L_1 = \frac{\partial (H + z)}{\partial x_1} + \frac{\partial H}{\partial x_1}$. The statistical parameters of the ln K_s data obtained from this analysis of the trench data are estimates of the variance, σ_f^2, and the vertical correlation length, λ_1. To calculate the actual degree of anisotropy using eqns (5) and (6), the variance of the mean pore size, σ_a^2, and the mean flow field characteristics (i.e. H and L_1) must be known; however, this study considers only the spatial correlation of ln K_s. Thus, only relative comparison of the functional dependence of the degree of anisotropy on the variance of ln K_s, σ_f^2, and vertical correlation length, λ_1, can be made.

Under drying conditions (see eqn (4)), the degree of anisotropy is not dependent on σ_f^2 and λ_1. Thus,

the difference in σ_f^2 and λ_1 values obtained from the two-dimensional analysis and from the detailed analysis will have no effect on the degree of anisotropy under drying conditions.

The use of the variance σ_f^2 obtained from the two-dimensional analysis ($\sigma_f^2 = 1.54$) as opposed to the variance obtained from the detailed analysis of the vertical transects ($\sigma_f^2 = 1.06$) should have little effect on the estimated degree of anisotropy for all flow conditions using eqns (5) and (6) because σ_f^2 is in the numerator and is added to other terms. The vertical correlation length, λ_1, varies from 0.5 m for the two-dimensional analysis to 0.15 m for the detailed analysis. In eqn (5), for wetting conditions, the degree of anisotropy will be much different depending on which correlation length is used because λ_1 is less than one for both analyses and it is in the denominator. As the correlation length decreases, the degree of anisotropy increases for wetting conditions. For steady-state conditions represented by eqn (6), the effect of changes in λ_1 is not as large unless $AL_1\lambda_1 >> 1$. For drying (see eqn (4)), there is no effect if an incorrect λ_1 is used.

One procedure for testing the stochastic approach to flow and transport in unsaturated soils as developed by Mantoglou and Gelhar (1987a, b, c) is to estimate the degree of anisotropy under specific flow conditions and compare the expected moisture profile to the field measurements. With the uncertainty in the estimation of the vertical correlation length and the strong dependence of the degree of anisotropy on λ_1 under wetting conditions, it may be difficult to test the stochastic theory conclusively with field measurements at the Las Cruces Trench Site. An inverse approach based on using moisture plumes from the field studies to estimate the statistical properties of the ln K_s might indicate the scale of spatial variability that needs to be considered in stochastic approaches to flow and transport.

Summary

A semivariogram analysis of the two-dimensional ln K_s data set obtained from the Las Cruces Trench Site (Wierenga et al., 1989) yielded estimates of horizontal and vertical correlation lengths of 2.5 and 0.5 m, respectively. A detailed semivariogram analysis of combined data from specific horizons indicated that horizons 3, 4, 5 and 6 were correlated in the horizontal direction with a correlation length of 2.0 m. The other horizons were uncorrelated, but influenced the results of the two-dimensional analysis through a nugget effect. A detailed semivariogram analysis of the combined data from the vertical transects produced a vertical correlation length of 0.15 m and no nugget effect. The sample semivariogram for the 90° direction produced by the combined data from all horizons indicated no correlation, thus these data contribute to the nugget effect found in the two-dimensional analysis.

The stochastic theory for flow and transport in the unsaturated zone developed by Mantoglou and Gelhar (1987a, b, c) uses the vertical correlation length in the definition of the effective anisotropic hydraulic conductivities for given flow conditions. The uncertainty in the estimation of the vertical correlation length (i.e. 0.5 m from the two-dimensional analysis as compared to the 0.15 m from the vertical transects analysis) will cause the degree of anisotropy in the effective hydraulic conductivities to vary because as the vertical correlation length decreases, the degree of anisotropy increases (Mantoglou and Gelhar, 1987c). Thus, a conclusive test of the stochastic theory by comparing predictions to field data may be difficult until the actual vertical correlation length which influences flow and transport in stratified soils can be identified.

Acknowledgments

Thanks are expressed to Tom Nicholson of the U.S. Nuclear Regulatory Commission (NRC), Glendon Gee of the Pacific Northwest Laboratory (PNL) and Peter Wierenga currently at the University of Arizona for their help in this work. In addition, Marjory Jones is thanked for editing this paper and Deborah Wilson for her publishing skills. This research was supported, in part, by the Desert Research Institute and by NRC under a U.S. Department of Energy contract DEAC06-76RLO 1830 while the author was at PNL.

Dr. Elizabeth Jacobson received her B.A. in Mathematics and Physics from California State University, San Bernardino, an M.S. degree in Atmospheric Physics from the University of Arizona and a Ph.D. in

Hydrology at the University of Arizona. In 1983, she joined the Hydrology Section of the Geosciences Department at Battelle Pacific Northwest Laboratories. In 1988, Dr. Jacobson joined the Water Resources Center of the Desert Research Institute, University of Nevada System, (7010 Dandini Blvd., Reno, Nevada 89512), as an Assistant Research Professor. She also teaches graduate level courses at the University of Nevada, Reno in the Geology Department. She specializes in the development and improvement of parameter estimation (inverse) methodology as it applies to ground water flow problems, and maintains an active research interest in geostatistics and kriging, conditional simulation, and sensitivity and uncertainty techniques as they apply to ground water flow systems.

References

David, M. 1977. Geostatistical Ore Reserve Estimation. Elsevier Scientific Publishing Company.

Journel, A.G. and Ch.J. Huijbregts. 1978. Mining Geostatistics. Academic Press.

Mantoglou, A. and L.W. Gelhar. 1987a. Stochastic modeling of large-scale transient unsaturated flow systems. Water Resour. Res., v. 23, pp. 37-46.

Mantoglou, A. and L.W. Gelhar. 1987b. Capillary tension head variance, mean soil moisture content, and effective specific soil moisture capacity of transient unsaturated flow in stratified soils. Water Resour. Res., v. 23, pp. 47-56.

Mantoglou, A. and L.W. Gelhar. 1987c. Effective hydraulic conductivities of transient unsaturated flow in stratified soils. Water Resour. Res., v. 23, pp. 57-67.

Reynolds, W.D. and D.E. Elrick. 1985. In situ measurement of field-saturated hydraulic conductivity, sorptivity, and the α-parameter using the Guelph permeameter. Soil Sci., v. 140, pp. 292-302.

Reynolds, W.D. and D.E. Elrick. 1986. A method for simultaneous in situ measurement in the vadose zone of field-saturated hydraulic conductivity, sorptivity, and the conductivity-pressure head relationship. Ground Water Monit. Rev., v. 6, pp. 84-95.

Wierenga, P.J., L.W. Gelhar, C.S. Simmons, G.W. Gee and T.J. Nicholson. 1986. Validation of stochastic flow and transport models for unsaturated soils: A comprehensive field study. NUREG/CR-4622, PNL-5875, prepared for the U.S. Nuclear Regulatory Commission, Washington, D.C.

Wierenga, P.J., A.F. Toorman, D.B. Hudson, J. Vinson, M. Nash and R.G. Hills. 1989. Soil physical properties at the Las Cruces Trench Site. NUREG/CR-5441, prepared for the U.S. Nuclear Regulatory Commission.

Stochastic modelling of contaminant movement in ground water

by Kevin K. Wolka and T. Al Austin

Abstract

A stochastic procedure is described for use in a ground water contamination exposure assessment. This procedure delivers more information about contaminant movement than single solution numerical or analytical solute transport models. Multiple solutions for contaminant movement are used to develop a probability distribution of results. The stochastic nature of this exposure assessment procedure is derived primarily from the spatial variability of hydraulic conductivity in geological formations and its effect on the uncertainty of contaminant movement in ground water. The Turning Bands Methods is used along with a deterministic random walk solute transport model developed by the Illinois State Water Survey to form a "joint probability distribution of contaminant concentration and duration of exposure".

The field data used in the modelling effort represent injections of low level radioactive wastes (tritium) from the Idaho Chemical Processing Plant (Idaho National Engineering Laboratory) into the Snake River Plain aquifer. Over 30 years of data, including injection flow rates and concentrations, and monitored well water levels and concentrations, were provided by the Idaho District of the US Geological Survey, together with a transmissivity map of the Snake River Plain aquifer at the INEL.

The spatial variability of hydraulic conductivity is a major cause of uncertainty for contaminant movement in ground water. The Turning Bands Method aids in quantifying the uncertainty by generating a specified number of hydraulic conductivity fields, each to be used as input to the solute transport model for a contaminant movement realization. Every one of the hydraulic conductivity fields is unique, but they all have the same statistical properties, i.e.. mean, standard deviation and correlation function. Each hydraulic conductivity field results in a corresponding unique contaminant movement pattern. The aggregation of these contaminant movement patterns results in the aforementioned "joint probability distribution".

The existing transmissivity study area has a mean hydraulic conductivity log value of 2.4427 and a standard deviation of 0.1226 in metric units. The correlation function is $r=e^{-0.904d2}$, where r is the correlation coefficient and d is the distance in km between two points in the aquifer. The computer model generated hydraulic conductivity fields with means within 1% to 2% of the input mean, and standard deviations approximately 15% from that entered. The joint probability distribution of contaminant concentration and duration of exposure stabilized after 100 realizations with the solute transport model for two separate tritium disposal events. A statistical description of the joint probability distributions was obtained using the logit transformation.

Kevin K. Wolka (Geraghty and Miller, Inc., 50 West Big Beaver Road, Troy, Michigan, 48084, USA) received a BS in civil engineering in 1972 and an MSCE in Water Resources Systems in 1974 from Purdue University. After working for engineering consulting firms in Chicago and Minneapolis-St. Paul, he joined the Iowa State University Civil Engineering Department in 1980. In 1986, he received his PhD in water resources from Iowa State University. His current

research interests include stochastic analyses of ground water contamination processes.

Dr. T. Al Austin (Iowa State University, Ames, Iowa, 50011, USA) is Professor of Civil and Construction Engineering and Director of the Water Resources Research Institute at Iowa State University. He received his BSc and PhD degrees from Texas Tech University and his MSc from Utah State University. Dr. Austin joined the faculty at Iowa State University in 1972 and has had extensive research work in water resources, hydrology and ground water hydrology since coming to ISU. In recent years, Dr. Austin has worked in modelling ground water transport processes. He has supervised seven PhD and more than 30 MSc student research theses.

Determination of Scales of Porosity Variability Through the Use of Image Analysis

by Lisa D. Shepherd, Jean M. Bahr, and Gerilynn R. Moline

Abstract

Recent theoretical and field results indicate the importance of heterogeneity in controlling fluid flow and mass transport in porous media. Variability in porosity and permeability can exist over a wide range of scales. The scales of variability in porosity are being investigated for the St. Peter Sandstone in the Michigan Basin. On a macroscopic scale the St. Peter Sandstone is a relatively homogeneous quartz sandstone. However, porosity varies from <1% to >20% between core samples obtained from a single well. Abrupt changes in the degree of cementation and porosity can be observed within single thin sections. If these small-scale variations in porosity generate areally extensive zones of low effective permeability, they could provide an explanation for the existence of pressure compartments within the St. Peter Sandstone. An image analysis system was used to quantify porosity variations from thin sections impregnated with blue-dyed epoxy. Images of the thin sections were projected onto a computer screen. The user set an upper and lower sensitivity limit to pigment color in order to discriminate between porosity and rock matrix. Geostatistical techniques are used to evaluate vertical and lateral spatial variability and to determine correlation scales. Comparison of these results to core descriptions and wireline log signatures can help to identify patterns of variability on a larger scale. Results of this work are being used to develop a regional hydrodynamic model for the Michigan Basin.

Introduction

Heterogeneity of hydraulic conductivity is important in controlling fluid flow and mass transport in porous media. In the St. Peter Sandstone in the Michigan Basin there is significant variability in porosity and cements throughout the basin. Because the St. Peter Sandstone is a relatively homogeneous quartz sandstone, most of the variability of hydraulic conductivity is controlled by secondary diagenetic processes. Identifying the scale of this variability is important in the development of fluid flow models to simulate migration and entrapment of hydrocarbons in the subsurface.

Recent work in the petroleum industry, summarized by Hunt (1990), indicates that most sedimentary basins contain two main hydrogeological systems, shallow and deep. The shallow system is basin-wide in extent and exhibits normal hydrostatic pressures. The deep system, where oil is generated, usually begins at approximately 3 km and is divided into several individual fluid "compartments" that exhibit anomalous pressures. The fluid compartments are bounded on all sides by low permeability zones called seals. As a result they may be in limited hydraulic communication with each other and with the overlying normally pressured system. The upper seal appears to be fairly horizontal and may cut across stratigraphic boundaries. The lateral seals, where they have been identified, are approximately vertical and are often associated with faults. These pressure compartments act as traps for oil and gas. Understanding the distribu-

tion and nature of these compartments can therefore have important implications for hydrocarbon exploration and reservoir development.

The purpose of this research was to investigate the scale and causes of pressure compartments in the Lower Paleozoic strata of the Michigan Basin, concentrating mainly on the St. Peter Sandstone, which is an active gas play. Because production is also obtained from the overlying Glenwood Formation in some areas, this unit was also examined. Due to the large size of the Michigan Basin initial research efforts were focused on areas with potentially anomalous pressures. Anomalously pressured zones can be identified using areal distributions of hydraulic head. Formation pressure data for head computations can be obtained from drill-stem tests (DST), repeat-formation tests (RFT), and bottom-hole pressure measurements during production tests. Although an RFT provides the most reliable data, this type of test has not been used extensively in Michigan. Therefore, the preliminary analysis of pressure distribution relied mainly on DST data, which was used to generate a preliminary map of hydraulic heads in the St. Peter Sandstone (Bahr, 1989). This preliminary analysis identified a fairly large area of high heads in the north-central part of the basin and west of Saginaw Bay (Figure 1A). The western

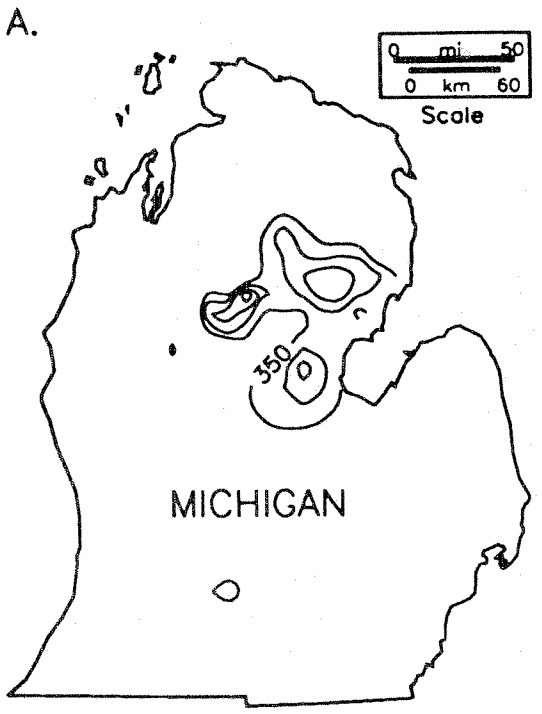

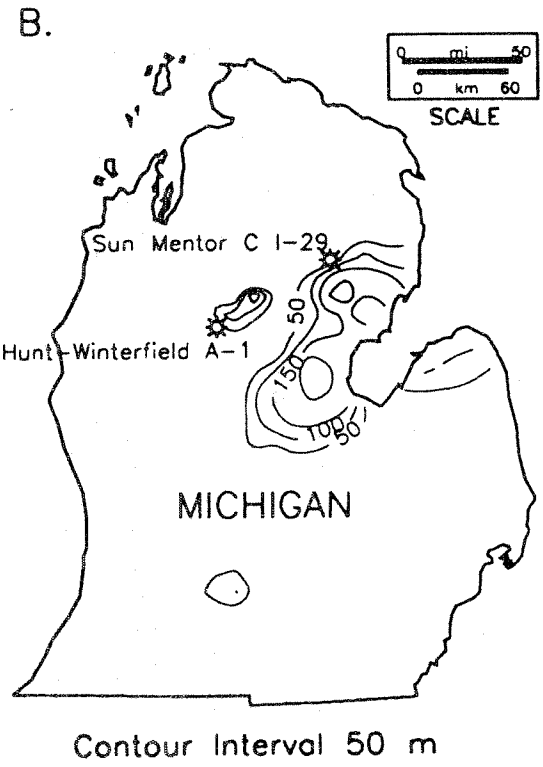

Figure 1. A. Map of Michigan showing areas of high hydraulic heads in the St. Peter Sandstone. Outlined are heads >350 m. B. Map showing areas where the computed hydraulic heads in the St. Peter Sandstone exceed surface elevation by at least 50 m. These areas represent anomalous pressures in the Michigan Basin. Locations of the Hunt Winterfield A-1 and the Sun Mentor C 1-29 wells are also shown.

part of this high-head region is an area of high surface topography that acts as a recharge area for the basin. In this case the high hydraulic heads might be explained by regional topographically driven flow. Figure 1B shows areas in which the computed hydraulic heads in the St. Peter Sandstone exceed surface elevation by at least 50 m. In these areas, which are concentrated west and north of Saginaw Bay, the high hydraulic heads are not consistent with a steady state regional flow system. Saginaw Bay is a regional discharge area and should have considerably lower hydraulic heads than the recharge area of the basin. The anomalously high hydraulic heads near Saginaw Bay indicate that a pressure compartment exists in this area.

Further evidence of fluid compartments in the Michigan Basin can be seen by looking at pressure-elevation curves. Figure 2A shows a pressure vs elevation curve for the St. Peter Sandstone, using extrapolated pressures from DST data across the entire basin. In this profile offsets toward greater pressure occur at elevations of 1775 m, 2440 m, 2650 m, and 2865 m, respectively. These offsets represent possible pressure compartments and suggest that there may be multiple stacked compartments in the St. Peter Sandstone. Similar offsets observed within the overlying Glenwood Formation (Figure 2B) suggest that at least some of the compartment seals cut across formation boundaries and are relatively horizontal. If pre-existing lithology is not the controlling factor in seal formation, then diagenetic processes must play an important role in generating the areally extensive low-permeability seals. Characterization of these seals is important in understanding the origin and maintenance of the pressure compartments.

This paper describes methods being used to quantify scales of porosity variability of potential seals within the St. Peter Sandstone and the Glenwood Formation. These porosity variations are likely to be the main source of hy-

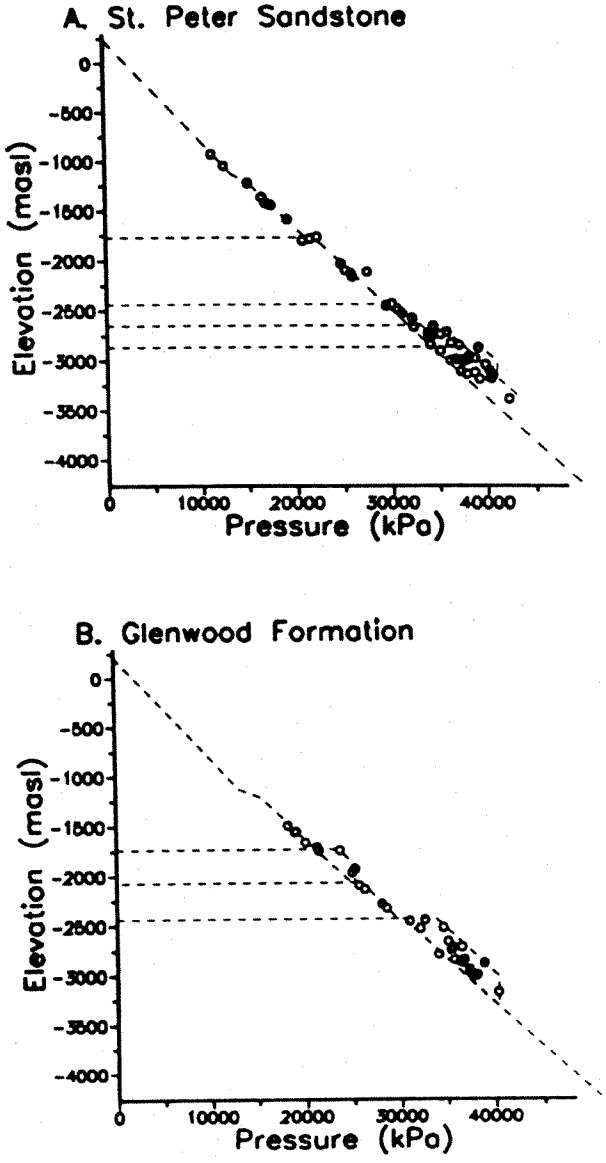

Figure 2. A. Pressure vs elevation curve for the St. Peter Sandstone. The dashed lines indicate where offsets toward greater pressure occur. These offsets represent possible pressure seals. B. Pressure vs elevation curve for the Glenwood Formation.

draulic conductivity variation in the seals and thus can play a major role in restricting hydraulic communication between the compartment and the regional flow system.

Banded Seals

It has been observed by Hunt (1990) that the top seal in many sandstone beds is layered with multiple horizontal bands of carbonate cement. These bands, which are produced to a large extent by diagenetic fluid-flow processes, can be on the scale of either millimeters or meters. This diagenetic banding creates a seal that can be very heterogeneous in both porosity and permeability throughout its thickness, with alternating layers of high and low permeability. Despite the presence of permeable lenses within the seal, the vertical permeability must be very low in order to isolate the compartment from the surrounding hydrogeological units (Hunt, 1990). A model has been developed by Dewers and Ortoleva (1990a) to explain the formation of banded cementation in sandstones. This model assumes that banding is mainly a result of differential compaction and cementation, due to mechanical and chemical interactions. This differential compaction/cementation is initiated originally by small heterogeneities in the texture of the rock, local stress, or chemistry of the formation water. These heterogeneities lead to localized chemical compaction, creating alternating zones of enhanced cementation and pressure solution. For example, small deviations in grain size in a relatively homogeneous sandstone can lead to large spatial variations in the amount of cementation and compaction that occur (Dewers and Ortoleva, 1990a). The smaller the grain size the higher the rate of intergranular pressure solution (IPS) (Houseknecht, 1988). As the finer-grained sandstone dissolves by IPS the silica will be exported to other zones and reprecipitated as quartz-overgrowths, causing porosity to decrease. As silica is exported, the fine grains in the sandstone will become smaller, allowing more IPS to occur. At the same time IPS is impeded in the quartz-overgrowth cemented areas, due to the larger contact surface area created by the silica cement. This creates a feedback mechanism that is self-perpetuating. This process will create a banded phenomenon, characterized by alternating zones of quartz-overgrowth cemented, low porosity sandstone and higher porosity, more compacted sandstone. This feedback mechanism illustrates that even a small initial heterogeneity in texture can lead to large, macroscopic variations in cementation and porosity in the system (Dewers and Ortoleva, 1990b). The quantitative data base on micro-scale porosity in the St. Peter Sandstone and the Glenwood Formation that is being generated as part of this research can be used to test this model.

Geological Setting

On the macroscopic scale, the St. Peter Sandstone is a relatively homogeneous quartz sandstone. It is Middle Ordovician in age and occurs at a depth of <1500 m in the west to >3350 m in the center of the basin. It reaches a maximum thickness of >335 m in the center of the basin and thins to zero at the basin margins (Fisher and Barratt, 1985). It is a thick succession of medium- to fine-grained, nearly pure quartz sandstones, with thin discontinuous silt/shale beds and dolomite-cemented sandstone layers. It may also contain up to 5% detrital feldspar, concentrated mainly in the finer-grained sandstones (Harrison et al, 1989). The dominant cement is quartz-overgrowths, with

minor amounts of dolomite and clay (mainly illite) cements. In general, the St. Peter Sandstone is dominated by two main facies: 1. a heavily bioturbated facies, most common in the upper part of the formation, with abundant vertical and horizontal burrows and quartz overgrowths, and 2. a laminated to cross-bedded facies with abundant stylolites, found in the lower part of the formation. Both of these facies suggest a predominantly shallow marine origin for the St. Peter Sandstone.

Overlying the St. Peter Sandstone is the Glenwood Formation, which is an interbedded siltstone/shale, sandstone, and carbonate unit. It is up to 60 m thick in some parts of the basin and thins to zero near the basin margin. Burrows are abundant in the sandstone units and may be quartz or dolomite cemented. Quartz, dolomite, and clay cements are all common, with the type and amount of cement varying vertically and laterally. Underlying the St. Peter Sandstone is the Prairie du Chien Group. It is composed of two main facies: 1. an interbedded silty sandstone and sandy dolomitic siltstone, quartz sandstone, and black shale, and 2. oolitic and silty dolomites.

Diagenesis and Porosity

Porosity variability in the St. Peter Sandstone is controlled to a large extent by secondary diagenetic factors. Primary porosity is occluded mainly by quartz-overgrowths, saddle dolomite, and illite, along with minor amounts of pyrite, anhydrite, and chlorite. Quartz-overgrowths are very common and are present basin-wide. These overgrowths completely occlude porosity in some areas, creating tight zones of low porosity and permeability. Where dolomite cement is present it may also completely occlude porosity. Bands of low porosity, dolomite-cemented sandstone have been observed, especially in the upper part of the St. Peter Sandstone. Secondary porosity is dominant, and results mainly from the dissolution of authigenic cements (Schmitt and McDonald, 1979). Clay occurs mainly as a pore lining/filling authigenic cement that was deposited fairly late in the diagenetic sequence.

Methods

Variability of porosity was evaluated using an image analysis system to measure porosity on the thin-section scale. The computerized image analysis system allows the user to quantify the pore space area in a thin section. The image analysis system used for this research is a color system that allows the user to measure specified objects in a user-defined area. Measurements completed to date are mainly for thin sections from the Hunt Winterfield A-1 and the Sun Mentor C 1-29 wells (see Figure 1B). Core samples and thin sections for these wells were obtained from Western Michigan University. Core samples were impregnated with a low-viscosity, blue-dyed epoxy before they were cut into thin sections. Images of the thin section are projected onto a computer screen. All of the porosity in these images (except for the microporosity in the clays) is stained blue from the epoxy. The computer generates a histogram from the image, assigning a range of gray-scale values from 0 - 255 to each color. The user then selects the color of interest (blue in the case of porosity) and the program highlights the areas in the image that fall within the range of gray-scale values assigned to that color. Dividing the highlighted area by total screen area, the program generates a value of the fractional area of porosity. The system can also be used in a similar manner to quantify the percentage of

clay and dolomite cement. It cannot be used to quantify the amount of quartz-overgrowth cement, however, because the system is not able to distinguish between the color of the overgrowth and the color of the detrital quartz grain.

A total of 20-50 images per thin section were analyzed. The number of images analyzed for a given section depended on the size of the thin section, as well as on the variability in porosity that was observed. An average area of porosity was then obtained for each thin section, along with a standard deviation, maximum, and minimum value. Assuming the samples are relatively isotropic, this two-dimensional area provides a good estimate of the three-dimensional porosity. The image analysis system was also used to measure the percentage of dolomite and clay cements. These results were then compared to core descriptions to determine if values obtained using the image analysis system can be correlated with facies observed in the core.

Results

Average thin section porosity of the St. Peter Sandstone varies from <1% to >20% between core samples obtained from a single well. In addition, abrupt changes in the degree of cementation and porosity were observed within single thin sections. More detailed descriptions of results for the Hunt Winterfield A-1 and the Sun Mentor C 1-29 wells are provided below.

Hunt Winterfield A-1

The Hunt Winterfield A-1 well is located in the northwest section of Clare County, in the north-central part of the Michigan Basin. It is located near the edge of one of the areas of high anomalous hydraulic heads in the central part of the basin (Figure 1B). The St. Peter Sandstone in this core (3232.7 - 3538.1 m) is a fine- to medium-grained, nearly pure quartz sandstone with approximately 5% detrital feldspar. Most of the grains are well sorted and subrounded to rounded. Many of the grains have sutured contacts, indicating widespread pressure solution and compaction throughout the core. There are abundant vertical burrows, and stylolites are locally common, especially in the lower St. Peter Sandstone. The dominant cement type is quartz-overgrowths, with some zones of dolomite cement; clay cement is virtually absent. The Glenwood Formation in this core contains interbedded siltstone, fossiliferous dolomicrite, and burrowed quartz sandstone. Some of the zones in the sandstone are cemented by diagenetic dolomite and there is abundant authigenic clay present (mainly illite). The clay acts mainly as a pore lining/filling cement.

A description of the Hunt Winterfield A-1 core is shown in Figure 3. In addition to the core description, Figure 3 shows the major and minor types of cement found in the core, the average grain size, and the average percent and range of porosity found in each thin section. The cement types and grain size were determined from core analysis

Figure 3A. (next page) Simplified columnar section of the core through the Glenwood Formation, St. Peter Sandstone, and Prairie du Chien Group in the Hunt Winterfield A-1 well. See Figure 1B for well location. The core description includes type of cement, average grain size, and average percent and range of porosity. Cements are, from left to right, clay, carbonate, and quartz. See Figure 3B for a key of the lithologies and structures used in this core description.

FIGURE 3A - HUNT WINTERFIELD A-1

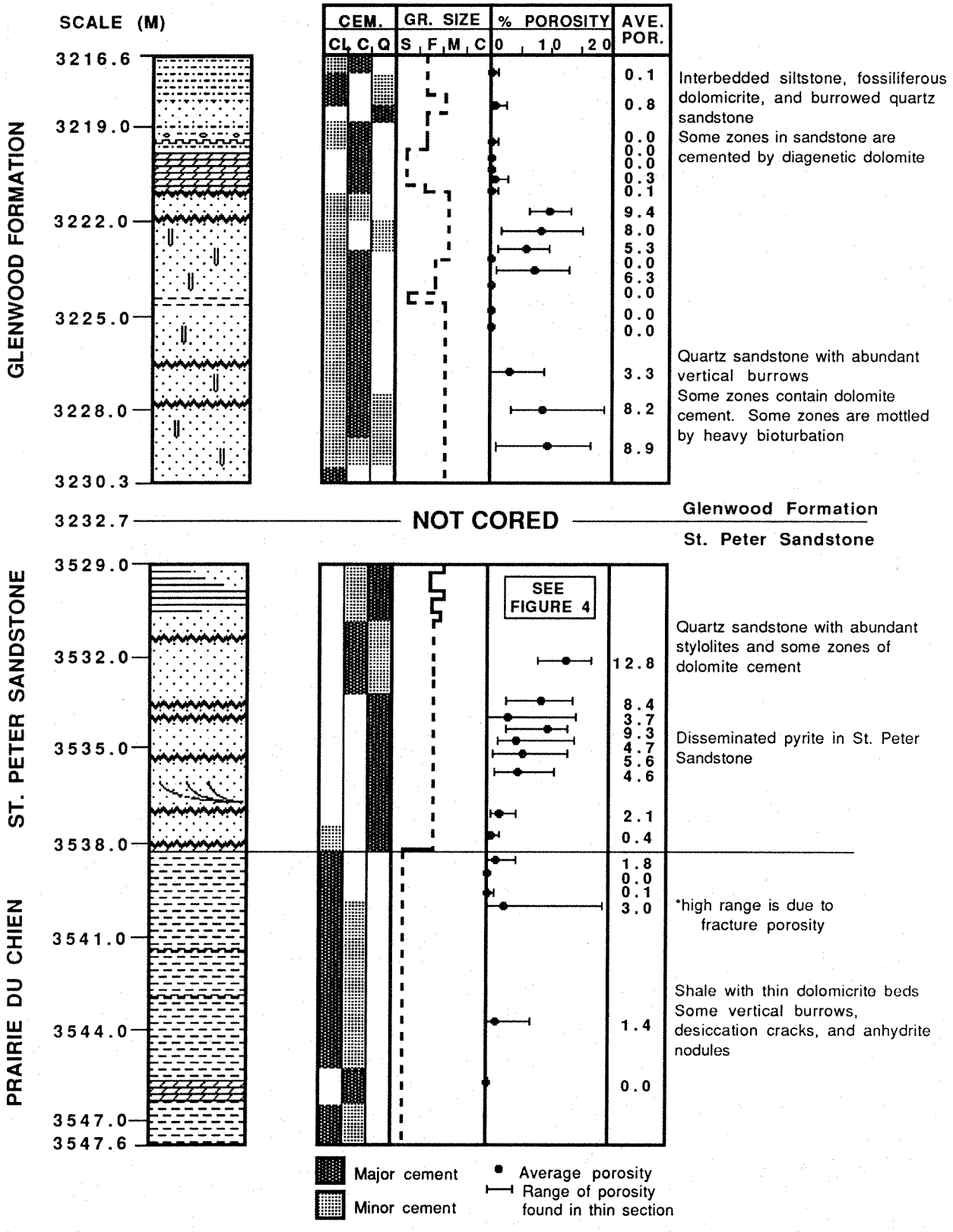

and thin sections, where available. Figure 4 is an enlarged section of the zone from 3529.3 - 3531.0 m, for which ten thin sections were available. The porosity values shown in Figures 3 and 4 indicate that there is significant variability in porosity, not only in a vertical direction but also within a single thin section. It should be noted that microporosity in clays is not included in these porosity measurements due to the limitations of the image analysis system. Porosity in clay-rich zones will therefore be underestimated. Average porosity varies from 0.0 - 9.4 % in the Glenwood Formation, with a possible seal existing from at least 3216.6 m (top of core) to approximately 3221 m. This interval is composed mainly of sandy-shale and fossiliferous dolomicrite zones and has an average porosity of <1%.

Average porosity of the St. Peter Sandstone ranges from 0.1 - 12.8%. Reservoir heterogeneity is especially apparent in the interval from 3529.3 - 3531.0 m. (see Figure 4). Over an interval of less than a meter, porosity changes from essentially zero to 12%, with the amount and type of cement also varying. This variability is illustrated in the following three thin sections. The thin section from a depth of 3530.0 m is a medium-grained, dolomite-cemented, quartz sandstone with an average porosity of 0.7% (range of porosity in the thin section is 0 - 2.4%). There is 25% dolomite cement and 5% quartz-overgrowth cement. The grains are not highly compacted, indicating an early origin for the dolomite cement. Description of the core from this depth indicates centimeter-scale variations in cement type, with alternating zones of quartz-overgrowth and dolomite cement. A short distance below (3530.2 m) the sandstone is very porous, with an average porosity of 12.0% (range 9.5 - 14.5%). It is cemented mainly by quartz-overgrowth cement (average 10%), with 2% clay cement lining the pores. Lower again (3530.5 m) porosity once again decreases to almost zero. In this case, however, porosity is occluded by quartz-overgrowth cement rather than by dolomite. The thin section from this depth shows a fine- to medium-grained, well compacted sandstone, tightly cemented by quartz overgrowths, with an average porosity of 1.2% (range 0 - 4.8%). There is approximately 15% quartz-overgrowth cement. These three thin sections represent variability in porosity and cement type on the scale of centimeters to decimeters. It is interesting to note that on the scale of the core, the interval from 3530.0 - 3530.5 m represents a single facies, characterized by fairly tight, quartz-cemented sandstone with abundant stylolites. There are also some centimeter-scale bands of dolomite cement. This interval illustrates that even within a single facies, porosity can be highly variable.

Abrupt changes in porosity can also be observed within a single thin section. This can be seen in the thin section from a depth of 3533.9 m. This thin section has an average porosity of 3.7%, with a range of 0 - 14%. The upper part of the thin section is a dolomite-cemented quartz sandstone with zero porosity. The grains are not very well compacted, with 25% dolomite cement. The lower part of the thin section is a medium-grained, poorly sorted quartz sandstone with approximately 5% quartz-overgrowth cement and 10% porosity.

Sun Mentor C 1-29

The Sun Mentor C 1-29 well is located in the southeast corner of Oscoda County, in the northeast part of the Michigan Basin. It is located within the high hydraulic head area shown in Figure 1A. Because the Sun Mentor C

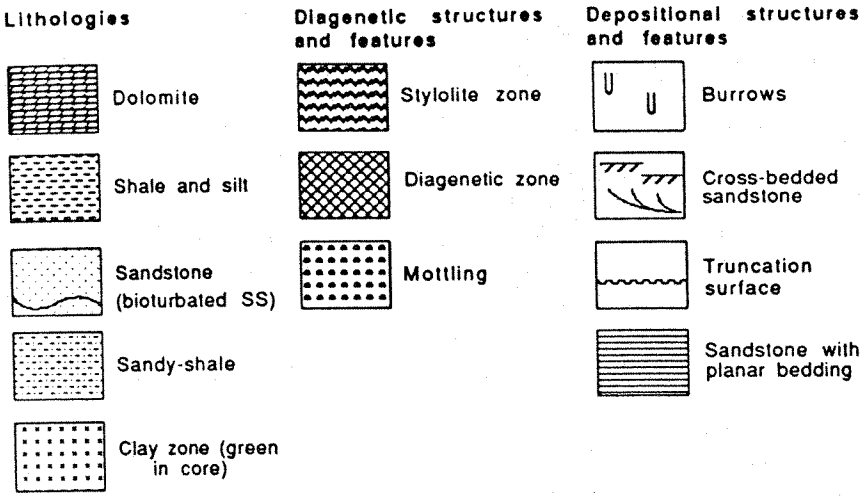

Figure 3B. Key of the lithologies and structures used in Figures 3A, 4, and 5.

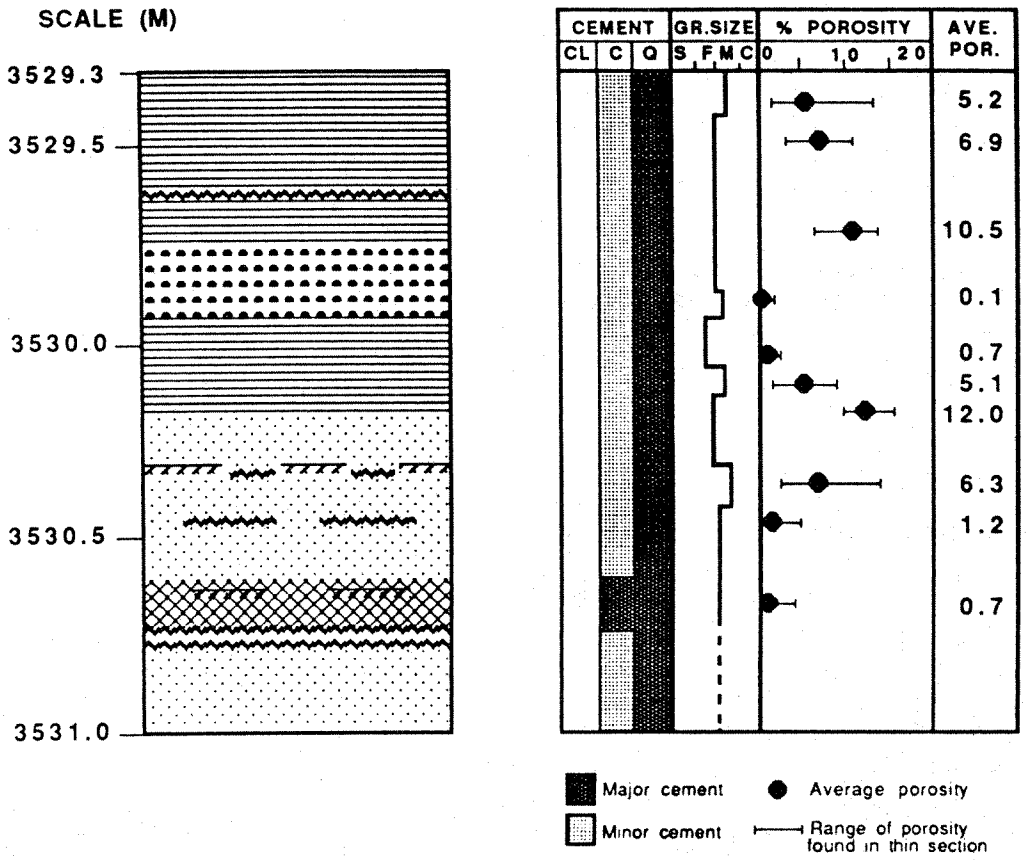

Figure 4. An enlarged section of part of the Hunt Winterfield A-1 core shown in Figure 3A. See Figure 3B for a key of the lithologies and structures used in this core description.

1-29 well is not located near a recharge area, high hydraulic heads represent anomalous pressure (Figure 1B).

A core description of this well is shown in Figure 5. The entire core consists of fine- to medium-grained quartz sandstone with 5-10% detrital feldspar, concentrated in the finer-grained sandstone. Sutured grain contacts are common throughout the core, indicating that pressure solution has occurred. The St. Peter Sandstone in this core (3074.5 - 3116.6 m) is a quartz-overgrowth cemented sandstone with planar bedding and vertical *Skolithos* burrows. There is minor clay lining/filling pores in some zones; dolomite cement is virtually absent. The lower part of the core (3098.3 - 3116.6 m) is characterized by millimeter-scale diagenetic banding. The banding is composed of interbedded white, quartz-overgrowth cemented layers and red, clay-cemented layers. The Glenwood Formation in this core (3062.3 - 3074.5 m) contains abundant vertical burrows, planar bedding, and some green clay-rich zones. Quartz, dolomite, and clay (mainly illite) cements are common.

Average porosity in the St. Peter Sandstone ranges from 0 - 12.6%. Porosity is especially low in the upper part of the St. Peter Sandstone (in the cored intervals from 3074.5 - 3077.6 m and 3098.3 - 3111.6 m) where average porosity ranges from 0 -5.6%. The low-porosity interval from 3098.3 - 3111.6 m is part of the core that is characterized by the millimeter-scale diagenetic banding discussed above. Porosity in the Glenwood Formation is more variable than in the St. Peter Sandstone, with average porosity ranging from 0.0 - 17.8%. The high porosity value (17.8%) is in one of the clay-rich zones.

Significant variability in porosity also occurs within single thin sections, as can be seen by the large ranges in porosity shown in Figure 5. For example, the thin section from a depth of 3068.7 m has an average porosity of 2.4%, with a range of 0 - 17.5%. In this thin section the amount of porosity is influenced by the type of cementation. The upper part of the thin section is a fine- to medium-grained dolomite-cemented quartz sandstone with zero porosity. The grains are not very well compacted (29% dolomite), suggesting an early origin for the dolomite cement. The lower part of the thin section is a fine-grained, more compacted quartz sandstone with high porosity (average 15%). The transition between the two porosity zones is fairly abrupt.

A second transition from a poorly cemented, porous zone to a tight zone was observed in a thin section from a depth of 3105.6 m. This thin section has an average porosity of 3.0%, with a range of 0 - 15%. Part of the thin section is a well compacted, medium-grained, quartz-overgrowth cemented sandstone with zero porosity. There is approximately 10% quartz cement, with some clay rimming the grains. The other part of the thin section is a more porous, fine- to medium-grained quartz sandstone with some quartz-overgrowth cement. Average porosity in this zone is 8%. It also has 5% pore filling Fe-rich clay. Description of the core from this depth indicates millimeter-scale diagenetic banding, with alternating bands of white, quartz-overgrowth ce-

Figure 5. (next page) Simplified columnar section of the core through the St. Peter Sandstone in the Sun Mentor C 1-29 well. See Figure 1B for well location. The core description includes type of cement, average grain size, and average percent and range of porosity. Cements are, from left to right, clay, carbonate, and quartz. See figure 3B for a key of the lithologies and structures used in this core description.

FIGURE 5 - SUN MENTOR C 1-29

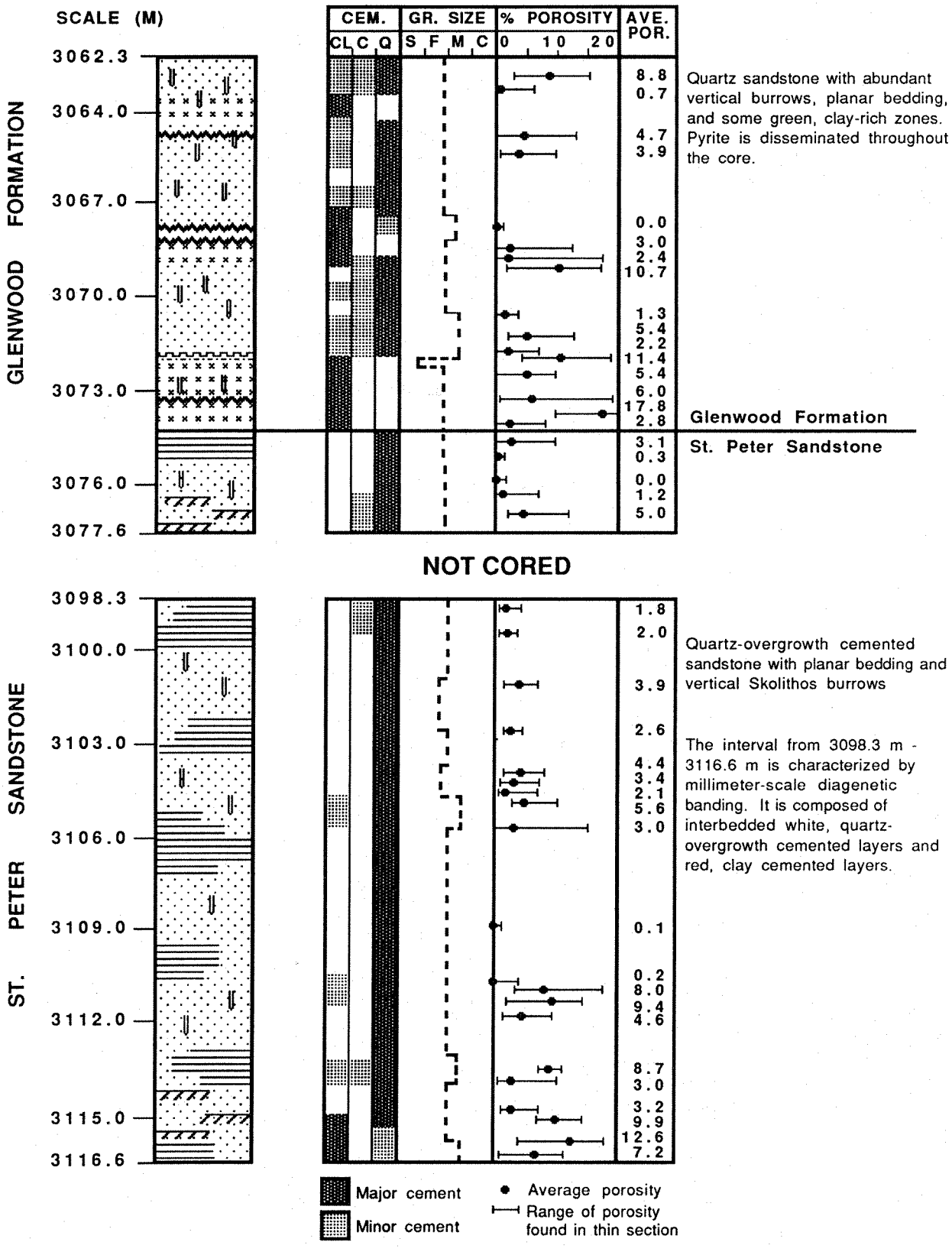

mented sandstone and red, clay cemented sandstone.

Discussion

These preliminary results from the Hunt Winterfield A-1 and the Sun Mentor C 1-29 cores indicate that there are abrupt changes in the degree of cementation and porosity on a relatively small scale. Although the St. Peter Sandstone is a relatively homogeneous quartz sandstone on the macroscopic scale, it is a relatively heterogeneous sandstone on the microscopic scale. Results from the image analysis system indicate that porosity and cement type vary not only on the core scale (scale of meters), but also on the centimeter and millimeter scale. Comparison of these results to core descriptions show that porosity is highly variable even within a single facies. This is consistent with the model for banding developed by Dewers and Ortoleva (1990b). Even in a relatively homogeneous sandstone like the St. Peter Sandstone, differential compaction and cementation significantly affect the amount of porosity in the system. Additional thin section analysis is required, however, to quantify the scale of this banding and to determine correlation lengths for porosity variability in the St. Peter Sandstone and the Glenwood Formation.

Future Work

Our work to date has demonstrated that porosity in the St. Peter Sandstone and the Glenwood Formation varies at several scales, as a function of both depositional facies changes and heterogeneity of cementation. In order to quantify this variability further, and to develop information on the statistical properties of porosity and hydraulic conductivity distributions, additional image analysis measurements are required, both for the cores already examined and for additional cores from nearby wells. These additional measurements will be used to examine trends in the mean and variance of porosity within individual wells and between wells completed in the same facies. Vertical autocorrelation functions of mean porosity will then provide additional information on scales of banding and other diagenetic features in individual wells.

Results of this porosity characterization, along with other petrographic studies of core samples, should aid in the interpretation of wireline log signatures that are being used to identify patterns of variability on a larger scale. The data will also be used to test the theoretical model of banding developed by Dewers and Ortoleva (1990b). Information on hydraulic parameters derived from this research will ultimately be used to develop a hydrodynamic model for the Michigan Basin.

Acknowledgements

This research is being funded by the Gas Research Institute. P. Drzewiecki and R. Vandrey provided core descriptions for the Hunt Winterfield A-1 and Sun Mentor C 1-29 cores. Core samples and some thin sections for these cores were provided by Western Michigan University. Extrapolated pressures from drill-stem tests were provided by R. Vugrinovich of the Michigan Department of Natural Resources.

Lisa D. Shepherd is an MS student in hydrogeology at the University of Wisconsin-Madison (Dept. of Geology and Geophysics, 1215 W. Dayton St., Madison WI. 53706). She received her BA in geology from Carleton College (Northfield, MN) in 1987. She has experience at the Water Resources

Division of the US Geological Survey working on geothermal and subsidence projects.

Jean M. Bahr is an assistant professor in the Department of Geology and Geophysics at the University of Wisconsin-Madison (Dept. of Geology and Geophysics, 1215 W. Dayton St., Madison, WI 53706). She has experience in geotechnical consulting and as a hydrologist with the US Geological Survey. Her current research interests include fluid flow and solute transport in shallow and deep systems.

Gerilynn R. Moline is currently pursuing a PhD in hydrogeology at the University of Wisconsin-Madison (Dept. of Geology and Geophysics, 1215 W. Dayton St., Madison, WI 53706). She received a BA in geology from the University of Southern Maine in 1986 and an MS in geophysics from the University of Wisconsin-Madison in 1989. Her current research focuses on hydrogeological modeling of deep basin pressure compartments under a grant funded by the Gas Research Institute.

References

Bahr, J. M. 1989. Evaluation of pressure distribution in the St. Peter Sandstone, Michigan Basin (Abs.). EOS, v. 70, p. 1097.

Dewers, T. and P. Ortoleva. 1990a. A coupled reaction/transport/mechanical model for intergranular pressure solution, stylolites, and differential compaction and cementation in clean sandstones. Geochim. Cosmochim. Acta, v. 54, pp. 36-52.

Dewers, T. and P. Ortoleva. 1990b. The interaction of reaction, mass transport, and rock deformation during diagenesis: mathematical modeling of intergranular pressure solution, stylolites, and differential compaction/cementation. In Predicting Reservoir Quality (eds. I. Meshri and P. Ortoleva). Am. Assoc. Petrol. Geol. Mem. (in press).

Fisher, J. H. and M. W. Barratt. 1985. Exploration in Ordovician of Central Michigan Basin. Am. Assoc. Petrol. Geol. Bull., v. 69, pp. 2065-2076.

Harrison, W. B., D. Barnes, C. Lundgren, and L. Wieczorek. 1989. Deep well drilling in the Michigan Basin. American Gas Assoc. Annual Proceedings.

Houseknecht, D.W. 1988. Intergranular pressure solution in four quartzose sandstones. J. Sediment. Petrol., v. 58, pp. 228-248.

Hunt, J.M. 1990. Generation and migration of petroleum from abnormally pressured fluid compartments. Am. Assoc. Petrol. Geol. Bull., v. 74, pp. 1-12.

Schmidt, V. and D. McDonald. 1979. Texture and recognition of secondary porosity in sandstones. In Aspects of Diagenesis (eds. P.A. Scholle and P. Schluger). Society of Economic Paleontologists and Mineralogists, Spec. Pub. 26, pp. 209-225.

A Multivariate Statistical Method For Using Geophysical Log Data To Delineate Hydrostratigraphy And Estimate Hydraulic Parameters: St. Peter Sandstone, Michigan Basin

by Gerilynn R. Moline, Jean M. Bahr and Lisa D. Shepherd

Abstract

A study is currently underway to investigate the occurrence of pressure compartmentation in the St. Peter Sandstone of the Michigan Basin. The St. Peter Sandstone reaches depths exceeding 3 km (10,000 ft) in much of the basin and is currently an active gas play. A regional flow model is being constructed as part of this investigation. Although more than 500 wells have been drilled to the St. Peter Sandstone or deeper, only a few cores and permeability analyses have been made available due to the proprietary nature of these data. Thus for the majority of the basin the only data available for determination of hydrostratigraphy are wireline logs. A means for correlating these data with lithology and hydraulic parameters is needed. Conventional methods for analyzing well log data utilize two- or three-dimensional cross-plots of log parameters which capitalize on the differences in log response to geological parameters. While useful for delineating large variations in lithology and porosity, conventional cross-plots are not sufficient to identify the subtle variations observed in the St. Peter Sandstone. An alternative approach being proposed in this study is a multivariate statistical analysis of the geophysical log data using a suite of geophysical logs available for most deep gas wells in the Michigan Basin. Data from two wells were examined to test the correlations between the multivariate log responses and the hydraulic parameters. The logs were segmented into homogeneous zones which were then grouped into electrofacies according to similarity of hydraulic characteristics. Permeability and porosity values were assigned to electrofacies on the basis of core analyses. The similarity of geophysical log responses for a given range of permeability indicates that an electrofacies model can be used to estimate hydraulic parameters. In future work, quantification of these correlations will provide a data base for statistical estimation of hydrogeological parameters at well locations for which only geophysical data are available.

Introduction

The St. Peter Sandstone in the Michigan Basin is a relatively homogeneous mature quartz sandstone of Middle Ordovician age. Depths to the top of the St. Peter Sandstone range from <1500m (5,000 ft) to >3350m (11,000 ft) in the central part of the basin. This sandstone, along with the overlying Glenwood Formation and underlying Prairie du Chien Group, has been the target of intense exploratory drilling for gas over the past decade, with more than 500 wells completed to the St. Peter Sandstone or deeper.

A study is currently underway at the University of Wisconsin - Madison to investigate the origin and occurrence of pressure compartments within the St. Peter Sandstone. A preliminary analysis of the basinwide hydraulic head distribution calculated from drill stem test (DST) data indicates zones of high hydraulic head inconsistent with the regional flow pattern (Bahr, 1989). Pressure vs elevation profiles construct-

ed from DST data indicate discontinuities in the pressure gradient at elevations of -1770, -2440, -2650 and -2865 m (-5800, -8000, -8700 and -9400 ft, respectively); see Shepherd et al. (1991, Figure 2).

A closer examination of permeability and porosity data from a number of different sources indicates that these parameters vary widely within this macroscopically homogeneous sandstone. At the scale of wireline logs (≈0.5 m; 1-2 ft), permeabilities calculated from Repeat Formation Tester (RFT) pressure buildup curves indicate variations of five orders of magnitude over intervals of a few meters to a few tens of meters (Figure 1). Core plug permeabilities, which sample a 2.5 cm (1 in) thickness at a frequency of ≈0.3 m (1 ft), indicate similar variations in permeability. Core plug porosity varies from <1% to >20% within the St. Peter Sandstone. On a microscopic scale the entire range of porosity is sometimes observed within a single thin-section (Shepherd et al., 1991).

An examination of geophysical log signatures and core samples indicates that the variations in hydraulic parameters result from variations in the abundance of quartz and dolomite cement, and that zones of intense stylolitization and diagenetic banding correlate strongly with zones of very low porosity and permeability. It is these zones that may constitute diagenetic seals for the pressure compartments within the St. Peter Sandstone.

As part of the effort to determine the origin of these seals, a basinwide hydrodynamic model is being constructed. For this purpose, the vertical and lateral variations in porosity and permeability need to be identified for the delineation of hydrostratigraphy within the St. Peter Sandstone and the assignment of hydraulic parameter values for the identified units. Because only limited core data are available due to their proprietary nature, geophysical logs are the most complete set of data available for basinwide studies. Thus a means for estimating hydraulic parameter values from the response of geophysical logging tools will provide the input parameters for regional flow modeling.

Concept of Electrofacies

The term *facies* has a wide variety of meanings and usages in the geological literature. This paper employs the general definition proposed by Moore (1949) which defines a facies as "any areally restricted part of a designated stratigraphic unit which exhibits characteristics significantly different from those of other parts of the unit." These characteristics are the result of primary depositional and secondary diagenetic processes.

Wireline logs measure the geophysical properties of stratigraphic units at depth. These properties are, in turn, a function of the chemical and structural properties of the rock matrix and pore fluids, including rock texture, mineralogical composition, fluid density, and fluid phase. Wireline logs differ in their sensitivity to these lithological and fluid properties. Each log therefore responds in a different manner to variations in subsurface characteristics. The sum of these log responses provides a composite picture of the rock and fluid properties within the volume influenced by the wireline geophysical tools (Serra, 1986).

It follows that an *electrofacies* constitutes a set of wireline log responses which characterizes a portion of the subsurface, permitting it to be distinguished from its surroundings (Serra and Abbott, 1982; Serra, 1986). The name arises from the common use of the term "electric logs" to include the entire suite of geophysical logs which measure acoustic, nuclear, and mech-

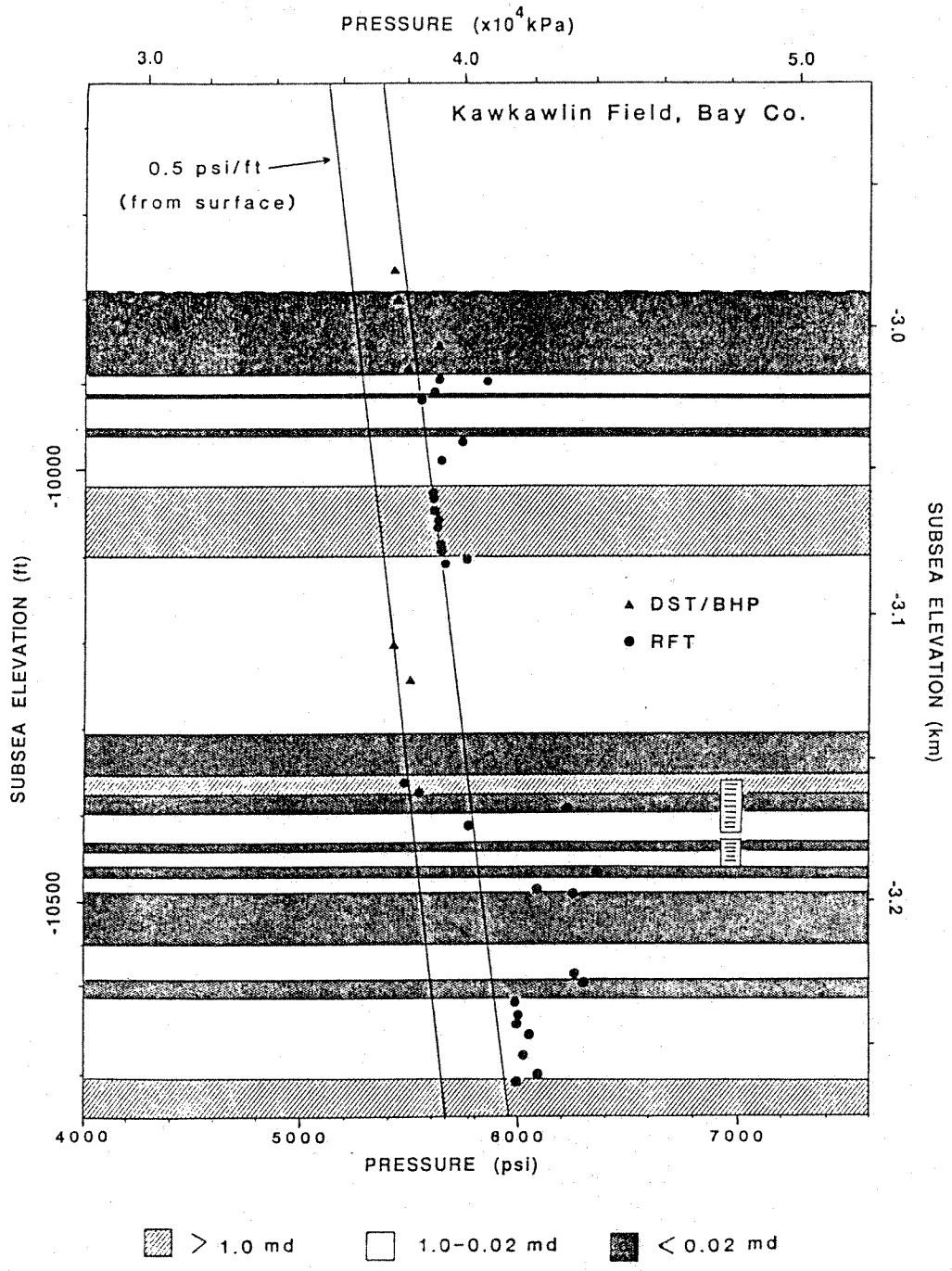

Figure 1. Pressure vs elevation for an interval within the St. Peter Sandstone. This well is located in the southcentral portion of the basin within a pressure anomaly. Permeabilities calculated from RFT pressure buildup curves indicate large variations over a few meters to tens of meters. Overpressuring is indicated by a shift in pressure relative to a hydrostatic gradient of (0.5 psi/ft). The gas producing zone is identified by the box near -10,400 ft.

anical as well as electrical properties.

Electrofacies differ from lithofacies in that the geophysical logging tools are sensitive to changes in pore fluids as well as lithology, so that more than one electrofacies may be associated with a single lithofacies type.

An electrofacies may be defined by any number of geophysical log parameters. For delineating sandstone and shale successions one to three parameters are usually sufficient, and standard cross-plots such as the MID Plot (Clavier and Rust, 1976) and M-N Plot (Burke et al., 1969) are used routinely in the petroleum industry. For a more detailed picture, particularly where lithologic changes are subtle, as in the St. Peter Sandstone, more log parameters need to be incorporated. For this study eight log parameters were used to define the electrofacies types: neutron porosity (ϕ_N), photoelectric factor (Pe), compensated density (ρ_b), microresistivity (R_{MSFL}), deep resistivity (R_{LLD}), sonic travel time (Δt), natural gamma ray (γ), and caliper (CAL).

To be detectable, variations in lithology and/or pore fluids must occur over an interval that is larger than the resolution of the logging tool, which ranges from ≈0.3 to 1 m (0.5 to 3 ft) depending on the tool (Serra, 1984). The log response to small thickness changes will be averaged over the measured interval.

Geophysical measurements are recorded at a frequency of once every 15 to 30 cm (6 to 12 in) within the borehole. Each multi-log measurement represents a point in multi-dimensional space. Measurements from intervals which are lithologically similar form clusters of data points which can then be grouped into electrofacies types. The scatter of points within each electrofacies is due to error contributed by tool measurement and borehole irregularities as well as to real lithologic and fluid variations. Some overlap between these clusters or facies types occurs as a result of differences in the sensitivity of the tools to a particular lithologic change.

Once the data are clustered into discrete electrofacies, discriminant analysis can be applied to each population to describe its distribution in multidimensional space to provide a means for assigning group membership to data from additional wells. The correlations between electrofacies, lith-, ology, and ranges of hydraulic parameter values can then be examined and quantified.

One means of graphically displaying electrofacies is through the use of rose or spider's web diagrams (Figure 2). Each axis of the plot represents a different wireline log scale. When the points on each axis are joined, a characteristic shape is formed which then allows rapid identification and correlation of electrofacies types.

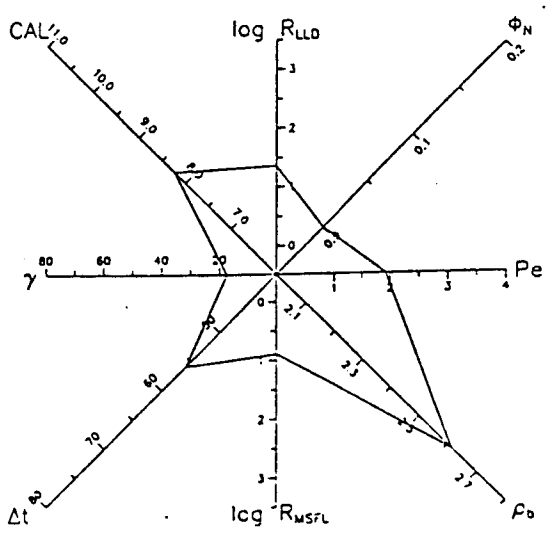

Figure 2. Spider's web plot showing the characteristic shape for an electrofacies. Log parameters are (clockwise from top): deep resistivity, neutron porosity, photoelectric factor, compensated density, microresistivity, sonic travel time, natural gamma ray, and caliper.

Method of Electrofacies Determination

The identification of electrofacies begins with the division of the logged interval into discreet zones or *electrobeds* having similar log characteristics (Serra, 1986). Data must be depth-corrected because cable stretch and tool sticking can result in shifts of a meter or more between log runs. Differences in the resolution between the various logging tools must also be taken into account.

Because borehole washouts can grossly distort the log response, the caliper log is examined and washed out intervals are eliminated from the analysis. The Compensated Neutron-Litho-density® and Borehole Compensated Sonic® logs adjust for the majority of the effects of borehole irregularity. Compensations are considered valid to ≈0.2 g/cm^3 for the bulk density (Asquith, 1982). Those intervals requiring greater adjustments, as indicated by the compensation curve, are also eliminated from the analysis.

The log values within each of the identified zones are compiled from a set of digitized data and arithmetically averaged, resulting in a multivariate mean for each log segment. These mean values, together with maximum and minimum values, are plotted on a spider's web diagram for each electrobed. Those zones with similar log responses, as reflected by their characteristic shapes, are assigned to the same electrofacies group.

Correlation with Hydraulic Parameters

Porosity and permeability are primarily controlled by the rock texture which is a function of the primary depositional environment and subsequent diagenetic processes during burial history. Because the components of texture such as grain size, shape, sorting, and degree and type of cementation (grain-grain, grain-matrix, and grain-cement bonding) also control the logging tool response, it is not surprising that a correlation exists between the log responses and the porosity and permeability.

As mentioned above, the hydraulic parameters vary dramatically over scales smaller than the resolution of the geophysical tools. However, because the geophysical tools average the variations in log response within the resolution of the tool, a correlation exists between that averaged log response and the averaged values of porosity and permeability within the same interval.

To examine these correlations, core porosity and permeability measurements were divided into zones which corresponded to the geophysical log zonation, after depth corrections were made. An average porosity and $\log_{10}$ permeability was calculated for each interval. Electrobeds were then grouped into electrofacies types according to orders of magnitude of permeability for comparison.

Application to Michigan Basin Wells

As an initial test, the electrofacies identification process described above was applied to two wells that were logged and cored in the uppermost portion of the St. Peter Sandstone. The Hunt Martin 1-15 well, located in the central portion of the basin, is not an active producing well; the Patrick Gilde 1-25 well is located within a producing field in the western flank of the basin (Figure 3).

The cored intervals of the geophysical logs were subjectively

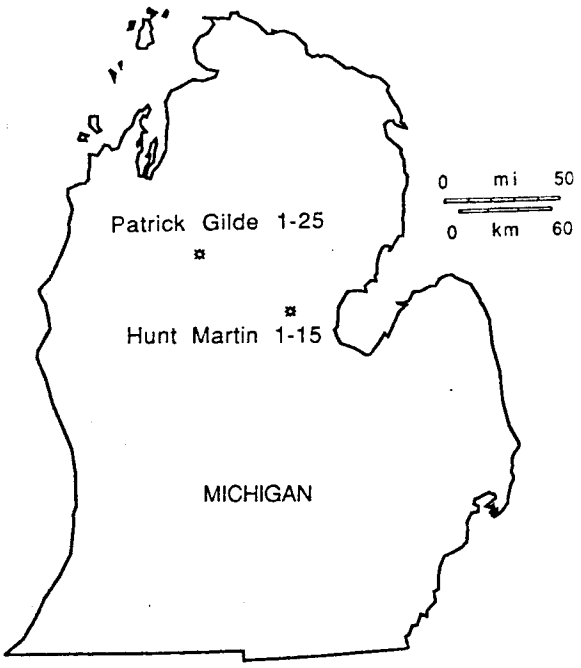

Figure 3. Map of the lower peninsula of Michigan showing the well locations.

segmented into electrobeds. This segmentation for the Hunt Martin 1-15 well is shown in Figure 4. Some variations in depth and thickness resolution are evident, but the depths at which changes in log response occur are relatively consistent. Zonation was determined primarily from the neutron, sonic (not shown), and density logs, because these logs are slightly less sensitive to changes in pore fluids than the resistivity logs. Both the Pe and gamma logs show only minor variation within the interval of interest, a reflection of the macroscopic lithologic homogeneity within this sandstone. The correlation between log responses and core hydraulic parameters can be seen in Figure 4.

An examination of the spider's web diagrams clustered by order of magnitude of $\log_{10}$ permeability reveals a similarity of characteristic shapes within each cluster (Figure 5A-D). Each cluster represents an electrofacies type. The characteristic shapes within each electrofacies exhibit some variability, but there is enough distinction between groups to allow an immediate electrofacies identification. A qualitative estimate of permeability for any given electrobed can then be made by simple comparison.

Spider's web diagrams for each of the electrobeds identified in the Hunt Martin 1-15 well are shown in Figures 6A and 6B together with the mean values for porosity and permeability. In a few cases (such as hm14, hm15, and hm16) where the shapes do not correlate well, the mean value of the permeability is skewed by wide variability within that depth interval.

A similar analysis was completed for the Patrick Gilde 1-25 well (Figure 7). The range of permeability values is not quite as large as in the Hunt Martin 1-15 well and this is reflected in the characteristic shapes. For a given permeability range the magnitude of the log parameters differ slightly between the two wells, but the characteristic shapes bear a qualitative similarity. For example, the Pe is lower and the gamma is higher in the Patrick Gilde 1-25 well, reflecting some lithologic differences between the two wells. This is not surprising, given the distance separating the two wells. However, it is encouraging that those parameters most sensitive to variations in permeability show consistent trends.

Parameter Sensitivity

Of the eight geophysical parameters employed in the electrofacies determinations, only five exhibited strong sensitivity to changes in porosity and permeability: microresistivity (R_{MSFL}), deep resistivity (R_{LLD}), compensated density (ρ_b), neutron porosity (ϕ_N,) and sonic travel time (Δt).

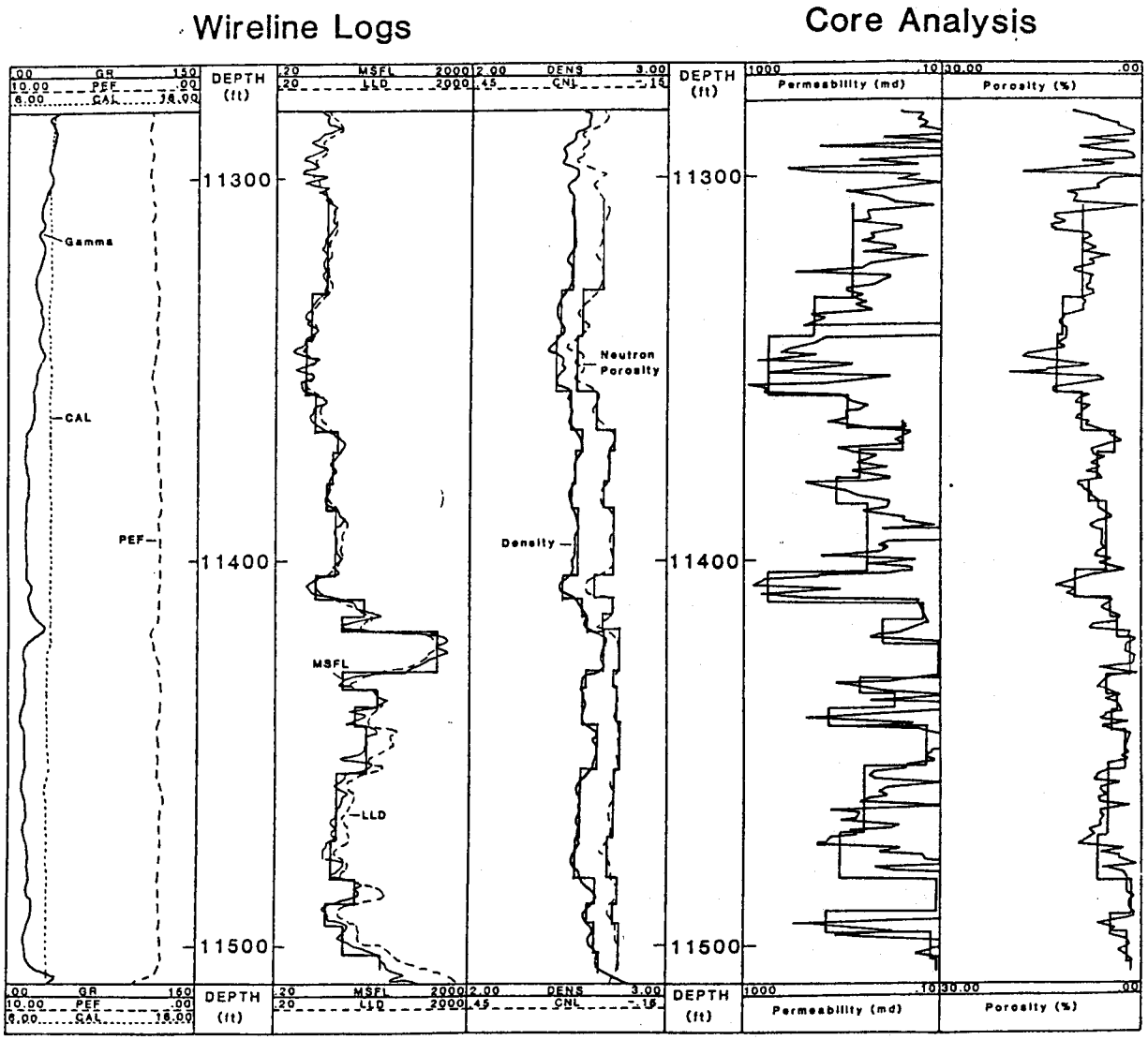

Figure 4. Wireline log zonation for the upper St. Peter Sandstone in the Hunt Martin 1-15 well. The logs were segmented on the basis of similarity of log values within the interval. Average values for both logs and core are superimposed over each trace.

The other three log parameters (γ, CAL, Pe) did not vary sufficiently to establish any recognizable trends. The γ and Pe logs reflect bulk lithology, which does not change significantly within the St. Peter Sandstone in the intervals examined, and the CAL is included only to identify washouts.

An examination of the characteristic shapes for the Hunt Martin 1-15 elec-

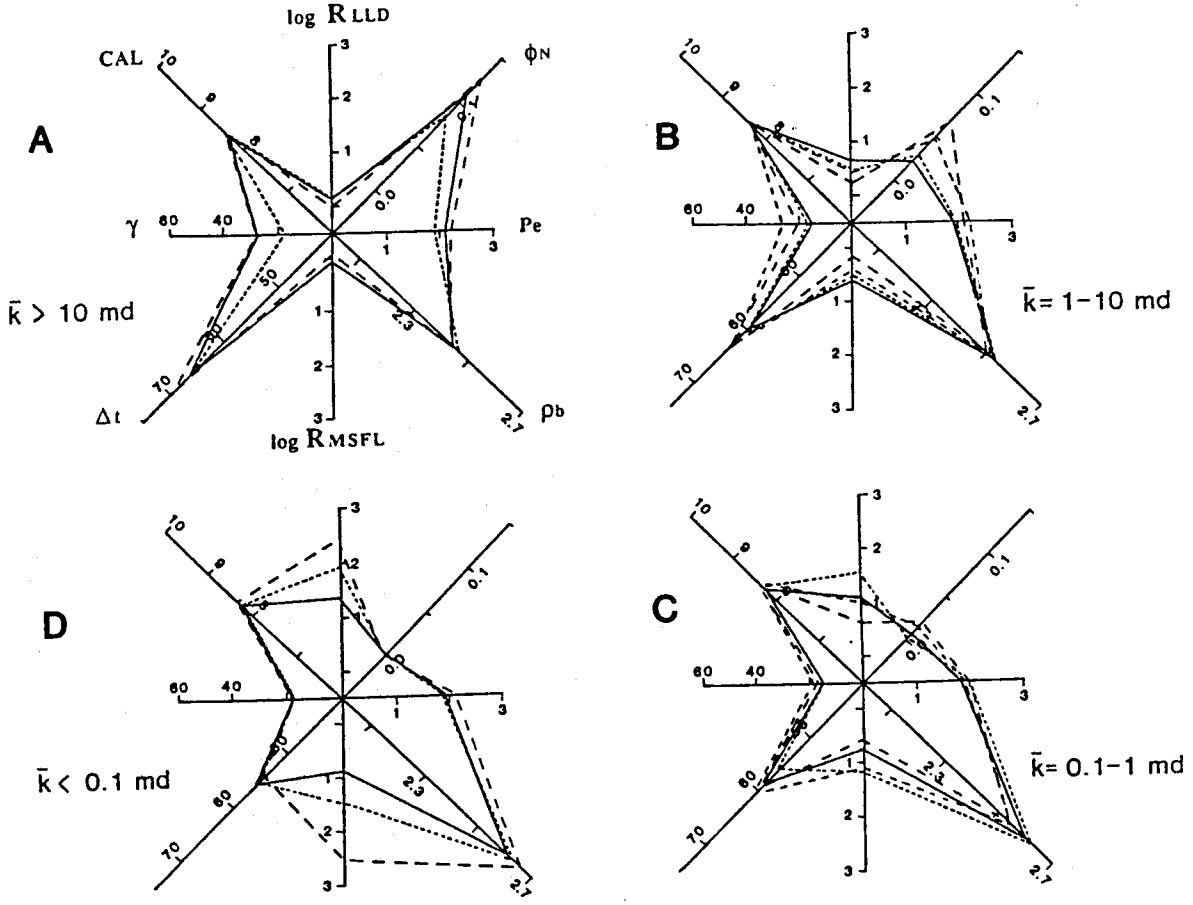

Figure 5. Characteristic shapes for the electrobeds from the Hunt Martin 1-15 well, grouped into electrofacies by order of magnitude of permeability.

trofacies types (Figure 5) shows the following trends with increasing permeability: decreasing R_{MSFL}, R_{LLD}, and ρ_b, and increasing Δt and ϕ_N. The strength of these correlations can be seen by plotting the average geophysical log values for each electrobed vs the average hydraulic parameter values. These plots are shown in Figures 8A-E.

Vertical and horizontal bars for the data points indicate the range of the data within each electrobed. The significant variability in porosity and permeability mentioned earlier is evident in these plots. However, the correlation is strengthened by using average values within each electrobed.

Conclusions

A preliminary examination of geophysical log data from two wells cored within the upper portion of the St. Peter Sandstone indicates that a strong correlation exists between the electrofacies types and porosity and permeability determined by core analyses. These findings support the idea that geophysical logs can be used to estimate average values for hydraulic parameters over discrete depth intervals.

Of the eight log parameters used to determine electrofacies types, five showed strong sensitivity to variations in porosity and permeability in both of

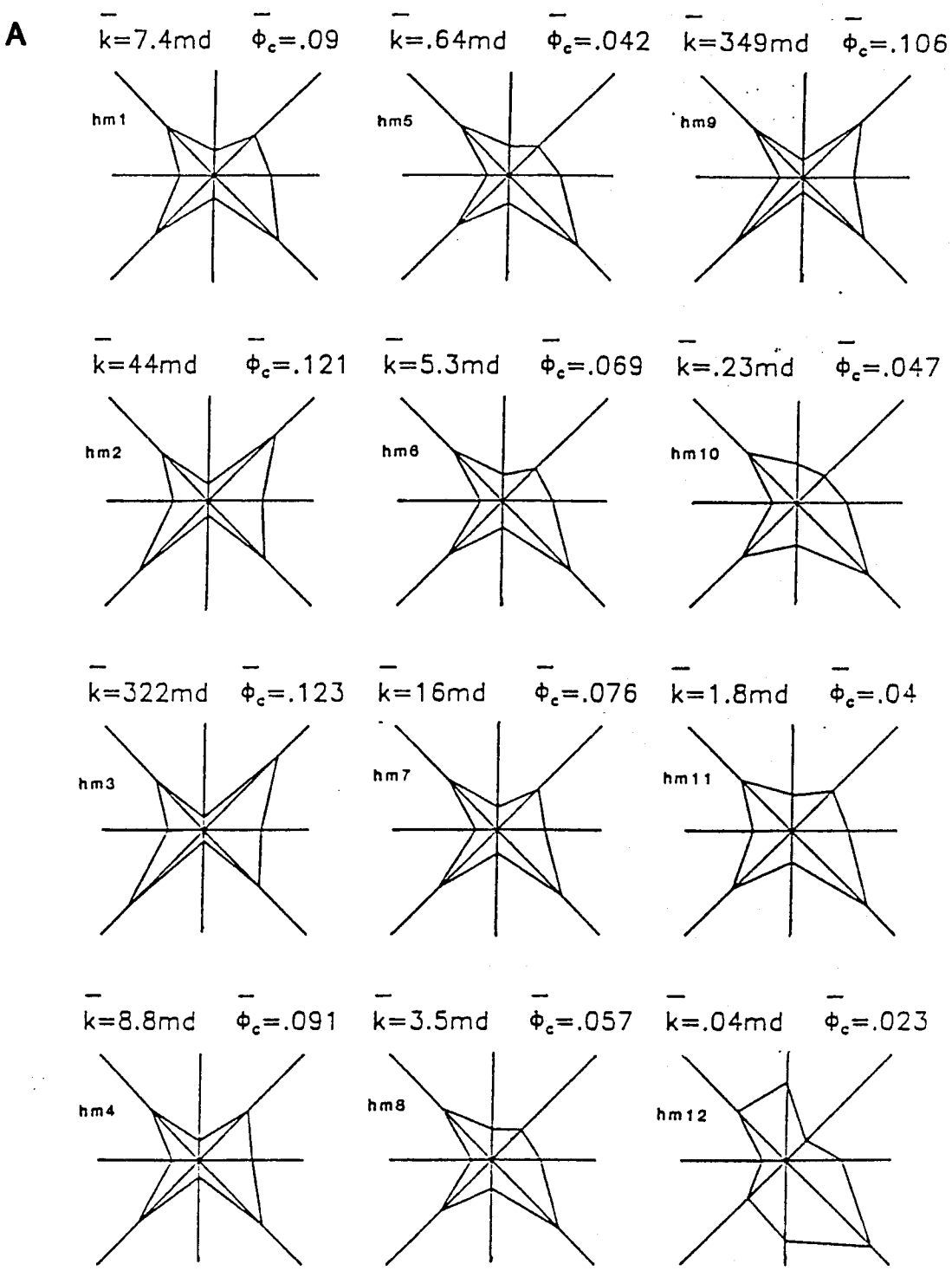

Figure 6. Characteristic shapes corresponding to each zone or electrobed from the Hunt Martin 1-15 well (see Figure 4). The plots are in order of increasing depth down the columns from left to right. Mean values for core porosity and permeability

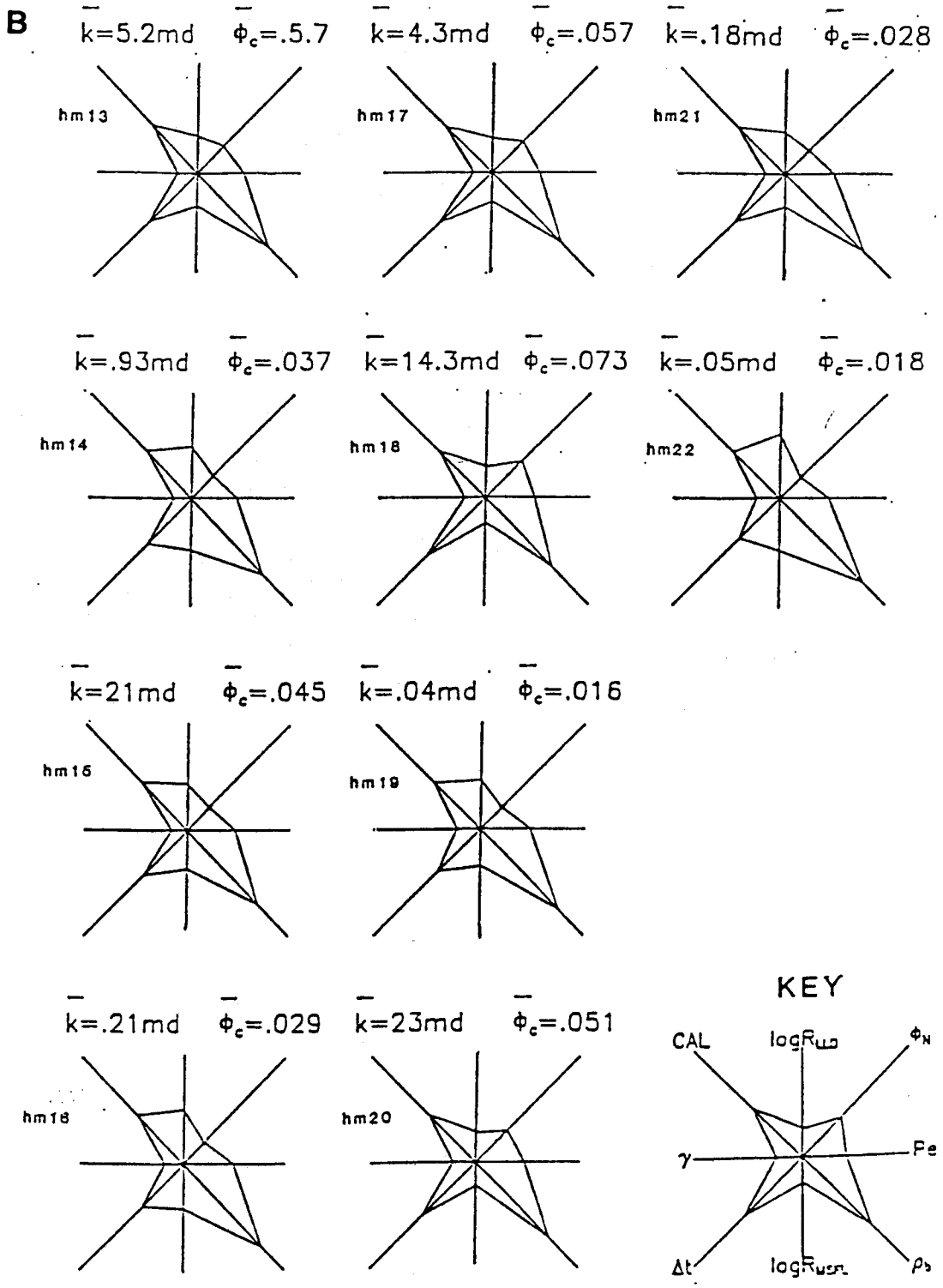

from corresponding log intervals are shown above each diagram. Note the similarities in shape for a given range of hydraulic parameter values. The key for the axis labels is shown above.

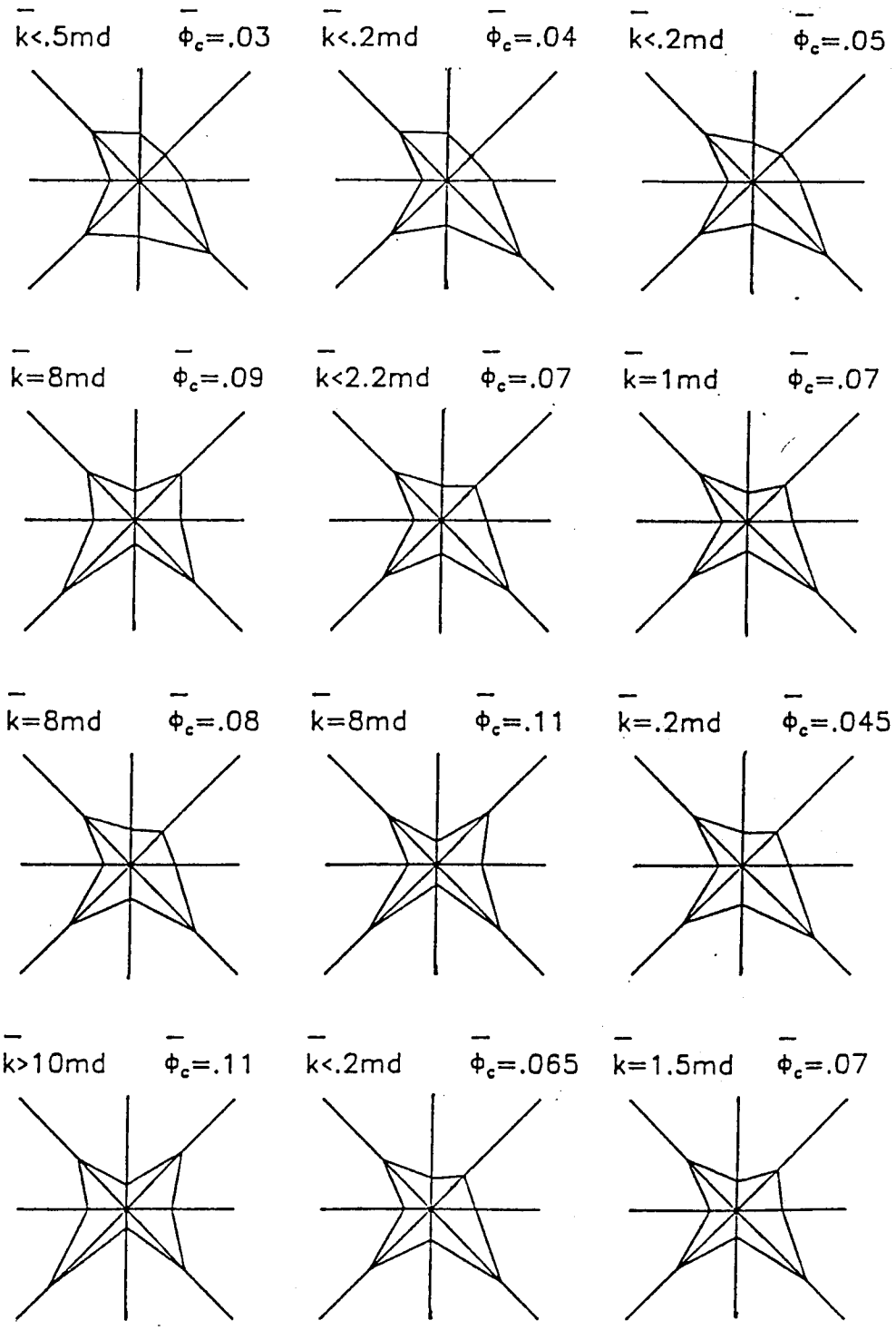

Figure 7. Characteristic shapes from zonation of the Patrick Gilde 1-25 well. Porosity and permeability variations are not as pronounced as in the Hunt Martin 1-15 well (Figure 5), but the evolution of the curves with increasing porosity and permeability is consistent between wells. (see Figure 6B for key.)

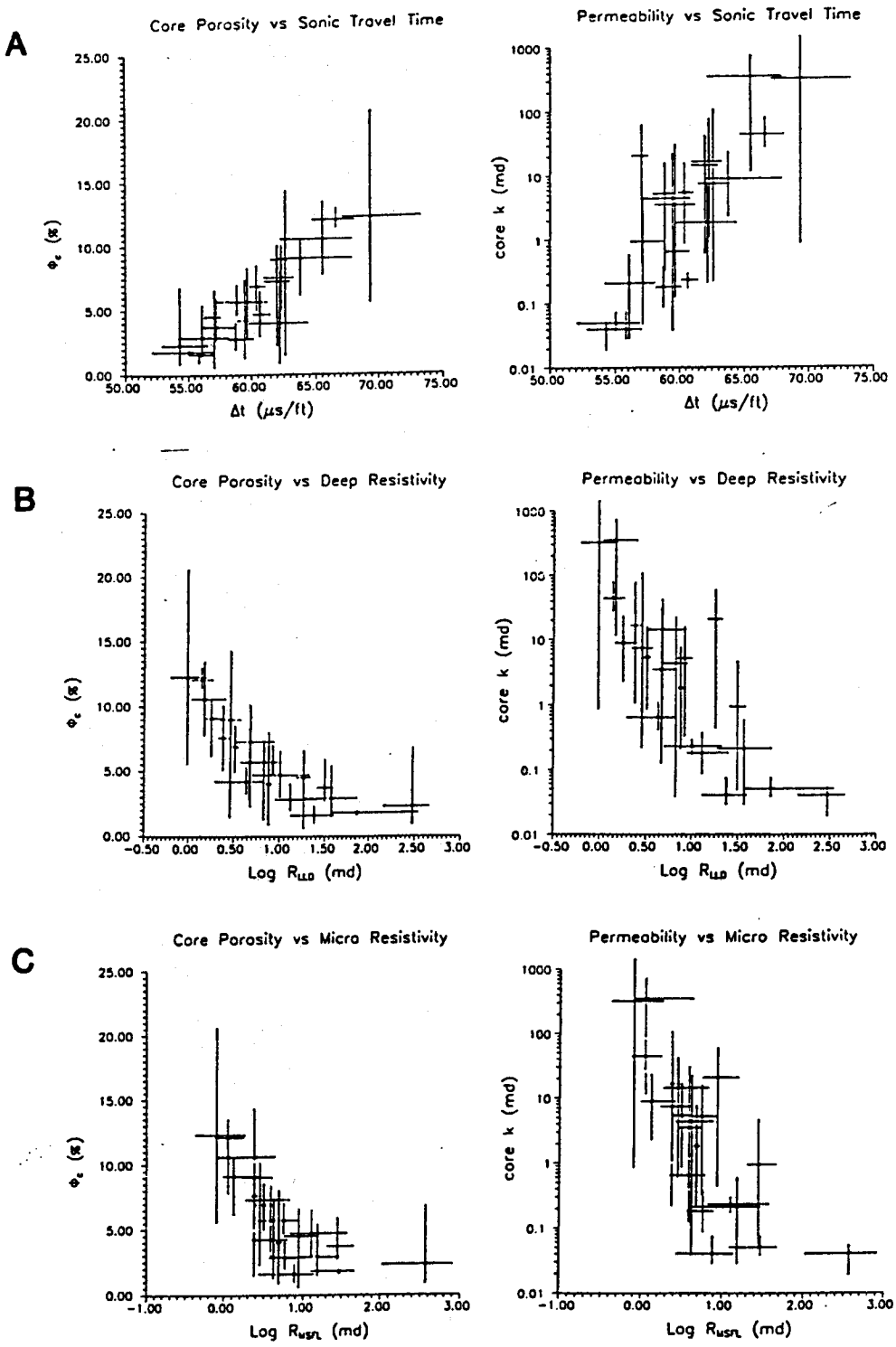

Figure 8. Mean values of hydraulic parameters plotted against mean values for individual geophysical log parameters. Each data point corresponds to an electrobed within the Hunt Martin 1-15 well (Figures 4-6). Vertical and horizontal bars indicate minimum and maximum values and demonstrate the

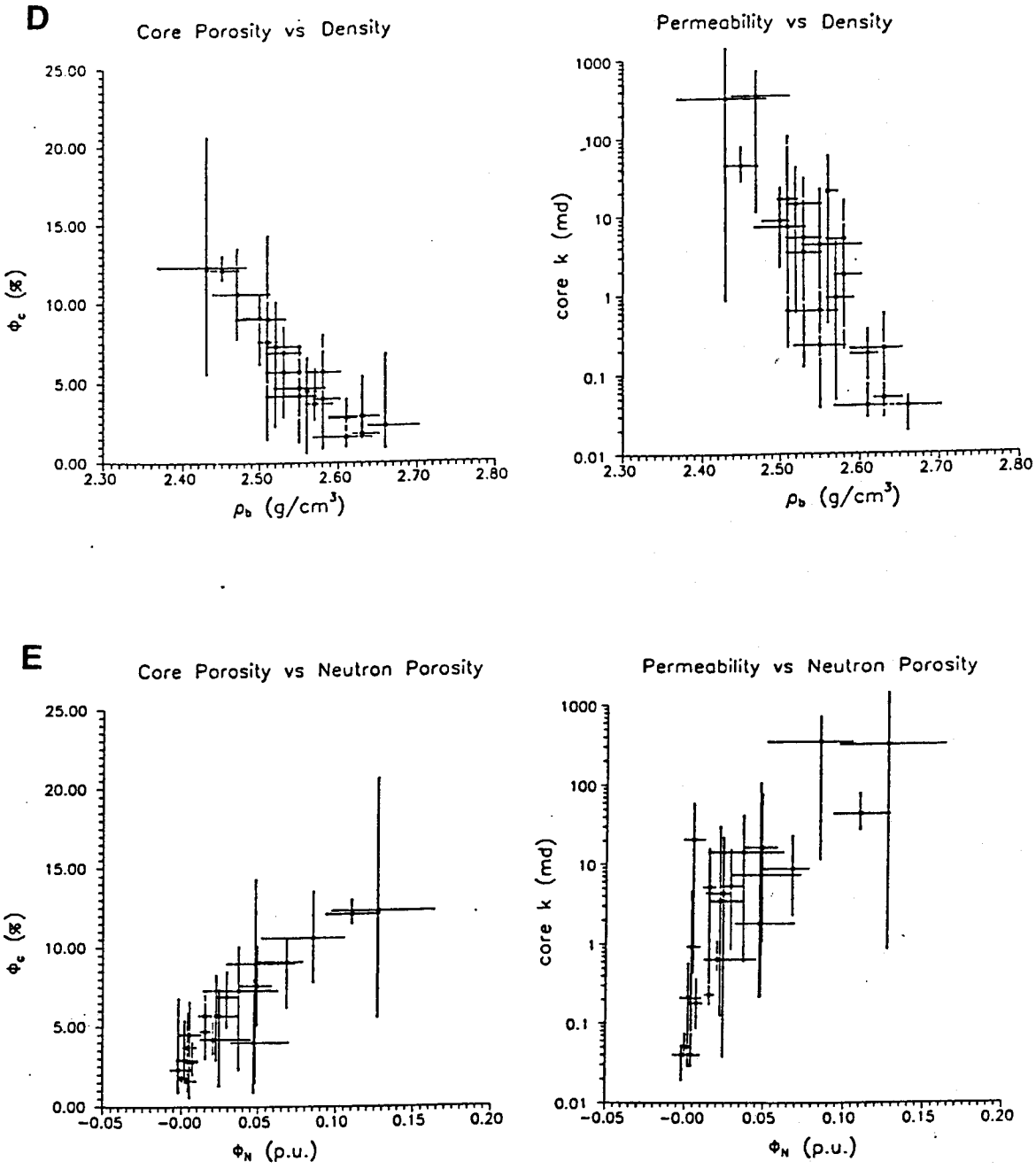

wide range of variability within the depth interval corresponding to individual electrobeds. Despite this variability, the mean values show distinctive trends. Those log parameters which did not correlate well with the hydraulic parameters are not shown.

the wells examined: microresistivity, deep resistivity, sonic travel time, neutron porosity, and compensated density. The other three parameters (caliper, gamma, and Pe) differed between the two wells and did not correlate well with variations in hydraulic properties.

The electrofacies associated with very low porosity and permeability are also associated with zones of stylolitization and diagenetic banding, suggesting diagenetic control of tight permeability consistent with the formation of pressure seals. This observation suggests that the technique of electrofacies identification has potential for identifying the location and extent of these pressure seals, even where abnormal pressuring no longer exists.

Future work will focus on the incorporation of additional well data within the upper part of the St. Peter Sandstone as well as the deeper facies. Automatic zonation will be used to apply objective and consistent criteria to the log segmentation process.

Unlike the initial test described in this paper, log segments will be clustered into electrofacies according to their geophysical characteristics, rather than their hydraulic characteristics. Discriminant analysis will then be applied to characterize the multivariate log response within each electrofacies and to provide a means for classifying additional geophysical log data. Correlations between electrofacies types and the associated porosities and permeabilities will then be used to estimate these parameters on the basis of electrofacies membership.

Once the quantitative statistical analysis has been completed, the predictive capability of this method will be tested in locations where other core is available. The method will also be tested against RFT-determined permeabilities which sample a larger volume than the core plugs and provide measurements under in situ conditions.

Acknowledgements

This work was supported by a grant from the Gas Research Institute. Core analyses and digital log data were provided by Western Michigan University. P. Drzewiecki and R. Vandry supplied the necessary core descriptions.

Gerilynn R. Moline is currently pursuing a PhD in hydrogeology at the University of Wisconsin-Madison (Department of Geology and Geophysics, University of Wisconsin-Madison, 1215 W. Dayton, Madison, WI 53706, USA). She received a BA in geology from the University of Southern Maine in 1986 and an MS in geophysics from the University of Wisconsin-Madison in 1989. Her current research focuses on hydrogeological modeling of deep basin pressure compartments.

Jean M. Bahr is an assistant professor in the Department of Geology and Geophysics at the University of Wisconsin-Madison (Department of Geology and Geophysics, University of Wisconsin-Madison, 1215 W. Dayton, Madison, WI 53706, USA). She has experience in geotechnical consulting and as a hydrologist with the US Geological Survey. Her current research interests include fluid flow and solute transport in shallow and deep systems.

Lisa D. Shepherd is an MS student in hydrogeology at the University of Wisconsin-Madison (Department of Geology and Geophysics, University of Wisconsin-Madison, 1215 W. Dayton, Madison, WI 53706, USA). She received her BA in geology from Carleton College in 1987. She has experience at the Water Resources Division of the US Geological Survey

working on geothermal and subsidence projects.

References

Asquith, G.B. 1982. Basic Well Log Analysis for Geologists. (ed. M.K. Horn). Am. Assoc. of Petrol. Geol.

Bahr, J.M. 1989. Evaluation of pressure distribution in the St. Peter Sandstone, Michigan Basin (Abs.). EOS, Trans. Am. Geophys. Union, v. 10(43), p.1097.

Burke, J., R. Campbell and A. Schmidt. 1969. The litho-porosity crossplot. Presented at the 10th Annual Logging Symposium, SPWLA, May 25-28, 1969.

Clavier, C. and D.H. Rust. 1976. MID Plot: a new lithology technique. The Log Analyst, v. 17(6), pp. 16-24.

Moore, R.C. 1949. The meaning of facies. Geol. Soc. of Am., Mem. 39, pp. 1-34.

Serra, O. 1984. Fundamentals of Well-Log Interpretation. Vol. 1: The Acquisition of Logging Data. Developments in Petroleum Science, v. 15A. Elsevier.

Serra, O. 1986. Fundamentals of Well-Log Interpretation. Vol. 2: The Interpretation of Logging Data. Developments in Petroleum Science, v. 15B. Elsevier.

Shepherd, L.D., J.M. Bahr, and G.R. Moline. 1991. Determination of scales of porosity variability through the use of image analysis. In Parameter Identification and Estimation for Aquifer and Reservoir Characterization (ed. S. Bachu). Proc. 5th Canadian/American Conf. on Hydrogeology. National Water Well Association, Dublin, Ohio. (this volume).

Regionalized Classification: Ideas and Applications

by Geoffrey C. Bohling , Jan Harff , and John C. Davis

Abstract

Regionalized classification involves mapping the results of a multivariate classification of a set of observations onto the physical space from which the observations were taken. The process identifies optimal boundaries between physically contiguous regions which are homogeneous in the statistical properties of the observations within them. The vector of observations at each observation point in space is used to estimate the probability of membership in each class at that point. The probability functions for the different classes are interpolated to a regular grid and compared in order to produce a map of class membership. It is also possible to produce a map of the probability of correct classification. The sharpness of the probability transitions at regional boundaries is a function of the degree of heterogeneity of the underlying variables in the boundary regions and of the density of observations.

An example based on groundwater chemistry data from the upper Dakota aquifer in western and central Kansas is used to illustrate the basic principles of regionalized classification.

Introduction

Many problems in hydrogeology and reservoir engineering involve an attempt to discretize space into regions which are relatively homogeneous in the statistical properties of some set of variables measured within them. For example, a researcher may wish to determine the optimal zonation of aquifer transmissivity for a groundwater flow model, or identify regions of distinct groundwater chemistry for a regional groundwater system. Regionalized classification is a technique which provides a quantitative means of transferring a multivariate classification of a set of observations onto the physical space from which the observations were taken.

Figure 1 illustrates the basic idea of regionalized classification. Two variables, A and B, are measured at a number of wells distributed throughout a study area. These observations can be plotted in variable space and classified by statistical techniques such as agglomerative cluster analysis. This process, referred to below as typification, might be used to identify, say, three classes of interest. The classes identified contain observations that are simultaneously as similar as possible to other observations in the same class and as distinct as possible from observations in other classes. Each observation can then be assigned a probability of membership in each class, which is essentially a transformation of the distance from each observation to a given group mean in variable space. Because the probabilities are smooth functions of spatially continuous variables, they can be interpolated to a regular grid in physical space and contoured. Comparison of the probability maps

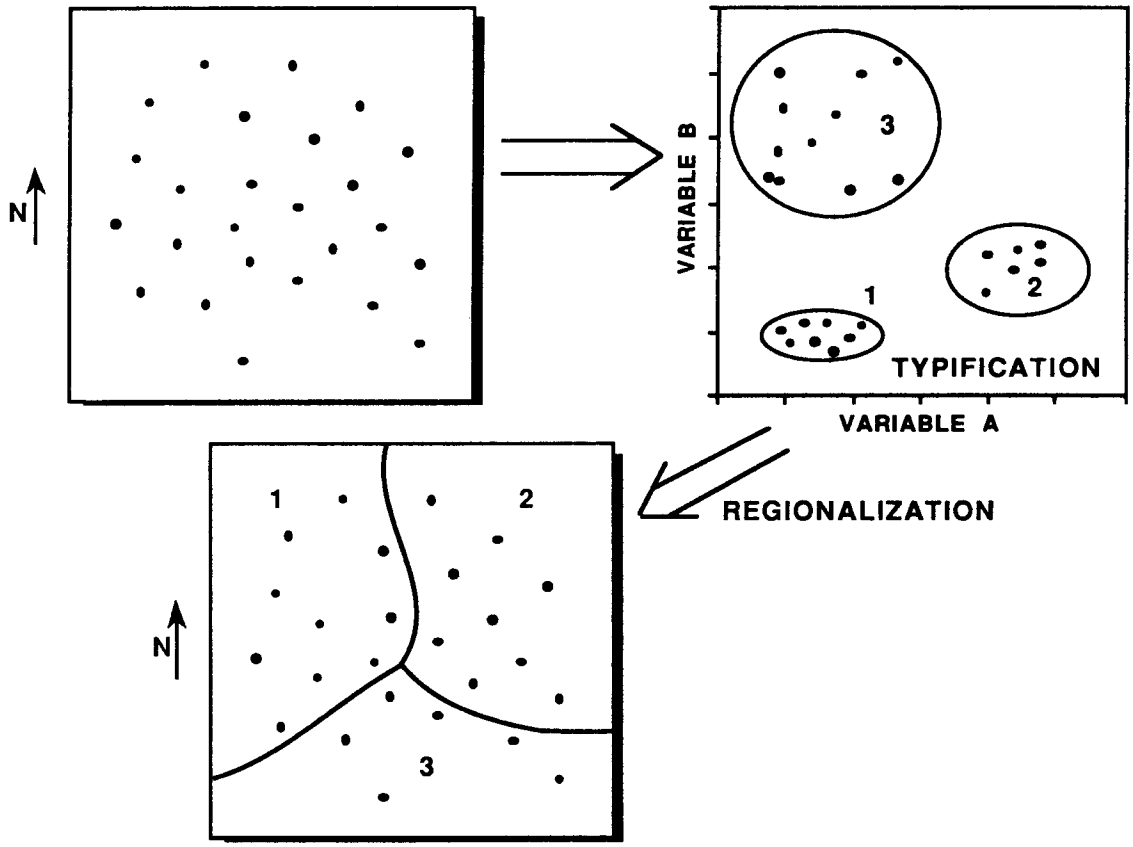

Figure 1. Schematic diagram of regionalized classification.

for different classes provides estimates of the locations of the boundaries between classes. This last step is the essential feature of regionalized classification. For more detailed discussions of the theory of regionalized classification, see Harff and Davis (1990) and Harff et al. (1990).

In many studies, a subset of the complete set of variables may have to be identified for use in the typification and regionalization processes. Thus, regionalized classification consists of three steps, variable selection, typification and regionalization. The variable selection process depends on the goals of the study. In some studies, regionalized classification may be used to explore the simultaneous variation of a number of equally important variables. In others there may be one variable of primary interest and a set of candidate explanatory variables for this target variable.

Here, the discussion of regionalized classification will be illustrated with an example involving groundwater chemistry data from the upper Dakota aquifer in western and central Kansas. The upper Dakota aquifer consists of sandstone in the Cretaceous Dakota Formation. This data is provided by the Kansas Geological Survey's ongoing Dakota aquifer program, a multidisciplinary effort to better

understand the resource potential of the Dakota aquifer in Kansas. The Dakota aquifer project is discussed in Macfarlane et al. (1990).

Variable Selection

Variable selection may be required to reduce computational effort or to avoid linear dependence among the variables used. In a problem involving a target variable, such as aquifer transmissivity, the researcher should try to identify variables which best explain the variation of the target variable, using statistical techniques such as discriminant analysis or multiple regression. For studies in which the simultaneous variation of a number of variables is of interest, techniques such as principal components analysis can be used to select a subset of important variables. Of course, expert appraisal may often be the best source of information for identifying the important variables.

A practical consideration in the variable selection process is the availability of data. Measurements on certain variables may be available at a large number of wells while others may be represented by relatively few observations. In particular, observations on a target variable may be more sparse than observations on the possible explanatory variables. For example, the data set may contain a limited number of observations on the hydraulic conductivity of a certain stratigraphic unit but a much larger number of observations on certain lithological properties of the unit which might be correlated with the conductivity. One approach to use in this situation is to perform the typification process using a subset of observations for which all the important variables are available. The target variable itself could be included in the typification. The regionalization process could then be performed using a more widely available subset of the typifying variables. In other words, the assignment of probabilities of class membership would be performed in a subspace of that used for typification.

In the Dakota aquifer example used in this paper, observations on six major ions, Ca, Mg, Na, HCO_3, SO_4 and Cl, are used for both the typification and regionalization processes. These were chosen for purposes of illustration.

Typification

Identification of the classes in variable space may be based on *a priori* descriptions of the classes or *a priori* assignments of each observation to a class. However, in our studies we have used agglomerative cluster analysis to identify the class divisions based on actual observations. For a discussion of clustering techniques see Davis (1986). Cluster analysis begins by computing the distances (or some other measure of similarity) in variable space between the individual observations. The most similar observations are then joined together to form a cluster. This cluster becomes a single object and the distances from all the observations to this cluster are computed. The two most similar objects (observations and/or clusters) in the new set are then joined in an identical fashion. The process continues until all objects have been linked.

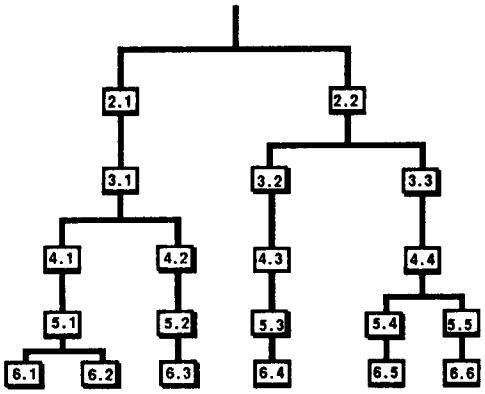

Figure 2. Dendrogram for two- through six-class levels of the hierarchical cluster analysis based on concentrations of six major ions from 217 wells in the upper Dakota aquifer. Classes are ordered from left to right on increasing Na (or Cl).

The clustering process can be represented with a dendrogram. The dendrogram for the Dakota aquifer geochemical data is shown in Figure 2. Class divisions are shown down to the six-class level. More dissimilar objects are joined as one moves up the dendrogram. In this example, the original data set was thinned before clustering was performed. Only one well from each township and range was used because observations which are tightly clustered in physical space would tend to represent a disproportionately large sample from a single cluster in variable space. Also, only wells with observations on all six variables could be used in the cluster analysis. Thus, 217 of the original 780 wells were used in the typification process.

Figure 3 shows the basic statistics of each class for the two-, four-, and six-class levels of the dendrogram. The concentrations, in mg/l, were converted to natural logs and then standardized before clustering. It is important to standardize each variable to zero mean and unit variance before the clustering process is performed, so that only relative and not absolute magnitudes of variation influence the clustering. The conversion of concentrations to natural logs was performed because concentrations of solutes in groundwater tend to be better represented by lognormal distributions than by normal distributions. In Figure 3, the groups have been ordered from left to right on increasing Na (or Cl) concentration. This is also true of the dendrogram in Figure 2, so that there is a direct correspondence between the group numbering on the two figures. This ordering is almost the same as the ordering on total dissolved solids (TDS), except that on the four-group level, group 2 is slightly higher in TDS than group 3; this also applies to groups 3 and 4 at the six-group level. However, the difference in TDS between these two groups is not significant. The means are plotted with ± one standard deviation error bars.

The characterization of the clusters shown in Figure 3 is based on only the first two moments of the data in each cluster. This is not intended to imply that the data in all the clusters are normally distributed (implying lognormally distributed concentrations). Some clusters exhibit significant deviations from normality. However, the set of plots shown in Figure 3 do show essentially the same information about the patterns of divisions as a corresponding set of (nonparametric) box plots.

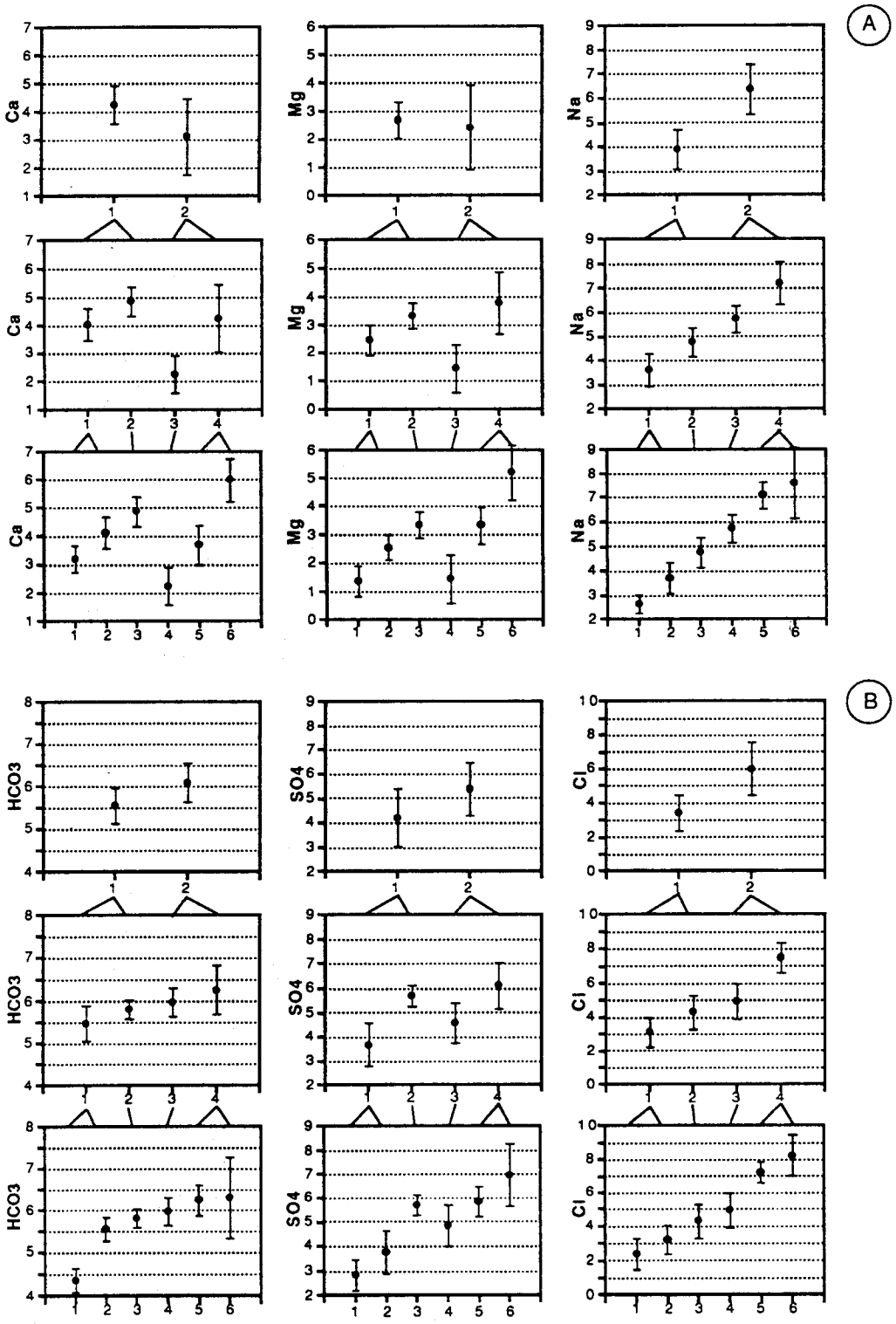

Figure 3. Statistics of classes on two-, four- and six-class levels for A. cations and B. anions. Scales shown are in natural logs of concentration in mg/l. Note the ranges of the scales are not the same across variables. Ordering of groups is the same as in the dendrogram in Figure 2.

The plots show that Na and Cl are the primary variables influencing the division of the observations into two groups. Similarly, the plots give some sense of the relative influence of different variables on the division of each group into subgroups. For instance, SO_4 exerts a major influence on the division of group 1 at the two-group level into groups 1 and 2 at the four-group level. Groups 1 and 6 at the six-group level are extreme groups and are both represented by only a few wells (in the typification set). Group 1 contains only seven wells, while group 6 has only ten.

Regionalization

The essential feature of regionalized classification is the development of a formal process for transferring the group memberships identified in variable space to the physical space from which the observations were taken. That is, the optimal locations of boundaries between different classes must be mapped. This task is accomplished in the following fashion. Every observation (well) can be assigned a probability of membership in each of the classes identified in the typification process. This probability is essentially a transformation of the Mahalonobis distance between the observation and a given group mean. The Mahalonobis distance is a standardized distance in variable space (Davis, 1986). The probability estimates used here are derived from Bayes' theorem and are based on the assumption that the identified clusters are drawn from multivariate normal distributions with equal variances (Harff and Davis, 1990).

As mentioned above, some of the identified clusters do violate the assumption of normality. Also, there are some statistically significant differences in variance among clusters. However, the regionalization technique is fairly robust. Violations of the assumption of equal variances among the clusters will tend to cause inflated estimates of the probability of misclassification, but the mapped pattern of class memberships will not be greatly affected. The effects of violations of the assumption of normality are somewhat harder to predict. However, it is expected that incorporation of higher moments in the estimation of probabilities of class membership would not significantly alter the general pattern of classification results.

The probability of membership in each class is a spatially continuous function, because it is a smooth function of variables which are themselves spatially continuous. Thus, each probability function can be interpolated to a regular grid. Figure 4A shows the probability of membership in class 1 of the two-group classification for the Dakota aquifer data. Figure 4B shows the probability of membership in class 2. Because there are only two classes and the probabilities of membership in all classes must sum to unity, the two probability functions are complementary. In general, probability of membership in class 1 is high in the southern and eastern portions of the study region and probability of membership in class 2 is high in the northern and western portions.

Each node in the grid is assigned to the class with the highest probability at that node.

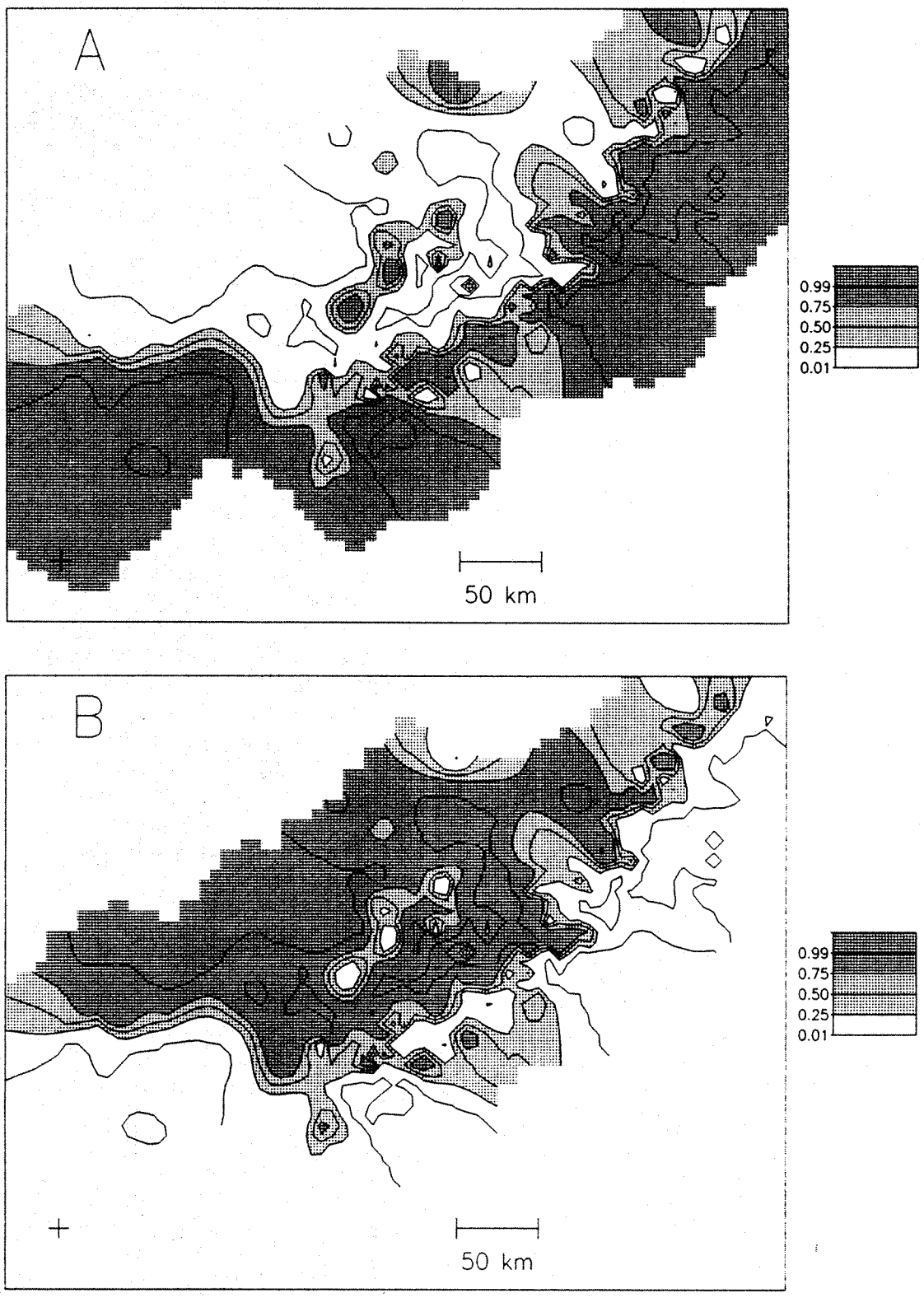

Figure 4. Probability of membership in A. group 1 and B. group 2 of two-group classification of Dakota aquifer major ion data. Contours are at the 1, 25, 50, 75 and 99% probability levels. The plus sign indicates the southwest corner of Kansas.

Memberships can then be coded and presented as a map, as shown in Figure 5A for the two-group classification. In addition, a map can be produced which shows the probability of membership in the class having the highest probability of membership at any given node, as shown in Figure 5B. This gives a map of probability of correct classification, a useful supplement to the classification map. The boundaries between classes on the classification map occur where probability functions for individual classes cross. These boundaries appear as valleys on the maximum probability map, Figure 5B. The boundary regions are areas of maximum uncertainty of classification.

The sharpness of the boundaries are determined by several factors, including the spatial structure of the underlying variables and the distribution of observations across the map area. In particular, if there is a fairly distinct transition or discontinuity in the variables under consideration and this transition is well documented by a good distribution of observations, then a sharp boundary will appear on the probability map. Less distinct transitions in the variables or more sparsely distributed observations will lead to more uncertain placement of the boundaries.

There are two different ways of producing the probability estimates at the grid nodes. The method used here is to determine the probability of membership in each class at each well, based on its vector of observations, and then interpolate the probabilities to a regular grid. This involves interpolating as many functions as there are classes. Another option would be to actually interpolate the individual variables to a regular grid and then assign probabilities of membership to each grid node based on the interpolated vector of observations at that node. The latter method has several advantages. First, it would help to overcome the problem of missing values on individual variables, because the interpolation process would help to fill in the holes on observations of any particular variable. The first method can only assign probabilities to wells with complete observation vectors, unless one uses mean substitution for the variables with missing values. The second method could also be based on sophisticated techniques such as multivariate kriging, possibly allowing a more optimal representation of the spatial characteristics of the variables. However, because there often may be more variables than classes, the second technique would usually be more computationally intensive than the first, especially if multivariate kriging were used.

Dakota Aquifer Regionalization

Figures 5, 6 and 7 show the results of the regionalization process for the two-, four- and six-group levels for the major ion chemistry of the Dakota aquifer. The wells that were used in the typification process are posted as solid triangles. Those which were not used for typification, but which were used in the regionalization process, are shown as open triangles. Figure 3 should be consulted as a key to the meanings of the identified classes.

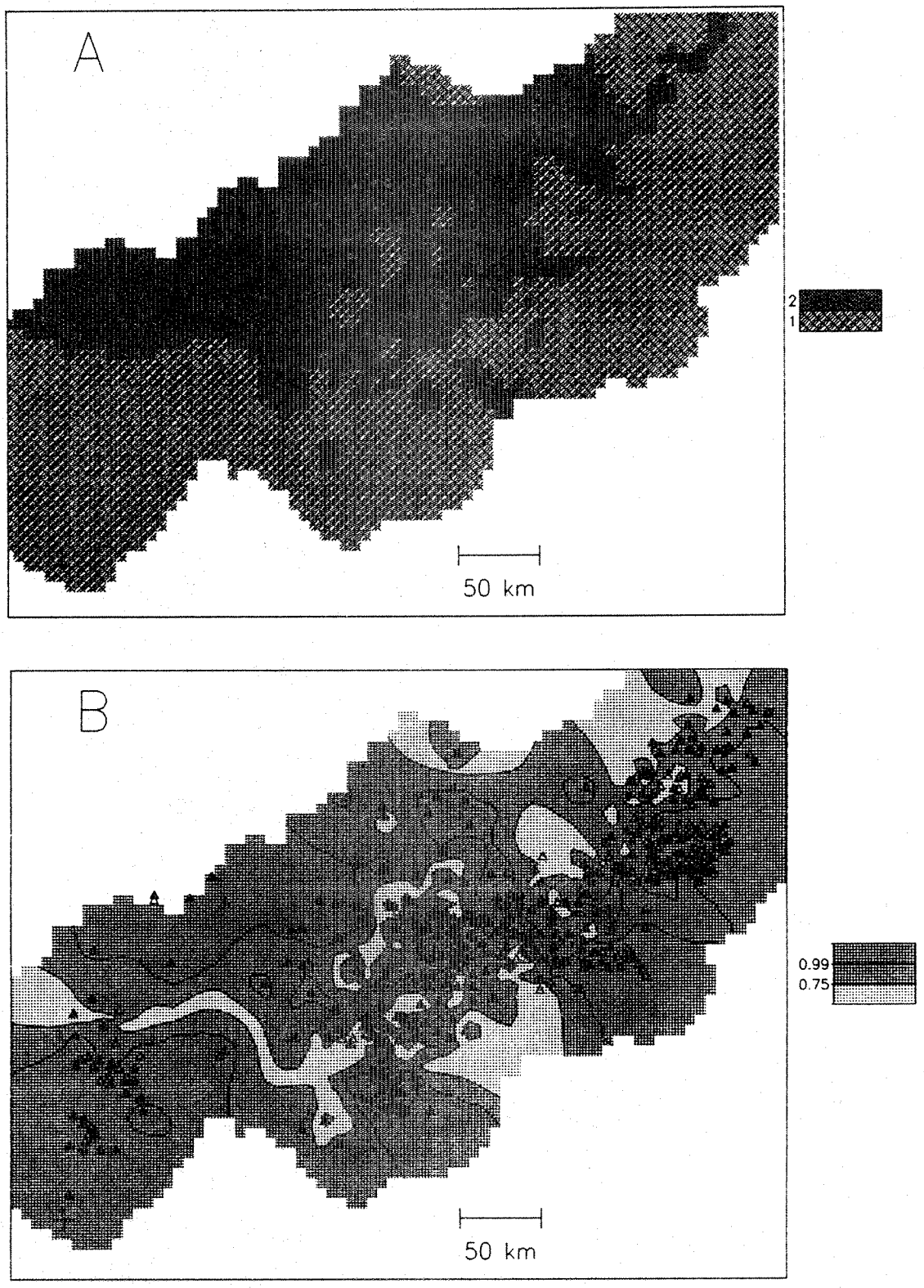

Figure 5. Maps of A. classification and B. probability of correct classification for two-group classification of Dakota aquifer major ion data. Probability contours are at the 75 and 99% levels. Numbering of classes is the same as on Figure 3.

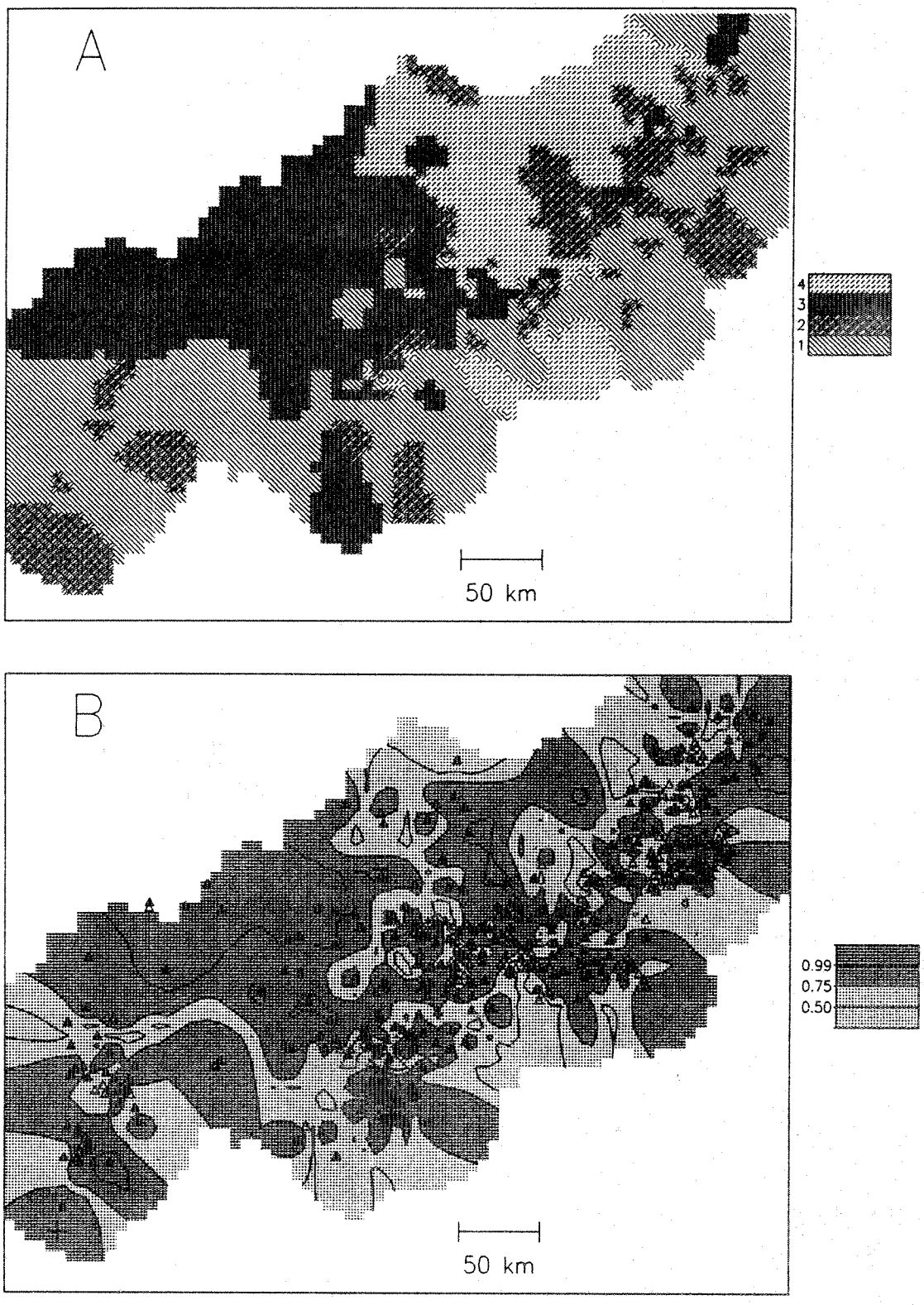

Figure 6. Maps of A. classification and B. probability of correct classification for four-group classification of Dakota aquifer major ion data. Probability contours are at the 50, 75 and 99% levels.

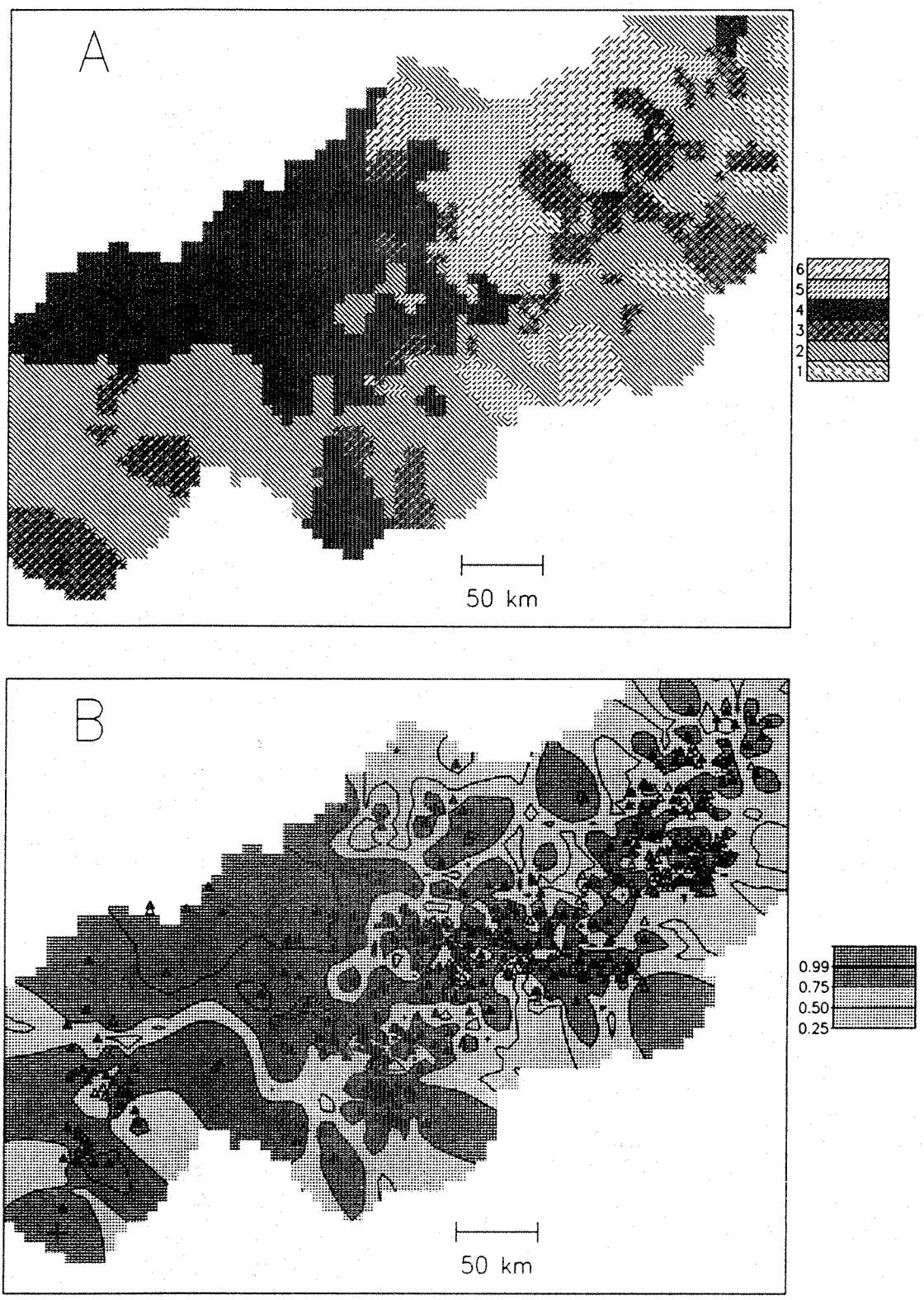

Figure 7. Maps of A. classification and B. probability of correct classification for six-group classification of Dakota aquifer major ion data. Probability contours are at the 25, 50, 75 and 99% levels.

The initial division into two groups (Figure 5) reveals a fairly sharp distinction between the waters associated with the outcrop/subcrop region of the Dakota aquifer (group 1), and those associated with the deeper, confined portions (group 2). Calcium-bicarbonate waters dominate in the outcrop zone because of solution of carbonate minerals and flushing of saline waters by fresh water recharge. The primary source of salt water in the deeper portions of the aquifer is upward flow from underlying aquifers in the Permian that contain evaporites (Macfarlane et al., 1990).

In the western portion of the study area, the four-group classification (Figure 6) preserves the distinction between waters associated with the outcrop/subcrop region and those associated with deeper portions of the aquifer. Here, outcrop/subcrop waters are represented by groups 1 and 2, with group 2 having somewhat higher concentrations overall on all six constituents, especially SO_4. Group 4, which is dominated by Na and Cl, shows up both in the northern and southern portions of the map. This coincides with a region where the upper Dakota aquifer is hydraulically connected with salt water-bearing aquifers in the Permian Cedar Hills Sandstone. Elsewhere, the Cedar Hills Sandstone is overlain by less permeable Permian strata (Macfarlane et al., 1990).

The four-group and six-group (Figure 7) classifications reveal the complicated pattern of water types in the eastern portion of the study area. In this area, the Upper Cretaceous aquitard overlying the Dakota aquifer is dissected by river valleys. In these valleys, the Dakota aquifer is hydraulically connected to the alluvial aquifers. Thus, there is considerable local variation in water quality. This is reflected in the low probabilities of correct classification in the eastern portions of the the four- and six-group probability maps.

Conclusions

The regionalization process can be applied to any set of observations on a number of variables measured at different points in space. The example discussed in this paper emphasizes the use of regionalized classification to produce maps summarizing a set of multivariate data. In this instance, a similar and perhaps more straightforward map could have been produced by simply assigning each well to a certain water type and posting an appropriate water type symbol at each well (Macfarlane et al., 1990). The assignment to classes or types could be based on pre-defined criteria or, as here, on the results of a cluster analysis.

The benefits of regionalized classification become more apparent when determining the locations of continuous boundaries between classes. An obvious application to hydrogeology and reservoir engineering would use regionalized classification to determine optimal zonation of a flow and/or transport model with spatially distributed parameters. Regionalized classification techniques could be used to assign a class membership to each node in a finite difference or finite element model. Each contiguous region in a

certain class would correspond to a zone of the model.

Regionalized classification is especially promising for problems in which a particular variable (such as aquifer transmissivity) is of primary interest, but there are relatively few observations of this variable in the data set. The multivariate classification can be based on the limited number of observations for which the variable of interest is measured. The entire set of observations can then be assigned to classes using a more widely available subset of the variables used in the classification process.

Acknowledgements

The authors thank the members of the Kansas Geological Survey's Dakota aquifer program for providing the data used in this study and for their interaction and comments concerning both the analysis and the manuscript.

Geoffrey Bohling earned a BA in English and a BSc in Physics-Geophysics from the University of Kansas in 1986. He received an MSc in Geology, with a concentration in hydrogeology, from the University of Wisconsin-Madison in 1988. He is now a Research Assistant in the Mathematical Geology Section of the Kansas Geological Survey (1930 Constant Avenue, Campus West, The University of Kansas, Lawrence, KS 66047). He is pursuing research on aquifer parameter estimation and participating in various projects involving mathematical and statistical applications in geology.

Jan Harff, a geologist from Germany, spent the 1989 spring semester as Visiting Research Scientist at the Kansas Geological Survey. Dr. Harff received his geological training at Humboldt University in Berlin and Arndt University in Greifswald, where he earned his doctorate in 1974. The GDR Academy of Science awarded him the DSc in 1986, when he also received the A. G. Werner medal. He was the 1989 recipient of the Academy's Stammberger Prize. In Potsdam, Dr. Harff is Chief of the Mathematical Geology Department of the Central Institute for Physics of the Earth (Bereich Geologie, Zentralinstitut für Physik der Erde, O-1561 Potsdam, Federal Republic of Germany).

John C. Davis received his PhD in Geology from the University of Wyoming in 1967. Currently he is Senior Scientist and Chief of the Mathematical Geology Section at the Kansas Geological Survey (1930 Constant Avenue, Campus West, The University of Kansas, Lawrence, KS 66047) and Professor of Chemical and Petroleum Engineering at the University of Kansas. Dr. Davis authored Statistics and Data

Analysis in Geology, *co-authored* Display and Analysis of Spatial Data *and* Probability Methods in Oil Exploration, *contributed to 15 other texts and compendiums, and author/co-authored more than 90 scientific articles and reviews. He served as President of the International Association for Mathematical Geology from 1984-89, and was awarded their Krumbein Medal in 1987.*

References

Davis, J. C. 1986. Statistics and Data Analysis in Geology. John Wiley and Sons.

Harff, J. and J. C. Davis. 1990. Regionalization in geology by multivariate classification. Math. Geol., v. 22, no. 5, pp. 573-588.

Harff, J., W. Eiserbeck, K. Hoth and J. Springer. 1990. Computer-assisted basin analysis and regionalization aid the search for oil and gas. Geobyte, v. 5, no. 3, pp. 11-15.

Macfarlane, P. A., D. O. Whittemore, M. A. Townsend, J. H. Doveton, V. J. Hamilton, W. G. Coyle III, A. Wade, G. L. Macpherson and R. D. Black. 1990. The Dakota Aquifer Program: Annual Report, FY89. Kansas Geol. Surv. Open-File Rep. 90-27.

State-of-the-Art Borehole Geophysics Applied to Hydrogeology

by Elliot N. Yearsley and Robert E. Crowder

Abstract

The application of borehole geophysics to hydrogeological problems is rapidly expanding, driven by the increased need for better in-situ characterization of ground water systems. A number of borehole geophysical technologies have recently emerged that are specifically developed to meet this need. This paper reviews those technologies, which include equipment and data processing capabilities that are new to the ground water industry, and existing borehole methods that have become particularly relevant in hydrogeological investigations.

For the purpose of this paper, these borehole geophysical applications are divided into three categories:

- Characterizing permeability profiles.
- Fracture analysis.
- Logging in the unsaturated zone.

Field examples demonstrate these applications, and briefly review their operational features. The field examples include full waveform sonic logs, flow meter surveys, borehole televiewer, and induction logging.

The primary focus of this paper is an overview of the state-of-the-art of borehole geophysical methods applied to hydrogeology. The paper's implicit theme is the documentation of the emerging awareness that ground water problems require borehole methods that are specifically developed to address issues in the ground water industry.

Introduction

The problem of subsurface interpretation and modeling requires the equally important components of geological intuition and information. Geological intuition must be earned through experience, and information is available from the rocks, well tests, or geophysics.

Geophysics has the capability for remote measurements of a much greater volume of the subsurface than other means of sampling or testing, and generally represents in-situ conditions. The science of geophysics has, over the years, revolutionized the petroleum industry to the extent that drilling a well without seismic control, or without obtaining geophysical well logs, is almost unthinkable. Managers in the petroleum industry understand that money spent on geophysics at the front end of a project pays for itself many times over.

Many of the advances in geophysics made in the petroleum industry can be converted to ground water applications. Two examples are reflection seismic methods applied to hazardous waste investigations (Irons and Lewis, 1990), and the application of full waveform sonic (FWS) analysis to fracture analysis (Paillet, 1982). Both these technologies, originally conceived in the petroleum industry, now have the capability to make profound contributions to hydrogeology.

As in the case of FWS logs, other borehole geophysical measurements can make a meaningful transition from petroleum to hydrogeology, notably density measurements from which quantitative porosity values can be derived. However, because the operating conditions and type of information needed in ground water studies differ from the petroleum industry, distinct technology and methods must be developed for the former. With regard to borehole geophysics, this means smaller logging probes, more portable data acquisition systems, different combinations of logs, and interpretation techniques that target information germane to hydrogeological studies. In some cases this means completely new methods must be developed.

Studies in the unsaturated zone, for example, require measurements and log interpretation techniques that are relevant to partially saturated conditions, an issue which is never addressed in petroleum logging. Also, flow meter methods discussed in this paper were developed to meet a specific need in ground water investigations, namely that of characterizing the vertical variation in permeability in greater detail than conventional pump test methods. This need is relevant for water supply, where delineation of primary flow is important, and in contaminant transport problems, where description of hydraulic heterogeneities is a goal.

This paper will not cover the more conventional borehole geophysical applications which nevertheless make a critical contribution to the geological understanding and subsurface interpretation of ground water problems. These applications are aptly described by Keys (1988), whose work was conducted under the auspices of the U.S. Geological Survey Water Resources Division (USGS WRD). The fine technical work by the USGS WRD continues, particularly in the areas of flow meter studies and fracture characterization in crystalline rock.

The examples and discussions presented herein review the current (1991) state-of-the-art of selected borehole geophysical methods applied to hydrogeological investigations. For the purposes of this paper those methods are divided into three categories:

- Characterizing permeability profiles.
- Fracture analysis.
- Logging in the unsaturated zone.

Because recent developments in borehole geophysics applied to hydrogeology are too numerous for a single symposium paper, not all the new technology is discussed in this paper. Some of those methods not discussed or otherwise referenced herein include the use of magnetic susceptibility measurements in the correlation of ash flow tuffs (Balch et al., 1987), the dielectric tool as a porosity log (Collier, 1989), and completion evaluation of PVC-cased monitoring wells with geophysical density logging (Yearsley et al., 1991).

Methods in Characterizing Permeability Profiles

For ground water investigations concerned with contaminant transport the need for determining the vertical variation in permeability with better definition than conventional pump tests is discussed in a number of publications, including Molz et al. (1989). Further, the recognition of high permeability zones can often be the most significant aspect of site characterization or water supply investigations.

In this paper the term permeability is used as the description of the intrinsic flow property of rocks which is not necessarily constrained to saturated rock. Hydraulic conductivity is used when citing the work of others who have used that term in their papers, or where the assumption of full saturation has been made.

Borehole geophysical methods that have demonstrated recent success in determining permeability profiles in ground water studies include: flow meter methods, tube wave amplitude, and the single well electrical tracer (SWET) test, and will be discussed in that order.

Flow Meter Methods

The most direct method for determining permeability profiles is the use of flow meter methods. Flow meters are downhole instruments that measure the vertical velocity profile of fluid flow in a borehole, either under natural conditions or during withdrawal or injection. Flow meter logs can provide horizontal hydraulic conductivity (K) profiles derived from the Cooper-Jacob equation used frequently in well hydraulics. The primary assumptions in the use of this equation are aquifer homogeneity and horizontal flow. The assumption of homogeneity is much less restrictive for flow meters than for conventional well tests because flow meter measurements are made in greater vertical detail (i.e. digital data collected at .03 m intervals [0.1]).

The most common flow meter is the impeller type (described in Rehfeldt, 1989), which can resolve fluid velocities down to about 1.5-3.0 m/min (5-10 ft/min), and are therefore normally used in conjunction with pump tests. Hess (1986) described a heat-pulse flow meter that can resolve fluid velocities as low as .03 m/min (0.1 ft/min), and can therefore be applied to the measurement of natural flow or very low induced flow in a borehole.

Morin (1988) has presented a heat- pulse flow meter case history of remarkable simplicity. A test was performed which consisted of adjusting the injection rate into an open borehole so that the flow out of the borehole equaled the injection rate (constant head condition). The absence of natural flow within the borehole was confirmed with a heat-pulse flow meter survey previous to the injection test, and the injection rate was low enough (5.7 l/min [1.5 gpm]) such that laminar flow predominated in the borehole. These conditions allowed the reasonable assumption that the hydraulic head change

from natural conditions was a constant (i.e. a constant equal to the increased head of injection). This assumption can be justified by considering that: 1. there are negligible friction losses during injection for laminar flow, and 2. that no natural head differentials existed prior to injection. The fluid velocity profile was measured during injection, and knowledge of the constant head change and the borehole diameter (a caliper log was available) allowed the application of the Cooper-Jacob equation to the calculation of the hydraulic conductivity profile. The resulting product, a continuous vertical profile of horizontal K, was acquired relatively inexpensively without the need for cumbersome straddle-packer tests.

Impeller flow meters are more widely available than the heat-pulse type at the present time, and have produced some very useful results. Molz et al. (1989) compared hydraulic conductivity profiles derived from impeller flow meter measurements to multilevel slug tests and single well electrical tracer (SWET) tests performed in the same wells. In their work, impeller meter and pressure transducer surveys were made for natural conditions and during steady state pumping (withdrawal). The difference between these two sets of surveys provided the data from which the vertical variation in horizontal hydraulic conductivity could be determined.

Molz et al. (1989) stated in their conclusions that results from the three methods (impeller, multilevel slug, and SWET) were quite similar in overall nature and K distribution (Figure 1). These authors further stated that the impeller meter method appeared better able to detect zones of higher K than did the multilevel slug approach, and that of the three types of data, impeller meter data were the most convenient to obtain.

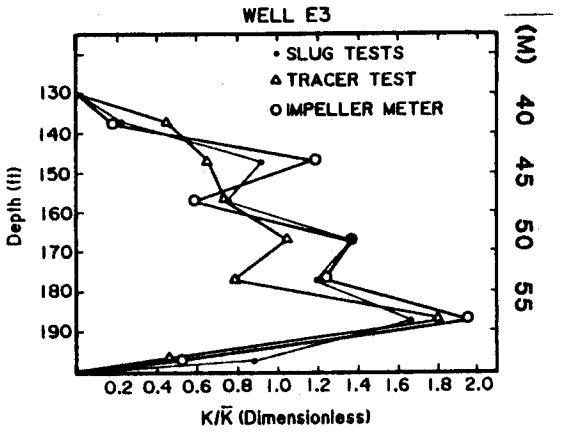

Figure 1. Comparison of multi-level slug, impeller flow meter, and single well electrical tracer data (Molz et al. 1989).

This paper will present an additional impeller flow meter example not previously published which demonstrates the delineation of K distribution for a multiple-screened completion in a water supply recharge well. This well is part of the Willows Water District (Arapahoe County, Colorado) recharge program which is designed to take off-peak treated surface water and inject it into deep non-tributary Denver Basin aquifers. Pump tests conducted in this well over a 215 m (700 ft) interval that consisted of 13 individual screened sections resulted in an average K of 1.6 m/d (5.2 ft/day) for the whole interval (Halepaska et al., 1990).

An impeller flow meter survey made during steady state pumping (withdrawal) provides flow data for the individual screened sections. The flow meter data is presented in Figure 2. Hydraulic conductivity was derived by calculating a constant of proportionality for each screened section between incremental flow per foot of screen and total discharge rate for the whole

interval, as given by the following (see Javandel and Witherspoon, 1969; or Molz et al., 1989):

$$K_i = C \times K_a$$

and, $$C = (Q_i/z_i)/(Q_p/B)$$

where:

C = constant of proportionality
K_a = average K for the whole interval (from a standard aquifer test)
K_i = K for the incremental screened section
z_i = incremental screened length
B = total length of screen
Q_i = flow rate for incremental screened section
Q_p = total discharge rate

It should be pointed out that the hydraulic conductivity results shown in Figure 2 are calculated based on the absence of natural flow. A static (non-pumping) impeller flow meter survey revealed that natural flow was indeed occurring in the wellbore prior to pumping. However, it was small compared to the pump rates during the impeller surveys and could therefore be neglected. The information regarding unequal aquifer heads was nonetheless valuable in terms of understanding natural conditions.

An operational issue important to keep in mind for impeller surveys which involve pumping is the requirement that the pump is temporarily removed while lowering the impeller instrument into the borehole. The pump must then be reinstalled for the test, removed again to retrieve the tool, and then reinstalled if other pumping is needed. Also, at least two pressure surveys along with the impeller surveys are needed for the quantitative calculation of hydraulic conductivity if significant natural flow exists.

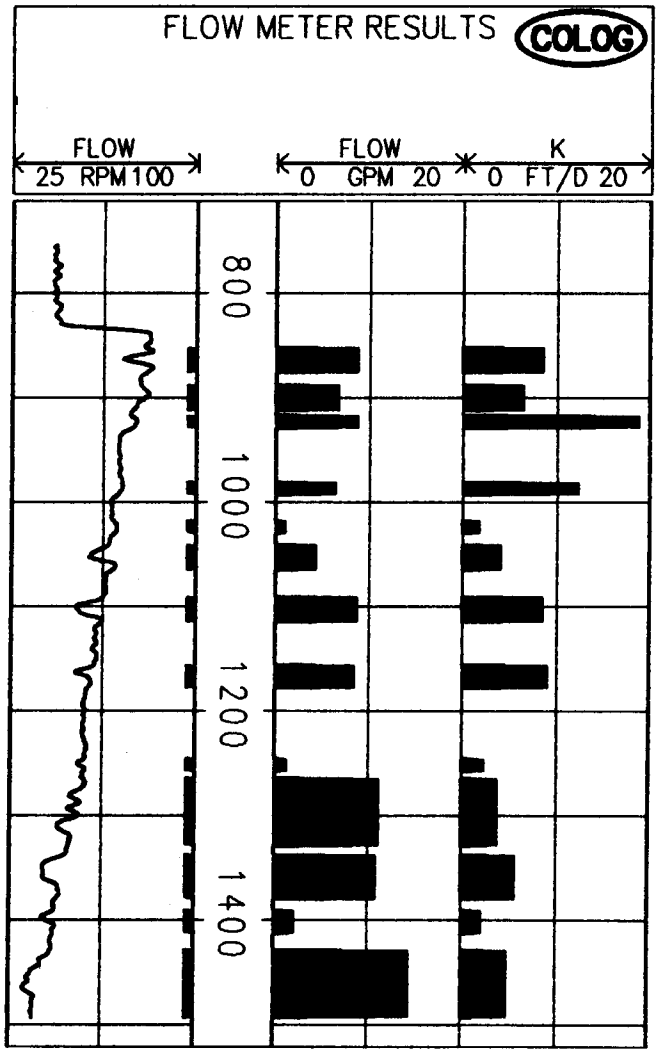

Figure 2. Impeller flow meter results for a multiple screened well. RPM is revolutions per minute of the impeller while logging. The black bars represent the magnitude of flow and hydraulic conductivity for each screened section.

Tube Wave Amplitude

Tube wave amplitude analysis from full waveform sonic logs provides promising insight into permeability variations measured in a borehole. Because no testing or pumping

is involved, this method has profound implications with regard to the economical appraisal of permeability profiles.

The full sonic waveform, recorded at downhole receivers in a borehole sonic probe, consists of interacting sonic waves generated by an acoustic energy pulse from the probe's transmitter. The propagation of these waves is controlled by the borehole wall/fluid interface, at which some types of waves are refracted and complicated wave reflections occur. An important wave which is present is the tube wave, which travels along the borehole wall and is sensitive to borehole wall permeability. Figure 3 illustrates an actual recorded wave with the compression and tube waves annotated.

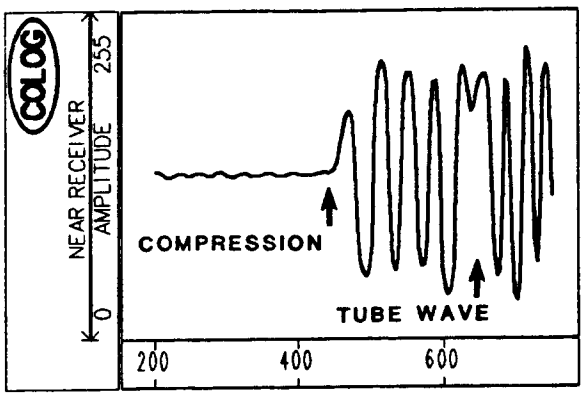

Figure 3: Full waveform to 800 μs, denoting the compression and tube waves.

Paillet and White (1982) presented theoretical work and field evidence that the amplitude content of the tube wave could be used to distinguish permeable fractures. Also, studies which focused on petroleum reservoirs (see for example Rosenbaum, 1974, or Williams et al., 1984) discussed tube wave (or Stonely wave) amplitude and permeability in porous rock. Crowder et al. (1991) have presented field examples of tube wave amplitude analysis applied to environmental and engineering investigations.

Though many complexities of tube wave attenuation related to permeability are not yet understood, the physical process is simple in concept. Tube wave energy is attenuated by fluid interaction between the borehole and the adjacent formation. Because open fractures or permeable porous media provide a path for this interaction, these conditions reduce the energy of the transmitted tube wave, resulting in lower tube wave amplitudes associated with more permeable rock.

Figure 4 shows the tube wave amplitude log and the variable density log (VDL) from a ground water monitoring well drilled in Tertiary fluvial sediments. The VDL is the vertically stacked display of the full waveforms and is characterized by its grey-scaled banded appearance which represents the amplitude variation of sonic waves. The velocity of the rock is indicated by the arrival time of the leading edge of the first black band.

In the example illustrated by Figure 4 the shale has a slower velocity as shown by later arrival times, the sandstone is faster, and the interbedded unit stands out because of its variable velocity profile. Note also on Figure 4 the lighter grey tone of the VDL in the sandstone interval from approximately 600 μs and later. This represents the lower amplitude of the tube wave portion of the wavetrain in that interval and is related to the higher permeability of the sandstone compared to the rock around it. The tube wave amplitude log (on the left) shows the qualitative permeability profile, with permeability increasing to the left.

The minimum tube wave values in Figure 4 are associated with the higher permeability sandstone, and the maximum tube wave

values are associated with the shale in the upper part of the borehole. Intermediate tube wave amplitudes are observed in the siltstone interval at the bottom of the well.

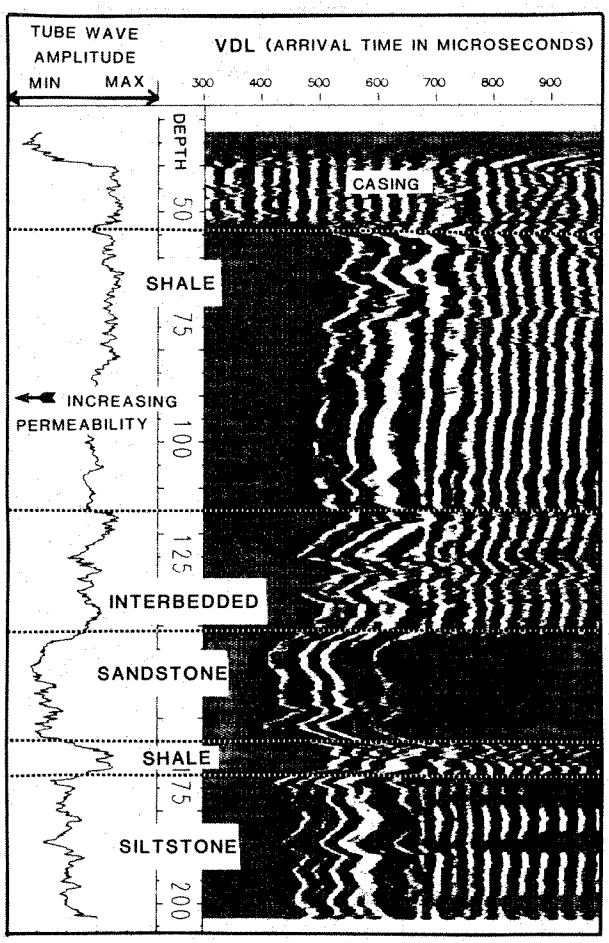

Figure 4. Full waveform logs in Tertiary fluvial sediments, including the tube wave amplitude (left) and the variable density log (VDL, right).

Single Well Electrical Tracer Test

The single well electrical tracer (SWET) test is a method by which the vertical variation in permeability can be observed with time lapse monitoring of fluid injected into the formation. The fluid is introduced under a known driving force, and is electrically conductive relative to the formation fluid so that its movement can be detected by a sequence of resistivity measurements. This method is described by Taylor et al. (1988), who also discussed the conditions for which quantitative hydraulic conductivities can be calculated.

The example shown in Figure 5 compares SWET test data with tube wave amplitude, core results, and field tests in a four inch borehole drilled in welded volcanic tuff. The SWET test data is displayed as a "difference log" which plots the profile of the difference in electrical conductivity between the base log (before fluid injection) and measurements taken 192 minutes after injection began. These electrical conductivity measurements were obtained with an induction logging probe which has a radial depth of investigation of approximately one meter (three feet).

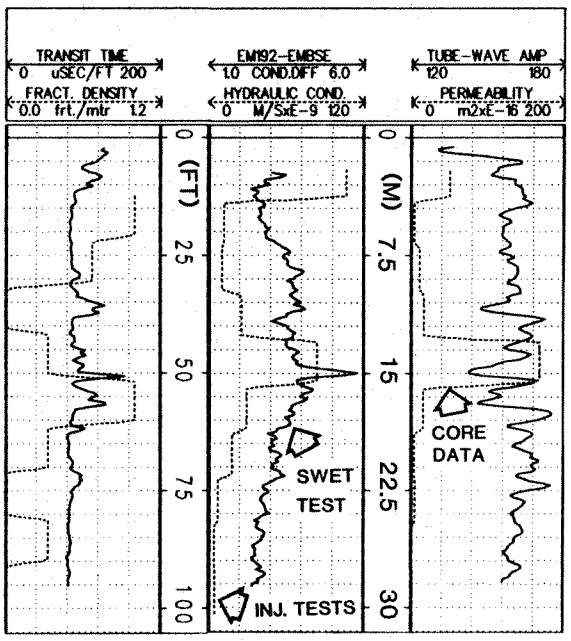

Figure 5. Single well electrical tracer test compared to tube wave amplitude, core analysis, and field tests.

The greatest difference in conductivity, which occurs at a depth of 15 m (50 ft), represents the most permeable flow zone based on the simple premise that the invasion of conductive fluid follows the most permeable path. Note that the zone of greatest conductivity difference from the SWET test corroborates the highest permeability as indicated by the minimum tube wave amplitude (also at the depth of 15 m). The core derived permeabilities (air injection tests performed on core retrieved from 3 m intervals) support both the SWET test data and tube wave amplitude. Also shown in Figure 5 is the hydraulic conductivity profile as derived from in-situ air injection tests, fracture density from core descriptions, and sonic travel time.

The disadvantage of the SWET test is that the injection of brine, or any fluid, is often prohibited at sites under investigation for ground water contamination. The case history shown here was performed at a research site reserved for the study of the physical properties of welded volcanic tuff. It is suggested here that the strategy of an off site research test facility that would accommodate investigations such as the SWET test could be beneficial to many projects. Variations of the SWET test could include the introduction of potable water to a dry hole in an unsaturated environment, or monitoring the vertical progress of a ponded wetting front over time. A site-specific relationship between the rate of change of electrical conductivity and permeability could be extremely valuable in contaminant migration studies.

Fracture Analysis

Fractures control the hydrogeology in many geological environments, including limestone, volcanic, intrusive, and metamorphic rocks. Borehole methods which have been used to locate fractures include sonic, resistivity, caliper, and neutron measurements (Paillet and Kapucu, 1989). However, in addition to locating fractures there is a need in hydrogeology to "characterize" fractures with regard to their capability to support hydraulic flow and their orientation and "connectivity".

Full waveform sonic logs (FWS) can be used both in the identification and permeability evaluation of fracture zones. Fractures are recognized on the VDL by late arrival times (lower velocity), lower tube wave amplitude, and the character of the grey-scaled banding (Crowder et al., 1991). Fracture permeability can be evaluated with tube wave amplitude analysis, as discussed in a previous section. Work by Davison et al. (1982) and Paillet (1989) has firmly established the link between fracture permeability and tube wave amplitude. Mathieu (1984) has presented a mathematical relationship between tube wave attenuation and permeability, and documented favorable comparisons between theoretical results and field packer tests in fractured rock.

Figure 6 shows a composite log from a borehole drilled in fractured granite. Significant fracture permeability is interpreted for the zones marked one through six.

The temperature log is shown in Figure 6 because the deviation from a linear thermal gradient is an excellent indication of fluid flow in or out of the borehole due to the effect of convective heat transfer (Keys, 1988, p. 249). Resistivity logs are a qualitative indication of fracture density because the presence of clay alteration or fluid in the fractures reduces the resistivity of the fractured rock compared to the competent rock matrix.

Independent confirmation of important fractures denoted by the numbered zones in Figure 6 is offered by the agreement of log responses, namely the tube wave amplitude, resistivity, and velocity minima, and corresponding temperature anomalies. A notable exception to this trend is zone six, for which no apparent temperature anomaly is present. This last point addresses one of the outstanding questions inherent in fracture analysis, and that is one of extent. For example, zone 6 could represent fractures that are open at the borehole wall and thus delineated by sonic and resistivity logs, but do not conduct hydraulic flow due to their limited extent, and therefore have no associated temperature anomaly.

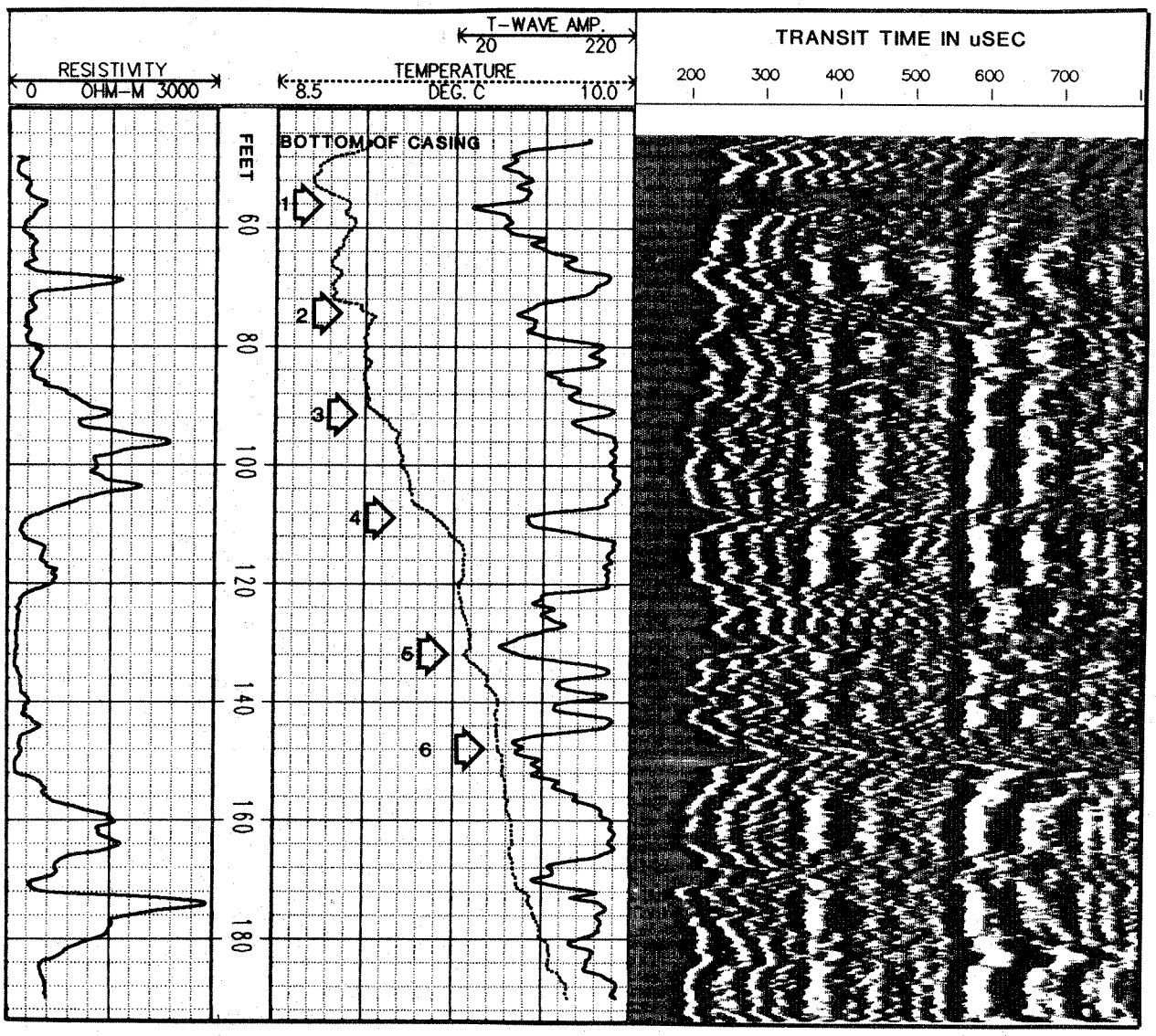

Figure 6. Composite fracture log with important fracture zones denoted by the numbered arrows 1-6. Resistivty is on the left, temperature and tube wave amplitude logs are shown in the middle track, and the variable density log (VDL) is shown on the right.

Orientation and Fracture Connectivity

The orientation (dip direction and azimuth) of the fractures can be derived from borehole televiewer (BHTV) measurements. The BHTV produces an image of the borehole wall with high frequency acoustic reflection. Significant BHTV work has been done by the U.S. Geological Survey Water Resources Division (Keys, 1984; Paillet et al., 1987), and excellent processing capabilities have been developed at Stanford University (Barton and Zoback, 1989). Borehole televiewer surveys combined with heat pulse flow meter measurements in multiple wells have produced valuable results with regard to fracture connectivity. Paillet et al. (1987) have performed BHTV fracture orientation surveys for a number of holes in crystalline rock, and also obtained heat-pulse flow meter data in four of the holes that were closely spaced (tens of meters apart). The flow meter data were collected while discharging one of the wells at a low rate, the results of which are shown in Figure 7.

Note that all of the flow from the three observation wells exits from a single location in each well. Furthermore, all of the incoming water to the pumped well originates from only one area, presumably a single fracture or fracture zone.

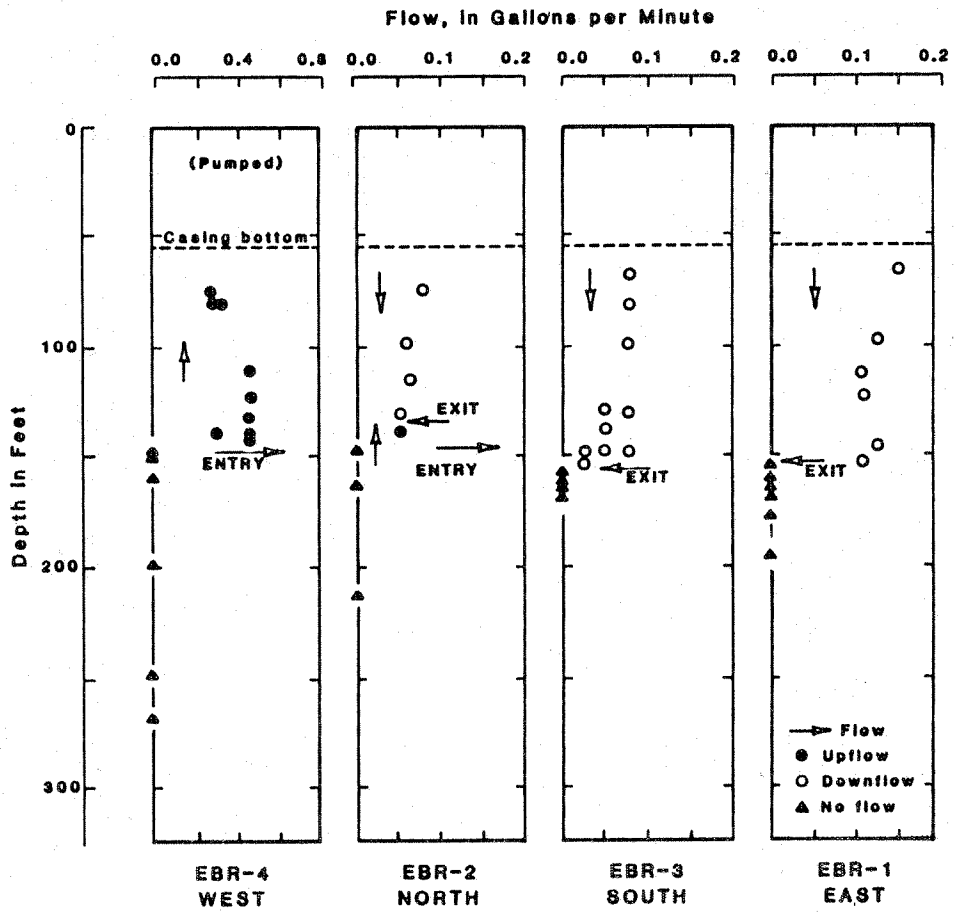

Figure 7. U.S. Geological Survey heat-pulse flow meter data showing entry and exit points of flow during low volume discharge pumping (Paillet et al., 1987).

Figure 8 is the interpretation offered by Paillet et al. (1987) for the BHTV surveys combined with the heat-pulse flow meter information. Those authors noted that though many fractures are identified by the BHTV, most of the observed fractures do not participate in the flow. They concluded that a major portion of the flow between the holes was conducted by relatively few fractures forming complex intersecting conduits.

These results concerning fracture connectivity are critical to understanding and modeling fracture flow, and cannot be derived from core analysis or stochastic methods.

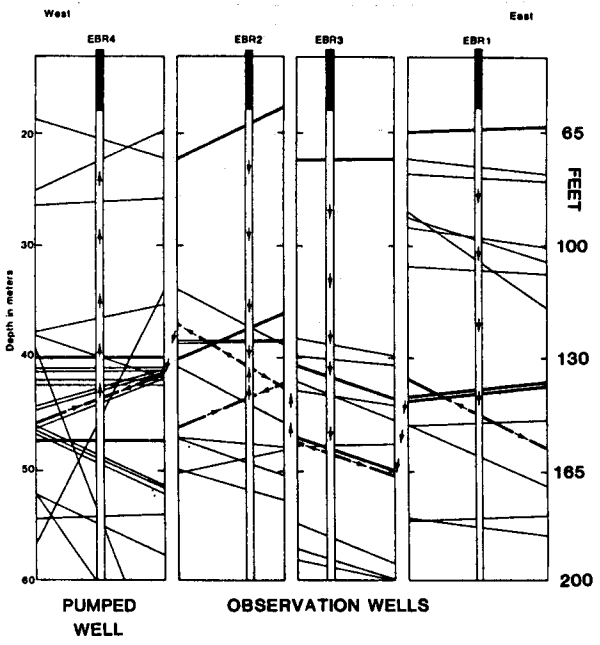

Figure 8. Interpretation of fracture flow between the four wells shown in Figure 7 (Paillet et al., 1987). The lines represent the fractures as interpreted from BHTV logs, and the arrows show direction of flow. Note that the vertical scale compression reduces the apparent dip of the fractures.

Logging in the Unsaturated Zone

Interpretation and modeling for unsaturated zone investigations, which include recharge and contaminant transport issues, requires an understanding of the controls on and time dependency of in-situ moisture conditions. The transport of fluid in unsaturated porous media is controlled by grain size, capillary potential, and gravity potential. The advance of a wetting front, for example, can be described by the depth below ground surface of the front, capillary potential, and storage capacity (Bear, 1972, page 514). The latter two parameters are functions of grain size and saturation. The extent of capillary rise above a phreatic surface, also, depends on grain size and degree of saturation.

The aspects of unsaturated hydrogeology which can be addressed with borehole geophysics include the time-dependent moisture content, lithology, and grain size distribution. Important borehole measurements in this regard are neutron, natural gamma, electromagnetic (EM), and density, all of which can be obtained either in air-filled or fluid-filled holes. Neutron measurements respond primarily to the Hydrogen density (and therefore water content) that surrounds the probe, and can be obtained in the open hole or through casing. Natural gamma logs are useful in delineating lithology and can be used in cased or open holes. The electrical resistivity of unsaturated media, which is controlled in part by its water content, can be measured with downhole EM probes in the open hole or through non-conducting casing. Open hole density measurements indicate the degree of saturation, and can be used in conjunction with neutron logs to identify perched water (Poeter, 1988).

The direct measurement of moisture content in the vadose zone with neutron probes has been documented by several authors including Brose and Shatz (1987), Hammermeister et al. (1985), and Tyler (1985). Those authors have calibrated downhole neutron count rates at specific sites to moisture contents measured in cores or compared to known moisture conditions in laboratory experiments. Kramer et al. (1990), and Kramer and Everett (1990) have studied the effects of well construction materials on neutron measurements, and discussed permanent neutron log access tubes to monitor temporal changes in moisture content.

Work done by Lawrence Livermore Laboratories related to the Yucca Mountain project has used high frequency (5-300 Mhz) electromagnetic (EM) methods to monitor in-situ moisture conditions. Daily and Ramirez (1989) discuss the interpretation of crosshole EM tomographs to monitor moisture movement and drying in a welded volcanic tuff environment, and Ramirez (1986) reviews the use of crosshole EM surveys and conductive fluid tracers to delineate fractures in unsaturated granitic rock.

Log Interpretation

Experience has shown that there exists meaningful physical relationships between geophysical measurements, moisture content, and the physical parameters that control the distribution of moisture in the unsaturated zone. Individual measurements discussed above (i.e. neutron, natural gamma, EM resistivity, and density) are related to specific physical conditions such as moisture content, grain size, and lithology, but their responses are not necessarily unique because of the influence of multiple variables. Therefore, multiple measurements are needed to provide solutions to unsaturated zone issues.

The analysis of multiple measurements is best approached with the method of crossplotting, a technique for comparing trend relationships between two or more geophysical logs. Figure 9, for example, shows a direct trend between neutron count rate and EM resistivity in a borehole drilled in 140 m (460 ft) of unsaturated alluvial sediments. This trend established the physical relationships between these logs and the water content and lithology. The implication is that the greater water content generally occurs in the more fine-grain sediments that contain abundant clay.

Support for this interpretation is shown in a second crossplot between EM resistivity and natural gamma in Figure 10, where the lower resistivity values are also associated with higher natural gamma readings. Core analysis in this well had established a direct relationship between natural gamma and clay content, and therefore one can now make the link between higher clay content and greater water content, which is physically intuitive. Conversely, the dryer coarse-grain material is represented by resistivity and neutron maxima, and natural gamma minima.

Departures from these established trends can be analyzed in terms of anomalous lithologic composition or water saturation. The group of log values shown by the arrow in Figure 9, for example, is anomalously resistive for its relative water content, and is interpreted as a highly cemented sandstone.

The polygons in Figures 9 and 10 enclose log values which represent the fine-grain lithologic end member of the sediments in this borehole. The geophysical properties associated with this end member lithology are low resistivity, high natural gamma, and

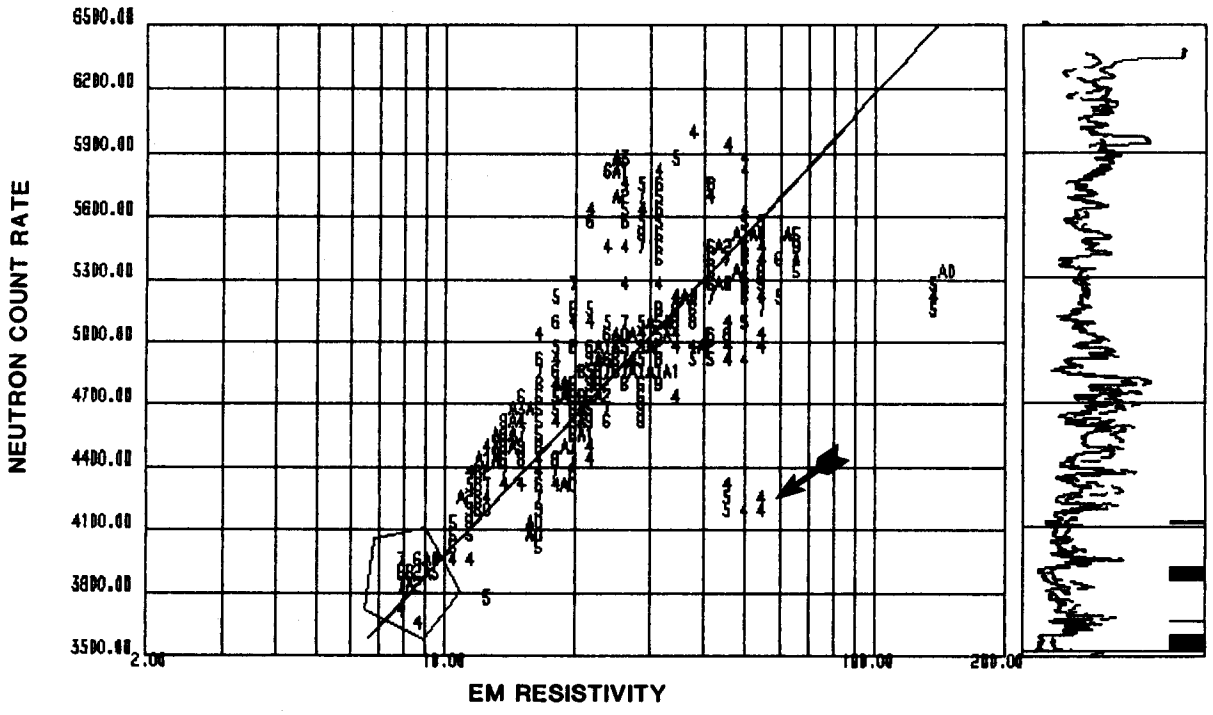

Figure 9: Crossplot illustrating trend between neutron count rate vs. EM resistivity in unsaturated allluvial sediments.

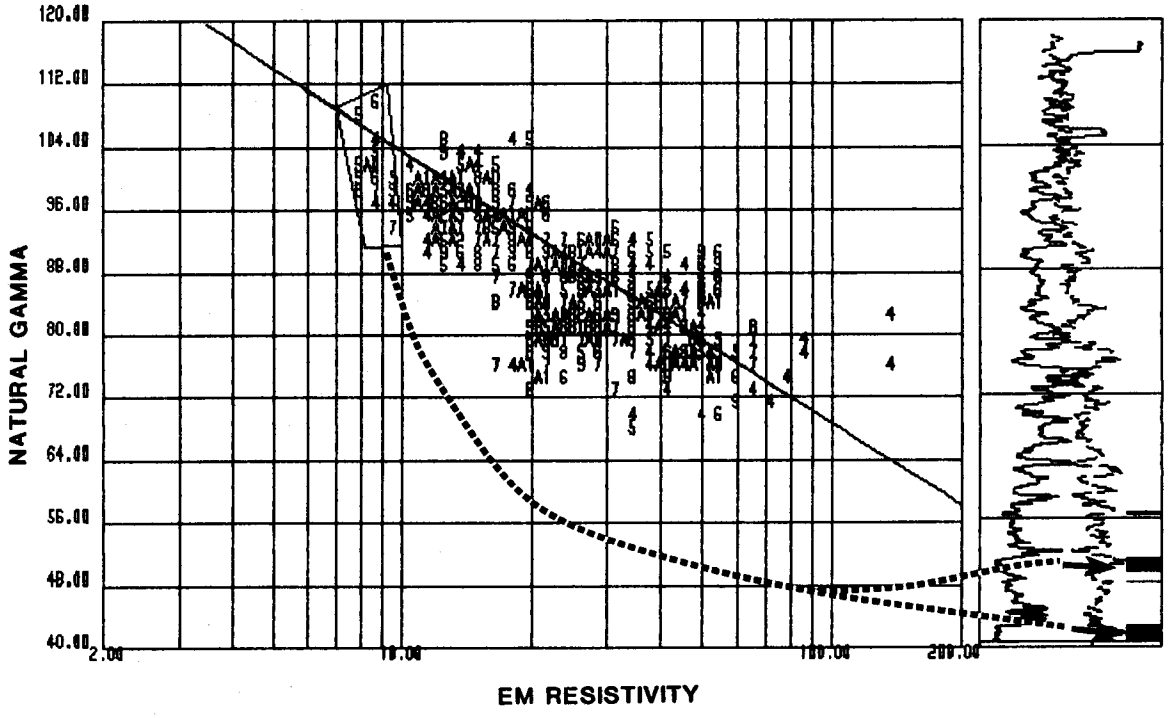

Figure 10: Crossplot of natural gamma vs. EM resisitivty for the same borehole as Figure 9.

low neutron count rate. The stratigraphic locations of those points are shown by the black bars adjacent to the logs on the far right of Figures 9 and 10.

In this example the approach of multiple log crossplots combined with core analysis has provided a defensible interpretation of the water content profile in the well, and the grain size and lithologic controls on the water content profile. Moreover, departures from established trends are important with regard to identifying anomalous lithology or moisture conditions (i.e. perched water).

Finally, a key element in transport issues in the unsaturated zone is the time dependency of moisture conditions. Long term monitoring programs over 20 years sampled quarterly are now being discussed in the environmental industry. Moisture monitoring techniques should therefore be repeatable, objective, and sensitive to small temporal changes in moisture over long periods of time. These attributes are found in borehole geophysical logs.

Conclusions

Borehole geophysical methods specific to ground water issues have evolved due to the increased need for better in-situ characterization of ground water systems. The application of conventional borehole geophysical methods has been supplemented with special techniques which address:

- Characterization of permeability profiles.
- Fracture analysis.
- Logging in unsaturated zone environments.

Because of the importance of permeability variations in both water supply and contaminant problems, the characterization of permeability profiles in boreholes has taken on a central role in hydrogeological borehole geophysics. This paper describes three methods which have been successful in addressing this issue: flow meter methods, tube wave analysis, and single well electrical tracer tests.

Flow meter methods are a direct measurement of ambient or stressed flow in a borehole from which the vertical variation in hydraulic conductivity can be derived. Sonic tube wave amplitude analysis has shown promising and economical results in permeability studies. The single well electrical tracer (SWET) test offers an independent evaluation of permeability variations and is compared in this paper to core data and tube wave analysis.

The goal of borehole geophysics applied to fracture analysis is the identification of fracture zones, their orientation, and assessment as to their relative hydraulic importance. Unique fracture connectivity studies using the heat-pulse flow meter and borehole televiewer logs have been performed by the U.S. Geological Survey Water Resources Division. Full waveform sonic data has the capability for both location identification and fracture permeability evaluation.

The emerging field of borehole geophysics applied to unsaturated zone studies has addressed such issues as in-situ moisture content, time-dependent moisture cycles, and controls on moisture distribution in the unsaturated zone. The analysis of multiple geophysical logs with crossplots offers an approach to unsaturated zone log interpretation from which grain size distribution, lithology, and moisture content can be evaluated.

Biographical Sketches

Elliot N. Yearsley is a Geological Engineer and Log Analyst for COLOG, Inc. (1019 8th Street, Golden, Co. 80401). He received his B.S. in Geological Engineering from the Colorado School of Mines (CSM) in 1981, later returning to CSM to earn a M.S. in Engineering Mechanics in 1989. In the interim between degrees Elliot was employed as a Geological Engineer for Tenneco Exploration and Production for six years, where he pioneered the use of Measurement While Drilling (MWD) log analysis. With COLOG he is currently working on new borehole geophysical techniques applied to geotechnical and hydrogeological investigations, including monitoring well completion evaluation and full waveform acoustic analysis applied to permeability determinations.

Robert E. Crowder is President of COLOG, Inc. (1019 8th Street, Golden, Co. 80401) and has 13 years diversified experience in borehole geophysical applications, including environmental, geotechnical, and mineral investigations. Prior to forming COLOG he was Operations Manager for Colorado Well Logging for eight years. He has taught numerous courses for client groups in borehole geophysical logging and log interpretation, both domestic and international. He received his degree in Engineering Geophysics from Colorado School of Mines in 1978.

References

Balch, S.J., W.A. Morris, D. Blohm and B. Thuma. 1987. Interpretation of borehole magnetic data for mineral exploration and lithological mapping. In Proceedings of the Second International Symposium on Borehole Geophysics for Minerals, Geotechnical, and Ground water Applications, unedited, pp. 179-188.

Barton, C.A. and M.D. Zoback. 1989. Utilization of interactive analysis of digital borehole televiewer data for studies of macroscopic fracturing. In Proceedings of the Third International Symposium on Borehole Geophysics for Minerals, Geotechnical, and Ground water Applications, unedited, pp. 623-653.

Bear, J. 1972. Dynamics of Fluid Flow in Porous Media. Dover Publications, Inc.

Brose, R.J. and R.W. Shatz. 1987. Neutron monitoring in the unsaturated zone. In Proceedings of the First National Outdoor Action Conference on Aquifer Restoration, Ground Water Monitoring, and Geophysical Methods, National Water Well Association, Dublin, Ohio, pp. 455-467.

Collier, H.A. 1989. Assessment of the dielectric tool as a porosity log. Proceedings of the Third International Symposium on Borehole Geophysics for Minerals, Geotechnical, and Ground water Applications, unedited, pp. 183-198.

Crowder, R.E., J.J. LoCoco and E.N. Yearsley. 1991. Application of full waveform borehole sonic logs to environmental and engineering investigations. In Proceedings of the Symposium for the Application of Geophysics to Environmental and Engineering Problems (in press).

Daily, W.D., and A.L. Ramirez. 1989. Preliminary evaluation of an electromagnetic experiment to map in situ water in heated welded tuff. Water. Resour. Res., v. 25, no. 6, pp. 1083-1096.

Davison, C.C., W.S. Keys and F.L. Paillet. 1982. Use of borehole geophysical logs and hydrologic tests to characterize crystalline rock for nuclear waste storage at Whiteshell and Chalk River, Canada. Office of Nuclear Waste Isolation Tech. Rept. No. ONWI-418.

Halepaska, J.C., K.T. Le and B. Lytle. 1990. Artificial recharge: Willows Water District Arapahoe aquifer recharge project. In Proceedings of the Ground Water Engineering and Management Conference. Colorado State University, pp. 269-284.

Hammermeister, D.P., C.R. Kneiblher and J. Klenke. 1985. Borehole calibration methods used in cased and uncased test holes to determine moisture profiles in the unsaturated zone, Yucca Mountain, Nevada. In Proceedings of the Conference on Characterization and Monitoring of the Vadose Zone, National Water Well Association, Dublin, Ohio, pp. 542-563.

Hearst, J.R. and P.H. Nelson. 1985. Well Logging for Physical Properties. McGraw-Hill.

Hess, A.E. 1986. Identifying hydraulically conductive fractures with a slow velocity borehole flow meter. Can. Geotech. Jour., v. 23, pp. 69-78.

Irons, L. and B. Lewis. 1990. Shallow high-resolution seismic reflection investigation at a hazardous waste site. In Proceedings of the Fourth National Outdoor Action Conference on Aquifer Restoration, Ground Water Monitoring and Geophysical Methods. National Water Well Association, Dublin, Ohio, pp. 1129-1142.

Javandel, I. and P.A. Witherspoon. 1969. A method of analyzing transient fluid flow in multilayered aquifers. Water. Resour. Res., v. 5, pp. 856-869.

Keys, W.S. 1984. A synthesis of borehole geophysical data at the Underground Research Laboratory, Manitoba, Canada. Office of Crystalline Repository Development Rept. No. OCRD-15.

Keys, W.S. 1988. Borehole geophysics applied to ground-water investigations. U.S. Geol. Surv. Open File Rept. No. 87-539.

Kramer, J.H., L.G. Everett and L.A. Eccles. 1990. Effects of well construction materials on neutron probe readings with implications for vadose zone monitoring. In Proceedings of the Fourth National Outdoor Action Conference on Aquifer Restoration, Ground Water Monitoring and Geophysical Methods. National Water Well Association, Dublin, Ohio, pp. 1303-1317.

Kramer, J.H. and L.G. Everett. 1990. Proactive post-closure vadose zone monitoring strategy using neutron logs. In Proceedings of the 20th Annual Western Region Solid Waste Management Symposium (in press).

Mathieu, F. 1984. Application of full waveform acoustic logging data to the estimation of reservoir permeability. M.S. Thesis, Massachusetts Institute of Technology.

Molz, F.J., R.H. Morin, J.G. Melville and O. Guven. 1989. The impeller meter for measuring aquifer permeability variations: Evaluation and comparison with other tests. Water. Resour. Res., v. 25, pp. 1677-1683.

Morin, R.H. 1988. Determining the vertical distribution of hydraulic conductivity in-situ by concurrent injection and geophysical logging. In Proceedings of the International Conference of Fluid Flow in Fractured Rocks, Georgia State University, pp. 346-354.

Paillet, F.L. and J.E. White. 1982. Acoustic modes of propagation in the borehole and their relationship to rock properties. Geophysics, v. 47, pp. 1215-1228.

Paillet, F.L., A.E. Hess, C.H. Cheng and E. Hardin. 1987. Characterization of fracture permeability with high-resolution vertical flow measurements during borehole pumping. Ground Water vol. 25, pp. 28-40.

Paillet, F.L. 1989. Analysis of geophysical well logs and flow meter measurements in boreholes penetrating subhorizontal fracture zones, Lac Du Bonnet batholith, Manitoba, Canada. U.S. Geological Survey Water Resour Invest Rept 89-4211.

Paillet, F.L. and K. Kapucu. 1989. Fracture characterization and fracture permeability estimates from geophysical logs in the Mirror Lake Watershed, New Hampshire. U.S. Geological Survey Water Resour Invest Rept 89-4058.

Poeter, E.P. 1988. Characterizing fractures at potential nuclear waste sites with acoustic waveform logs. The Log Analyst, vol. 28, no. 5, pp. 453-461.

Ramirez, A.L.. 1986. Recent experiments using geophysical tomography in fractured granite. In Proceedings of Inst. of Electrical and Electronic Engr., vol. 74, pp. 347-352.

Rehfeldt, K.R. 1989. Application of the borehole flowmeter method to measure the spatially variable hydraulic conductivity at the macro-dispersion experiment site. In Proceedings of the Conference for New Field Techniques for Quantifying the Physical and Chemical Properties of Heterogeneous Aquifers, National Water Well Association, Dublin, Ohio, pp. 419-442.

Rosenbaum, J.H. 1974. Synthetic microseismograms: logging in porous formations. Geophysics, v. 39, pp. 14-32.

Taylor, K., F. Molz and J. Hayworth 1988. A single well electrical tracer test for the determination of hydraulic conductivity and porosity as a function of depth. In Proceedings of the Second National Outdoor Action Conference on Aquifer Restoration, Ground Water Monitoring, and Geophysical Methods, National Water Well Association, Dublin, Ohio. pp. 925-938.

Tyler, S. 1985. Moisture monitoring in large diameter boreholes. In Proceedings of Conference on Characterization and Monitoring of the Vadose Zone. National Water Well Association, Dublin, Ohio. pp. 97-106.

White, J.E. 1983. Underground Sound: Application of Seismic Waves. Elsevier Publishing, New York.

Williams et al. 1984. The long spaced acoustic logging tool. In Transactions of the 25th Annual Logging Symposium of the Society of Professional Well Log Analysts, Paper T.

Yearsley, E.N. and R.E. Crowder. 1991. Monitor well completion evaluation with borehole geophysical density logging. Ground Water Monitoring Review, v. 11, no. 1, pp. 103-111.

Aquifer Parameters Defined by Borehole Geophysics

by Bruce Manchon

Abstract

In the environment field borehole geophysics is used primarily for correlation of equivalent strata from one borehole or well to the next, to determine lithology, but not to delineate the nature of fluids in aquifers. Borehole geophysical interpretation provides a means of determining not only the lithology of the beds but also the composition of aquifer fluids.

Groundwater contaminated with waste migrating from a landfill, surface spill, leaking underground storage tank, by injection, or salt water intrusion, exhibits distinctive borehole geophysical log signatures. The interpretation of the distinctive contaminated log signatures and the log signatures of the native conditions from upgradient wells, aids in the identification of hydrogeological parameters of the aquifer and associated contaminant plume.

Borehole geophysical interpretation techniques can be applied effectively to a variety of environmental settings. They are especially effective in terrains where strata are locally continuous and a resistivity or radioactive contrast exists between the formation water and the contaminants. These techniques can provide data about the dimensions of a contaminant plume, contaminant concentrations in the ground water, and water saturations, or to verify model plume predictions.

This paper demonstrates, by theoretical, qualitative, quantitative, and empirical borehole geophysics interpretation techniques, how to identify and estimate parameters of the lithology and fluids of an aquifer.

Bruce Manchon is a project hydrogeologist with International Technology Corporation (4585 Pacheco Blvd., Martinez, California 94553, USA).

Quantification of Ionic and Hydrocarbon-Type Contaminants with Geophysical Resistivity Surveys and Drill Hole Sample Data

by Joe O. Davis

Abstract

The use of geophysical methods in the petroleum, geotechnical engineering and mining industries is common; its use is increasing on environmental projects for site characterization. The major advantage of geophysical methods over drill and sample techniques is cost savings; yet many projects are too complex to be described accurately by any amount of drilling. They are not a replacement for drilling, but can save the majority of 'dry' (non-contamination intersecting drill holes). When geophysics is used in combination with drill hole data cost effectiveness is maximized, while other techniques can be used to give additional data.

This talk outlines some methods which derive total contamination amounts through the novel use of geophysical resistivity data and drill hole sample data. These methods are approximate, yet are usually surprisingly accurate.

The talk shows the final interpretation techniques which are used after a three-stage site characterization process which includes: a primary resistivity survey, drilling and sampling, and final interpretation which combines data types to give additional information.

Joe O. Davis is an independent consultant (Omega Geophysics Ltd., 203 - 888 Burrard Street, Vancouver, British Columbia V6Z 1X9, Canada) offering specialized services for environmental projects, hydrogeological applications, and engineering design. He graduated with a BSc in geophysics from the University of Calgary in 1987.

The Inversion of E-SCAN Resistivity Data in the Solution of Ground Water Contamination and Enhanced Oil Recovery Problems

by P.R. McGillivray and D.W. Oldenburg

Abstract

The DC (direct current) resistivity method has seen widespread use as an aid to characterizing properties of aquifers, and to a lesser extent petroleum reservoirs. The method allows one to construct an electrical resistivity model of the subsurface based on an interpretation of surface voltage measurements. The electrical model can then be used to infer a hydrogeological model based on theoretical and experimental relations between electrical resistivity and the aquifer parameters of interest.

The success of a DC resistivity survey requires that assumptions made in the interpretation of the data be consistent with the true earth. In hydrogeological applications, the interpretation of resistivity data has been almost exclusively limited to the matching of field data to type curves based on 1D (horizontally layered) model assumptions. Since lateral changes cannot be represented in the 1D model, this assumption reduces the reliability of the interpretation in areas where the geology is even moderately complicated. In particular, where lateral changes in the near-surface resistivity are encountered, these simple interpretation techniques can lead to very misleading results. For problems involving lateral changes in the geology, a more complete analysis of the data is needed to correctly resolve subsurface structures. To meet this need, a parametric inversion algorithm was developed to invert resistivity data for more complicated 2D earth structures. In order to allow the inversion as much flexibility as possible a large number of parameters (of the order of 1000) was used to represent the earth. A global model norm was also minimized, insuring that the final model was smooth relative to some specified reference model. This smoothness requirement helps control the inherent non-uniqueness, and makes the algorithm less sensitive to noise. A re-parameterization, based on the sensitivity of both the data and the global model norm to changes in the model parameters, was also used to reduce the computational size of the problem. As a test of the algorithm, several synthetic data sets from an E-SCAN resistivity survey were inverted. The results illustrate the ability of the algorithm to recover smoothed estimates of the subsurface resistivity structure, even in the presence of near-surface inhomogeneities.

Introduction

The DC (direct current) resistivity method has been used in the geophysical exploration of the subsurface for many years. The good depth of penetration of the method and its low cost make it an economical alternative to detailed drilling

and testing. Although there are many variations of the DC resistivity technique, the basic idea is to establish a subsurface current distribution by injecting current into the ground between two electrodes. A series of voltage differences are measured between pairs of potential electrodes in a line or grid, and are then interpreted to yield information about the electrical resistivity distribution beneath the study area.

Numerous ways of arranging the current and potential electrodes in a resistivity survey are possible. Both the geometric configuration of the electrodes (i.e. the array used) and the relative spacing between electrodes can vary from survey to survey. Because both the depth of penetration and vertical resolution depend on the particular arrangement of electrodes used (Roy and Apparao, 1971; Roy, 1972), a proper choice of array is crucial to the success of the experiment. This choice must be based on the nature of the target (such as depth of burial and resistivity contrast), as well as on the complexity of the surrounding medium. Arrays which are frequently encountered include the pole-pole array (best depth of penetration, poorest resolution), pole-dipole, and dipole-dipole array (poorest depth of penetration, best resolution). These are illustrated in Figure 1.

The most common way of acquiring resistivity data is to make use of one or more traverse lines oriented perpendicular to strike. To image lateral changes in the subsurface, the center of the array is moved along one of the traverse lines while keeping the electrode separations fixed. This mode of acquisition is referred to as profiling. Expanding the electrode array about a fixed point to image successively deeper regions of the earth is referred to as depth sounding. Combining the two techniques into a depth sounding/profiling survey is also possible.

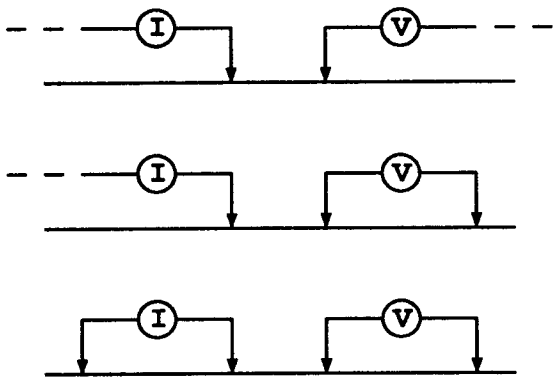

Figure 1. Electrode configuration for the pole-pole, pole-dipole and dipole-dipole arrays. Dashed lines indicate electrodes located at infinity.

The E-SCAN Resistivity Experiment

The E-SCAN experiment is a relatively new DC resistivity technique based on the pole-pole array. The survey involves recording a set of pole-pole measurements using a grid of electrodes set up over a survey area (Figure 2). An operator sweeps across the grid, injecting current into the ground through one electrode and measuring the resulting voltage at each of the remaining electrodes. Other DC resistivity responses (i.e. pole-dipole, dipole-dipole) can then be computed from the pole-pole measurements, or can be measured directly.

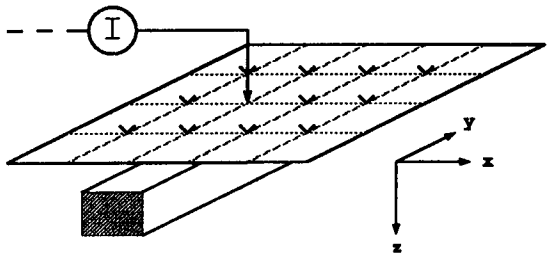

Figure 2. Electrode configuration for an E-SCAN survey. The potential electrodes are indicated by the symbol "v".

Because of the high density of data which is measured, the E-SCAN technique has the potential for resolving more complicated earth structures than standard linear surveys. Thus far the technique has been used primarily in the exploration for structures associated with mineral deposits and in the study of hydrothermal areas. Other possible applications include the evaluation of groundwater resources, detection and monitoring of groundwater contamination, and the monitoring of enhanced oil recovery (EOR) processes.

Applications To Groundwater Resource and EOR Problems

The close relation between electrical current flow and porous media transport has stimulated considerable interest in the application of DC resistivity methods to groundwater and EOR problems. The resistivity technique has been used extensively in the detection and mapping of groundwater contamination (Klefstad et al., 1975; Stollar and Roux, 1975; Kelly, 1976; Berk and Yare, 1977; Urish, 1983). Considerable work has also been done on applying the technique to the evaluation of groundwater resources and in the quantitative evaluation of aquifer parameters which control groundwater flow (Schwartz and McClymont, 1977; Kelly, 1977; Kosinski and Kelly, 1981; Sri Niwas and Singhal, 1981, 1985). More recently, resistivity measurements have been used directly in the geostatistical extrapolation of aquifer parameters away from well control (Bardossy et al., 1986; Ahmed et al., 1988). The use of geoelectric methods in the monitoring of EOR processes has also been described (Beasley, 1989).

Relation Between Electrical Resistivity and Parameters Characterizing the Aquifer or Reservoir

Much of the attention in recent years has focused on the relations between electrical resistivity and parameters governing porous media flow (Worthington, 1976; Frohlich and Kelly, 1985; Mazac et al., 1985; Huntley, 1986). Often these relations are based on experiment, and can only be applied to very specific situations. Nonetheless, they provide a way of characterizing properties of the aquifer or reservoir once the electrical structure has been recovered.

The starting point for most studies is to relate the bulk electrical resistivity ρ_b to the resistivity of the pore fluid ρ_f using a constant formation factor F, where,

$$F = \frac{\rho_b}{\rho_f} \qquad (1)$$

Assuming the formation factor is indeed constant, this allows one to determine the ionic content of the pore fluid (i.e. the water quality) once the bulk resistivity has been estimated. The assumption of a

constant formation factor, as pointed out by Worthington (1976), will be invalid for problems where matrix conduction is significant. In these cases, more complicated formulas must be considered.

For problems where the porous medium is non-homogeneous, theoretical relations like Archie's law,

$$F = a\phi^{-m} \qquad (2)$$

can be used to relate the formation factor to the porosity ϕ. Combining eqn (1) and eqn (2), one obtains,

$$\phi = \log_m \left(a\rho_f/\rho_b\right) \qquad (3)$$

which can be used to determine the porosity of the medium, given an estimate of its bulk electrical resistivity.

Relations between formation factor and other aquifer parameters like hydraulic conductivity and permeability have also been examined (Frohlich and Kelly, 1984; Mazac et al., 1985; Huntley, 1986). Hydraulic conductivity can be correlated directly with porosity, or it can depend on other parameters (e.g. grain size, packing) which are related to porosity. One can thus observe either a direct or an inverse relation. The formation factor can also display a direct or inverse correlation with porosity, depending primarily on the mode of conduction. The need to establish the correct relation between electrical resistivity and the aquifer parameter of interest is essential to the success of any geoelectric survey. This is usually done by comparing the resistivity sounding results to aquifer parameters estimated from pump tests at nearby wells.

Characterization of Subsurface Electrical Resistivity from Surface Electrical Measurements

Having established a relation between electrical resistivity and the aquifer parameter of interest, the problem of characterizing the subsurface electrical resistivity given a set of surface electrical measurements still remains. The first step in a typical interpretation of resistivity data is to convert the measured voltages into apparent resistivities – the apparent resistivity, ρ_a, being the resistivity of a homogeneous earth corresponding to the particular voltage measurement $\mathrm{v}\,(x,y,z)$. For the pole-pole experiment the apparent resistivity is given by,

$$\rho_a = \frac{2\pi}{I}\cdot\sqrt{(x-x_s)^2+(y-y_s)^2+(z-z_s)^2}\cdot \mathrm{v}\,(x,y,z) \qquad (4)$$

Apparent resistivity data obtained from profiling surveys are usually displayed as pseudo-sections or contoured iso-depth maps and interpreted qualitatively. Data from depth soundings are most often presented as apparent resistivity vs electrode separation plots, and are interpreted using type curves generated from simple layered-earth models. A more elaborate interpretation of sounding data makes use of the auxiliary point method (Parasnis, 1986). This involves matching successive branches of the sounding plots to two- or three-layer type curves, thereby constructing a more complete multi-layer cross-section.

Limitations of the DC Resistivity Technique

Although DC resistivity methods have proved their usefulness in groundwater resource and contamination studies, several

limitations have been documented. Stollar and Roux (1975) discuss the limitations of the resistivity method in general, and note that the geological environment must not be overly complicated if the use of type curves is to be meaningful. They also point out that the nature of the target (i.e. depth of burial, resistivity contrast, thickness) can preclude it from being detected. Klefstad et al. (1975) conclude that the heterogeneity associated with alluvial deposits can easily obscure apparent resistivity anomalies associated with groundwater contamination.

In general, many of the limitations of the resistivity technique can be attributed to incorrect assumptions made at the interpretation stage. If curve matching based on 1D earth models is to provide reliable information, the geology of the aquifer must be reasonably consistent with the 1D assumption. Because lateral changes in the electrical properties of the aquifer (e.g. near surface inhomogeneities, regional changes in the lithology) cannot be represented in the 1D model, their influence can easily lead to an incorrect interpretation. This is particularly true when the zone of interest is relatively deep or the resistivity contrast between the target and background is small. In these cases the interpretation of resistivity data measured over a laterally varying earth requires a more complete analysis based on 2- or 3-dimensional model assumptions. Because the use of type curves and forward modeling for these higher dimensional problems is impractical, it becomes necessary to use more formal inverse techniques to characterize the subsurface resistivity distribution.

Solution of the Inverse Problem

The ultimate goal of an inversion is to recover a model that adequately reproduces the measured data. Because only a finite number of data are measured over what can be an arbitrarily complicated earth, the inverse problem is inherently non-unique – there are many diverse earth models which can fit the given data. One is thus faced with the problem of restricting the solution to models which are realistic in terms of the known geology. One way of doing this is to greatly reduce the number of unknowns in the problem by subdividing the region of interest into a small number of zones of constant electrical resistivity. The form of the parameterization (i.e. the number and shape of zones) must be based on prior knowledge of the true earth structure. Although this approach is commonly used, it can lead to very poor results if the model is parameterized incorrectly. To overcome this problem, as fine a parameterization as possible was used, so that no *a priori* information was needed to decide on the form of parameterization. The non-uniqueness was then controlled by requiring that the final solution be in some sense "simple". This was achieved by fitting the observed data while also minimizing the "distance" of the solution relative to a reference model.

For the 2D resistivity problem the model was parameterized by dividing the subsurface into a set of horizontal, infinitely long prisms (Figure 3). The elements of the model vector $\vec{m}$ were then taken to be the log resistivities of each of the prisms. The observed data $\vec{e}_{obs}$ were taken to be the measured voltages (or voltage differences) normalized by their standard deviations. The predicted data

$\vec{e}(\vec{m})$ for a given model $\vec{m}$ were computed numerically using an integrated finite difference scheme (Dey and Morrison, 1979).

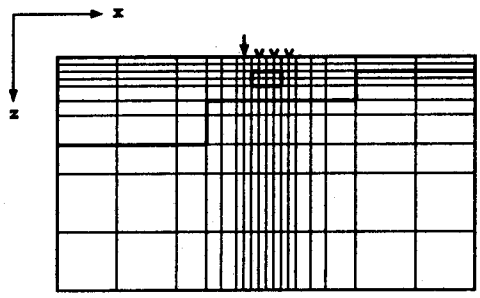

Figure 3. Cross-section showing how the model is parameterized for the 2D resistivity problem. Dark lines indicate geological boundaries corresponding to discontinuities in electrical resistivity.

Because of the non-linear relation between the data and the model parameters an iterative solution to the inverse problem must be considered, where at the n^{th} iteration a perturbation $\Delta\vec{m}$ to the previous model estimate $\vec{m}^{n-1}$ is to be determined. The data misfit function,

$$\Phi(\Delta\vec{m}) = \left\|\vec{e}\left(\vec{m}^{n-1} + \Delta\vec{m}\right) - \vec{e}_{obs}\right\|^2 \quad (5)$$

and the global model norm,

$$\Psi(\Delta\vec{m}) = \left\|W\left(\vec{m}^{n-1} + \Delta\vec{m} - \vec{m}_{ref}\right)\right\| \quad (6)$$

are first defined, where W is a weighting matrix used to control the nature of the recovered model. In the present study, the Laplacian weighting matrix

$$W = \left[\cdots, 1, \cdots, 1, -4, 1, \cdots, 1, \cdots\right] \quad (7)$$

was used, although other weighting matrices are also possible. This particular choice of W requires $\vec{m} - \vec{m}_{ref}$ be smooth in order to minimize Ψ. The reference model $\vec{m}_{ref}$ can be a smoothed estimate of the true electrical resistivity structure (if enough is known about the regional geology), or simply a half-space assigned some average resistivity.

At each iteration in the inversion a model perturbation is sought which minimizes the global model norm, while reducing the data misfit to some prescribed value ξ. Using the method of Lagrange multipliers, the model perturbation is found by minimizing,

$$\Theta(\Delta\vec{m}, \lambda) = \left\|W\left(\vec{m}^{n-1} + \Delta\vec{m} - \vec{m}_{ref}\right)\right\|^2 + \lambda\left(\left\|\vec{e}\left(\vec{m}^{n-1} + \Delta\vec{m}\right) - \vec{e}_{obs}\right\|^2 - \xi\right) \quad (8)$$

Setting the derivative of eqn (8) with respect to λ and $\Delta\vec{m}$ to zero yields,

$$\left\|\vec{e}\left(\vec{m}^{n-1} + \Delta\vec{m}\right) - \vec{e}_{obs}\right\|^2 = \xi \quad (9)$$

and,

$$2W^T W\left(\vec{m}^{n-1} + \Delta\vec{m} - \vec{m}_{ref}\right) + 2\lambda J^T\left(\vec{e}\left(\vec{m}^{n-1} + \Delta\vec{m}\right) - \vec{e}_{obs}\right) = 0 \quad (10)$$

where $J = \frac{\partial\vec{e}}{\partial\vec{m}}$ is the Jacobian or sensitivity matrix. Elements of the sensitivity matrix can be computed by numerically solving an "adjoint" forward problem. The formulation of the adjoint problem is described in McGillivray and Oldenburg (1990).

The change in the predicted data that results from perturbing the model is linearized using,

$$\vec{e}\left(\vec{m}^{n-1} + \Delta\vec{m}\right) \approx \vec{e}\left(\vec{m}^{n-1}\right) + J\Delta\vec{m} \quad (11)$$

Eqn (10) is then rearranged to yield,

$$\left(\lambda J^T J + W^T W\right) \Delta\vec{m} = \lambda J^T(\vec{e}\,(\vec{m}^{n-1}) - \vec{e}_{obs}) - W^T W\left(\vec{m}^{n-1} - \vec{m}_{ref}\right) \quad (12)$$

The minimum is obtained by carrying out a line search over a range of λ values. For each value of λ, a model perturbation $\Delta\vec{m}$ is computed using eqn (12) and a set of predicted data is generated for the updated model $\vec{m}^{n-1} + \Delta\vec{m}$. The value of λ that results in the desired decrease in misfit, as given by eqn (9), is then selected. Eqn (12) is then used to compute the final model perturbation.

Having found a model perturbation that minimizes the global model norm and achieves the desired decrease in misfit, the new model $\vec{m}^n = \vec{m}^{n-1} + \Delta\vec{m}$ is formed for the next iteration. The algorithm terminates when the desired misfit is achieved and the global model norm no longer changes from iteration to iteration.

Generalized Subspace Technique

For problems involving more than a few hundred parameters one finds that the direct use of eqn (12) becomes impractical because of the size of the matrix $\lambda J^T J + W^T W$ that must be inverted repeatedly at each iteration. To reduce the size of the matrix which must be inverted, an approach similar to the subspace technique described by Kennett and Williamson (1987) and Kennett et al. (1988) was used. Note that although the dimension of the perturbation $\Delta\vec{m}$ is often quite large, the amount of independent information provided by the data can be relatively small. It is thus reasonable to re-parameterize the problem by restricting $\Delta\vec{m}$ to lie within a subspace of the perturbation space. The model perturbation can then be written as the linear combination,

$$\Delta\vec{m} = \sum_{k=1}^{M_b} \alpha_k \vec{v}_k = G\vec{\alpha} \quad (13)$$

where,

$$G = \begin{bmatrix} | & | & | & & | \\ \vec{v}_1 & \vec{v}_2 & \vec{v}_3 & \cdots & \vec{v}_{M_b} \\ | & | & | & & | \end{bmatrix} \quad (14)$$

is the matrix of basis vectors $\vec{v}_k$ which span the subspace. Substituting eqn (13) into eqn (8) and carrying out the minimization, yields the expression,

$$G^T\left(\lambda J^T J + W^T W\right) G\vec{\alpha} = \lambda G^T J^T(\vec{e}\,(\vec{m}^{n-1}) - \vec{e}_{obs}) - G^T W^T W\left(\vec{m}^{n-1} - \vec{m}_{ref}\right) \quad (15)$$

The matrix $G^T\left(\lambda J^T J + W^T W\right) G$ that must be inverted to obtain $\vec{\alpha}$ is now only of order M_b.

The success of the subspace approach hinges on a proper selection of the basis vectors. In particular, they should be chosen so that both the data misfit function and global model norm are sensitive to model changes in those directions. The basis vectors must also be reasonably independent. For this particular problem a partial data misfit function $\Phi_k(\Delta\vec{m})$ was associated with each current electrode, and the corresponding steepest descent directions (with respect to changes in $\|W\vec{m}\|$) were selected as basis vectors. Thus for each current electrode the basis vector,

$$\vec{v}_k = -\left(W^T W\right)^{-1}\vec{g}_k, \quad k = 1, \ldots, N_{cur} \quad (16)$$

was defined, where $\vec{g}_k = \vec{\nabla}\Phi_k(\Delta\vec{m})$. Similarly, the basis vector,

$$\vec{v}_{N_{cur}+1} = -\left(\vec{m}^{k-1} - \vec{m}_{ref}\right) \qquad (17)$$

corresponding to the gradient of the global model norm, was also defined.

To stablize the inversion of the matrix in eqn (15) it is necessary to form an orthonormal set of basis vectors from the original set of vectors. This is most easily done using the singular value decomposition,

$$G = U\Lambda V^T \qquad (18)$$

where Λ is the matrix of eigenvalues of G, and U and V are the matrices of left and right eigenvectors, respectively. The columns of U are then used to form the orthonormal basis set.

Examples

As an illustration of the generalized subspace technique, synthetic data sets generated for the model shown in cross-section form in Figure 4 were inverted. The model consists of a 400 m wide, 10 Ωm conductive plug within a faulted 100 m thick, 100 Ωm layer. The layer is buried within a resistive 1000 Ωm background. This particular model could represent either a contamination plume moving through an aquifer, or a flood front in an EOR problem. The model was parameterized using a rectangular mesh extending from −4000 m to 4000 m in the x direction, and 0 m to 2000 m in the z direction, yielding a total of 1000 parameters. Note that only the portion of the grid below the survey area is shown in Figure 4 and in subsequent cross-sections.

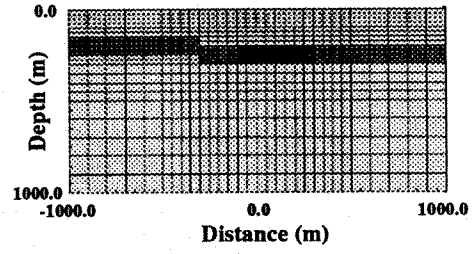

Figure 4. Cross-section through the model used in the first example. The model consists of a 400 m wide 10 Ωm conductive plug within a faulted 100 m thick 100 Ωm layer. The layer is buried within a resistive 1000 Ωm background.

To image the region of interest, 11 current electrodes were placed along the surface every 200 m from −1000 m to 1000 m. Forty potential electrodes were placed 200 m apart in a grid around each current electrode (Figure 5).

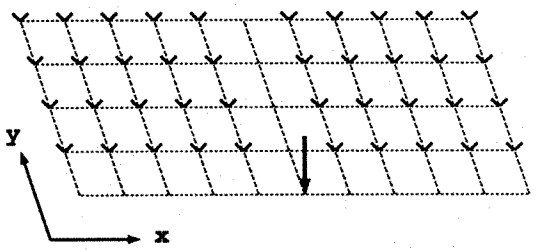

Figure 5. E-SCAN pole-pole array used in examples. The current electrode is indicated by an arrow; the potential electrodes are indicated by the symbol "v".

The integrated finite difference program was then used to model the 440 pole-pole potentials to be used in the inversion examples.

For the first example, 5% Gaussian noise was added to the modeled pole-pole

potentials, and the data were then inverted using the generalized subspace algorithm. A 1000 Ωm half-space was used as both the starting model and reference model. A total of 12 basis vectors (one corresponding to each current electrode and an additional one corresponding to the gradient of the global model norm) were used to form the model subspace in this example. After 10 iterations the desired RMS misfit of 5% was achieved and the global model norm reached a minimum. The result is shown in Figure 6.

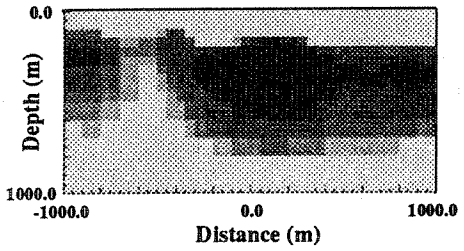

Figure 6. Pole-pole inversion result for the model in Figure 4. The model achieved an RMS misfit of 5% after 10 iterations.

Although the final model is quite diffuse, the extent of the conductive plug and the presence of the layer are easily discerned. The diffuseness of the result is due to both the low resolution of the pole-pole data and the smoothness imposed by our choice of the matrix W in eqn (6). By comparing the apparent resistivities computed for the final inversion result to the modeled data with and without noise (Figure 7), it is clear that the algorithm is relatively insensitive to the added noise. This robustness is again due to our requirement that the final model be globally smooth.

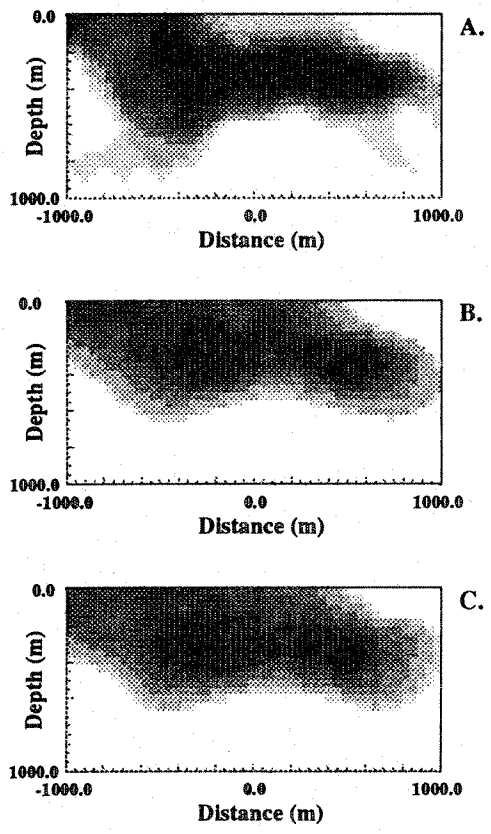

Figure 7. Apparent resistivity pseudo-sections computed from A. data used in the pole-pole inversion (5% Gaussian noise added), B. potentials generated by inversion result in Figure 6, and C. data before noise added.

In the second example, the modeled pole-pole potentials were used to compute 342 pole-dipole data, to which 5% Gaussian noise was again added. The corrupted data were inverted, and the result after 10 iterations is shown in Figure 8. The improvement in resolution over the pole-pole result was quite dramatic. Both the conductive plug and the layer were well defined, and the recovered resistivities were closer to their true values;

a resistivity of 30 Ωm was obtained for the conductive plug using the pole-dipole data compared to 50 Ωm using the pole-pole data. The RMS misfit to the data achieved in this example was 7%, somewhat higher than the desired misfit of 5%. This was a result of attempting to fit the higher resolution pole-dipole data with a globally smooth model. To allow for a closer fit to the data, a larger number of basis functions could be used in the inversion. The objective function could also be modified to allow for rougher models, although this would tend to increase its sensitivity to noise.

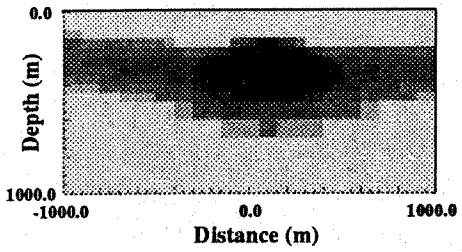

Figure 8. Pole-dipole inversion result for the model in Figure 4. The model achieved an RMS misfit of 7% after 10 iterations.

As a final example, a 200 Ωm conductor was included in the model to simulate a near-surface channel (Figure 9). A synthetic pole-dipole data set with 5% Gaussian noise was then inverted using the generalized subspace algorithm.

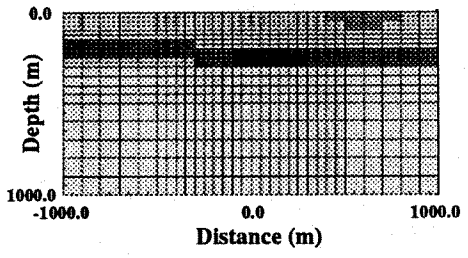

Figure 9. Cross-section through the model used in a more complicated example. In this model a 200 Ωm conductor was included to simulate a near-surface channel.

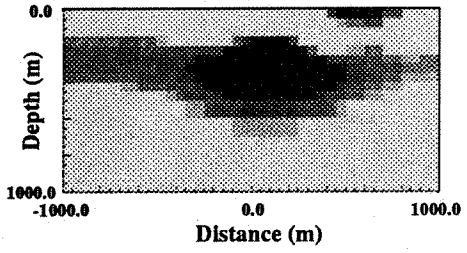

Figure 10. Pole-dipole inversion result for the model in Figure 9. The model achieved an RMS misfit of 8% after 10 iterations.

After 10 iterations the result shown in Figure 10 was achieved, yielding an RMS misfit of 8%. Both the conductive plug and the near-surface channel were well defined, as was the left segment of the layer. Imaging of the right segment of the layer was somewhat weaker because of a loss of signal from current channeling within the near-surface conductor. The success of this example indicates that the inversion can resolve structures below near-surface inhomogeneities providing that enough current reaches the target.

Summary and Conclusions

An algorithm for inverting resistivity data to recover smoothed estimates of the subsurface resistivity structure was described. The algorithm was used to invert synthetic E-SCAN resistivity data generated over structures typically encountered in groundwater contamination and EOR problems. A fine parameterization involving of the order of 1000 parameters allowed the inversion algorithm to have maximum flexibility in fitting the data. Problems with slow convergence and instabilities due to an incorrect parameterization were thus avoided. In order to make it computationally feasible to solve for such a large number of parameters, a generalized subspace approach was developed and used to re-parameterize the model perturbations. In spite of the significant decrease in the effective number of parameters, the algorithm was able to adequately reproduce the data after a small number of iterations. By minimizing a global model norm, and thereby imposing a smoothness constraint on the recovered model, the non-uniqueness inherent in the inverse problem was also addressed. It was found that the smoothness constraint also allowed the algorithm to filter out most of the noise from the data. Because small changes in the data can translate into large changes in the recovered model, this robustness is necessary if the inverse problem is to be well posed.

The ability of the algorithm to recover smoothed estimates of the subsurface resistivity distribution, even with a variable near-surface, was clearly demonstrated. A comparison of pole-dipole and pole-pole inversions showed that the resolution of the recovered model was a function of the electrode array used. The more highly resolved pole-dipole result suggested that the pole-dipole array may be more useful for near surface imaging. For problems where greater depth of penetration is required, the pole-pole configuration will likely lead to better results.

P.R. McGillivray received his B.Sc. in geophysics from the University of British Columbia in 1984. He was employed as an exploration geophysicist by Canadian Superior Oil Ltd. and Mobil Oil Canada Ltd. from 1984 to 1986. He is presently a Ph.D. candidate in the Department of Geophysics and Astronomy at The University of British Columbia (2219 Main Mall, Vancouver, British Columbia V6T 1W5, Canada). His current research interests include the solution of large-scale modeling problems using adaptive multigrid techniques and the solution of inverse problems in groundwater and geophysics.

D.W. Oldenburg received a B.Sc.(Hons.) in physics in 1967 and an M.Sc. degree in earth science in 1969, both from The University of Alberta and a Ph.D. degree in earth sciences in 1974 from Scripps Institute of Oceanography. He was a Killam postdoctoral fellow at The University of Alberta from 1974 to 1976. Since 1977 he has been with the Department of Geophysics and Astronomy at the University of British Columbia (2219 Main Mall, Vancouver, British Columbia V6T 1W5, Canada) where he is currently a professor. His interests center around the application of inverse theory to problems in electromagnetic and seismic data processing. He is a member of SEG, EAEG and the CSEG.

References

Ahmed, A., G. de Marsily, and A. Talbot 1988. Combined use of hydraulic and electrical properties of an aquifer in a geostatistical estimation of transmissivity. Ground Water, v. 26, pp. 78–86.

Bardossy, A., I. Bogardi and W.E. Kelly 1986. Geostatistical analysis of geoelectric estimates for specific capacity. J. of Hydrol., v. 84, pp. 81–95.

Beasley, C.W. 1989. Cross-borehole resistivity inversion: theory and application to monitoring enhanced oil recovery. Ph.D. thesis, Department of Geology and Geophysics, The University of Utah.

Berk, W.J. and B.S. Yare 1977. An integrated approach to delineating contaminated ground water. Ground Water, v. 15, pp. 138–145.

Dey, A. and H.F. Morrison 1979. Resistivity modeling for arbitrarily shaped two-dimensional structures. Geophys. Prospect., v. 27, pp. 106-136.

Frohlich, R.K. and W.E. Kelly 1985. The relation between hydraulic transmissivity and transverse resistance in a complicated aquifer of glacial outwash deposits. J. of Hydrol., v. 79, pp. 215–229.

Huntley, D. 1986. Relations between permeability and electrical resistivity in granular aquifers. Ground Water, v. 24, pp. 466–474.

Kelly, W.E. 1976. Geoelectric sounding for delineating ground-water contamination. Ground Water, v. 14, pp. 6–10.

Kelly, W.E. 1977. Geoelectric sounding for estimating aquifer hydraulic conductivity. Ground Water, v. 15, pp. 420–425.

Kennett, B.L.N. and P.R. Williamson 1987. Subspace methods for large scale nonlinear inversion. In Mathematical Geophysics: A Survey of Recent Developments in Seismology and Geodynamics. (eds. N.J. Vlaar, G. Nolet, M.J.R. Wortel and S.A.P.L. Cletingh). D. Reidel, Dordrecht.

Kennett, B.L.N., M.S. Sambridge and P.R. Williamson 1988. Subspace methods for large inverse problems with multiple parameter classes. Geophys. J., v. 94, pp. 237–247.

Klefstad, G., L.V.A. Sendlein and R.C. Palmquist 1975. Limitations of the electrical resistivity method in landfill investigations. Ground Water, v. 13, pp. 418–427.

Kosinski, W.K. and W.E. Kelly 1981. Geoelectric soundings for predicting aquifer properties. Ground Water, v. 19, pp. 163–171.

Mazac, O., W.E. Kelly and I. Landa 1985. A hydrogeophysical model for relations between electrical and hydraulic properties of aquifers. J. of Hydrol., v. 79, pp. 1–19.

McGillivray, P.R. and D.W. Oldenburg 1990. Methods for calculating Fréchet derivatives and sensitivities for the non-linear inverse problem: a comparative study. Geophys. Prospect., v. 38, pp. 499–524.

Parasnis, D.S. 1986. Principles of Applied Geophysics. Chapman and Hall.

Roy, A. and A. Apparao 1971. Depth of investigation in direct current methods. Geophysics, v. 36, pp. 943–959.

Roy, A. 1972. Depth of investigation in Wenner, three-electrode and dipole-dipole DC resistivity methods. Geophys. Prospect., v. 20, pp. 329–340.

Schwartz, F.W. and G.L. McClymont 1977. Applications of surface resistivity methods. Ground Water, v. 15, pp. 197–202.

Sri Niwas and D.C. Singhal 1981. Estimation of aquifer transmissivity from Dar-Zarrouk parameters in porous media. J. of Hydrol., v. 50, pp. 393–399.

Sri Niwas and D.C. Singhal 1985. Aquifer transmissivity of porous media from resistivity data. J. of Hydrol., v. 82, pp. 143–153.

Stollar, R.L. and P. Roux 1975. Earth resistivity surveys – a method for defining ground-water contamination. Ground Water, v. 13, pp. 145–150.

Urish, D.W. 1983. The practical application of surface electrical resistivity to detection of ground-water pollution. Ground Water, v. 21, pp. 144–152.

Worthington, P.F. 1976. Hydrogeophysical equivalence of water salinity, porosity and matrix conduction in arenaceous aquifers. Ground Water, v. 14, pp. 224–232.

A Conceptual Framework for the Geostatistical Approach to the Inverse Problem

by Peter K. Kitanidis

Abstract

An overview of the geostatistical approach to the inverse problem is presented, with emphasis on the conceptual basis of the methodology. In particular, the problem is viewed as one of prediction with incomplete information, rather than a classical statistics or frequency analysis problem. The principles of maximum entropy and Bayes' inference are explained and it is shown that, under certain assumptions, they lead to a geostatistical approach. This interpretation sheds light on the meaning of the probabilistic model and the error bounds on the predictions; the strengths and limitations of the normality assumption; and the relevance of maximum likelihood estimation. Further, the insight leads to new algorithms appropriate for, among others, large-variance problems.

Peter Kitanidis is a hydrologist with the Department of Civil Engineering, Stanford University (Stanford, California 94305-4020, USA).

Optimization Methods in Inverse Solution of Groundwater Flow Systems

By **Jiannan Xiang** and **Derek Elsworth**

Abstract

Inverse solution may be effectively used to determine in situ hydraulic parameters at field scale. Where data are limited to m spatially distributed values of transmissivity and n distributed hydraulic head magnitudes, the distributions of transmissivity and hydraulic head in the remainder of the domain may be determined using any suitable inverse method. Indirect methods are widely used in this class of problem because of their flexibility and ability to handle nonlinear parameters and constraints. However, the effectiveness of these methods varies considerably with the adopted optimization technique. A comparison was completed between six well-known optimization methods in the minimization of a multidimensional functional. The relative performance of these methods was then compared using an example. The differential equation of flow was represented by a low-order finite element that has been shown to perform well. Five cases were studied under different levels of data completeness or incompleteness. Results indicated that all methods perform well for complete data but may be ranked according to solution time. With incomplete data sets, computational requirements are increased, with the Quasi-Newton method yielding the most accurate results. The Levenberg-Marquardt method performed with high accuracy and exhibited rapid convergence, although the CPU requirements are greater than for the Gauss-Newton method. Where different initial estimates were used to start the iteration, unique transmissivity distributions resulted for cases of complete data. With incomplete data the results are non-unique. To improve the solution, an objective function using an average value of transmissivity is presented. The computed results show that the accuracy of the solution was improved and the CPU time remained at the same magnitude.

Introduction

The difficulty with which in situ hydraulic parameters may be obtained by direct measurement makes parameter estimation by inverse methods an attractive procedure. Observations may be limited to m spatially distributed values of transmissivity and n distributed hydraulic head magnitudes. A complete distribution of these parameters over the entire domain may be determined by any suitable and robust inverse method. Both direct and indirect methods are available to solve the inverse problem. In the direct method a technique such as Kriging may be used to interpolate initial hydraulic head magnitudes, which must then be inverted by a suitable procedure to obtain the transmissivity distribution. Success of the method is dependent on the initial estimate of hydraulic head distribution. This method (Frind and Pinder, 1973) may give poor results where the measured gradients of head are low, as demonstrated by Weir (1989).

Alternatively, the indirect method requires that hydraulic head and transmissivity distributions are obtained by minimizing an objective function relating these two parameters. The major requirement is that the objective function must be defined to enable solution. This method works well where the complete data set is available. Since, in the finite element method, the sizes and shapes of elements can easily be changed to match the spatial distribution of observations, the indirect method with complete data works very well. The parameters within each element can be obtained using interpolation of the basis function. The indirect method is also used widely for inverse problems with incomplete data or for problems in which measurements are fewer than unknowns . A variety of optimization methods may then be used in the solution. Yeh et al. (1983) presented a similar method for an unsteady state groundwater flow model. The parameters are optimally determined by a generalized matrix inversion scheme. Aral

(1986) presented an optimization approach for the identification of aquifer parameters in mutilayer systems. Many optimization approaches are available for inverse solution. However, it is very important to determine the efficiency of these optimization methods to perform parameter estimation under both complete and incompleted data sets because, for a real problem, the dimensions of the parameter are very large and an ineffective method will result in high computational cost or an unreasonable solution. In this paper, six methods are tested using a multidimensional example for a variety of starting vectors and different data densities. All of the methods are widely used in inverse solution and some of them are very effective for optimization of nonlinear equations. To make these optimization methods more effective in the estimation of parameters, an objective function combined with *a priori* information is presented.

Governing Equation and Objective Functions

Differential Equation

The basic assumptions for the one- or two-dimensional problems of groundwater flow considered in the following are that the aquifer is horizontal, inhomogeneous from point to point and continuous in the region. Only confined problems are considered where the transmissivity is directionally isotropic. The governing equation for a groundwater flow system can be written as:

$$\frac{\partial}{\partial x_i}\left(T\frac{\partial h}{\partial x_i}\right) = \Sigma Q_w(t)\Pi\delta(x_i - x_w) + S\frac{\partial h}{\partial t} \quad (1)$$

where i = 1, 2, 3.

For a two dimensional problem, the equation can be rewritten as:

$$\frac{\partial}{\partial x}\left(T\frac{\partial h}{\partial x}\right) + \frac{\partial}{\partial y}\left(T\frac{\partial h}{\partial y}\right) = \Sigma Q_w(t)\,\delta(x - x_w)\delta(y - y_w) + S\frac{\partial h}{\partial t} \quad (2)$$

and must satisfy the following conditions:

$$h(x,y,0) = h_0(x, y) \qquad x, y \text{ in } R$$

$$h(x,y,t) = h_1(x,y,t) \qquad x, y \text{ in } dR_1$$

$$T\frac{\partial h}{\partial n} = h_2(x,y,t) \qquad x, y \text{ in } dR_2$$

where h(x,y,t) is hydraulic head at point (x,y), T(x, y) is transmissivity at (x,y), S is storage coefficient, Q_w is source-sink term, x, y are coordinates in two-dimensional space, t is time, R is the flow region, dR is the boundary of the aquifer ($dR_1 \cup dR_2 = dR$), h_0, h_1, h_2 are specified functions, $\delta(x)$ is the Dirac delta function with $\delta(x) = \infty$ for $x = 0$ and $\delta(x) = 0$ for $x \neq 0$, and x_w, y_w are the coordinates of a well.

Governing Equation

Using a low order finite element (Xiang and Elsworth, 1990), eqn (2) for the steady state condition is readily transferred to a system of linear equations . The equation may be written as:

$$\mathbf{T}H = Q_w + q = Q \quad (3)$$

or

$$\mathbf{H}T = Q \quad (4)$$

where $\mathbf{T}$ is a matrix representing the transmissivity distribution of the domain, $\mathbf{H}$ is a matrix representing the hydraulic head distribution within the domain, H is a vector of nodal hydraulic head magnitudes, T is a vector of elemental transmissivity magnitudes, Q_w is a vector of source-sink values, **q** is a vector of boundary discharge and Q is a vector of discharge.

Objective Function for Minimization

In the indirect method, the solution must satisfy an error criterion. The purpose is to determine the transmissivity parameter, T, from a limited number of observations scattered throughout the field. An objective function is necessary for minimization. In this paper, two objective functions based on the least square error are used. One is the scalar function f defined as:

$$f = (H^* - H)^T(H^* - H) + (T^* - T)^T(T^* - T) \quad (5)$$

where f is a scalar function, H^* is the observed head vector and T^* is the observed transmissivity vector. Another objective function is a vector function $\underline{f}$, where the element f_i is given by

$$f_i = (H_i^* - H_i)^2 + (T_i^* - T_i)^2 \quad (6)$$

The procedure for the calculation of functions f and f_i include the following steps:

1. Input the predicted vector of transmissivity;
2. Formulate the matrix $\underline{T}$;
3. Solve eqn. (3) for hydraulic head H;
4. Compute function f or f_i.

It is noted that the linear system of equations must be solved once for hydraulic head, H, in each calculation of function f or f_i.

The Methods Studied

A total of six methods were used in the comparison, as shown in Table 1. The type of method and constraint are also shown in Table 1. A brief description of each method is given in the following section.

Table 1
Six Methods Studied for Comparison

Method	Name	Type	Constraint
1	Quasi-Newton	Local	no
2	Global Minimization	Global	yes
3	Gold Section Powell	Local	no
4	Fletcher Powell	Local	no
5	Gauss - Newton	Local	yes
6	Levenberg - Marquardt	Local	no

Quasi-Newton Method

In this method, it is assumed that the gradient vector:

$$g(T) = (\partial f/\partial T_1, \partial f/\partial T_2, \partial f/\partial T_3, \ldots\ldots \partial f/dT_n)$$

and Hessian matrix:

$$H_e = \frac{\partial^2 f}{\partial T_i \partial T_j} \quad (7)$$

exist in the study region. The computations of gradient vector and Hessian matrix are carried out by updating the initial Hessian with each iterative step.

Global Minimization

The Global Minimization method is used to obtain a global minimum for a constrained problem. This constrained minimization problem is transformed to unconstrained minimization by the following equation

$$T_i = a_i + (b_i - a_i)\sin^2 y_i \quad (8)$$

where $a_i \le T_i \le b_i$ with a_i and b_i being the lower and upper bounds, respectively.

Therefore, the constrained minimization problem is equivalent to minimizing an unconstrained problem such as:

$$f = f(a_1 + (b_1 - a_1)\sin^2 y_1 + \ldots\ldots a_n + (b_n - a_n)\sin^2 y_n) . \quad (9)$$

Using this transformation, each possible global minimum, including any one on the boundary, is transformed into a local minimum (Box, 1966). The remainder of the solution is carried out by the Quasi-Newton method.

Golden Section Powell Method

The Golden Section Powell method is a search method. The search is started in a selected direction at the initial point by the Powell method (Powell, 1964). The Powell method has been shown to be effective in a comparison with several optimization methods (Box, 1966). The Powell procedure may be outlined as,

1. For r =1,2...n, calculate λ^r so that $f(T^{r-1} + \lambda^r \xi^r)$ is a minimum and define

$$T^r = T^{r-1} + \lambda^r \xi^r; \quad (10)$$

2. Find the integer m, so that
   $\Delta = f(T^{m-1}) - f(T^m)$ is a maximum;
3. Calculate $f^3 = f(2T^n - T^o)$, $f^1 = f(T^o)$ and $f^2 = f(T^n)$;
4. If $f^3 \geq f^1$ or $(f^1-2f^2 + f^3)*(f^1-f^2-D) \geq D(f^1-f^3)^2/2$, use the old directions for the next iteration and use T^n for the next T^o, otherwise
5. Use $\xi = T^n - T^o$ and go to i).

In the directional search, the Golden Section technique is used to find λ^r, a scalar. This produces a better solution with reduced search time. The advantage of this method is that the minimization problem does not require the calculation of derivatives and has an improved solution over the pure Powell method.

Fletcher-Powell Method

A function f(x) may be extended as:

$$f(T+\delta T) \approx f(T) + J\,\delta T + H_e \delta T/2 \quad (11)$$

where J is a Jacobian matrix, H_e is defined as before, and δT is an increment vector of T.

In this method, the Hessian matrix which contains the second derivative terms is needed. In fact, an accurate Hessian matrix is difficult to obtain, therefore, the inverse of the Hessian matrix is approximated by another matrix, G, which iteratively approaches H^{-1}_e. The first Fletcher-Powell iteration is equivalent to the steepest descent method, but successive iterations are better approximations for H^{-1}_e to improve the search direction.

An approximation of G^{n+1} is found using the parameter change ΔT and also the gradient change:

$$Y = \text{gradient}(T') - \text{gradient}(T) \quad (12)$$

where $T' = T + \Delta T$, and

$$G^{n+1} = G^n + \alpha_1 \Delta T \Delta T^T - \alpha_2 G^n Y (G^n Y)^T \quad (13)$$

where the scale factors α_1 and α_2 are given by:

$$\alpha_1 = Y^T \Delta T \quad (14)$$

$$\alpha_2 = Y^T G Y \quad (15)$$

Gauss-Newton Minimization

This algorithm is widely used to perform minimization in parameter estimation (Jahns et al. Jacquard and Jain, 1966; Yeh, 1986; and Aral, 1986). The advantages of this method are that it does not require the calculation of the Hessian matrix, as is required by the Newton method, and the rate of convergence is high (Yeh, 1986). The algorithm generates the following parameter sequence for an unconstrained minimization problem:

$$T_{n+1} = T_n - \delta T_n \quad (16)$$

and

$$(J_n^T J_n)\, d_n = J_n^T (H^* - H(T_n)) \quad (17)$$

$$\delta T_n = \rho_n \delta_n \quad (18)$$

where ρ_n is step size;

δT is defined as before;

d_n is Gauss- Newton direction vector;

J_n is Jacobian matrix at T_n; the elements in J_n are first derivatives and may be estimated using the forward difference method as:

$$\frac{\partial f}{\partial T_i} = \frac{f(T + \varepsilon \upsilon) - f(T)}{\varepsilon} \quad (19)$$

where υ is a unit vector and ε is scalar, (one may use $\varepsilon = c\,T_i$, where c is a very small number).

The step size ρ_n is a scalar. In this paper it is determined by a trial-and-error procedure until the current error is less than the previous error, such that:

$$f(T_n - \rho_n \delta_n) < f(T_n) \quad (20)$$

To limit the number of iterations, the constraints $T_{min} \leq T_i \leq T_{max}$ are added to this method.

Levenberg-Marquardt

For m nonlinear functions, $f_1, f_2, \ldots\ldots f_m$ of a vector parameter T, one desires to minimize the function f:

$$f = f_1(T)^2 + f_2(T)^2 + \ldots\ldots f_m(T)^2 \qquad (21)$$

When fitting a nonlinear model to data, the function f_i should be defined as before. Newton's procedure is used and

$$T^{n+1} = T^n - [\beta_n D_n + J_n^T J_n]^{-1} J_n^T f(T_n) \quad (22)$$

where J_n is the Jacobian matrix at T_n, D_n are the elements of the diagonal of matrix $J_n^T J_n$, β_n is a positive scaling constant (Marquardt parameter).

Comparison

A comparison of the different methods was completed using the square error criterion for various physical cases. The effects of data density, initial values and objective function on the accuracy are discussed below. Prior information was used to increase the reliability of the solution.

Example and Cases Studied

The example problem is one of unidirectional flow in an inhomogeneous aquifer. The width of the aquifer is uniform and equal to unity.

The constraints are:

$$h_a = 1.0;\ h_b = 3.0$$
$$T_a = 1.0;\ T_b = 2.0$$

The theoretical solution is:

$$h(x) = 2.8854 \ln(x/6 + 1) + 1$$
$$T(x) = x/6 + 1.$$

where h_a and h_b are the hydraulic heads and T_a and T_b are the transmissivities at each end of the aquifer; and x is the longitudinal coordinate. To investigate the behavior of different methods to the data density, five cases are studied, as shown in Table 2. The six methods studied are described in Table 1.

Table 2
Five Cases Studied for Different Methods

Case	Description	Data density (%)
1	complete data	100
2	incomplete data	86
3	incomplete data	71
4	incomplete data	57
5	incomplete data	43

Results

All computations were run on a mainframe IBM 3090. The initial values, observations and boundary conditions were the same in the computations for all methods. The computed results for five cases by all six methods are shown in Tables 3 and 4. In order to describe

Table 3
Sums of Square Errors Between the Theoretical and Computed Heads

Case	Method 1	Method 2	Method 3	Method 4	Method 5	Method 6
1	1.6260e-7	1.3817e-7	1.6855e-7	1.7250e-7	1.9801e-7	1.7725e-7
2	2.7504e-7	2.3187e-7	1.6387e-7	2.1445e-7	3.8532e-7	2.2796e-7
3	1.4536e-5	7.0933e-2	9.9610e-5	3.2276e-3	1.6688e-4	1.2613e-5
4	6.4217e-4	1.9826e-1	2.2285e-3	2.0553e-3	7.3824e-1	8.2021e-4
5	7.2075e-3	2.2494e-1	7.5686e-3	9.3419e-3	2.0919e-1	1.1220e-2

Table 4
Sums of Square Errors between the Theoretical and Computed Transmissivities

Case	Method 1	Method 2	Method 3	Method 4	Method 5	Method 6
1	1.5160e-5	9.6428e-5	1.6494e-5	1.3126e-5	1.5070e-5	9.7645e-6
2	2.6779e-4	2.2823e-5	3.5130e-5	2.0658e-5	2.1824e-5	2.2374e-5
3	5.1427e-3	1.9490	3.9386e-3	1.2450e-1	8.0980e-3	4.3786e-4
4	1.3926e-2	29.875	5.9818e-2	7.9721e-2	4.6871	1.8103e-2
5	5.8372e-2	0.1783	6.2088e-2	1.7772e-1	5.1787	1.1028e-1

the methods easily, we refer to these methods by numbers defined in Table 1. The sum of the square error of hydraulic head and transmissivity are presented. It is noted that the error in head distribution is related to that in transmissivity distribution. Comparing Table 3 with Table 4, it is apparent that the errors in hydraulic head are almost two orders of magnitude less than those in transmissivity, and with an incomplete data set the square errors of hydraulic head are very small for all methods.

The Quasi-Newton method (method 1) performed very well. The errors both in transmissivity and in head are very small compared with other methods. This fact may be attributed to the evaluation of second derivatives in each iteration. With an incomplete data set, although the accuracy decreases, this method still gives a better solution than other methods. The required CPU time is in the middle range of the six methods. With more observations, more CPU time is required because the objective function requires more iterations to be minimized within a certain tolerance, as shown in Table 5.

The Global minimization method (method 2) requires an upper bound and lower bound. The search seeks to find a global minimum among all local minimums. In the computation, the minimum was found, from several iterations, to continue to convergence by the Quasi-Newton method for the final result. With a complete data set, this method produced good results for the parameter estimated, as shown in Table 4

Table 5
CPU Time Used for Computations by Different Methods (in 10^{-6} s)

Case	Method 1	Method 2	Method 3	Method 4	Method 5	Method 6
1	867	69530	1537	10655	140	188
2	731	69376	2815	10089	138	176
3	706	68927	396	3960	138	175
4	622	68771	561	7429	113	176
5	498	68216	133	8697	192	140

(method 2, case 1). However, because more iterations are required in this method, the CPU time used is about two orders of magnitude larger than that used by methods 1, 5 and 6. Table 5 also shows that the CPU time changes very little when the data density decreases. For incomplete data sets, the solutions deviate from the real solution. The reason is that the real solution may not be the global minimum for a problem with incomplete observations. This implies that the solution of this problem is not unique. This non-uniqueness is described in the Appendix. To improve the solution, one may specify a reduced range for the upper bound and lower bound. Different cases of reduced ranges were evaluated and are shown in Table 6. It is noted that when the upper bound is changed from 5.0 to 2.5 and the lower bound from 0.5 to 0.75, the square error of estimated transmissivity is changed from 9.643e-5 to 1.0614e-5 for case 1. However, this method may not be suitable for the inverse problem with low data density because the results are not reliable and too much CPU time is required.The errors from the solution of the Golden Section Powell method (method 3) are in the central range of errors, compared to the other methods. Although it is not required to evaluate the first and second derivatives of the objective function, the errors both in hydraulic head and transmissivity are relatively small, especially in the case where more observations are not available. The CPU time required varies significantly with variation of data availability. This fact implies that this method will require increased CPU time for multi-dimensional problems.

Table 6
Sums of Square Errors Between the Theoretical and Computed Transmissivities for Different Upper and Lower Bounds

No.	Case	Method 2	Method 5
1*	1	9.6428e-5	1.5070e-5
1	2	2.2823e-5	3.5130e-5
1	3	1.9490	8.0980e-3
1	4	29.875	4.6871
1	5	1.7830e-1	5.1787
2	1	1.0164e-5	1.5070e-5
2	2	2.2632e-5	2.1824e-5
2	3	7.8729e-1	8.0980e-3
2	4	1.6906	1.9700
2	5	2.6180e-1	2.1836
3	1	1.0272e-5	1.5070e-5
3	2	2.2231e-5	2.1824e-5
3	3	1.7142e-1	8.0980e-3
3	4	2.3261e-2	1.1630e-2
3	5	7.0338	8.8927e-1

*where for No. 1, T_{max} = 5.0 and T_{min} = 0.5; for No. 2, T_{max} = 2.5 and T_{min} = 0.75; for No. 3, T_{max} = 2.1 and T_{min} = 0.9.

The Fletcher-Powell method (method 4) requires evaluation of the first and second derivatives of the objective function. The results are very good in the case of complete data. One disadvantage is that this method needs considerable CPU time to attain the required precision because of the calculation of the inverse of the Hessian matrix in each iteration. This method, however, requires less CPU time than method 2, as shown in Table 5.

The Gauss-Newton method (method 5) works very well for a complete data set. For low data density, the solution may not converge to the true solution. By narrowing the bounds, an improved solution can be obtained, as shown in Table 6. An attractive advantage is that the CPU time required by this method is the least among all six methods, as noted in Table 5.

The Levenberg-Marquardt method (method 6) can give excellent results in the case of high data density compared with those by other methods with the exception of method 1. The CPU time required was only slightly greater than that by the Gauss-Newton method. In fact, when the coefficient β_n in eqn (22) is zero, both methods are the same. However, the Levenberg-Marquardt method is more efficient, especially in the case where the determinant of J^TJ is very small or equal to zero, because in this case the modification of transmissivity are difficult to obtained correctly. Using this method, one can avoid such numerical difficulties and obtain a reasonable solution.

Convergence of Solution

For a complete data set, all methods perform very well and the square errors are very small. For incomplete data sets, the errors both in hydraulic head and transmissivity distribution increase as the data availability decreases. Two behaviors may be noted. The first one exhibits linear behavior in the relation between the logarithm of square error and the percentage data density. This behavior may be indicated by methods 1, 3 and 6 in both Figures 1 and 2. The second one may be indicated by methods 2, 4 and 5. The errors by these three methods increase in a nonlinear manner as data density decreases, as shown in Figures 1 and 2. Comparing curves in both Figures 1 and 2, it is apparent that methods 1 and 6 have the least error as the data density decreases.

Because most methods are based on local minimization and because global minimization may be questionable with incomplete data sets, a series of tests based on different initial values was carried out. The results indicated that when data are incomplete, almost all methods are sensitive to the initial values except the global method (Table 7). The variations of errors for the case with complete data are very small compared with those cases with incomplete data sets. All results by different methods, and initial values in Table 7, show that the solutions by local minimization methods are nonunique when the data density is low.

Table 7
Sums of Square Errors between the Theoretical and Computed Transmissivities for Different Initial Values

T_o	Case	Method 1	Method 2	Method 3	Method 4	Method 5	Method 6
1.5	1	1.5160e-5	9.6428e-5	1.6494e-5	1.3126e-5	1.5070e-5	9.7645e-6
1.5	2	2.6779e-4	2.2823e-5	3.5130e-5	2.0658e-5	2.1824e-5	2.2374e-5
1.5	3	5.1427e-3	1.9490	3.9386e-3	1.2450e-1	8.0980e-3	4.3786e-4
1.5	4	1.3926e-2	29.875	5.9818e-2	7.9721e-2	4.6871	1.8103e-2
1.5	5	5.8372e-2	0.1783	6.2088e-2	1.7772e-1	5.1787	1.1028e-1
1.0	1	1.5128e-5	9.6087e-6	4.7077e-6	1.0243e-5	1.4101e-5	1.4092e-5
1.0	2	2.9784e-5	2.2557e-5	8.4437e-1	3.6597e-4	3.0114e-5	2.2247e-5
1.0	3	1.0555	1.9505	1.1059	1.5134	1.3889	8.4227e-1
1.0	4	1.0220	19.030	9.2388e-1	1.4997	1.6276	8.0069e-1
1.0	5	1.1376	20.181	1.1716	1.3314	1.52055	1.3055
2.0	1	1.5494e-5	9.9575e-6	8.5452e-6	1.5386e-5	1.4344e-5	1.7585e-5
2.0	2	3.2006e-5	2.2340e-5	5.4082e-5	2.2684e-5	2.3644e-5	2.2301e-5
2.0	3	7.2706e-1	1.9504	1.0703	3.3719e-1	2.2971	7.4167e-1
2.0	4	8.8922e-1	29.800	7.8025e-1	6.5407e-1	2.1709	7.1534e-1
2.0	5	9.7019e-1	21.005	9.1515e-1	5.9963e-1	15.397	3.4837e-1
random	1	1.4000e-5	1.0396e-5	5.1117e-6	6.4459e-5	1.2644e-5	1.6903e-5
random	2	3.2099e-4	2.2660e-5	5.7951e-6	2.9804e-5	2.8532e-5	2.2345e-5
random	3	1.3063e-1	1.9544	4.1205e-2	6.3602e-1	1.5524	3.0665e-1
random	4	8.8392e-2	19.6418	1.5886e-1	6.4422e-1	9.4895	2.6519e-1
random	5	4.1972e-1	20.179	4.0722e-1	6.6548e-1	6.8498e-1	6.6420e-1

where T_o is the initial value, a constant means all initial values are the same; random means that each initial value was chosen randomly.

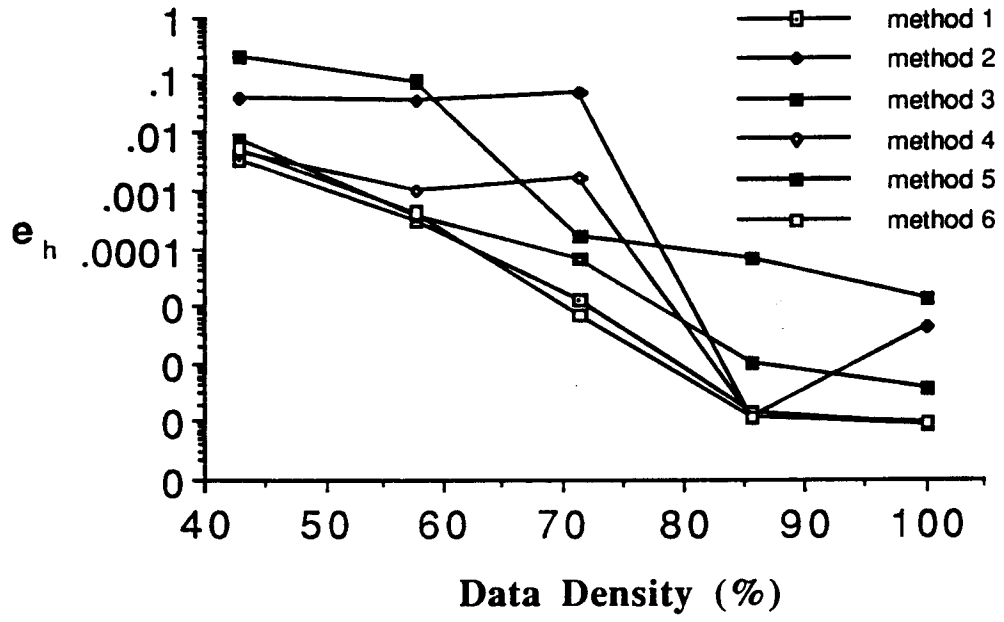

Figure 1. The relation between the data density and square error of estimited head, e_h.

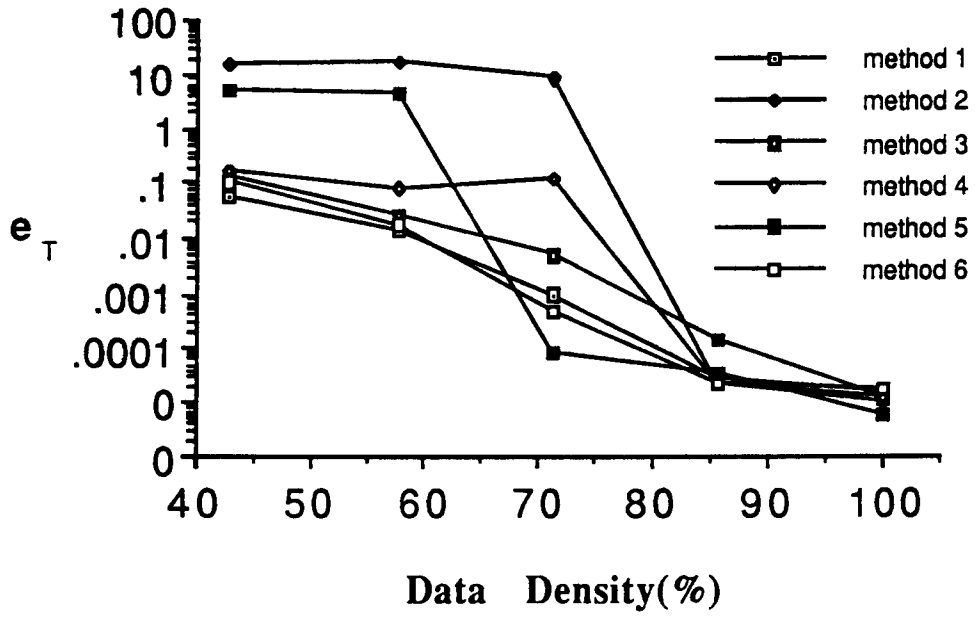

Figure 2. The relation between the data density and square error of estimited transmissivity, e_T.

Modification of Objective Function

As mentioned above, most solutions are nonunique when the data are incomplete. Different initial values may lead to intangible solutions even if the objective function is minimized. Therefore, it is difficult to find a correct solution for an incomplete data set using any minimization method mentioned above. Gavalas et al. (1976) applied a Bayesian estimation method which incorporates prior information to parameter identification. This method performs well only for a linear model when the measurement errors are normally distributed. It may also be noted that it is difficult to find a suitable value of λ ($0<\lambda<1$). Several tests for the same example were conducted to find a better solution. The computed results show that only when λ is very small, can the accuracy be improved, and then only slightly. However, the computation also showed that the mean value of transmissivity is a very important parameter for finding a unique solution. This value may be obtained from field boundary discharge and the average hydraulic head, or by using a statistical method.

Considering the fact that average values of estimated and measured transmissivities in the whole domain should be same, the objective function can be modified as:

$$f = (H^* - H)^T(H^* - H) + (T^* - T)^T(T^* - T) + (T^*_m - T'_m)^2 \quad (23)$$

where T'_m is $(\Sigma T_i)/k$, predicted average transmissivity for the domain, a scalar; k is number of parameter dimensions; T^*_m is measured average transmissivity for the studied area, a scalar.

Because T^*_m is a scalar, this objective function cannot be used for the Gauss-Newton and Levenberg-Marquardt methods. The computations for five cases with different initial values were carried out. The results are shown in Table 8. Comparing Table 8 with Table 7, one may note that results by using the above objective function are much better. In most cases, the square error by this objective function is one or two orders of magnitude less than those by the previous objective function. It also indicates that when the data density is < 60%,

Table 8
Sums of Square Errors Between the Theoretical and Computed Transmissivitie for Modified Objective Function

T_o	Case	Method 1	Method 2	Method 3	Method 4
1.5	1	4.6127e-6	4.4326e-6	4.1073e-6	3.8875e-5
1.5	2	4.8498e-6	4.5872e-6	4.2295e-6	1.2227e-5
1.5	3	5.5720e-6	5.5651e-6	5.5926e-6	8.6572e-5
1.5	4	1.3560e-2	1.5033	1.1647e-3	5.0497
1.5	5	5.5363e-1	2.0294	5.1083e-2	3.4924
random	1	4.6699e-6	4.3926e-6	4.2466e-6	1.3456e-5
random	2	4.8403e-5	4.5872e-6	4.9299e-5	9.1651e-6
random	3	5.5732e-6	5.5651e-6	5.6388e-6	3.2561e-5
random	4	1.0947e-2	1.0335	1.2407e-2	4.3352
random	5	6.3324e-2	2.0294	7.3866e-2	3.2438

the square error is much larger for all four methods used. When random initial values are used, the variations of square errors are very small compared with those using a constant initial value. Interestingly, the CPU time required remains of the same order of magnitude, except in method 3, where the CPU time required is increased (Table 9).

3. The Quasi-Newton method performs best of the six methods for the example problems with incomplete data sets in terms of accuracy and CPU time, especially when the mean value of the parameter is available, though it requires about three times more CPU time than the Gauss-Newton method.

Table 9
CPU Time Used for Computations by Different Methods (in 10^{-6} s) for Modified Objective Function (Random Initial Values)

Case	Method 1	Method 2	Method 3	Method 4
1	554	68846	39735	6534
2	676	68519	40283	7478
3	765	68631	634	5353
4	632	68414	714	5547
5	368	68313	403	3873

Conclusions

The relative performance of six optimization methods for parameter identification in groundwater flow systems are compared. To determine the effects of incomplete data on the accuracy of parameter estimation, many cases with different initial values and objective functions were considered. The computed results show that:

1. For complete data sets all methods perform very well and the results are independent of the initial values. The Levenberg-Marquardt method may be considered as the best method for complete data sets in terms of CPU time and efficiency on different problems, though the Gauss-Newton method needed the least CPU time.

2. The square error of the estimated hydraulic head is about two orders of magnitude less than that of the estimated transmissivity, indicating the insensitivity of the system to transmissivity distribution. This has further ramifications in the determination of unique transmissivity distributions.

4. In problems with incomplete data sets, supplementary information is necessary for a correct solution. The objective function presented, which uses the mean value of the parameter, can improve the solution.

5. For incomplete data sets, global minimization may not be attainable without considerable increases in the required CPU time or requiring addition of more constraints.

Acknowledgments.

This research was supported by U.S. Department of the Interior through the National Mine Land Reclamation Center under agreement No. C0388026. The authors also thank reviewers for their help and commands.

Jiannan Xiang earned his Master of Engineering degree from the Graduate School of the Institute of Water Conservation and Hydroelectric Power Research (IWHR), China. After working at IWHR and the Mathematical Modeling Department of ISMES in Italy, he obtained his Master of Science

degree in the Department of Mineral Engineering, The Pennsylvania State University. Following completion of his Ph.D. in the same department in December, 1990, he is currently Post-doctoral Researcher in the Department of Soil and Environmental Sciences, University of California, Riverside (Department of Soil and Environmental Sciences, University of California, Riverside, California, 92521-0424). His research interests focus on the numerical modeling, computer applications and various areas of computational mechanics.

Derek Elsworth is currently Associate Professor in the Department of Mineral Engineering at the Pennsylvania State University (Department of Mineral Engineering, The Pennsylvania State University, 104 Mineral Sciences Building, University Park, Pennsylvania, 16802, USA), following faculty positions at the Universities of Toronto and Waterloo in Canada. His research interests center on flow and transport of fluids in deformable porous and fractured geological media.

References

Aral,M. 1986. Optimization approach to the identification of aquifer parameters in multilayer systems, Sixth International Conference on Finite Elements in Water Resources, Lisbon, Portugal.

Box, M.J. 1966. A comparison of several current optimization methods and the use of transformation in constrained problems. Computer J. v. 9, pp.67-77.

Frind E. and G. Pinder 1973. Galerkin solution of the inverse problem for aquifer transmissivity. water resources research, v.9, pp 1397-1410.

Gavalas, G.R., P.C. Shah and J.H. Seinfeld 1976. Reservoir history matching by bayesian estimation, Society of Petroleum Engineers Journal, pp.337-350.

Jahns, H.O. 1966. A rapid method for obtaining a two-dimensional reservoir description from well response data, Soc. Petrol. Eng. J., Trans. AIME, v.237, pp.315-327.

Jacquard. P. and C. Jain, 1966. Permeability distributions from field pressure data, Soc. Petrol. Eng. J., Trans., AIME, v.. 234.

Powell, M.J.D. 1964. An efficient method for finding the minimum of a function several variables without calculating derivatives, Computer. J. v.7, pp.155-162.

Weir, G. (1989) The direct inverse problem in aquifers. Water Resources Research, v. 25, pp. 749-753.

Xiang, J. and D. Elsworth 1990. Low-order finite elements for parameter identification in groundwater flow, Applied Mathematical Modeling (in press).

Yeh, W.W-G., Y.S. Yoon and K.S. Lee 1983. Aquifer parameter identification with kriging and optimum parametrization. Water Resources Research, v.19, pp.225-233.

Yeh,W. 1986. Review of parameter identification procedures in groundwater hydrology: the inverse problem. Water Resources Research, v. 22, pp.95-108.

Appendix
Proof of Non-global Minimum for the Inverse Problem with Incomplete Data

A complete proof showing that the real solution for a problem with incomplete data may not give a global minimum objective is difficult to develop. However, if one can find an incorrect solution for the problem that has at least an equal minimum objective value, the problem may be proved.

Let

$$H_1=\begin{Bmatrix}H'_1\\H''_1\end{Bmatrix},\quad H_2=\begin{Bmatrix}H'_2\\H''_2\end{Bmatrix},\quad T_1=\begin{Bmatrix}T'_1\\T''_1\end{Bmatrix},\quad T_2=\begin{Bmatrix}T'_2\\T''_2\end{Bmatrix} \tag{A 1}$$

where H''_i is a vector of computed hydraulic head at n locations of observation for solution i; H'_i is a vector of computed hydraulic head at locations without observations for solution i; T''_i is a vector of computed transmissivity at m locations of observation for solution i; T'_i is a vector of computed transmissivity at the locations without observations for solution i.

Let the objective functions for solutions 1 and 2

$$f_1 = (H^*-H''_1)^T(H^* - H''_1) + (T^* - T''_1)^T(T^*- T''_1) \quad (A\ 2)$$

$$f_2 = (H^*- H''_2)^T(H^* - H''_2) + (T^* - T''_2)^T(T^*- T'') \quad (A\ 3)$$

where H* and T* are observations of hydraulic head and transmissivity, respectively.

Now, assume T_1 is the real parameter of the problem, then the solution H_1 from equation

$$\mathbf{T}_1 H_1 = Q_1 \quad (A\ 4)$$

must be a real solution for the problem because matrix $\mathbf{T}_1$ is only dependent on vector T_1. This will result in the objective function

$$f_1 = (H^*- H''_1)^T(H^* - H''_1) + (T^* - T''_1)^T(T^*- T''_1) = 0 \quad (A\ 5)$$

Similarly, one can solve the following equation for H_2,

$$\mathbf{T}_2 H_2 = Q_2 \quad (A6)$$

with boundary condition

$$H''_2 = H^*$$

where, for the same problem, $Q_2 = Q_1$, T_2 is a matrix depending only on T^* and T'_2. The vector T'_2 may contain arbitrary entries. Therefore, in general, $T_1 \neq T_2$ because $T'_2 \neq T'_1$, though $T^* = T''_2 = T''_1$.
The solution $H_2 \neq H_1$, but it may minimize the objective function f_2 as

$$f_2 = (H^*- H''_2)^T(H^* - H''_2) + (T^* - T''_2)^T(T^*- T''_2) = 0 \quad (A7)$$

Therefore, even though $H_1 \neq H_2$ and $T_1 \neq T_2$, one still has $f_1 = f_2$.

Inverse Modeling in the Frequency Domain: The Example of Estimating Transmissivity From Observations of the Combined Solid Earth Tide and Atmospheric Pressure Influence

by Robert W. Ritzi, Jr.

Abstract

The parameter estimation schemes which include frequency domain models of ground water flow and mass transport have traditionally been posed with estimation criteria based upon modulus or phase transformations of the model frequency response function (FRF) and the sample FRF. A better approach is to use an estimator with a complex vector estimation criterion because it has less bias, less variance, and it is more robust. This has been demonstrated in considering the estimation of transmissivity (T) from well response to the combined Earth tide and atmospheric pressure influences.

Regardless of which criterion is used, T is only identifiable if the data are sufficiently informative. An estimation scheme using the *combined* solid Earth tide and atmospheric pressure information (CSA), when compared to schemes using only the *individual* Earth tide or atmospheric pressure information, gives the greatest probability that sufficient information is contained in a data record so that T is indeed identifiable. The CSA scheme also gives estimates with the greatest precision, and requires the shortest length of time-series data.

Introduction

Water level within a well is known to fluctuate as a result of natural influences. This is shown, for example, in Figure 1. Of particular interest are those variations which are due to the influence of the solid Earth tide (SET) and atmospheric pressure variation (APV). The scope of this paper is a review of recent developments in the extraction of information about the hydraulic properties of a ground water flow regime from these data. In particular, the goal is to consider the estimation of the transmissivity (T) of an aquifer or aquitard. This requires a consideration of the dynamic response of water level to the SET and APV, which is to be distinguished from past work by Bredehoeft (1967), Jacob (1940), and Van der Kamp and Gale (1983) who considered only the hydrostatic response in the estimation of the storage properties of a reservoir.

Estimates of T are usually obtained through conducting pumping tests. However, in the investigation of a hydrogeological regime it may not always be possible to impose pumping stresses on the system. For example, the system may be undergoing a period of baseline monitoring, during which time any anthropogenic disturbances are undesirable. In the investigation of high level nuclear waste repositories, a period of baseline monitoring may be required and may last a considerable number of years. Another example arises within the investigation of areas in which ground-

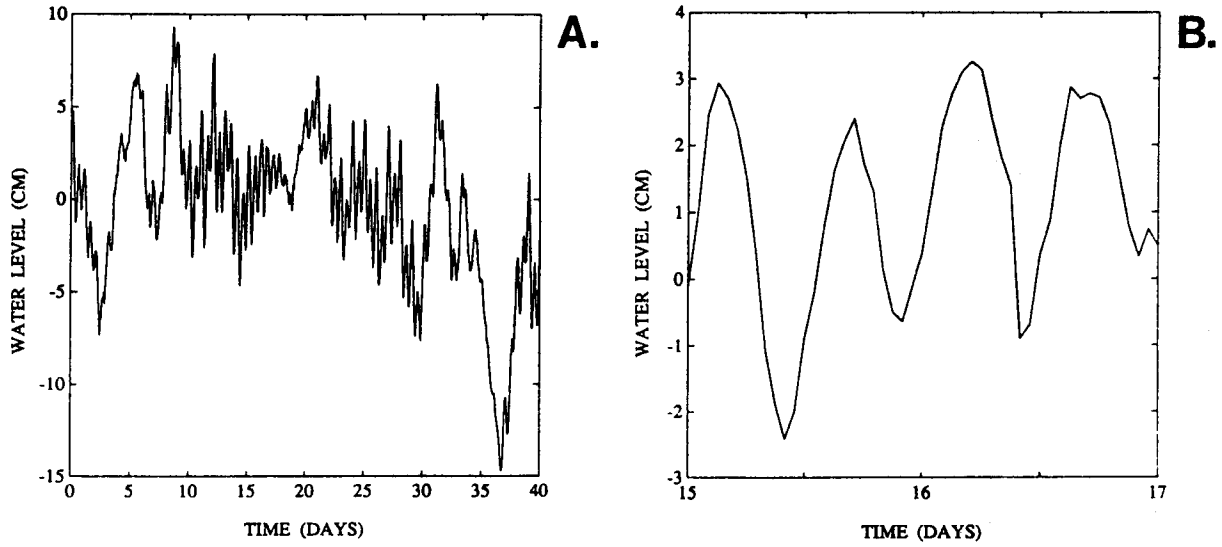

Figure 1.

A. Water level variations observed in a well near Parkfield, CA. Data are from Hsieh et al. (1987). Hourly observation over 40 d are plotted. B. Blow up of 48 h of data showing an obvious semidiurnal periodicity.

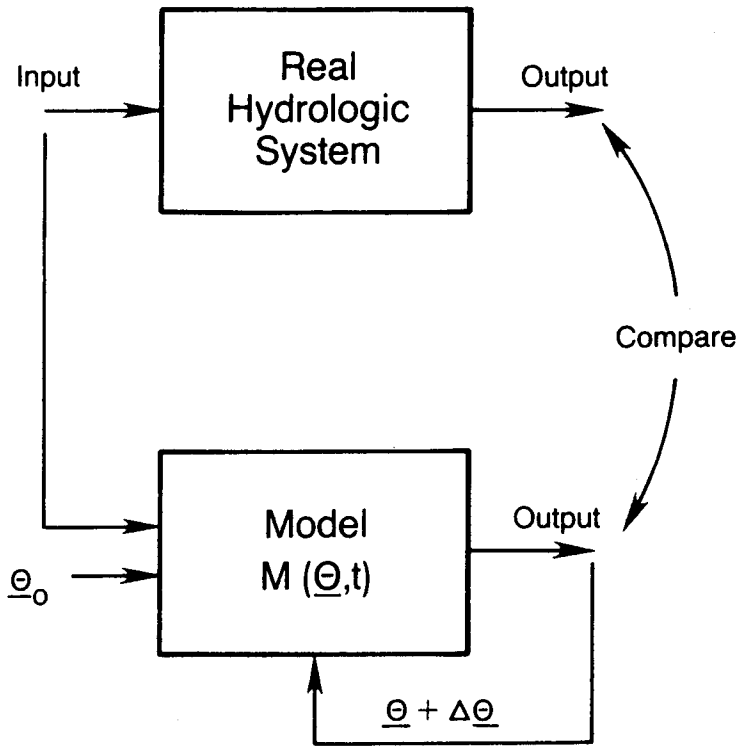

Figure 2.

Schematic showing the general approach to the parameter estimation problem, where M($\underline{\Theta}$,t) is the mathematic model, $\underline{\Theta}$ is a vector of model parameters, $\underline{\Theta}_o$ is an initial guess for the parameters, and $\Delta\underline{\Theta}$ is an incremental change in the parameter values.

water contamination has already occurred. In this case, pumping tests create tremendous costs associated with the disposal of the produced contaminated water, which under regulation cannot simply be returned to the same subsurface regime. Finally, in the investigation of aquitards which are extremely impermeable, pumping tests may not be physically possible due to very low well yields.

In these cases, it might be desirable to utilize stresses other than pumping stress in the parameter estimation methodology. Natural stresses acting on the system are seen as an alternative. By considering investigative methodologies which utilize natural forces, and thus do not require pumping, it may still be possible to obtain parameter estimates to aid in building conceptual and mathematical models of the hydrogeological regime.

The general parameter estimation problem, illustrated in Figure 2, involves finding values for model parameters, Θ, from the set of all possible choices, such that by some reasonable criteria the model is "closest" to the real process (Gupta and Sorooshian, 1985). The models which might be used in this procedure are discussed in the following section. These models have been developed in the frequency domain, and the advantage of consequently adopting a frequency domain approach to the estimation problem will be discussed in this paper along with a recommendation for the choice of an estimation criterion to decide upon the "closest" fit. Finally, the relation between the type of input data used in the estimation methodology and the resulting parameter estimates will be discussed.

Models

It is helpful for the purposes of this discussion to take a Linear Systems approach, and consider the change in fluid pressure at a fixed point in the well, δP_w, as the *output* of a well-aquifer system in response to some input(s). For the purposes of this discussion δP_w is seen as being caused by *two inputs*. One of these inputs is the changing pore fluid pressure in the formation, δP_f, and the other input is the changing atmospheric pressure at the water level surface within the well, δP_A.

While the mechanics of well response to the Earth tide and atmospheric pressure are well known, they are reviewed here to emphasize their differences. Consider the Earth tide influence first. An Earth tide dilitation causes a proportional change in aquifer stress, part of which is born by a change in pore fluid pressure according to the relation of Terzaghi. As pore fluid pressure is changed a pressure disequilibrium between the fluid in the wellbore storage and the pore fluid is created, resulting in flow into or out of the well. The corresponding δP_w (the system output) will be positive for a positive change in δP_f.

A change in atmospheric pressure at the Earth's surface, when transmitted through a confining bed, causes a change the rock stress, and part of this change is borne by a change in pore fluid pressure. It is known that δP_f is proportional to δP_A by the loading efficiency, ξ: $\delta P_f = \xi * \delta P_A$, where $\xi = 1/(1+\phi C_w/C_e)$, ϕ is the formation porosity, C_w is the fluid compressibility, and C_e is the matrix compressibility (Ritzi, 1989). At the same time fluid pressure within the wellbore storage will change by an amount equal to δP_A, because the well is directly open

to the atmosphere. Note that the pressure change in the wellbore storage will always be greater than the change in pore fluid pressure, and the resulting disequilibrium will cause fluid to flow into or out of the well. The corresponding δP_w will, for example, be negative for the case of a positive change in atmospheric pressure and a positive change in pore fluid pressure.

The discussion is further facilitated by representing the components of this system in the frequency domain. Let $\Gamma_{ww}(\omega)$ be the power spectrum of $P_w(t)$, the system output, where ω is the angular frequency. Ritzi et al. (1991b) have shown that the inputs can be represented by $\Gamma_{(f-A)(f-A)}(\omega)$ which is the power spectrum of the difference between $P_f(t)$ and $P_A(t)$. The transfer function for this system will have the form:

$$\Gamma_{ww}(\omega) = \Gamma_{(f-A)(f-A)}(\omega)\ |H(\omega)|^2$$

where $H(\omega)$ is the frequency response function for the system.

The term $|H(\omega)|^2$ gives the attenuation in power, and the argument of $H(\omega)$ gives the phase shift, $\eta(\omega)$, between the input and output. For the case of a confined aquifer, mathematical models for $H(\omega)$ have been given by Hsieh et al. (1987) for the SET forcing, by Rojstaczer (1988) for the APV forcing, and by Ritzi (1989) and Ritzi et al. (1991b) for the combined forcings (CSA). Further, Rojstaczer (1988) and Rojstaczer and Riley (1990) have developed models for $H(\omega)$ in the case of a semi-confined aquifer under APV forcings, and of an unconfined aquifer under CSA forcings.

Consider a confined aquifer penetrated by a well, with well-bore storage, under both SET and APV influences. For this case an analysis of the model shows that the attenuation and phase shift will be a function of 1. the frequency of the variation, f; 2. the transmissivity of the formation, T; and 3. the radius of the well casing, r_c; and to a negligible extent 4. the storativity, S; and 5. the radius of the well screen, r_s (Hsieh et al., 1987; Rojstaczer, 1988; Ritzi et al., 1991b). This is illustrated in Figure 3 which graphically shows the attenuation in power and the phase shift which occur between the input and the output of the system. These are plotted with the solid line against dimensionless transmissivity (T_d) as the abscissa, where T_d is equal to T/fr_c^2. It can be seen that within the stipple pattern the attenuation and phase shift increase with decreasing T_d. At T_d above this zone there is no attenuation or phase shift, and below it there is complete attenuation.

The variation in the curves of Figure 3 will be negligible for variations in Sr_s^2/r_c^2 over even several orders of magnitude (the value of this parameter used in Figure 3 is $1x10^{-5}$). This leads to a uniqueness problem in estimating S as is discussed by Ritzi et al. (1991b). Fortunately, there is little correlation between estimates of S and T based upon this model, and thus estimates of T are possible without accurate information regarding S.

Estimation of Transmissivity

Within the context of this paper, the estimation of T is posed in the frequency domain. Thus, the schematic for the parameter estimation problem shown in Figure 2 must be modified to that shown in Figure 4. When estimating T from APV and SET data the solution involves:

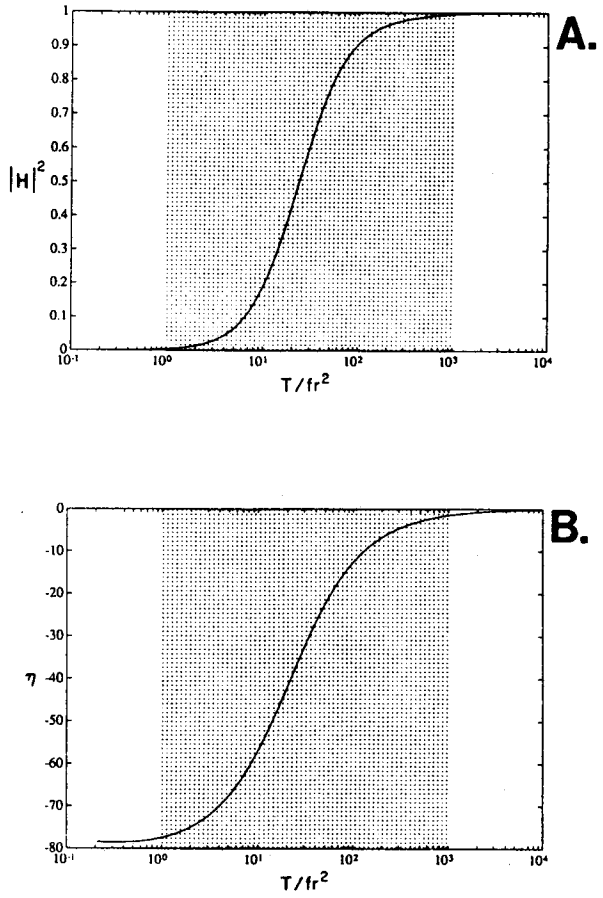

Figure 3.
Model for the frequency response function for well response to the combined SET and APV influences (from Ritzi et al., 1991b)

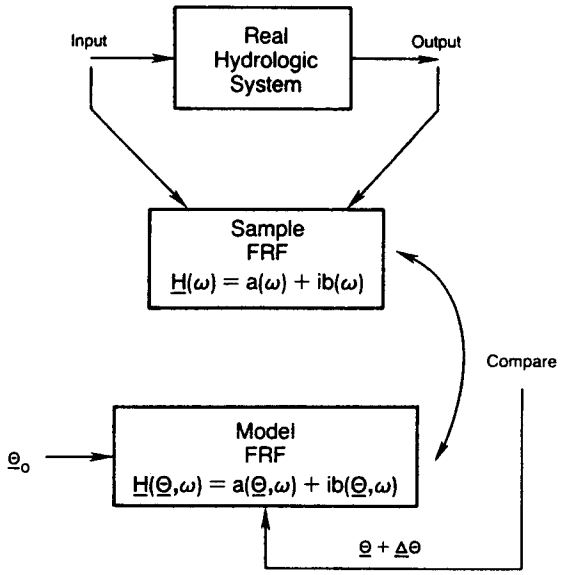

Figure 4.
Schematic showing the frequency domain approach to the parameter estimation problem.

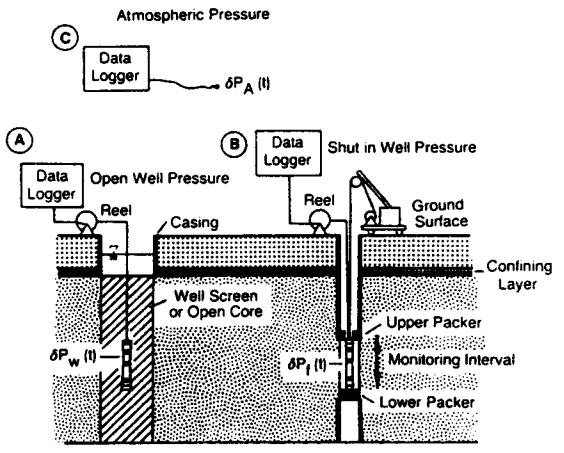

Figure 5.
Instrumentation for data acquisition (from Ritzi et al., 1991b).

1. the collection of input-output data from the physical system;
2. the calculation of the sample frequency response function, $H^o(\omega)$, from the data; and
3. finding T such as to achieve the "best fit" between model, $H(T_d)$, and the observed, $H^o(\omega)$.

Ritzi (1989) discussed the advantages to this approach as compared to estimating parameters in the time domain. Estimates of the impulse response function obtained in the time domain have unsatisfactory statistical properties arising from the fact that neighboring estimates of the function are highly correlated. In comparison, estimates of the frequency response are uncorrelated at neighboring frequencies. Further, by posing the problem in the frequency domain, important frequencies of the process can be included while undesirable frequencies can be filtered out.

It is important to note that the data requirements differ depending upon which influences are to be considered in the estimation process: the SET, the APV, or the combined (CSA) influences. If the CSA scheme is used, three time series records are involved (Figure 5):

1. Natural hydraulic head or pressure measurements from a well open to the atmosphere;
2. Formation pressure from a shut in well (not open to the atmosphere); and
3. Atmospheric pressure.

However, only the first two time series are required for the SET scheme, so that the atmosphere need not be monitored. Only the first and last time series are needed for the APV scheme if ξ is estimated in addition to T, so that the shut in well is not required. It is important to point out that the SET and the APV influences on water level variations differ; there are differences: 1. in the mechanics of the cause in the water level disturbance, and 2. in the frequencies at which they occur (these differences will be described in more detail in a following section). Thus, not only does the data for each scheme contain different information, which is expressed at different frequencies, but also note that it will take different amounts of effort to collect the data required for each different scheme.

Complex Vector Estimator

In the list of steps in the solution to the parameter estimation problem given above, step 3 involved finding the "best fit" between the computed FRF and the observed. This best fit is quantified through the choice of an estimation criterion, which might for example be the minimization of the sum of squared differences. Traditionally, the problem of estimating parameters by fitting frequency domain models to the transfer function of SET and APV data has been approached by choosing estimation criteria (EC) based upon modulus and phase representations of $H(\omega)$:

$$EC(T)_{mod} = \sum (\, |H^o(\omega_i)| - |H(T_{d_i})| \,)^2$$

and

$$EC(T)_{phs} = \sum (\, arg\{H^o(\omega_i)\} - arg\{H(T_{d_i})\} \,)^2$$

(e.g. Hsieh et al., 1987; Rojstaczer, 1988; Rojstaczer and Riley, 1990).

However, an alternative is the complex vector estimation criterion given by Ritzi et al. (1991a):

$$EC(T)_{cv} = \sum (H^{o}(\omega_i) - H(T_{d_i}))^2$$

which is equivalent to minimizing the sum of the real and imaginary squared differences between the computed and observed FRF values. In a set of Monte Carlo experiments, Ritzi et al. (1991a) compared estimators based upon the EC*mod*, EC*phs*, and EC*cv* criteria. One thousand replications of synthetic data were used to estimate values for T, with the results being illustrated in the histograms of Figure 6. It is apparent that the complex vector estimation criterion is the minimum variance, the minimum bias, and the most robust estimator when compared to the modulus and phase estimators, and thus is a better choice.

Ritzi et al. (1991a) used the complex vector estimation criterion within a Gauss-Marquardt nonlinear optimization algorithm. An example of the result of a fit of $H(T_d)$ to $H^{o}(\omega)$ is illustrated in Figure 7, representing the former with 'x's and the latter with 'o's. Note that the curve is not being fitted to the 'o's. Rather, the curve is fixed (or relatively so; it will change negligibly with Sr_s^2/r_c^2). The location of a point on the curve is a function of T_d. For a given r_c and ω, a point 'x' will shift along the curve toward the origin with decreasing T. The estimator adjusts the distribution of 'x's along the curve in satisfying the EC_{cv}. In this example there were 2048 harmonic numbers in the FRF values resolved. However, as pointed out by Ritzi et al. (1991b) most of the harmonic numbers resolved are associated with components of the input signal which have very little power, and thus are extremely affected by noise. Ritzi et al. (1991b) suggested a method for excluding frequencies which optimizes the number of frequencies using a confidence interval criterion. For the example above, the minimum width of the confidence intervals associated with an estimate of T occurs with the inclusion of 27 harmonic numbers as is illustrated in Figure 8.

Evaluation of the Estimation Methodology in Relation to Data Informativeness

In the discussion which follows, it will be critical for the reader to understand that the APV and SET influences occur at differing frequencies. While this is not a new insight, it nevertheless is reviewed here for the sake of clarifying this point for the reader.

Differences Between the Set and APV Influences

Figure 9D shows the fast Fourier transform of the water level time series previously shown in Figure 1. The combined influences of the Earth tide (represented by the tidal potential in Figure 9A) and atmospheric pressure variation (Figure 9B) on dilitation (given as a proxy for actual pore pressure changes) can be seen in Figure 9C, and ultimately on downhole pressure in Figure 9D.

It is evident that the tidal influence occurs most significantly at the principal lunar and solar *diurnal* tidal frequencies (O1, K1), and at the principal lunar and solar *semidiurnal* frequencies (M2, S2).

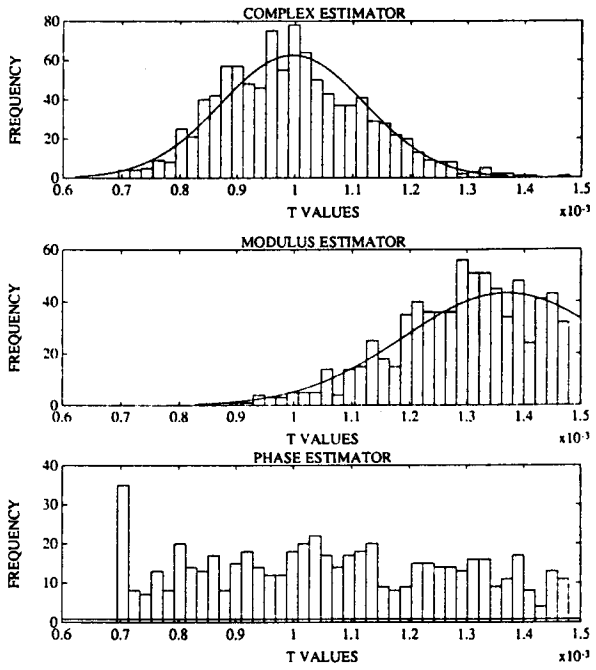

Figure 6.

Results from a Monte Carlo experiment comparing T estimates from each of the estimators: A. Complex vector; B. Modulus, and C. Phase. The true value for T is $1x10^{-3}$. Note that the complex vector estimator has less bias (from Ritzi et al., 1991a).

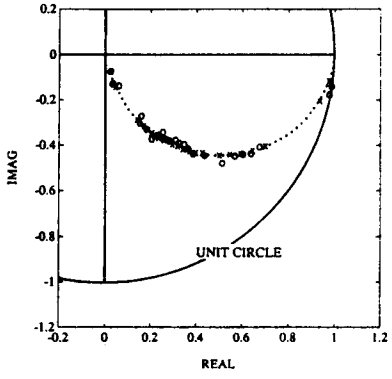

Figure 7.

CSA data. Results of complex vector estimator with optimal 27 frequencies used. Dotted line is the model curve. The 'O' are the estimated FRF at the 27 frequencies considered. The 'X' represent the model based upon the value of T determined by the estimation methodology (adapted from Ritzi et al., 1991b).

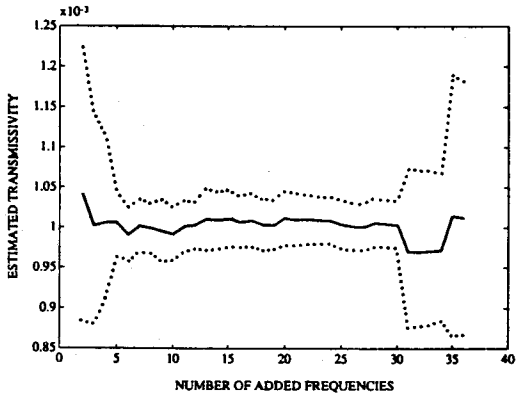

Figure 8.
Estimate of T is given by the solid line. Dotted line shows 95% confidence bands on the estimate (from Ritzi et al., 1991b)

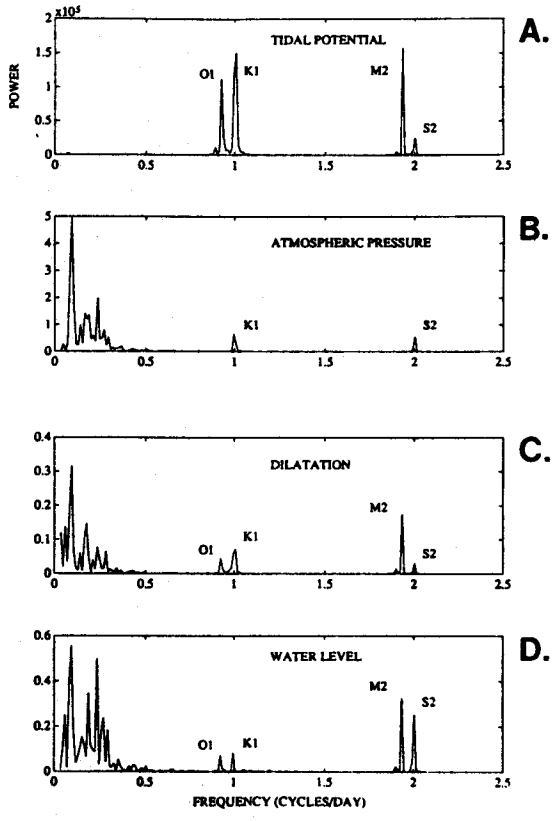

Figure 9.
Amplitude spectrum of A. tidal potential; B. atmospheric pressure; C. dilatation; and D. well pressure.

Of the many lines in the tidal spectrum, our experience shows that only these four are of significant power to be of practical use for our intended purposes.

In the barometric pressure spectrum shown in Figure 9B, only the solar tidal frequencies are present. The atmospheric pressure tide is primarily thermally driven, with the gravimetric component negligible and thus the lunar atmospheric tides can be ignored. The barometric pressure spectrum also has significant power at frequencies < 0.5 cycles/d due to macroscale phenomena including general circulation and synoptic scale changes. Thus, in contrast to the purely periodic nature of the Earth tide forcing, the barometric changes include both periodic and a-periodic components. Microscale atmospheric turbulence exists at the intertidal and the supertidal frequencies (Kimball and Lemon, 1970), however, it has very little power as compared to the tidal and the macroscale phenomena.

Relationship Between the Ability to Estimate *T* and the Type of Data Which are Available

In some cases, depending upon the information in the data, or the system from which is was collected, it may not be possible to estimate T. In this context, the advantage of having CSA data over just the individual APV and SET data is made clear through the following example.

Although it has been pointed out in the previous section that the actual estimation is best done in the complex plane, it is still helpful to consider the power spectral response function $|H(T_d)|^2$, and phase, $\eta(T_d)$, representations of the models as illustrated in Figure 3. Note that T will be identifiable [i.e. single value for T gives rise to a given $|H(T_d)|^2$ or $\eta(T_d)$] only when T_d is such that it falls within an "identifiability window", which is shown with the stipple pattern. Above the identifiability window $|H(T_d)|^2$ is unity and $\eta(T_d)$ is zero, regardless of the value of T. Below the window $|H(T_d)|^2$ is zero. Note that in the complex plane $H(T_d)$ will plot at the intersection of the model curve and the unit circle for all T_d above the window, and will plot at the intersection of the model curve and the origin for all T_d below the window.

The term "intermediate range" is used by Ritzi et al. (1991b) in order to refer to a specific range of the sample FRF, $H°(\omega)$ along the ordinate axis of Figure 3, which is to be distinguished from the concept of the identifiability window which refers to a specific range of T_d along the abscissa. In the context of the estimation methodology, T will be identifiable only if the data are such that $H°(\omega)$ can be determined within an intermediate range (IR) of values where $|H(T_d)|^2$ takes on values between (and different from) zero and unity, and $\eta(T_d)$ takes on values between zero and -78° for this particular model curve. In this case the estimation algorithm will search over values of T such that T_d is within the identifiability window. $H°(\omega)$ should thus be examined before attempting to apply the estimation algorithm. If $H°(\omega)$ is not within the IR at the ω for which the data allow its determination, and thus T is not identifiable, then only an upper or a lower bound can be given for the value of T. Noise in the data may prohibit the distinction of $H°(\omega)$ close to the endpoints of the IR, and thus the actual width of the window will depend upon the level of this noise.

Therefore, interest is in obtaining data with information content sufficient for the

determination of $H^*(\omega_i)$ at some ω_i for which the $H^*(\omega_i)$ values fall within the IR. The SET, APV and CSA estimation schemes each use different data having differing information contents. With the SET scheme data only the two lunar tidal frequencies may be resolved in the sample FRF because the solar tidal frequencies are contaminated by barometric effects. Similarly, the APV scheme cannot include the solar tidal frequencies because of the SET influence in pore fluid pressure at those frequencies, and thus only non-tidal frequencies which have significant power can be considered. Here, an advantage of the CSA scheme becomes apparent, because CSA data allow for the inclusion of all four tidal frequencies as well as the non-tidal frequencies in the analysis and thus uses data with the maximum information content. To illustrate this point further, two hypothetical ground water systems are considered. System 1 has a $T = 2.5 \times 10^{-4}$ m^2/h, and System 2 has $T = 2.5 \times 10^{-1}$ m^2/h. Both systems have a casing radius of 0.1 m.

First, consider the analysis associated with the SET estimation scheme. For System 1 the O1 and M2 frequencies correspond to T_d which falls below the identifiability window as is shown in Figure 10. If, however, the barometric information is included in the analysis by using the APV or CSA schemes, a range of additional frequencies are available to use in the analysis. As shown by Rojstaczer (1988) and Ritzi (1989), beside the tidal frequencies, the low frequency barometric components (< 0.5 cycles/d) have enough power in the input signal to be of practical use in the analysis. It is apparent that this range of low frequency components defines a range of T_d which falls within the identifiability window.

Consider System 2. If only the APV data are available then again the tidal frequencies cannot be used in the analysis, leaving the barometric low frequencies for consideration. It is apparent in Figure 11 that they define a range of T_d which falls above the identifiability window. The SET scheme uses the two lunar tidal frequencies which define T_d, and which are within the window. For the CSA case, all four tidal frequencies can be used for which the associated T_d fall within the identifiability window.

In this example, data associated with the CSA scheme contains adequate information so that the estimation of T is possible for both hypothetical systems. This is not true for the SET and APV schemes. Thus, the advantage in using the CSA scheme is apparent.

Other Issues Associated with the Type of Data

Note that even in the case that data from all three schemes make it possible to identify an estimate for T, the estimates may differ in their precision. Ritzi et al. (1991b) have shown that the CSA estimates are the most precise as compared to SET and APV estimates, as one would intuitively expect because, in general, more frequencies, and thus more degrees of freedom are included in the estimation process.

Parameter Precision and the Number of Observations

Assuming that observations are to be made discretely, there are two fundamental considerations involved in

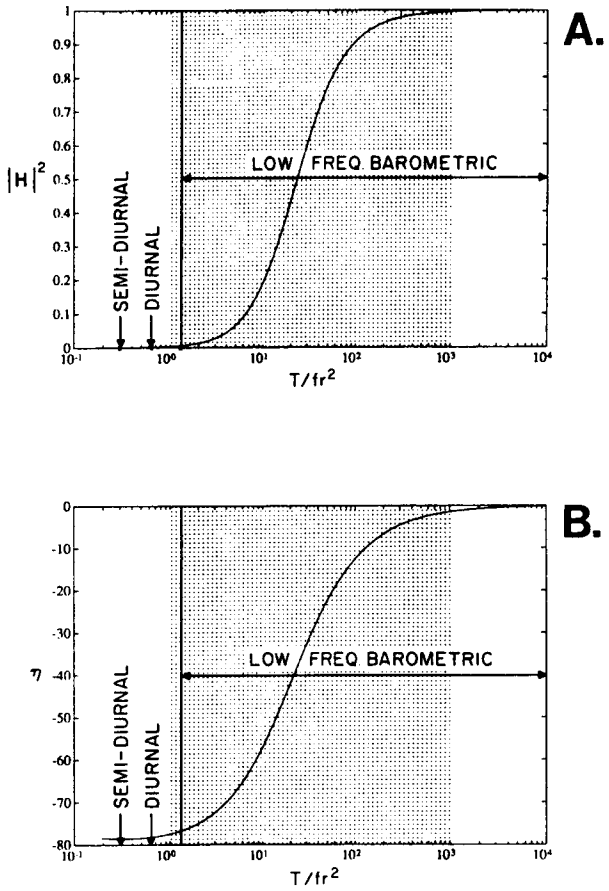

Figure 10.
Illustration of a case where the tidal frequencies are below the identifiability window, but the barometric low frequencies are within the identifiability window (from Ritzi et al. 1991b).

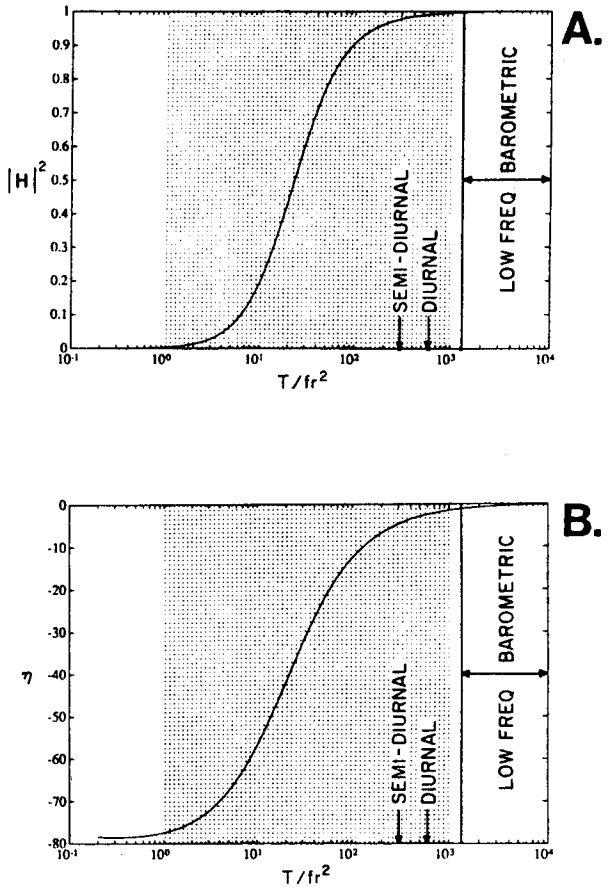

Figure 11.
Illustration of a case where the barometric low frequencies are above the identifiability window, but the tidal frequencies are within the identifiability window (from Ritzi et al., 1991b).

the collection of data. These considerations include the choice of:

1. Δ_t, the sampling interval, (length of time between samples); and

2. W, the number of observations (dimensionless).

The total length of the monitoring period is then $W\Delta_t$.

The time series must be at least competently sampled, i.e. Δ_t must be small enough so that there are no significant frequency components greater than the Nyquist frequency, $1/2\Delta_t$, to avoid aliasing in the spectra. Therefore, considering that the highest frequency in any of the time series with significant power is the solar diurnal, a Δ_t at least as small as 6 h is necessary. By sampling every hour as opposed to every 6 h, a desirable margin for error is established between the Nyquist frequency and the diurnal tidal frequencies. Indeed, an hourly sampling rate is commonly used in tidal analysis, and is adopted here.

In considering the choice of W it is important to realize first that the number of frequencies obtained in the FRF is equal to W/2+1 (in digital spectral analysis without subdividing the data and averaging subsequences, and considering only positive frequencies). Second, the resolution between frequencies, Δ_f, will be $1/(W\Delta_t)$. Thus, assuming that Δ_t is fixed, increasing W will provide a greater number of frequencies by increasing Δ_f. The greater the number of frequencies obtained, the more frequencies there are which possibly can be used in the estimation of T and thus possibly add to the confidence of the estimate.

Note that collecting data at smaller Δ_t over a given monitoring period will not increase the resolution between frequencies because the product $W\Delta_t$ will not change. The number of frequencies will only increase by adding new frequencies at the high frequency end. Assuming, for example, that the data are initially collected hourly, increasing the sampling frequency will only result in including more high frequencies which do not have enough associated power in the input signals to be of practical importance in the analysis. In order to increase resolution, the length of the monitoring period must be increased.

Ritzi et al. (1991b) performed experiments using synthetic data with increasingly smaller numbers of observations. The results show that the CSA scheme will require a considerably shorter monitoring period, compared to the APV scheme. The fact that the CSA scheme requires a shorter monitoring period can be explained by considering, for example, the extreme case of W equal to 64 and Δ_t equal to 1 h. At this point, all of the low frequency barometric power of the input and output spectra has been lumped into one frequency class. Thus the APV scheme will only contain information at one frequency not significantly affected by noise, when at least two frequencies are required in the estimation of T and ξ. For the CSA scheme, the power in the diurnal range and in the semidiurnal range will be lumped into separate classes, which are each separate from the class containing the low frequency barometric power. Thus in comparison, the CSA scheme will have information at a total of three frequencies not significantly affected by noise, which are widely separated in the spectrum, and the CSA scheme only

requires one frequency in the estimation of T.

Discussion and Conclusions

Models exist for the response of water levels in wells to the SET and APV influences, combined or individually, in confined, unconfined, and semi-confined aquifers. For the case of confined aquifers, estimates for transmissivity (T) using the response of water levels in wells to the solid Earth tide (SET), to the atmospheric pressure variation (APV), and to the combined influences (CSA) may be possible depending upon the value of dimensionless transmissivity (T_d) for the system being monitored. The true T and the r_c^2 of the system, and the frequencies at which the FRF can be determined must be such that the T_d falls within the identifiability window in the estimation methodology. The CSA scheme will always determine the FRF at the most number of usable frequencies, and thus gives the greatest probability that sufficient information is contained in the data in order that T may be estimated.

When estimating T the complex vector estimator is superior to the modulus and phase estimators. It is better because it has less bias and variance in the estimates, and is more robust to errors which violate the implicit assumptions.

Within the estimation methodology, the computation of the sample FRF is greatly affected by error in the data at frequencies which do not contain significant power in the input. These include the intertidal and supertidal frequencies. Thus, only a range of low frequencies below 0.5 cycles/d, in addition to the tidal frequencies give good definition of the FRF. The number of low frequencies to include in the APV and CSA schemes can be optimized based upon minimizing the confidence intervals associated with the estimates of T.

The SET, APV, and CSA estimation schemes each require a different type of data. Because each type of data contains different information about the system, the parameter estimates from each scheme will be different, even during the same period of monitoring. The results of applications to synthetic data indicate that the CSA scheme gives the transmissivity estimate with the most precision, with all other factors being equal. Further, the CSA scheme requires a shorter monitoring period, all other factors being equal.

When designing a sampling program, there will be a trade off between the length of time required for monitoring vs the cost of installing the monitoring instrumentation. When considering the cost of collecting data, the APV scheme requires data from only one open well, which is a fairly common situation, in addition to atmospheric monitoring which are easy to instrument. The APV scheme minimizes the cost of monitoring instrumentation, because the SET or CSA requirements also include a second shut-in well with extra effort and expense needed to successfully pack the pressure transducer off from the atmosphere. In fact, given that the shut-in well is the limiting factor in data collection, and that monitoring the atmosphere is relatively easy, if the shut in well is completed one is likely to adopt the CSA scheme over simply using the SET scheme.

Thus, a very practical conclusion can be drawn which is that if the analysis is not urgent, one is best advised to initially adopt the APV scheme. Once the

minimal monitoring period has expired (> 43 d of hourly sampled data were required in experiments with synthetic data by Ritzi et al., 1991b), the sample frequency response function would be computed. If a system response is observed within the intermediate range, then the APV estimation scheme can be applied to estimate *T*. Otherwise, an additional shut in monitoring well would be installed to collect the additional data necessary for the CSA estimation scheme (> 2.7 d of hourly sampled data were required in experiments with synthetic data by Ritzi et al., 1991b). The additional information obtained by using the CSA scheme may allow frequencies in the FRF to be obtained such that a system response in the IR is now observed. If so, then T_d in the analysis now will fall within the identifiability window and the estimation algorithm can be initiated. Conversely, it may be that minimizing the length of monitoring time has a higher priority than minimizing the costs of monitoring instrumentation. In this case one is advised to skip the APV monitoring and adopt the CSA approach from the start.

Acknowledgements

This paper was written and presented with the support of a Research Challenge Award from the School of Graduate Studies at Wright State University.

Robert William Ritzi, Jr. is a faculty member in the Department of Geological Sciences at Wright State University (Dayton, Ohio, 45435, USA). He received the Ph.D. in 1989 from the Department of Hydrology and Water Resources in the College of Engineering and Mines at the University of Arizona. He has the M.S. and the B.A. degrees in Geological Sciences from Wright State University and Wittenberg University, respectively.

References

Bredehoeft, J. D. 1967. Response of well-aquifer systems to earth tides. J. Geophys. Res., v. 72, n. 12, pp. 3075-3087.

Gupta, V. K. and S. Sorooshian. 1985. The relationship between data and the precision of parameter estimates of hydrologic models. J. of Hydrology, v. 81, pp. 57-77.

Hsieh, P. A., J. D. Bredehoeft and J. M. Farr. 1987. Determination of aquifer transmissivity from earth tide analysis. Water Resour. Res., v. 23, pp. 1824-1832.

Jacob, C. E. 1940. On the flow of water in an elastic artesian aquifer. Trans. Amer. Geophys. Union, v. 21, pp. 574-586.

Kimball, B. A. and E. R. Lemon. 1970. Spectra of air pressure fluctuations at the soil surface. J. Geophys. Res., v. 75, pp. 6771-6777.

Ritzi, R. W. 1989. The use of well response to natural forces in the estimation of hydraulic parameters. Ph.D. Dissertation, The University of Arizona.

Ritzi, R. W., S. Sorooshian and V. K. Gupta. 1991a. On the estimation of parameters for frequency domain models. Water Resour. Res. (*in press*).

Ritzi, R. W., S. Sorooshian and P. A. Hsieh. 1991b. The estimation of fluid flow properties from the response of water levels in wells to the combined atmospheric and earth tide forces. Water Resour. Res. (*in press*).

Rojstaczer, S. 1988. Determination of fluid flow properties from the response of water levels in wells to atmospheric loading. Water Resour. Res., v. 24, pp. 1927-1938.

Rojstaczer, S. and F. S. Riley. 1990. Response of the water level in a well to earth tides and atmospheric loading under unconfined conditions. Water Resour. Res., v. 26, pp. 1803-1818.

Van der Kamp, G., and J. E. Gale. 1983. Theory of earth tide and barometric effects in porous formations with compressible grains, Water Resour. Res., v. 19, no. 2, 538-544.

Modelling a Multi-unit Aquifer System with Uncertain Aquifer Geometry

by Malcolm Reeves and Rebecca Yost Grambo

Abstract

Recently, it has become common practice in aquifer modelling to employ Monte Carlo techniques in stochastic simulations to take account of uncertainties. Geostatistical methods have been applied to estimate the spatial distribution of many parameters including aquifer characteristics, thickness and piezometric surface. These methods are particularly useful in allowing for variance reductions associated with scale when "point" data are used to predict values for large "blocks" in numerical models.

Here a methodology is outlined for treating uncertainty in both aquifer properties and aquifer geometry for a glacial, multi-unit, sand and gravel, aquifer complex. The procedure uses interpreted well-logs together with more subjective geological and geomorphological models of the geometry of glacial sediments, to constrain sets of bounding surfaces for permeable sand and gravel bodies within a relatively impermeable clay-till matrix. For each set of surfaces, analysis of "overlap" is used to assign vertical conductances to a multi-layer numerical model. Horizontal hydraulic conductivities are estimated using a geostatistical model for spatial variability.

Groundwater flow models were run for standardized recharge conditions to quantify groundwater interchange between the various sub-units within the aquifer complex. The ultimate objective of the research is to establish probability functions for inter-aquifer flows and their associated covariance structure.

The case-study area is centred on the city of Regina, Saskatchewan. Approximately 900 wells, many quite shallow, were available to characterize an area of ~ 3000 km^2, where significant sand and gravel bodies are found at five distinct stratigraphic horizons. Post-depositional erosion and solution collapse features have resulted in added potential for interconnection between permeable units. The degree of interconnection between the various aquifers has major implications for the assessment of the risk of groundwater contamination.

Introduction

Although areal variations of transmissivity (T) and hydraulic conductivity (K) are often important controls on groundwater flow patterns, in many situations, the spatial "interconnectedness" between aquifers can exert a much stronger influence than changes of K within aquifers. Fogg (1986) has pointed out that "many so-called sandstone aquifers are actually multiple aquifer systems consisting of discontinuous sand bodies distributed complexly in a matrix of lower-permeability silts and clays." This model is an excellent description of the glacial

sands and gravels which make up the Regina aquifer system in Saskatchewan.

The aquifer involves at least five "correlatable" sand and gravel bodies with typical hydraulic conductivities from 10^{-3} to 10^{-4} m/s in a matrix of silts, tills and clays with typical hydraulic conductivities from 10^{-7} to 10^{-8} m/s. The sand-bodies are commonly 5-15 m thick and are separated by 0-30 m of low-permeability "till matrix".

More than 900 well-logs were analyzed to construct models of sand-body tops and thicknesses. Although much of the variance of the interpreted data for tops and thicknesses can be explained by combinations of trend or drift and local stochastic variations, there remains significant uncertainty in the extent of spatial interconnection between sand-bodies. In order to estimate inter-aquifer flows, a model was required to describe the distribution of sand-bodies in space and, in particular, to predict where aquifers come into contact.

To generate such a model a Monte Carlo technique was used to create a large number of realizations of the bounding surfaces of the sand-bodies. From these realizations the frequency per unit area with which connections are indicated was recorded. These relative frequencies were used to assign vertical hydraulic conductivities in a multiple aquifer flow model. This paper emphasizes the K_v (vertical hydraulic conductivity) and K_h (horizontal hydraulic conductivity) parameter identification with brief reference to their subsequent application in numerical models of groundwater flow.

In this paper, the term trend is used for regional-scale variation of the mean value, modelled by fitting a single polynomial or Fourier surface to the entire data set before analysis for spatial autocorrelation. The term drift is used to indicate local scale removal of variations in the mean value by piecewise polynomials, simultaneous with the analysis for spatial autocorrelation.

Methodology

The methodology employed involved four principal steps:

1. Acquisition and analysis of lithological and electrical logs of wells including construction of many cross-tied sections.
2. Decomposition of thickness and top elevation data sets into low-frequency trend-drift components, local stochastic components that exhibit spatial correlation, and residual "nugget" components that exhibit no spatial correlation; fitting of models to predict the spatial variability of tops and thicknesses.
3. Simulation of many realizations of the bounding surfaces to examine sand-body interconnection and to create possible spatial patterns for K_h and K_v (horizontal and vertical hydraulic conductivity).
4. Numerical modelling of inter-aquifer flows and hydraulic heads using simulated K-patterns for standard boundary conditions.

Data Acquisition and Reduction

The raw data is comprised of well-log information obtained from the Saskatchewan Research Council for an area of > 3000 km^2. The grid coordinate origin for the study is the intersection of the northern limit of Tp 21 and the eastern edge of R 21, W 3 Mer, to the

northwest of the city of Regina, Saskatchewan. Figure 1 shows the approximate grid coordinates of various place-names (mentioned in the text) with the styllized locations of the principal water courses (the Qu'Appelle River, Boggy Creek and Wascana Creek).

Both lithological and electrical logs (when available) were examined to extract the top and bottom elevations of all sand and gravel intervals. The Sierra Stratlog (tm) computer package was used to construct and cross-correlate more than 25 cross-sections marked in Figure 2, involving more than 500 wells and in excess of 60 cross-ties (intersection points). The study area boundaries are also located in Figure 2.

The geological correlation of well-logs in glacial terrain is not a trivial task. It is particularly difficult in the absence of cores or cuttings because recognition of till units is based on factors such as colour, staining, jointing and carbonate content. Not all well-logs are recorded in sufficient detail to be certain of which sand and till units are represented. The sands and gravels show large variations in thickness and grain-size and represent a fluvial complex. Correlations were based primarily on lithological evidence combined with an attempt to minimize changes in elevation of correlated units between adjacent wells. The interpretation may not be correct but it is objectively reproducible from the data set, that is, the rules for correlation picked unique surfaces.

The preliminary picks and correlations were verified by construction of trend surface maps for the unit tops. The trend surface program is based on the code given by Davis (1973). Because the

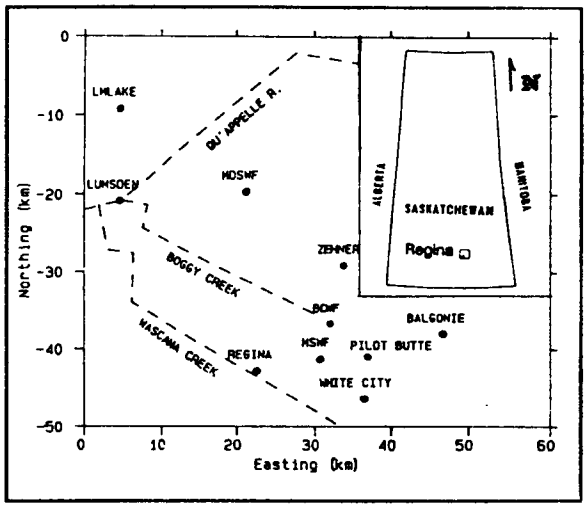

Figure 1. Place-name location map for Regina aquifer system. BCWF = Boggy Creek Well Field; MSWF = Mallory Springs Well Field; MDSWF = Mound Springs Well Field; LMLAKE = Last Mountain Lake.

correlation procedure implied a relatively smooth bed top, all extreme-point residuals (outside 2σ) were reviewed and corrected when in error. This procedure eliminated most mistaken picks and data transposition errors. It also drew attention

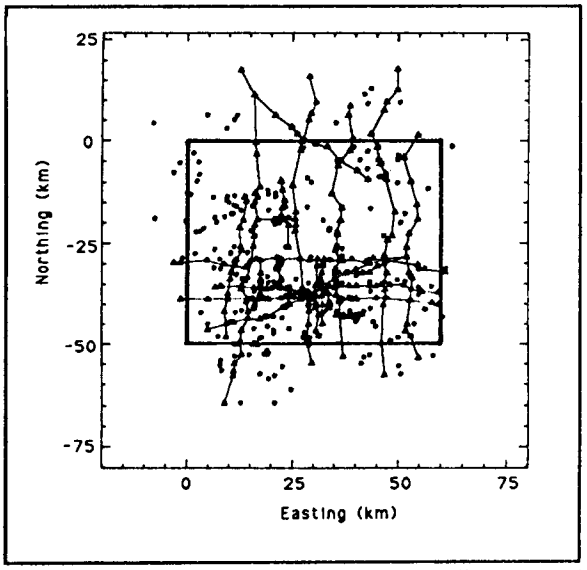

Figure 2. Location of wells and geological sections.

to anomalous subregions, which in this case are usually associated with salt-collapse features.

Five sand-bodies were identified but only three are discussed here, the Condie, Upper Floral and Lower Floral. The three stratigraphic units combine to form the Condie, Regina, Zehner, Richardson, and Northern aquifers of Maathuis and Van der Kamp (1988) which are named primarily on the basis of geographical location. The glacial stratigraphy of the region has been summarized by Christiansen (1979). The usage of the terms Condie, Lower Floral and Upper Floral in this paper may be formally incorrect, but for the purposes of this study these terms are synonymous with the first, second and third correlatable sand zones in the local succession. In particular, the Upper Floral sand-body may include the "interglacial" sediments of Christiansen (1979).

Modelling of Sand-bodies

Trend surface analysis revealed that much of the variance of the sand-body tops (>80%) could be removed by subtraction of fourth or fifth order trend surfaces from the data (Figures 3, 4, and 5). These surfaces are geologically credible and identify major features of the subsurface topography: for example, the N-S trending, northward plunging Regina glacial valley on the western edge of Figures 4 and 5. The Condie sand-body top reveals a consistent dip to the west, falling perhaps 4 m/km across the 50 km east-west extent of the unit in the study area. Table 1 gives the trend surface correlation coefficients and the unexplained variance of the residuals in square metres.

To check for small-scale spatial correlations in the top-surface data sets, the trend surface residuals were used to construct variograms, and an attempt was made to model these residuals. The Environmental Protection Agency GEO-EAS computer package (Englund and Sparks, 1988) was used for this analysis. Relatively little reduction in error-variance was obtained by kriging residuals, and cross-validation tests were unsatisfactory.

Table 1

Trend Surface Correlations and Residual Variances

Unit	R	$\sigma^2(m^2)$
Condie	.918	128
U.Floral	.909	288
L.Floral	.842	710

Table 2 shows that three trend surfaces correlate strongly with each other. Analysis of the well data showed that it was relatively unusual for wells to penetrate all three sand units. For this reason it is thought that cokriging might be successful in improving the top-surface prediction model. The cokriging method has not yet been tried on the Regina aquifer system data set.

Table 2

Correlations between Sand-body Tops

Unit	Condie	U.Floral	L.Floral
Condie	1.000		
U.Floral	.857	1.000	
L.Floral	.692	.910	1.000

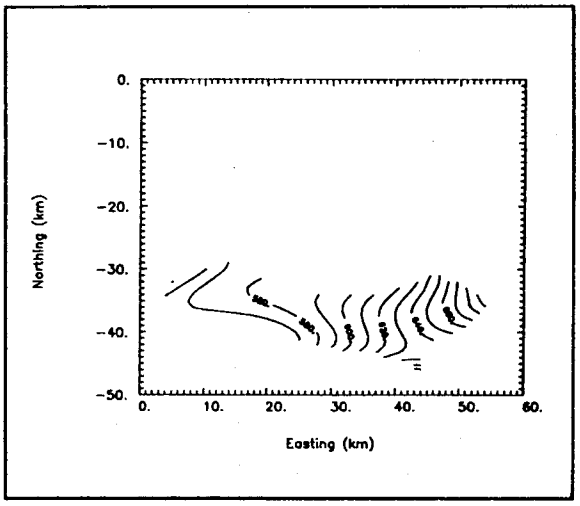

Figure 3. Fourth-order trend surface of Condie sand-body top (contour interval 10 m, R = 0.918).

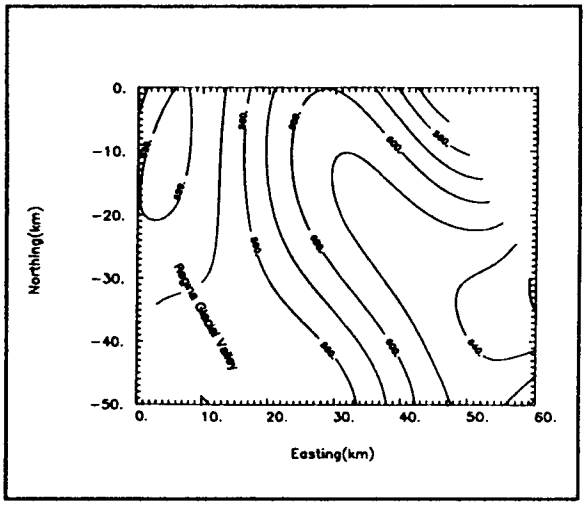

Figure 5. Fifth-order trend surface of Lower Floral sand-body top (contour interval 20 m, R = 0.842).

Because trend/drift and the stochastic component of spatial variability are often difficult to isolate individually (Russo and Drury, 1987), a second analysis was carried out on the top-surface data sets. A universal kriging model was implemented using the U.S. Geological Survey 2D spatial statistics computer package (Grundy and Miesch, 1988). For universal kriging, with a first-order,

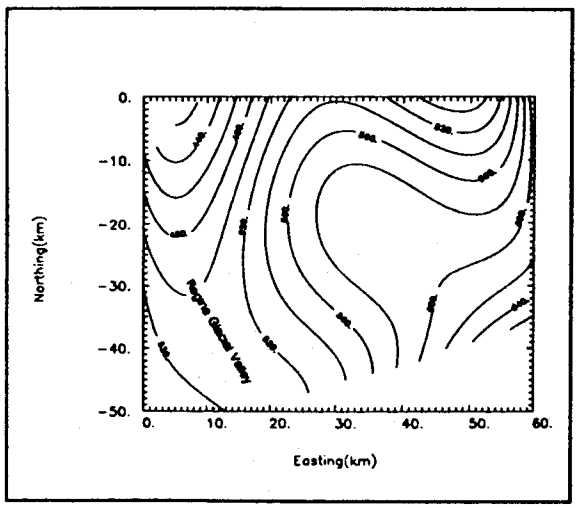

Figure 4. Fifth-order trend surface of Upper Floral sand-body top (contour interval 20 m, R = 0.909).

moving-neighbourhood drift model, the drift model removed ~ 80% of the variance and the stochastic spatially correlated component contributed little. The trend surface and universal-kriging-drift components were very similar to each other so the decision was made to adopt a regional trend surface model for unit tops.

The thickness data sets were similarly analyzed, and it was found that the total variances were much smaller than those for the tops. Trend surfaces or universal-kriging-drift explained only a relatively small amount of these variances (13-35%). Figures 6, 7, and 8 show spherical variogram models for the raw thickness data (no drift/trend removal), for the Condie, Upper Floral and Lower Floral sand-bodies, respectively. The variograms were "fitted" by a weighted least squares (WLS) technique as recommended by Cressie (1985) and used by Ahmed and De Marsily (1987). The latter authors refer to "assigning appropriate weights" based on the distance (h) and the number of pairs. A

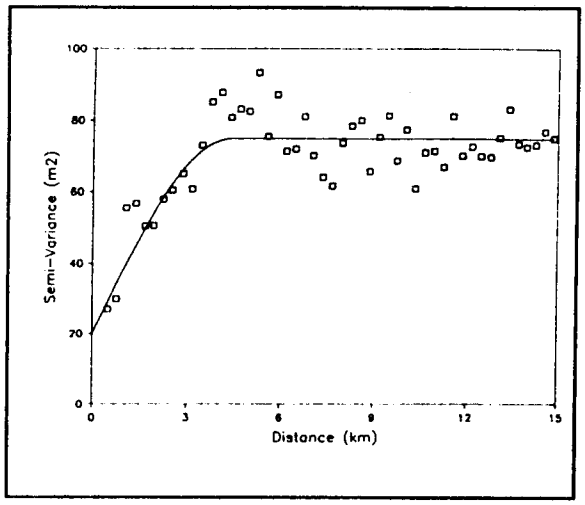

Figure 6. Experimental and model variogram for Condie sand-body thickness (Co = 20.0 m², Cs = 54.9 m², a = 4.38 km)

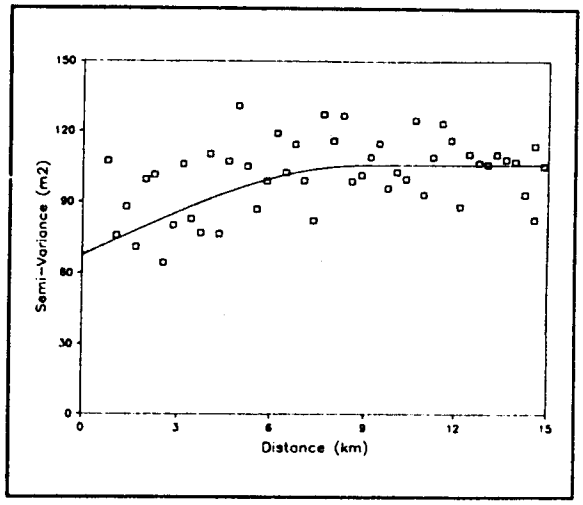

Figure 8. Experimental and model variogram for the Lower Floral sand-body thickness (Co = 67.7 m², Cs = 37.9 m², a = 9.05 km).

similar weighting scheme was adopted for the Regina study.

Considerable effort was expended in developing an objective technique to identify variogram parameters. The technique used identified the three variogram parameters nugget (c_o), sill (c_s) and range (a) using a Turbo Pascal implementation of the WLS algorithm given by Press et al. (1986). A starting value was assumed for range and a linear least squares minimization was performed for the nugget and sill. Iteration was carried out to find the range value which gave the smallest chi-squared statistic for goodness-of-fit. The procedure did not constrain the parameters in any way; for example, the nugget values were not constrained to be positive. The WLS method in general, and this procedure in particular, may well produce biased parameter estimates as indicated by the work of Russo and Jury (1987). The parameters were tested by cross-validation and it was found that small increases in the "fitted" sill and range would return slightly improved cross-validation statistics. Nevertheless, for the data sets in this study, parameter identification by the WLS procedure outlined, proved to be insensitive to variations in number of lags and the size of the lag interval and appeared to generate "reasonable" if not "optimal"

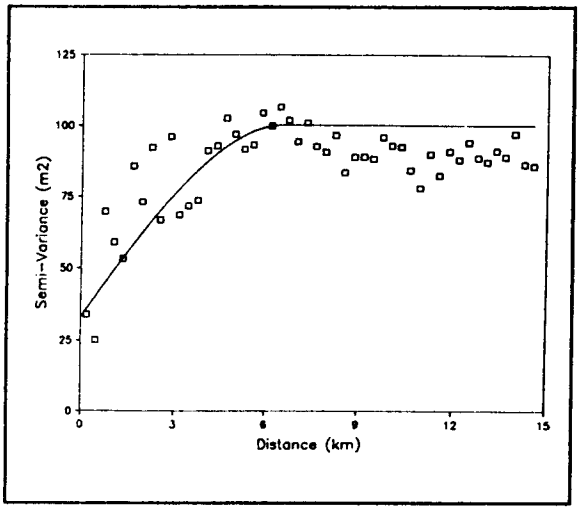

Figure 7. Experimental and model variogram for Upper Floral sand-body thickness (Co = 33.1 m², Cs = 67.3 m², a = 6.55 km).

parameters.

The results are reported only for isotropic variograms. Table 3 shows the "fitted" variogram parameters and associated errors of estimation. The range values of 4-9 km are comparable with earlier data for ln(T) variograms by Hoeksema and Kitanidis (1984) for unconsolidated glacial deposits mapped over ~ 1000 km².

Table 3

Thickness Raw-Data Variogram Parameters

Unit	C_o (m^2)	C_s (m^2)	a (km)	X^2 dof
Condie	20.0	54.9	4.37	43.1
	±4.2	±4.6	±1.37	31
U.Floral	33.1	67.3	6.55	55.3
	±3.3	±4.3	±1.20	21
L.Floral	67.7	37.9	9.05	77.4
	±5.9	±6.5	±2.52	44

The variograms of thickness residuals after trend surface removal, fitted by the WLS algorithm, are given in Table 4. For both the Upper and Lower Floral sand-bodies, the fitted nugget, sill, range values do not change significantly, but for the Condie sand-body the range of the trend-residuals variogram is reduced from 4.37 to 1.50 km.

Figure 9 shows the trend-surface model for the Condie sand-body. The observed range-reduction may reflect the success of the trend model in predicting the thickness variations normal to the "long-axis" of the Condie sand-body. The trend/drift models do little to reduce the error-variance for the Upper and Lower Floral sand-body thickness predictions.

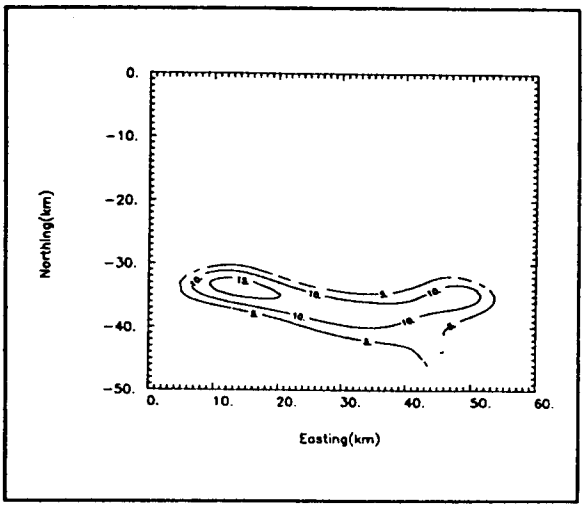

Figure 9. Fifth-order trend surface for Condie sand-body thickness (contour interval 5 m, R = 0.426).

The fitted variograms were used to krige the thickness residuals, either after trend removal or concurrently with drift removal, in order to further remove the spatially correlated stochastic component from the data. The final residuals, after removal of trend-drift and local spatial correlations, are then expected to be random.

Table 4

Thickness Trend-Residual Variogram Parameters

Unit	C_o (m^2)	C_s (m^2)	a (km)	X^2 dof
Condie	0.5	47.5	1.50	12.5
	±8.9	±9.1	±2.53	21
U.Floral	32.3	64.5	6.04	57.4
	±3.4	±4.2	±1.14	24
L.Floral	68.8	31.3	8.35	83.7
	±6.2	±6.8	±2.74	44

Ordinary kriging with trend removal and universal kriging models were cross-

validated to determine their acceptability as models of the data set. Two cross-validation procedures were used.

1. Jackknifing, where each data point in turn was eliminated from the data set and it's value estimated from the remaining points.
2. Sample splitting, where the data was divided into two approximately equal sets of points by random selection. Each subset was then used to estimate the point values in the other set.

Tables 5 and 6 show typical results of jackknifing cross-validation of thickness for a trend-removal case.

Table 5

Cross-Validation Parameters

Unit	Data SDev (m)	Krig SDev (m)	Krig Mean Err	Krig RMS Err
Condie	6.58	5.76	-.027	.852
U.Floral	8.08	7.82	.014	.970
L.Floral	8.32	9.47	.003	.883

Underlined values fail test.

Table 6

Cross-Validation Correlations

	RMS Kriging Error Est			
Unit	x	y	Est	Data
Condie	.070	-.077	-.185	.642
U.Floral	-.003	.024	.119	.486
L.Floral	.000	.008	.154	.223

Underlined values fail test.

Grundy and Miesch (1988) list a number of "tests" that can be made on the cross-validated data and used as criteria for acceptability of a model:

1. The mean kriging error (column 4, Table 5) should be close to zero, that is, the kriged estimates should be unbiased.
2. The standard deviation of the data before kriging (column 2, Table 5) should be greater than the standard deviation of the kriged data (column 3, Table 5), that is, the variogram model should account for a spatially correlated component.
3. The standard deviation of the standardized errors or the reduced root mean square kriging error (column 5, Table 5) should be close to unity, Delhomme (1976).
4. The standardized errors should be independent of (uncorrelated with) the kriged values (column 4, Table 6), Journel and Huijbregts (1978).
5. The standardized errors should be independent of spatial location (columns 2-3, Table 6), that is, the errors show no spatial trend.
6. The kriged values should be positively correlated with the raw data values (column 5, Table 6), that is, the model is a good predictor of the data.
7. The model variograms are "good fits" to the experimental variograms (see Chi^2 values in Tables 3 and 4, column 5).

Note that the degrees of freedom in the final columns of Tables 3 and 4 are the number of variogram points used to calculate the WLS "goodness of fit" not the number of point-pairs used to compute the variance. The number of point-pairs for each variogram point were always > 30 and typically > 200.

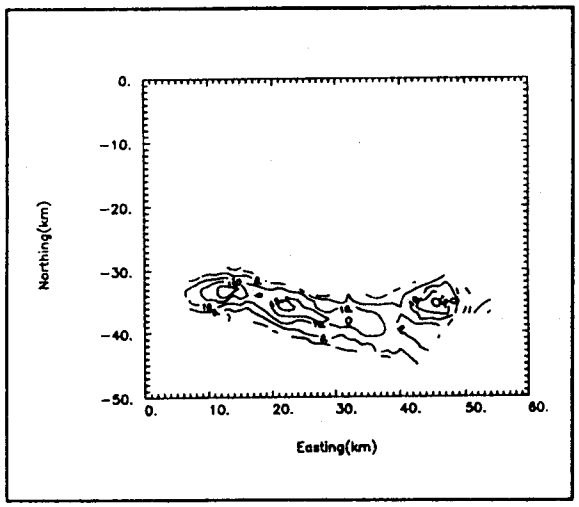

Figure 10. Block-kriged thickness of Condie sand-body (contour interval 5 m, 1km x 1km blocks).

For the Condie and Upper Floral models, the acceptability criteria are satisfied. The Lower Floral model is less successful in this respect. Fortunately, because the Lower Floral thickness model is not used in the prediction of the unit top (only for the bottom), this has little or no influence on the Condie-Upper Floral and Upper Floral-Lower Floral intersections.

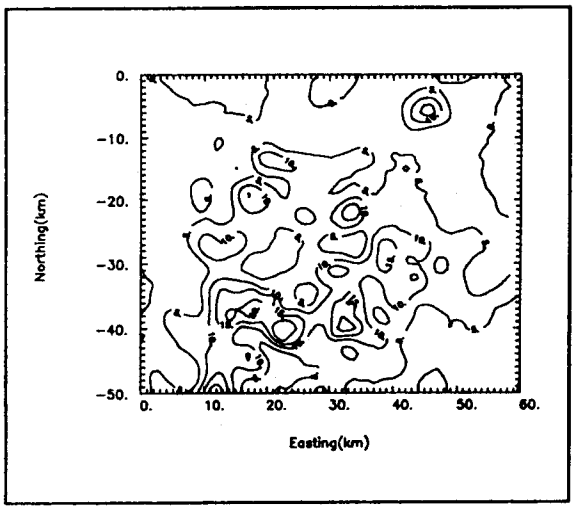

Figure 11. Block-kriged thickness of Upper Floral sand-body (contour interval 5 m, 1km x 1 km blocks).

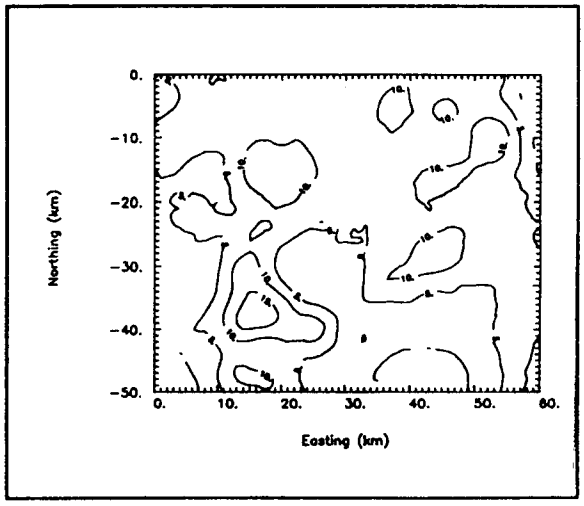

Figure 12. Block-kriged thickness of Lower Floral sand-body (contour interval 5 m, 1km x 1km blocks).

The fact that the kriging variance exceeds the data variance for the Lower Floral model reflects the poor variogram, fitted with the WLS algorithm. The Lower Floral thickness shows little discernable, local-scale, spatial structure.

Table 7

Estimate-Observed Correlations

Surface	R	Model Type
Condie Top	.918	Trend
U.Floral Top	.909	Trend
L.Floral Top	.842	Trend
Condie Thickness	.814	Trend-Krig
U.Floral Thickness	.586	Trend-Krig
L.Floral Thickness	.361	Krig

Table 7 gives the correlation coefficients between observed tops and thicknesses and the final model estimates. The Lower Floral thickness model does not include a trend/drift component and because of the low correlation coefficient, that is, the Lower Floral thickness shows little

regional-scale trend. The Lower Floral thickness estimator is thus little better than a random variable.

Block-kriged thicknesses for the Condie, Upper Floral and Lower Floral sand-bodies were generated and are shown in Figures 10, 11 and 12 respectively. These thicknesses were subtracted from the tops (modelled by trend surfaces) to obtain a set of bottom bounding surfaces for the three sand-bodies. The six surfaces (3 tops and 3 bottoms) are the best estimate of the bounding surfaces and together with the block-kriged thicknesses they are subsequently referred to as "reference surfaces".

The direct modelling of formation bottoms as trend surfaces was also investigated. Trend surface top and bottom models involved much higher error-variances for overlap predictions than for trend surface tops combined with kriged thicknesses.

Further analysis has shown that the deposits may be better represented by anisotropic variograms. This result was anticipated for "channel" sands, but it has yet to be shown that the error-variances for predicted surfaces and overlap are reduced by the adoption of anisotropic models.

Monte Carlo Simulation

To predict sand-body intersections it is necessary to model the high-frequency variations which are smoothed by trend surface and kriging models. For this purpose Monte Carlo simulation techniques were applied. Both conditional and unconditional simulations have been carried out to create multiple realizations of the sand-body geometry. Since many more runs of the unconditional simulations have been completed, only these results can be reported at this time.

Unconditional simulations take account of intercorrelations between top-surfaces and thicknesses but do not preserve the local-scale spatial correlations of the thickness models. Much of the work has been confined to unconditional simulations for two reasons:

1. The local spatial component is less than 15% of the total variance for all surfaces, and thus the reduction in estimation error is not expected to be large.
2. Full conditional simulations require very large linear transformations and the computational resources needed are much more significant.

The simulation programs were written in Turbo Pascal and used the additive congruential algorithm suggested by Knuth (1981) for portable random number generation, based on code given in Press et al. (1986). A gaussian distribution of random numbers was used for the simulation study.

The reference model residuals were found to be approximately gaussian and uncorrelated with either x, y, or the predicted tops and thicknesses. Some of the residuals were quite strongly correlated with each other as shown in Table 8. These correlations were incorporated into both the conditional and unconditional simulations using a principal-components technique (Haan, 1977).

Principal components analysis transforms a set of n correlated variables into n uncorrelated or othogonal components. These components are the eigenvectors

of the correlation matrix. The orthogonal independent variables can be created readily with the random number generator and transformed to variables with the required correlation structure by linear combination of eigenvectors. The principal components method is equivalent to the decomposition of the

Table 8

Correlation between Residuals for Tops and Thicknesses

	C.Tp	U.Tp	L.Tp	C.Th	U.Th	L.Th
C.Tp	1.00					
U.Tp	.45	1.00				
L.Tp	.21	.64	1.00			
C.Th	-.38	.06	.15	1.00		
U.Th	-.18	-.15	.11	-.12	1.00	
L.Th	-.01	-.03	.08	-.02	.43	1.00

C.Tp = Condie Top; U.Tp = Upper Floral Top; L.Tp = Lower Floral Top; C.Th = Condie Thickness; U.Th = Upper Floral Thickness; L.Th = Lower Floral Thickness.

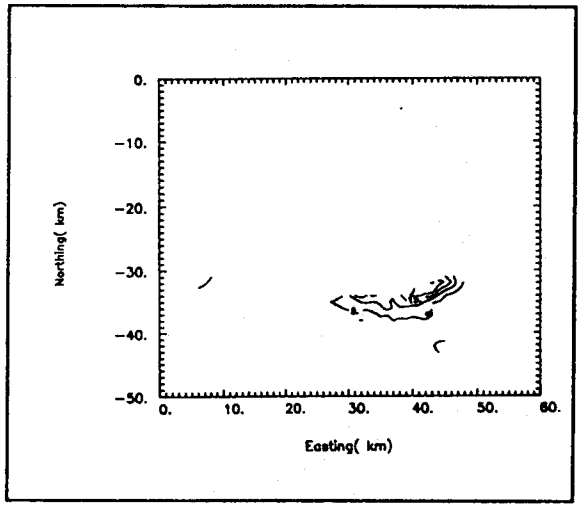

Figure 13. Condie-Upper Floral percentage interconnection (contour interval 5%).

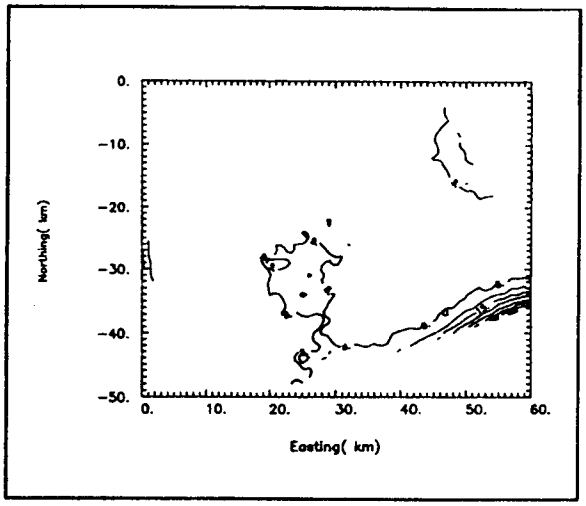

Figure 14. Upper Floral-Lower Floral percentage interconnection (contour interval 5%).

covariance matrix (Σ = A.A') into a product of a lower triangular matrix (A) and its transpose (A'). The linear tranformation Y = A.X transforms the independent variables X into the correlated variables Y.

The physical reason for the observed correlations seems to be salt-collapse depressions which cause localized high-amplitude, coherent disturbances in both thicknesses and tops on a scale too small to be identified by either drift or variogram models. These points could (and perhaps should) have been removed as outliers for the cross-validation procedures. They are too few in number to influence the variogram "fits" strongly, but their influence was apparent in the first 2 or 3 lags using a 300 m lag interval. Subsequent analysis showed that their exclusion reduced the nugget in all cases and led to a reduced kriging error. The results reported here do not exclude these points and the simulated variances may therefore be somewhat high.

Conditional simulations are carried out using the same decomposition technique employed for incorporating correlations between thicknesses and tops. The main difference is in the size of the vectors and matrices involved in the linear transformations. To account for correlations between surfaces, the transformation matrix A is 6 x 6. For full conditional simulation of the local-scale spatial variability, the transformation matrix is up to 3111 x 3111.

More than 5,000 unconditional realizations of sand-body tops and bottoms were analyzed for overlap using a grid (1 km x 1 km) of 3111 (61 x 51) points. Random deviates (based on point-kriged thickness variances) with the appropriate correlation structure (Figures 6-8) were added to the modelled reference surfaces. The percentage of realizations where sand-bodies were found to be connected are shown in Figures 13 and 14 for Condie-Upper Floral and Upper Floral-Lower Floral, respectively. It should be noted that the reference model surfaces showed minimal intersection and a model based on these surfaces would fail to identify areally significant regions of vertical continuity.

In Figure 13, the Condie and Upper Floral sand-bodies show 5-25% probability of overlap on the northern edge of the Condie unit eastward from the Boggy Creek Well Field between Grid Refs. (28,-35) and (48,-32). These contact areas for the Condie and Upper Floral sand-bodies are confirmed by the constructed geological sections which provide a few indications of possible overlap.

The Upper Floral-Lower Floral interconnection (Figure 14) is more complex. There are three principal areas where probabilities of interconnection are in excess of 5%.

1. 5-10%, in the northeast of the study area around Grid Ref. (48,-15) in the Northern aquifer.
2. 5-45% (mostly <20%), in the Mallory Springs - Pilot Butte - Balgonie area and eastward between Grid Refs. (30,-40) and (60,-35) in the Zehner aquifer and its eastward extension.
3. 5%, around Grid Ref. (23,-30) due south of the Mound Springs Well Field.

The high percentage (45%) for predicted overlap around Grid Ref. (47,-37) is confirmed by the southernmost E-W geological cross-section shown on the location plan (Figure 2).

Analysis of interconnection summary maps (Figures 13 and 14) in isolation can be misleading. For significant interflows to be associated with overlap additional criteria must be satisfied:

1. units must have non-zero thickness;
2. units must be saturated; and
3. units must have lateral continuity with the main body of the aquifer.

For areas 2 and 3, the thickness and saturation criteria may not be met.

A further difficulty in interpretation is that the overlap maps are cumulative results of 5000 individual realizations. It is possible, for any particular realization, to predict non-zero thickness for saturated, vertically connected points that are horizontally isolated from the main body of the aquifer. This is a common feature of regions where the sand-bodies are thin (accentuated by the strong cross-correlations of the residuals). Full

conditional simulations, including the variogram model, reduce the tendency to generate laterally isolated points with vertical connections, relative to unconditional simulations. Conditional simulation may be essential for adequate modelling of such regions.

It is noteworthy that the simulations predict all three aquifers are interconnected in the vicinity of the major area of groundwater discharge, Boggy Creek Well Field; Grid Refs. (26,-32) to (30,-32).

Spatial Distribution of K

There are relatively few spatially located measurements of T or K available from published sources for the Condie, Upper Floral and Lower Floral sand-bodies. Those field test measurements that are available are strongly clustered (around the well fields) making the task of extracting spatial statistics (variograms) more difficult. Nevertheless, the values of T and K appear to follow a lognormal distribution with a mean value of K corresponding to about 6×10^{-4} m/s. For the lognormal distribution the interval $\pm\sigma$ is 2×10^{-4} to 2×10^{-3} m/s and the Chi-squared value for goodness of fit with 18 degrees of freedom is 8.2.

There is a strong relation between K and T (Figure 15) and a preliminary variogram appears to have a range of 5-6 km. Hoeksema and Kitanidis (1984) indicate ranges from 5.3 to 13.0 km (median 8.0 km) for seven sets of glacial deposits with sample sizes (23-71) comparable to the present set of 27 values. The comparison of variogram ranges for glacial sands and gravels may be naive because of the wide variation in scale and style of heterogeneity, but it of some

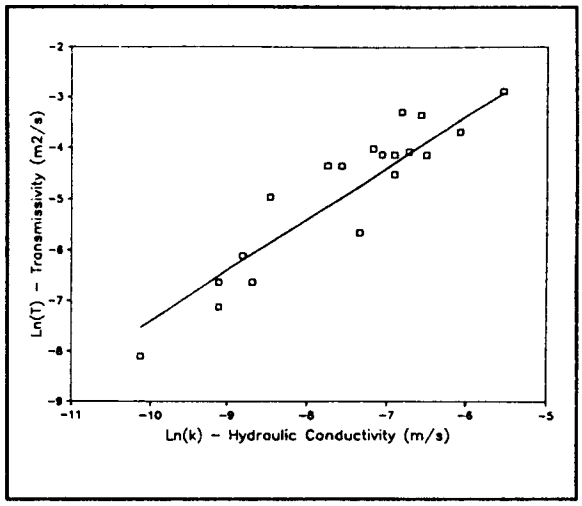

Figure 15. Log transmissivity-hydraulic conductivity linear regression (Ln(T) = 1.006 Ln(K) + 2.657, R = 0.891).

comfort, when forced to deal with a small data set, that the range is of similar magnitude to those reported in the literature for comparable sediments. Because the hydraulic conductivity data is of limited exyent, a simple model for K was adopted. K was assumed to be independent of thickness and the preliminary variogram was used only to reduce the variance of K appropriately for estimates of 1 km x 1 km model grid regions. Values of T were obtained by multiplying K by the block-kriged thickness estimate, corrected for the water-table or piezometric surface position.

The final step was to assign K_v where sand-bodies are in contact. For a simple layered system, it can be argued that a geometric mean K values might be appropriate. However, the variation of lithologies within sand-bodies is as much as that between them and one cannot therefore have great confidence that the data set is sufficiently large to even estimate the horizontal K_h mean. As a working hypothesis, K_v was selected from

the same lognormal population as K_h by arbitrarily subtracting one standard deviate from the simulated K_h value to give a K_v estimate. This value was multiplied by the fractional connection probability estimate obtained by simulation.

The assumption for the K_v-K_h relation was made because no K_v values were available from field tests. Careful re-analysis of the raw data from field pump tests and falling head tests may provide a more satisfactory estimate of the K_v-K_h relation in the future.

Modelling of Groundwater Flows

The ultimate purpose of identifying the K-structure of the aquifer system was to model flows. The U.S. Geological Survey package MODFLOW (McDonald and Harbaugh, 1984) is presently being used to generate steady-state flows and hydraulic heads for a large number of K-patterns. This work proceeds much more slowly than either the conditional or unconditional simulations to identify parameters because each realization involves a 3111 node, 5 layer, steady-state model run. Flow models use block-kriged reference model thickness for K_h, and identical recharge conditions and stream bed conductances. K_v values are based on the probabily of overlap generated by simulation. The assumptions for recharge are based on the information given by Maathuis and van der Kamp (1988).

Preliminary results of flow modelling suggest that the "barrier" between the Regina and Zehner aquifers, approximate Grid Ref. (27,-37), reported by Maathuis and van der Kamp (1988) might be explained by local thinning of the Upper Floral sand-body combined with the loss of connection with the overlying Condie. This causes an abrupt reduction of sand thickness eastward, from 25-30 m down to 6-7 m. This corresponds to a simulated reduction in T by an average factor of ~ 4 but often very much more. In some realizations the Upper Floral sand is predicted to be patchy (horizontally discontinuous) in this immediate area.

Conclusions

The methodology described here has proved a viable method for the interpretation of 3D spatial interconnections of sand-bodies. Simulation of the bounding surfaces of the sand-bodies that comprise the Regina aquifer system has furnished results that are consistent with the principal hydrogeological features of the area. The extent of these predicted connections were not apparent from the "deterministic" reference model surfaces. Simulation of thickness variations has also assisted in the interpretation of flow barriers.

Careful examination of individual stochastic realizations is essential to take account of particular, rather than average, conditions. In particular, areas where the reference model predicts thin units with finite vertical connection may actually comprise many small isolated patches with no horizontal continuity. Conditional simulation may be necessary under these circumstances to more faithfully represent local-scale horizontal continuity. Calculation of quantitative flows for individual realizations is necessary for complete analysis of inter-aquifer connections.

Acknowledgements

Garth van der Kamp and Harm Maathuis of the Saskatchewan Research Council are thanked for their help in evaluating and extracting well records, logs and maps for this project. The paper has benefited considerably from the helpful suggestions of the two anonymous referees.

Malcolm Reeves has been involved in groundwater modelling since 1970. In the United Kingdom, between 1970 and 1976, he worked at the Water Resources Board, Water Research Centre and the Central Water Planning Unit of the Department of the Environment. Before coming to Canada in 1982 he was Lecturer in Engineering Geology at the University of Durham, England. Dr Reeves is a professional engineer and a professor in Geological Engineering in the Department of Geological Sciences at the University of Saskatchewan (Saskatoon, Saskatchewan S7N 0W0, Canada). He also holds an associate appointment in the Department of Civil Engineering.

Rebecca Yost Grambo graduated from the South Dakota School of Mines in 1985 with a BE degree in Geological Engineering. She is currently enrolled in a PhD program in the Department of Geological Sciences at the University of Saskatchewan (Saskatoon, Saskatchewan S7N 0W0, Canada). Her thesis topic is a regional model study of the Regina aquifer system. Mrs Grambo is a member of the Association of Engineering Geologists and has gained practical experience of hydrogeology from summer jobs in southern California.

References

Ahmed, S. and G. De Marsily. 1987. Comparison of geostatistical methods for estimating transmissivity using data on transmissivity and specific capacity. Water Resour. Res., v. 23, pp. 1717-1737.

Christiansen, E. A. 1979. The Wisconsinan deglaciation of southern Saskatchewan and adjacent areas. Can. J. Earth Sci., v. 16, pp. 913-938.

Cressie, N. 1985. Fitting variogram models by weighted least squares. J. Int. Assoc. Math. Geol., v.17, pp. 563-586.

Davis, J. C. 1973. Statistics and data analysis in geology. John Wiley and Sons Inc.

Delhomme, J.P. 1976. Kriging in the hydrosciences. Advances in Water Resour., v.1, pp.251-266.

Englund, E. and A. Sparks. 1988. GEO-EAS Geostatistical Environmental Assessment Software. Computer Oriented Geological Society, Denver, Colorado.

Fogg, G. E. 1986. Groundwater flow and sand body interconnectedness in a thick, multiple-aquifer system. Water Resour. Res., v. 22, pp. 679-694.

Grundy, W. D. and A. T. Miesch. 1988. Brief descriptions of STATPAC and related statistical programs for the IBM Personal Computer. U.S. Geol. Surv. Open File Rept. 87-411-A.

Haan, C. T. 1977. Statistical methods in hydrology. The Iowa State University Press.

Hoeksema, R. J. and P. K. Kitanidis. 1984. An application of the geostatistical approach to the inverse problem in two-dimensional groundwater modeling. Water Resour. Res. v. 20, pp. 1003-1020.

Journel, A. G. and C. J. Huijbregts. 1978. Mining Geostatistics. Academic Press.

Knuth, D.E. 1981. The Art of Computer Programming, v. 2, Seminumerical Algorithms, 2nd Ed., Addison-Wesley.

Maathuis, H. and G. van der Kamp. 1988. Comprehensive evaluation of groundwater resources in the Regina area. Saskatchewan Research Council Rept. No. 209.

McDonald, M. G., and A. W. Harbaugh. 1984. A modular three-dimensional finite-difference ground-water flow model. U.S. Geol. Surv. Open File Rept. 83-875.

Press, W. H., B. P. Flannery, S. A. Teukolsky, and W. T. Vetterling. 1986. Numerical Recipes: the Art of Scientific Computing. Cambridge University Press.

Russo, D. and W. A. Jury. 1987. A theoretical study of the estimation of the correlation scale in spatially variable fields, 2, Nonstationary fields. Water Resour. Res. v. 23, pp. 1269-1279.

Assessment of the Rational Set of Field Tests in Heterogeneous Aquifers on Imitation Models

by V.A. Mironenko

Abstract

The theory and practice of aquifer tests involve several unsolved problems, including: 1. evaluation of the quality of estimated parameter values in view of their use in subsequent forecasts; 2. quantitative comparison of the quality of different kinds of test results; and 3. justification of the optimum number of aquifer tests and their distribution by types and operation stages within the area under investigation. Imitation modelling provides new possibilities for studying these problems. It helps in the study of a complex system with uncertain structure, using multivariate experiments with an adaptively constructed model, in the course of which the probabilistic structure of the system, its possible behaviour, and its optimal functioning conditions are found.

In the present case, the sequence 'aquifer - field tests - engineering structure (water intake, drainage, etc.)' is studied in this way. Imitation experiments, using a numerical flow model, are planned and carried out by two independent groups of experts. One group (hydrogeologists) represents (invents) the input data about the aquifer system and simulates its 'true' behaviour during the course of its exploration and exploitation. The other group plans and carries out field tests, interprets the results, and designs an engineering structure and predicts its behaviour, i.e. simulates the work of the hydrogeologists under conditions of uncertainty. Comparison of the estimated effects of the numerical experiments performed by the second group with the 'true' effects simulated by the first group, gives an idea of the quality of the field test results and forecast estimates.

This type of study has been carried out for a number of simulated typical situations with different characteristics of the spatial variability of aquifer properties, and with simulation of typical test shortcomings. The experiments resulted in obtaining the relations between the number of tests and their cumulative error, as well as pertinent relations for the forecast error. The resulting measure of the test quality is the relation between the number of tests and total cost, which includes the test costs and the risk of economic losses in the course of water-intake operation due to lack of and errors in, information about flow parameters.

The practical conclusions concern the evaluation of regional parameters from a suite of local test results, the relative reliability and informativeness of different types of tests in heterogeneous aquifers, and the advisable number of various tests. These results are demanding the appreciable rise in the quantity of relatively large-scale and expensive multi-well tests, as well as the expense of hydrogeological surveys, compared to currently adopted empirical standards.

Introduction

Great attention is paid to the application of probabilistic models in ground water hydraulics. The results from using traditional deterministic models in this field often contradict the uncertainty typical of the hydrogeological situation under investigation, and the information about it. On the other hand, it is hard to rely on a purely statistical approach, and so neglect the deterministic nature of flow systems in particular, because this cannot really be supported by the practice of determination of the initial hydrogeological data. The most promising prospects in using stochastic models are expected in solving different kinds of optimization of flow problems, or

more widely, in investigations of behaviour of complex flow systems. Through the imitation of typical flow systems using *a priori* specified properties one can approach the solution of hydrogeological optimization problems, which remained until now beyond the possibilities of conventional investigative methods of hydrogeology. In this paper an attempt is made to present this idea in connection with aquifer tests.

Corresponding concepts and methods are connected to a great extent with 'imitation' modelling, which can be regarded as exploration of a complex system with uncertain structure by means of multivariate experiments on a gradually constructed model. This process reveals the probabilistic structure of the system, describes its possible behaviour, and allows evaluation of the conditions of its optimal functioning (Shannon, 1975). It is extremely important, in using imitation modelling, that the hydrogeologist knows the input parameters of the system, which are to be used as an exact standard for comparison, and that he can vary the experimental situation repeatedly. All this enables the effective use of probabilistic methods in planning, proceeding and interpretation of aquifer tests. In particular it allows to take into account the impact of uncertainties connected with interaction of a great number of natural and engineering factors to be taken into account, as well as with deficiency and inconsistency of information about the hydrogeological situation.

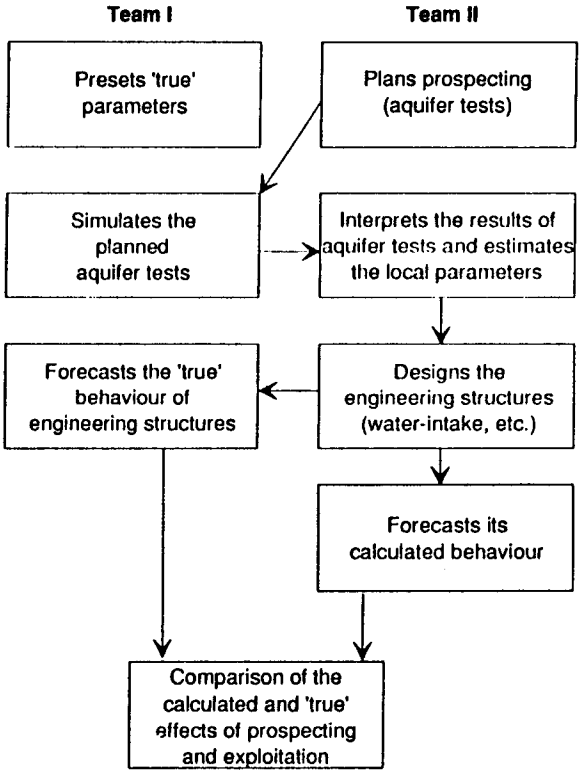

Figure 1 General scheme of imitation modelling.

Imitation Experiments

In the present paper, consideration is given to the sequence 'aquifer-hydrogeological prospecting (aquifer tests) - design of engineering structure'. Imitation experiments on a numerical flow model are planned and conducted by two independent teams of experts (Figure 1). The first team 'presets' the initial system and simulates its 'true' behaviour during hydrogeological prospecting and water intake exploitation. The second team plans and carries out prospecting (aquifer tests) on the simulated situation, interprets the results, and designs the engineering structure and forecasts its behaviour, i.e. imitates the work of the hydrogeologist under conditions of uncertainty. Comparison of the predicted effects of prospecting and exploitation (the results of numerical experiments by the second team) with the 'true' effect (the results of the first team) provides an estimation of the quality of aquifer tests as well as forecasts made on their basis

- depending on the types, amount and location of the aquifer tests.

Investigations of this kind have been carried out on several typical hydrogeological situations, with different parameters of two-dimensional spatial variability of aquifer properties and with simultaneous imitation of the major imperfections of the aquifer tests.

Special attention was paid to the problem of substantiation of the input data. In conducting the computer experiments, simulation of the individual field tests, and of the whole set of aquifer tests, the model took into account the following factors, which have a probabilistic (or quasiprobabilistic) nature:

1. The spatial variability of aquifer flow properties (the variability of external boundary conditions is not considered here);
2. The completeness of the data on parameter variability, which in this case is essentially defined by the data density, the spatial distribution and the character of aquifer tests, with due account for scale effects. These are all of great importance here, and they depend on interrelations between the scale of parameter variability and amount of tests, as well as on the location of testing sites relative to the elements of heterogeneity;
3. The errors of individual tests, which include both systematic and random components. Typically they are errors in interpretation related to defects in diagnostics of the experimental situation; this refers not to the subjective errors in diagnostics, but to the objective constraints caused by such factors as: 1. lateral nonuniformity and vertical heterogeneity of the aquifer; 2. skin-effect and storage of wells; 3. uneven operation of pumping equipment; and 4. errors in drawdown evaluation.

Treatment of Aquifer Heterogeneity

The impact of heterogeneity depends on the ratio (λ) of the effective radius of test influence (R) and the characateristic size of heterogeneous elements or correlation scale. One can distinguish the small-scale ($\lambda >$ 5 to 10) and large-scale (0.5 to 1.0 $< \lambda <$ 5 to 10) 'effective' heterogeneity. For very large values of λ (a few tens - hundreds) or for values much smaller than 1, the aquifer manifests itself as quasihomogeneous.

In simulating individual aquifer tests ('local' models), attention was focussed on the statistical representation of heterogeneity with a lognormal distribution of conductivity and a large variance. The size of the heterogeneous elements was also varied within a wide range. The choice was dictated by the typical conditions of single-well tests in confined aquifers, in which case the radius of influence usually does not exceed a few tens to hundreds of metres, compared with the testing distribution, which is measured in hundreds of metres, sometimes in kilometres. On the other side, the experiments cannot practically consider natural heterogeneous elements which do not exceed a few metres.

As to heterogeneity within the domain of influence of an engineering structure ('regional' models), the simplest exponential-type correlation was used, with an integral scale of autocorrelation equal to a few hundreds of metres to kilometres. This corresponds to a wide range of confined aquifers in sedimentary formations of various origin.

The manifestation of vertical heterogeneity can be taken into account indirectly through the characteristic time of its influence, t_h. It is assumed that after a period of time $t > t_h$, the plot of the drawdown vs ln(t) approaches its linear asymptote. In particular we considered two types of heterogeneous aquifers, two-layered unconfined, and stratified confined aquifers, for which a typical value of t_h is 0.1 - 1 d. Through the

typical time t_r one can also take onto account the effect of pumping history during interpretation of recovery plots. Similarly, the combined effects of two other factors are included, namely, well storage and the skin-effect of pumping and observation wells, which, as a rule, substantially increase the lag of the main section of the plot (Mironenko and Shestakov, 1978). Essentially, in many practically important situations these factors cause severe distortions of the most representative sections of the plot where the drawdown rate is at a maximum, and hence the error in calculated drawdown is minimal.

Simulation of Aquifer Tests

The technical aspects of simulating individual tests can be described as follows. It is supposed that each set of tests is conducted within a locally uniform aquifer with a deterministic trend of mean values, with the heterogeneity characteristic scale substantially exceeding the testing scale, and random variations of transmissivity. Note that the field for each set of tests is considered to be stationary. It is assumed that the effective zone of influence for each test does not intersect other zones of influence, and no zones reach the aquifer boundaries. For the simulation of such local models a special numerical pattern of 2500 elements was used. Depending on the heterogeneity scale, the number of zones with different values of transmissivity varied from 81 to 257. In the case of small-scale heterogeneity there is no need to consider the variations of pumping well positions relative to the main zones of heterogeneity; therefore, the position of the well was fixed at the central element of the grid. On the contrary, for cases of large-scale heterogeneity, the position of the pumping well was one of the most important, so that the position was varied randomly within the central zone of 100 elements.

Main Results of Imitation Modelling

The first result relates to the quality and representativeness of the local estimates of flow parameters obtained by testing of aquifers with lateral heterogeneity (in a stochastic sense).

1. The calculated transmissivity T and its deviation from the initial field vary substantially with increase of λ. In the case of large-scale heterogeneity, the calculated values of transmissivity change considerably depending on test characteristics such as duration and location. In the case of small-scale heterogeneity, the transmissivity is effectively constant. In all cases, however, it is less than the initial mean value $\bar{T}$, the difference increasing with the variation coefficient of transmissivity, W_T. This difference is described by the relation $T = \bar{T}(1+0.5\,W_T)^{-1}$ (Shvidler, 1963).
2. The variance of calculated transmissivity values is considerably less than the initial value. For $\lambda \sim 2$ to 3 this difference usually accounts for at least two orders of magnitude, which confirms the strong 'smoothing down' effect of pump tests on aquifer heterogeneity. It emphasizes, once again, the high degree of uncertainty in solving the inverse problem with respect to the determination of field transmissivity.
3. The lateral nonuniformity of transmissivity, even if comparatively low, causes rather high errors in the value of diffusivity, in particular for observation points adjacent to the pumping well. The uncertainties of all estimates are greatly increasing for type-curve matching methods.
4. A reliable evaluation of parameters for aquifers with lateral heterogeneity could be achieved only by using the linear asymptote of the drawdown vs ln(t) plot. In doing so, it is highly desirable for multiwell tests to specify parameters for the central zone which includes the pumping well.

One of the prime advantages of imitation modelling is its ability to evaluate the reliability of calculated parameters for the system under study, depending on the number of various tests. The exact solution of this problem makes it necessary to identify interrelations between the errors of parameter identification and the errors of forecasts. The first stage of analysis, however, can be confined to comparison between the calculated parameters and the mean value of the initial distribution. Limitations of such an approach are evident, because the correct estimate of the mean value of a parameter distribution does not guarantee a reliable forecast. The reliability of transmissivity estimation based on test results can then be expressed by the difference between its current value (i.e. accumulated mean value for the current number of tests N) and its asymptotic mean value. This difference serves as an initial standard of reliability because it represents, jointly, the spatial variability of properties, the errors of individual tests, their location and their amounts. In particular, incrementing the deviation curve (Figure 2) by increasing the number N of similar type tests, results in obtaining the objective estimation of the relation between the informativeness and reliability of the current value of the parameter (accumulated mean) and the number of aquifer tests of different kinds. By using this approach for a representative number of numerical experiments (40-50 numerical tests in each run) the following results were obtained.

1. The asymptotic estimates of transmissivity (i.e. those which cannot be improved by increasing the number of tests) are commonly lower than the initial mean values, and generally similar to results of individual tests in heterogeneous aquifers. So, for a large degree of heterogeneity (W_T>1) the reliability of calculated parameters

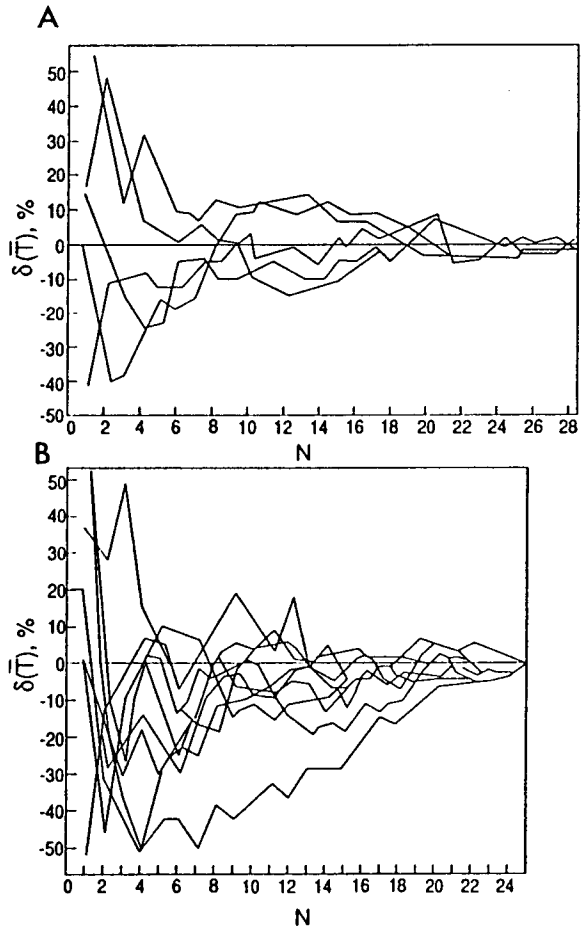

Figure 2 Examples of curves of deviations of calculated transmissivity values from their asymptotic value: (A) where lateral heterogeneity is the only complicating factor; (B) showing the aggregated effect of all complicating factors.

remains low even for a great number of tests.

2. Because of both the combined influence of the above-mentioned factors on the test results, and the uncertainty of diagnostics (choice of representative section on the drawdown plot), it is difficult or even impossible (particularly for single-well tests) to obtain a reliable estimation of asymptotic parameters using only a limited number of tests. For example, in case of large-scale effective heterogeneity with an average amount of variability (W_T~0.5 to 0.6) the advisable number of tests, N_o, is 20-25 when using only s=f(t) plots (single-well tests). For tests with two or more observation wells, N_o decreases to 10-12 due to the possibility of also using the s=y(r) plot.

3. When lateral heterogeneity was the only complicating factor, 'time tracing' (s=f(t)) generally provided a better estimate than the 'areal' one (s=y(r)). After including other sources of errors in the model, however, the results were quite opposite, especially for low degrees of lateral heterogeneity. This shows that the separate estimation of the influence of each newly added factor on the results of aquifer tests can lead to essentially erroneous evaluations. Thus, in view of the effects of individual factors, the optimization of tests does not provide the optimal results for the system as a whole. This emphasizes once again the advantages of imitation modelling as providing a systems approach to the problem.

4. With further increase in the degree of lateral heterogeneity until it becomes the prevailing factor, the rational number of tests appears to be less and less dependent on either the scale of heterogeneity (in the examined range of λ) or on the tracing method. Thus the lateral hetgerogeneity is the principal factor limiting the possibility of improving the parameter identification process through increasing the number of multi-well tests vs single-well tests. That is, as the degree of heterogeneity grows, the advantages of multi-well tests decrease. This tendency becomes more significant still, because even the very accurate evaluation of local parameters for aquifers of this type does not guarantee the identification of major errors in estimations of generalized (calculated) parameters for subsequent forecasts.

The upper limit for the number of various aquifer tests, established through the error curves on imitation models, can be used as an initial reference level. The same curves roughly establish a reasonable correspondence between information obtained by a number of single-well tests, compared with one multi-well test at different exploration stages. After establishing this correspondence, the distribution of the total number of various aquifer tests can be determined based on economic considerations. Finally, the same curves (more exactly, their gradients) can be used to determine the distribution of the types of aquifer tests among different prospecting stages. This can be done by comparing the rates of approach of the current calculated parameters values toward their 'best' values - for different kinds of tests. The overall tendency is clear enough: sharp predominance of single-well tests at early stages and a relative increase of multi-well tests at later stages. Notwithstanding the limitations of such an approach to the determination of the required type of aquifer tests, the method gives minimally distorted estimates for many typical hydrogeological situations, taking into account the high cost of exploitation as compared with the cost of exploration.

The final optimization criterion can be based of the minimum of the interrelation curve between the number of tests (N) and the total expenses. The latter include costs of testing and risk of economical losses during water-intake operations due to incomplete and erroneous data on the flow parameters.

A typical curve is presented in Figure 3. The sharp asymmetry shows that the deviation from the optimal number of tests (N_{opt}) to the larger side is connected with essentially less nonproductive expenses than is the case of its similar deviation toward the minor side. In other words, overkill in exploration is rather less dangerous than is underkill. Similar results have been obtained in oil exploration (Frolov et al., 1976).

The final task for subsequent imitation modelling for the problem under study can be specified as the development of optimization principles for hydrogeological prospecting, with due account of feedback relations with designed engineering constructions. Only by such a comprehensive approach it is possible to speak about optimization of the overall system, rather than its individual elements. It can be proven in particular that economically important hydrogeological situations remain underexplored in many typical cases. This results in great additional costs of exploitation which make necessary the notable increases in the expense of hydrogeological prospecting as a whole. The latter presupposes the tendency toward the increase of weight of relatively expensive but more effective kinds of aquifer tests during the overall hydrogeological exploration.

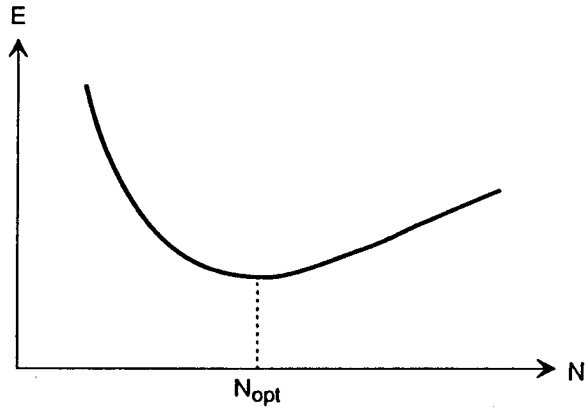

Figure 3 Typical curve of total expenses vs the number of aquifer tests.

Conclusions

1. Imitation modelling is a powerful instrument for the assessment and revision of various physical assumptions used in the study of flow processes, as well as in the estimation of the degree of uncertainty of the models. On the other hand, stochastic representation of the exploration process allows an estimate to be made of the model uncertainty, as this is related to incomplete and improper initial information. All this makes it possible to evaluate, simultaneously and from the same point of view, both a mean forecast estimate and possible errors.

2. Imitation modelling provides a systems approach to the investigation of flow problems, due to its ability to represent the overall main influencing factors and to consider interrelatedly (within one model) all development stages of the flow system and its data compilation - starting from exploration up to exploitation.

3. Within the physically substantiated stochastic models, imitation modelling allows the use of the advantages of a flexible heuristic approach to model construction, combining the theoretical knowledge of the investigator, with his/her practical experience and intuition. Thereby, the requirements to form a mathematical basis to the model are not so stringent, and relatively greater attention is paid to the logical substantiation and stepwise schematization of the model. Subsequent application of adaptation and feedback principles allows the quick detection of even the most narrow place in the hydrogeological scheme. Through imitation models one can accomplish the idea of hydrogeological exploration as a continuous 'self-teaching' experiment, which is the most effective way for exploration optimization.

4. Special attention should be paid to the possible application of imitation modelling for inspecting the quality of expert estimates, training and teaching.

Valery A. Mironenko was born in Leningrad, graduated from the Leningrad Mining Institute as a specialist in hydrogeology and engineering geology, and subsequently from the Leningrad State University with a specialization in mathematics and mechanics. Since 1969 he has been a professor at the Leningrad Mining Institute in the Department of Hydrogeology (21 Linija, 2 Leningrad 199026, USSR). The main direction of scientific activities include: ground water hydraulics, mining hydrogeology and engineering geology, hydrogeological tests and observations, and modelling of hydrogeological processes. Dr. Mironenko is a UN expert on water resources and a member of the American Institute of Hydrology, and a corresponding member of the USSR Academy of Sciences.

References

Frolov E.F. et al. 1976. Optimal Prospecting of Oil Deposits. Nedra, Moscow, (in Russian).

Mironenko V.A. and V.M. Shestakov. 1978. Theory and Methods for Interpretation of Aquifer Tests. Nedra, Moscow, (in Russian).

Shannon R.E. 1975. Systems Simulation - the Art and Science. Prentice-Hall, Inc.

Shvidler M.I. 1963. Seepage flow in heterogeneous medium. Gostoptechizdat, Moscow, (in Russian).

New Approaches to the Simulation of Field-Scale Solute Transport in Fractured Rocks

by Leslie Smith, Tom Clemo, and Mark D. Robertson

ABSTRACT

Two methods are described with the view to developing the capability to model solute transport at the field scale in geological media where fractures provide the dominant pathways for fluid flow. Both approaches start with the assumption that statistical data characterizing the geometric and hydraulic properties of a fracture network are available from fracture mapping and hydraulic testing. For geological media with a spatially-regular fracture pattern, a statistical continuum model is described that predicts the ensemble mean distribution of solute. This approach, introduced by Schwartz and Smith, has been modified to yield better estimates of the second moment of the spatial distribution of mass. For geological media where fractures occur with a range in their characteristic length scales, a hybrid model based on delineating a hierarchy among the fracture sets has shown promise. The approach, known as dual permeability modeling, is specifically designed to handle solute transport in those geological settings where conventional continuum concepts are not applicable.

INTRODUCTION

Predictions of rates and patterns of solute transport in geological media where fractures provide the dominant pathways for fluid flow present hydrogeologists with a problem for which conventional transport models may not be well-suited. Fracture patterns seen in outcrop or in underground adits provide striking visual evidence for inferring the presence of connected networks of fractures that form the hydraulic backbone for solute transport. It is not a given that models based on equivalent porous medium approximations provide valid representations of fracture-dominated systems, even when the solute migrates over distances of many tens to hundreds of meters. The alternative modeling approach, discrete network simulation, which by its nature does not require the identification of volume-averaged network properties, appears to be limited to problems of near-field simulation, that is, tens of meters or less. For problems at larger scales, currently there is little alternative but to model solute transport using porous medium equivalent models.

Two key questions arise when addressing the influence of the geometry of a fracture network on larger-scale spreading patterns and concentration distributions: 1. What models describe the spatial pattern of fractures within a rock mass, and how are these models dependent upon the lithologic and structural properties of the rock mass? 2. What approaches are available to transform a geometric description of a fracture network into a hydraulic and solute transport model? Statistical properties of fracture networks were reviewed by Dershowitz and Einstein (1988) and Barton and Hsieh (1989). Major issues yet to be resolved include the development of methodologies for inferring fracture dimensions given only borehole observations, and the need for an improved understanding of the scale-dependent description of fracture patterns. The focus in this paper is on the second issue, specifically, how a geometric description of a fracture system can be used as the basis for developing a solute transport model.

Solute transport in fractured media reflects the interaction of processes occurring at several scales. Processes of importance include: 1. advective transfer of mass at the average groundwater velocity, 2. dispersion due to tortuous pathlines and

2. dispersion due to tortuous pathlines and channeling within the plane of individual fractures, 3. dispersion due to routing of mass through fracture intersections that results in mass following pathways through the fracture network that are of differing length and with differing fluid velocities, 4. diffusive mixing at fracture intersections, 5. diffusion of mass from fractures into the rock matrix and vice versa, and 6. chemical reaction, including sorption. The cumulative influence of these processes is: 1. the appearance of erratic behavior in near-source regions because of a strong dependence on the precise structure of pathways through the fracture network, and 2. a typically asymmetric breakthrough curve with a rapid rise to a peak concentration and a long tail. Furthermore, because fractures tend to occur in sets with preferred orientations, spreading patterns vary with the orientation of the hydraulic gradient. That is, solute transport is an anisotropic process.

Two methods are described here with the objective of developing the capability to model solute transport in the case where the length scale of interest is of the order of tens to hundreds of meters or more. Both approaches start with the assumption that statistical data characterizing the geometric properties of a fracture network are available from fracture mapping and hydraulic testing. The first method, a statistical continuum approach, is applicable in the case where it is possible to identify, at the scale of interest, representative volume-averaged parameters describing the transport process. The second method, called the dual permeability approach, is designed to handle the case where multiple scales of fractures occur in a rock mass, a situation where a representative volume may not be definable at the scale of interest. Both approaches preserve the unique influence of the geometry of a fracture network on the transport process.

Throughout this paper, a number of simplifications are made. The intact rock matrix is assumed impermeable with zero porosity, thus no mass moves through the rock matrix. At fracture intersections, a complete mixing model is adopted, where mass leaving an intersection is distributed in the outflow branches in direct proportion to the fluid fluxes. The flow system in the fracture network remains at steady state. In addition, there is no coupling between the hydraulic, geochemical, and mechanical regimes.

MODELING APPROACHES

There are three approaches to simulate solute transport in fractured rock; discrete network simulation, continuum models based either on porous medium equivalent assumptions or statistical representations of mass transfer, and hydrid models that combine elements of both discrete fracture models and continuum approximations.

Discrete Network Simulation

Transport simulations carried out using two-dimensional representations of discrete fracture networks have proven to be useful to examine requirements for characterization of a fracture network as an equivalent porous medium (Endo et al., 1984; Schwartz and Smith, 1988), to examine the scale dependence of the dispersion process (Schwartz et al., 1983), to examine how network geometry influences spreading patterns (Smith and Schwartz, 1984), and to examine issues related to the worth of data on fracture position and orientation (Andersson and Thunvik, 1986). However, to describe the range in possible behaviour fully, simulations must eventually be carried out in three dimensions. This factor imposes severe restrictions on discrete network simulation. Even after simplifying a three-dimensional fracture network to a system of one-dimensional flow branches, and eliminating a significant fraction of low-permeability fractures, Cacas et al. (1990) could only model solute transport in a region only several tens of meters about an adit at the Fannay-Augeres mine in France.

Further, it was not possible to carry out a comprehensive stochastic interpretation of tracer tests because only a limited number of realizations could be examined. It is our judgement that while discrete models are useful analytical tools, alternative methods will be required at the field scale.

Conventional Continuum Models

The conventional form of the transport equation for a nonreactive solute is

$$\frac{\partial}{\partial x_i}\left[D_{ij}\frac{\partial c}{\partial x_j}\right] - v_i\frac{\partial c}{\partial x_i} = \frac{\partial c}{\partial t} \qquad (1)$$

where D_{ij} is the dispersion tensor and v_i the mean advective velocity. In using this equation to represent solute migration in a fractured rock mass, three basic issues arise. First, it must be determined that it is valid to approximate solute transfer through the fracture network using concepts of an equivalent porous medium, an assumption implicit in the use of the advection-dispersion equation. Second, if the first criterion can be met, then to compute an advective velocity, the effective porosity of the rock mass must be estimated. Third, coefficient values for the anisotropic dispersion tensor (D_{ij}) are required. All three issues pose considerable technical challenges.

To represent solute transport through a fracture network with a continuum model, whereby the specific geometry of the fluid pathways through the network are approximated with volume-averaged coefficients, several conditions must hold. The continuum elements must be large enough to encompass a representative sample of the connected fractures and their variable influences on the flow and transport behavior of the network. This factor defines the size of a representative elemental volume (REV).

For the fluid flow process, the concept of a representative sample means that it is possible to define a symmetric permeability tensor, independent of small changes in averaging volume, that predicts a stable relation between specific discharge and the orientation of the hydraulic gradient (e.g. Long et al., 1982). Several viewpoints are possible with respect to the transport process. One approach looks at the existence of an effective hydraulic porosity that is independent of the orientation of the hydraulic gradient (Endo et al., 1984). A second approach considers whether or not, at a given distance away from the source location (or a given time after solutes enter the flow system), the plume has encountered a statistically representative suite of fluid velocities in the hydraulically open fractures within the rock mass (Schwartz and Smith, 1988). Characteristic values for this length scale in different geological media are not known.

Evidence is accumulating that fluids are channeled within a fracture network, so that a relatively small set of fractures may dominate the larger-scale hydraulic and transport properties of the rock mass. Transport distances needed to meet the requirements for representative volume averages can be expected to be substantially larger than the length scale characterizing the dominating fractures within the rock mass.

Additional conditions for adopting a continuum approach are that the statistical properties of network geometry be uniform over a distance that is larger than that of the continuum element for transport, and that the domain of interest must be larger than that defining the representative volume. For example, if a prediction is required at a distance 100 m from a source location, and continuum approximations are inappropriate at scales < 200 m, then a conventional transport model will fail to provide a meaningful prediction.

If it can be determined that a continuum representation is a reasonable approximation at the scale of interest, and eqn (1) is adopted, then numerical values for the dispersion tensor must be estimated. One possible approach is to carry out a tracer test, and through

calibration, estimate values for the dispersion coefficients. In practical terms, this approach is limited to distances of meters to a few tens of meters. Unfortunately, it is not at all clear to what extent observations on this scale can be extrapolated to larger scales. Two alternatives have recently been discussed in the literature. A statistical continuum model has been proposed by Schwartz and Smith (1988) that is based on using representative statistics on particle motion observed within a discrete fracture network, rather that estimating values of D_{ij}. The second, proposed by Neuman and Depner (1988), adopts stochastic transport theory for an anisotropic porous medium, and uses estimates of hydraulic conductivity from single-borehole and cross-hole hydraulic tests to estimate coefficient values in the dispersion tensor. In this paper only the first model is discussed.

Statistical Continuum Models

Schwartz and Smith (1988) proposed a statistical continuum approach to simulate anisotropic dispersion in a network of finite length, randomly-located fractures of variable aperture. Particle tracking is at the core of the method. Transport is modeled by first collecting statistics on particle motion in a subdomain model using a discrete network simulation, and then using these statistics in a continuum model to simulate transport at a larger scale. Subdomain statistics adopted by Schwartz and Smith (1988) were the mean and standard deviation in fluid velocity for each possible direction of particle motion, probabilities on direction of motion away from fracture intersections, and the probability distribution on distances between fracture intersections for a given fracture set. In the statistical continuum model, this latter probability distribution describes decision points at which a possible change in direction of particle motion can occur, and at which a new fluid velocity will be chosen from the appropriate probability density function. Fluid velocities in the continuum model are generated assuming a lognormal probability distribution. Note that because mass seeks preferential pathways through the network, statistics based solely on a static analysis of the flow distribution within a fracture network are not equivalent to those sampled by a large set of reference particles.

This approach is based on continuum approximations and as such, several requirements must be satisfied to apply the method. The discrete subdomain model must be large enough to encompass a sufficient number of fracture pathways to obtain representative probability distributions on particle motion. There is also the requirement that the statistical properties of the fracture network at the subdomain scale be identical to those of the larger-scale continuum. Finally, the subdomain must still be small enough to be computationally feasible as a discrete network simulation. While this latter requirement is easily met in a two-dimensional analysis, the subdomain statistics for three-dimensional applications have yet to be determined. In this paper recent progress in the development of the statistical continuum method is reported.

To evaluate the accuracy of the approach, a discrete network model is used as a "stand-in" for a field trial. Subdomain statistics are collected from a discrete model at one scale, and then a second discrete network simulation and a statistical continuum prediction compared in a larger- scale domain. Schwartz and Smith (1988) did not carry out such a comparison because of computational limitations at that time in the size of a discrete network model that they could consider.

Figure 1A shows the network used in this comparison. Statistics for both fracture sets are identical, with parameter values chosen to be consistent with the earlier simulations of Schwartz and Smith (1988). See Table 1. No variability is included in fracture aperture. The hydraulic gradient is aligned

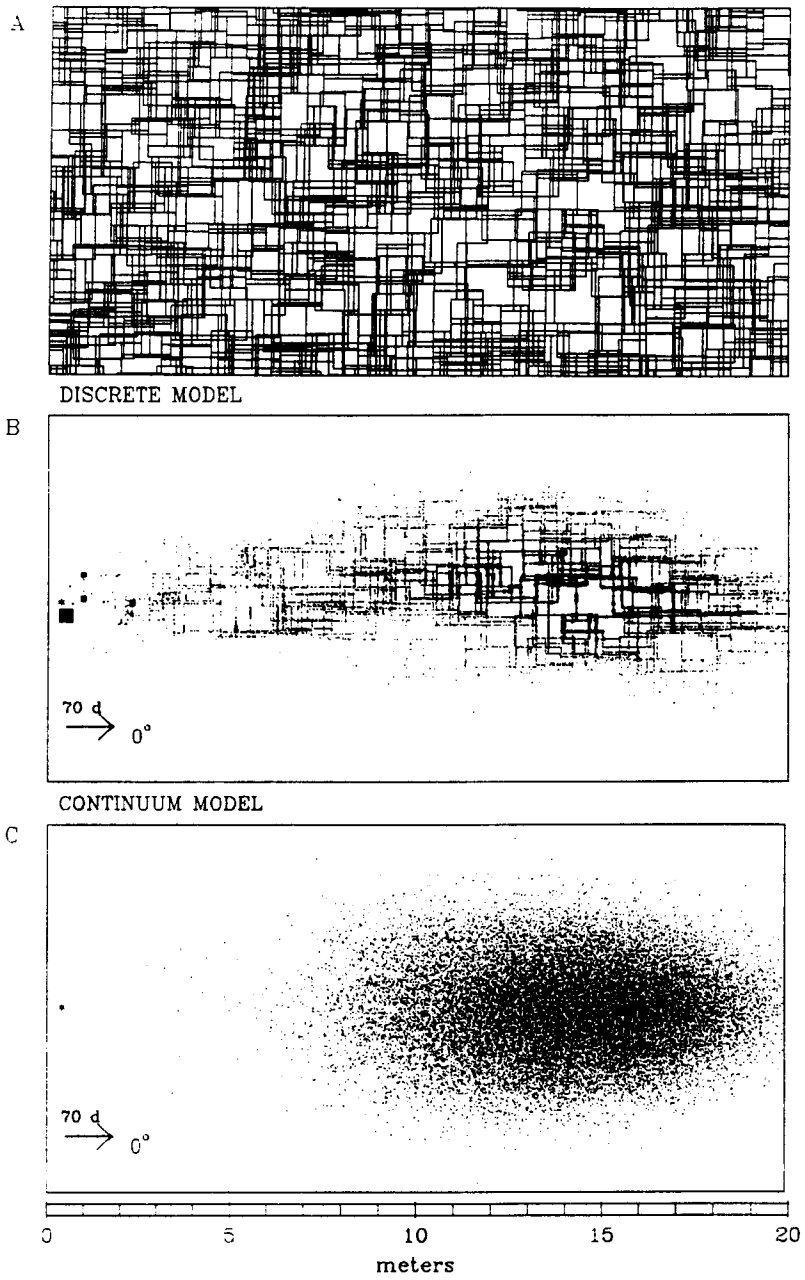

Figure 1. Comparison of discrete network simulation and statistical continuum prediction for the case with all fractures having a uniform aperture. A. Fracture network. B. Discrete network simulation for T = 70 d. c. Corresponding statistical continuum prediction.

Table 1

Geometric Properties of Fracture Network and Simulation Parameters, Statistical Continuum Model

Number of horizontal fractures	904
Number of vertical fractures	904
Mean horizontal fracture length	0.4 m
Mean vertical fracture length	0.4 m
Minimum horizontal fracture length in the network	1.2 m
Minimum vertical fracture length in the network	1.2 m
Log mean horizontal fracture aperture (aperture in m)	-4.5
Log mean vertical fracture aperture (aperture in m)	-4.5
Log standard deviation, horizontal fracture aperture	0.0
Log standard deviation, vertical fracture aperture	0.0
Hydraulic gradient in direction of flow	0.01
Number of reference particles	50000

in the direction of the horizontal fractures. The subdomain used to collect statistics on particle motion is 10 m by 10 m.

Figure 1B is a discrete network simulation for T = 70 d, by which time the center of mass of the plume has moved into the second half of the domain. The asterisk shows the source location. A total of 50,000 particles are used in the simulation. The dot size is scaled to be proportional to the number of particles located within a square region of dimension 0.05 m. The larger boxes near the source region denote a group of particles that entered a fracture segment with a low fluid velocity, and thus have not had a significant opportunity to disperse.

Figure 1C shows the corresponding statistical continuum prediction. The approach used here is the same as that of Schwartz and Smith (1988), except that where they collected discrete subdomain statistics from a single realization of a fracture network, here statistics on particle motion are averaged over 100 realizations of the discrete subdomain. This additional step removed noise in the discrete subdomain statistics that occurs because the subdomain model, for this particular network geometry, is close to the threshold of REV behaviour for solute transport. Analyses not reported here show that using 100 realizations to estimate subdomain statistics, and 50,000 particles to mimic continuum behaviour, yield results that are insensitive to further increases in the values of these simulation parameters.

Several features can be noted in Figure 1. First, the continuum nature of the simulation is obvious, the plume in the lower plot represents an "average prediction" of the mass distribution, and the local character of the mass distribution in the discrete fracture network is not preserved. By taking fracture porosity into account, this plot could be reinterpreted as an estimate of ensemble mean concentrations. Second, while the statistical continuum model is successful in approximating the leading edge and central body of the plume, it fails to preserve the long tail seen in the discrete fracture model. The first two moments of the particle distribution (s_X,s_{XX},s_Z,s_{ZZ}) provide a basis for comparison. Here, s_{XX} and s_{ZZ} are the variances in the spatial distribution of mass about the center of gravity (s_X,s_Z) of the plume. In large part because of the tail in the mass distribution, the variance predicted in the continuum model is approximately one half of that observed in the discrete model; a value of 5.5 in the continuum model, vs 11.7 in the discrete network simulation. This result was

not apparent in the results presented earlier by Schwartz and Smith (1988) because they based their tests on a comparison of the breakthrough curve at the downstream boundary. Effectively, this type of comparison places less emphasis on the tail of the plume. Breakthrough curves for these two simulations are compared in Figure 2.

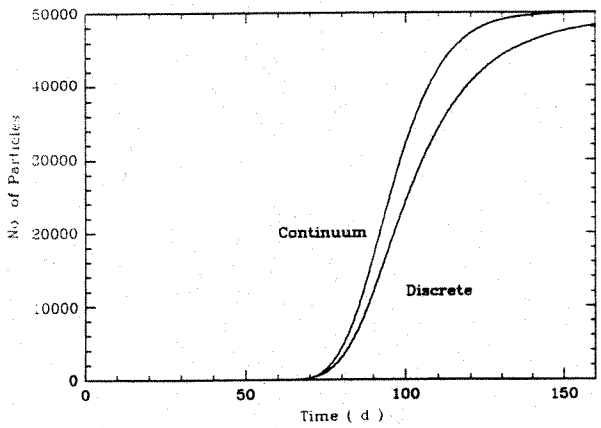

Figure 2. Comparison of cumulative breakthrough curve at the downstream boundary for the discrete network and statistical continuum models, see Figure 1.

Additional simulations not reported here show that differences in the statistical moments for a discrete network simulation and its corresponding continuum prediction are even greater in the situation where aperture variability is included in the analysis. This feature is apparent in Figures 3A and 3B, which compare the mass distribution in a discrete network model and a corresponding statistical continuum prediction, for a trial where the standard deviation in log-aperture is 0.20. A value of this magnitude results in apertures that vary by approximately one order of magnitude. The fracture network is the same as that shown in Figure 1. Note that the introduction of aperture variability leads to a plume that moves at a higher mean advective velocity than in the uniform aperture case. The simulation time is T = 35 d. A poor reproduction of the spatial distribution of mass is apparent. These and similar results provide the motivation to examine the use of alternate subdomain statistics in an attempt to mimic, more precisely, the discrete network motion in the continuum model.

Figure 3C shows the results of using a different set of rules to mimic particle motion in the continuum simulation. Two basic changes have been implemented from those developed by Schwartz and Smith (1988). First, instead of representing fluid velocity by a lognormal probability distribution, a two-parameter gamma distribution is used. The gamma distribution leads to a better representation of the histogram of fluid velocities collected in the discrete subdomain simulation than does the lognormal model. Second, account is taken of the temporal correlation structure in fluid velocity recorded as a particle migrates through the discrete subdomain model. In the earlier model of Schwartz and Smith (1988), fluid velocities generated for a new time step as a particle moves away from a decision point in the continuum model were not conditioned on the value selected during the prior time step.

In this study, a lag-one correlation for movement in a given direction is defined as the correlation between the value of the particle velocity on the downgradient side of a fracture intersection, with respect to the value of particle velocity the last time it was moving down a fracture segment in the same direction. This formulation measures the correlation structure for a particle moving in a given direction, and it includes occurrences where a particle may have entered a second fracture set before continuing to move in the first fracture set again. The lag-two correlation coefficient extends back through two fracture segments in the same direction of motion. In the example shown in Figure 3A, the estimated correlation coefficients are 0.68 and 0.51 for the lag-one and lag-two values, respectively for a particle that moves in the positive x direction.

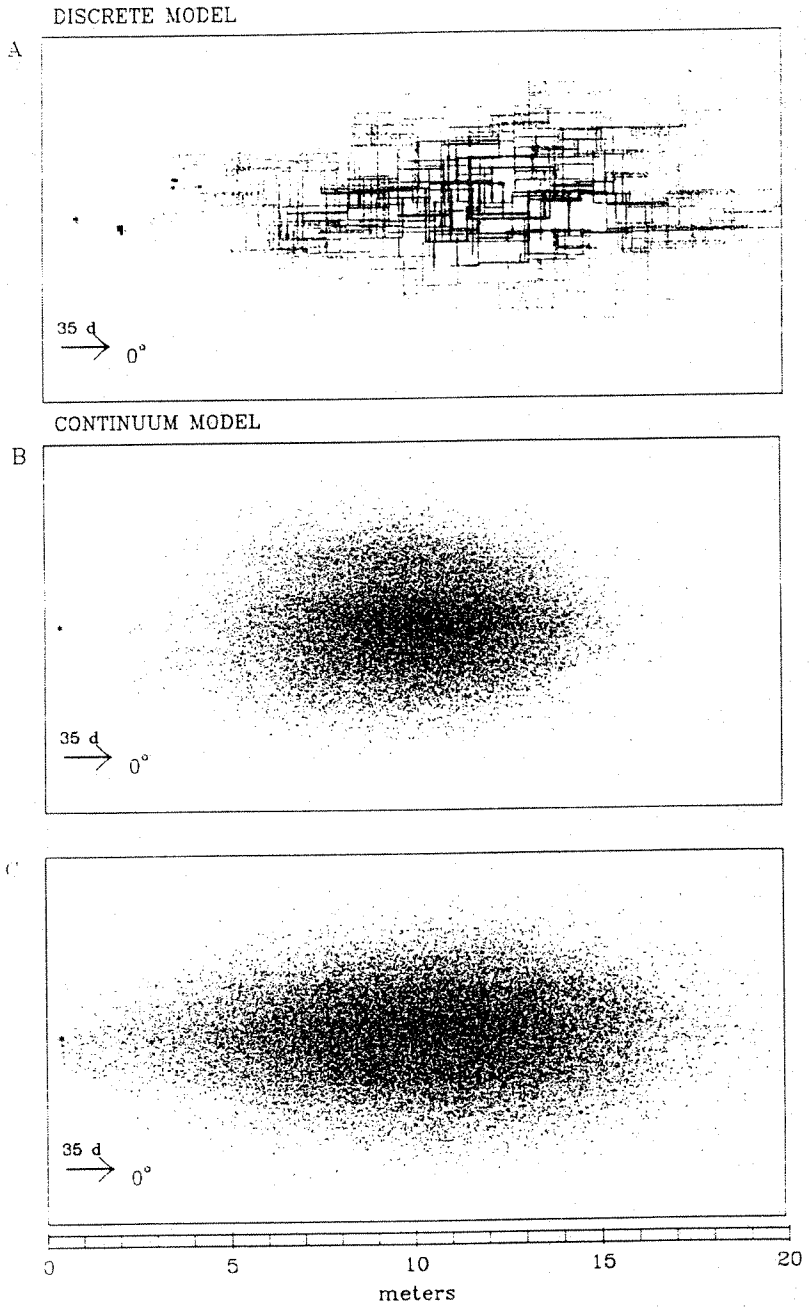

Figure 3. Comparison of discrete network simulation and statistical continuum predictions for the case where the log aperture standard deviation is 0.20. A. Discrete network simulation at T=35 d. B. Corresponding statistical continuum prediction using the method described in Schwartz and Smith (1988). C. Statistical continuum prediction based on a gamma distribution for particle velocity, and a second order autoregressive temporal correlation structure.

Particle velocities are sampled in the continuum model by representing this correlation structure with a second order autoregressive model (Box and Jenkins, 1976). A probability transform is used to generate random variates with a gamma distribution, given an AR(2) gaussian model. Figure 3C shows that the revised continuum model is better able to represent the spatial distribution of mass in the discrete network, especially with respect to the tail of the distribution.

The growth of the variance in the spatial distribution of mass in the x direction (s_{xx}) is plotted as a function of time in Figure 4. The various curves reflect different assumptions used in the continuum simulation to mimic motion in the discrete network. The solid curve is the time-dependent increase in s_{xx} estimated from the discrete network simulation. It is obtained as an average of 100 realizations of the discrete model. The lowermost curve, labelled gaussian-(0), corresponds to the

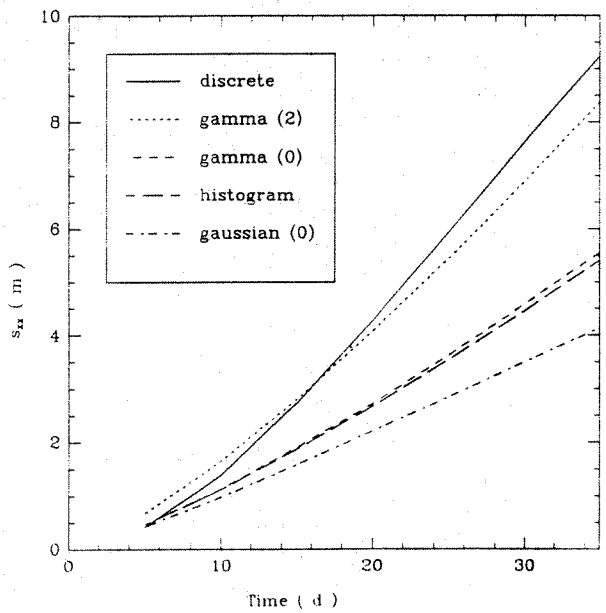

Figure 4. Estimated ensemble variance in the spatial distribution of mass in the x direction, using several different models to represent particle motion in the statistical continuum model. See text for explanation of individual curves.

method adopted by Schwartz and Smith (1988). The curve labelled "histogram" is obtained by generating particle velocities in the continuum model directly from the sample histogram formed from the subdomain simulation, without incorporating a temporal correlation structure in particle velocity. The curve lying just above that (gamma-(0)) results when sampling particle velocities from a gamma distribution are fitted to the sample histogram.

These comparisons show: 1. the improvement in representing the temporal growth of the discrete network plume by not imposing the assumption of a lognormal distribution for particle velocity, and 2. that the gamma distribution provides a good approximation to the sample histogram, considered from the perspective of the transport simulation. However, none of these three models properly captures the spatial distribution of mass in the discrete network model. A much better representation of the second moment of the plume is obtained by taking account of the correlation structure in particle velocity (curve gamma-(2)). Work is ongoing to evaluate these revised methods in collecting discrete subdomain statistics, and in mimicking transport patterns in the larger scale continuum (Robertson and Smith, 1991).

Dual Permeability Models

It is conceivable that there may be many field settings where the transport process is not adequately represented by continuum approximations. Unfortunately, computational limitations in the application of discrete network models do not provide a way around this problem. A method with the potential to model far larger volumes of fractured rock than can be accommodated with the discrete approach, without resorting to continuum approximations, is presently being developed. The basic concept is to delineate a hierarchy among the fractures forming a network. Those fractures that are deemed more important

to the flow and transport process, which are called primary fractures, are modeled individually. The majority of the fractures are modeled in groups using a lumped-parameter representation called network blocks. A schematic example of the concept is shown in Figure 5. Together, the combination of primary fractures and network blocks form the dual permeability model. While smaller-scale fractures submerged within network blocks are individually of less importance, their collective effect is on a par with that of the primary fractures. The method seems well-suited to modeling solute transport in fracture networks where fractures occur with a broad range of length scales.

Network blocks are an approximation to the effects of a group of adjacent fractures. They are not a continuum in the sense of an equivalent porous medium because the blocks are sub-REV in size. Each block is different, just as each discrete fracture is different. Network blocks are bounded by primary fractures which define the geometry of the network blocks, and thus their hydraulic properties. Note that the dual permeability concept is distinct from the dual porosity model. The "dual" in dual permeability reflects the division of fracture permeability into two categories (primary fractures and network blocks), and it should not be thought of as two overlapping continua linked by a transfer function as in a dual porosity model.

A dual permeability model contains two sub-models. The flow model determines the fluid flux in the network blocks and primary fractures. Using a Galerkin finite element method, network blocks are represented by two-dimensional rectangular elements, and primary fractures by line

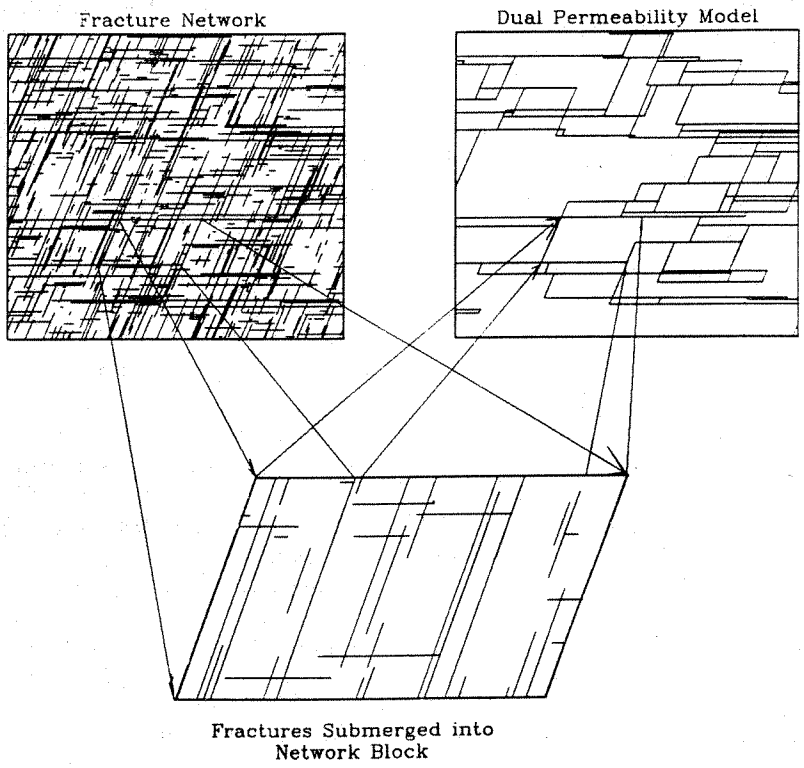

Figure 5. Creation of a dual permeability model for a fracture network. Primary fractures are retained as individual, discrete fractures. Most fractures are submerged into network blocks, as shown for the single block that has been isolated in this schematic representation.

elements. The hydraulic conductance of each network block is calculated knowing the hydraulic properties of the fractures that it replaces. In the transport

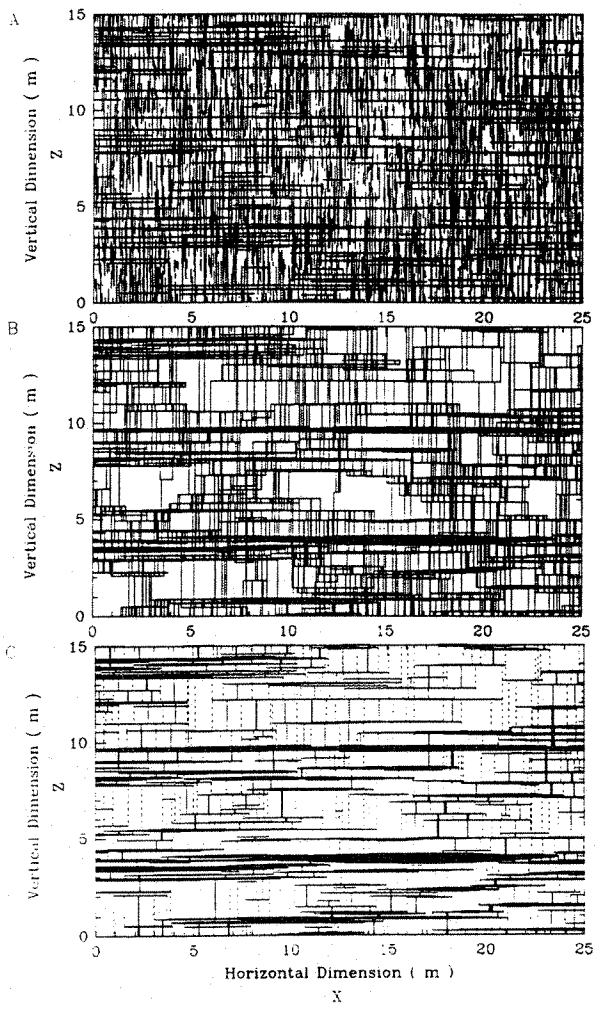

Figure 6. An example of a dual permeability model. A. Fracture network. B. Distribution of fluid flux within the network, where each fracture segment that is part of the active network is plotted with a line width that is proportional to the flow rate in the fracture. Flux calculated using a discrete network model. See text for details. C. Fluid flux predicted by the dual permeability model, the dashed vertical lines identify boundaries of network blocks.

model these fluid fluxes are used as the basis for moving discrete particles through the flow domain. Mass transfer across network blocks is expressed in terms of stochastic residence time functions on travel time and on exit location to a down-gradient primary fracture. These probabilities are calculated from the statistical parameters of the smaller-scale fracture sets, the orientation of the local hydraulic gradient, and the location of the larger-scale primary fractures which define the geometry of the network blocks. Details of the computational procedure are given in Clemo and Smith (1991).

Figure 6 illustrates the method. The network shown in Figure 6A is one realization from a statistically defined network composed of two orthogonal fracture sets. The horizontal fractures, while less abundant, have a greater length scale and higher mean aperture than the vertical fracture set (an average length of 6 m and mean aperture of 50 microns, vs an average length of 1 m and mean aperture of 10 microns). The vertical scan line density is two fractures per meter, the horizontal scan-line density is ten fractures per meter. The aperture standard deviation is 0.10. The boundary conditions are defined by a uniform hydraulic head gradient of 0.01 at an angle 80^{o} counterclockwise from the x direction.

Figure 6B shows the flow distribution in the rock mass calculated using the discrete network simulation model. Each fracture segment that is part of the active network is plotted with a line width proportional to the flow rate in the fracture. Fractures that carry < 3% of the greatest flow rate are all plotted with a line width 3% of the maximum width.

Figure 6C shows the flow distribution predicted by the dual permeability model. Recall that many of the vertical fractures are not modeled as discrete features, as they are in Figure 6B. The dashed lines are the vertical boundaries used to define the set of network blocks. The solid line plotted in the center of most network blocks represents the total flow through the

blocks. Fluid flow through the network blocks is only plotted if it is greater than the 3% threshold. Note that some of the network blocks will be assigned zero conductance if no fractures cross between the bounding primary fractures.

Heterogeneity of flow within the domain is evident in Figures 6B and 6C. Many of the horizontal fractures have relatively low flow rates. High flows are seen in large aperture fractures that are well connected to other horizontal fractures. Although individually the vertical fractures rarely have flow rates > 3% of the greatest flow, taken collectively they provide essential connectivity to the network.

Figure 7 compares the breakthrough curves at the downstream vertical boundary calculated using both a discrete network model, and the dual permeability model. Figure 7A compares the particle arrival integrated along the entire downstream vertical boundary, Figure 7B compares the particle arrival at vertical position 9.66 m

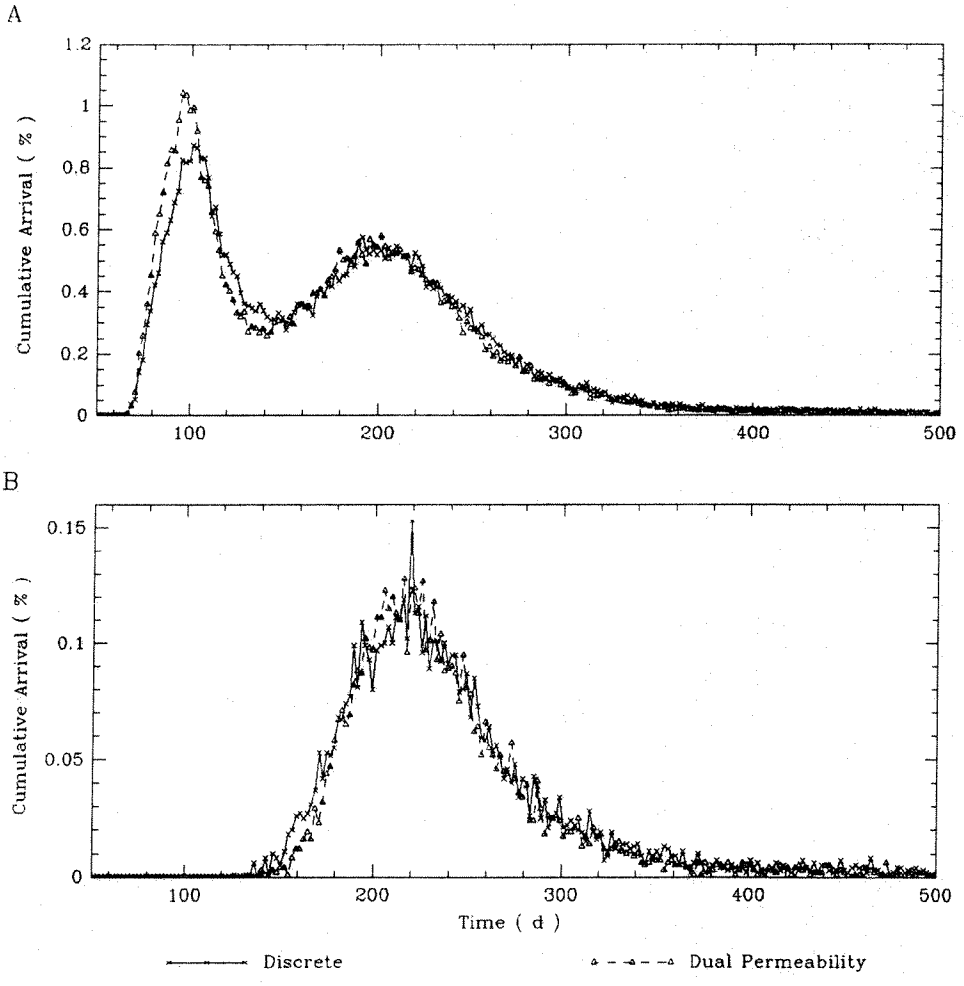

Figure 7. Comparison of breakthrough curves formed at the downstream vertical boundary, for the discrete network and dual permeability simulations. A. Particle arrival integrated along the entire downstream vertical boundary. B. Particle arrival at vertical position 9.66m on the downstream boundary.

on the downstream boundary. The match is considered to be excellent in both cases. Considerably less computational effort was needed to obtain the dual permeability results. The flow component of the discrete network model required the solution of 7430 equations, the dual permeability model required the solution of 1392 equations. Particle tracking in the dual permeability model is also less computer intensive, although this is less of a factor than the efficiencies in determining the fluid fluxes. It is these efficiencies, coupled to the concept of sub-REV simulation and identification of primary fractures, that hold considerable promise in moving toward field-scale simulation. Studies are underway to extend the computational procedures to allow more general fracture geometries than that illustrated in Figure 6.

SUMMARY

In this paper we have reviewed our recent progress in developing field-scale simulation models describing solute transport in fractured rock masses. Two methods are described, both of which start with the assumption that statistical data characterizing the geometric properties of a fracture network are available from fracture mapping and hydraulic testing. For those geological settings with a spatially-regular fracture pattern and a single scale of fracturing, a statistical continuum model shows promise for prediction of the ensemble mean distribution of mass. The approach is being refined to determine a set of subdomain statistics on particle motion that best replicates moment estimates. The dual permeability model is a hybrid approach that is suited to simulating solute transport in rock masses where fractures occur on a range of scales. The method is based on delineating a hierarchy among the fractures (or fracture sets) that form a network, and then treating them computationally as primary fractures and network blocks. Mass transfer is represented in terms of stochastic residence time functions for the network blocks, combined with particle tracking in the primary fractures. This method yields predictions of mass breakthrough at downstream boundaries.

ACKNOWLEDGEMENTS

This research has been supported by grants from the Natural Sciences and Engineering Research Council of Canada, and a research contract from the Idaho National Engineering Laboratory.

Biographical Sketches

Leslie Smith is a Professor of Geological Sciences at the University of British Columbia in Vancouver, British Columbia (6339 Stores Road, Vancouver, B.C. V6T 1Z4). He has conducted research in the areas of solute transport in heterogeneous porous media, transport processes in fractured rocks, and the influence of groundwater flow on the thermal regime of the upper crust.

Tom Clemo is a Ph.D. student in the Geological Engineering Program at the University of British Columbia (6339 Stores Road, Vancouver, B.C. V6T 1Z4), on leave from the Idaho National Engineering Laboratory. He holds degrees in Mechanical Engineering from the University of California, Davis, and in Nuclear Engineering from the University of California, Berkeley.

Mark Robertson is a consultant for Mackie Martin and Associates in Brisbane, Australia. He holds B.A.Sc. and M.A.Sc. degrees in Geological Engineering from the University of British Columbia.

REFERENCES

Andersson, J. and R. Thunvik. 1986. Predicting mass transport in discrete fracture networks with the aid of geometrical field data. Water Resour. Res., v.22, pp. 1941-1950.

Barton, C.C. and P.A. Hsieh. 1989. Physical and hydrologic-flow properties of fractures. Field Guide Book, Twenty-ninth Inter. Geol. Cong. Field Trip T385.

Box, G. and G. Jenkins. 1976. Time Series Analysis Forecasting and Control, Holden-Day, San Francisco.

Cacas, M.C., E. Ledouc, G. de Marsily, B. Tillie, A. Barbreau, E. Durand, B. Feuga and P. Peaudecerf. 1990. Modeling fracture flow with a stochastic discrete fracture network: Calibration and validation 1. The flow model. Water Resour. Res., v.26, pp. 479-489.

Clemo, T. and L. Smith. 1991. Solute transport in fractured media: Dual permeability models (in prep.).

Dershowitz, W.S. and H.H. Einstein. 1988. Characterizing rock joint geometry with joint system models. Rock Mech. and Rock Eng., v.21, pp.21-51.

Endo, H.K., J.C.S. Long, C.R. Wilson and P.A. Witherspoon. 1984. A model for investigating mechanical transport in fracture networks. Water Resour. Res., v.20, pp.1390-1400.

Long, J.C.S., J.S Remer, C.R. Wilson and P.A. Witherspoon. 1982. Porous medium equivalents for networks of discontinuous fractures. Water Resour. Res., v.18, pp.645-658.

Neuman, S.P. and J.S. Depner. 1988. Use of variable-scale pressure test data to estimate the log hydraulic conductivity covariance and dispersivity of fractured granites near Oracle. J. Hydrol., v.102, pp.475-501.

Robertson, M. and L. Smith. 1991. Extensions to a statistical continuum model for mass transport in fractured media (in prep.).

Schwartz, F.W., L. Smith and A.S. Crowe. 1983. A stochastic analysis of macroscopic dispersion in fractured media. Water Resour. Res., v.19, pp.1253-1265.

Schwartz, F.W. and L. Smith. 1988. A continuum approach for mass transport in fractured media. Water Resour. Res., v.24, pp. 1360-1372.

Smith, L. and F.W. Schwartz. 1984. An analysis of the influence of fracture geometry on mass transport in fractured media. Water Resour. Res., v.20, pp. 1241-1252.

Controls on porosity and permeability in fracture-flow/conduit-flow rocks of the Knox Group, Southern Appalachian Fold-and-Thrust Belt, USA

by James C. Redwine,
Richard R. Parizek and Fred J. Molz

Abstract

Alabama Power Company's Logan Martin reservoir is located on folded, faulted, fractured and solutioned rocks of the Cambro-Ordovician Knox Group in east-central Alabama, USA. The reservoir loses significant quantities of water through the underlying fracture-flow/conduit-flow aquifer system, which diminishes hydroelectric power generation at the site. For this and other reasons, subsurface investigations have been ongoing at the Logan Martin site for the past 30 years. Major categories of information include studies of aerial photography and remotely-sensed imagery; approximately 265,000 piezometer readings; dye and tracer test data; surface and subsurface geological mapping and modelling; temperature information; water chemistry data; surface and downhole geophysics; packer (hydraulic conductivity) testing; grouting records; and sinkhole mapping. Recently, this information has been pulled together to identify and estimate flow and transport parameters, particularly controls on porosity, permeability, and discrete flow paths. Major geological controls include the upper Knox/lower Knox contact; various rock types; fold structures; regional and local thrust faults; local normal faults; regional cross-structural discontinuities; fracture systems of various ages; near-vertical zones of fracture concentrations; present karst and paleokarst horizons; mappable features of unknown origin; and combinations and interactions of the various controls. Work is presently underway to detect discrete flow paths with borehole flowmeters using both state-of-the-art and prototype equipment. This quantitative hydraulic testing, when combined with the previous hydrogeological work, will be used to develop a methodology or procedure for quantifying flow and physical transport parameters in complex geological terrain. The investigators can develop a hierarchy of controls, and because of the extensive site investigations, determine the most cost-effective methods for parameter identification and assessment. This work applies not only to ground water problems in fracture-flow and conduit-flow aquifers, but also to oil and gas exploration and development in such rocks.

James C. Redwine is a senior hydrogeologist/engineering geologist and is presently working with the Earth Science and Technology Department of Southern Company Services (PO Box 2625, Birmingham, Alabama 35202, USA. Mr. Redwine's responsibilities range from project development to ground water investigations to geological resource evaluations. The subject matter of this presentation is part of his dissertation research performed in partial fulfillment of requirements for his PhD in geology at the Department of Geosciences, Pennsylvania State University.

Fred J. Molz works in the Civil Engineering Department at Auburn University (Auburn, Alabama 36849-3501, USA).

Characterization and Modeling of Groundwater Flow in a Heterogeneous Aquifer System to Evaluate Contaminant Migration

by Fred G. Baker and Hannah F. Pavlik

Abstract

The hydrogeological regime and extent of groundwater contamination were characterized at a federal Superfund site in the Sacramento River valley, northern California. Wood-preserving compounds, primarily pentachlorophenol (PCP) and creosote have been detected in the soil and groundwater. A plume of dissolved PCP up to ~2.4 km (1.5 mi) long has been detected in groundwater south of the site.

Aquifer heterogeneity is dominated by the juxtaposition of channel-fill gravel and sand facies against less permeable flood plain clays and debris-flow units which act as aquitards. The aquifer consists of a complex multizoned system of permeable gravels and sands composed of units from four geological formations deposited by the ancestral Feather River. Fluvial channel gravels form the principal aquifer zones and contain overbank clay and silt deposits, which locally form clay lenses or more continuous aquitards. Two incised paleo-channels of the Laguna Formation are inset into the older Mehrten Formation near the site, complicating the aquifer stratigraphy. The geometric mean horizontal hydraulic conductivities for channel gravels range from 37 to 161 m/d (120 to 530 ft/d). Mean vertical aquitard hydraulic conductivity is 2×10^{-2} m/d (0.07 ft/d). Groundwater flow is generally southward, with a velocity 145 to 305 m/a (470 to 1,000 ft/a). Groundwater flow is largely advection-dominated in this system.

The spatial distribution of dissolved PCP in the aquifer documents the interactions between major permeable zones. Hydrostratigraphic evidence pointing to the separation of aquifer zones is supported by the major ion chemistry of groundwater. This indicates that hydrodynamic separation exists between the upper and lower zones of the aquifer, limiting the vertical movement of the PCP plume. A 3-D numerical groundwater model, based on the conceptual hydrogeological model described here, was developed for use as a tool for design of a groundwater extraction and treatment system.

Introduction

The heterogeneous nature of fluvial sand and gravel aquifers is of direct concern in investigations of groundwater contamination because the heterogeneity often adds a level of complexity that hinders understanding of aquifer system behavior. The scale of the heterogeneity, the approximate dimensions and spatial distribution of high and low permeability units, and the relative contrast in permeabilities all have a direct influence on the movement of groundwater and any dissolved constituents through the aquifer system. Ironically, a large number of hazardous waste sites associated with chemical plants, refineries, wood-treatment plants and manufacturing facilities are located on heterogeneous fluvial geological deposits due to proximity to water

supplies, water transportation routes and available land. The study summarized here represents a case study of the investigation and modeling of groundwater flow and contaminant migration in a heterogeneous aquifer system.

Soil and groundwater contamination in the vicinity of a wood-treatment plant near Oroville, northern California, have contributed to the migration of dissolved chemical constituents into groundwater offsite. The plant is situated along the eastern margin of the Sacramento Valley, in the floodplain of the Feather River, which is bounded by Plio-Pleistocene fluvial terraces rising 15 to 35 m (50 to 120 ft) above the valley floor (Figure 1). The primary chemicals of concern are wood preservatives such as pentachlorophenol (PCP) and polynuclear aromatic hydrocarbon (PAH) compounds.

Due to the complexity of the local aquifer system, several site investigations were undertaken to characterize hydrogeological conditions near the wood-treatment

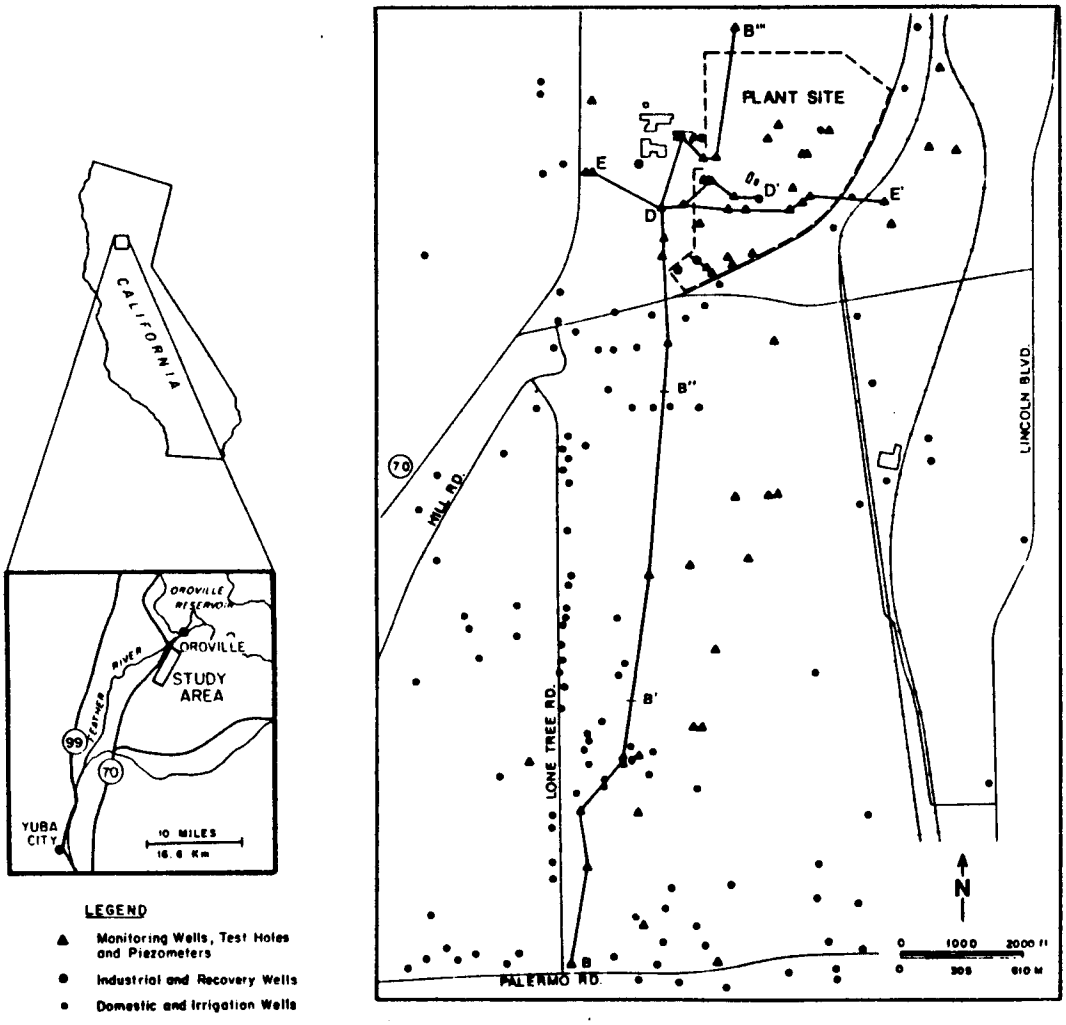

Figure 1. Map of the study area showing plant site, wells and cross-section locations.

plant. Early hydrogeological investigations produced conflicting interpretations of the uniformity of groundwater flow and the magnitude of the PCP plume migration. The initial site investigation (California Department of Water Resources, 1973) relied on geological data obtained largely from ground surface and shallow boreholes, and suggested that groundwater from the plant flowed toward the west and southwest through a series of shallow unconfined gravels. This interpretation was supported by groundwater quality data and measured groundwater hydraulic gradients. A more comprehensive study conducted more than a decade later (Schmidt, 1984) found that groundwater flow was to the south, as indicated by the presence of a PCP plume extending nearly 2.4 km (1.5 mi) south from the plant. As a result of the 1984 findings, a CERCLA (Comprehensive Environmental Response, Compensation and Liability Act.) Remedial Investigation/Feasibility Study (RI/FS) was undertaken beginning in early 1986. As a part of the overall RI/FS work, detailed information was collected to characterize the physical properties of soil and aquifer units, and the extent of contamination in soil, air, surface water and groundwater (Dames and Moore, 1988a, b). Subsurface information obtained included geological logs from 32 newly constructed monitoring wells and exploration test holes. In addition, groundwater quality data were obtained from water samples collected from more than 100 wells and test holes (see Figure 1).

The purpose of the hydrogeological investigation presented here was to define the nature of the heterogeneous aquifer system, to determine the influences of heterogeneity on groundwater flow in the vicinity of the wood-treatment plant, and to evaluate the distribution and transport of PCP and other chemical constituents throughout the aquifer system. Information gained from the site investigation was initially used to identify key hydrostratigraphic units within the fluvial deposits. The resulting description of the aquifer system and its behavior served as the basis for development of a three dimensional groundwater flow and solute transport model of the site (Dames & Moore, 1988a). The transport model was used to simulate the spatial distribution of the dissolved PCP plume in groundwater and to predict the rate and extent of movement of PCP and other compounds in groundwater under "no-action" conditions, for use in risk evaluation and in the feasibility study. In addition, the model was used for preliminary evaluation of possible groundwater recovery and treatment alternatives (Dames & Moore, 1989).

Specific objectives of the study that are emphasized in the following sections are: 1. definition of the principal hydrostratigraphic units that constitute the large scale heterogeneity of the aquifer system; 2. characterization of the hydraulic properties of the principal permeable units of the aquifer; and 3. development of a three-dimensional model to describe groundwater flow and solute transport for use in evaluation of remedial alternatives.

Hydrostratigraphy

The principal stratigraphic units in the Oroville area include the Eocene-age Ione Formation, the Oligocene-Pliocene-age Mehrten Formation, the upper Pliocene Nomlaki Tuff, and the

upper Pliocene - Holocene Laguna Formation (Blair and Baker, 1990). Locally, the aquifer system near the plant can be generalized into four major hydrostratigraphic zones: A, B, C and D (Dames & Moore, 1988a). The characteristics and stratigraphic relations of these zones are summarized in Table 1 and in a series of simplified stratigraphic cross-sections (Figures 2 and 3) the locations of which are shown in Figure 1. The A zone is a permeable gravelly unit of the Laguna Formation (Table 1) found south of the plant site. It is not present in the vicinity of the plant due to the presence of a marked stratigraphic transition that occurs at the margin of the present Feather River floodplain. In most areas south of the plant, the A zone is underlain by the Nomlaki Tuff (unit AB in Table 1), which acts as a major aquitard to confine the B zone. In general, the shallow gravels of zone A are relatively unimportant for assessing contaminant migration from the site because they occur only sparingly and are water-bearing only in the southern portion of the study area where sources of contamination are not known. The highly permeable gravelly units of the B and C hydrostratigraphic zones comprise the uppermost aquifer of interest to this study. Depending on location, B and C zone gravels and sands can belong to either the Laguna, Mehrten or Ione Formations, which are interwoven in a relatively complex and highly variable stratigraphic environment (Figures 2 and 3). The B and C zones are separated in many areas by interbedded clay units which locally form the BC aquitard. The upper aquifer forms the major potential pathway for transport of dissolved chemicals offsite,
and elevated concentrations of PCP occur in groundwater samples collected from both the B and C zones.

Two paleo-channels of Laguna age have been identified in the study area (Blair and Baker, 1990). One channel is located in the area occupied by the current Feather River floodplain, (Section B"-B"', Figure 2) and the other occurs in the area south of the plant site. In addition, older Mehrten channel gravels have been identified south of the plant. The Laguna paleo-channels cut through permeable units of the Mehrten Formation, juxtaposing Laguna channel gravels against gravels of the Mehrten Formation.

A generalized hydrostratigraphic interpretation of the site is presented in cross-sections B"-B"' and E-E' (Figures 2 and 3). Figure 2 illustrates the complex stratigraphic relations that exist between the principally channel-fill deposits of the Laguna Formation onsite and the older Ione, Mehrten and Nomlaki Formations (where they occur) south of the site. The cut-and-fill morphology typical of channel deposits can be seen quite clearly in the B"-B"' transect (Figure 2), where Laguna gravels wedge out sharply to the south between test hole F (TH-F) and groundwater monitoring well MW-22, decreasing in thickness from ~82m (~270 ft) at TH-F to only 9m (30 ft) at MW-22.

In general, groundwater flowing south from the plant moves through Laguna gravels in hydrostratigraphic zones B and C and enters the permeable units of adjacent formations (Figure 2). Groundwater in zone B moves from relatively less permeable Laguna gravels found onsite into somewhat more permeable Mehrten gravels; groundwater in Laguna gravels found onsite in hydrostratigraphic zone C flows into the permeable units of the Ione Formation in the vicinity of MW-22

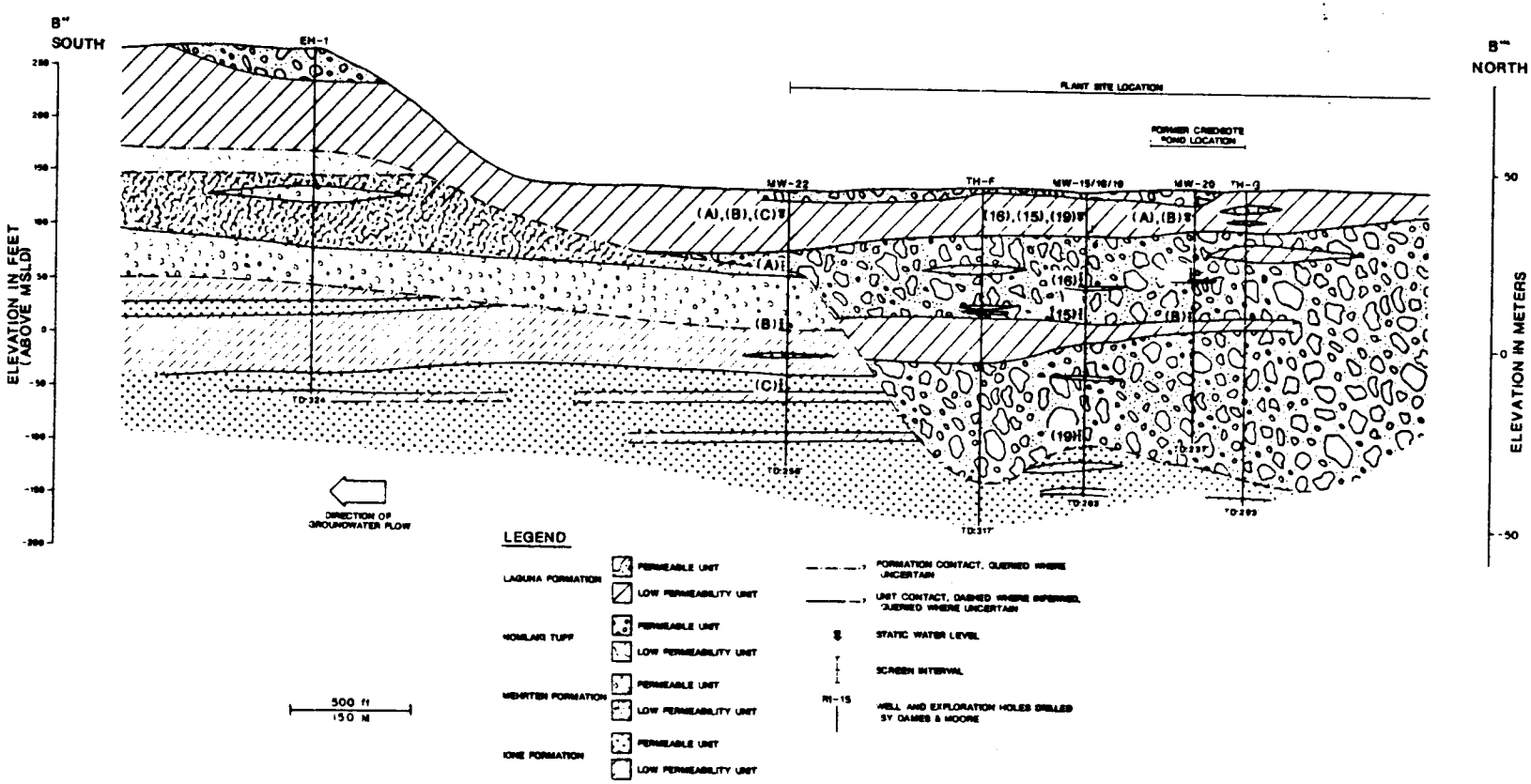

Figure 2. Geological cross-section B"-B'''.

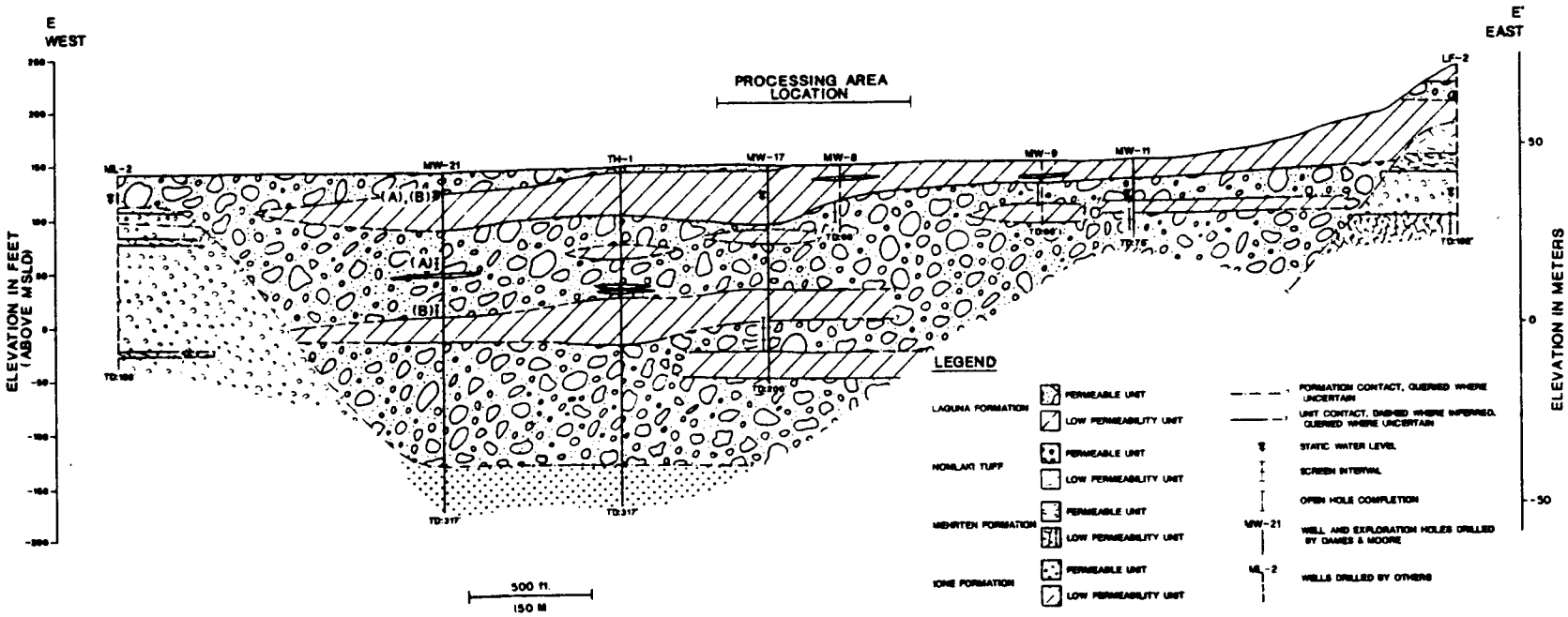

Figure 3. Geological cross-section E-E'.

Table 1

Generalized Hydrostratigraphic Unit Characteristics

Unit	Description
A	Permeable, gravelly unit of the Laguna Formation (upper Pliocene-Holocene). Found south of the plant site. Water-bearing only in southern portion of the study area.
AB	Nomlaki Tuff, aquitard (upper Pliocene age). Spatially significant confining unit in the south and southwest.
B	Highly permeable gravel units of the Mehrten Formation (Oligocene-Pliocene) in the southern and western part of the study area. Also comprised of highly permeable gravels of the Laguna Formation on the southeast side of the study area where a paleochannel has been incised into the Mehrten Formation gravels. Contains discontinuous clay lenses. Composed of a thick accumulation of Laguna Formation gravels onsite, which wedges out along a paleochannel wall just south of the plant site.
BC	Aquitard unit or series of discontinuous low-permeability units. Between MW-22 P-1, EH-1, and RI-5, this is a thick siltstone of the Ione Formation (Eocene). Farther south, it is apparently discontinuous, composed of clayey, silty lenses in the Mehrten and Laguna Formations. In the far south, near P-2 and RI-15, tuffaceous and siltstone units form a locally continuous stratum. Onsite it forms a substantial Laguna Formation clay layer that is juxtaposed against the BC siltstone of the Ione, maintaining separation between the B and C zones.
C	Permeable gravels of the lower Mehrten, lower Laguna, and Ione Formations south of RI-4 and RI-5, and the B and C aquifer zones appear to form a thick gravel unit separated by discontinuous clay lenses. Farther south, they are apparently separated again by the BC aquitard. It is composed of lower Laguna gravels onsite. It appears that the B and C gravels combine to form a locally thick permeable unit in the northern portion of the site, where no intervening clay is found.
CD	Deep, largely continuous, low-permeability stratum composed of Ione Formation clays and silts (Eocene).
D	Deep sandstone in Ione Formation (Eocene) at well P-1.

and into Mehrten gravels and less permeable Ione sandstone units to the east. As shown in section B"-B"' (Figure 2), the BC aquitard is formed by low permeability interbeds of the Laguna and Ione Formations juxtaposed against each other along the side wall of the paleo-channel. This juxtaposition of sediments provides hydraulic continuity between permeable units across the channel boundary but it also prevents the mixing of B and C zone groundwater. The permeable gravels of hydrostratigraphic zone B comprise the principal aquifer along which dissolved PCP was able to migrate.

A different perspective on the hydrostratigraphy of the site can be seen in cross-section E-E' (Figure 3) which traverses the plant site from west to east. The BC clay thins and pinches out to the east allowing direct communication between B and C gravels in the vicinity of the wood-processing area. During the drilling of monitoring well ML-2, shown on the west side of the cross section, a thick succession of Mehrten gravels and sands was encountered juxtaposed against channel-fill deposits of the Laguna Formation. The Nomlaki and Mehrten Formations were both encountered at shallow depths in well LF-2, indicating that gravels of the Mehrten Formation are in direct hydraulic contact with gravels of the Laguna Formation at this location. Mehrten gravels also define the eastern margin of the incised Laguna paleo-channel seen near this well.

Hydraulic Properties

Eighteen aquifer pumping tests were conducted to estimate the hydraulic properties of the Band C aquifer zones (Dames & Moore, 1988a). The hydrostratigraphic units in which aquifer tests were conducted are clayey sands and gravels that contain a significant fine-particle fraction. The silt, clay and fine-sand fractions of these geological materials appear to reduce the effective permeability of the observed formations, perhaps reducing aquifer permeability to the lower end of the range of hydraulic conductivities expected in fluvial sand and gravel deposits. Based on the pumping test results, the B and C hydrostratigraphic zones appear to be semiconfined. The aquitards that act to confine the permeable zones are leaky, and results from the pumping tests have been used to estimate the vertical permeability of these aquitards. Because of leaky aquitard conditions, most pumping test analysis methods used are those that can be applied to tests in semi-confined aquifers. These methods include the Hantush inflection point method (Hantush, 1956), the method of Walton (1962), and the Jacob straight-line method under specific conditions (Cooper and Jacob, 1946).

Aquifer test results are summarized in Figure 4 where they are grouped according to the hydrostratigraphic unit in which the test wells were completed. Observed log-transformed hydraulic conductivity values are plotted on the normal probability graph presented in Figure 4A, which shows that the populations representing hydraulic conductivity data from all tests K(all) and data from three individual groups of tests, (K Mehrten; K Laguna south; and K Laguna plant) all plot in a nearly linear fashion. The close-to-linear fit indicates that the observed hydraulic conductivity distribution is approximately log-normal. It should be noted that the three sub-datasets plotted in Figure 4A, representing three distinguishable hydrogeological units, appear to form

overlapping subdistributions which, when superimposed, form a combined, nearly log-normal distribution (black dots). Because the three subdistributions partially overlap, there does not appear to be a clear distinction between the hydraulic conductivity range of one hydrostratigraphic unit versus that of another.

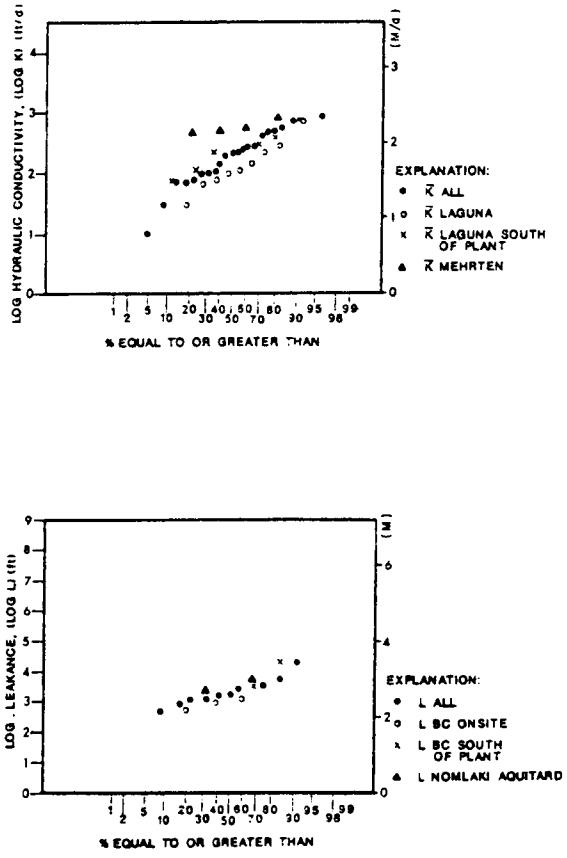

Figure 4. A. Log-probability distribution of hydraulic conductivity of the Laguna Formation gravels at the plant, Laguna gravels south of the plant and Mehrten gravels.

B. Log-probability distribution of leakance of the Laguna Formation clays at the plant, Laguna clays south of the plant and the Nomlaki aquitard.

Based on the pumping test data, transmissivity (T) estimates for Laguna channel gravels on the plant site range from 9.3 to 1670 m^2/d (100 to 18,000 ft^2/d), with a geometric mean value of 288 m^2/d (3,100 ft^2/d). The geometric mean hydraulic conductivity value (K_g measured in the Laguna Formation onsite is 4.6 m/d (150 ft/d), ranging between 3 and 205 m/d (10 and 670 ft/d). Storativity (S) for Laguna gravels on the plant site arithmetic mean is 0.0025 as a whole, but estimates cover a broad range from 0.00002. to 0.011.

The geometric mean transmissivity based on three aquifer pumping tests performed in Laguna Formation channel gravels south of the plant site is 2,490 m^2/d (26,800 ft^2/d). The corresponding geometric mean hydraulic conductivity for Laguna gravels in this area is 160 m/d (530 ft/d) ranging from 64 m/d to 260 m/d (210 ft/d to 850 ft/d). No estimates of storativity could be made from observation wells completed in Laguna gravels south of the plant site.

The results of aquifer pumping tests performed in wells that are completed in permeable units within the Mehrten Formation yield a geometric mean transmissivity of 930 m^2/d (10,000 ft^2/d) and a geometric mean hydraulic conductivity of 67 m/d (220 ft/d). Storativities measured in the Mehrten Formation have an arithmetic mean 0.00017. The average storativity in the Mehrten is lower than that observed in the nearby Laguna Formation, confirming the influence of the Nomlaki confining unit on the Mehrten gravels.

As mentioned previously, comparison of hydraulic conductivity estimates obtained for the Laguna and Mehrten Formations suggests that, in

general, the three aquifer pumping test groups yield a similar range of values (Figure 4A). The similarity in hydraulic conductivity between formations is important because it indicates that hydrostratigraphic units which are juxtaposed against each other along the sides of paleo-channels are in hydraulic communication. This implies that a given permeable zone can act as a continuous hydraulic unit and conduct groundwater flow even though there may be some local differences in the sedimentary composition of the zone.

The aquifer pumping test data also provide useful information about the hydraulic properties of aquitards that confine the principal aquifer zones. In this case, leakance (L) and hydraulic conductivity (K') values were calculated for selected aquitards using the Walton method (Walton, 1962). Test results from the Laguna BC aquitard located on the plant site, the uppermost Laguna aquitard located south of the plant site, and the Nomlaki aquitard are shown in Figure 4B. Leakance estimates plotted in the log probability graph approximate a straight line, suggesting that the data are log-normally distributed. In general, K' values estimated for the three acquitards are relatively similar: 3.5 x 10^{-5} cm/s (0.1 ft/d) for the Laguna BC aquitard on the plant site; 4.6 x 10^{-5} cm/s (0.13 ft/d) for the uppermost Laguna aquitard south of the plant site; and 1.4 x 10^{-5} cm/s (0.04 ft/d) for the Nomlaki Tuff. The overall geometric mean K' is 2.4 x 10^{-5} cm/s (0.07 ft/d) which is approximately three orders-of-magnitude lower than the hydraulic conductivity (K) of the permeable gravel units.

Hydraulic Gradients and Groundwater Flow

Groundwater in the study area flows generally southward through the permeable gravels of the B and C aquifer zones. Hydraulic gradients throughout the area are uniform except in the immediate vicinity of the wood-treatment plant (Figure 5). Within aquifer zone B, the hydraulic gradient ranges from 0.0013 to 0.0028 and groundwater velocity ranges from 0.4 m/d to 0.85 m/d (1.3 ft/d to 2.8 ft/d) southward. Gradient and velocity estimates are based on a geometric mean hydraulic conductivity of 91 m/d (300 ft/d) estimated south of the plant, and an estimated effective porosity of 0.3. These parameters appear to vary little based on a measurement period of 2.5 a. From the above data, the estimated rate of groundwater movement in the southern portion of the study area ranges from 145 m/a to 305 m/a (470 ft/a to 1000 ft/a) southward.

Vertical hydraulic gradients have been evaluated at eleven locations in the vicinity of the plant, in areas where well clusters provide water level measurements in more than one aquifer zone. In general, hydraulic gradients within the B aquifer are downward west of the plant site, possibly in response to recharge from irrigation ditches and ponds. Vertical gradients in the aquifer B zone on site are generally upward, with occasional fluctuations in magnitude and direction probably caused by the strong influence of local pumping wells. Although observed vertical gradients may help to explain the distribution of PCP in groundwater in some areas, in general, transport across aquitards does not appear to be an important factor in PCP movement into offsite areas.

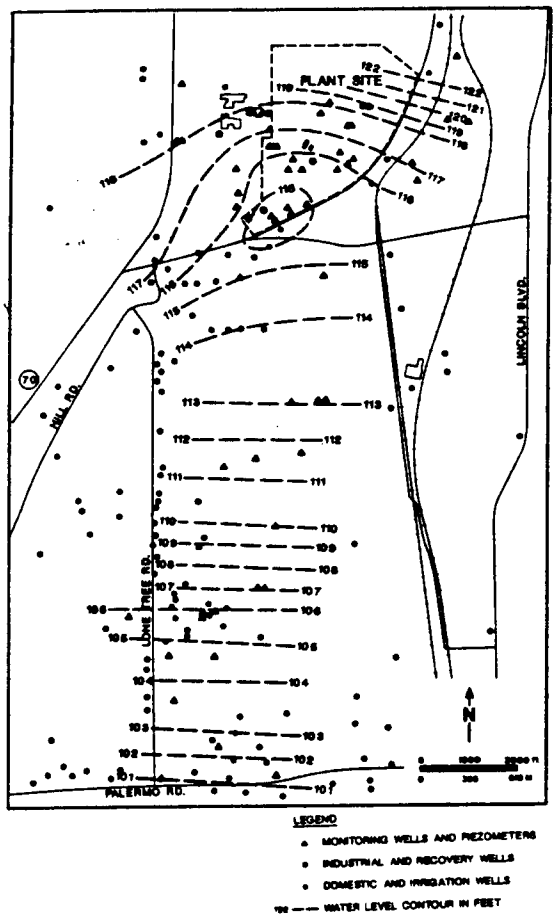

Figure 5. Piezometric head surface contours for the aquifer B zone.

PCP Distribution in Groundwater

During the RI/FS program conducted at the wood-treatment site, groundwater quality conditions were monitored in 39 onsite and 105 offsite wells. As a result, the concentrations of a broad spectrum of chemical constituents of groundwater, including PCP and PAH compounds, were determined providing a thorough description of the overall water chemistry of aquifer zones A, B, C, and D.

Analysis of water quality data collected during the RI/FS program indicates that aquifer zone B is the major pathway for movement of the PCP plume in groundwater. Zone C gravels appear to contain dissolved PCP to a lesser extent, primarily near the plant site. The spatial distribution of PCP detected in onsite and offsite monitoring wells screened in aquifer zone B is shown in Figure 6. The outermost PCP concentration isopleth shown in the figure represents a concentration of 30 µg/l. The direction of PCP movement is generally to the south in a well-defined plume that appears to exhibit little transverse dispersion. Based on the distribution of PCP in the B and C zones, it is clear that migration of PCP occurs along separate pathways; which may communicate in areas where the returning aquitard is absent. This is consistent with the advection-dominated transport conditions observed in the study area.

Groundwater Flow and Solute Transport Modeling

The site investigation provided sufficient information for the formulation of a detailed conceptual model of the heterogenous aquifer system. This conceptual model served as the basis for development of a three-dimensional numerical model of the aquifer system in which a large measure of the aquifer heterogeneity could be retained.

The key elements of the conceptual model included the spatial location of permeable aquifer zones, spatial distribution of aquitards, hydraulic properties of the geological materials, groundwater elevation data, hydraulic inputs and outputs to the system (such as well use, irrigation, rainfall, and stream losses), aquifer boundary

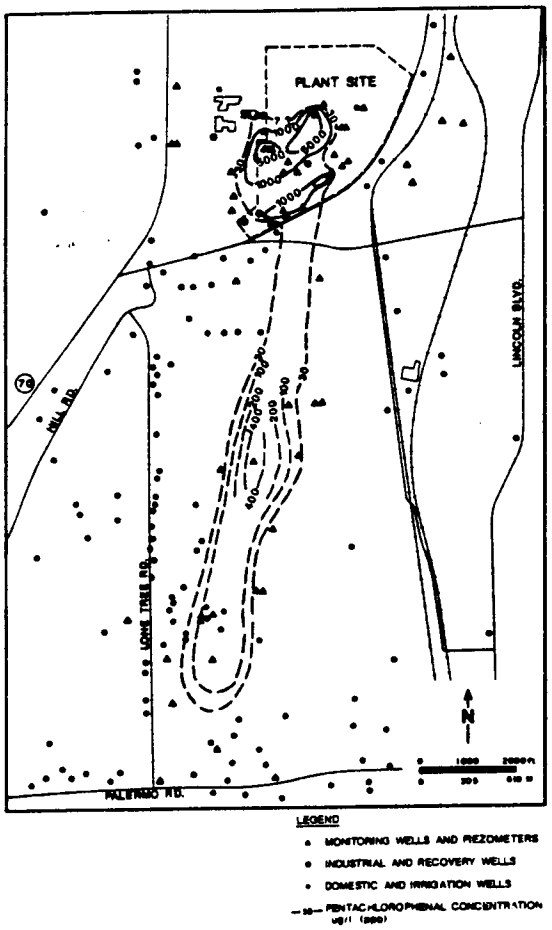

Figure 6. PCP plume distribution in the aquifer B zone (fall, 1987)

.

conditions, and contaminant source information. The above elements were subsequently integrated into the three-dimensional numerical groundwater flow and solute transport model that was developed to describe the aquifer system (Dames & Moore, 1988a). The numerical code selected for model simulations was TARGET-3DS, a three-dimensional, saturated, density-coupled, transient groundwater flow and solute transport model developed by Dames & Moore (Dames & Moore, 1985). This model employs an integrated finite-difference solution technique which utilizes a hybrid differencing formulation of the advection-dispersion equation. All model runs were performed on a Compaq 80386 microcomputer.

The primary purpose of the modeling analysis was to develop a numerical model that realistically represented past and present groundwater flow and contaminant transport for the heterogeneous aquifer system. The transport model was used to simulate the spatial distribution of PCP contamination and to predict the rate and extent of movement of PCP and other compounds in groundwater under "no-action" conditions, for use in risk evaluation and for preliminary evaluation of possible groundwater recovery and treatment alternatives (Dames & Moore, 1989). Specific objectives included:

1. Calibration and evaluation of the sensitivity of the simulated hydrogeological system to variations in key hydraulic and transport parameters;

2. Prediction of the current and future extent of groundwater contamination for use in evaluation of remedial alternatives; and

3. Evaluation of the effectiveness of groundwater remediation alternatives.

A brief summary of the modeling analysis and simulated results for hydrodynamics and PCP transport are presented next. The model grid was oriented over the study area (Figure 7A) and aligned with the predominant groundwater flow direction. The western boundary of the grid was set along the Feather River while the other boundaries were positioned to include data from groundwater monitoring wells

located farthest from the site. The dimensions of the grid were ~4.5 km (~2.8 mi) in the i-direction (east-west or x-axis) and 6.1 km (3.8 mi) in the j-direction (north-south or y-axis). The bottom of the model grid was defined at a depth where a substantially thick clay unit of the Ione-Formation provided a convenient natural boundary (no flow boundary) for the bottom of the grid, thus creating a vertical grid dimension of ~80m (260 ft). A minimum grid spacing equal to 61 m (200 ft) in the i and j directions 6.1 m (20 ft) in the vertical (k-direction) grid was selected. This resulted in a grid with dimensions of 33 by 56 by 15 in the i, j, and k dimensions, respectively. Based on modeling requirements and on numerical constraints, a time step of 1a was selected for all model runs.

During the course of the site investigation, groundwater monitoring data indicated that groundwater levels vary uniformly across the modeled area and horizontal hydraulic gradients do not appear to vary seasonally across the domain. The Feather River, located in the northwest portion of the grid, was modeled as a constant fixed-head boundary because variations in river stage do not influence water levels in the area of interest. Other groundwater flow boundaries were also treated as fixed hydraulic head boundaries based on observed field data.

Groundwater withdrawals due to well pumping were accounted for through use of annual average pumping rates obtained from public records and documents. Recharge from rainfall, irrigation, rivers, streams and impoundments were allocated as annual averages and distributed spatially based on land use and natural processes.

The naturally occurring aquifer units were classified into six hydraulic material types that were used to define the hydrostratigraphy of the model domain (Dames & Moore, 1988a). They are: 1. highly permeable gravels (Laguna and Mehrten Formation gravels off-site, represented by hydrostratigraphic units B and C); 2. medium permeability gravels (Laguna gravels located in zones B and C); 3. dredge tailings; 4. Ione Sandstone (zone C); 5. low permeability Nomlaki Tuff (the AB aquitard); and 6. low permeability clays of Laguna and Mehrten channel deposits, off-site. Based on the results of aquifer and physical tests, the hydraulic properties of the low permeability clays were found to be similar, justifying their representation as a single material type in the model. The hydraulic conductivities of all six material types were assumed to be isotropic in the horizontal plane.

For each of the six materials described above, the numerical model required input data to define horizontal and vertical hydraulic conductivity, storativity, porosity, and longitudinal and transverse dispersivities. The values used in the model were initially derived from field and laboratory measurements (Dames & Moore, 1988b) and from the literature. Estimates of a few of these properties were later modified during calibration to optimize the model fit to observed hydraulic gradients and solute transport rates. Final calibration values for these parameters are summarized in Table 2.

Retardation parameters and degradation rates for the solutes of interest in groundwater were estimated from studies reported in the literature. Criteria used to evaluate the applicability of literature data included

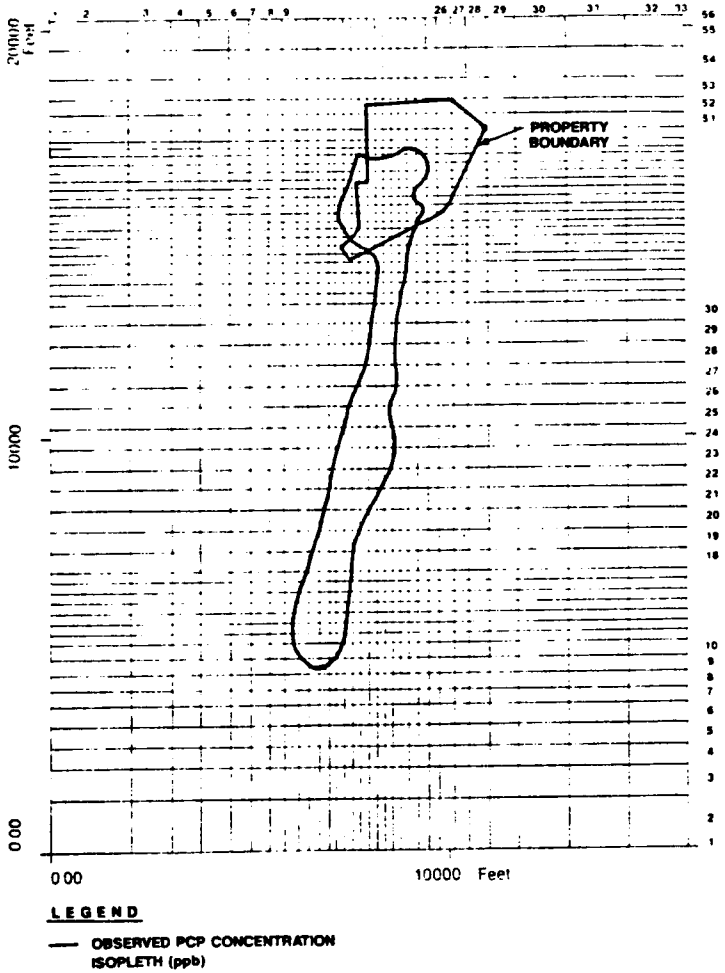

Figure 7. A. Simulated PCP plume in aquifer zone B at calibration.

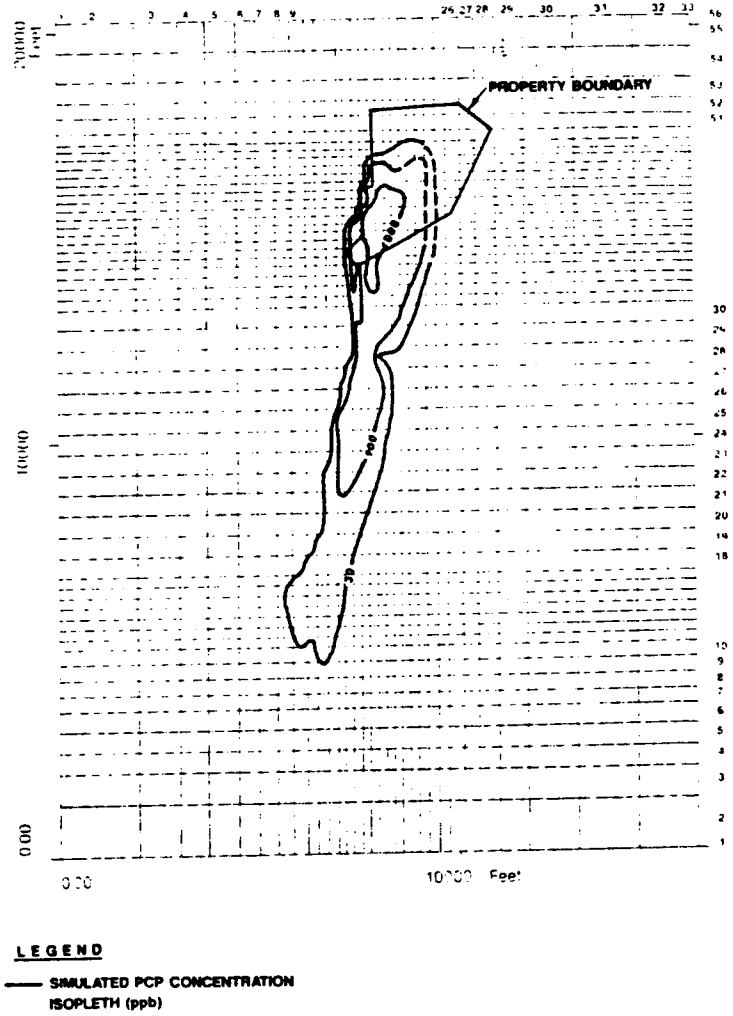

Figure 7 B. Observed PCP plume in aquifer zone B (1987).

Table 2

Geologic Material Types and Hydraulic Properties At Calibration

Model Material Type	Description	Hydraulic Conductivity (m/d)		Storage Coefficients		Effective Porosity	Dispersivity(m)	
		Horizontal	Vertical	Storativity	Yield		Longitudinal	Transverse
1	Highly permeable gravels	106	10.6	0.0022	0.25	0.21	36	3.6
2	Medium permeable gravels	55	5.5	0.0024	0.25	0.21	36	3.6
3	Dredge tailings	84	8.4	0.0002	0.25	0.25	36	3.6
4	Ione sandstone	55	5.5	0.0022	0.25	0.25	36	3.6
5	Low permeability Nomlaki tuff	0.15	0.0015	0.0002	0.01	0.35	36	3.6
6	Low permeability clay	0.019	0.019	0.0002	0.01	0.30	36	3.6

site stratigraphy, nature of geological materials, chemical composition of groundwater, total organic -C content of the aquifer and other aquifer properties. The transport parameters selected for PCP as a result of model calibration were: retardation factor R = 1.11 and degradation half-life $t_{1/2}$ = 12 a. The degradation half-life based on observed field conditions was more than an order of magnitude greater than the values reported from laboratory studies. The laboratory defined values from the literature were not used because they were thought to be unrepresentative of actual field conditions.

Significant areas of groundwater contamination identified on the plant site were represented in the model by grid cells in which solute-laden infiltration water was introduced into the uppermost saturated cell of the aquifer. The areas of groundwater contamination represented by the model were approximately proportional to the total estimated area of the sources of contamination observed in the field. The rate and duration of releases of contaminants from each source area during the predictive runs were estimated from observed concentrations, infiltration rates, and chemical solubility data (Dames & Moore, 1988b).

The numerical flow and solute transport model was initially calibrated for hydrodynamics to match water level and flow conditions and then for solute transport based on the spatial distribution of the PCP plume. the best match between simulated results and observed data was obtained when PCP was introduced into groundwater during a 25a period beginning in 1963. Simulations of the PCP 25-a calibration period (Figure 7A) compared favorably with the observed present-day PCP plume (presented in Figure 7B at the same scale). In addition, the vertical distribution of PCP in the heterogeneous aquifer was quite representative of the distribution observed in the field.

Conclusions

Based on the hydrostratigraphic evidence presented in this paper, it is plausible that groundwater originating in Laguna gravels present on the wood-treatment site can migrate downgradient (southward) along parallel but seemingly distinct pathways through the B and C aquifer zones to a location at least midway between wells RI-5 and RI-11/12, where the intervening BC clay may not be present. In this area, some missing between the two zones may occur, allowing the PCP plume to cross over from the B zone into the deeper C zone gravels. Hydraulic gradient, groundwater flow, and water chemistry data suggest that within permeable aquifer zones, groundwater moves relatively freely across formational and incised paleo-channel boundaries. Hydraulic conductivities of Laguna and Mehrten gravels support field observations of free groundwater movement across the Laguna/Mehrten geological contacts. This finding is significant because it helps to explain why the groundwater regime in the study area is not dominated by flow along the gravelly paleo-channels, but instead contains a much more uniform flow field than might otherwise be expected.

The groundwater modeling analysis resulted in the development of a numerical groundwater flow and solute transport model that realistically

represents the movement of groundwater and PCP in the heterogeneous hydrogeological system associated with the wood-treatment site. The calibrated model yields predictions which compare favorably with field observations of hydraulic gradients and PCP concentrations. Predictions of solute movement are consistent with the observed hydrostratigraphy and behavior of the hydrogeological system; therefore, the underlying conceptual model upon which these predictions were made is believed to be valid.

Modeling results suggest that predictions of PCP solute transport are sensitive to the degradation rate of the compound in groundwater. Review of laboratory studies reveals that relatively short degradation half-lives of a few months have been reported for PCP under controlled conditions. Modeling results, however, suggest that a realistic half-life is of the order of 12 a in the groundwater environment encountered on this site. The apparent differences between literature and modeled degradation rates may be due to the media and other conditions under which the rates were estimated. The calibrated model of PCP movement is believed to be representative of actual degradation of PCP under field conditions at this site.

Acknowledgements

The authors wish to thank Dames & Moore, Sacramento, California, and both Koppers Industries, Inc., and Beazer East, Inc., of Pittsburgh, Pennsylvania for permission to publish this manuscript. This work was conducted while both authors were at Dames & Moore's Sacramento office.

Fred G. Baker is Leader of the Hydrogeology Program for Ebasco Environmental (143 Union Boulevard, Lakewood, Colorado 80228-1824, USA). He obtained a BS in Geology and an MS in Soil Science at the University of Wisconsin-Madison, and an MS in Cvil Engineering and PhD in Geology at the University of Colorado-Boulder. His areas of interest include groundwater flow and solute transport under saturated and unsaturated conditions, mass transport modelling, in situ and laboratory testing of aquifer and soil transport properties. He has been actively involved in research and consulting for more than 17 years.

Hannah F. Pavlik is Leader of the Geochemistry Group for Ebasco Environmental (143 Union Boulevard, Lakewood, Colorado 80228-1824, USA). She obtained her PhD in Geochemistry at the University of Colorado.-Boulder Her areas of expertise include aqueous geochemistry, water-rock interactions and solute mobility and transport. She has more than 10 years of experience in consulting and university research.

References

Blair, T.C. and F.G. Baker. 1990. Cenozoic fluvial facies architecture and aquifer heterogeneity, Oroville, California Superfund Site and vicinity. In Three Dimensional Facies Architecture of Clastic Sediments (ed. A.D. Miall and N. Tyler). Soc. Econ. Paleo. Mineral (in press).

California Department of Water Resources. 1973. Groundwater Quality Investigation, Roundhouse Subarea, Oroville.

Cooper, H.H. and C.E. Jacob. 1946. A generalized graphical method for evaluating formation constants and summarizing well field history. Am. Geophys. Union Trans., V 27 pp. 526-534.

Dames & Moore. 1985. TARGET: Dames & Moore Mathematical Model of Ground-Water Flow and Solute Transport.

Dames & Moore. 1988a. Groundwater Summary Report, RI/FS, Feather River Plant, Oroville, California. Project Report for Koppers Company, Inc., Pittsburgh, Pennsylvania.

Dames & Moore. 1988b. Remedial Investigation Report, RI/FS, Feather River Plant, Oroville, California. Project Report for Koppers Company, Inc., Pittsburgh, Pennsylvania.

Dames & Moore. 1989. Feasibility Study Report, RI/FS, Feather River Plant, Oroville, California. Project for Koppers Industries, Inc., Pittsburgh, Pennsylvania.

Hantush, M.S. 1956. Analysis of data from pumping tests in leaky aquifers. Am. Geophys. Union Trans., V. 37, pp. 702-714.

Schmidt, K.D. 1984. Trace Organic Chemical Constituents in Groundwater South of the Koppers Oroville Plant, Results of the Phase II Investigation. Prepared for Koppers Company, Inc., Pittsburgh, Pennsylvania.

Walton, W.C. 1962. Selected analytical methods for well and aquifer evaluation. Illinois State Water Surv. Bull., no. 49.

A Percolation Model for Hydraulic Conductivity in Porous Media

by B. Berkowitz and I. Balberg

Abstract

While percolation theory has been studied extensively in the field of physics, and the literature devoted to the subject is vast, little use of its results has been made to date in the field of hydrology. In the present study, Monte Carlo computer simulations were carried out on a percolating model representative of a porous medium. The model considers intersecting conducting permeable spheres (or circles, in two dimensions) which are randomly distributed in space. Two cases are considered: 1. all intersections have the same hydraulic conductivity, and 2. the individual hydraulic conductivities are determined by the degree of overlap of the intersecting spheres. It was found that the critical behavior of the hydraulic conductivity of the system, K, follows a power-law dependence defined by $K \alpha (N/N_c-1)^x$, where N is the total number of spheres in the domain, N_c is the critical number of spheres for the onset of percolation, and x is an exponent which depends on the dimensionality and the case. Both cases yield a value of $x \approx 1.2 \pm 0.1$ in the two-dimensional system, while $x \approx 1.9 \pm 0.1$ was found in the three-dimensional system for only the first case. In the second case, $x \approx 2.3 \pm 0.1$. These results are in agreement with the most recent predictions of the theory of percolation in the continuum. Thus percolation theory is seen to provide useful predictions as to the structural parameters which determine hydrological transport processes.

Introduction

While the theory of percolation was first introduced some time ago to describe problems in porous media (Broadbent and Hammersley, 1957), and the literature devoted to the subject, primarily in the field of physics, is vast (e.g. Stauffer, 1985; Balberg, 1987), little use of its results has been made to date in the field of hydrology (Thompson et al., 1987). The principal advantage of percolation theory is that it provides universal laws which determine the geometrical and physical properties of the system. These laws are usually manifested by a power-law behavior of the type.

$$A \alpha (V-V_c)^x \qquad (1)$$

where A is a geometrical or physically observable quantity, V is the fractional volume of the conducting phase, V_c is its critical value for the onset of percolation (i.e. system connectivity), and x is a "critical exponent" specific to this quantity. The value of x, in the so-called "universal" case, depends only on the dimensionality of the system. When the observed x differs from that value, the behavior is described as "non-universal". With the availability of powerful, high-speed computers, complicated media can be examined and universal relations between such critical parameters have been identified (e.g. Stauffer, 1985; Aharony, 1986).

Several advances in the application of percolation theory for the understanding of flow in porous media (Halperin et al., 1985) have been made in the last few years, with evidence that some percolation models can

account for transport phenomena observed in porous rocks (e.g. Balberg 1986; Gueguen and Dienes, 1989). In view of these developments, it seems plausible that various other ideas from percolation theory may be applied to more specific problems in the study of porous media.

Historically, most relations between hydraulic conductivity and porosity have been developed theoretically by representing the pore space of a porous rock as a bundle of capillary tubes. The most frequently cited relations developed in this manner are the Kozeny (1927) and Kozeny-Carman equations (Carman, 1956), although numerous modifications have since been made to these equations. Other purely empirical expressions relate hydraulic conductivity to a mean (or "effective") grain diameter (e.g. Krumbein and Monk, 1943, in Bear, 1972), or to packing and sand-shape factors (e.g. Fair and Hatch, 1933). In fact, analyses of pore structures indicate that the pore space is characterized by a wide distribution of channel sizes, and that random networks more closely represent actual pore spaces (e.g. Doyen, 1988).

One may describe fluid flow through a disordered (random) medium by a so-called "percolation process" (e.g. Stauffer, 1985). In the present study, Monte Carlo computer simulations were carried out on a percolating model representative of some porous media. The model considers intersecting conducting permeable "pores" - spheres (in three dimensions), or circles (in two dimensions) - which are randomly distributed in space. The local hydraulic conductivity at the intersection between any two permeable spheres (or circles) is either prescribed, or determined by the local geometry. Therefore, two cases are considered: 1. all intersections have uniform conductivity, and 2. conductivities are determined by the degree of overlap of the intersecting spheres. The model is used to analyze the relation between conductivity and the number of pores (or their volume) in the system. These results are then compared with the predictions of percolation theory in the continuum.

Description of the Model

The conductivity behavior of a highly idealized representation of a porous is examined by computer simulation. The simulations are unique in the consideration of the case where the local geometry of the conducting pores is also taken into account.

The porous medium model employed in this study was applied previously to the problem of electrical conduction and electrical resistance noise (Balberg et al., 1988), and is adopted here for the problem of hydraulic conductivity. The model is composed of conducting permeable spheres (or circles, in two dimensions) which are randomly distributed in space. In this model, a local non-zero conductance is associated only with intersecting spheres. The hydraulic conductivity at each intersection between two permeable spheres is either prescribed, or is determined by the local geometry. The permeable spheres are assumed to have constant radius, a, and are distributed randomly in a unit cube. If two spheres overlap, they are considered connected, and the onset of percolation is at a concentration of spheres, N_c, which is associated with the formation of a continuous path of connected spheres between two opposite faces of the cube. The overall conductivity of the system is them computed as function of $(N/N_c - 1)$, where N is the total number of spheres in the cube. The relation

between N_c and V_c of eqn (1) is well-known (e.g. for spheres, V_c = 0.29, where the sample cube is of a volume of unity; see Balberg, 1987), so that (N/N_c-1) is proportional to (V/V_c-1).

In the two cases considered in this work, the local conductivities were assigned as follows. In the first case, all intersections were simply assumed to have a uniform hydraulic conductivity. In a continuum model, such as the one used here, the local conductivity can be alternatively correlated with the actual local geometry, in contrast to cases in which no such relation exists. Thus the local conductivity at the intersecting region of two spheres (the so-called "neck") was correlated with the neck geometry, as has been done previously for the electrical resistance (Feng et al., 1987; Balberg et al., 1988). In the second case, it was assumed that the local hydraulic conductivity depended only on one variable geometrical parameter, ε, which is a measure of the degree of overlap of the spheres. As is well-known, the dominant feature affecting the hydraulic conductivity is due to the narrowest portion of the neck. As such, it is well-approximated (Feng et al., 1987) by a cylinder with length, L, of the order $2(a\varepsilon)^{1/2}$ and radius, r, of the order $(a\varepsilon)^{1/2}$ (see Figure 1).

The Hagen-Poiseuille law for the rate of flow through a capillary tube is given in the three-dimensional case by (e.g. Batchelor, 1967)

$$Q = \frac{\pi r^4}{8\mu}\frac{\Delta p}{L} \equiv k\cdot\Delta p \qquad (2)$$

where Q is rate of flow, r is the radius of the capillary tube, μ is the dynamic fluid viscosity, L if the length of the tube, and Δp is the pressure difference across the tube. In this study, for convenience in comparison to electrical resistance studies, the local hydraulic conductivity (denoted here by k) was defined by (in three dimensions)

$$k = \frac{\pi r^4}{8\mu L} \alpha \frac{A^2}{L} \qquad (3)$$

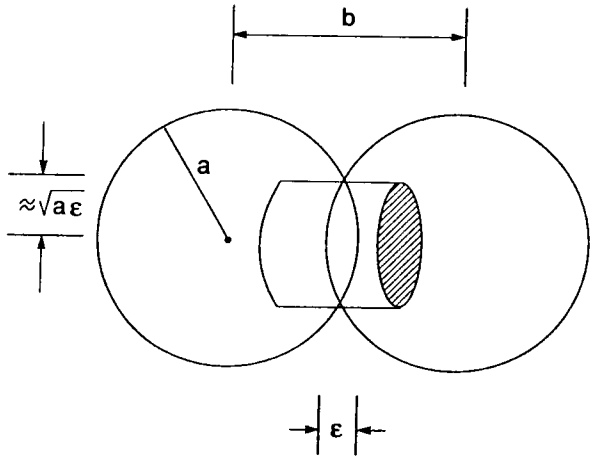

Figure1.The geometry of intersecting permeable spheres. The cylinder represents the region which yields the dominant contribution to the hydraulic conductivity of the corresponding "neck".

where A denotes the cross-section of the capillary tube. Generalization to dimension d implies that k is proportional to $r^{2(d-1)}/L$. Thus, in the presently discussed "neck-cylinder" geometry, the local hydraulic conductivity has the dependence

$$k \alpha \varepsilon^{1/2} \qquad (4)$$

in two dimensions and

$$k \alpha \varepsilon^{3/2} \qquad (5)$$

in three dimensions. In the present simulations, the constant of proportionality is assumed equal to one.

In the build-up of the sample, spheres of radius, a, are randomly distributed in the cube, one at a time. As each sphere is implanted, a check is made for percolation. This procedure is repeated until the onset of percolation (i.e. a continuum path of overlapping spheres from one edge of the cube to the opposite edge), and the critical number of spheres, N_c, is recorded for that particular system realization. Calculations for the overall hydraulic conductivity, K, are then made. Additional spheres are placed in the system, until the total number of spheres reaches some specified factor of N_c. At each step, the overall conductivity of the system is determined. This process of adding spheres and calculating the conductivity is repeated here, for $N = 1.1N_c$, $1.2N_c$ $1.3N_c$,..., $2.0N_c$. A more detailed description of the procedure can be found in Balberg and Binenbaum (1985).

The overall hydraulic conductivity of the system is calculated as follows. For each system of spheres, two values of the local hydraulic conductivity are given for each intersection, by 1. assigning a constant value, and 2. using eqns (4) and (5). In this second case, the distance between the centers, b, of each pair of intersecting spheres is determined, and the value of $\varepsilon = 2a-b$ recorded. A unit discharge across the cubic domain is assumed in one direction; other faces are assumed impermeable. By writing a volumetric balance equation for every node (using eqn (2)), and by applying Kirchhoff's law (Balberg and Binenbaum, 1986) which requires that the algebraic sum of the fluxes at a node equal zero, a set of linear algebraic equations with a symmetrical coefficient matrix is obtained. These equations can be solved under the imposed boundary conditions, to yield the pressure at each intersection. From the calculated pressure gradient across the inlet and outlet faces of the domain, and the prescribed unit discharge across the inlet and outlet faces, the overall hydraulic conductivity of the system is determined.

In this work, the above sets of equations are solved by use of a pre-conditioned conjugate-gradient algorithm, which enables solution of very large systems of equations. The method is particularly useful when the coefficient matrix of the system of equations is sparse, and solves the system by iterative methods. The use of a preconditioning matrix improves the rate of convergence. Further details of the algorithm can be found, for example, in Meyer et al. (1989) or Balberg et al. (1988).

It is noted that in the determination of the overall hydraulic conductivity, an idealization of real systems was employed, because multiple overlaps of spheres were considered as separate overlaps, and, in the second case, the local hydraulic conductivities were estimated according to the geometry of the cylindrical necks. Near the percolation threshold, however, these simplifications are expected to play a minor role. The neck approximation improves the smaller the overlap (i.e. the smaller the conductivity), and it is known that, near N_c, the smaller conductivities determine the critical behavior (e.g. Feng et al., 1987). The multiple overlaps also represent parallel connections which form "miniblobs"; however, the effect of such blobs on overall hydraulic conductivity decreases with proximity to the threshold (due to the dominant effect of the "singly-connected bonds"; Feng et al., 1987) and for lower dimension (e.g. Stauffer, 1985).

Results and Discussion

To make the best analysis possible, results were obtained which represented averages of five large samples (realizations), with percolation thresholds of the order of N_c~10,000 spheres (or circles). Apart from relatively small statistical variations, similar values of N_c and K (for given N) were obtained. The calculated values of K (for the five samples) were then averaged for each given N. With the completion of these calculations, values of the overall hydraulic conductivity were plotted as a function of (N/N_c-1), and the exponents of the best-fit lines were obtained by using regression (see also Balberg and Binenbaum, 1985). These exponents were determined, in each of the two cases of local hydraulic conductivity, for both the two- and three-dimensional systems. Following the expected power-law dependence (see eqn (1), $K \alpha (N/N_c-1)^x$), data are presented on log-log scales.

Figure 2 shows results obtained for the two-dimensional system. As can be seen from the results, a linear dependence (on the log-log plot) was obtained, and the hydraulic conductivity exponent was found to be $x \approx 1.2 \pm 0.1$, in both cases i.e. the differing local hydraulic conductivities had no influence on the dependence of the overall conductivity. These results are in excellent agreement with the most recent predictions of percolation theory for such a system of permeable circles (Feng et al., 1987); the value x = 1.3 is the known universal exponent of electrical and hydraulic conductivities for two-dimensional systems (Aharony, 1986).

Figure 3 presents results obtained for the three-dimensional system. In the first case of local hydraulic

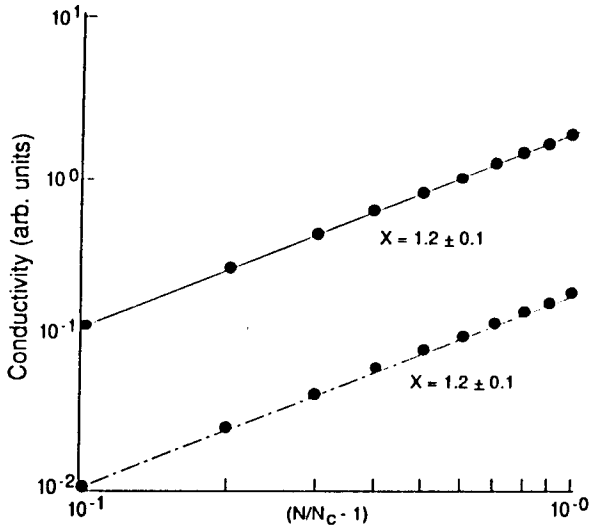

Figure2.The dependence of the sample hydraulic conductivity on the proximity to the percolation threshold in the two-dimensional random pore system (——— uniform local conductivities; —·—·— local conductivities determined by overlap). Each data point represents an average of five different samples.

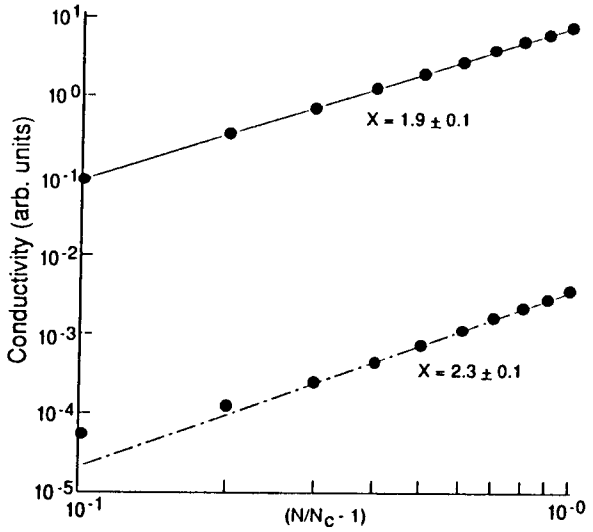

Figure3.The dependence of the sample hydraulic conductivity on the proximity to the percolation threshold in the three-dimensional random pore system (——— uniform local conductivities; —·—·— local conductivities determined by overlap). Each data point represents an average of five different samples.

conductivity, the exponent was found to be $x \approx 1.9 \pm 0.1$, which is in agreement with the universal exponent of $x = 2.0$ in three dimensions (Aharony, 1986). In the second case, an exponent of $x \approx 2.3 \pm 0.1$ was obtained. The points that clearly deviate from the best-fit line are typical in such simulations, and can be attributed to finite-size effects. Again, these results follow the predictions of continuum percolation theory, which provides conditions under which non-universal behavior may be expected to arise (Balberg, 1987; Feng et al., 1987). The simplest presentation of this theory is as follows. Define g to be a transport property of the medium (such as hydraulic conductivity), f(g) to be the distribution function of g in the system, and $h(\varepsilon)$ to be a distribution function of the single relevant geometrical parameter, ε (e.g. in the present case, the degree of overlap of intersecting spheres). The relation between f(g) and $h(\varepsilon)$ is given by (Sen et al., 1985)

$$f(g) = h(\varepsilon)(d\varepsilon)/dg) \qquad (6)$$

Assuming that $h(\varepsilon)$ is a constant as $\varepsilon \rightarrow 0$, and substituting (4) and (5) into (6) (where $k = g \alpha \varepsilon^{u}$), yields

$$f(g) \alpha g^{-1+1/u} \equiv g^{-a} \qquad (7)$$

Considering (4) and (5), it is apparent that for the problem under discussion, u=1/2 and u=3/2 in two and three dimensions, respectively. Thus, it follows that a = -1 (i.e. a non-diverging distribution at small g) in two dimensions, while a = 1/3 (i.e. a diverging distribution at small g) in three dimensions. Hence, the above two-dimensional case as well as the uniform conductivity case essentially represent the condition whereby a finite average g is representative of the conductors in the system. This is then the same case as that of a uniform conductivity (Balberg, 1987).

It is well-known (Kogut and Straley, 1979) that non-universal behavior arises if $0 < a < 1$ (i.e. if there is a divergence of f(g) for $g \rightarrow 0$), with a critical behavior characterized by the exponent $x + a/(1-a)$ rather than x. Thus, it was expected that in the present study, the two-dimensional system would yield a universal behavior, while the three-dimensional system would not. Rather, from (7) and the u=3/2 value, the expected critical exponent is $x+1/2 = 2.5$ in the latter case. In physical terms, the non-universality arises in cases where f(g) diverges as $g \rightarrow 0$ due to an accelerated drop in the sample conductivity beyond the effect of fewer and fewer conductors (i.e. as the percolation threshold is approached from above). This is not only since the number of conductors decreases (which leads to the universal behavior), but also since the average participating conductor has a lower conductance as a result of the diverging f(g) (Kogut and Straley, 1979).

In the second case of the three-dimensional system, the actual results for x are somewhat lower (2.3 ± 0.1 vs 2.5) than those expected for an infinite sample using exact methods of percolation theory. This is not surprising, because finite-size effects weaken the divergence near the percolation threshold, in general (Kim et al., 1987), and for electrical properties in particular (Wagner and Balberg, 1987; Balberg and Binenbaum, 1985). Indeed, the existence of finite size effects was confirmed by application of the simulations described here for smaller samples (average of five samples of $N_c \sim 5000$), which yielded $x \approx 2.1 \pm 0.1$ in three dimensions (case 2). Comparison of this value with that of Figure 3 also indicates that the value of the critical exponent converges to the higher,

expected value as the sample (i.e. N_c) is increased.

The connection between models of the type presented in this study and the porosity and hydraulic conductivity of real rocks has been discussed by several authors, including, for example, Wong et al. (1984), Balberg (1986), and Thompson et al. (1987). In fact, many real rocks exhibit non-zero hydraulic conductivities at extremely small porosities, which in these cases indicates a percolation threshold approaching zero. However, Balberg (1986) showed that while the scaling dependence of hydraulic conductivity on porosity is valid for different porosities, it is sensitive to the microscopic structure of the pores. For example, for spherical pores, the critical porosity (i.e. porosity for the onset of percolation) is 0.29, while for pores shaped as thin disks, the critical porosity approaches zero. Thus, there is no inherent contradiction in applying percolation theory to describe conductivity properties of porous media. Furthermore, the results obtained here are qualitatively consistent with relations such as the Kozeny-Carman equation, in their similar power-law dependence of the hydraulic conductivity on porosity.

It should also be noted that the hydraulic conductivity can vary by orders of magnitude among rocks of the same porosity (due to different microscope pore structures), which might suggest that the coefficient of equality may be of greater practical significance than the critical exponent. Unfortunately, this coefficient is difficult to calculate, because the microscopic structure and details of the particular porous medium under consideration must be taken into account. Percolation theory does not address this aspect of the problem. Furthermore, results from percolation theory are based on systems near the percolation threshold, and the proximity of real porous rocks to the threshold is also a matter of question. However, the practical importance of percolation theory results such as those demonstrated here is that, while not providing absolute answers, they enable prediction of the hydraulic conductivity behavior of a system given its porosity and knowledge of the basic pore structure, based on results for similar systems. Moreover, while not discussed in this paper, percolation theory also provides information on the average number of intersections with any given object (see , e.g. Balberg, 1987), which provides information on the general topological structure of a porous medium.

Finally, it should be mentioned that the connection between the continuum percolation and discrete network model (lattice percolation) approaches has been examined by several authors (e.g. Halperin et al., 1985; Balberg, 1987). It has been shown that, due to universality, many scaling relations of geometrical and transport properties are valid in both the discrete and continuum approaches.

Conclusions

It is found that the critical behavior of the hydraulic conductivity of the system, K, near the percolation threshold, follows a power-law dependence defined by $K \alpha (N/N_c - 1)^x$, where N is the total number of spheres (or circles) in the domain, N_c is their concentration at the percolation threshold, and x is an exponent which depends on the dimensionality and the case. These calculated exponents are in excellent agreement with those predicted by percolation theory in the continuum. In particular, both universal and non-universal behaviors were identified. Thus percolation theory is seen to provide useful predictions as to the structural parameters that determine hydrological transport processes.

Studies such as these, apart from their theoretical interest, may serve as a guide in the analysis and understanding of transport properties of many types of porous rocks. The method described here can be modified to permit examination of other types of systems, both in terms of different pore shapes (e.g. cylinders and disks), and in terms of other definitions of local hydraulic conductivity. Further analysis of conditions under which universal exponents do not appear will allow extension of percolation theory results and their application in understanding of structural parameters and hydraulic characteristics of porous media.

Brian Berkowitz is a research hydrologist with the Hydrological Service of Israel (Hydrological Service, Water Commission, Ministry of Agriculture, P.O.B. 6381, Jerusalem 91063, Israel). He completed his BSc and MSc in applied mathematics at The University of Alberta, Canada, and his DSc at Technion, Israel. He was awarded the Israel Hydrology Association Goldschmidt Prize in 1986. His major field of interest is transport phenomena in porous and fractured media.

Isaac Balberg is a professor of physics at the Racah Institute of Physics, Jerusalem (The Hebrew University of Jerusalem, Jerusalem 91904, Israel). He holds MSc and PhD degrees from the Hebrew University. During 1970-72 and 1979-80 he was a member of the technical staff at RCA Laboratories, Princeton. He has been a senior scientist in many research institutions and laboratories from 1974 to date. He is currently acting as secretary of the Israel Physical Society. His field of interest is transport in disordered media.

References

Aharony, A. 1986. Percolation, In Directions in Condensed Matter Physics. (eds. G. Grinstein and G. Mazenko). World Scientific, Singapore, pp. 1-50.

Balberg, I. 1986. Excluded-volume explanation of Archie's law. Phys. Rev. B, v. 33, pp. 3618-3620.

Balberg, I. 1987. Recent developments in continuum percolation. Phil. Mag., v. 56, pp. 991-1003.

Balberg, I. and N. Binenbaum. 1985. Cluster structure and conductivity of three-dimensional continuum systems. Phys. Rev. A, v. 31, pp. 1222-1225.

Balberg, I. and N. Binenbaum. 1986. Direct determination of the conductivity exponent in directed percolation. Phys. Rev. B, v. 33, pp. 2017-2019.

Balberg, I., N. Wagner, D.W. Hearn and J.A. Ventura. 1988. Critical behavior of the electrical resistance and its noise in inverted random-void systems. Phys. Rev. Lett., v. 60, pp. 1887-1890.

Batchelor, G.K. 1967. An introduction to Fluid Dynamics. Cambridge University Press.

Bear, J. 1972. Dynamics of Fluid in Porous Media. Elsevier.

Broadbent, S.R. and J.M. Hammersley. 1957. Percolation processes: 1. Crystals and mazes. Proc. Camb. Phil. Soc. v. 53, pp. 629-641.

Carman, P.C. 1956. Flow of Gases Through Porous Media. Butterworths.

Doyen, P.M. 1988. Permeability, conductivity, and pore geometry of sandstone. J. Geophys. Res., v. 93(B7), pp. 7729-7740.

Fair, G.M. and L.P. Hatch. 1933. Fundamental factors governing the streamline flow of water through sand. J. Am. Water Works Assoc., v. 25, pp. 1551-1565.

Feng, S., B.I. Halperin and P.N. Sen. 1987. Transport properties of continuum systems near the percolation threshold. Phys. Rev. B, v. 35, pp. 197-214.

Gueguen, Y. and J. Dienes. 1989. Transport properties of rocks from statistics and percolation. Math. Geol., v. 21, pp. 1-13.
Halperin, B.I., S. Feng and P.N. Sen. 1985. Differences between lattice and continuum percolation transport exponents. Phys. Rev. Lett., v. 54, pp. 2391-2394.
Kim, D.Y., H.J. Hermann and D.P. Landau. 1987. Percolation on a random lattice. Phys. Rev. B, v. 35, pp. 3661-3662.
Kogut, P.M. and J. Straley. 1979. Distribution-induced non-universality of the percolation conductivity exponents. J. Phys. C, v. 12, pp. 2151-2159.
Kozeny, J. 1927. Uber kapillare Leitung des Wassers im Boden. Sitzungsber. Akad. Wiss. Wien, v. 136, pp. 271-306.
Meyer, P.D., A.J. Valocchi, S.F. Ashby and P.E. Saylor. 1989. A numerical investigation of the conjugate-gradient method as applied to three-dimensional groundwater flow problems in randomly heterogeneous porous media. Water Resour. Res., v. 25, pp. 1440-1446.
Sen. P.N., J.N. Roberts and B.I. Halperin, 1985. Nonuniversal critical exponents for transport in percolating systems with a distribution of bond strengths. Phys. Rev. B, v. 32, pp. 3306-3308.
Stauffer, D. 1985. Introduction to Percolation Theory. Taylor and Francis, New York.
Thompson, A.H., A.J. Katz and C.E. Krohn. 1987. The microgenity and transport properties of sedimentary rock. Adv. Phys., v. 36, pp. 625-694.
Wagner, N. and I. Balberg. 1987. Anomalous diffusion and continuum percolation. J. Stat. Phys., v. 49, pp. 369-382.
Wong, P., J. Koplik and J.P. Tomanic. 1984. Conductivity and permeability of rocks. Phys. Rev. B, v. 30, pp. 6606-6614.

Computed Effect of Heterogeneity on Well-to-Well Tracer Results

by Saleem G. Ghori and John P. Heller

Abstract

Knowledge of the permeability heterogeneity of underground strata is a major requirement for the efficient operation of enhanced oil recovery projects. But the problems in quantifying the variability in the permeability include both the lack of direct field data and of computational methods to use the indirect information that is available from well-to-well tracer studies. A new numerical technique considers both convection and physical dispersion during flow of the tracer and approaches the solution differently than do conventional finite difference methods. An equation of motion, which contains both Darcy and dispersive terms, allows tracking of isoconcentration lines. This numerical method is stable and avoids any numerical dispersion. The numerical solutions for the homogeneous flooding patterns (observed when the heterogeneity variance has been reduced to zero) are compared with the known approximate analytical solutions. The flooding patterns considered are the five-spot pattern and other developed patterns.

Random permeability fields are generated by the source point method (SPM). An approximate relation is developed to prespecify the correlation length in the SPM. The desired random field of permeability can be obtained by adjusting two parameters: the correlation length (related to the number of source points, N_{sp}) and the variance (α) in the generators.

Results show that the tracer output concentration profile is affected by geometry of the well pattern, channeling due to permeability heterogeneity, and dispersive mixing. Channeling, even in a single layer, produces multiple peaks in the tracer output concentration. The effect of channeling increases with the increase of the correlation length. Channeling exists even if the correlation length is a small fraction of the total flow domain. Dispersivity introduces more mixing and smooths the tracer output concentration curve. Comparison of these curves with the profile obtained in a real field tracer production test can give an estimate of the dispersivity and permeability variability.

Introduction

It has been recognized that reservoir heterogeneity is one of the most important characteristics that influence oil recovery. This is especially so in enhanced oil recovery projects (EOR) where displacement patterns are more critical (Lasseter et al., 1986; Weber, 1986). The most important aspect of reservoir heterogeneity may be the spatial permeability variations. It is impossible to quantify this by single values, but the spatial distribution can be described by probabilistic theory (Journel and Huijbregts, 1978; Matheron, 1973; Marsily, 1984). Unfortunately, not enough actual field permeability data are available to define the spatial permeability variation statistically. In general, to characterize the heterogeneity of a reservoir, one needs to know not only the distribution parameters (the mean and the variance) but also the parameters describing the auto-correlation of nonuniformities in the field. The correlation structure, in fact, has been observed at different scales from pore level to interwell distance (Bahralolom and Heller, 1989; Goggin et al., 1989).

Radioactive or chemical tracers have long been used in reservoir floods to give information about reservoir and flow characteristics (Wagner, 1977; Carpenter et al., 1952; Strum and Johnson, 1951). Operating engineers use output

concentration at the production well to predict the behavior of the reservoir qualitatively (Wagner, 1977) but these tests do not reveal quantitative information about the permeability heterogeneity.

Mathematically, the flow of a miscible tracer in a reservoir is described by the well-known convective-dispersion equation. The exact analytical or numerical solutions for a nonuniform flow field are not available. Existing numerical simulation procedures may show instability problems or suffer from numerical dispersion, especially at the large field scale (Peaceman and Rachford, 1962; Fanchi, 1983). Several techniques are described in the literature (Chaudhari, 1971; Stone and Brian, 1963; Larson, 1982; Garder et al., 1964; Laumbach, 1975) that attempt to minimize the effect of numerical dispersion, but its elimination has not been completely achieved.

This paper imparts a better understanding of the effect of permeability heterogeneity on the displacement of a miscible tracer in flooding patterns such as the five-spot, the staggered-line drive, and the direct-line drive. A single component, single phase, miscible tracer with unit mobility ratio for numerical computations is considered. The aquifer is assumed to have only a single layer.

The computations are performed in several steps. In the first of these steps, a synthesized permeability field is generated by the Source Point Method (SPM) (Heller, 1972). Second, an efficient computer simulator is used to obtain solutions to pressure equations for the Darcy velocity. A new numerical method is presented to compute the changing fluid composition for the solution of the convective-dispersion equation. This numerical technique was originated by Heller (1986). After the application of this technique, the tracer concentration curves of the produced fluid are then computed to determine the effect of two parameters of the SPM and of the dispersivity of the rock.

Derivation of the Equation of Motion

The state of displacement of a fluid by a miscible solvent in a porous medium can be specified by two macroscopic variables: a vector $\boldsymbol{u}$, which describes the Darcy velocity, and a scalar C, which represents the concentration of the displacing fluid; the latter can be taken as ranging from 0 to 1. Variation of concentration of a displacing fluid is related to the velocity field by the partial differential equation:

$$\frac{\partial C}{\partial t} = -\frac{\boldsymbol{u}}{\phi}\cdot\nabla C + \nabla\cdot\boldsymbol{D}\cdot\nabla C \qquad (1)$$

Here, ϕ is the porosity and $\boldsymbol{D}$ is the second order symmetric tensor which represents the coefficient of dispersion for the fluid matrix system. Even for a homogeneous and isotropic porous system, the dispersion is direction dependent. Following de Jong (1958) and Bear (1961), the dispersion coefficient is often taken as a symmetric tensor with its principal direction parallel to the Darcy velocity, leaving only two independent components, D_L and D_T. Further, these components are dependent on the value of $\boldsymbol{u}$. Experimental studies by Blackwell (1962), and by Perkins and Johnston (1963) with relatively homogeneous packs and rock cores show that dispersion can be approximated by:

$$D_L = \frac{D_m}{\phi F} + \frac{\lambda_L |u|}{\phi} \qquad (2)$$

where λ_L is the dispersivity constant (or the dispersivity distance) in the longitudinal direction. In the transverse direction, a similar equation seems valid with λ_L replaced by λ_T.

Motion of the Isoconcentration Surfaces

The description of the two-state variables (u,C) in miscible displacement may be given in terms of a family of moving iso-concentration surfaces. The concentration is represented by a scalar function of two quantities, space and time $C(r,t)$. The total derivative of the concentration is:

$$dC = \nabla C \cdot dr + \frac{\partial C}{\partial t} dt \qquad (3)$$

The substantive time derivative of concentration can then be written as:

$$\frac{DC}{Dt} = \nabla \cdot C \frac{dr}{dt} + \frac{\partial C}{\partial t} \qquad (4)$$

The substantive time derivative of concentration about a test point that remains on a given isoconcentration surface will be zero. In this situation, dr/dt represents the velocity of a point in the isoconcentration surface and can be represented by a vector v. Equation (4) then becomes:

$$v \cdot \nabla C = - \frac{\partial C}{\partial t} \qquad (5)$$

Here, v is the displacement velocity vector, or front velocity vector, of the isoconcentration surface. Combining eqns (1) and (5), results in

$$v \cdot \nabla C = \frac{u}{\phi} \cdot \nabla C - \nabla \cdot D \cdot \nabla C \qquad (6)$$

Like the convective-dispersion eqn (1), eqn (6) also has a convective part and a dispersive part. For the dispersive part in eqn (6), a modification is required to deal with the tensorial nature of dispersion. In a one-dimensional flow system, eqn (6) can be solved numerically by a variety of techniques. For a multidimensional flow system, however, the numerical solution of eqn (6) can be performed most easily if the flow vector is parallel to one of the coordinates of the flow system. But in most multi-dimensional miscible displacements, for example in a five-spot pattern, the flow vectors are not oriented simply with respect to the coordinate axis (Aziz and Settari, 1979). In this study, the grid produced by the family of streamlines (Ψ = constant) and isopotential lines (Φ = constant) was used as the base of the curvilinear orthogonal coordinate system in the numerical computations.

Equation of Motion of Isoconcentration Surfaces in Φ-Ψ Coordinates

By using tensorial analysis (Ghori, 1988), the equation of motion of the isoconcentration lines, i.e. the velocity of the isoconcentration surfaces in the normal direction, was derived. The tensorial analysis can be summerized in the following steps: 1) represent the dispersion tensor in a general curvilinear coordinate system; 2) transform each derivative term in eqn. (6) into general curvilinear coordinates; 3) change the transformed equation into an orthogonal coordinate system; 4) choose a two-dimensional coorindate system (Φ, Ψ) such that the flow direction coincides with one of the axes (Φ-coordinate). This will reduce the dispersion tensor into only two components. The resulting equation can be written as:

$$v = \frac{|u|}{\phi} \frac{\partial C/\partial \Phi}{|\nabla C|} - \frac{1}{h\,|\nabla C|} \left(D_L \frac{\partial^2 C}{\partial \Phi^2} + \frac{\partial D_L}{\partial \Phi} \frac{\partial C}{\partial \Phi} + D_T \frac{\partial^2 C}{\partial^2 \Psi} + \frac{\partial D_T}{\partial \Psi} \frac{\partial C}{\partial \Psi} \right) \qquad (7)$$

where h = scale factor, with the dimensions L^2T^2/M.

This is the equation of motion of isoconcentration surfaces in a two dimensional ($\Phi-\Psi$) coordinate system.

This analytical expression is used directly in the computation of two-dimensional miscible displacements in five-spot or other patterns. The method computes the concentration following the injection of a tracer slug. The leading and trailing edges of the slug are not assumed to be discontinuous, but initially of a ramped or trapezoidal shape with concentration values assigned to the distribution ranging from 0 to 1. This concentration profile is divided into 17 isoconcentration lines or points. In its motion, each isoconcentration line is subjected to the influences of convection and dispersion, and the outward, or front, velocity along each designated streamline of the flooding pattern is calculated.

Numerical Method

The numerical computations have been divided into three major parts. The first section computes the Darcy velocity; the second part computes the motion of the isoconcentration surfaces; and the last section calculates the integrated output concentration profile that would be observed at the production well.

Determination of Darcy Velocity

The equation of motion of the isoconcentration lines requires computed values of the Darcy velocity along prespecified streamlines. While this velocity can be obtained analytically by solution of the Laplace equation for the homogeneous case, there exists no analytical solution in fields where the permeability varies arbitrarily from point to point. If the spatial permeability pattern is known, or can be approximated, the pressure field can be computed numerically by solution of an equation similar to that of Laplace:

$$\nabla^2 p + \nabla P \cdot \nabla \ln k = 0 \qquad (8)$$

With some statistical justifications, only one quarter of the flooding pattern is considered.[1] A successive over relaxation (SOR) method was used to solve eqn (8) for pressure. The Darcy equation was then used to compute the flow velocity at any point. The position of the displacement front on a particular streamline was then obtained by the iterative use of the equations:

$$\Delta x = u_x \Delta t \qquad (9a)$$

$$\Delta y = u_y \Delta t \qquad (9b)$$

Once the Darcy velocity and the positions of the streamlines, together with the potentials, are known, the movement of the miscible tracer slug can be obtained from eqn (7).

Numerical Solution of the Equation of Motion

The computations in the numerical scheme are quite straightforward. At each of the isoconcentration lines, the value for both the first and second derivatives of concentration can be approximated by a simple

[1] Theoretical considerations in a homogeneous aquifer provide symmetry properties in a system of wells like a five-spot pattern. For a heterogeneous aquifer, the permeabilities for all four quarters of the five-spot pattern were assumed to come from the same distribution. Further, the flow rates at the four production wells of the pattern are kept constant (one-fourth of the total injection toward each producer). This makes it possible to consider any or all of the four quarters of a five-spot pattern for numerical analysis.

finite difference scheme. The numerical technique eliminates the use of any outer boundary conditions. An initial condition is required to start the computations of tracer band movements. The initial time value is not zero, but is equal to the fill-up time from the well bore to the center of the initial concentration distribution. It is presumed that the actual tracer band is initially introduced as a flat-topped slug with ramp-shaped inner and outer edges, in which the concentration varies linearly from 0 to 1 and from 1 to 0, respectively. These ramps can be quite steep; the thickness of the flat-top portion then determines, independently, the amount of injected tracer. This initial concentration profile is assigned to all the predetermined streamlines of the flooding pattern. The concentration profile on each streamline is divided into 17 isoconcentration points. Once the velocities of the points on the isoconcentration lines have been computed from eqn (7), their new positions are determined by using a suitable time step.

Only a short time after the injection of the flat-topped tracer slug, the combination of the geometric peak narrowing effect and dispersion causes the leading and following edges of the slug to approach each other. The result of continued dispersion then decreases the peak concentration from its initial value of unity. In fact, it continues to decrease. The calculation scheme used here enables only isoconcentration points themselves to be followed. To calculate the peak concentration at any particular time, an approximation is made as follows: it is first recognized that, as the distance from the injection well increases, the shape of the peak approaches that of a normal distribution because of the dispersive term in the equation of motion. In the near neighborhood of the maximum concentration, this curve is well fitted by a parabola, resulting in an easily calculated peak concentration from a quadratic fit to the points nearest the center of the slug profile.

As the computation proceeds, the middle isoconcentration lines gradually approach each other and round the corners of the concentration distribution. A moment will come when the two isoconcentration points on opposite sides of the peak will come together and then disappear as the peak concentration falls below that level. When half of the isoconcentration lines have been lost in this way, the calculation procedure then doubles their number by starting new ones between each of the remaining lines. In addition to the calculation of the peak concentration at different times, the thickness of the tracer band at the 50% isoconcentration lines is also calculated.

Integrated Output Concentration Profile

The third section of the computer simulator computes the output tracer concentration. The previous computation gave the output concentration profiles as a function of time along all of the streamlines entering the production well. At any particular time, the overall effluent tracer concentration, $\overline{C}(t)$, from the system would then be given by the integral:

$$\overline{C}(t) = \frac{\int_0^{\pi/2} q(\Psi) C(\Psi, t)\, d\Psi}{q_t/4} \qquad (10)$$

where $C(\Psi, t)$ is the concentration that enters the production well from a streamline, at a time t, and $q(\Psi)$ is the flow rate on that streamline. Although the flood front consists of an infinite number of streamlines, this has been approximated for a computer by a smaller number. Originally, 81 streamlines were followed. This number was then increased to 275 in those cases where the dispersivity distance was particularly small.

Generation of a Random Permeability Field

The main objective of this study was to quantify the effects of a statistical variation of the permeability. This can be achieved by comparing the output concentration profile at the production well obtained from the simulator with that of the tracer production curve from a real field. In practice, not enough permeability data are available to enable a complete statistical analysis to be made. Therefore, synthetic permeability data were generated to use as input in the simulator.

Several methods of generating random permeability fields are available in the literature (Smith and Freeze, 1979; Montoglou and Wilson, 1982; Gutjahr, 1989). The method used here was first presented by Heller (1972) and is called the source point method (SPM). This method generates a random but somewhat "smooth" permeability field.

The SPM requires generating $3x N_{sp}$ (where N_{sp} = number of source points) random numbers. The first two N_{sp} numbers, generated from a uniform distribution, are used to compute x and y coordinates of the "source points" in the field. The last N_{sp} numbers are generated from a normal distribution and denoted as *s(j)*. These represent the local minima or maxima of the log-permeabilities at the location of the source points. An inverse square assumption is then used to compute the log-permeability values at the specified grid points as:

$$Sg(N,M) = \frac{\sum_{j=1}^{N_{sp}} \frac{s(j)}{[(x(j)-x_g(N))^2+(y(j)-y_g(M))^2]}}{\sum_{j=1}^{N_{sp}} \frac{1}{[(x(j)-x_g(N))^2+(y(j)-y_g(M))^2]}} \qquad (11)$$

Figure 1 shows the log permeability surfaces for realizations that were computed using $N_{sp}=50$ (Figure 1A) and $N_{sp}=250$ (Figure 1B). In these figures, the local minima and maxima are the valleys and peaks of the log-permeability distribution. The log-permeability distribution obtained by this method follows a normal distribution (Sultan et al., 1990).

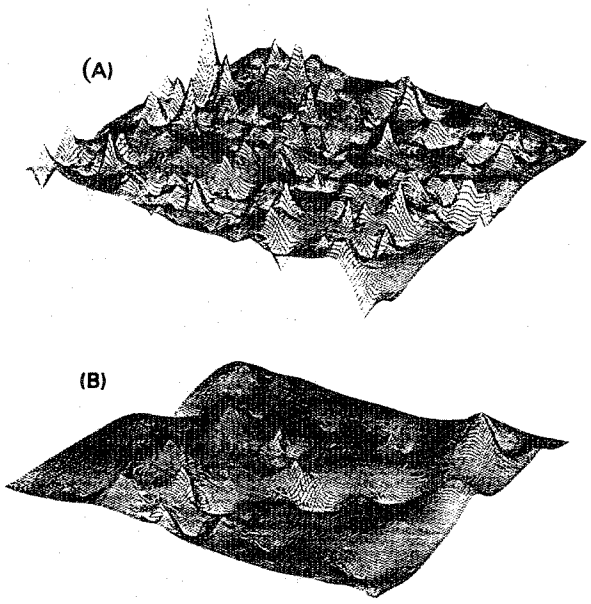

Figure 1. Log permeability surfaces from the SPM: (A) $N_{sp}=250$; (B) $N_{sp}=50$.

The permeability values at each grid point are then calculated as:

$$K(N,M) = K_0\, e^{\alpha S_g(N,M)} \qquad (12)$$

where, K_0 is the base permeability and α is the parameter defining the width of the permeability distribution. With this method, it is possible to generate a random permeability field with some correlation structure. The correlation length can be computed from the number of source points.

Correlation Length

The spatial correlation of a permeability distribution depends upon the method of its generation. To evaluate the correlation length from the SPM, a number of numerical experiments were performed with the method, and variograms for the different values of N_{sp} were constructed (Figure 2). It is obvious from Figure 2 that the correlation length increases with the decrease of the number of source points. The correlation lengths obtained from the variogram were plotted against the square root of the ratio of the area of the field to the number of source points. A least square method was then used to obtain the best fit.

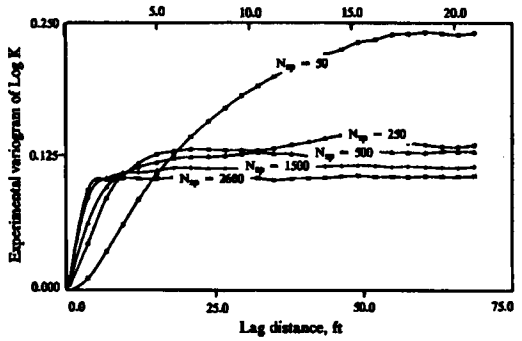

Figure 2. Semi-variogram of log-K for different number of source points.

The following equation, with a correlation coefficient of .95, was obtained from the least square fit:

$$L_c \cong 2.0\left(\frac{Area}{N_{sp}}\right)^{1/2} \qquad (13)$$

It is evident that the crrelation length is proportional to the average spacing of the source points. By the convention used, it is exactly twice that average distance.

Results and Discussion

It was observed that the effect of transverse dispersion is negligible as compared to the longitudinal dispersion (Ghori, 1988). Therefore, the results presented here do not include the component of the dispersivity tensor in the transverse direction. Several simulations were made. In order to check the validity of the simulator, numerical results were compared with the known analytical solution of a homogeneous aquifer. Figure 3 shows the comparison of the numerically obtained output tracer concentration with the approximate analytical solution of a five-spot pattern as given by Abbaszadeh and Brigham (1983). It is apparent that the agreement between the two is excellent, except at the peak. The disagreement at the peak is perhaps due to the differences in the assignment of the initial tracer concentration distribution.

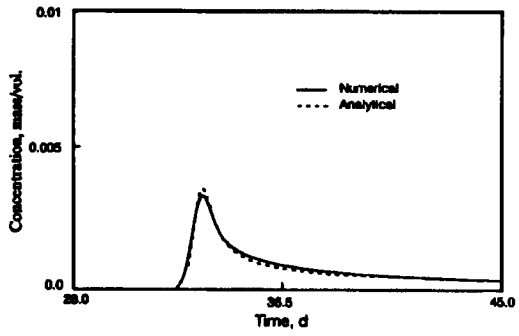

Figure 3. Comparison of numerical solution with analytical solution of a homogeneous five-spot pattern, $\lambda = 0.8$ ft (~ 0.25 m).

The two parameters, α and N_{sp}, of the SPM determine the degree of heterogeneity. The N_{sp} determines the correlation length; the greater the number of source points, the smaller the correlation length, and vice versa. A large correlation implies that the displacement pattern in this reservoir will show a highly channeled structure, whereas

a small correlation length means a less channeled flow pattern. The value of α, which determines the width of the permeability distribution, also contributes toward channeling in the displacement pattern. A large value of α shows more channeling. Figure 4 shows front locations of the 50% isoconcentration lines at different values of the pore volume injected for a five-spot pattern. Figures 4A and 4B show the front locations for $N_{sp} = 250$ and α as 0.3 and 2.0, respectively. It can again be noted that an increase in the α value corresponds to more channeling. Similar conclusions can be drawn from Figures 4C and 4D. Comparison of Figures 4B and 4D shows that for $N_{sp} = 250$ ($L_c \sim 5.8$ m; ~ 19 ft) less channeling is observed, whereas for $N_{sp} = 50$ ($L_c \sim 12.8$ m; ~ 42 ft), more channeling is evident.

The time history of the tracer concentration at the production well shows the combined effect of the geometry of the flow pattern, the degree of heterogeneity, and the dispersivity of the aquifer. The effect of the geometry is due to the great variation of the arrival times at the production well of the tracer that has moved along different streamlines. Because of the geometrical effect alone, the peak of the output concentration profile is considerably < 100% even in the absence of heterogeneity and dispersive mixing. The degree of heterogeneity and dispersive mixing induce further dilution in the tracer concentration at the production well.

Heterogeneity of the reservoir, as described by the values of N_{sp} and α, results in an output concentration profile quite different from that observed in a homogeneous aquifer. For a large N_{sp} and small α value, the tracer concentration is comparable with that of a homogeneous aquifer (Figure 5A). The increase in the channeling effect produces output concentration profiles with multiple peaks (Figures 5A through 5D). It has not been reported previously that a single layered

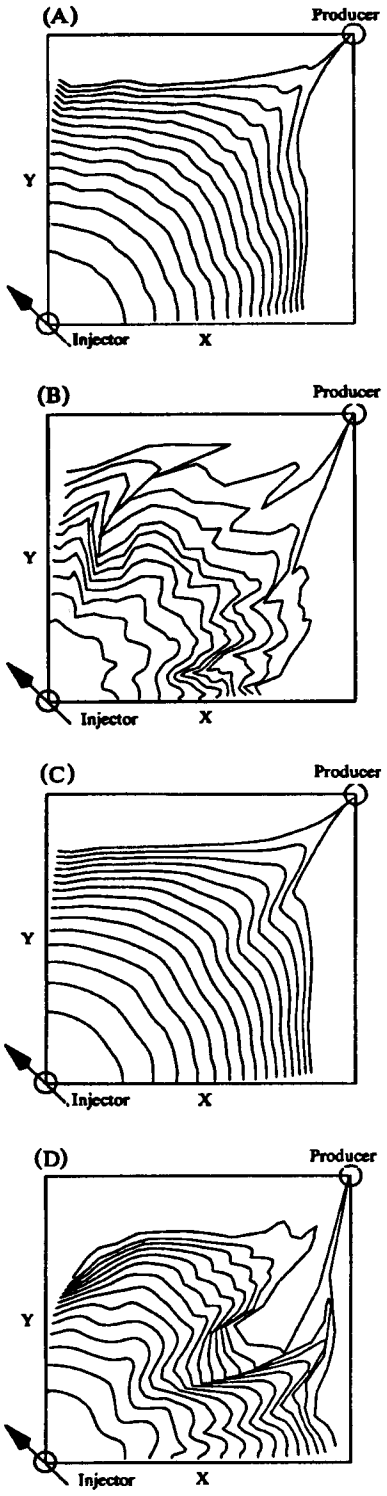

Figure 4. Front locations of 50% isoconcentration lines: (A) $N_{sp} = 250$, $\alpha = 0.3$; (B) $N_{sp} = 250$, $\alpha = 2.0$; (C) $N_{sp} = 50$, $\alpha = 0.3$; (D) $N_{sp} = 50$, $\alpha = 2.0$.

reservoir can produce results, as if the aquifer has multiple layers. The existence of peaks and valleys is because of the areal variation of the permeability. Results not presented here have shown that the details of these multiple peaks are unique for a particular realization of the permeability field. The number and position of the multiple peaks depend upon the correlation lengths with respect to the total flow dimension. For small correlation lengths, the multiple peaks are very similar for different realizations.

Dispersivity affects the sweep efficiency of the displacing front and the spreading of the tracer slug as it moves through the reservoir. For an aquifer with high dispersivity, a larger amount of the displacing fluid is required. Dispersivity values as low as 1.5×10^{-3} m (0.005 ft) for a Berea sandstone to 0.6 m (2.0 ft) for field cores are reported in the literature. In the present study, we have considered three values of dispersivity distance (1.8×10^{-2} m, 1.8×10^{-1} m, and 1.8 m; 0.06 ft, 0.6 ft, and 6.0 ft, respectively) to cover all possible ranges of dispersivity in the field. It has been found that more streamlines are required to define the output concentration curve as the dispersivity distance used in the calculation is decreased. This was observed in the simulation of the homogenous aquifer.In that case, the number of streamlines was increased until a smooth output concentration was obtained. Figure 6 shows the output tracer concentration from a homogeneous aquifer for different values of dispersivity. In the tracer output concentration curve from a single-layered homogeneous aquifer, only a single real peak occurs; if the aquifer is heterogeneous, several peaks appear in the output curve. The fact that the positions of these peaks do not change, between calculations that used different values of the dispersivity distance, confirms that a sufficient number of streamlines has been used, and that the peaks and valleys shown are real. Figures 5A to 5D show the effect of dispersivity on the tracer output concentration. It is apparent that the increase in the dispersivity smooths the profile by introducing more dilution.

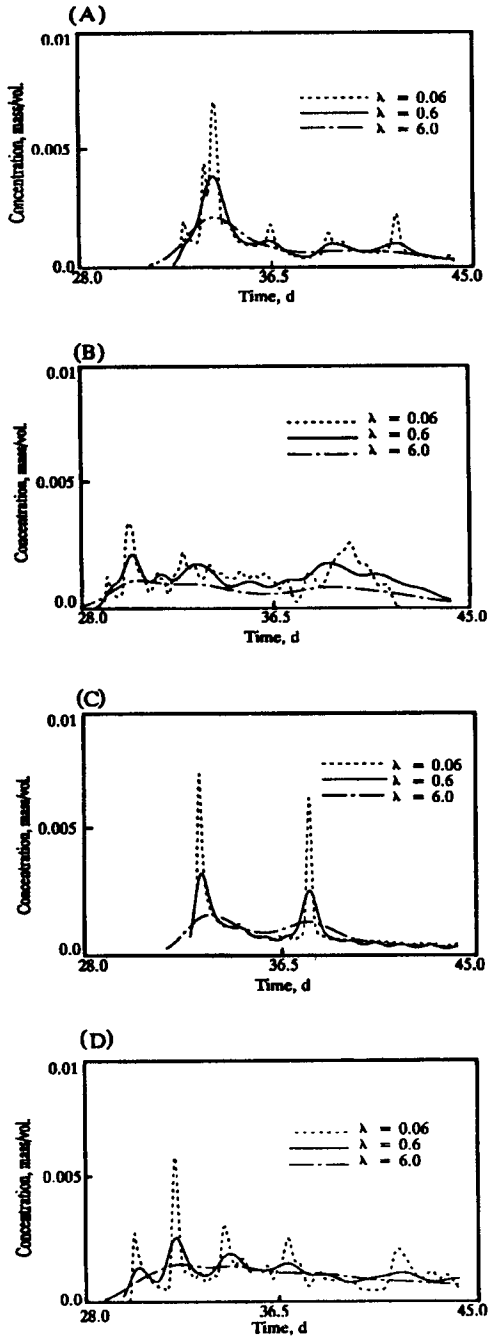

Figure 5. Integrated tracer output concentration for a five-spot pattern: (A) $N_{sp} = 250$, $\alpha = 0.3$; (B) $N_{sp} = 250$, $\alpha = 2.0$; (C) $N_{sp} = 50$, $\alpha = 0.3$; (D) $N_{sp} = 50$, $\alpha = 2.0$.

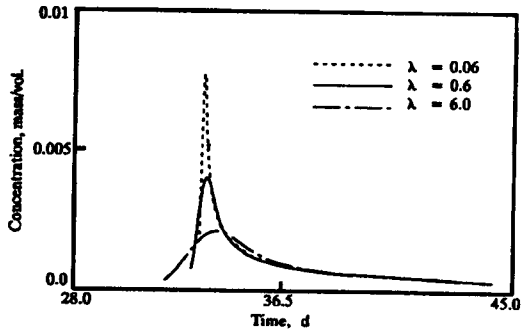

Figure 6. Effect of dispersivity distance on the integrated tracer output concentration for a homogeneous five-spot pattern.

Some results have also been obtained for other flooding patterns; for example, a staggered line drive and a direct line drive. The flooding area considered in both these patterns is the same as that of the five-spot pattern. The staggered line drive is similar to a five-spot pattern, except that the boundaries are not square. Front locations of the 50% isoconcentration lines, for $N_{sp} = 250$ and $\alpha = 2.0$, is shown in Figure 7A. It was observed that for a heterogeneous aquifer, earlier breakthrough of the tracer occurs compared with the homogeneous case (Figure 7B). The shape of the output tracer concentration curve for the heterogeneous aquifer is not very different from the homogeneous case. Similarly, the direct line drive is similar to a five spot-pattern, except the wells are at the center of the sides of the boundary. The front locations and the output concentration are given in Figures 8A and 8B. Here, the output concentration profile has more peaks and valleys, which are apparently associated with the distortion in the flood front (Figure 8A).

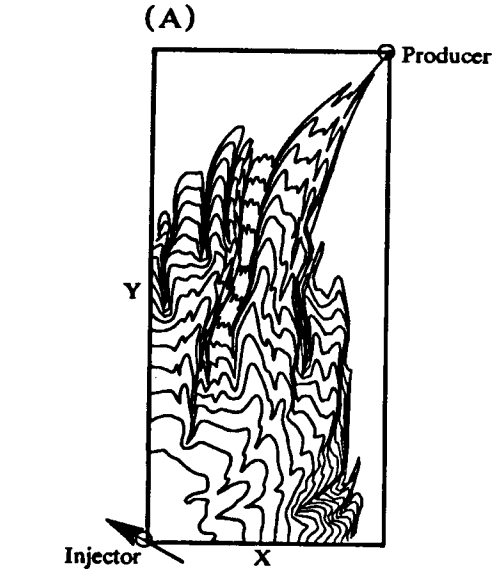

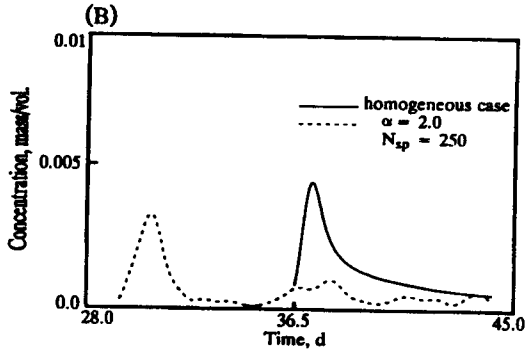

Figure 7. (A) Front locations of the 50% isoconcentration lines for a staggered line drive, $N_{sp} = 250$, $\alpha = 2.0$; (B) Integrated tracer output concentration for a staggered line drive, $\lambda = 0.8$ ft (~ 0.25 m).

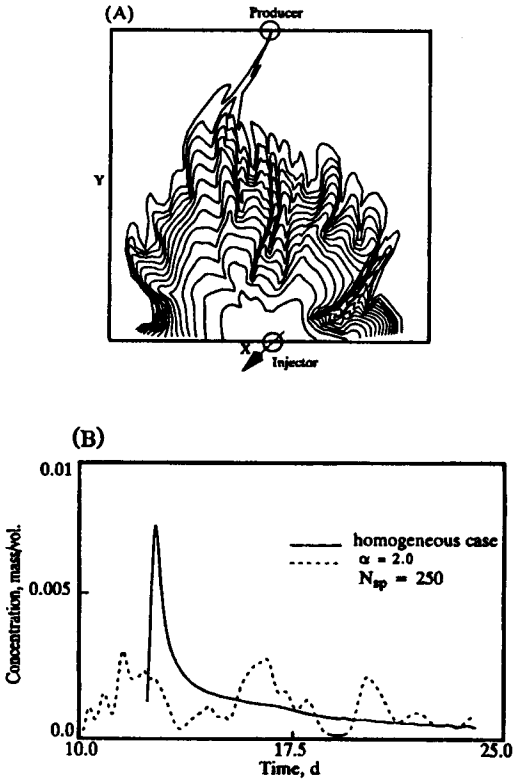

Figure 8. (A) Front locations of the 50% iso-concentration lines for a direct line drive, $N_{sp} = 250$, $\alpha = 2.0$; (B) Integrated tracer output concentration for a direct line drive, $\lambda = 0.8$ ft (~.25 m).

In order to quantify the permeability heterogeneity, the results obtained from the simulator can be compared with the field tracer tests. There are three parameters involved: the correlation length (defined by the N_{sp}), the value of α, and the dispersivity distance. One approach is to use an optimization technique that can minimize the error between the observed values and simulated values. Another approach is to produce a catalogue of tracer production curves from the simulator in a "type curve" fashion. These proposals are now being considered, and along with the inclusion of the effect of layering, will be presented in the next paper resulting from this research.

Conclusions

The tracer production curve reflects the effect of the flow process in underground reservoirs. Therefore, tracer production history can be used as a diagnostic tool in the determination of permeability heterogeneity. The following conclusions have been drawn from the results of this work:

1. A new numerical method has been presented to follow the progress of a miscible fluid displacement process by computing the successive positions of the floodfront in a reservoir with arbitrary permeability distribution.

2. The numerical method allows the value of the dispersion coefficient to be varied independently so that its effect may also be studied.

3. The source point method (SPM) was used for the generation of the random permeability field. An approximate relation was developed so that the correlation length can be prespecified in the SPM generator.

4. The numerical method has been applied to the study of the effect of permeability heterogeneity on several production patterns in well-to-well tracer studies for single-layer reservoirs. These studies included the five-spot, the staggered line drive, and the direct line drive. Results show marked differences among them.

5. Heterogeneity generally causes an increase of the time interval over which the tracer emerges from the production well.

6. The tracer output concentration at the production well is affected by the geometry of the well pattern, and by the channeling resulting from the permeability heterogeneity as modified by the dispersive mixing.

7. The geometrical effect produces a nonuniform velocity field which, in turn, induces variability in the arrival time of a tracer on different streamlines. Because of this effect, the tracer output concentration is diluted with the geometrical effect alone.

8. The channeling resulting from the permeability heterogeneity also causes variation in the arrival time of a tracer at the production well. Therefore, the integrated output profile, even for a single layered reservoir, shows peaks and valleys and more mixing.

9. Unless dispersivity is unusually large, the tracer production pattern is characterized by a number of peaks and valleys, apparently caused by the variability of streamline paths in the heterogeneous aquifer. These peaks and their distribution can be used to evaluate the heterogeneities. Channeling increases with the increase of the correlation length of the permeability field. It is evident from the results that correlation of permeabilities in even a small fraction of the flow domain produces noticeable channeling.

Saleem G. Ghori received a B.S. degree in petroleum engineering from the University of Engineering and Technology, Lahore, Pakistan, in 1981. After graduation, he worked as an assistant production engineer with Pakistan Petroleum Ltd., at the Sui gas field. He earned an M.S. degree in petroleum engineering from The New Mexico Institute of Mining and Technology (NMIMT) in Socorro, NM, in 1988. He is currently a Ph.D. candidate in petroleum engineering at NMIMT.

John P. Heller received his B.S. and Ph.D. in physics, with a mathematics minor, at Queens College, New York, in 1944, and at Iowa State University, Ames, Iowa, in 1953, respectively. He has performed research in petroleum operations and in enhanced oil recovery since 1953, first at the Mobil Oil Company Field Research Laboratory (now the Dallas Research Division) and at the Petroleum Recovery Research Center at NMIMT. He is presently a senior scientist and head of the CO_2 Mobility Control and Flow Heterogeneities Group at the Petroleum Recovery Research Center (New Mexico Institute of Mining and Technology, Socorro, NM 87801).

References

Abbaszadeh, D. M. and W. E. Brigham. 1983. Analysis of unit mobility ratio well-to-well tracer flow to determine reservoir heterogeneity. DOE/SF/ 11564-1.

Aziz, K. and A. Settari. 1979. Petroleum Reservoir Simulation. Applied Science Publ. Ltd.

Bahralolom, I. and J. P. Heller. 1989. Core sample heterogeneity from laboratory flow experiments. Proc. 2nd Internat. Res. Char. Tech. Conf., Dallas. Academic Press, NY (to be published).

Bear, J. 1961. On the tensor form of dispersion in porous media. J. Geophys. Res., v. 66, pp. 1185-1198.

Blackwell, R. J. 1962. Laboratory studies of microscopic dispersion phenomena. Trans. AIME, v. 1 (225), pp. 1-8.

Carpenter, P. G., T. D. Morgan and E. D. Parson. 1952. Use of boron compounds as water flood tracers. Prod. Monthly, v. 16, no. 12, pp. 12-19.

Chaudhari, N. M. 1971. An improved numerical technique for solving multidimensional miscible displacement equations. Soc. Petrol. J., pp. 277-284.

de Jong, G. deJosselin. 1958. Longitudinal and transverse diffusion in granule deposits. Trans. Am. Geophys. Union, v. 39, pp. 67-74.

Fanchi, J. R. 1983. Multidimensional numerical dispersion. Soc. Petrol. J., pp. 327-339.

Garder, A. O., D. W. Peaceman and A. L. Pozzi. 1964. Numerical calculation of multidimensional miscible displacement by the method of characteristics. Soc. Petrol. J., v. 4, pp. 26-36.

Ghori, S. G. 1988. Numerical Simulation of Miscible Displacement of a Tracer Slug in Homogeneous Five-Spot Patterns. Master's Thesis, NMIMT, Socorro, NM.

Goggin, D. J., M. A. Chandler, G. Kocurek and L. W. Lake. 1989. Permeability transits in eolian sands in their use in generating random permeability fields. 64th Annual Tech. Conf., paper SPE 19586, pp. 149-163.

Gutjahr, A. L. 1989. Fast Fourier Transforms for Random Field Generation. New Mexico Institute of Mining and Technology. Project Rept. LANL Contract 4-R58-2690R.

Heller, J. P. 1986. Tracer distribution in radial flow. Mobility control for CO_2 injection. DOE/MC/16426-19, pp. 111-136.

Heller, J. P. 1972. Observations of mixing and diffusion in porous media. Proc. Second Symp. Fundamentals of Transport Phenomena in Porous Media, IAHR-1SSS, Ontario, pp. 1-26.

Journel, A. G. and C. J. Huijbregts. 1978. Mining Geostatistics. Academic Press.

Lake, L. W. and J. L. Jensen. 1989. A review of heterogeneity measures used in reservoir characterization. NMT Centennial Symposium (SPE) pp. 223-234. To be published.

Larson, R. G. 1982. Controlling numerical dispersion by variably timed flux updating in one dimension. Soc. Petrol. J., pp. 399-408.

Lasseter, T. J., J. R. Waggoner and L. W. Lake. 1986. Reservoir Heterogeneities and Their Influence on Ultimate Recovery. Reservoir Characterization, Eds. L. W. Lake and H. B. Carrol, Academic Press, pp. 545-559.

Laumbach, D. D. 1975. A high-accuracy finite-difference technique for treating the convection-diffusion equation. Soc. Petrol. J., pp. 517-531.

Marsily, G. 1984. Spatial Variability of Properties in Porous Media: A Stochastic Approach. Fundamental of Transport Phenomena In Porous Media, Eds. Bear and Corapcioglu, pp. 721-769.

Matheron, G. 1973. The Intrinsic Random Functions and Their Applications. Advan. Appl. Prob., pp. 439-468.

Montoglou, A. and J. L. Wilson. 1982. The turning bands method for simulation of random fields using line generation by a spectral method. Water Resour. Res., v. 18, no. 5, pp. 1379-1394.

Peaceman, D. W. and H. H. Rachford. 1962. Numerical calculation of multidimensional miscible displacement. Soc. Petrol. J., pp. 327-339.

Perkins, T. K. and O. C. Johnston. 1963. A review of dispersion and diffusion in porous media. Soc. Petrol. Eng. J., no. 3, pp. 70-84.

Smith, L. and R. A. Freeze. 1979. Stochastic analysis of steady state ground water flow in a bounded domain, 1. One-dimensional simulations. Water Resour. Res., v. 15,pp. 521-528.

Stone, H. L. and P. L. T. Brian. 1963. Numerical solution of convective transport problems. A.I.Ch.E. J., v. 9, pp. 681-688.

Strum, P. W. and W. E. Johnson. 1951. Field experiments with chemical tracers in flood waters. Prod. Monthly, v. 15, no. 2, pp. 11-18.

Sultan, A. J., J. P. Heller and A. Gutjahr. 1990. Generation and Testing of Random Fields and the Conditional Simulation of Reservoirs. International Technical Meeting. CIM/SPE 90-98.

Wagner, O. R. 1977. The use of tracers in diagnosing interwell reservoir heterogeneities—Field results. J. Petrol. Tech., pp. 1410-1416.

Weber, K. J. 1986. How Heterogeneity Affects Oil Recovery. Reservoir Characterization, Eds. L. W. Lake and H. B. Carrol, Academic Press, pp. 487-544.

Nomenclature

$S_g(N,M)$ = log of permeability values at $(N,M)^{th}$ grid point
C = concentration mass/volume
$\overline{C}(t)$ = integrated concentration at a particular time, mass/volume
u = Darcy velocity vector, L/T
v = frontal velocity vector, L/T
ϕ = porosity
D = dispersion tensor, L^2/T
D_m = molecular diffusion coefficient, L^2/T
F = formation resistivity factor
K = permeability, md
Ψ = stream function, M/LT^2
Φ = potential, M/LT^2
q_t = total flow rate into the pattern, L^3/T
$q(\Psi)$ = flow rate into a stream tube, L^3/T
$C(\Psi,t)$ = concentration entering the production well from a stream tube at a particular time, mass/volume
x_g,y_g = coordinates of the specified grid in the flow domain, L
x,y = coordinates of the source points, L
L_c = correlation length of the permeability field, L
$s(j)$ = maxima, or minima, of the source points

Simulating Fluid Flow Through a Geologically Realistic Permeable Medium

by Larry W. Lake

Abstract

For the past five years the outcrop of the Page Sandstone in northern Arizona has been studied as a prototype for eolian oil reservoirs and aquifers. The work has encompassed detailed geological studies and highly intensive descriptions of the distribution of hydraulic conductivity or permeability. The point has now been reached of using this information to evaluate predictions about fluid flow through naturally occurring sandstones. Work on this topic is the subject of this presentation.

The first step in the study was to establish a 'truth case', a standard against which to measure the success of alternative procedures for flow prediction. This truth case consisted of a highly detailed (> 11,000 finite element nodes) numerical simulation of a miscible displacement through a portion of the outcrop wherein each nodal property was assigned according to the actual value existing at that point. This intensively deterministic simulation also allowed the evaluation of the extent of geological detail necessary for a good prediction; mobility ratio and the distribution of average permeability were the most important quantities governing fluid flow. Permeability anisotropy, fourth order bounding surfaces and dispersion are much less important.

With the 'truth case' in hand, the simulations were recalculated based on the amount of data that would normally be available for subsurface conditions. In this case, of course, it was the generation of interwell properties which was being tested. The work investigated two basic procedures; pseudofunctions and conditional simulation. The pseudofunction approach generated effective relative permeabilities (a concept borrowed from immiscible flow) to model the effects of heterogeneities on a gross or flow unit scale. The effective relative permeabilities then depended on the size of the flow unit, the mobility ratio and the nature of the distribution of the permeability within the flow unit. The conditional simulation approach generated interwell properties statistically, and evaluated each procedure according to whether the distribution of the simulation results agreed with the results of the 'truth case'.

Pseudofunctions rely almost exclusively on geological information and conditional simulation on statistics. It is hoped to be able to infer the merits and drawbacks of each method from this work.

Larry Lake is Chairman of the Department of Petroleum Engineering at the University of Texas at Austin (Austin, Texas 78712, USA) and Director of the Enhanced Oil Recovery Research Program. His research areas are enhanced oil recovery, reservoir characterization and in situ leaching.

Visualization of flow and transport in heterogeneous media

by John L. Wilson

Abstract

Spatial variation or heterogeneity of porous media properties influences the flow of fluids, and the transport of colloids and dissolved species. The influence of heterogeneous permeability has been the subject of recent mathematical modelling in hydrology, soil science, and reservoir engineering. Less attention has been given to the other properties of the media, e.g. capillarity.

The use of flow visualization in etched glass micromodels is explored to help elucidate the influence of heterogeneities on several different flow and transport mechanisms. The micromodels are physical models of a pore space, created by etching a pattern onto two glass plates which are then fused together. The resulting pores have complex three-dimensional cross-sections, although the pore network is only two dimensional. Models of this type have been used to study multiphase flow, miscible displacement, and foam behaviour in petroleum engineering. Recently, they have been applied to hydrology and pollutant transport issues. The usual focus of a micromodel study is on pore-level behaviour, but it has been found that bulk properties can also be observed. For example, the pore network can be constructed to emulate an aggregated soil, with well defined preferential flow paths, or an interbedded aquifer or reservoir material, with lenses of a one material buried in a matrix of another material. Observation of behaviour in a micromodel containing many such paths or lenses reveals behaviour that is missing from mathematical models, and may help to define appropriate equivalent homogeneous or pseudo-properties in those models.

Miscible displacement, two- and three-phase immiscible flow, and colloid transport were examined. The visualizations were recorded on film and videotape. It has been found, for example, that media heterogeneities dominate two phase displacement and trapping mechanisms, with implications for aquifer remediation and oil recovery. Non-wetting fluids selectively travel through the coarser and more permeable portions of heterogeneous media, bypassing finer-grained regions. Later, during a natural or imposed flood of a wetting fluid, capillary forces can relegate the flow of the wetting fluid to finer-grained regions, by-passing the coarser non-wetting fluid-filled regions. The amount of by-passing depends on the heterogeneity, and a balance of capillary and viscous forces. Following the recovery of non-wetting phase, the residual saturation left behind in, say, a heterogeneous material composed of disconnected coarse lenses, tends to be larger than in a homogeneous material, and depends on the history of the recovery. It is not a constant media property as assumed by conventional mathematical models.

John L. Wilson is Professor of Hydrology and Director of the Hydrology Program at the New Mexico Institute of Mining and Technology (Department of Geoscience, New Mexico Institute of Mining and Technology, Socorro, New Mexico 87801, USA).

The Impact of Large Scale Heterogeneities on Hydrocarbon Recoveries

by Sait Kocberber and R. Eugene Collins

Abstract

In this study, a fundamental method for incorporating large scale heterogeneities into reservoir studies in a general way is presented. This is achieved by utilizing representations for relative permeabilities and capillary pressures conditioned by absolute permeabilities and employing initial distributions of fluid saturations based on capillary-gravity equilibrium in a three-phase, three-dimensional simulator.

A small scale model is used to evaluate recovery by solution gas drive from a black oil system in a three-dimensional, rectangular block containing a cross-bed lamina. The block is depleted by fluid withdrawal at one face while the other faces of the block are sealed. The results indicate that the recovery history is strongly dependent on the configuration of the cross-bed lamina and the direction of flow. Capillary effects cause high water saturation build-up in the tight lamina. Because of its low relative permeability, the lamina acts as a flow barrier to hydrocarbon flow causing very non-uniform recovery patterns.

Results of these studies indicate that many common practices in previous simulation studies are not representative of real reservoir behavior.

Introduction

Sandstone reservoirs exhibiting cross-bedded structure represent a large fraction of world oil reserves. Detailed descriptions of clastic depositional systems (Davis, 1983; Galloway and Hobday, 1983) clearly indicate that cross-bedding is a major architectural feature in essentially every clastic depositional system. Furthermore, shale intercalations are known to exist within all such deposits. It is widely anticipated that cross-bedding affects hydrocarbon recovery dramatically. Indeed, Tyler *et al.* (1984), in a detailed study which ranked Texas oil reservoirs by percent ultimate recovery, showed that deltaic and slope-basin reservoirs operating under solution-gas drive exhibit the lowest ultimate recoveries of all sandstone reservoirs. These, of course, do have significant cross-bedding in their structure.

Weber *et al.* (1972) and Weber (1982) provided the first detailed studies of the relation of small-scale cross-bedding to large-scale anisotropy of permeability. Kortekaas (1985) carried these concepts further with a scaling-up process using simple models in simulation experiments. He analyzed flow parallel and perpendicular to foreset laminae to generate pseudo relative permeability and capillary pressure curves for a simple element of uniform laminae. These were then applied to a simulated pattern water flood. On the large scale, the reservoir was represented as a homogeneous anisotropic system in which the normally scalar characteristics of relative permeabilities were replaced by tensor properties.

Lasseter *et al.* (1986) also employed a uniform anisotropic representation for a cross-bedded reservoir in a linear waterflood simulation. However, this representation assumed isotropic relative permeabilities and omitted capillary pressure; thus, the simulation was not totally realistic. However, this study did include effects of fluid density, viscosity differences and gravity effects. These studies showed that for single-phase flow, these systems could be functionally represented on the large scale as uniform with anisotropic horizontal permeability. It was demonstrated that a much greater recovery at breakthrough resulted for flooding such that the foreset dip was upward in the flooding direction rather than downward. That is, when the tendency for gravity under-running of water and that for permeability-directed water over-running were opposed rather than in a common direction. Thus, simply reversing the direction of flooding dramatically altered the recovery history.

Recently, Kasap and Lake (1989) have provided quantitative descriptions of cross-bedded outcrops and some calculations of miscible displacements in cross-bedded systems.

While these limited studies demonstrate the significant effects of cross-bedding on fluid displacement processes, they cannot be viewed as providing a complete basis for evaluating the impact of cross-bedding on hydrocarbon recovery. There have been no reported studies of the effects of cross-bedding on primary

recovery; for example, by solution-gas drive.

Most recently, Kocberber and Collins (1990) studied the impact of heterogeneities on the initial distribution of hydrocarbons. Critical to the evaluation of effects of permeability heterogeneities in their study were representations for capillary pressure functions and relative permeability functions, parameterized by absolute permeability. These incorporated representations for the critical saturations, that is, residual gas and oil saturations, and minimum connate water, as a function of absolute permeability. Hence, for a configuration of absolute permeability in the reservoir, the assignment of realistic capillary pressure and relative permeability functions was automatically accomplished for all elements in the reservoir. This system incorporated a very realistic representation of capillary effects in heterogeneous rocks. These relative permeability and capillary pressure relations were then employed to compute initial fluid saturation distributions in composite rocks based on capillary-gravity equilibrium. Severe discontinuities in saturation and effective permeability were demonstrated. It was clearly shown that heterogeneity of permeability dominates initial fluid distributions and causes very non-uniform drainage patterns.

It is essential that capillary pressure and relative permeabilities, parameterized by absolute permeability, be properly included not only during the evaluation of initial fluid saturation distributions but also during the subsequent recovery process. In this study we extend this approach to study the impact of reservoir heterogeneity on hydrocarbon recoveries.

Mathematical Model

The equations solved are formulated in terms of three-dimensional, three-phase, immiscible flow of oil, gas and water based upon Darcy's law and conservation of mass of water and of each of the two components of the hydrocarbon system. To simulate the impact of cross-bedding on hydrocarbon recoveries, a black oil model which uses a finite element method for space discretization, as described by Becker *et al.* (1981), has been developed. This three-dimensional, three-phase model simulates flow of compressible fluids including capillary, viscous and gravity effects. Because capillarity is an important factor in the formulation, and the time derivatives of capillary pressures cannot be ignored, the model utilizes a simultaneous solution method having three primary dependent variables at each node. The saturation derivatives of capillary pressures can be quite large, therefore to make the coefficient matrix diagonally dominant, the phase pressures are chosen as the primary dependent variables. All nonlinearities and space discretization are treated implicitly to improve the stability and convergence of the calculations. The formulation of the model can be summarized as follows.

Governing partial differential equations for the black oil model are (Collins, 1991): (D is vertical distance above a gravitational datum while the other symbols should be familiar)

$$\nabla\cdot\left[\frac{\lambda_w}{B_w}\left(\nabla P_w + \rho_w g \nabla D\right)\right] = \frac{\partial}{\partial t}\left(\frac{\phi S_w}{B_w}\right) + q_w \tag{1}$$

$$\nabla\cdot\left[\frac{\lambda_o}{B_o}\left(\nabla P_o + \rho_o g \nabla D\right)\right] = \frac{\partial}{\partial t}\left(\frac{\phi S_o}{B_o}\right) + q_o \tag{2}$$

$$\nabla\cdot\left[\frac{\lambda_g}{B_g}\left(\nabla P_g + \rho_g g \nabla D\right)\right] + \nabla\cdot\left[\frac{R_s\lambda_o}{B_o}\left(\nabla P_o + \rho_o g \nabla D\right)\right] = \frac{\partial}{\partial t}\left[\phi\left(\frac{S_g}{B_g} + \frac{R_s S_o}{B_o}\right)\right] + q_g + R_s q_o \tag{3}$$

Auxiliary equations

$$S_w + S_o + S_g = 1 \tag{4}$$

$$P_{cow} = P_o - P_w \tag{5}$$

$$P_{cgo} = P_g - P_o \tag{6}$$

and B_w, B_o, B_g and R_s are specified functions of pressure and temperature. Initial conditions are determined by capillary-gravity equilibrium as described above. In these differential equations, the saturation derivatives are converted to pressure derivatives based upon representations of capillary pressures as functions of only one fluid saturation, specifically, $P_{cow}(S_w)$ and $P_{cgo}(S_g)$. Thus:

$$\frac{\partial S_w}{\partial t} = \frac{dS_w}{dP_{cow}}\frac{\partial P_{cow}}{\partial t} = \frac{dS_w}{dP_{cow}}\left(\frac{\partial P_o}{\partial t} - \frac{\partial P_w}{\partial t}\right) \tag{7}$$

$$\frac{\partial S_o}{\partial t} = -\frac{dS_w}{dP_{cow}}\left(\frac{\partial P_o}{\partial t} - \frac{\partial P_w}{\partial t}\right) - \frac{dS_g}{dP_{cgo}}\left(\frac{\partial P_g}{\partial t} - \frac{\partial P_o}{\partial t}\right) \tag{8}$$

$$\frac{\partial S_g}{\partial t} = \frac{dS_g}{dP_{cgo}}\frac{\partial P_{cgo}}{\partial t} = \frac{dS_g}{dP_{cgo}}\left(\frac{\partial P_g}{\partial t} - \frac{\partial P_o}{\partial t}\right) \tag{9}$$

In this way we obtain three partial differential

equations with only pressures as the primary dependent variables. The complete expansion of time derivatives can be found in Aziz and Settari (1979).

Simulation Experiments

To illustrate the impact of cross-bedding on hydrocarbon recovery by solution gas drive, simulation experiments on a 3-D cross-bedded block with 2-D symmetry are exhibited. The initial fluid distribution, determined by capillary-gravity equilibrium for a rock with a single tight lamina with 35% average water saturation, is shown in Figure 1. Initial pressures are above the bubble point pressure everywhere. Because the system is under capillary-gravity equilibrium, it has capillary pressure continuity and hence the saturation distributions are discontinuous. Note that the tight rock exhibits a much higher water saturation than the high permeability rock. Boundary conditions for well representations, or flow boundaries, in the simulation system are an important consideration in this investigation. Boundary conditions are "no flow" or constant pressure drawdown with "ramping" in time to avoid excessive initial spatial truncation errors.

The fluids are depleted by constant pressure withdrawal at one face while the other faces of the block are sealed. Figure 2 shows fluid saturation distributions after 157 d of production. Shown in Figure 3 are effective permeabilities to water and oil after 157 d of production from a uniform block and a block with a single lamina, as in Figure 1. These dramatically demonstrate the impact of cross-bedding on recovery of oil. Most of the oil behind the low permeability lamina remains unproduced. Fundamentally, continuity of pressure, for each fluid phase, across the reservoir-well interface is a prime condition. This leads, of course, to the water hold-up boundary effect because of capillarity, as seen in Figure 2. Severe water build-up exists in the tight rock and at the outflow face due to the capillary end effect (Collins, 1991). Indeed, these results show very clearly that naturally occurring heterogeneities in permeability have a major impact on recovery of oil and gas.

In Figure 4 we compare oil saturation after 200 d of production from a block with a single lamina to that of a homogeneous block. Also, superimposed as a dashed line on the oil saturation plot for the block with a single lamina is the oil saturation profile at the bottom of the homogeneous block. These results show that there is considerable difference between the two cases. The heterogeneous block shows more production on the produced side of the lamina whereas the isolated part of the block is untouched. One would grossly underestimate the field size by looking at the homogeneous block.

Conclusions

Heterogeneous permeability configurations dominate reservoir behavior. Severe saturation and effective permeability discontinuities provide great numerical challenges and can only be handled by a finite element method. These effects are most dramatic in water-wet systems; the higher capillary pressures in the low permeability laminae of a cross-bedded system cause high water retention, with correspondingly low hydrocarbon permeabilities, over the entire range of average saturations. Thus, such "tight streaks" literally become permeability barriers to hydrocarbon flow and create very non-uniform reservoir drainage patterns; extensive pockets of trapped hydrocarbons result.

Flow geometry in heterogeneous reservoirs is complicated beyond the effect of absolute permeability variation. These reservoirs contain flow barriers not only because they contain sections with low absolute permeability but also because these low absolute permeability sections are filled mostly with non-mobile wetting phase. This is a direct result of the effect of absolute permeability on the relative permeability and capillary pressure properties of the rocks and the fact that hydrocarbon migration to create initial fluid distributions in water-wet reservoirs is a drainage process. Thus it is not surprising that a correct simulation of any flow process in a heterogeneous system must incorporate not only relative permeability and capillary pressure but also the effects of absolute permeability on relative permeability and capillary pressure. Further, all simulation studies in heterogeneous reservoirs which use single phase flow or a single relative permeability and capillary pressure relation are inadequate, especially if these studies are directed toward the effect of heterogeneity on flow behavior. A correct study must include all relevant phases and assign the correct capillary pressure and relative permeability relations as well as other related parameters including absolute permeability and porosity to every grid block. This is evident if actual relative

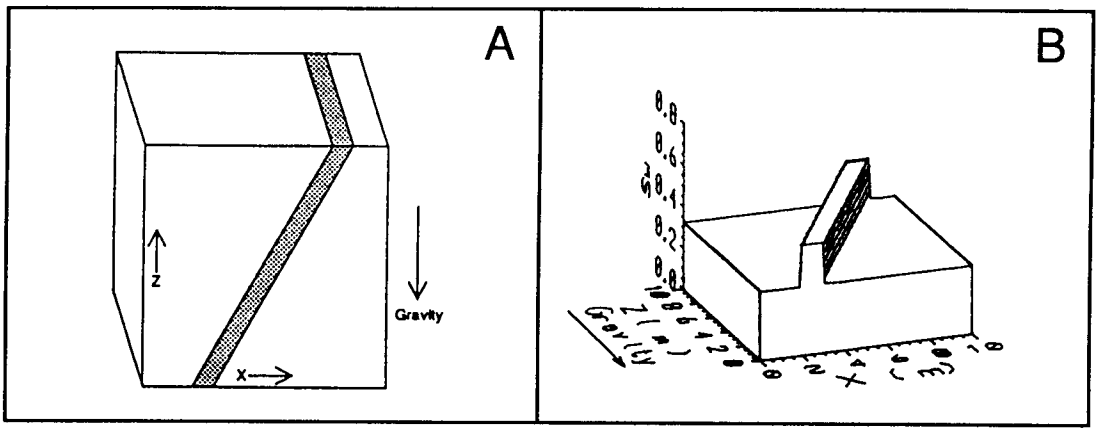

Figure 1. Cross-bedded rock specimen (A) and the corresponding initial water saturation distribution (B) used in studies.

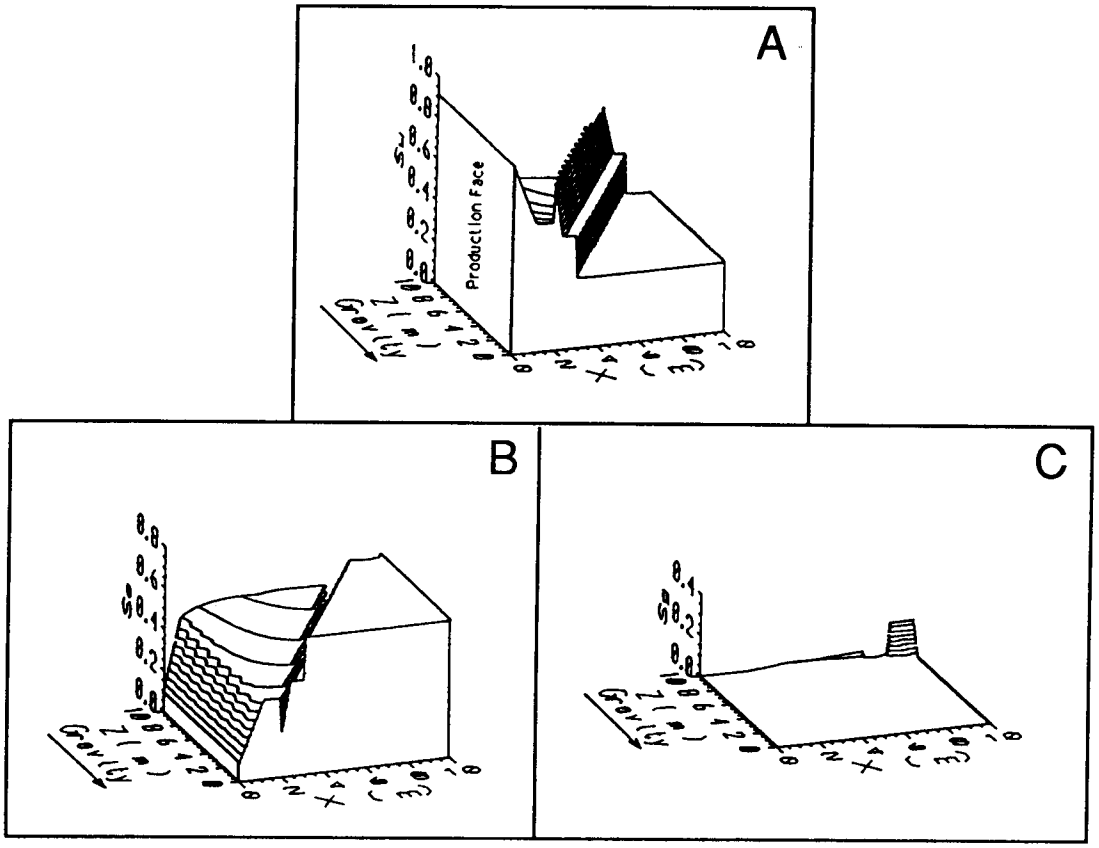

Figure 2. Water (A) oil (B) and gas (C) saturation distributions after 157 d of production from the cross-bedded rock specimen.

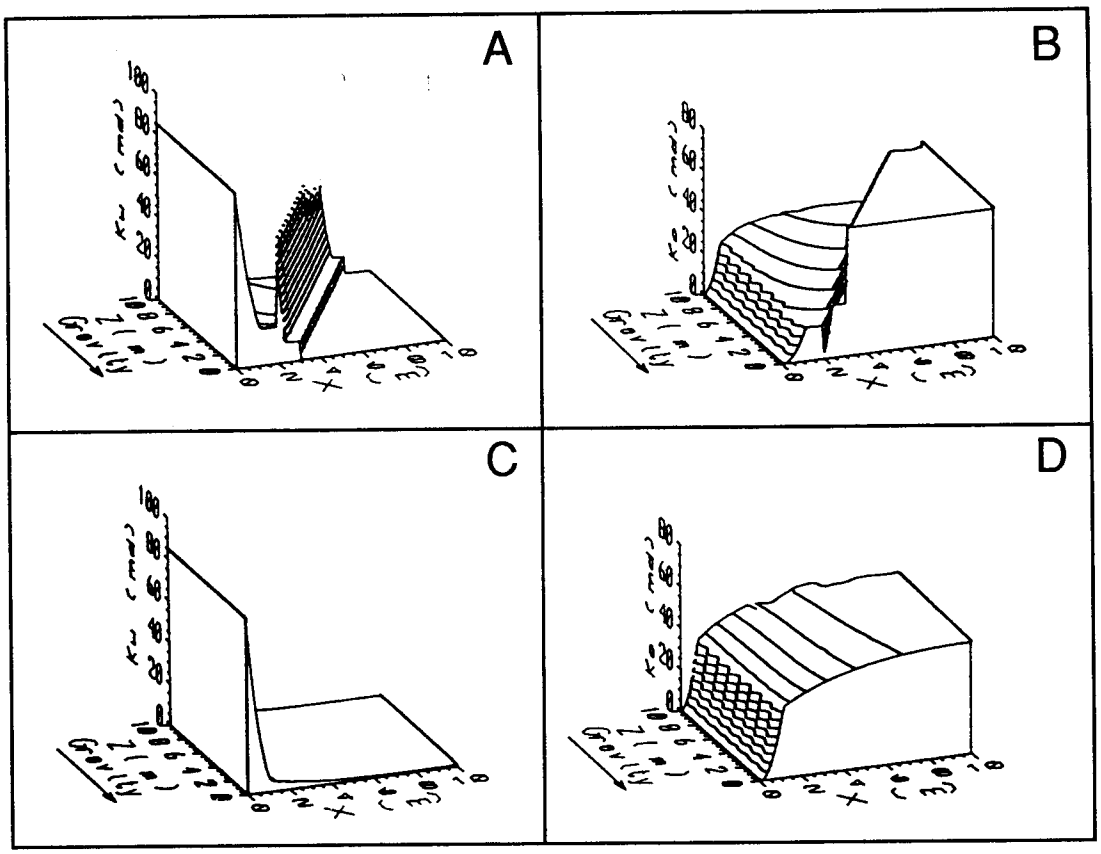

Figure 3. Comparison of effective permeabilities after 157 d of production: A (water) and B (oil) in a cross-bedded rock; C (water) and D (oil) in a homogeneous rock.

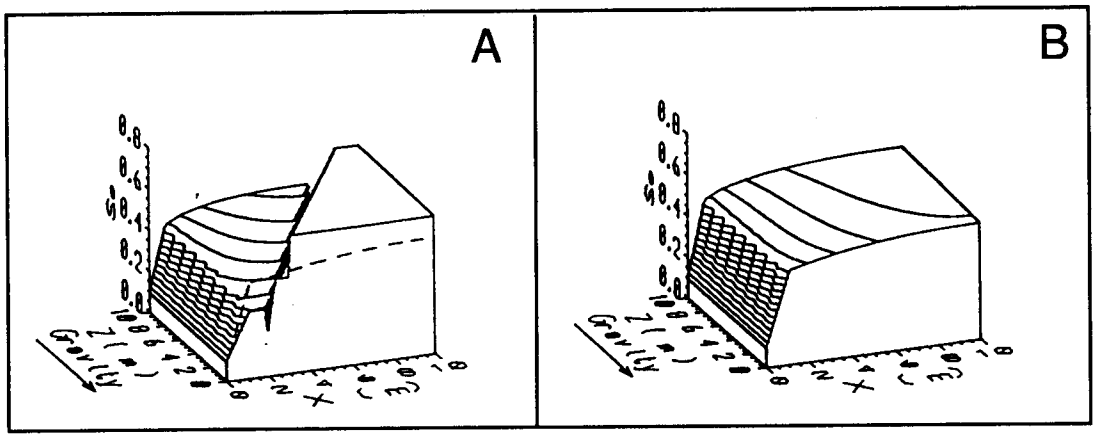

Figure 4. Oil saturation distributions after 200 d of production:
A. Cross-bedded rock; B. Homogeneous rock.

permeability and capillary pressure relations are compared for rocks of different absolute permeabilities.

It is common practice in the petroleum industry to assign uniform initial saturations and identical capillary pressures and relative permeability relations regardless of absolute permeability for heterogeneous systems. For example, Chase and Todd (1984) in their multi-layer simulation study of CO_2 flooding in which permeability varied between 0.7 millidarcies and 20 millidarcies used a single set of relative permeability and capillary pressure functions and assigned uniform initial saturations. Although this type of approach alleviates the numerical difficulties involved (saturation and effective permeability contrasts that exist in reality are greatly reduced) it does not represent real phenomena. These conventional simulation techniques are bound to be insufficient and new numerical techniques should be devised for heterogeneous systems.

Sait Kocberber is a Senior Engineer with Research & Engineering Consultants, Inc. (5445 DTC Parkway, Suite 640 Englewood, Colorado 80111, U.S.A.). He received his BS in petroleum engineering from Middle East Technical University, Turkey, his MS in petroleum engineering from Stanford University and his PhD in petroleum engineering from the University of Texas at Austin. Sait came to the U.S.A. on Turkish Government scholarships and specialized in simulation and simulator development while at university. He is now involved in developing simulation techniques for heterogeneous reservoirs, specifically oil recovery from cross-bedded systems.

Gene Collins is a physicist and mathematician by training, a petroleum engineer, biophysicist and hydrologist by avocation and a registered professional engineer in Texas. He received his BS degree form the University of Houston, his MS and PhD from the Texas A&M University, all in physics. He has forty years experience, in research positions with Exxon, Mobil, Amoco and the Texas Petroleum Research Committee, academic appointments as professor of physics and biophysics at the University of Houston, the W. A. "Monty" Moncrief Chair in Petroleum Engineering at the University of Texas at Austin and the Champlin Professorship in Petroleum Engineering at Montana Tech. He is currently the President of Research & Engineering Consultants, Inc. (5445 DTC Parkway, Suite 640 Englewood, Colorado 80111, U.S.A.). He has consulted for many large companies and government agencies over the years and has published more than 100 technical articles and books including the classic text "Flow of Fluids Through Porous Materials", first published in 1961 and later translated into Russian and Japanese. He also authored the graduate level text, "Mathematical Methods for Physicists and Engineers", published in 1968 and most recently, "Characterization of Heterogeneous Reservoirs", published in 1985.

References

Aziz, K. and A. Settari. 1979. Petroleum Reservoir Simulation. Applied Science Publishers Ltd.

Becker, E. B., G. F. Carey and J. T. Oden. 1981. Finite Elements: An Introduction. Prentice-Hall Inc.

Chase, C. A., Jr. and M. R. Todd. 1984. Numerical simulation of CO_2 flood performance. Soc. Petrol. Engr. J. v.24, pp. 597 - 605.

Collins, R. E. 1991. Flow of Fluids Through Porous Materials. Research & Engineering Consultants, Inc.

Davis, R. A., Jr. 1983. Depositional Systems. Prentice-Hall Inc.

Galloway, W. E. and D. K. Hobday. 1983. Terrigenous Clastic Depositional Systems. Springer-Verlag, Inc.

Kasap, E. and L. W. Lake. 1989. An analytical method to calculate the effective permeability tensor of a grid block and its application in an outcrop study. Paper SPE 18434 presented at the 1989 Reservoir Simulation Symposium, Houston, TX, Feb. 6-8.

Kocberber, S. and R. E. Collins. 1990. Impact of reservoir heterogeneity on initial distribution of hydrocarbons. Paper SPE 20547. Presented at 1990 SPE Annual Tech. Conf. New Orleans, LA.

Kortekaas, J. F. M. 1985. Water-oil displacement characteristics in cross-bedded reservoir zones. Soc. Petrol. Eng. J., v.25, pp. 917-926.

Lasseter, T. J., J. R. Waggoner and L. W. Lake. 1986. Reservoir heterogeneities and their influence on ultimate recovery. reservoir characterization.
(L. W. Lake and H. B. Carroll, Jr., eds.) Academic Press.

Tyler, N., W. E. Galloway, C. M. Garrett, Jr. and T. Ewing. 1984. Oil accumulations, production characteristics and targets for additional

recovery in major oil reservoirs of Texas. The University of Texas, Bureau Econ. Geol. Circ. 84-2.

Weber, K. J., R. Eijpe, D. Leiznse and C. Moens. 1972. Permeability distribution in a holocene distributary channel-fill near Leerdam (The Netherlands). Geol. en Mijnbouw, v. 51, pp. 53-62.

Weber, K. J. 1982. Influence of common sedimentary structures on fluid flow in reservoirs. J. Petrol. Tech., v. 34, pp. 667-672.

Estimation of Reservoir Parameters in Heterogeneous Gas Storage Reservoirs under Aquifer Support

by *I. Ershaghi, H. Calisgan, J. Chang*
University of Southern California
and *Y. Shikari*, GRI

Abstract

A composite model for gas storage reservoirs representing a gas bubble, transition zones and an aquifer has been formulated to study gas/water interface effects on parameter estimation. A procedure is recommended where average pressure in gas storage reservoirs may be obtained without the estimate of drainage areas and shape factors for individual wells

Introduction

For monitoring the inventory and for continuous testing of the competency of gas storage reservoirs, periodic pressure build-up and fall-off tests are needed. For a typical storage field, this may require simultaneous testing of several wells. It would be ideal if operators could afford to equip gas storage wells with permanently installed sensitive downhole pressure recorders and continuously monitor well pressure responses during routine cycles. This would provide valuable information about the condition of the wells and their interrelations. Further, one could use the information from such a data base to generate maps representing reservoir heterogeneity effects and movement of gas/water interfaces.

Because of the high cost of such an installation, compromised approaches are employed. These include methods such as monitoring wellhead pressure on all or a selected number of wells, short time bottomhole monitoring of only a few wells and spot pressure reading. Because of the influence of wellbore storage and skin on the early data, and fluid interfaces and boundary effects on the late time, recorded pressures with low resolution are often inconclusive with respect to accurate estimation of static reservoir pressure and other reservoir properties.

Gas storage reservoirs are distinguished from conventional gas reservoirs because of the cyclical nature of their operation. Gas is injected during certain periods and produced in other times providing opportunities for pressure buildup and pressure fall-off tests. A systematic monitoring plan can be implemented where data from a low pressure stage are used for the next high pressure stage or vice versa.

During the low or high pressure stages, the fluid interfaces may move, thus affecting the effective drainage volume for the wells. Further, because of interaction among wells, test results from different cycles are influenced by changing and variable drainage areas. Interaction among wells and influence of moving boundaries warrants careful examination of single-well test formulation for the interpretation of data from gas storage fields. Improved interpretation techniques need to be implemented.

Estimation of static pressure for a gas storage reservoir has traditionally been based on weighted average responses of individual wells. Pressure response to perturbation caused by withdrawal or injection (buildup or fall-off tests) in individual wells is controlled

by wellbore and near-wellbore effects, reservoir effects and boundary conditions. Within a prescribed period, when a number of wells are being tested, the response for individual wells may vary from one strongly affected by wellbore and near-wellbore effects to one representing multiple layers, and/or boundary and interface effects.

The standard practice for estimation of reservoir static pressure, $\bar{p}$, has been the extrapolation of the semilogarithmic plot of shut-in pressure vs. a dimensionless time function. Static pressure, is then estimated from consideration of drainage area and wellsite configurations (shape factor). Beside the inadequacy of pressure response data, a number of issues can interfere with the accuracy of such an approach. These include reservoir heterogeneities, layering, fluid interfaces, reservoir boundaries, and interferences among wells.

A dry gas reservoir during its lifetime may experience several periods of buildup and drawdown testing. An important characteristic of such a system is the one directional change in reservoir pressure. This change for depleting-type reservoirs follows a declining path unless it is augmented by aquifer support. For wells close to the gas/water interface, three intervals can be identified, a gas bubble, a water-invaded zone and the aquifer. The size of the water invaded zone tends to increase with time and the gas bubble will shrink.

For gas storage wells, because of the alterative periods of injection and withdrawal, the interface between gas bubble/water invaded intervals goes through an expansion/shrinkage cycle. Pressure transient tests examining the bulk of the reservoir will then characterize the location of the interface between gas bubble/water invaded at different distances from a well. But for a well in a dry gas reservoir, under aquifer support and experiencing a decreasing size bubble, the test duration to investigate the effective size of the gas bubble decreases.

The changing size of the gas bubble affects the average reservoir pressure and the drainage area. Accordingly, appropriate corrections must be made in the use of prediction methods, such as the back pressure deliverability equation. Other complications can develop where extended periods of testing are required. For example, if the formation consists of a number of layers with different permeabilities, the presence of a tight zone can result in a lag during pressure stabilization, even after extended periods of shut-in.

Statement of the Problem

Pressure buildup or fall-off test data obtained on gas storage wells, when interpreted based on a single well model in an infinite medium, are expected to follow a trend as shown in Figure 1.

Detection of the flat portion on this plot is essential in correct interpretation of the test data and estimation of reservoir properties and static reservoir pressure. This capability does not exist when the test duration is short, wellbore storage is large, or only spot pressure recordings are available. In the absence of such imperfections, and given a set of adequately designed and conducted test data, the next issue is the application of the appropriate model representing reservoir boundaries, location of the gas/water interface and interference effects among wells.

In a gas storage reservoir under water influx and efflux, the reservoir volume around each well consists of at least three, and perhaps four, intervals. These intervals are defined here only with respect to the type of fluid saturation and not the change in intrinsic properties of the reservoir. Lateral variations in permeability, porosity and thickness could by themselves create additional in-

tervals with sharp or smooth transitions superimposed upon or separate from the fluid boundaries. The problem of two fluid or reservoir intervals has been mathematically modeled by several authors, including, Guerrero and Loucks (1961), Ramey (1970) and Kazemi *et al.* (1972). For the purpose of this study, a formulation was developed for a reservoir consisting of up to four intervals. From this modeling effort, focus was directed to its implication on pressure responses obtained in gas storage wells. This analytical modeling at best could verify the response of an individual well. The question of well interference needed scrutiny by use of a numerical model. The numerical model was calibrated vs. an analytical solution.

Analytical Solution

Consider a single well in a gas storage reservoir in which four intervals surround the well. A gas bubble (I), a gas transition interval (II) where $S_w = S_{wc}$, a water transition (III) where $S_g = S_{gc}$, and the aquifer (IV) where $S_w = 1.0$ Figure 2. For intervals I and II where gas is mobile, the diffusivity equation is written using the pseudo pressure function $m(p) = 2\int_{p_b}^{p} \frac{p}{\mu(p)z(p)}dp$. For intervals III and IV, the conventional form of the diffusivity equation is used where real pressures are monitored. To establish fluid and pressure continuity among the intervals, the following boundary conditions are used:

For intervals I and II , the real gas equation may be written as :

$$\frac{1}{r}\frac{\partial}{\partial r}(r\frac{\partial m}{\partial r}) = \frac{\phi\mu_g c_g}{k_g}\frac{\partial m}{\partial t},\ r_w \leq r \leq r_2 \quad (1)$$

where $m = m(p)$.

The diffusivity equation for zones III and IV can be written as:

$$\frac{1}{r}\frac{\partial}{\partial r}(r\frac{\partial p}{\partial r}) = \frac{\phi\mu_L c_L}{k_L}\frac{\partial p}{\partial t},\ r_2 \leq r \leq r_e \quad (2)$$

With the following boundary conditions :

$$(\frac{\partial p_2}{\partial r})_{r=r_e} = 0 \quad (3)$$

$$p_1 = p_2,\ r = r_3 \quad (4)$$

$$\eta_{w_1}\frac{\partial p_1}{\partial r} = \eta_{w_2}\frac{\partial p_2}{\partial r},\ r = r_3 \quad (5)$$

$$m_2 = m(p_2),\ r = r_2 \quad (6)$$

$$\eta_{g_2}\frac{\partial m_2}{\partial r} = \eta_{w_1}\frac{\partial m(p_2)}{\partial r},\ r = r_2 \quad (7)$$

$$m_1 = m_2,\ r = r_1 \quad (8)$$

$$\eta_{g_1}\frac{\partial m_1}{\partial r} = \eta_{g_2}\frac{\partial m_2}{\partial r},\ r = r_1 \quad (9)$$

$$\frac{C}{\eta_{g_1}}\frac{\partial m_w}{\partial t} - (\frac{\partial m_1}{\partial r})_{r=r_w} = 1 \quad (10)$$

$$m_w = [m_1 - S(\frac{\partial m_1}{\partial r})]_{r=r_w} \quad (11)$$

Converting the above equations into dimensionless form , the following equations are obtained :

$$m_D = \frac{(m_i - m(r,t))}{\frac{P_{sc}q_{sc}T}{\pi k_g h T_{sc}}} \quad (12)$$

and

$$t_D = \frac{k_a t}{(\phi\mu c)_{g_1} r^2{}_w} \quad (13)$$

for the gas (I) and the gas transition (II) intervals,

$$\frac{1}{r_D}\frac{\partial}{\partial r_D}(r_D\frac{\partial m_{1_D}}{\partial r_D}) = \frac{1}{k_{r_{g_1}}}\frac{\partial m_{1_D}}{\partial t_D} \quad (14)$$

$$\frac{1}{r_D}\frac{\partial}{\partial r_D}(r_D\frac{\partial m_{2_D}}{\partial r_D}) = \frac{1}{k_{r_{g_2}}\frac{\mu_{g_1}}{\mu_{g_2}}}\frac{\partial m_{2_D}}{\partial t_D}, \quad (15)$$

and the dimensionless pressure equations for intervals (I) and (II) are:

$$p_D = \frac{(p_i - p(r,t))}{\frac{q\mu_w}{2\pi k_w h}} \quad (16)$$

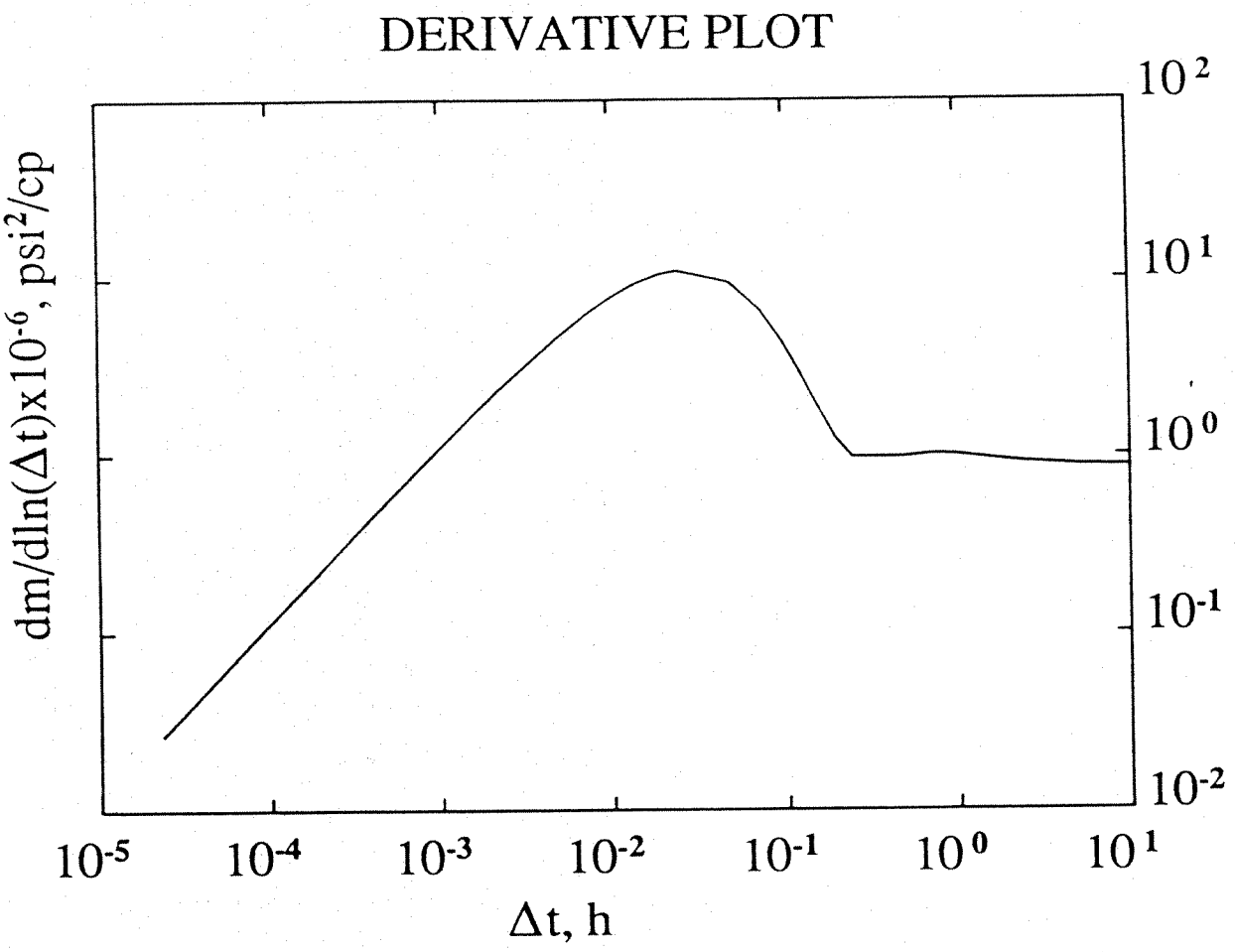

Figure 1 Pressure derivative plot for an infinite acting well

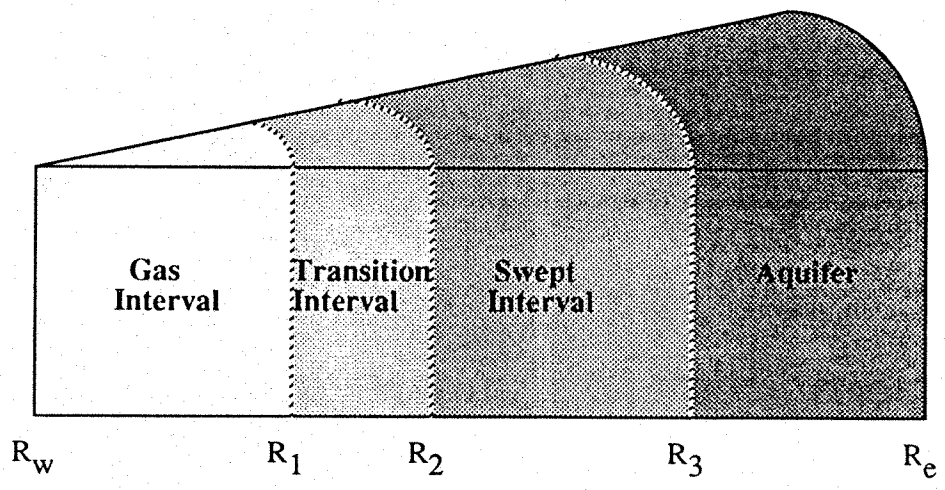

Figure 2 Schematic of the composite reservoir

$$\frac{1}{r_D}\frac{\partial}{\partial r_D}(r_D\frac{\partial p_{1_D}}{\partial r_D}) = \frac{1}{k_{r_{w_1}}\frac{\mu_{g_1}}{\mu_{w_1}}}\frac{\partial p_{1_D}}{\partial t_D} \quad (17)$$

$$\frac{1}{r_D}\frac{\partial}{\partial r_D}(r_D\frac{\partial p_{2_D}}{\partial r_D}) = \frac{1}{k_{r_{w_2}}\frac{\mu_{g_1}}{\mu_{w_2}}}\frac{\partial p_{2_D}}{\partial t_D}. \quad (18)$$

Expressing them in the Laplace domain, we obtain :

For intervals (I) and (II):

$$\frac{d^2\bar{m}_{1_D}}{dr_D{}^2} + \frac{1}{r_D}\frac{d\bar{m}_{1_D}}{dr_D} = \frac{s}{\eta_{g_1}}\bar{m}_{1_D},\ 1 \leq r_D \leq r_{1D} \quad (19)$$

$$\frac{d^2\bar{m}_{2_D}}{dr_D{}^2} + \frac{1}{r_D}\frac{d\bar{m}_{2_D}}{dr_D} = \frac{s}{\eta_{g_2}}\bar{m}_{2_D},\ r_{1D} \leq r_D \leq r_{2D} \quad (20)$$

and for the intervals (III) and (IV):

$$\frac{d^2\bar{p}_{1_D}}{dr_D{}^2} + \frac{1}{r_D}\frac{d\bar{p}_{1_D}}{dr_D} = \frac{s}{\eta_{w_1}}\bar{p}_{1_D},\ r_{2D} \leq r_D \leq r_{3D} \quad (21)$$

$$\frac{d^2\bar{p}_{2_D}}{dr_D{}^2} + \frac{1}{r_D}\frac{d\bar{p}_{2_D}}{dr_D} = \frac{s}{\eta_{w_2}}\bar{p}_{2_D},\ r_{3D} \leq r_D \leq r_{e_D}. \quad (22)$$

Boundary conditions in dimensionless Laplace domain are :

$$(\frac{\partial\bar{p}_{2_D}}{\partial r_D})_{r_D=r_{e_D}} = 0 \quad (23)$$

$$\bar{p}_{1_D} = \bar{p}_{2_D},\ r_D = r_{3_D} \quad (24)$$

$$\eta_{w_1}\frac{\partial\bar{p}_{1_D}}{\partial r_D} = \eta_{w_2}\frac{\partial\bar{p}_{2_D}}{\partial r_D},\ r_D = r_{3_D} \quad (25)$$

$$\bar{m}_{2_D} = \bar{m}_D(\bar{p}_{2_D}),\ r_D = r_{2_D} \quad (26)$$

$$\eta_{g_2}\frac{\partial\bar{m}_{2_D}}{\partial r_D} = \eta_{w_1}\frac{\partial\bar{m}_D(\bar{p}_{2_D})}{\partial r_D},\ r_D = r_{2_D} \quad (27)$$

$$\bar{m}_{1_D} = \bar{m}_{2_D},\ r_D = r_{1_D} \quad (28)$$

$$\eta_{g_1}\frac{\partial\bar{m}_{1_D}}{\partial r_D} = \eta_{g_2}\frac{\partial\bar{m}_{2_D}}{\partial r_D},\ r_D = r_{1_D} \quad (29)$$

$$C_D\frac{s}{\eta_{g_1}}\bar{m}_{w_D} - (\frac{\partial\bar{m}_{1_D}}{\partial r_D})_{r_D=1} = \frac{1}{s} \quad (30)$$

$$\bar{m}_{w_D} = \left[\bar{m}_{1_D} - S(\frac{\partial\bar{m}_{1_D}}{\partial r_D})\right]_{r_D=1}. \quad (31)$$

The solution to the above equations in terms of the Bessel equation is :

$$\bar{m}_{1_D} = AI_0(r_D\sqrt{\frac{s}{\eta_{g_1}}}) + BK_0(r_D\sqrt{\frac{s}{\eta_{g_1}}}) \quad (32)$$

$$\bar{m}_{2_D} = CI_0(r_D\sqrt{\frac{s}{\eta_{g_2}}}) + DK_0(r_D\sqrt{\frac{s}{\eta_{g_2}}}) \quad (33)$$

$$\bar{P}_{1_D} = EI_0(r_D\sqrt{\frac{s}{\eta_{w_1}}}) + FK_0(r_D\sqrt{\frac{s}{\eta_{w_1}}}) \quad (34)$$

$$\bar{P}_{2_D} = GI_0(r_D\sqrt{\frac{s}{\eta_{w_2}}}) + HK_0(r_D\sqrt{\frac{s}{\eta_{w_2}}}) \quad (35)$$

Applying the boundary conditions, we can obtain the coefficients A, B, C, D, E, F, G, and H. The numerical solution was then obtained using the algorithm of Stehfest (1970).

Drawdown response of a single well producing from such a composite reservoir is generated and shown in Figure 3A. For comparison purposes, the case of a bounded single phase gas reservoir is also shown in Figure 3B. The reservoir boundary is at $r_{eD} = 1000$ and the intervals are at dimensionless distances shown on the graph. Three cases are compared with the base case, these include gas in interval I and water in the next three intervals, gas in interval I, a gas transition zone with $S_g = .30$ and water in the next two intervals, and finally a gas transition interval with $S_g = .50$. The pressure derivative plot shows the distinct breaks in the pattern exhibiting fluid interfaces. The nature of this plot thus differs for individual well tests depending on their proximity to the gas/water interface. For any particular well the pattern for the low pressure stage will be different from that for the high pressure case.

Study of well interference effects during multiple well buildup or fall-off tests can best be done using a numerical solution approach. A gas reservoir simulator was used for this purpose. The simulator was first calibrated against the analytical solution. Figure 4 shows a comparison for a dry gas reservoir.

(3A)

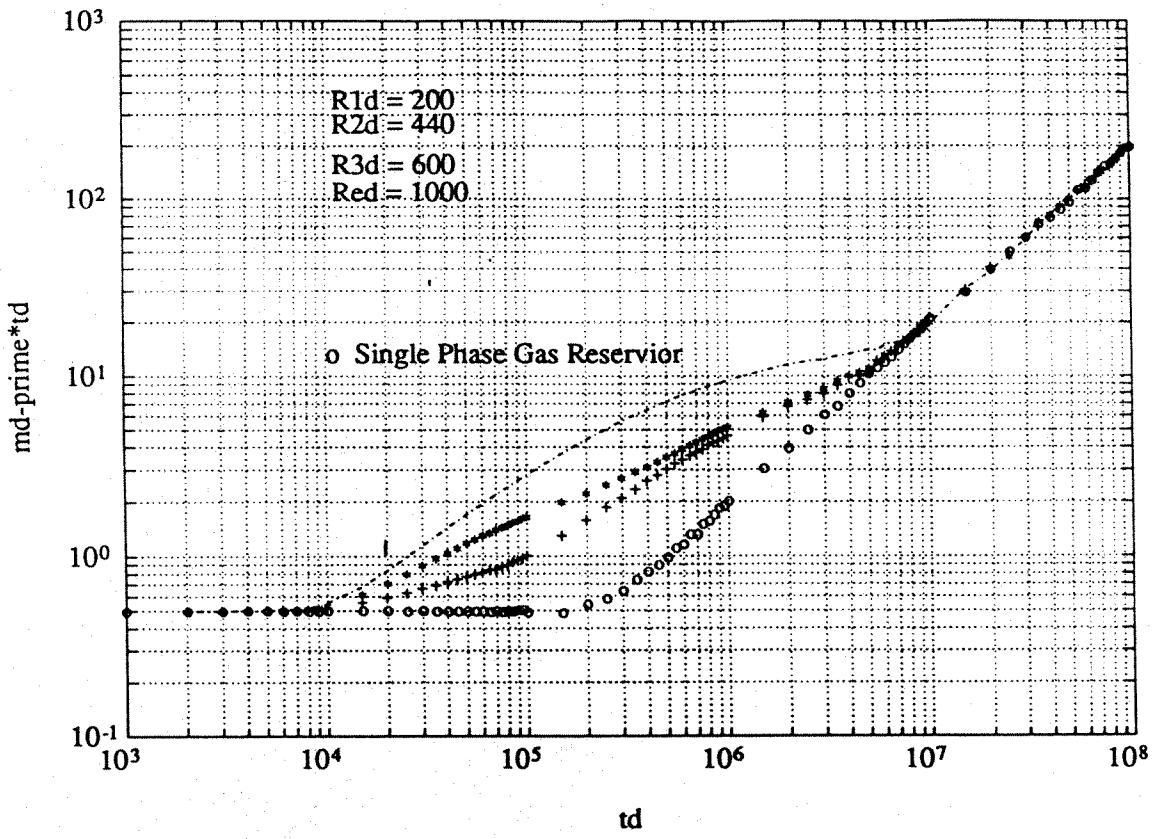

(3B)

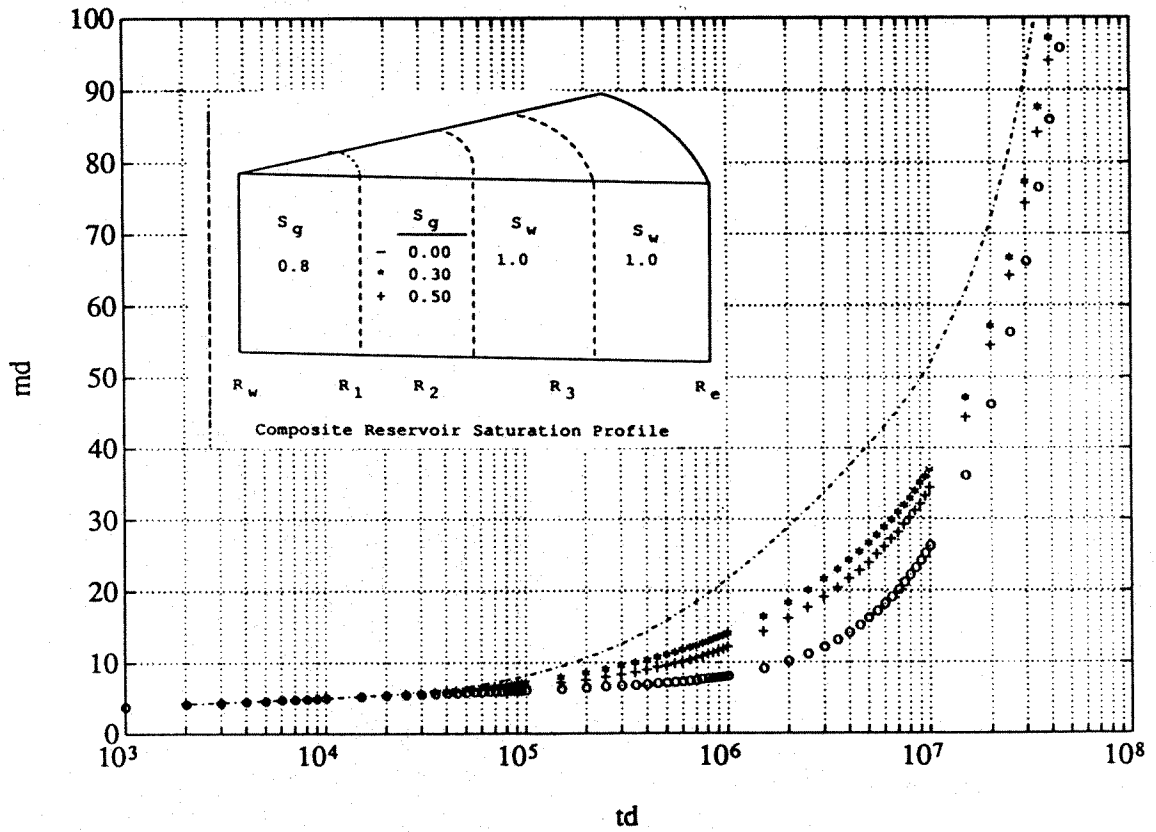

Figure 3 Pressure response for four composite cases

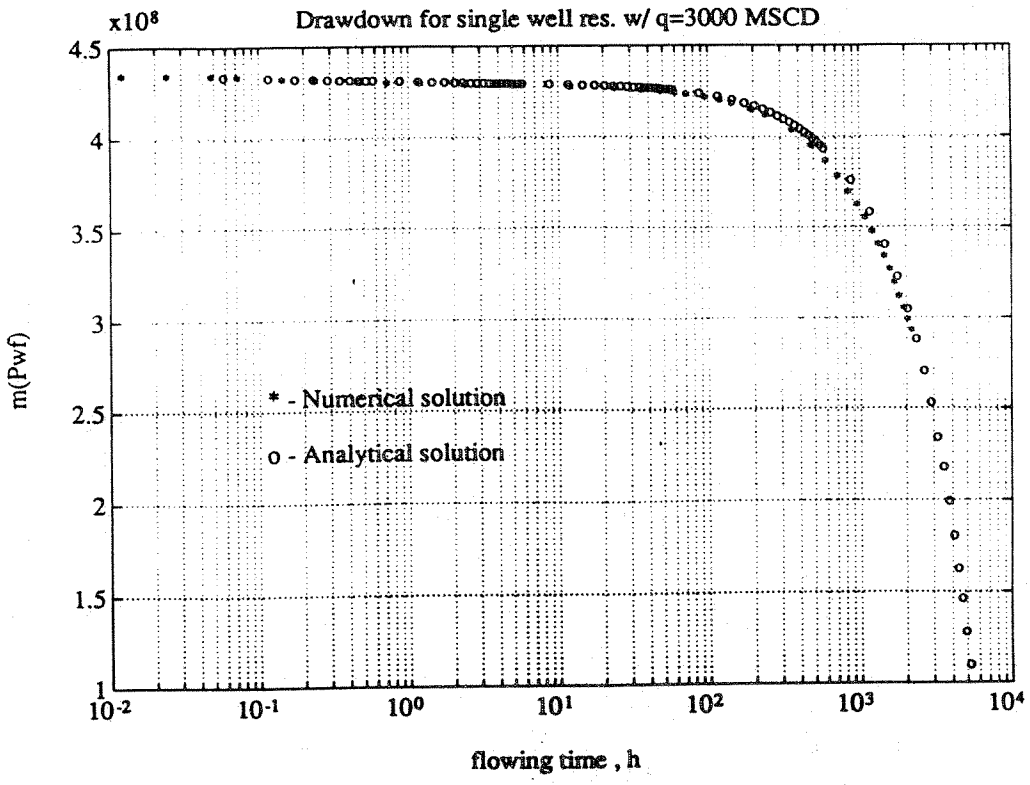

Figure -4 Comparision of analytical and the numerical solution for a single well

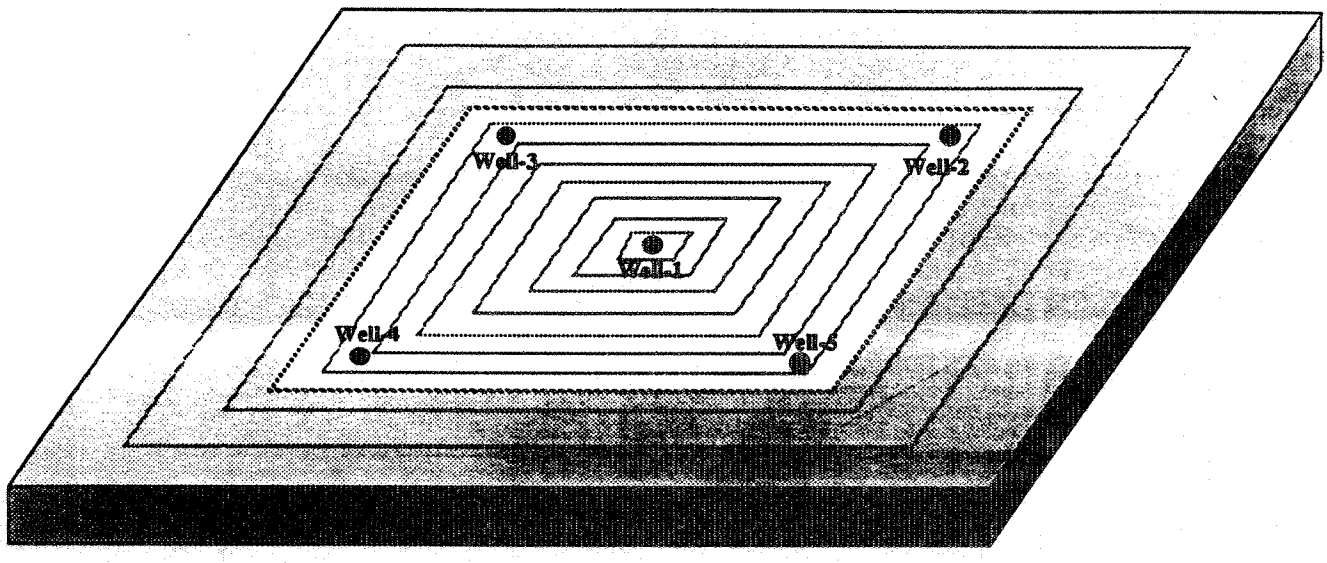

Figure 5 - General well configuration for interference and aquifer studies

The two solutions compare well, and the negligible departures found, when the reservoir boundaries are felt are because of differences between the circular nature of boundary for the analytical cases and the square shape used for the numerical model.

The simulator was used to study the behavior of a number of wells simultaneously being tested under different wellbore, reservoir and boundary conditions. Figure 5 shows the location of five wells used in these case studies. Sensitivity studies were conducted using variations in reservoir fluid interfaces, reservoir permeability, wellbore storage, skin and producing rates.

Using a software developed at the University of Southern California (USCGAS), the pressure responses generated for individual wells were analyzed and estimation of average pressure, permeability, skin and wellbore storage obtained from well test analyses were compared with those used in the simulation.

One of the issues of primary concern was the estimation of static reservoir pressure. The conventional method practiced by the gas industry consists of estimating static pressure for individual wells and obtaining the reservoir pressure using a weighted average approach. For the success of the method, one needs an estimation of drainage area and the shape factor for individual wells.

Because in gas storage reservoirs, periodic tests are conducted during the high and low pressure stages, an estimation of static pressure from one stage can be used to arrive at static pressure for a successive stage using a procedure proposed by Odeh and Al-Hussainy (1971). The only requirement is that the production or the injection period should be long enough to achieve a pseudo-steady state condition. This procedure needs only an estimation of shape factor, P^* and m' (slope of semilog plot of pressure data) as given below:

$$\frac{m(p_i) - m(p^*)}{m'} = \frac{m(p_i) - m(p_s)}{m'} - \log \frac{m(p_i) - m(p_s)}{m'} - \log C_A + 0.74 \quad (36)$$

While the requirement for the size of the drainage area of individual wells is apparently eliminated, one still has to estimate the shape factors. This requires an estimation of the location and the boundaries of the drainage areas.

A composite plot approach was suggested by Guppy *et al.* (1988) from work done for the American Gas Association. These authors, however, did not incorporate the effects of wellbore storage, skin and fluid boundaries. In the current study the composite plot procedure was examined more carefully for its applicability and under realistic conditions. Certain improvements have also been incorporated in the procedure to correct for pressure dependent variables among wells.

The basis for the method is the development of a composite plot incorporating data from all interfering wells and representing the entire well count by a pseudo well. The location of the psuedo well is computed at the center of gravity of the field. Pressure buildup or fall-off data for individual wells are averaged, as shown below:

$$m(p)_{(\Delta t)_i} = \frac{\sum_{j=1}^{J=n} q_j m(p)_{(\Delta t)_{(i)}}}{\sum_{j=1}^{j=n} q_j} = \frac{\sum_{j=1}^{j=n} q_j m(p)_{\Delta t_i}}{Q_t} \quad (37)$$

where j refers to the wells and i is the time step.

The location of the pseudo well is estimated from the following equations:

$$x = \sum_{j=1}^{j=n} \frac{q_j x_j}{Q_t} \quad (38)$$

$$y = \sum_{j=1}^{j=n} \frac{q_j y_j}{Q_t} \quad (39)$$

Based on the location of the pseudo well with respect to the reservoir as a whole, a shape factor is computed using the method of images and assuming a pseudo steady state prevails in the reservoir.

From the derivative plot and the semilog plot, the correct slope, m', is estimated and $\bar{p}$ is obtained using the Odeh and Al-Hussainy (1971) proposed procedure. For estimation of permeability, skin and wellbore storage average properties as formulated below are used:

$$\gamma = \sum_{j=1}^{j=n} \frac{q_j \gamma_j}{Q_t} \quad (40)$$

$$\phi = \sum_{j=1}^{j=n} \frac{\phi_j V_j}{V_t} \quad (41)$$

$$r_w = \frac{\sum_{j=1}^{j=n} (r_w)_j}{n} \quad (42)$$

Case Studies

Basic input data used for simulation studies are shown in Table 1. Results obtained for a number of cases are summarized in Tables 2 and 3. In general, in all cases where by the virtue of large producing time or high permeability, computations were done for large values of t_{DA} of satisfying the pseudo steady state condition, the composite method produced $\bar{p}$ similar to the one obtained from gas reservoir simulators.

The derivative plots for individual wells show deviations from the expected behavior of a single well and this is attributed to interference among wells. For a single well with and without aquifer support, Figures 6A and 6B show the influence of the gas/water interface on the derivative plot. Adding a second well to the reservoir introduces interference effects as seen in Figures 6C to 6D. For a 5-well case, we studied a number of reservoir and well properties. For the case of uniform permeability with no water influx, as shown in Figure 7, derivative plots for individual wells differ depending on location and boundary effects. The composite plot results in correct estimation of $\bar{p}$ and the slight difference between the computed k and assumed k is attributed to approximation in conversion of pressure, p, to the pseudo pressure, $m(p)$. A similar case but with the influence of an aquifer, was also analyzed. The derivative plots exhibit the lateral change in fluid mobility before the reservoir boundaries are felt Figure 8. Studies with low permeability and for the same producing time resulted in a deviation of estimated $\bar{p}$ from that obtained from the simulator. This is caused by insufficient duration of flow. Behavior of a reservoir with a totally random permeability distribution but within a given range was also studied. Significant changes in the trends of the derivative plots were observed as affected by local permeabilities. The composite plot results in a smooth trend.

We further studied the effect of variable rate with and without water influx. The behavior of individual wells was different on the derivative plot. A smooth plot is obtained for the composite case resulting in a fairly good estimate of $\bar{p}$ and reservoir permeability.

For a heterogeneous reservoir with individual wells each behaving differently, the estimation of $\bar{p}$ from the composite plot is improved with increasing number of wells being monitored and incorporated in the calculation. One significant advantage of this method is the need for estimation of only one shape factor for the pseudo well and elimination of the need to guess the drainage areas and shape factors for individual wells.

To study the effect of water influx and efflux, a 5-well reservoir was modeled with water invasion, and then the wells were shut in for a pressure build-up test. After a period

Table 1 Simulation input data for both aquifer supported ans dry gas

Aq. Support	Dry Gas	Parameters					
Well ID	Well ID	k, md	skin	C, bbls/psi	Q, MSCFD	# of wells	C_A
1z2k2	1z1k2	25	20	0.01	1000	1	31
2z2k2w1	2z1k2w1	25	20	0.01	1000	1	8.8
2	2	"	"	"	"	2	19.1
z2k2w1	z1k2w1	25	20	0.01	1000	1	31
2	2	"	"	"	"	2	26
3	3	"	"	"	"	3	"
4	4	"	"	"	"	4	"
5	6	"	"	"	"	5	"
z2k4w1	z1k4w1	25	1	0.01	3000	1	18
2	2	"	5	"	2000	2	23
3	3	"	10	"	1500	3	12
4	4	"	15	"	1000	4	0.7
5	5	"	20	"	500	5	"
z2p5w1	z1p5w1	33.37	5	0.01	2000	1	8.3
2	2	31.43	10	"	1500	2	1.3
3	3	15.09	20	"	500	3	0.03
4	4	19.20	15	"	1000	4	4.0
5	5	47.94	1	"	3000	5	26.0

Table 2 Comparison of computation from the single well and composite well studies with simulation results without aquifer support

Well ID	k, md	skin	C, bbls/psi	est. p_{avg}, psi	sim. $p_{stab.}$, psi	C_A
1Z1K2	25	20	.0092	2482.2	2482.6	31
2Z1K2W1	24	20	.0092	2468	2466.1	8.8
2	25	20	"	2461.5	"	19.1
Comp	20	16	.0095	2466.0	"	20.9
Z1K2W1	23	18.0	.0109	2412	2414.2	31
2	22	17.5	.0112	2415	"	26
3	"	"	.0091	"	"	"
4	"	"	.0094	"	"	"
5	"	"	"	"	"	"
Comp	"	17.4	.0096	2413.7	"	31
Z1K4W1	22	2.2	.0096	2361	2360.2	18
2	25	6.3	.0092	2353	"	23
3	23	9.5	.0093	2359	"	12
4	25	15.1	.0094	2372	"	0.7
5	26	20.0	.0096	2370	"	0.7
Comp	18	5.1	.0084	2355.7	"	29
Z1P5W1	31.8	5.8	.0116	2353	2360.4	8.3
2	31.3	10.5	.0119	2366	"	1.3
3	14.2	18.2	.0092	2389	"	0.03
4	19.3	15.3	.0112	2370	"	4.0
5	47.5	2.5	.0103	2322	"	26.0
Comp	15.0	3.4	.0086	2357.7	"	26.4

Table 3 Comparison of computation from the single well and composite well studies with simulation results with aquifer support

Well ID	k, md	skin	C, bbls/psi	est. p_{avg}, psi	sim. $p_{stab.}$, psi	C_A
1Z2K2	24	19	.0097	2453.4	2453.8	31
2Z2K2W1	22	18	.0094	2409.5	2406.0	8.8
2	20	16	.0081	2401.0	"	1.9
Comp	20	16	.0097	2403.0	"	10
Z2K2W1	22	17.0	.0094	2266	2264.0	31
2	21	16.2	."	2265	"	2.7
3	"	"	.0096	"	"	"
4	"	"	.0098	"	"	"
5	"	"	.0093	"	"	"
Comp	22	17.2	.0098	2259.2	"	31
Z2K4W1	23	2.1	.0104	2124	2120.5	18
2	22	5.1	.0098	2120	"	0.8
3	26	10.5	.0088	2115	"	2.1
4	24	14.2	.0097	2127	"	3.8
5	29	21.3	.0096	2133	"	12
Comp	22	6.0	.0088	2108.9	"	27
Z2P5W1	32.3	5.5	.0101	2121	2120.9	8.3
2	31.2	10	.0116	2124	"	0.5
3	14.7	18	.0115	2142	"	19
4	19.6	15	.0113	2137	"	0.4
5	50.3	2	.0106	2072	"	0.5
Comp	15.5	3.3	.0099	2108.5	"	20

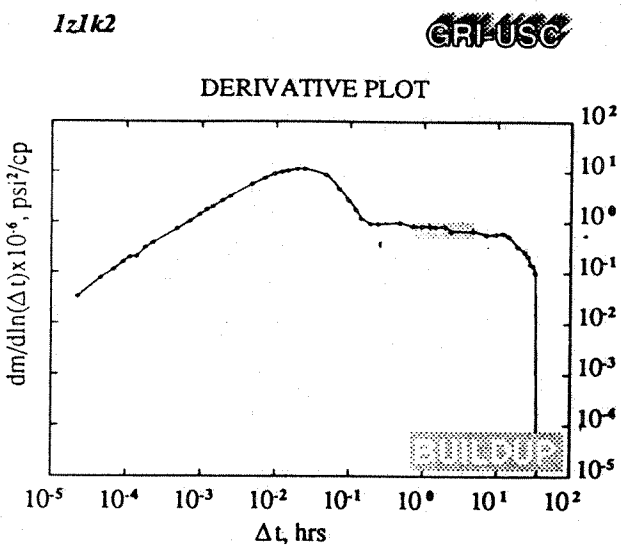

Figure -6A Behavior of a single well without aquifer support

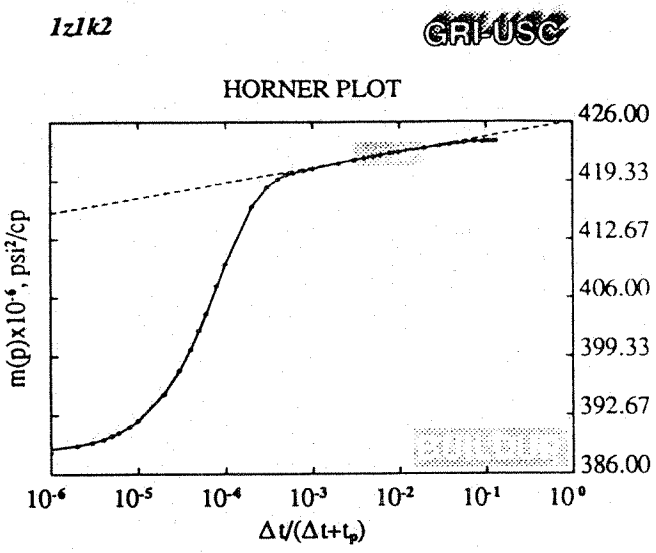

slope= 1.73, k= 25.05md, skin= 20.17
m(p*)=426.04, p*= 2489 psi, CA=30.88
Ramey-Cobb: $m(p_{avg})$=423.98, p_{avg}= 2483 psi
Odeh: m(ps)=423.86, ps=2482.21 psi

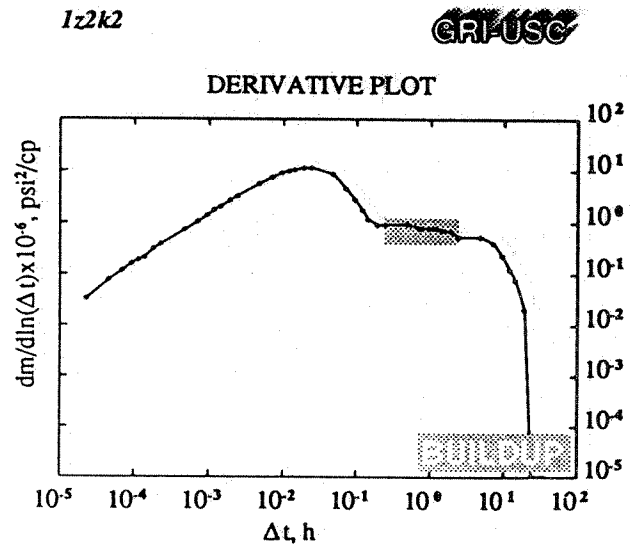

Figure -6B Behavior of a single well with aquifer

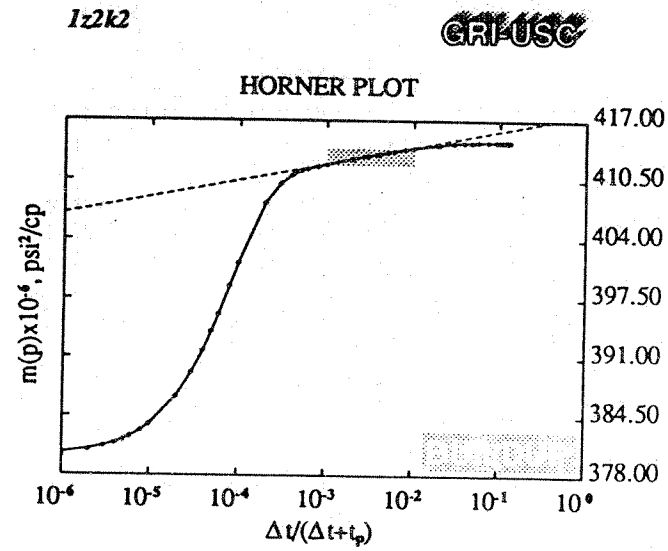

slope= 1.81, k= 23.83md, skin= 19.01
m(p*)=417.72, p*= 2463 psi, CA=30.88
Ramey-Cobb: $m(p_{avg})$=414.79, p_{avg}= 2454 psi
Odeh: m(ps)=414.71, ps=2453.41 psi

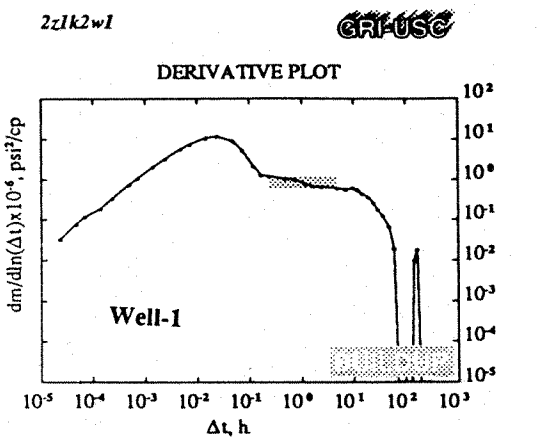

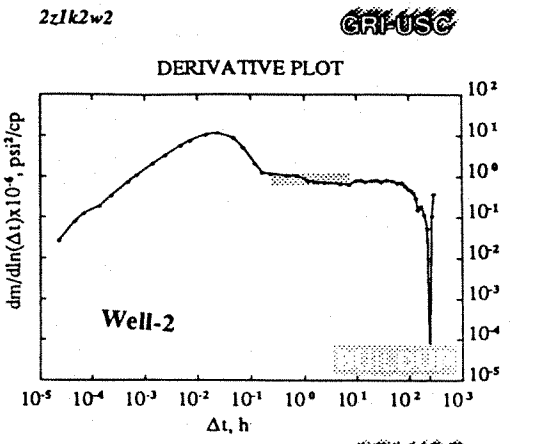

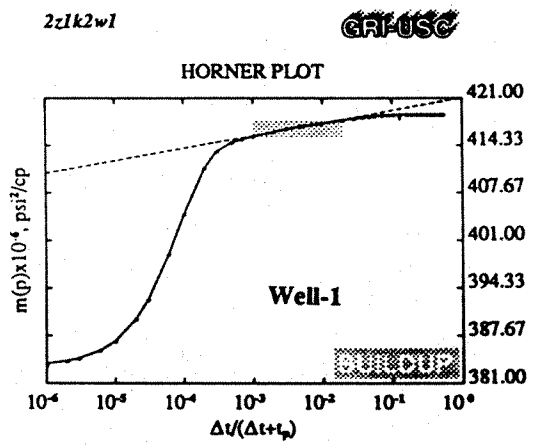

slope= 1.77, k= 24.42md, skin= 19.55
m(p*)=421.04, p*= 2473 psi, CA= 8.83
Ramey-Cobb: m(p_{avg})=419.37, p_{avg}= 2468 psi
Odeh: m(ps)=419.33, ps=2467.98 psi

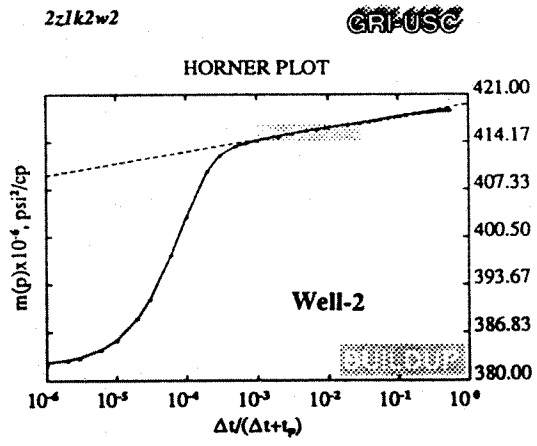

slope= 1.72, k= 25.12md, skin= 20.15
m(p*)=419.67, p*= 2469 psi, CA=19.09
Ramey-Cobb: m(p_{avg})=417.45, p_{avg}= 2462 psi
Odeh: m(ps)=417.27, ps=2461.51 psi

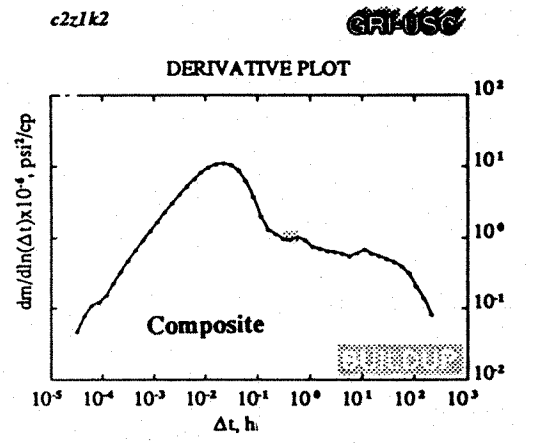

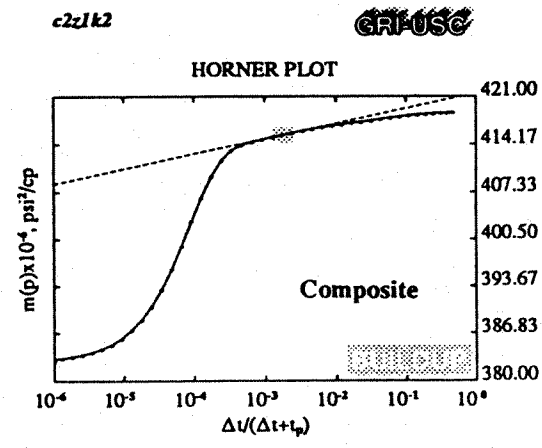

slope= 2.16, k= 20.04md, skin= 15.82
m(p*)=421.46, p*= 2475 psi, CA=20.86
Ramey-Cobb: m(p_{avg})=418.80, p_{avg}= 2466 psi
Odeh: m(ps)=418.70, ps=2465.99 psi

Figure -6C Behavior of a two well system without aquifer

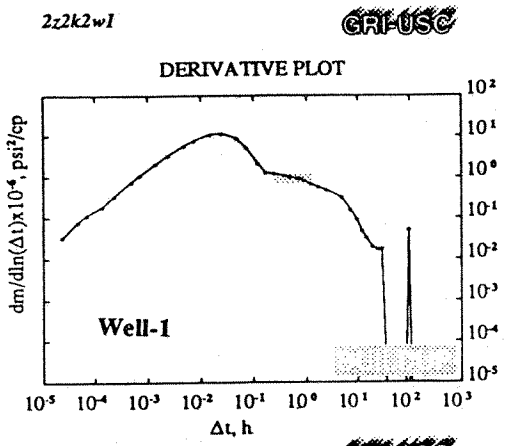

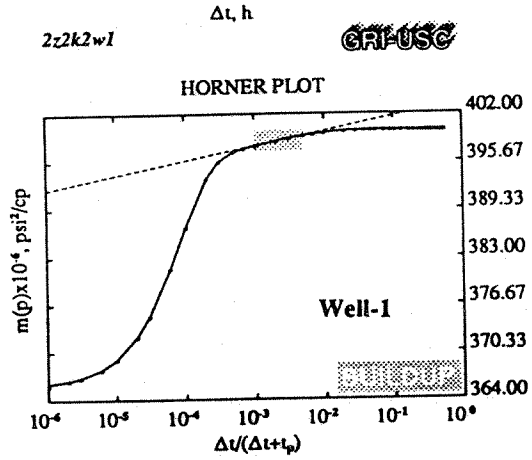

slope= 1.92, k= 22.46md, skin= 17.71
m(p*)=403.57, p*= 2418 psi, CA= 8.76
Ramey-Cobb: m(p_{avg})=400.98, p_{avg}= 2410 psi
Odeh: m(ps)=400.92, ps=2409.53 psi

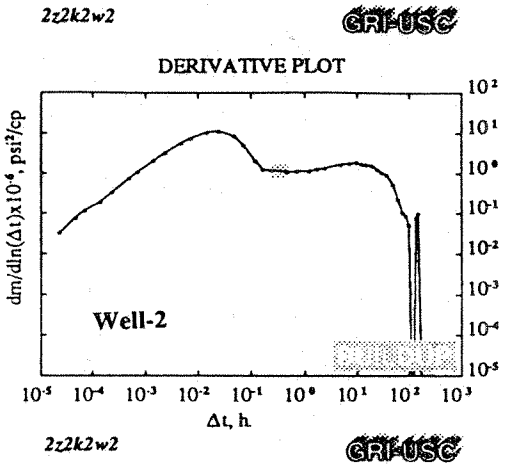

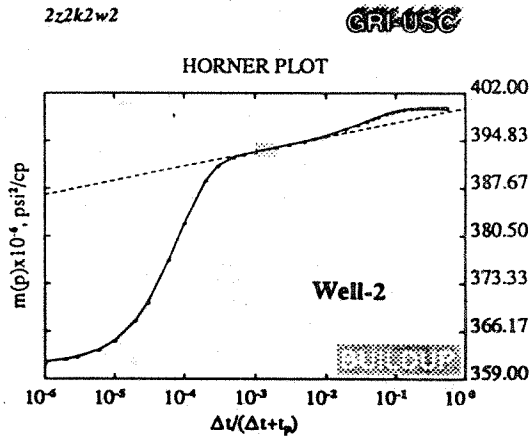

slope= 2.18, k= 19.86md, skin= 15.55
m(p*)=399.74, p*= 2406 psi, CA= 1.85
Ramey-Cobb: m(p_{avg})=398.40, p_{avg}= 2401 psi
Odeh: m(ps)=398.25, ps=2400.96 psi

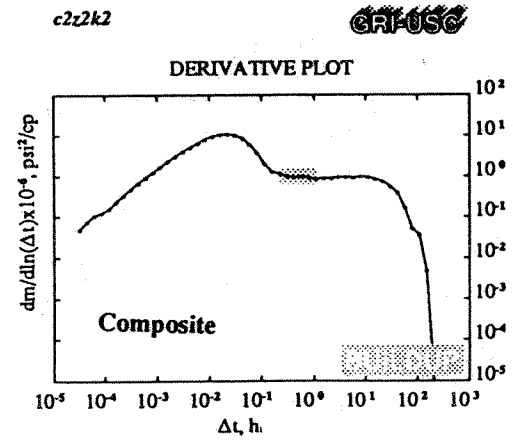

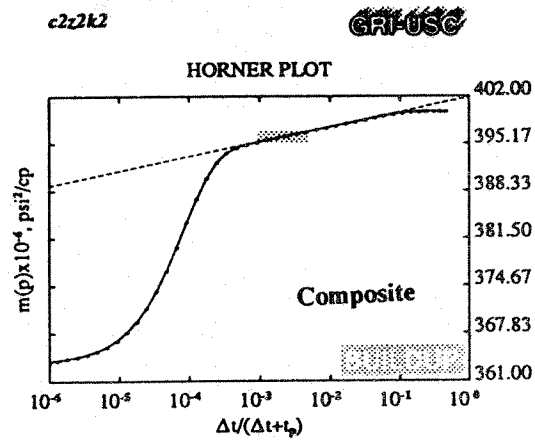

slope= 2.13, k= 20.28md, skin= 15.89
m(p*)=401.88, p*= 2413 psi, CA= 9.68
Ramey-Cobb: m(p_{avg})=399.02, p_{avg}= 2403 psi
Odeh: m(ps)=398.89, ps=2403.02 psi

Figure -6D Example of a two well system under aquifer support

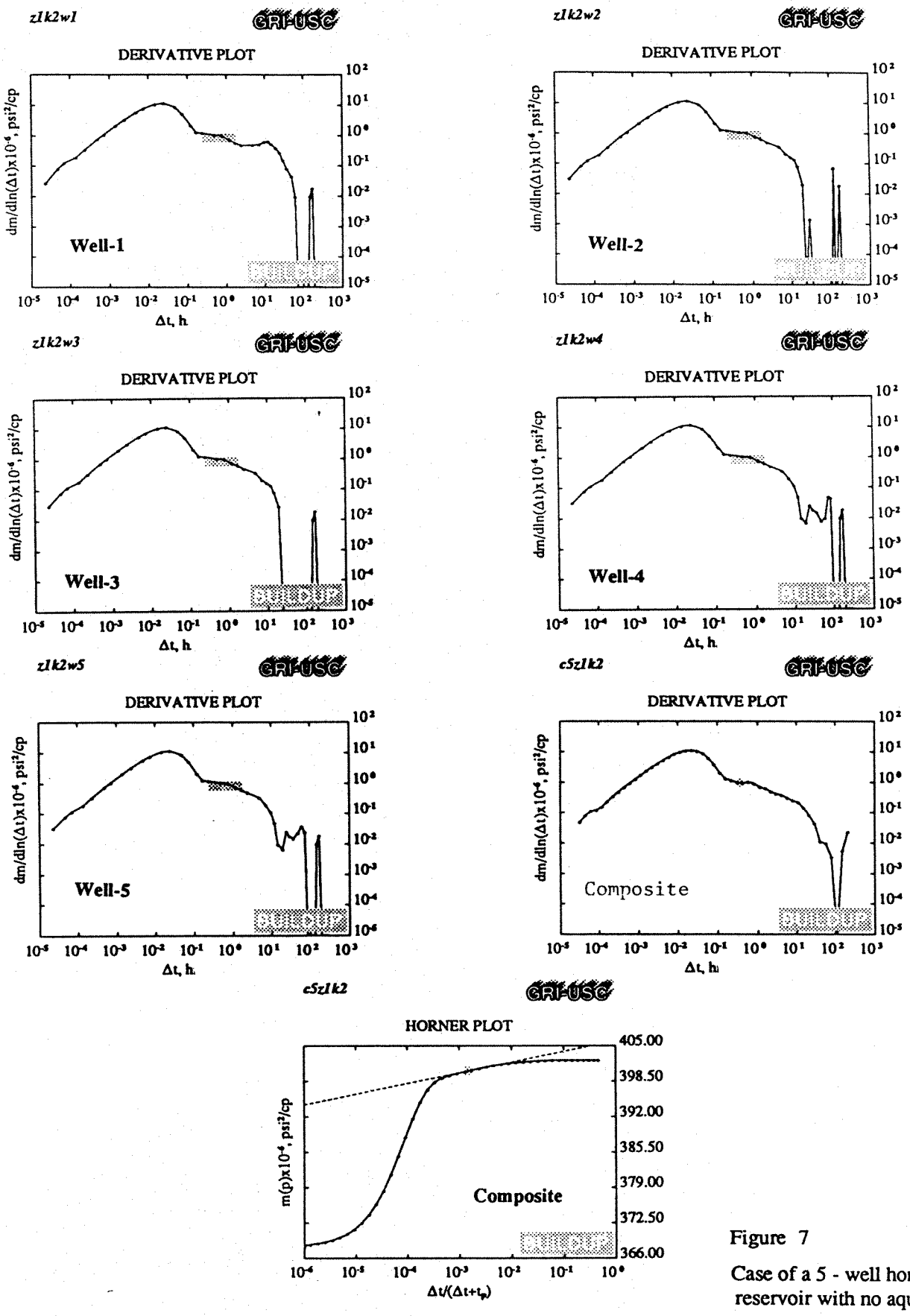

slope= 1.96, k= 22.09md, skin= 17.42
m(p*)=405.93, p*= 2426 psi, CA=30.88
Ramey-Cobb: $m(p_{avg})$=402.34, p_{avg}= 2414 psi
Odeh: m(ps)=402.22, ps=2413.70 psi

Figure 7

Case of a 5 - well homogeneous reservoir with no aquifer support

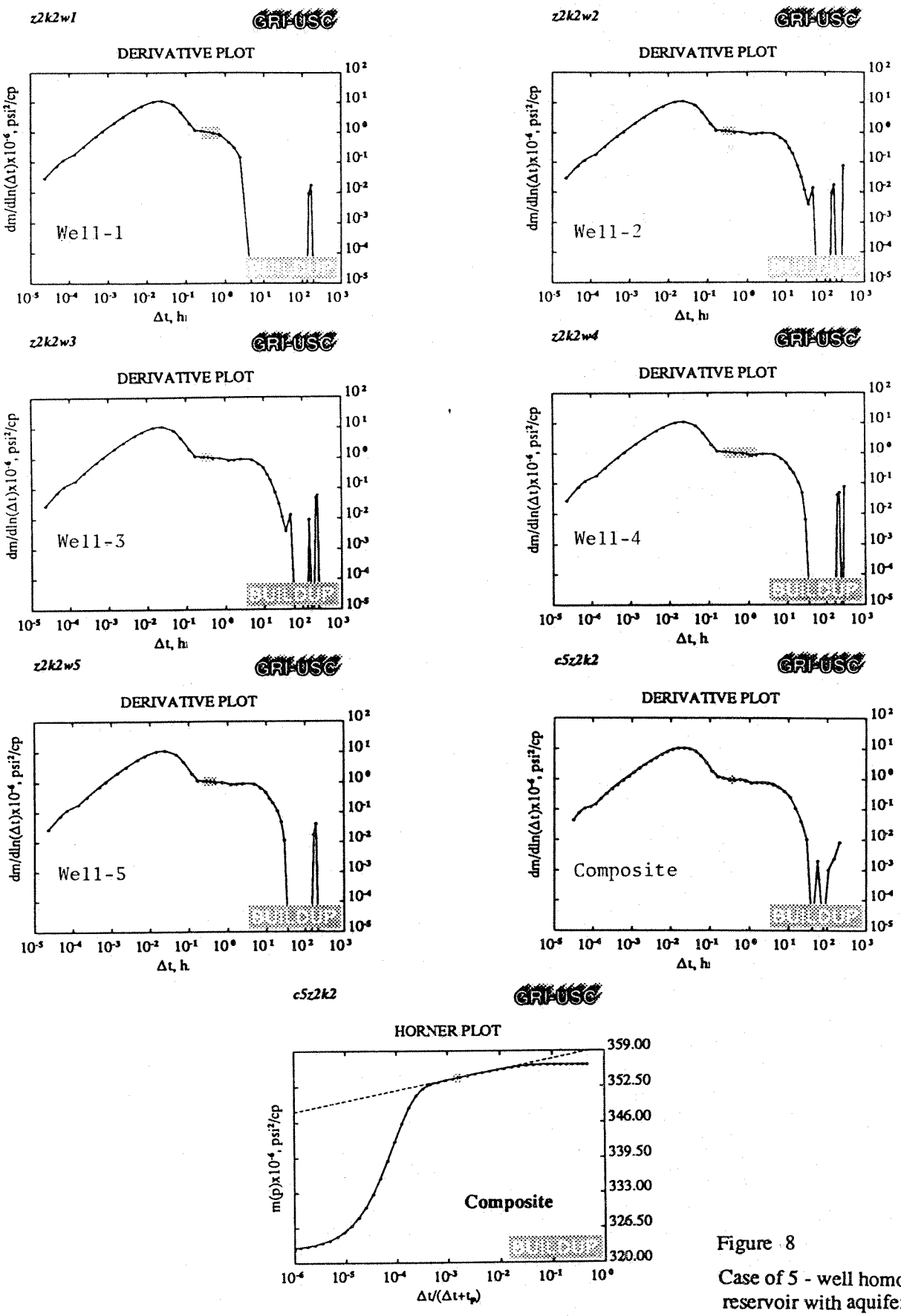

slope= 1:94, k= 22.24md, skin= 17.16
m(p*)=359.59, p*= 2274 psi, CA=30.88
Ramey-Cobb: $m(p_{avg})$=355.18, p_{avg}= 2260 psi
Odeh: m(ps)=355.06, ps=2259.18 psi

Figure 8

Case of 5 - well homogeneous reservoir with aquifer support

of injection, pushing the water out of the gas bubble, a fall-off test was conducted. Derivative plots for individual wells under influx and efflux are shown in Figure 9. Changes in the location of the gas-water interface influence the derivative plots. Note that in both cases the composite plot result is a good estimate of reservoir parameters.

An important observation from the results presented above is the inadequacy of using spot pressure data. Because of unclear location of the spot pressure and time on the derivative plot, any type of extrapolation may be subject to significant errors.

Conclusions

In gas storage reservoirs, because of opportunities to conduct periodic shut-in tests (buildup and fall-off), the effects of cyclical water influx and efflux can be monitored from the derivative plots. Analytical modeling of a reservoir consisting of a gas bubble and gas/water transition intervals indicates the influence of the interfaces on the pressure derivative plots. Using the procedure described in this paper, a composite of individual well behaviors can be used to estimate average reservoir pressure. Areal variation in reservoir permeability coupled with lateral variations in fluid saturation can affect the shape of the derivative plots. In the composite plot approach, these effects are averaged and a fairly good estimate of $\bar{p}$ and reservoir permeability can be obtained. An important requirement in the use of the composite plot is the establishment of pseudo steady state condition prior to the buildup or fall-off test. Only in extreme cases when a single well may exhibit long duration of afterflow or with very early response of boundary conditions, are certain errors introduced in the composite plot. In such cases, the behavior of these wells may be excluded from the composite plot.

Acknowledgement

This study was supported by the Gas Research Institute. Assistance of Judy Lee in typing the manuscript is much appreciated.

References

- Guerrero, E. T. and Loucks, T. L., (1961) Pressure drop in a composite reservoir, *Soc. Pet. Engr. Journal* pp. 170.
- Guppy, K.H., Babur, A. and Ramezani, R., (1988) Estimation of average reservoir pressure in underground storage reservoirs, *AGA*, PR-193-707.
- Kazemi, H., Merill, L. S. and Jargon, J. R., (1972) Problems in interpretation of pressure fall-off tests in reservoirs with and without fluid banks, *J. Petrol. Tech.* pp. 1147-56.
- Odeh, A.S. and Al-Hussainy, R., (1971) A method for determining the static pressure of a well from buildup data, *J. Petrol. Tech.*, pp. 621-624.
- Ramey, H. J. Jr., (1970) Approximate solutions for unsteady liquid flow in composite reservoirs, *J. Can. Pet. Tech.* pp. 32-37.
- Stehfest, H., (1970) Algorithm 368, numerical inversion of laplace transformation [D5]," *Comm. ACM* **13** No.1, pp. 47-49.

Nomenclature

c_g = gas compressibility, vol/vol/psi

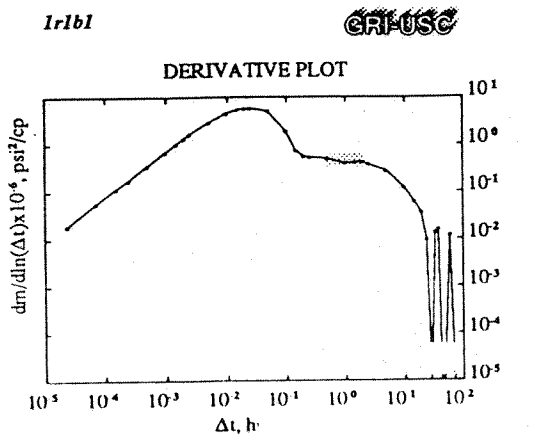

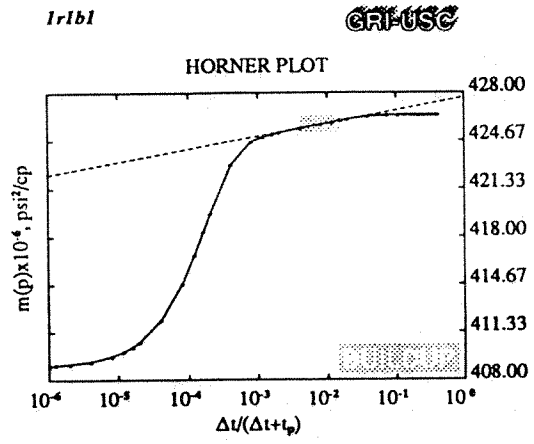

slope= 0.89, k= 24.24md, skin= 19.25
m(p*)=427.66, p*= 2494 psi, CA=30.88
Ramey-Cobb: m(p_{avg})=426.49, p_{avg}= 2490 psi
Odeh: m(ps)=426.52, ps=2490.54 psi

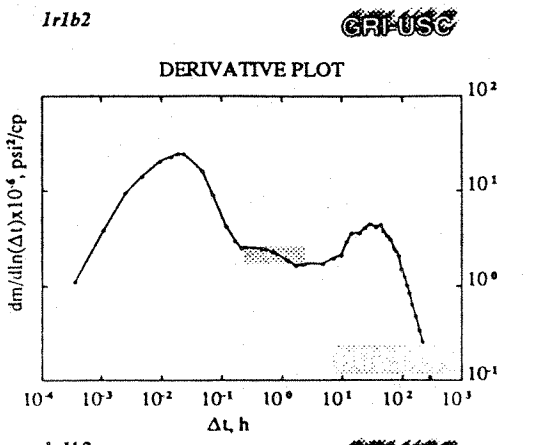

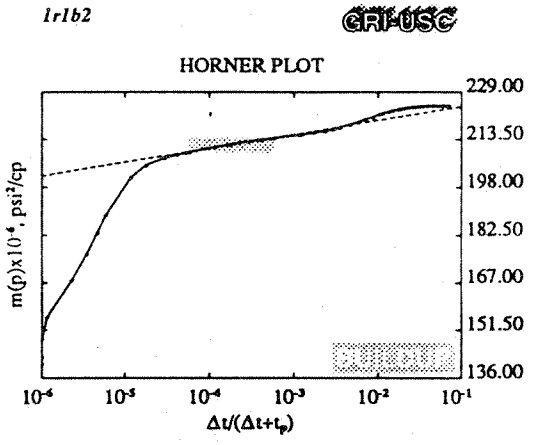

slope= 4.52, k= 23.91md, skin= 18.73
m(p*)=228.81, p*= 1797 psi, CA=30.88
Ramey-Cobb: m(p_{avg})=216.43, p_{avg}= 1747 psi
Odeh: m(ps)=217.90, ps=1752.99 psi

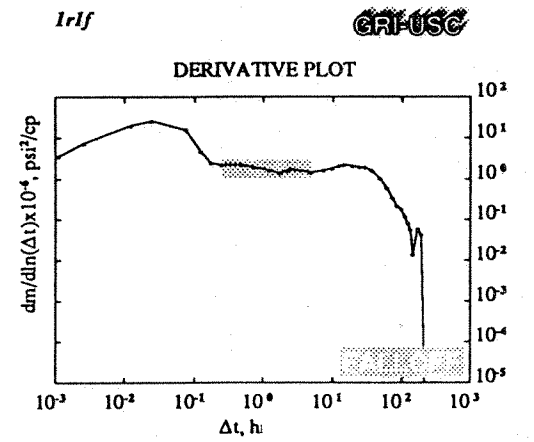

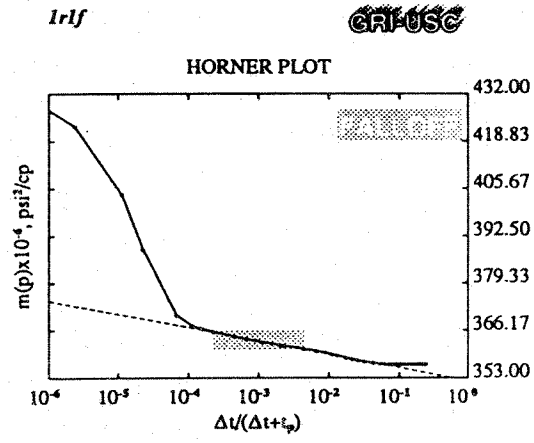

slope= -3.71, k= 23.33md, skin= 19.13
m(p*)=352.14, p*= 2249 psi, CA=30.88
Ramey-Cobb: m(p_{avg})=360.25, p_{avg}= 2277 psi
Odeh: m(ps)=360.71, ps=2278.11 psi

Figure 9 Derivative and Horner plots for the build up -1, build up -2 and the fall off tests

C = wellbore storage coefficient, BbL/psi

k = permeability, md

$m = m(p)$ = pseudo pressure, psi^2/cp

m' = slope of the semilog plot of pressure vs $\frac{t + \Delta t}{\Delta t}$, psi/cycle

n = number of wells

p = pressure, psi

q = production or injection rate of single well, MSEF/D

$$Q_t = \sum_{j=1}^{j=n} q_j$$

r = radius, ft

S = skin factor

s = Laplace transform parameter

S_w = water saturation, fraction

S_{wc} = irreducible water saturation, fraction

S_{g_c} = critical gas saturation, fraction

t = production or injection time, hours

Δt = shut-in time, hours

μ = viscosity, cp

z = gas derivation factor, dimensionless

ϕ = porosity, fraction

η = hydraulic diffusivity, md. ft/cp

SI Metric Conversion Factors

bbl	x	1.589,873	E-01 = m^3
cu ft	x	2.831,685	E-02 = m^3
ft	x	3.048*	E-01 = m
in.	x	2.54*	E+00 = cm
lbm	x	4.535,924	E-01 = kg
psi	x	6.894,757	E+00 = kPa

*Conversion factor is exact.

Iraj Ershaghi *is a professor and the Director of the Petroleum Engineering Program at the University of Southern California, University Park, Los Angeles, CA 90089-1211. His research interests are in the areas of well testing, formation evaluation and reservoir characterization. He has supervised many experimental and analytical graduate studies and research projects. He received a BS degree in petroleum and mining engineering from the University of Teheran in 1965 and MS and PhD degrees in petroleum engineering from the University of Southern California in 1968 and 1972, respectively. He has been with USC since 1972. He has also served as a reservoir engineering consultant and has published numerous papers in areas ranging from properties of rocks and fluids at high temperatures to formation evaluation techniques including well testing.*

Huseyin Calisgan *is a graduate student at the University of Southern California, University Park, Los Angeles, CA 90089-1211. He received his BSc degree from the Middle East Technical University in Ankara in 1987. His research interests are in well testing and numerical modeling of thermal recovery processes.*

Jincai Chang *is a PhD student at the University of Southern California, University Park, Los Angeles, CA 90089-1211. He received his BS and MS degrees in petroleum engineering from Southwestern Petroleum Institute, China and USC, respectively. His research interests include well testing and characterization of heterogeneous reservoirs.*

Yusuf A. Shikari *is Manager, Storage Research at the Gas Research Institute, 8600 West Bryn Mawr Avenue, Chicago, IL 60631. He is responsible for the overall planning, procurement and management of gas storage related to research and development programs for the US natural gas industry. He is also responsible for providing analytical and strategic support to GRI's executive management in the overall budgeting of its transport and storage research. Prior to working with GRI, Mr. Shikari was Research Business Analyst at IIT Research Institute. He holds BS and MS degrees in mechanical engineering and an MBA in finance and statistics.*

Regional Characterization of Variable-Density Fluid Flow in Sedimentary Basins: Implications of Model Interpretation

by Rainer K. Senger

Abstract

Characterization of regional ground-water flow in sedimentary basins requires estimates of regional-scale hydraulic properties that are difficult to determine. Alternatively, permeabilities may be calibrated in regional flow models using measurements of fluid pressure and/or hydraulic head. However, in aquifers with saline formation waters, fluid pressures are affected by fluid densities and pressure, or head gradients may not reflect actual ground-water flow patterns. In addition to the well-known problems of hydraulic-parameter and boundary-condition uncertainties, modeling strategies for regional, variable-density ground-water flow require consideration of uncertainties associated with fluid densities and evaluation of fluid pressures or equivalent fresh-water heads.

Effects of significant fluid-density variation on regional ground-water flow are studied in the Palo Duro Basin, Texas, where fluid densities vary between 1000 and 1150 kg/m^3. Steady-state flow of variable-density ground water is simulated on the basis of computation of equivalent fresh-water heads and stream functions, incorporating fluid densities that vary in space but are time invariant. Simulated equivalent fresh-water heads, in the variable-density model significantly increase with depth in comparison with simulated heads, assuming uniform fresh-water density. Constructed surfaces of equivalent fresh-water heads in saline aquifers may exhibit large local variations owing to vertical offset between test intervals in adjacent wells. Permeability variations and boundary conditions in the variable-density model have much smaller effects on simulated heads than they do in the constant-density model, which is important for model calibration. Modeling indicates that the overall ground-water flow pattern in the Palo Duro Basin is not significantly affected by variations in fluid densities, indicating that the flow component arising from the present-day topographic relief dominates buoyancy forces associated with dense fluids. However, during the recent geological past, prior to maximum basin uplift, when the topographic relief across the Palo Duro Basin was much lower than it is today, a buoyancy-dominated flow pattern may have existed, characterized by continuous overturn of fluids in the deep aquifers.

Introduction

In mature sedimentary basins, where mechanical compaction is negligible, fluid flow is driven by the potential energy represented by the shallow water table and generally follows the topography. Ground-water flow is generally inferred from the potential distribution, which is measured as hydraulic head or fluid pressure. Ground-water flow is said to be gravity-driven as it moves from topographic highs to topographic lows. Regional gravity-driven flow systems are typically assumed to be under steady-state conditions; that is, the ground-water flow pattern and velocity do not change with time and are governed by the basin geometry, the topography, and the permeability distribution throughout the basin (Tóth, 1962, 1963; Freeze and Witherspoon, 1966, 1967, 1968). Determination of regional-scale hydraulic properties in sedimentary basins is difficult because of the large number of permeability data necessary and the high costs associated with permeability measurements; alternatively, permeabilities may be calibrated in regional flow models on the basis of data on fluid pressures and/or hydraulic heads.

Regional flow systems can include both shallow aquifers with fresh water and deep aquifers with saline water, leading to spatially variable fluid densities. Flow patterns of variable-density ground water cannot be accurately inferred from pressure or head gradients because a single potential field does not exist in such an environment (Hubbert, 1940). Especially in sedimentary basins containing (or that once contained) thick evaporites, formation water in deep aquifers can have densities greater than 1100 kg/m^3 (total dissolved solids > 200,000 mg/L), and the ground-water flow direction may differ significantly from hydraulic head gradients observed in the aquifers because of buoyancy effects associated with the saline ground water. In cases where buoyancy forces dominate the hydraulic head or pressure gradient arising

from topographic relief, complex ground-water flow patterns may result, characterized by continuous overturn of fluids. Such flow patterns are typically associated with thermal or thermohaline convection caused by fluid instability (Nield, 1968; Combarnous and Bories, 1975). Herbert et al. (1988) described continuous overturn of fluids in numerical flow experiments of salt dissolution in a fresh-water aquifer, characterized by stratified fluid densities.

Characterization of subsurface hydrological regimes has become a critical component in the context of waste isolation problems for the assessment of safe disposal of radioactive and chemical wastes. For this purpose, it is crucial to understand the regional hydrogeological conditions and to identify rates and direction of subsurface fluid movement.

In this paper, the effects of variable-density fluids on regional ground-water flow is discussed. The focus is on describing regional-scale flow patterns of variable-density ground water; transient solute transport aspects associated with variable fluid density are not considered. It is assumed that solute concentrations and fluid density remain constant over time but can vary spatially. This assumption is considered valid in regional flow systems in which salinities change very slowly over geological time and in which fluid pressures are in equilibrium with fluid densities. In the first part of the paper, the relation between the two driving forces, hydraulic gradient and buoyancy force will be discussed. Simulated flow of variable-density ground water will be examined in an idealized flow scenario to determine the effects of variable fluid densities on the head distribution and to evaluate under what conditions buoyancy-dominated flow patterns may occur. In the second part, regional-scale flow of variable-density ground water will be analyzed using a cross-section flow model. The regional hydrodynamics of the Palo Duro Basin, an intracratonic basin of Permian age, is the focus of this study, which was initiated to investigate the suitability of this basin for high-level nuclear waste disposal.

Hydrogeological Setting

The general hydrogeology of the Palo Duro Basin has been previously described in detail by Bassett and Bentley (1982), Bair et al. (1984), Smith et al. (1985), and Senger and Fogg (1987). The general geometry of the major depositional facies is depicted along a west-east cross section through the Palo Duro and adjacent basins (Figure 1). Major features include a thick Permian

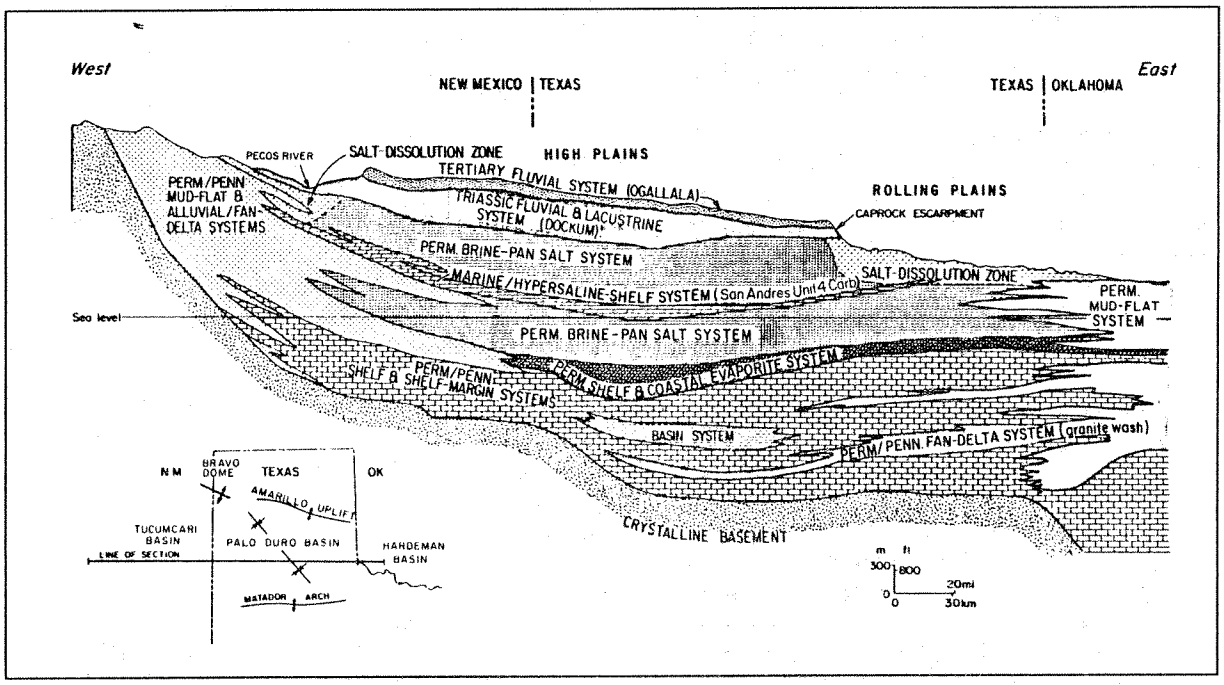

Figure 1. Regional west-east cross section schematically illustrating the spatial relations of the major depositional systems in the Palo Duro Basin (modified from Bentley, 1981).

evaporite sequence (evaporite aquitard) separating the underlying deep aquifer, which is composed of Lower Permian (Wolfcampian) and Pennsylvanian carbonates and arkosic sandstones, from the shallow fresh-water aquifers of the High Plains. Arkosic sandstones ("granite wash") represent an important permeability facies (Senger and Fogg, 1987). The major topographic features are the Pecos Plains in eastern New Mexico, the High Plains bounded on the east by the eastern Caprock Escarpment, and the Rolling Plains (Figure 1).

Pressure data from the Palo Duro Basin indicate that the deep aquifer is underpressured on a regional scale (Orr and Kreitler, 1985). These underpressured conditions are expressed in equivalent fresh-water heads of the deeper aquifer, which are as much as 350 m below the shallow water table of the High Plains along the cross-sectional traverse (Figure 1). Possible leakage through the evaporite aquitard overlying the deep aquifer is assumed to be mostly vertical. Although the potential for vertical flow has been identified in some parts of the basin, the dominant flow component within the deep aquifer is horizontal (Orr and Kreitler, 1985).

Potentiometric surfaces for the deep aquifer (Figure 2) and individual hydrostratigraphic units have been constructed from equivalent fresh-water heads that are based on fluid pressures measured in well tests (Bair et al., 1984; Smith et al., 1985; Wirojanagud et al., 1986). These potentiometric surfaces were used to evaluate lateral flow pat-

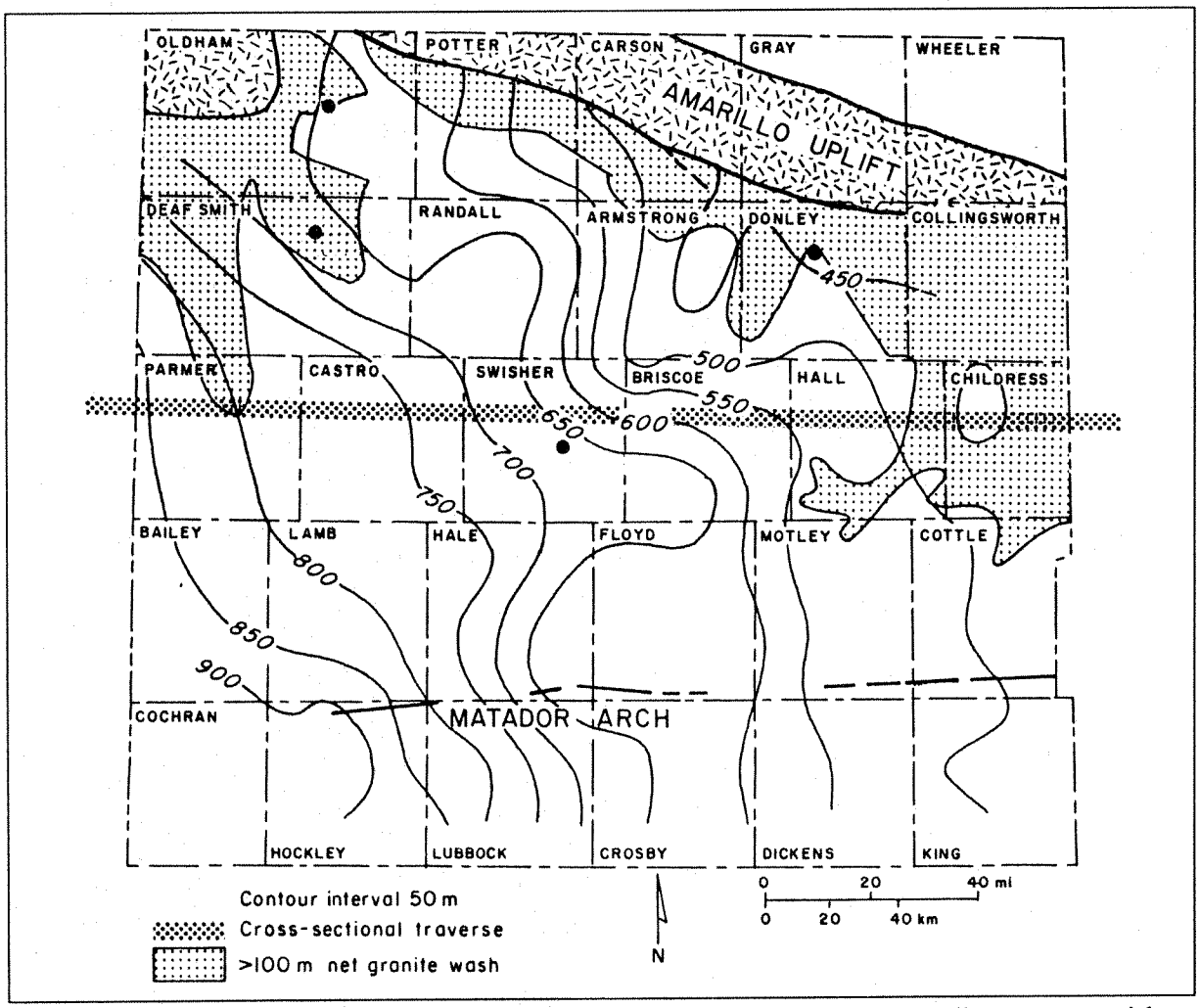

Figure 2. Average equivalent fresh-water head distribution of the entire deep aquifer constructed from kriged estimates of fresh-water hydraulic head. Distribution of the Permian/Pennsylvanian fan delta system (granite wash) is shown with net granite wash greater than 100 m (from Senger and Fogg, 1987).

terns. Contours of equivalent fresh-water heads indicate horizontal ground-water flow generally from west to east with a northward component in the central part of the Palo Duro Basin (Bair et al., 1984; Smith et al., 1985; Wirojanagud et al., 1986).

Studies of lateral and vertical salinity distributions within the Palo Duro and surrounding basins suggest recharge of fresh ground water from the west into the Lower Permian and Pennsylvanian strata (Figure 1) that underlie the evaporite aquitard (Fisher and Kreitler, 1987; Bein and Dutton, 1988). Because of the high fluid densities of the formation waters in the deep aquifer, it is possible that buoyancy phenomena may affect ground-water flow patterns.

Modeling Variable-Density Flow

Regional flow of variable-density ground water is simulated using stream functions and equivalent fresh-water heads. Contouring of computed stream-function values leads to a family of streamlines that provide a direct representation of the ground-water flow pattern and flow rates where fluid densities vary spatially. By comparison, equivalent fresh-water heads and fluid densities describe the two driving forces, hydraulic gradient and buoyancy force. The approach used in this study for simulating variable-density ground-water using equivalent fresh-water head and stream function is described in detail in Senger and Fogg (1990a) and is briefly summarized below.

The flow equation for variable fluid density, written in terms of equivalent fresh-water head (Bear, 1972), is

$$q_i = -K_{ij}\left[\frac{\partial h}{\partial x_j} + \rho_r \frac{\partial z}{\partial x_j}\right], \qquad (1)$$

where i and j are space coordinates and q_i is the specific discharge in the i direction. The equivalent fresh-water head, h, the relative density, ρ_r, and hydraulic conductivity, K, are defined by

$$h = \frac{p}{\rho_o g} + z, \qquad (2)$$

where p is the fluid pressure, ρ_o is a reference density, and z is the elevation, and by

$$\rho_r = \frac{\rho}{\rho_o} - 1 \qquad (3a)$$

and

$$K = \frac{k \rho_o g}{\mu}, \qquad (3b)$$

where k is the intrinsic permeability, μ is fluid viscosity, ρ is fluid density, and g is gravitational acceleration. Fluid flow in eqn (1) is interpreted to be caused by two driving forces: (1) the piezometric head difference, where the head refers to a fictitious homogeneous fluid of density, ρ_o, and (2) a buoyancy force acting on a fluid of density, ρ, embedded in a fluid of density, ρ_o.

For two-dimensional flow, variable-density fluid flow defined in terms of stream functions is expressed as

$$q_x = -\frac{\partial \Psi}{\partial z} \qquad (4a)$$

and

$$q_z = +\frac{\partial \Psi}{\partial x}. \qquad (4b)$$

The stream function Ψ is constant along a streamline, and the difference in Ψ values corresponds to the specific discharge between these streamlines irrespective of the fluid properties involved (De Josselin de Jong, 1960, 1969).

Assuming that the fluids and aquifer are incompressible and no sources and sinks exist, the steady-state continuity equation in a two-dimensional flow field oriented in the vertical plane, written in terms of equivalent fresh-water head, is given by

$$\frac{\partial}{\partial x}\left[K_x \frac{\partial h}{\partial x}\right] + \frac{\partial}{\partial z}\left[K_z \frac{\partial h}{\partial z} + K_z \rho_r\right] = 0. \qquad (5)$$

The corresponding stream-function equation, describing variable-density flow is given by

$$\frac{\partial}{\partial x}\left[\frac{1}{K_z}\frac{\partial \Psi}{\partial x} + \rho_r\right] + \frac{\partial}{\partial z}\left[\frac{1}{K_x}\frac{\partial \Psi}{\partial z}\right] = 0. \qquad (6)$$

The horizontal flux in the continuity eqn (6) is expressed by the stream-function gradient and a relative density term. The lateral density gradient expresses the rotation of the fluid due to variable density. In comparison, the vertical flow component in the continuity eqn (5) is represented by the head gradient and a density term, which incorporates the buoyancy of variable-density fluids. For further information on numerical aspects of the solution of stream functions and equivalent fresh-water heads using finite elements, refer to Senger and Fogg (1990a).

Evaluation of Driving Forces

The relation between the two driving forces, hydraulic gradient and buoyancy, and its effect on

equivalent fresh-water head and flow pattern in variable-density ground water is demonstrated using the salt-water intrusion example of Henry (1964). This example is commonly used for testing variable-density flow codes and involves a cross-sectional study of sea-water intrusion into a confined aquifer. The model dimensions are 2×1 m; fresh water recharges at a constant rate from the landward boundary and mixes with denser salt water before discharging at the sea-water boundary. Steady-state fluid densities for the salt-water intrusion scenario were obtained by simulating coupled flow and solute transport of high-salinity water using the finite-element model SUTRA (Voss, 1984). The computed fluid-density distribution is used as known input to simulate steady-state flow of variable-density ground water with the finite-element programs FRSURF/VDF and FRESTR/VDF (Senger and Fogg, 1990a), which compute equivalent fresh-water heads and stream functions, respectively (Figure 3). The programs FRSURF/VDF and FRESTR/VDF were modified from the original version of the finite-element program FREESURF (Neuman and Witherspoon, 1970) to account for variable-density fluids and to calculate discrete fluxes for each element.

Contours of simulated equivalent fresh-water heads are generally not orthogonal to the computed streamlines, except in the left part of the model where fresh water is recharged (Figure 3). Toward the sea-water boundary, the discrepancy between the head gradient and the actual flow vectors increases. In the lower right corner, where sea water is recharging and fluid density is highest, equivalent fresh-water head gradients are almost vertical upward; the buoyancy force associated with relatively dense sea water is vertical downward (Figure 3). The resultant of the two driving forces yields a relatively small, lateral flow component causing sea-water movement into the model, as shown by the streamlines and flow vectors (Figure 3). In the fresh-water section, the flow direction is perpendicular to the equivalent fresh-water head contours. The greater the magnitude of the buoyancy force compared with the magnitude of the equivalent fresh-water head gradient, the greater is the error in flow direction inferred from the head gradients. Moreover, the relatively high density of sea water produces a buoyancy-dominated flow system on the right side of the model, characterized by a clockwise overturn of saline water (Figure 3).

Comparing the magnitude of driving forces according to the flow equation (1) for this example (Figure 3) shows that the overall lateral head gradient associated with the prescribed recharge rate of fresh ground water along the left boundary is 0.0125, whereas the magnitude of buoyancy forces associated with the density of seawater (ρ = 1025 kg/m^3) relative to fresh water (ρ_o = 1000 kg/m^3) is 0.025, indicating a 2 to 1 ratio of buoyancy forces and lateral head gradient. Note

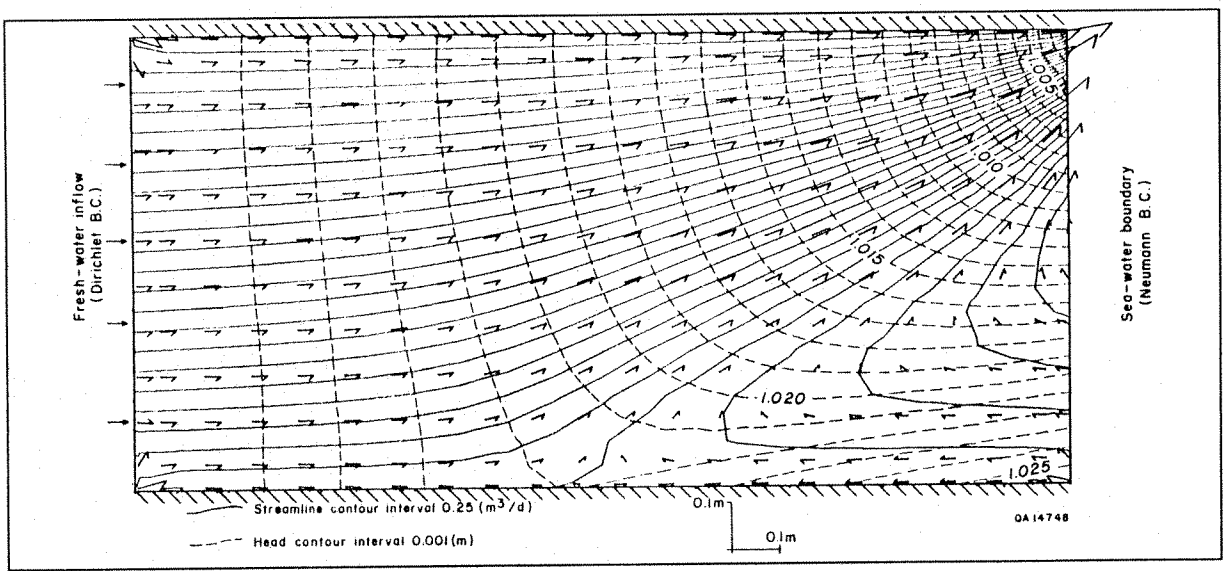

Figure 3. Distribution of equivalent fresh-water heads, streamlines, and flow velocities based on steady-state simulation of variable-density flow using FRSURF/VDF and FRESTR/VDF, respectively. The simulation incorporates steady-state fluid density distributions.

that the magnitude of the buoyancy force associated with sea-water density is reflected in the overall vertical head gradient along the sea-water boundary (Figure 3).

One can expect that by increasing the lateral head gradient across the model, the buoyancy-dominated flow system on the right side of the model (Figure 3) would disappear. This is demonstrated in Figure 4, where steady-state flow was simulated using the same distribution of fluid densities as that in the previous simulation (Figure 3) but where prescribed recharge rates were increased by a factor of 2 along the left boundary. The result is an increase in the overall lateral head gradient from 0.0125 (Figure 3) to 0.020 (Figure 4). Although the head gradient is slightly smaller than the magnitude of the buoyancy force associated with the sea-water boundary, the simulated flow pattern (Figure 4) does not indicate a buoyancy-dominated flow system in the right part of the model. Note, however, that computed flow velocities and equivalent fresh-water head are significantly affected by the high-density fluids (viscosity is assumed to be constant in these simulations). Although the computed heads and flow velocities (Figure 4) are based on steady-state assumption, the simulation implies that the dissolved mass, represented by the fluid densities, is not in equilibrium with the modified boundary condition. If coupled flow and solute transport were simulated, the increased recharge of fresh ground water along the left boundary would change the fluid-density distribution due to solute transport. This would cause subsequent changes in equivalent fresh-water head distribution and in the flow pattern. However, as shown in Senger (1989), simulation of steady-state flow of variable-density fluids gives an accurate representation of the ground-water flow pattern for a given fluid-density distribution, even though fluid densities may not represent steady-state conditions because fluid pressures readily adjust to changes in fluid density. Such conditions may not be uncommon in sedimentary basins where fluid pressures equilibrate relatively rapidly to topographic changes caused by basin uplift and erosion, but the distribution of dissolved mass responds more slowly to hydrodynamic changes.

The simulations indicate that buoyancy-dominated flow patterns occur if the magnitude of buoyancy forces associated with variable-density fluids becomes significantly greater than the magnitude of the head gradient arising from topographic relief (recharge flux). However, anisotropy and aquifer thickness will strongly affect the potential for buoyancy-dominated flow. It can be shown that by decreasing vertical permeability in the aquifer, the height of the flow cell will be reduced and eventually disappear completely. Furthermore, by reducing the aquifer thickness, the overall increase in equivalent fresh-water head along the sea-water boundary will be smaller and will reduce the driving-force component that causes the clockwise overturn of saline water.

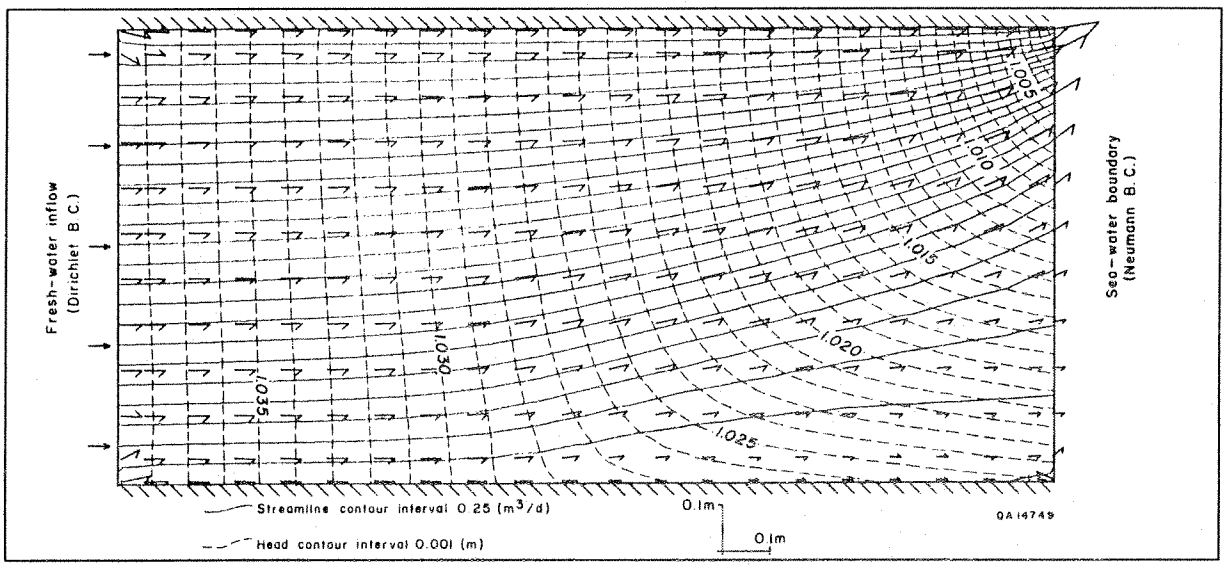

Figure 4. Distribution of equivalent fresh-water heads and flow velocities using increased recharge rates along the left boundary (from Senger and Fogg, 1990b).

Variable-Density Flow Simulations, Palo Duro Basin

The effects of variable-fluid density on regional ground-water flow are studied in a two-dimensional model along the west-east cross section (Figure 1). The finite-element mesh incorporating the basin geometry and the different hydrostratigraphic units (Figure 5) corresponds to that used in the previous investigation of the regional hydrodynamics of the Palo Duro Basin (Senger et al., 1987). Studies of lateral and vertical salinity distributions within the Palo Duro Basin and surrounding basins indicate large variations of fluid densities throughout the basin (Fisher and Kreitler, 1987; Bein and Dutton, 1988). The potential effects of high fluid densities on the head distribution is important for model calibration. Furthermore, evaluating the potential for buoyancy-dominated flow patterns is crucial for the interpretation of basin hydrology, which is difficult to infer from the head distribution.

Simulation Approach

Fluid densities in the different hydrostratigraphic units were estimated from limited information on salinity and temperature throughout the Palo Duro Basin and adjacent basins and is described in more detail in Senger and Fogg (1990b). Salinities range from less than 1000 mg/L in the shallow aquifers to as much as 300,000 mg/L within the evaporite confining system. Within the deep brine aquifers of the Palo Duro Basin, salinities generally increase with depth from less than 100,000 mg/L within the Lower Permian Wolfcampian strata to more than 250,000 mg/L in the underlying Pennsylvanian strata. At the eastern boundary in Oklahoma, salinities in the deep brine aquifers decrease from more than 200,000 mg/L to less than 150,000 mg/L. Computed fluid densities generally increase with salinity ranging from 1000 to 1169 kg/m^3 throughout the cross-sectional model (Figure 6). Fluid viscosities generally

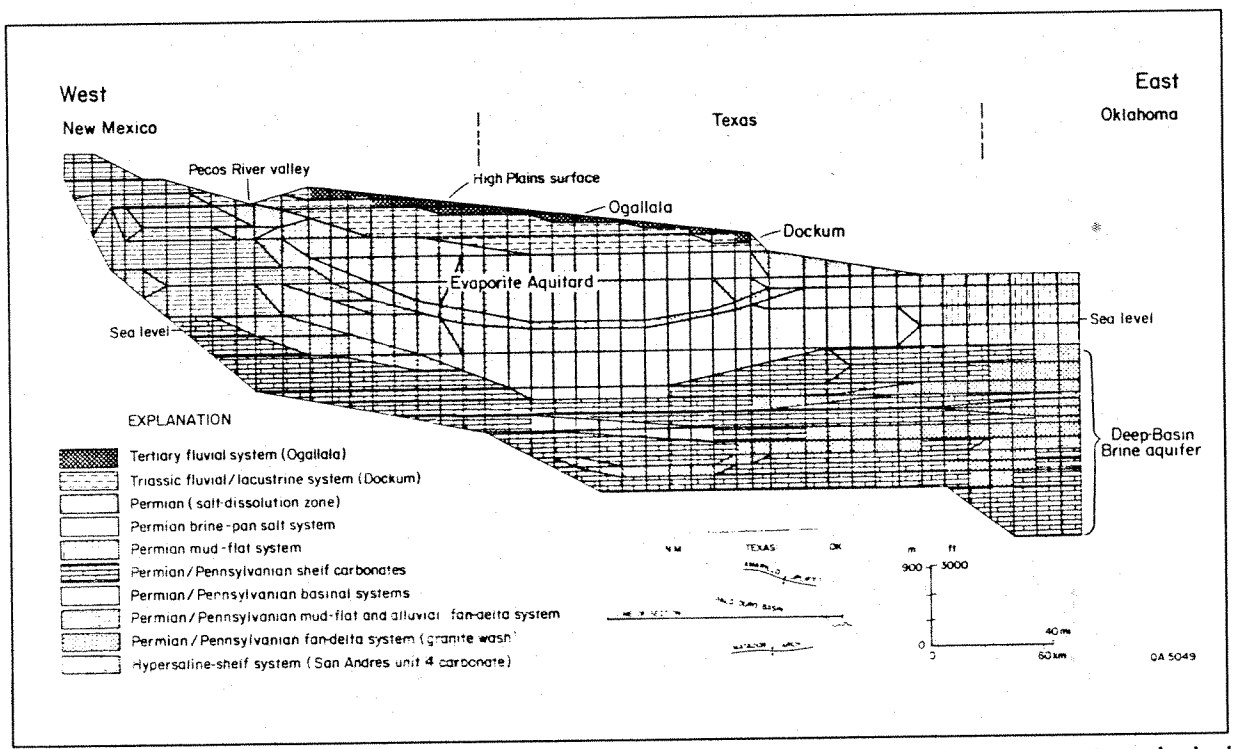

Figure 5. Finite-element mesh representing the major hydrologic units along the west-east geological cross section (Figure 1). Each element is assigned a hydraulic conductivity value. The upper surface of the mesh is represented by prescribed head boundary conditions representing the water table. The lower surface of the mesh is a no-flow boundary, which corresponds to the contact between the deep brine aquifer and the basement rock. The eastern boundary is a flow boundary represented by prescribed heads (from Senger and Fogg, 1987).

decrease with depth owing to a corresponding increase in temperature and range from 36 to 106 kg/m/d (0.42 to 1.23 cP). The pattern of fluid densities (Figure 6) resembles that of the salinity distribution, with relatively high fluid densities in the evaporite section and a wedge of low fluid densities in the western part of the deep aquifers. The wedge-shaped salinity pattern in the western part suggests recharge of meteoric water with lower total dissolved solids from the west, preferentially into the Lower Permian strata that underlie the evaporite confining system (Fisher and Kreitler, 1987; Bein and Dutton, 1988). The salinity pattern may represent some steady-state condition with regard to advective-dispersive transport. On the basis of analytical solutions for idealized conditions, Domenico and Robbins (1985) described wedge-shaped recharge plumes displacing connate fluids that represent steady-state conditions if the recharge area does not include the entire width and depth of the hydrological unit.

Ground-water flow is simulated in the cross-sectional model (Figure 5) using both the equivalent fresh-water head solution and the stream-function solution. Two different simulations are performed: Simulation V-1 assumes uniform values for both densities and viscosities equivalent to fresh water, and Simulation V-2 incorporates variable fluid densities and viscosities. Permeabilities used in the two simulations (Table 1) correspond to those used in Simulation A-2 of Senger et al. (1987). Fluid properties in Simulation A-2 were based on an average temperature of 60 °C and an average salinity of 130,000 mg/L of the deeper units, yielding an average fluid viscosity of 72 kg/m/d (Wirojanagud et al., 1986).

Boundary Conditions

No-flow boundaries are assumed along the lower surface of the mesh, and the topographic surface is represented by prescribed head boundaries corresponding to the shallow water table. In both simulations, horizontal flow conditions are imposed for the deep aquifers along the eastern boundary in accordance with pressure-depth data. In Simulation V-1, where fresh-water density is assumed, prescribed heads at the eastern boundary are uniform with depth and equal to the shallow water-table elevation. Pressure data obtained from drill-stem tests in Jackson County, Oklahoma, at the eastern boundary of the model indicate a pressure-depth gradient of ~ 0.01 MPa/m (0.47 psi/ft) suggesting brine hydrostatic conditions and concomitantly lateral flow

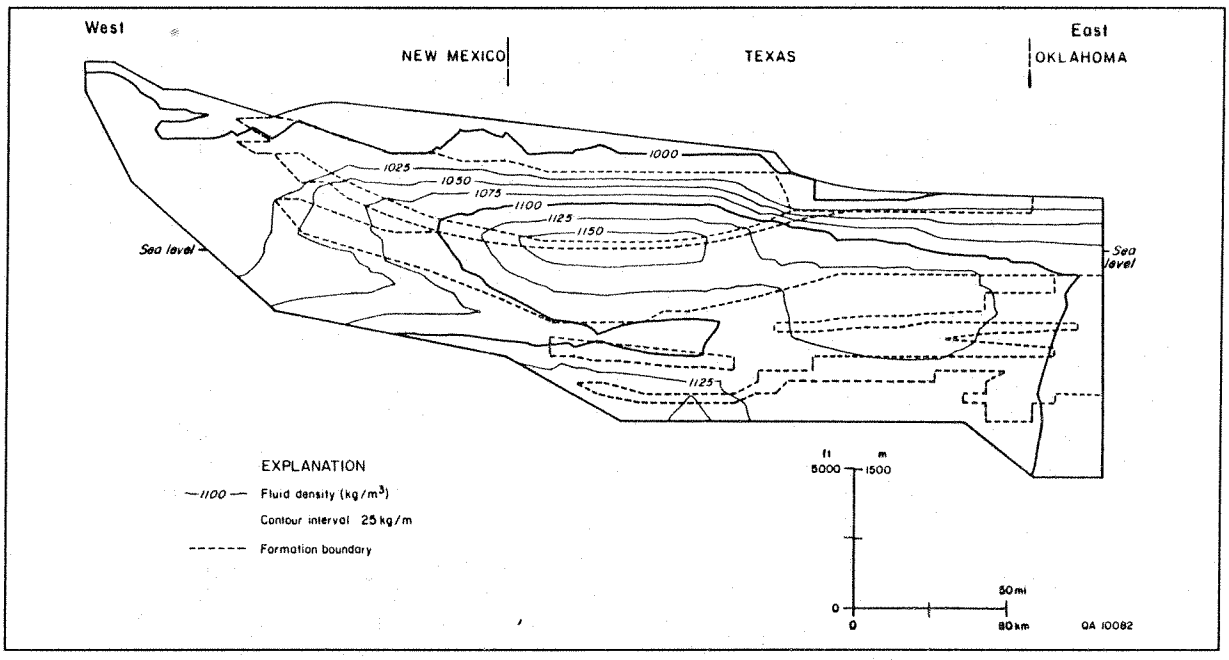

Figure 6. Distribution of fluid densities calculated from limited data on salinity and from temperature distributions based on linear geothermal gradients along the cross-sectional traverse (from Senger and Fogg, 1990b).

Table 1

Assigned permeability values for the major hydrologic units of the model. Permeabilities correspond to those used in Simulation A-2 in Senger and others (1987).

Hydrologic Unit	k_x (m^2)	k_z (m^2)
Tertiary fluvial system (Ogallala)	9.4×10^{-12}	9.4×10^{-13}
Triassic fluvial/lacustrine system (Dockum)	9.4×10^{-13}	9.4×10^{-14}
Permian salt dissolution zone	7.0×10^{-14}	7.0×10^{-16}
Permian brine pan salt system	2.7×10^{-19}	2.7×10^{-19}
Permian mud-flat system	7.0×10^{-17}	7.0×10^{-17}
Permian/Pennsylvanian shelf carbonates	1.2×10^{-14}	1.2×10^{-16}
Permian/Pennsylvanian basinal system	9.4×10^{-20}	9.4×10^{-20}
Permian/Pennsylvanian mud-flat and alluvial-fan delta system	7.0×10^{-15}	7.0×10^{-17}
Permian/Pennsylvanian fan delta system (distal granite wash)	1.0×10^{-14}	1.0×10^{-16}
Permian/Pennsylvanian fan delta system (proximal granite wash)	1.0×10^{-13}	1.0×10^{-15}
Normal marine/hypersaline shelf system	9.8×10^{-17}	9.8×10^{-17}

of brines in the deep aquifers (Senger and Fogg, 1987).

In Simulation V-2, where variable fluid density is assumed, Dirichlet boundary conditions for the head solution are represented by prescribed equivalent fresh-water head values that are calculated from fluid pressures on the basis of average fluid densities of the boundary elements (Figure 6). If one assumes that the flow along the entire eastern boundary is horizontal (i.e., the pressure-versus-depth regression line represents hydrostatic conditions), the computed fluid pressures and, in turn, the prescribed equivalent fresh-water heads in the deep aquifers become significantly greater than measured values, although the overall gradient agrees with the observed gradient. In order to reduce the prescribed head values along the eastern boundary, the observed depth intercept of the pressure-depth regression line, which is generally interpreted as the average depth to the water table below land surface, was assumed to represent a downward flow component across the shallow aquitard section (Senger and Fogg, 1990b). That is, the rate of pressure increase with depth must be smaller than the brine hydrostatic gradient causing downward flow across the shallow aquitard. With this adjustment, equivalent fresh-water head values along the boundary increase from 430 m at the upper surface to ~ 610 m at a depth of about 3000 m.

Within the overlying confining section (Figure 5) prescribed head values, assigned along the boundary, were assumed to increase linearly from 430 m at land surface to 435 m at the base of the confining unit. Despite the head increase with depth, downward flow conditions result from the buoyancy force associated with dense brines in the section. The increase in prescribed head values within the deep aquifers reflects the observed pressure-depth gradient of 0.01 MPa/m (0.47 psi/ft). Also, the range of prescribed head values agrees reasonably well with equivalent fresh-water heads based on kriged equivalent fresh-water head surfaces in eastern Oklahoma for the Wolfcampian and pre-Pennsylvanian aquifers, representing the uppermost and lowermost units, respectively, within the deep aquifers (Smith et al., 1985). In previous studies (Senger et al., 1987), the potential for vertical flow through the Permian mud-flat system in the easternmost part of the cross section (Figure 5) was not considered because the inferred lateral flow conditions in the deep aquifers, based on the pressure-depth data, were represented along the entire vertical boundary with uniform hydraulic head values with depth.

Modeling Results

Constant Fluid Density

In the first simulation, fluid densities and viscosities are uniform at 1000 kg/m³ and 98.6 kg/m/d (1.14cP), respectively. These values correspond to shallow ground water having 1000 mg/L salinity at 15 °C. The same fluid properties will be assigned to the boundary nodes along the upper topographic surface in the subsequent simulation. The viscosity of 98.6 kg/m/d, used in Simulation V-1, is somewhat higher than the viscosity of 72 kg/m/d assumed for the deeper units in Simulation A-2 in Senger et al. (1987).

Hydraulic heads and streamlines computed in Simulation V-1 are shown in Figure 7. Regional ground-water flow in the Palo Duro Basin is characterized by a shallow flow system governed primarily by topography and a deeper flow system recharging in New Mexico and passing beneath the Pecos River into the deeper part of the Palo Duro Basin (Figure 7). Based on a series of steady-state simulations, effects of topography and hydrostratigraphy on the regional flow system were investigated in Senger and Fogg (1987). Observed underpressuring in the deep aquifer underlying the High Plains surface was shown to be the result of the regional topography and geology. The shallow Ogallala water table is relatively high owing to the high topographic elevation of the High Plains. Hydraulic heads in the deep aquifer are relatively low owing to the draining effect of permeable granite wash and very low recharge rates, enhanced by the Pecos River. The evaporite confining unit effectively separates the two aquifer systems, thereby maintaining the large hydraulic-head differential (Senger and Fogg, 1987).

Variable Fluid Density

Effects of spatially variable fluid densities (Figure 6) and viscosities on the regional groundwater flow pattern are investigated in Simulation V-2. Simulated equivalent fresh-water heads and velocity vectors calculated for each element are shown in Figure 8. The head contours generally show a downward gradient across the evaporite confining system. Within the deep aquifer, computed heads increase with depth. This upward-oriented head gradient within the deep aquifer becomes steeper toward the eastern boundary where prescribed heads increase with depth, re-

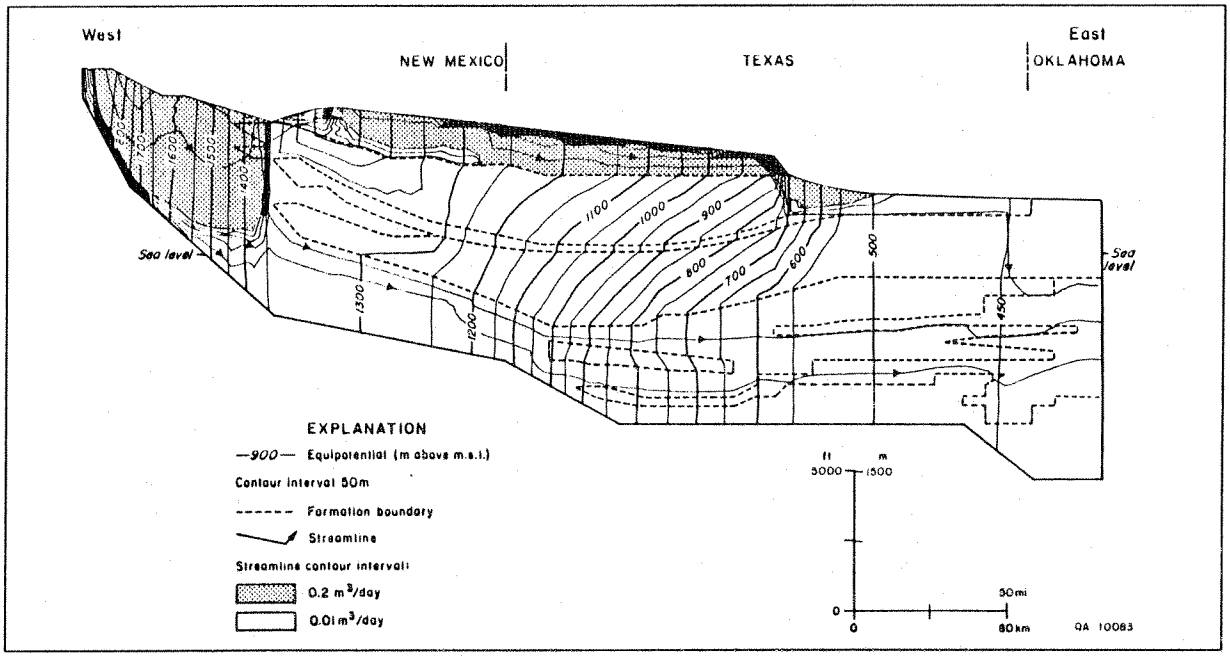

Figure 7. Flow net from initial Simulation V-1 using uniform fluid density and viscosity of shallow ground water throughout the entire cross section. Permeabilities are based on those used in Simulation A-2 of Senger et al. (1987).

flecting brine hydrostatic conditions and lateral flow out of the model.

Flow velocities for each element (Figure 8) are computed from the equivalent fresh-water heads, taking into account the buoyancy forces associated with variable fluid density. The regional flow pattern shown by flow vectors in Figure 8 is similar to that indicated by streamlines obtained from Simulation V-1 (Figure 7).

Streamlines and corresponding velocity vectors computed from the stream-function solution in Simulation V-2 are shown in Figure 9. Flow velocities computed by the stream-function solution (Figure 9) differ slightly from those computed by the head solution in the western part of the cross section (Figure 8). As discussed in more detail in Senger and Fogg (1990a), velocities computed from stream functions do not show oscillations between adjacent elements (Figure 9) because the vertical discretization is much finer than the horizontal one, and the potential errors associated with the centroid-only, velocity-consistent method are not significant. It can be shown that when using isotropic permeabilities, the discrepancy between centroid-consistent velocities computed from the head solution and stream-function solution becomes more apparent; the head solution yields an unrealistic, completely irregular velocity pattern throughout the cross-sectional model, whereas stream functions show accurate flow patterns, which one would expect.

Discussion of Model Results

Limited information on fluid pressures or equivalent fresh-water heads is typically used to calibrate regional ground-water flow models. In the following, results from the uniform-density and variable-density simulations are compared, and potential inconsistencies in regional flow modeling assuming uniform fluid density are evaluated by examining available information on equivalent fresh-water heads and fluid densities.

Comparison of Simulations

Comparison of streamlines in Simulation V-1 (Figure 7), where uniform fluid densities were assumed, with those in Simulation V-2 (Figure 9), indicates that the regional flow pattern in Simulation V-2 is largely unaffected by varying fluid density. An exception is at the eastern boundary of the model, where Simulation V-2 shows a considerable downward flow component across the shallow aquitard (Figure 9), as compared with the essen-

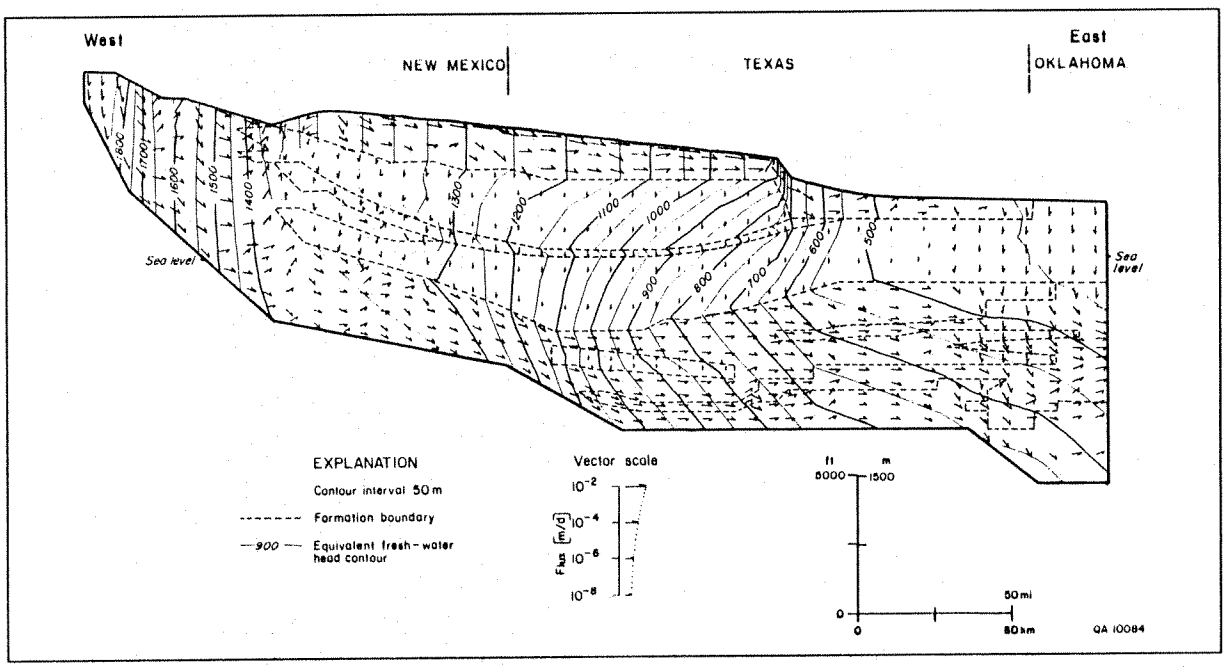

Figure 8. Distribution of equivalent fresh-water heads and computed element fluxes from Simulation V-2. Fluid densities are based on those shown in Figure 6 (from Senger and Fogg, 1990b).

tially horizontal flow shown at the same locality in Simulation V-1 (Figure 7). Even though simulated fresh-water heads within the deep aquifer are higher than the land surface (Figure 8), flow vectors show a downward direction across the confining unit as a result of buoyancy forces.

In Simulation V-1 (Figure 7), where fresh-water density was assumed, the potentia for vertical flow through the Permian mud-flat system in the easternmost part of the cross section (Figure 5) was not considered. Instead, brine hydrostatic conditions were assumed along the entire eastern boundary, which were represented by uniform hydraulic-head values equivalent to land-surface elevation.

The downward flow component in the variable-density model (Simulation V-2) is imposed by the prescribed head conditions along the upper part of the eastern boundary, as discussed earlier. The somewhat higher permeability assigned to the easternmost confining section, as compared with the evaporite section beneath the High Plains (Figure 5, Table 1), allows increased vertical leakage. This causes streamlines to deflect downward within the deep aquifer (Figure 8). Salinities within the deep section decrease toward the eastern boundary of the model, and overall fluid densities decrease with depth near the eastern boundary owing to higher temperature (Figure 6). Although uncertainty exists in the prescribed boundary conditions because of limited fluid-pressure data, the resulting vertical recharge of shallow ground water may explain the observed lateral decrease in salinities within the deep aquifer from > 200,000 mg/L in the eastern part of the Texas Panhandle to > 150,000 mg/L in western Oklahoma. Furthermore, the general decrease in density with depth near the eastern boundary results in greater buoyancy forces in the upper part of the deep aquifer (Figure 6), thereby accentuating the downward flow component in the eastern part of the deep aquifer (Figure 9).

Computed hydraulic heads in Simulation V-1 are mostly uniform with depth within the deep aquifer (Figure 7), whereas in Simulation V-2 (Figure 8) equivalent fresh-water heads significantly increase with depth, exceeding land-surface elevation by as much as 200 m in the eastern part of the model. Further, computed heads in Simulation V-2 (Figure 8) are as much as 100 m higher at the top of the deep aquifer than are heads in Simulation V-1 (Figure 7). Obviously, the extent of underpressuring expressed in the maximum head difference between the deep aquifer and the Ogallala aquifer on the High Plains was not reproduced by the variable-density simulation (Figure 8).

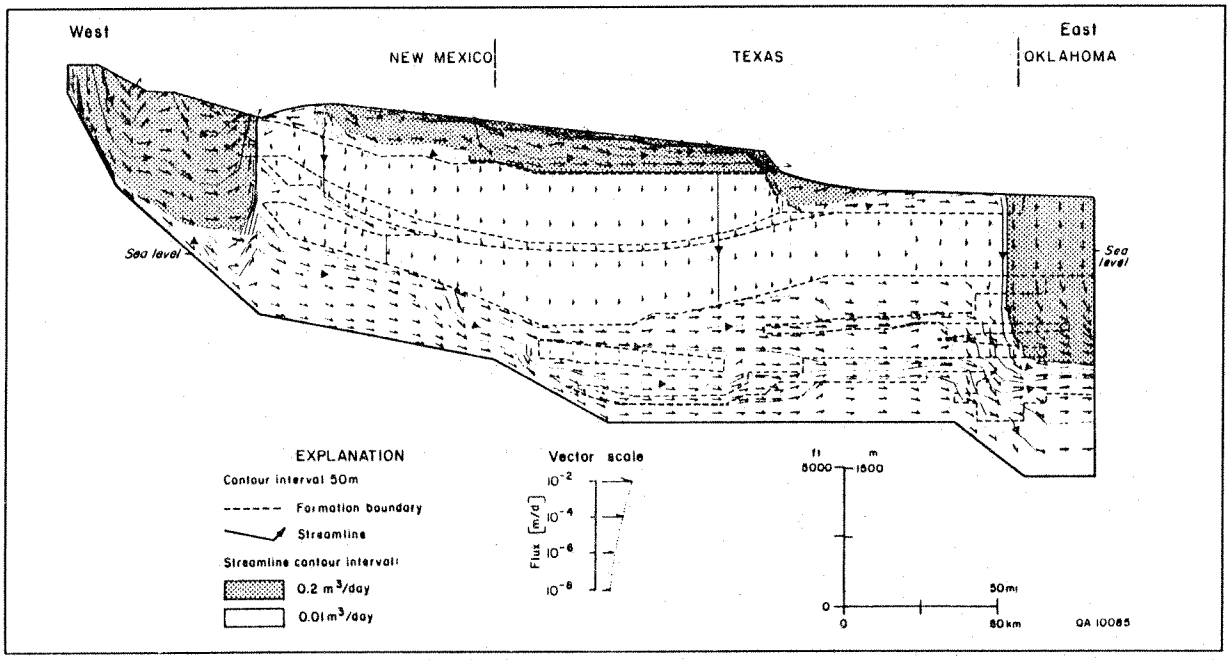

Figure 9. Distribution of streamline contours and computed element fluxes from Simulation V-2. Fluid densities are based on those shown in Figure 6 (from Senger and Fogg, 1990b).

The discrepancies between the two simulations can be related primarily to buoyancy effects of dense brines and to the effects of salinity and temperature variation on fluid properties that are incorporated in Simulation V-2. The upward gradient of equivalent fresh-water heads in the deep aquifer (Figure 8) counteracts buoyancy forces associated with dense brine, resulting in overall lateral flow (Figure 9). The reduction of maximum head difference across the evaporite confining system from ~ 350 m in Simulation V-1 (Figure 7) to > 250 m in Simulation V-2 (Figure 8) can be attributed to increased recharge to the deep aquifer from the west and to a lesser extent to increased vertical leakage (Figure 9) resulting from reduced viscosity at depth. Viscosities in Simulation V-2 are as much as 66 kg/m/d lower in the deepest part of the model than the uniform viscosity assumed in Simulation V-1. Reduced viscosities yield higher hydraulic conductivities, thereby increasing flow rates through the deep section.

Evaluation of Observed Data

In the following, equivalent fresh-water head data are examined for calibrating a constant-density model and for calibrating a variable-density model. In the previous study (Senger et al., 1987) the conceptual flow model, having uniform fresh-water density, was tested by comparing simulated hydraulic heads with a kriged surface of equivalent fresh-water heads for the deep aquifer. The head data were obtained by converting results from drill-stem tests into equivalent fresh-water heads. A block-kriged contour map was used to smooth large local variations in the head data, so that regional trends could be observed (Figure 2).

Equivalent fresh-water heads are expected to increase with depth where predominantly lateral flow occurs within an aquifer of highly saline formation water (Figure 8). Ideally, a kriged surface of equivalent fresh-water heads based on measured fluid pressures should represent average heads within the aquifer unit at a particular location. In reality, however, the distribution of equivalent fresh-water head values can exhibit large local variations not only because of differences in quality of the drill-stem test data but also because of vertical offset between adjacent intervals. If pressure data are obtained predominantly from test intervals in the upper part of the aquifer in a certain area, the resulting head surface will be biased toward lower heads in that particular area. This could affect the distribution of lateral gradients of equivalent fresh-water heads and, concomitantly, the interpretation of lateral flow patterns.

Fluid pressures were measured in two Department of Energy (DOE) wells in the central part of the High Plains (Figure 10): J. Friemel No. 1 (Deaf Smith County, Texas) and Mansfield No. 1 (Oldham County, Texas), located just east of the

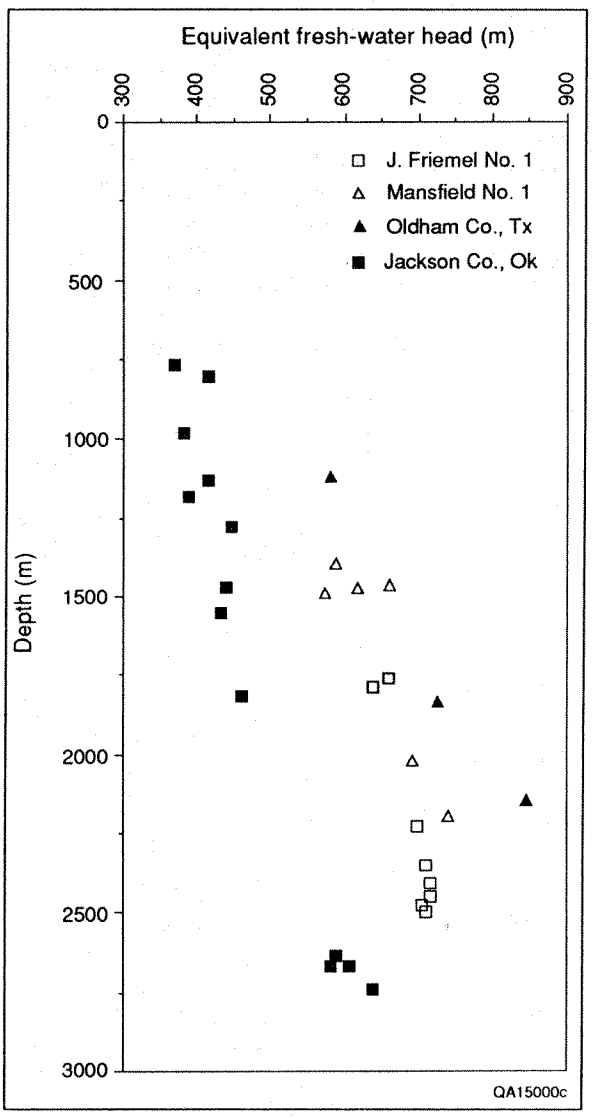

Figure 10. Equivalent fresh-water head vs. depth calculated from fluid-pressure measurements from the deep aquifer in Department of Energy (DOE) J. Friemel No. 1 well (Deaf Smith County, Texas), DOE Mansfield No. 1 well (Oldham County, Texas), Class A pressure data from Oldham County, and Class A data from Jackson County, Oklahoma, that correspond to the eastern boundary of the model.

New Mexico–Texas boundary to the north of the cross-sectional traverse (Figure 1). Equivalent fresh-water heads calculated from pressures in these two wells linearly increase with depth within the deep aquifer by as much as 80 and 160 m, respectively, over an ~ 1500-m depth interval (Figure 10). Similarly, equivalent fresh-water heads from Jackson County, Oklahoma, at the eastern boundary of the model show a distinct increase with depth by as much as 180 m (Figure 10). These data largely agree with results of the variable-density model (Simulation V-2; Figure 8).

Fluid pressures in two other DOE wells, Zeeck No. 1 well (Swisher County, Texas), located in the eastern part of the High Plains, and Sawyer No. 1 (Donley County, Texas), located east of the Caprock Escarpment and just north of the cross-sectional traverse, did not indicate a clear trend of increasing equivalent fresh-water heads with depth (Figure 11). In addition, equivalent fresh-water heads calculated on the basis of Class A pressure data (Smith et al., 1985) from the eastern part of the Texas Panhandle show a large scatter, generally increasing with depth. However, equivalent fresh-water heads from individual counties, most notably Childress County, located just west of the Texas–Oklahoma boundary, indicate rather uniform heads with depth (Figure 11), contrary to the results of the variable-density model (Figure 8).

One way to lower simulated equivalent fresh-water heads in the deep section in the eastern part of the model (Figure 8) is to reduce fluid densities, thereby reducing the upward gradient of equivalent fresh-water heads required to counteract the buoyancy force associated with dense brines. The salinity distribution used in this model is based on recent studies by Bein and Dutton (1988). The prescribed equivalent fresh-water head values calculated from fluid pressures based on estimated salinities and temperatures along the boundary agreed with the observed pressure-depth gradient. This supports estimates of at least 150,000 mg/L total dissolved solids in the eastern part of the basin.

Nevertheless, uncertainty exists regarding the density distribution in the deep aquifers. For example, total dissolved solids in a water sample from the upper part of the deep aquifer in the DOE Sawyer No. 1 well, just east of the eastern Caprock Escarpment, was only 140,000 mg/L (Fisher and Kreitler, 1987), whereas salinities of > 200,000 mg/L are used in the model. Furthermore, fluid densities in the model are computed assuming Na-Cl brines. Such brines occur mainly in the western part of the basin; however, brines from the central and eastern part of the basin are Ca-Cl brines (Fisher and Kreitler, 1987), which are characterized by somewhat higher fluid densities than Na-Cl brines at equivalent concentrations. Even with somewhat lower fluid densities owing to possibly lower salinities, one would expect a distinct increase in equivalent fresh-water heads with depth unless a significant vertical flow component exists.

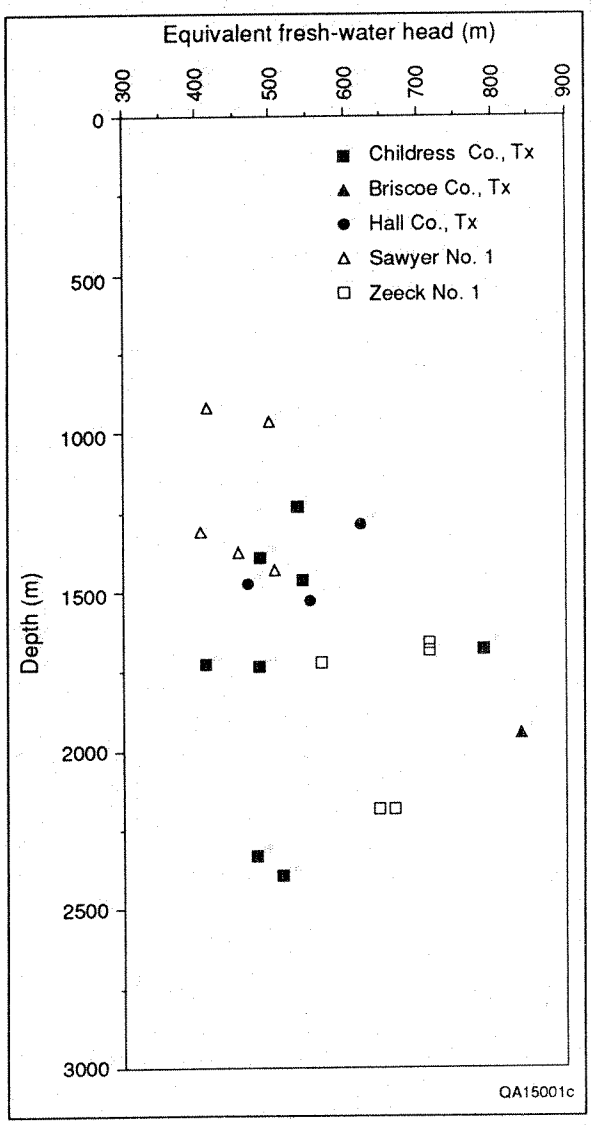

Figure 11. Equivalent fresh-water head vs. depth calculated from fluid-pressure measurements from the deep aquifer in DOE Zeeck No. 1 well (Swisher County, Texas), DOE Sawyer No. 1 well (Donley County, Texas), and Class A pressure data from various counties.

Implications of Model Interpretation

Modeling results, based on fresh-water fluid density (Senger et al., 1987), indicate that the relatively permeable granite-wash deposits drain the deeper section more effectively than it is recharged, and that changes in granite-wash permeability significantly affect the hydraulic-head distribution, particularly in the eastern part of the model. Uniform hydraulic-head values equivalent to a water-table elevation of 430 m were prescribed along the eastern boundary in Simulation A-2 (Senger et al., 1987) and in Simulation V-1 to simulate lateral flow in that area (Figure 7). In Simulation V-2, however, brine hydrostatic conditions implying lateral flow in the deep aquifer across the eastern model boundary result in an increase in prescribed heads from 430 to 610 m (Figure 8) to counteract buoyancy forces associated with fluids having relatively high density (Figure 6). Although granite-wash deposits still allow for good hydraulic communication between the deep section in the center of the model and the eastern boundary, it would appear that the simulated heads in the deep section have to adjust to higher prescribed heads in Simulation V-2 than to those in Simulation V-1 where fresh-water density is assumed.

Senger et al. (1987) indicated that the potential draining effect of the relatively permeable granite-wash deposits is not fully taken into account in the west-east cross-sectional model (Simulation A-2 in Senger et al., 1987, which corresponds to Simulation V-1 in Figure 7) because relatively permeable granite-wash deposits are also located to the northeast of the cross section along the Amarillo Uplift (Figure 1). To consider the possible draining effect of granite-wash deposits along the Amarillo Uplift, Senger et al. (1987) used artificially high permeability values for the Permian/Pennsylvanian fan-delta system along the entire cross section (Figure 5). Smith et al. (1985) suggested that the equivalent fresh-water heads in the relatively thick granite wash (predominantly Pennsylvanian age) along the uplift are much lower than the kriged head contours of the aquifer representing the entire Pennsylvanian section. Perhaps the relatively high equivalent fresh-water heads in Jackson County, Oklahoma (Figure 10), may not represent appropriate boundary conditions for the cross-sectional model because most of the flow is to the northeast, toward the relatively permeable granite-wash deposits along the Amarillo Uplift.

Similar to the situation in Simulation A-3 in Senger et al. (1987), where permeability assigned to the granite-wash facies was artificially increased to account for the possible draining effect toward the granite-wash deposits to the northeast of the cross section, permeability was increased from 1.0×10^{-14} m^2 in Simulation V-2 to 2.5×10^{-14} m^2 in Simulation V-3 (Figure 12). Prescribed equivalent

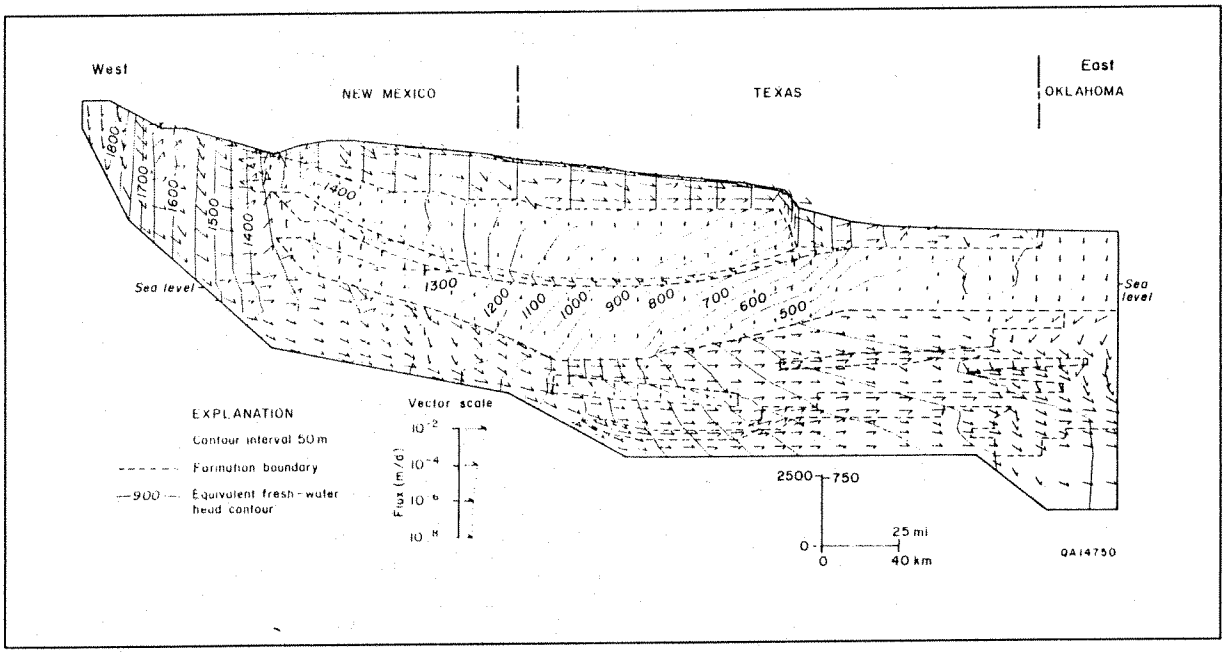

Figure 12. Distribution of equivalent fresh-water heads and computed element fluxes from Simulation V-3. Fluid densities are based on those shown in Figure 6.

fresh-water heads along the eastern boundary were also lowered by as much as 180 m, resulting in uniform heads with depth, to account for possible lower heads in granite-wash deposits. Further, the vertical permeability of the entire Permian and Pennsylvanian section was decreased by two orders of magnitude relative to the previous simulations (Table 1). Results from Simulation V-3 (Figure 12) indicate that the computed heads in the interior of the model maintained the characteristic head increase with depth. Only in the immediate vicinity of the boundary did simulated heads reflect the change in boundary condition (Figure 12). However, together with the uniform prescribed heads, the extreme anisotropy of the deep aquifer (K_x/K_z=10,000) shows locally uniform heads with depth within the relatively permeable granite wash deposits in the eastern part of the model. However, the simulation could not reproduce the observed uniform heads that extend over much greater depth ranges (Figure 11) than those shown in Simulation V-3 (Figure 12).

Significant uncertainties exist in pressure data obtained from drill-stem tests, in the kriged surfaces of equivalent fresh-water heads, and in estimated fluid densities, boundary conditions, and permeabilities. More detailed model calibration may yield a better agreement with observed heads. However, considering the hydrodynamic changes that occurred in the Palo Duro Basin during the recent geologic past, transient conditions affecting the distribution of fluid pressures in the deep aquifer cannot be excluded.

Previous modeling results (Senger et al., 1987), based on transient simulations describing the hydrodynamic development of the Palo Duro Basin, indicated that hydraulic heads have largely equilibrated to effects of basin uplift that started about 10 to 15 Ma ago. However, if the major pulse of uplift occurred more recently, as suggested by Eaton (1986), fluid pressures in low-permeability sections may not have equilibrated and heads could differ by as much as 40 m from steady-state heads (Senger et al., 1987). Another possibility is that local subnormal fluid pressures in thick basinal shale units, caused by erosional decompaction associated with the eastward retreat of the Caprock Escarpment, may perturb fluid pressures in the deep aquifer. This is similar to the scenario described for the shallow confining section (Senger et al., 1987). Such conditions may explain the absence of a typical head increase with depth and the wide scatter of equivalent fresh-water head values calculated from pressure data in the east-central part of the Palo Duro Basin (Figure 8).

Potential for Buoyancy-Dominated Flow

The hydrodynamic development of the Palo Duro Basin during recent Cenozoic time was characterized by changes in topography as a result of basin uplift and erosion. Senger et al. (1987) described the changes in the gravity-driven flow regime and indicated that basin uplift and tilting, starting 10 to 15 Ma ago, caused increased flow rates as a result of the increased hydraulic gradient across the basin. Before basin uplift, the overall gradient across the basin was much lower than that of today. This suggests that buoyancy phenomena may have been important in the Palo Duro Basin before the present-day hydrodynamic regime was established and when topographically induced hydraulic gradients were relatively small. Transient simulations indicated that fluid pressures in the Palo Duro Basin have largely equilibrated to changes in hydraulic boundary conditions (Senger et al., 1987); however, the distribution of dissolved mass evolves over much longer time periods, and the observed solute distribution in the basin may represent some past state of the system.

The potential for buoyancy-dominated flow patterns associated with paleohydrologic conditions is described in Simulation VT-2. For this purpose, steady-state simulation of variable-density flow is performed using the general distribution of fluid density (Figure 6) and viscosity that are inferred from observed salinities and temperature gradients. However, it is assumed that the observed wedge of low-density fluids in the western part of the basin (Figure 6) is a result of the increased recharge rate caused by basin uplift. Therefore, to represent hydrodynamic conditions prior to maximum basin uplift, the salinity distribution was modified to reflect a steeper increase in salinities downdip, thereby eliminating the low-TDS wedge in the western part of the deep aquifer (Senger, 1989). Simulation VT-2 represents hydrodynamic conditions during the initial phase of basin uplift, which incorporates fluid densities that are still responding to the hydrodynamic changes associated with basin uplift. Similar to the modeling approach in a previous study (Senger et al., 1987), the geometry of the mesh is not changed to represent the changes in topography associated with basin uplift. However, the mesh was modified near the Pecos River to represent the topography before the Pecos River valley erosion that occurred predominantly after basin uplift and tilting (Senger et al., 1987). Prescribed heads along the upper surface of the mesh are used to represent the

changes in the shallow water table associated with the changes in topography.

In Simulation VT-2, prescribed hydraulic heads along the upper surface of the model linearly increase by as much as 500 m to represent hydrodynamic conditions during basin uplift; that is, the shallow water-table elevation increases from 600 m at the eastern edge to 1100 m at the western edge. Maximum basin uplift was 1100 m relative to the eastern boundary of the model as described in the previous constant-density Simulation T-2 in Senger et al. (1987), where prescribed heads increased from 600 m at the eastern edge to 1800 m at the western edge of the model.

Stream functions and flow velocities from Simulation VT-2 are shown in Figure 13. Permeabilities of the evaporite confining unit and its eastern extension, the Permian mud-flat system (Figure 5), were reduced by two orders of magnitude, assuming that permeability-enhancing salt-dissolution phenomena were associated mainly with the erosional events during the last 5 Ma, following basin uplift (Senger et al., 1987).

Computed flow rates through the deep basin are much lower in Simulation VT-2 (Figure 13) than in Simulation V-2 (Figure 9) representing present-day hydrological conditions. In the western and eastern parts of the basin, closed streamlines and the calculated velocity vectors indicate circular flow cells (Figure 13). Even though brine hydrostatic conditions were prescribed along the eastern boundary, implying lateral flow across the vertical boundary, computed velocities indicate upward flow associated with the convection cell near the boundary.

Simulation VT-2 indicates that buoyancy phenomena may have been important in the recent geological past, affecting the paleohydrology of the basin. The model indicates that buoyancy-dominated flow could have produced convection cells in the western and eastern parts of the basin. Estimated fluid densities in the eastern part of the deep aquifers (Figure 6) show a slight decrease with depth due to higher temperatures and assumed constant salinities. The resulting density inversion indicates that thermohaline convection causes the continuous overturn of fluids in the eastern part of the basin (Figure 13). In the western part, however, fluid densities increase with depth (Figure 6), and the convection cell is characterized by clockwise rotation of fluids, similar to the flow pattern in the sea-water intrusion example (Figure 3) and to that described by Herbert et al. (1988).

With continued uplift and subsequent erosion, buoyancy-driven flow phenomena diminish, and

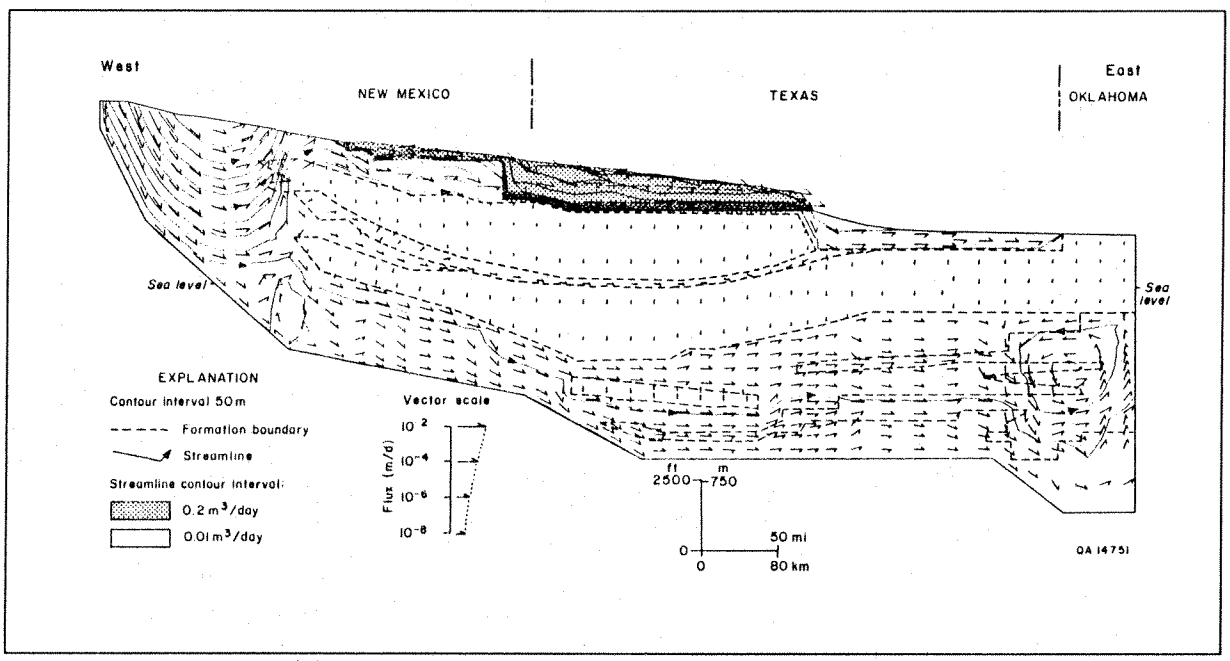

Figure 13. Computed streamlines and flow velocities from Simulation VT-2, representing hydrodynamic conditions during basin uplift that started 10 to 15 Ma ago. Fluid densities are based on those shown in Figure 6.

the flow component arising from topographic relief becomes more important. Consequently, present-day hydrodynamic conditions do not indicate buoyancy-dominated flow patterns despite relatively high fluid densities in the deep aquifer (Figures 8 and 9). Note, however, that the limited data on salinity and temperature that were used to calculate fluid densities (Figure 6) and viscosities in the model show relatively gradual changes across the basin. Possible local variations in salinities and temperatures may result in localized flow patterns dominated by buoyancy phenomena.

Conclusions

The results of these flow simulations indicate that fluid densities will significantly affect the distribution of equivalent fresh-water heads. Consequently, the uncertainty in fluid properties, as compared with the uncertainty in hydraulic properties, may pose a major problem for model calibration. With highly saline brines, the effect of fluid density on the distribution of equivalent fresh-water heads could obscure the effects of variations in hydraulic properties on the head distribution. Calibrating hydraulic parameters from a variable-density model is difficult when significant uncertainty in fluid-density distribution exists.

Present-day hydrodynamic conditions in the Palo Duro Basin, Texas, indicate that the gravity-driven flow component arising from topographic relief dominates the buoyancy forces associated with dense brines. That is, the regional groundwater flow pattern is not significantly affected by the relatively high fluid densities in the deep aquifer. However, during the recent geological past, prior to maximum basin uplift, when the topographic relief across the basin was much lower than it is today, buoyancy phenomena may have produced convection cells in the western and eastern parts of the basin. These buoyancy-dominated flow patterns significantly affect recharge of shallow ground water and displacement of basinal brines.

Acknowledgments

This research was supported by the U.S. Department of Energy Salt Repository Project Office. The conclusions of the author are not necessarily endorsed or approved by the Department of Energy. The author thanks Saleem Akhter of the Bureau of Economic Geology, The University of Texas at Austin, for his review. Editing was by Bobby Duncan. Figures were drafted by the cartographic section of the Bureau of Economic Geology under the supervision of Richard L. Dillon.

Rainer K. Senger is a Research Associate with the Bureau of Economic Geology, The University of Texas at Austin (University Station Box X, Austin, Texas 78713-7508, USA). He received an M.A. in Geology in 1983 and a Ph.D. in Geology in 1989, both from The University of Texas at Austin. His research interests include applications of numerical models for simulating fluid flow in aquifers and hydrocarbon reservoirs, evaluation of aquifer and reservoir properties, hydrogeologic characterization of carbonate aquifers, and development of well-head protection strategies in confined aquifers.

References

Bair, E. S., T. P. O'Donnell and L. W. Picking. 1984. Hydrogeologic investigations based on drill-stem test data, Palo Duro Basin area and New Mexico. Stone and Webster Engineering Corporation, Topical Rept., ONWI/SUB/84, E512-05000-T14.

Bassett, R. L. and M. E. Bentley. 1982. Geochemistry and hydrodynamics of the deep formation brines in the Palo Duro and Dalhart Basins, Texas, USA. J. Hydrol., v. 59, pp. 331–372.

Bear, J. 1972. Dynamics of Fluids in Porous Media. Elsevier.

Bein, A. and A. R. Dutton. 1988. Distribution of Na-CL and Ca-Cl brines in the southern great plains (U.S.A.) ground-water flow system and displacement of connate water (abs.). Geol. Soc. Am. Abstr. Programs, v. 20, p. 363.

Bentley, M. E. 1981. Regional hydrodynamics of brine aquifers, Palo Duro and Dalhart Basins, Texas. *In* Geology and Geohydrology of the Palo Duro Basin, Texas Panhandle. A report on the progress of nuclear waste isolation feasibility studies (T. C. Gustavson et. al., eds.). The University of Texas at Austin, Bureau of Economic Geology, Geol. Circ. 81-3, pp. 93–101.

Combarnous, M. H. and S. A. Bories. 1975. Hydrothermal convection in saturated porous media. Advances in Hydrologic Science, v. 10, pp. 231–307.

De Josselin de Jong, G. 1960. Singularity distributions for the analysis of multiple fluid flow through porous media. J. Geophys. Res., v. 65, pp. 3739–3758.

De Josselin de Jong, G. 1969. Generating functions in the theory of flow through porous media. *In* Flow Through Porous Media, (R. J. M. de Wiest, ed.), Academic Press, pp. 377–400.

Domenico, P. A. and G. A. Robbins. 1985. The displacement of connate water from aquifers. Geol. Soc. Am. Bull., v. 96, pp. 328–335.

Eaton, G. P. 1986. A tectonic redefinition of the Southern Rocky Mountains. Tectonophysics, v. 132, pp. 163–194.

Fisher, R. S. and C. W. Kreitler. 1987. Origin and evolution of deep-basin brines, Palo Duro Basin, Texas. The University of Texas at Austin, Bureau of Economic Geology, Rept. of Invest. No. 166.

Freeze, R. A. and P. A. Witherspoon. 1966. Theoretical analysis of regional ground-water flow. Part 1, Analytical and numerical solutions to the mathematical model. Water Resour. Res., v. 2, pp. 641–656.

Freeze, R. A. and P. A. Witherspoon. 1967. Theoretical analysis of regional ground-water flow. Part 2, Effect of water-table configuration and subsurface permeability variation. Water Resour. Res., v. 3, pp. 623–634.

Freeze, R. A. and P. A. Witherspoon. 1968. Theoretical analysis of regional ground-water flow. Part 3, Quantitative interpretations. Water Resour. Res., v. 4, pp. 581–590.

Henry, H. R. 1964. Effects of dispersion on salt encroachment on coastal aquifers. U.S. Geol. Surv., Water Supply Paper No. 1613-C, pp. C71–C84.

Herbert, A. W., C. P. Jackson and D. A. Lever. 1988. Coupled groundwater flow and solute transport with fluid density strongly dependent upon concentration. Water Resour. Res., v. 24, pp. 1781–1795.

Hubbert, M. K. 1940. The theory of ground-water motion. J. Geol., v. 48, pp. 785–944.

Neuman, S. P. and P. A. Witherspoon. 1970. Finite element method of analyzing steady seepage with a free surface. Water Resour. Res., v. 6, pp. 889–897.

Nield, D. A. 1968. Onset of thermohaline convection in a porous media. Water Resour. Res., v. 4, pp. 553–560.

Orr, E. D. and Kreitler, C. W. 1985. Interpretation of pressure-depth data from confined underpressured aquifers exemplified by the Deep-Basin Brine aquifer, Palo Duro Basin, Texas. Water Resour. Res., v. 21, pp. 533–544.

Senger, R. K. 1989. Hydrodynamics of gravity-driven flow systems in sedimentary basins: example of the Palo Duro Basin, Texas. The University of Texas at Austin, Ph.D. dissertation.

Senger, R. K. and G. E. Fogg. 1987. Regional underpressuring in deep brine aquifers, Palo Duro Basin, Texas. Part 1, Effect of hydrostratigraphy and topography. Water Resour. Res., v. 23, pp. 1481–1493.

Senger, R. K. and G. E. Fogg. 1990a. Stream functions and equivalent fresh-water heads for

modeling regional flow of variable-density ground water. Part 1, Review of theory and verification. Water Resour. Res., v. 26, pp. 2089–2096.

Senger, R. K. and G. E. Fogg. 1990b. Stream functions and equivalent fresh-water heads for modeling regional flow of variable-density ground water. Part 2, Applications and implications for modeling strategy, Water Resour. Res., v. 26, pp. 2097–2106.

Senger, R. K., G. E. Fogg and C. W. Kreitler. 1987. Effects of hydrostratigraphy and basin development on hydrodynamics of the Palo Duro Basin, Texas. The University of Texas at Austin, Bureau of Economic Geology, Rept. of Invest. No. 165.

Smith, D. A., M. S. Akhter and C. W. Kreitler. 1985. Ground-water hydraulics of the Deep-Basin Brine aquifer system, Palo Duro Basin, Texas Panhandle. The University of Texas at Austin, Bureau of Economic Geology, Open-File Rept. OF-WTWI-1985-16.

Tóth, J. 1962. A theory of groundwater motion in small drainage basins in central Alberta. J. Geophys. Res., v. 67, pp. 4375–4387.

Tóth, J. 1963. A theoretical analysis of groundwater flow in small drainage basins. J. Geophys. Res., v. 68, pp. 4795–4812.

Voss, C. I. 1984. SUTRA. A finite-element simulation model for saturated-unsaturated fluid-density-dependent ground-water flow with energy transport or chemically-reactive single-species solute transport. U.S. Geol. Surv. Water Resour. Invest. Rept. 84-4369.

Wirojanagud, P., C. W. Kreitler and D. A. Smith. 1986. Numerical modeling of regional groundwater flow in the Deep-Basin Brine aquifer of the Palo Duro Basin, Texas Panhandle. The University of Texas at Austin, Bureau of Economic Geology, Rept. of Invest. No. 159.

Use of Noble Gases to Determine Boundary Conditions in Groundwater and Petroleum System Models

by Emanuel Mazor and Adi Bosch

Abstract

Atmospheric Ne, Ar, Kr and Xe and radiogenic He and Ar provide means to formulate boundary conditions necessary for the construction of hydrological conceptual models of large groundwater and petroleum systems. Examples include: 1. recharge temperatures, deduced from atmospheric noble gas (ANG) concentrations; 2. porous vs conduit controlled flow in the aerated zone, interpreted from the ANG-derived recharge temperatures; 3. identification of of karstic flow, interpreted from the ANG-derived recharge temperatures; 4. depth of groundwater, determined by comparison of ANG recharge temperatures with emergence temperatures; 5. identification of brines formed by underground dissolution of salts and residual evaporation brines, by comparison of ANG concentrations as in air-saturated freshwater vs lower concentrations in evaporative brines; 6. check of hydraulic interconnections and suggested flow directions, based on distribution of He concentrations; 7. identification of gas caps, using ANG concentrations in produced fluids in excess over the concentrations in air-saturated water (ASW); 8. losses and gains of volatiles and reconstruction of initial gas concentrations, by comparison of measured ANG concentrations with those in ASW; 9. He and Ar dating of underground fluids: 10. establishing the degree of drainage of confined systems, by comparison of He-derived and Ar-derived ages with the respective hydraulic age; 11. identification of mixing of old and young waters, through the comparison of He- and Ar-derived ages with ages derived by other techniques; 12. identification of water-gas and water-oil associations, by comparison of ANG abundance patterns with those predicted from solubility data; and 13. He and Ar dating of hydrocarbons.

Introduction

Hydrological research dealing with systems that are hundreds kilometers across and thousands of meters deep, faces a high degree of complexity and a large number of uncertainties. Fluids involved include water with a wide range of isotopic compositions, and varying concentrations of dissolved ions and gases. These systems are accompanied by varying amounts of oils and natural gases of a multitude of compositions.

The research strategy in such case studies follows the sequence: observations and measurements > deduction of constraining boundary conditions > construction of conceptual models > mathematical modelling > formulation of criteria to check the models, and > conductance of further measurements. The present communication deals with the

formulation of the boundary conditions.

Equations describing the dynamics of crustal fluids are based on a large number of assumptions. The values of the parameters of these equations are often poorly constrained. This situation may be improved by incorporation of as many physical, chemical and isotopic parameters as possible. The use of noble gas data to define boundary conditions for subsurface fluid dynamics is discussed in the present communication.

Crustal fluids contain noble gases of two major sources: 1. atmospheric noble gases, and 2. non-atmospheric ^4He ($^4He_{NA}$) and ^{40}Ar ($^{40}Ar_{NA}$). The non-atmospheric components include a radiogenic contribution from the associated crustal rocks (He_C and Ar_C) and a mantle-derived contribution (He_M and Ar_M). The amount of He_{NA} is calculated from the accompanying ANG, and Ar_{NA} is calculated from the measured Ar concentration and the excess of the $^{40}Ar/^{36}Ar$ ratio over the atmospheric value of 295.5. Measured $^3He/^4He$ ratios serve to separate the measured concentration of He into He_C and He_M (e.g. Hooker et al., 1985), and Ar_C and Ar_M are estimated from He_C concentration and the calculated crustal production ($^4He/^{40}Ar$) ratio.

The ANG in cold and warm groundwaters have been shown to occur in concentrations expected in air-saturated water under the pressure (altitude dependent) and temperature prevailing in the recharge area.The solubilities of noble gases depend also on the salinity of the water, but in most cases salinity has a negligible effect. This observation proves that the noble gases are retained in closed system conditions in cold and warm groundwater, even of old ages (Mazor, 1972; Andrews and Lee, 1979; Herzberg and Mazor, 1979; Zaikovsky et al., 1987). However, dissolved gases are partitioned between liquid and gas (or vapor) phases, whenever the water boils (and steam is separated; Mazor and Truesdell,1984) and whenever the water comes into contact with gas and oil phases (Bosch and Mazor,1989a).

Boundary Conditions Deduced from noble Gas measurements

Recharge Temperature

The concentration of ANG in groundwater reflects the physical conditions that prevailed at the base of the aerated zone at the site of recharge, just before enclosure in the saturated zone. Knowing the altitude of the water table at the studied area, one can use the noble gas concentrations to read the recharge temperature from solubility graphs (Mazor,1972; Herzberg and Mazor, 1979).

Mode of Flow in the Aerated Zone

The noble gas deduced intake temperature, T_{INT}, may be compared with the average annual ambient temperature, T_{AA}, and the average temperature of the rainy recharge season, T_{RS}. The value of T_{RS} is low for winter rains and snow melt. The relation $T_{INT} = T_{AA}$, indicates the recharge water was delayed in the aerated zone to a degree that its temperature equilibrated to the average annual temperature. This, in turn, indicates recharge through a granular medium. In contrast, $T_{INT} =$

T_{RS} indicates negligible temperature equilibration during infiltration in the aerated zone, and hence fast conduit-controlled flow (Herzberg and Mazor, 1979).

Karstic Recharge

Excess air has been observed in certain groundwater samples by ANG concentrations higher than those in ASW and by ANG abundance patterns (relative to ASW) of Ne > Ar > Kr > Xe. Syphoning of air bubbles has been shown to typify recharge in some of these cases (Herzberg and Mazor,1979; Mazor et al., 1983). Thus, two independent ANG indicators for conduit controlled recharge are at hand: $T_{INT} = T_{RS}$, and excess air.

Depth of Groundwater Circulation

Subtraction of the noble gas deduced intake temperature, T_{INT}, from the temperature of emergence, T_{EM}, provides the geothermal temperature added to the water, ΔT. Division of ΔT by the local geothermal heat gradient provides the depth of water circulation. This is a minimum value because some conductive cooling may occur. The application of ANG to deduce the intake temperature liberates us from the need to assume the location of recharge and the mode of infiltration in order to estimate the intake temperature.

Identification of the Source of Dissolved Salts in Deep Brines

Noble gas solubility in water depends on the salinity, e.g. Weiss (1970), Smith and Kennedy (1983) and Weiss and Price (1989). During equilibration with the atmosphere, saline water (e.g. residual evaporation brines), dissolves significantly less ANG than does fresh water. However, fresh water that dissolves salts during its flow in the saturated zone, preserves the original ANG concentrations under the prevailing hydrostatic pressure. Thus, measurement of the ANG concentrations in saline groundwater enables the distinction between surface or deep sources of dissolved salts.

Check of Hydraulic Continuity and Suggested Flow Direction

The component He_C is constantly released from rocks and dissolves in associated water, providing an age indicator. Hence, water is expected to become enriched in He along its underground flow path. This is notable in large systems with old enough water (Mazor and Bosch, in press). Thus, gradual increase in He_C concentration along a suggested groundwater flow direction supports the hypothesis. However, abrupt change in the concentration of He_C calls for changes in the hydrological model. For example, abrupt decrease in the concentration of He_C suggests additions of young water, or the presence of separate water bodies.

Identification of Gas caps

Multiplication of the concentration of the ANG in the dry gas of a well (expressed as cc/cc dry gas) by the dry gas/water production ratio (ccSTP dry gas/ g water), provides the ANG concentrations in ther produced water (ccSTP ANG/g water). The ANG concentrations in the produced water, which are similar to the corresponding values

in recharge water (air-saturated sea water or fresh water), indicate a liquid feed to the produced fluid. Further, ANG concentrations distinctly higher than those predicted for the recharge water indicate the presence of a gas cap (Mazor and Kharaka, 1981).

Losses and Gains of Volatiles

Division of observed concentrations of ANG in a sample by the concentration in the assumed recharge water, ASW, provides the degree of ANG depletion or enrichment that took place.

Reconstruction of Concentrations of Volatiles in an Initial Liquid

A fluid sample depleted or enriched in the ANG due to boiling or gas release has been depleted or enriched to a similar degree in He, CO_2 and CH_4. Division of the measured gas concentration by the observed fractional ANG retention or enrichment factor, provides the respective initial concentration, He_{INI}, $CO_{2\ INI}$ and $CH_{4\ INI}$.

Spatial Exploitation Effects

The presence of fluids, in an exploration drill-hole, with He concentrations lower than those reconstructed for He_{INI}, implies that the hole was drilled into a part of the reservoir that is already reached by existing wells and there is no sense in making it operational. If, however, the concentration of He in a new drill-hole equals He_{INI}, an untouched niche of the field is tapped and the well should be operated.

Dating of Groundwater

It is possible to derive the semi-quantitative ages of groundwater systems by applying the calculated He_{INI} concentrations (Mazor and Bosch, 1990). This, in turn, is related to several hydrological issues, e.g. the check of hydraulic continuity and flow direction, discussed above, a well as the degree of drainage of a system.

Drainage Index

Hydraulic ages are calculated using information on the length of the flow path, the loss of hydraulic head, transmissivity, and other related parameters. In a number of deep confined water systems hydraulic and He ages are available, and the He ages are significantly higher (e.g. in the Paris Basin, Marty et al., 1988). Mazor and Bosch (1990) suggested that the studied systems lack drainage at present, as a result of subsidence that disconnected them from their original drainage basins. In the Paris Basin, for example, water in the Jurassic Dogger aquifer is located at a depth of -1600 to -1850 masl.

Assuming the hydraulic and He ages are properly calculated, then the hydraulic age portrays the system behavior under the assumption of free drainage (equivalent to the open end of the tube in Darcy's experiment), whereas the He age portrays the real situation. We would like to suggest the term drainage index, DI, to describe the degree of through flow in a confined system. The drainage index is derived by division of the calculated hydraulic age by the He age. DI = 1 indicates free drainage (and, hence, active recharge), and DI = 0 indicates lack of drainage (and, hence, lack of

recharge). Intermediate values indicate partial, or restricted drainage. The calculation of DI values enables comparison of the extent of drainage in different systems.

Identification of Mixing of Old and Young Waters

Mixing of old and young waters can be identified by a 'forbidden' combination of significant concentrations of short-lived age indicators, e.g. tritium or C-14, together with significant concentrations of He , which is a cumulative age indicator, effective for high ages. Examples for such forbidden combinations observed in mixed groundwaters have been reported from Switzerland (Mazor et al., 1986), from the Canadian Shield (Bottomley et al., 1984) and other locations. The application of different age indicators is vital in hydrological studies because it provides a check on: 1, the validity of a calculated age (agreeing or disagreeing ages); 2. hydraulic continuity (steady composition vs abrupt changes or reversal of age trends), and 3. leaks from one aquifer to another due to pumping installations.

Identification of Water-Natural Gas-Oil Associations

Bosch and Mazor (1988a) proposed that the ANG in petroleum fluids originated in groundwater (with ANG concentrations as in ASW). The ANG abundance patterns were predicted for natural gas and for oil, both at equilibrium with water. The patterns depend on the water/petroleum ratio, and the solubilities of the noble gases in water and in oil (or gas separated from oil) reveal distinct ANG patterns, which are similar to those predicted for water-natural gas and water-oil equilibration (Bosch and Mazor, 1988a; and unpublished data). The distinct ANG signatures enable the identification of oil-associated natural gas and natural gas which has never been in contact with oil.

Amounts of Water 'Seen' by Oil During its Evolution

The observation of ASW-derived ANG abundance patterns in oils leads to the conclusion that groundwater is the sole (or major) source of ANG in petroleum. Comparison of ANG patterns observed in oil samples with patterns predicted from the model (Bosch and Mazor, 1988a) indicates that the volume of water to which oil deposits were exposed during their subsurface evolution is high, i.e. > 30 cc/cc/

Dating of Oil and Natural Gas

Helium-4 and argon-40 are released from rocks and accumulate in associated hydrocarbons, as they do in water, providing the basis for semi-quantitative dating of hydrocarbon deposits. Helium dating (as well as Ar dating) is an essential tool to understand the dynamics of petroleum fluids; e.g. a He-derived age similar to the reservoir age indicates the presence of a connate fluid of a limited migratory history, where as presence of a fluid in older or younger reservoir rocks indicates that migration occurred. Also, He ages are relevant in placing boundary conditions on the identification of possible hydrocarbon source rocks. The He data of a gas sample from Zuk-Tamrur 1 well (western border of Dead Sea graben) indicates an age

of 10^8 a (Bosch and Mazor, 1988b). Two alternative source rocks were proposed for Zuk-Tamrur hydrocarbons: 1. recent generation in bituminous Upper Cretaceous rocks buried under the Dead Sea (Rullkotter et al.,1985); and 2. generation in Triassic and Paleozoic rocks west of the Dead Sea graben (S. Salhov, pers. commun., 1988). The He-derived age is compatible with the latter alternative. Thus the He-dating method may complement geological considerations in the reconstruction of the dynamic evolution of hydrocarbon deposits.

Conclusions

1. The noble gases provide (in addition to other measurable parameters) means to estimate or check a long list of basic hydrological features. These contribute to the formulation of boundary conditions constraining hydrological conceptual models. By applying information deduced from noble gas measurements, the number of proven assumptions and well estimated parameters required for mathematical modeling are increased.

2. Dating based on He is an essential tool to reconstruct the dynamic history of groundwater systems. A major result is the establishment of the occurrence of very old groundwaters, occasionally connate, up to 10^8 a old; and 2. buried, large groundwater systems that retained their water since the operation of the geological processes that disconnected them from their original bases of drainage.

3. It is highly recommended that noble gas measurements will become a routine part of studies of underground fluids.

Acknowledgements

Warm acknowledgement is made to the donors of The Petroleum Research Fund, administered by the American Chemical Society, for partial support of this research. Support by the MINERVA Foundation, Munich, Germany, is warmly acknowledged.

Biographical Sketch

Emanuel Mazor holds the F.W. Considine Professorial Chair in Hydrological Research at the Department of Environmental Sciences and Energy Research, the Weizmann Institute of Science, Rehovot. His research interests include terrestrial noble gases, groundwater hydrology and geology of the Ramon National Geological Park. (Rehovot, 76100, Israel).

Adi Bosch is currently a Phd student with the Department of Environmental Sciences and Energy Research of the Weizmann Institute of Science, Rehovot. Her current research interests include noble gases in crustal fluids. (Rehovot, 76100, Israel).

References

Andrews, J.N. and D.J. Lee. 1979. Inert gases in groundwater from the Bunter Sandstone of England as indicators of age and paleoclimatic trends, J. Hydrol., v. 41, pp.233-252.

Bosch, A. and E. Mazor. 1988a. Natural gas association with water and oil as depicted by atmospheric noble gases: case studies from the south eastern Mediterranean coastal

plain. Earth Planet. Sci. Lett., v. 87, pp. 338-346.

Bosch, A. and E. Mazor. 1988b. He and Ar as age indicators in natural gases from the Zuk Tamrur 1, Kidod 3 and Gurim 2 wells, Arad area, Israel. Israel Geol. Soc. Ann. Meet., Ein Boqeq, Abst. pp. 5-16.

Bottomley, D.J., J.D. Ross, and W.B. Clarke. 1984. Helium and neon isotope geochemistry of some ground waters from the Canadian Precambrian Shield. Geochim. Cosmochim. Acta, v. 48, pp. 1973-1985.

Herzberg, O. and E. Mazor. 1979. Hydrological applications of noble gases and temperature measurements in underground water systems: examples from Israel. J. Hydrolo., v. 41, pp. 217-231.

Hooker, P.J., R.K. O'Nions and E.R. Oxburgh. 1985. Helium isotopes in North Sea gas fields and the Rhine rift. Nature, v. 318. pp. 273-275.

Marty, B., A. Criaud and C. Fouillac. 1988. Low enthalpy geothermal fluids from the Paris Sedimentary Basin-1. Characteristics and origin of gases. Geothermics, v. 17, pp. 619-633.

Mazor, E. 1972. Paleotemperatures and other hydrological parameters deduced from noble gases dissolved in groundwaters: Jordan Rift Valley, Israel. Geochim. Cosmochim. Acta, v. 36, pp. 1321-1336.

Mazor, E. and Y.K. Kharaka. 1981. Atmospheric and radiogenic noble gases in geopressured-geothermal fluids: northern Gulf of Mexico Basin. Proc. 5th Conf. Geopressured-Geothermal Energy (eds. D.C. Bebout and A.L. Bachman), pp. 197-200.

Mazor, E., R.O. Everdingen and H.R. Krouse. 1983. Noble gas evidence for geothermal activity in a karstic terrain: Rocky Mountains, Canada. Geochim. Cosmochim. Acta, v. 47, pp. 1111-1115.

Mazor, E. and A.H. Truesdell. 1984. Dynamics of a geothermal field traced by noble gases: Cerro Prieto, Mexico. Geothermics, v. 13, pp. 91-102.

Mazor, E., F.C. Jaffe', J. Flück and J.D. Dubois. 1986. Tritium corrected ^{14}C and atmospheric noble gas corrected ^{4}He, applied to deduce ages of mixed groundwaters: examples from the Baden region, Switzerland. Geochim. Cosmochim. Acta, v. 50, pp. 1611-1618.

Mazor, E. and A. Bosch. 1987. Noble Gases in formation fluids from deep sedimentary basins: a review. Appl. Geochem., v. 2, pp. 621-627.

Mazor, E. and A. Bosch. In press. He as a semiquantitative tool for groundwater dating in the range of 10^4 to 10^8 years. In Isotopes of Noble Gases as Tracers in Environmental Studies. IAEA, Vienna.

Rullkotter, J., B. Spiro and A. Nissenbaum. 1985. Biological marker characteristics of oils and asphalts from carbonate source rocks in a rapidly subsiding graben, Dead Sea,

Israel. Geochim. Cosmochim. Acta, v. 49, pp. 1357-1370.

Smith, S.P. and B.M. Kennedy. 1983. The solubility of noble gases in water and in NaCl brine. Geochim. Cosmochim. Acta, v. 47, pp. 503-515.

Weiss, R.F. 1970. The solubility of nitrogen, oxygen and argon in water and seawater. Deep Sea Res., v. 17, pp. 721-735.

Weiss, R.F. and B.A. Price. 1989. Dead Sea gas solubilities. Earth Planet. Sci. lett., v. 92, pp. 7-10.
Zaikowsky, a., B.J. Kosanke and N. Hubbard. 1987. Noble gas composition of deep brines from the Palo Duro Basin, Texas. Geochim. Cosmochim. Acta, v. 51, pp. 73-84.

Boundary Conditions Needed for Groundwater Modeling, Derived from Isotopic, Chemical and Physical Measurements: Mediterranean-Dead Sea Transect

by Emanuel Mazor and Levy Kroitoru

Abstract

Hydrochemical, physical, chemical and isotopic measurements serve to define boundary conditions, to be accounted for in the construction of detailed hydrological conceptual models. Models derived in this mode pave the way for mathematical modeling with a minimum of unknown parameters, that otherwise have to be assumed. The methodology is demonstrated for a hydrological transect from the Mediterranean Coastal Plain, through the Judean Mountains to the Rift Valley.

The boundary conditions reached from the various measured parameters indicate that recharge at the Judean Mountains is rapid and karstic. The western drainage of the system toward the Coastal Plain has an upper slow flow system and a deeper fast-karstic flow system. The eastern drainage toward the Rift Valley has a flow path that is the reverse of the western drainage, namely, an upper fast-karstic flow system emerging in the Judean Desert springs, and a deeper slow flow system encountered by deep water wells.

Introduction

Mathematical modeling of groundwater flow is commonly based on declared and 'hidden' assumptions (Mazor ,1986): 1. modes of flow are assumed (commonly flow through porous media, neglecting flow in conduits); 2. water level data applied pertain to wells that are hydraulically interconnected; 3. derived direction of groundwater flow is not checked by independent criteria; 4. number of water groups involved is known (commonly presence of a single water group is implied); 5. possible hydraulic barriers, causing hydraulic discontiuities, are ignored; and 6. full drainage is assumed, as in the open-end tube of Darcy's experiment. As a result, the number of real unknowns exceeds the number of equations in conventional hydrological modeling. A major challenge of contemporary hydrological research is the increase of the confidence level of hydrological calculations by definition of boundary conditions, reached with the aid of as many measurable parameters as possible. These provide the base for the construction of plausible conceptual models that, in turn, provide the basis of mathematical modeling.

The topic of checking assumptions and establishment of groundwater flow characteristics, is discussed in the present communication in light of a transect across Israel, from the Mediterranean Coastal Plain,

through the Judean Mountains to the Dead Sea Rift Valley.

The Mediterranean Coastal Plain-Judean Mountains-Dead Sea Hydrological Transect Case Study

General Lay Out

Nearly 40 wells and 8 springs were selected along a 5 to 10 km band, about 60 km long, crossing the Judean Mountains anticlinorium at Jerusalem, the eastern flank of the Judean Desert, and the western flank of the Foot Hills and Shefela Plain (Figure 1). The study (Kroitoru,1987) included time-series data of physical, chemical and isotopic measurements (Figure 2).

Boundary Conditions Derived from the Depth of the Aerated Zone

The depth of the aerated zone is 60 to 260 m. This thick aerated zone facilitates the hydrochemical interpretation in two aspects: 1. the water table is below the depth of any roots, ruling out any short cuts of atmospheric CO_2 being brought into the saturated zone by tree respiration, a fact important in the C-14 data interpretation; 2. if a thick aerated zone would be composed solely of well-packed granular material, infiltrating recharge water would be retarded for 100 a or more. This is not the case in the Judean Mountains recharge area, because post-bomb tritium and C-14 are observed (Figure 2), indicating dominance of well developed karstic conduits. This conclusion is in accord with the karstic features that are abundant in the terrain.

Rapid, Karstic Recharge Through the Aerated Zone, Indicated by Tritium Data

Bomb tritium was observed in the Judean mountains groundwater at an early inspection, e.g. in the Ein Karem 1 well 68 TU were observed in November 1964 (Carmi and Gat, 1973). Thus, arrival of recharge water to the saturated Zone is in <8 a. This rate of recharge infiltration is fast, taking into account the thickness (60 to 260 m) of the aerated zone. Thus, karstic conduit controled recharge through the aerated zone is demonstrated.

Rapid Recharge and Karstic Flow, Confirmation From Temperature Data

Average annual temperature in the Judean Mountains is ~18°C, whereas the average rainy season (winter) temperature is ~10°C. The local geothermal gradient has been determined by Bartov and Bein (1977) to be 1.8°C/100m. The water temperature expected in wells may, thus, be calculated, assuming slow water flow and complete temperature equilibration. The Ein Karem well 17 has a water table at a depth of 170 m, and its total depth is 520 m (thickness of the water column: 350 m). The equilibrium temperature at the top of the phreatic aquifer is, thus, expected to be 18+(1.7x1.8)=21.3°C and the temperature at the bottom of the well should be 21.3+(3.5x1.8)=27.6°C. Assuming that pumping brings up mixed water in the well column, with an average groundwater temperature, a value of (21.3+27.6)/2= 24.5°C is expected to be found at the well head if full temperature equilibration took place. The

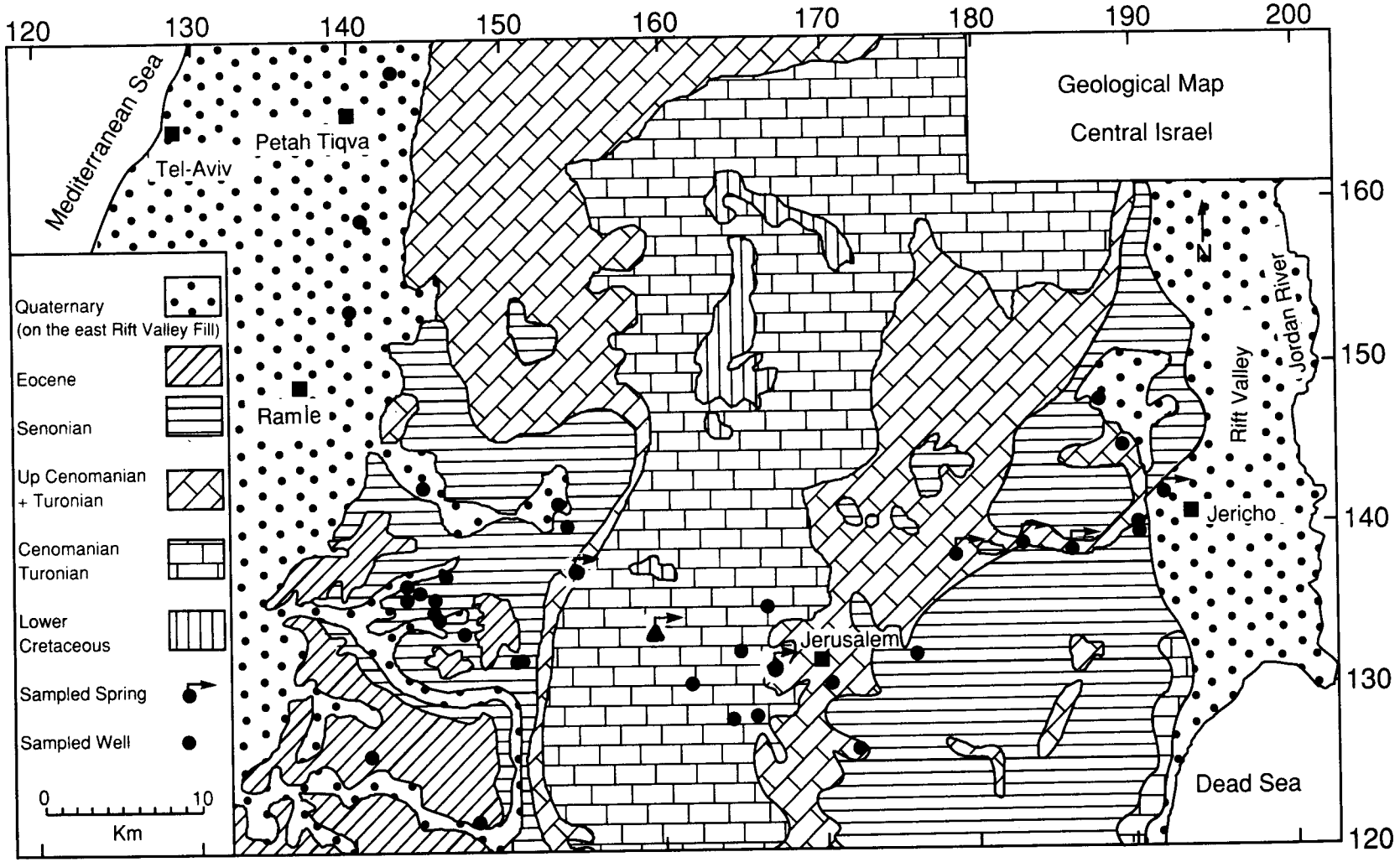

Figure 1. Geological map, central Israel.

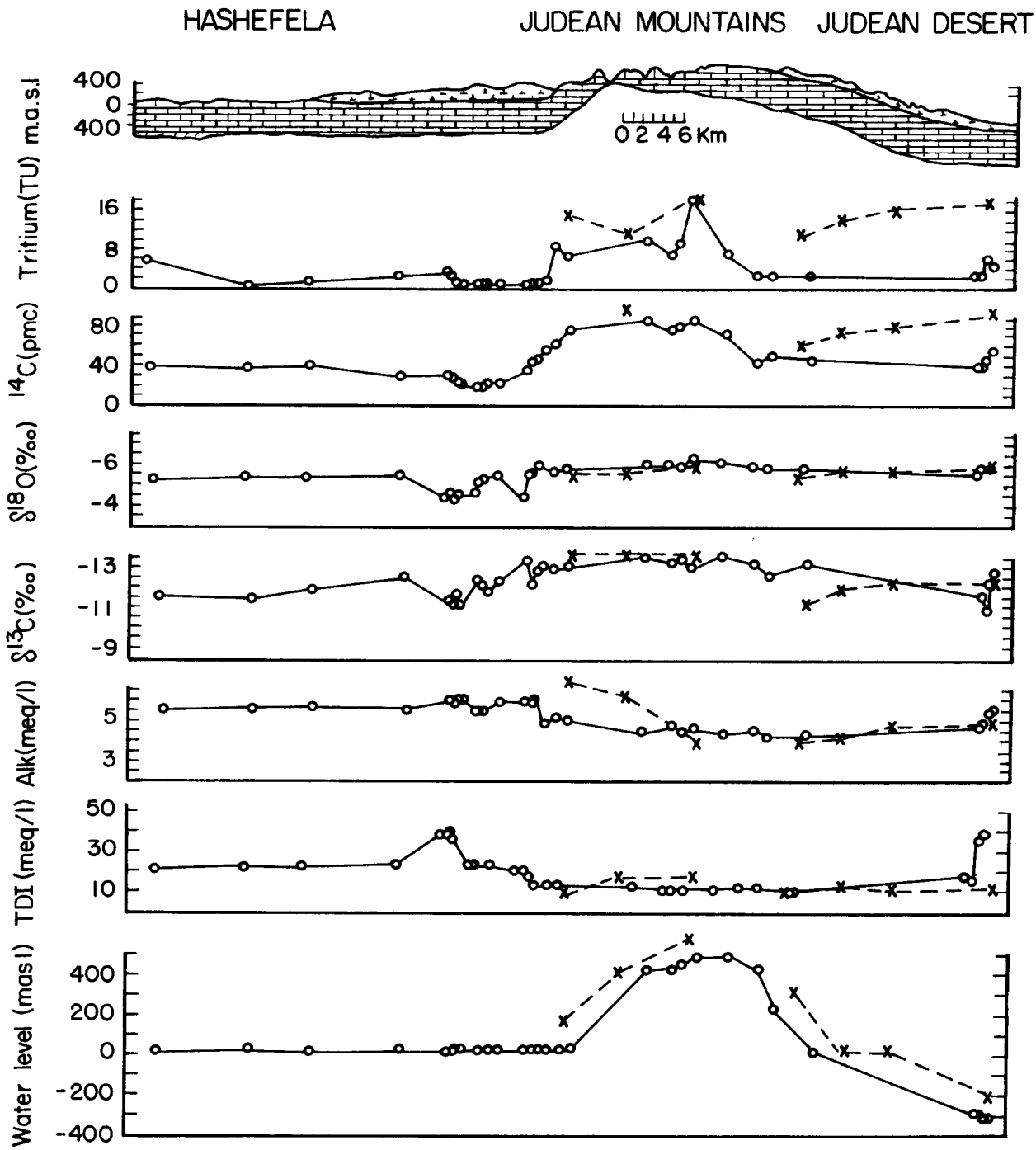

Figure 2. Schematic east-west transect through the Judean Mountains of the Judean Group groundwater system. Isotopic, chemical and physical parameters of samples wells (o) and springs (x).

observed temperature, 19.5°C, is lower by 5°C, indicating 'memory' of the colder rainy winter season and, hence, indicating rapid recharge via karstic conduits in the aerated and saturated zones. A second example is the Eshtaol 7 well, that reached water at a depth of 600 m (the water rose to 200 m below the surface). The well was drilled to a depth of 1226 m and the temperature of the pumped water was 24.5°C. The temperature of complete equilibration at the upper part of the water column should be 18+(6x1.8)=28.8°C and at the bottom of the well a temperature of 18+(12.3x1.8)=41°C should prevail. Thus, an average temperature for the pumped water should be (28.8+41)/2=35°C. The observed temperature of 24.5°C is 10.5°C lower, demonstrating memory of the cold rainy winter season, even in this part of the Judean Group groundwater system. Thus karstic recharge is again demonstrated.

Rapid Water-Rock Interaction in the Aerated Zone, Based on Observations of Fast Recharge

The Mountains' groundwater is fresh, but compared to the composition of rain water it is seen that the major part of the dissolved ions is picked up by water-rock interaction. Most important is the CO_2 take-up in the soil and consequent dissolution of calcite and dolomite, beside dissolution of slight amounts of halite and gypsum. These interactions seem to be rapid, because their results were observed: 1. in the fast recharged local springs; 2. in tritium-rich samples taken from pumped wells, a few years after the bomb tets; and 3. in groundwater that preserved the rainy season temperature.

Confirmation of Rapid Water-Rock Interaction, Deduced from Compositional Constancy in the Phreatic Aquifer

Lack of changes in the concentration of dissolved ions, $\partial^{13}C$ and $\partial^{18}O$ is observed along the mentioned westward flow (Figure 2), as well as ∂D. This is taken as a proof that water-rock interaction is completed upon arrival of recharge water into the saturated zone and no further ionic or isotopic interactions take place along the 20 km westward flow in the Judean Mountains.

General Flow Directions in the Judean Anticlinorium

Water levels (Figure 2) indicate that the groundwater flow is likely to occur from the Judean Mountains to the western and eastern flanks, in accordance with the topography, the anticlinal structure, and the regional distribution of rains. This flow pattern has to be checked for hydraulic interconnections before it may be accepted in a straight forward way.

Flow Direction in the Phreatic Aquifer

Ein Karem 9, 1, 17, 13, and 6 have water tables of 450 to 500 masl. Westward, the Eshtaol 5, Modiim 2, Eshtaol 7 and Gimzu 1 wells, tapping the same phreatic aquifer, have water tables of 20 masl. Thus the water table in the phreatic aquifer drops $>$430 m over a distance of $\sim$20 km and the direction of flow in the discussed part of the phreatic aquifer is to the west.

Confirmation of Flow Direction in the Phreatic Aquifer, Based on Tritium and C-14 Data

A change in the tritium value is seen along the westward flow: 6 to 17 TU in the upper (eastern) group of wells; and only 1 to 8 TU in the lower (western) group. Similarly, the C-14 values of the upper wells are 71 to 87 pmc, compared to 57 to 74 pmc in the western wells. These slight, but distinct, differences in the concentrations of the two age-indicating isotopes confirm the conclusion of a westward flow in the phreatic aquifer: the upper wells revealed, at the time of sampling (1986), dominance of post-bomb water, whereas the western wells seemed to contain also components that arrived a few years prior to the bomb tests.

Suggested Interconnection of Wells and Springs in the Judean Mountains, Based on Compositional Similarities

The springs in the Judean Mountains have parametric values that are indistinguishable from those of the Judean Mountains phreatic aquifer (Figure 2). Thus, from the composition point of view the wells and springs may have hydraulic interconnections. This is in agreement with observed distribution of water levels in the wells and emergence altitude of the springs.

Phreatic-Confined Aquifer Discontinuies, Deduced from Composition Differences

Most conspicuous in the hydrochemical transacts are the abrupt changes observed at the transition from the Judean Mountains phreatic aquifer to the Foothills confined aquifer (Mazor and Kroitoru, 1987): tritium, C-14 (Figure 2), dissolved O_2 and NO_3 drop significantly going westward through the transition zone, whereas the electrical conductivity, TDI, Na, K, Ca, Mg, Cl, SO_4, HCO_3 and H_2S increase. Thus, hydraulic communication between the phreatic and confined zones seems to be limited. Similarly, at the transition of the Judean Mountains to the Judean Desert deeper aquifer, reached by the wells, a significant drop is observed in the tritium and C-14, not accompanied by significant changes in the other parameters. The drop in the age-indicating parameters reveals that hydraulic interconnection between the phreatic Judean Mountains aquifer and the confined Judean Desert aquifer is also restricted. The data reveal a basic difference between the confined system of the western flanks of the anticlinorium and the eastern confined system: the western one is reducing and somewhat more saline, and the eastern one preserves the oxidizing environment and is salt-poor.

Interconnection of Judean Desert Springs and the Judean Mountains Phreatic Aquifer, Deduced from Compositional Similarities

The Judean Desert springs (Fara, Fawar, Kelt and Elisha) reveal tritium, C-14 and dissolved ions values that are similar to those of the phreatic aquifer of the Judean Mountains. Thus, the two systems seem to communicate hydraulically, in contrast to the discontinuity observed between the Judean Mountains phreatic aquifer and the deeper confined Judean Desert aquifer (Figure 3).

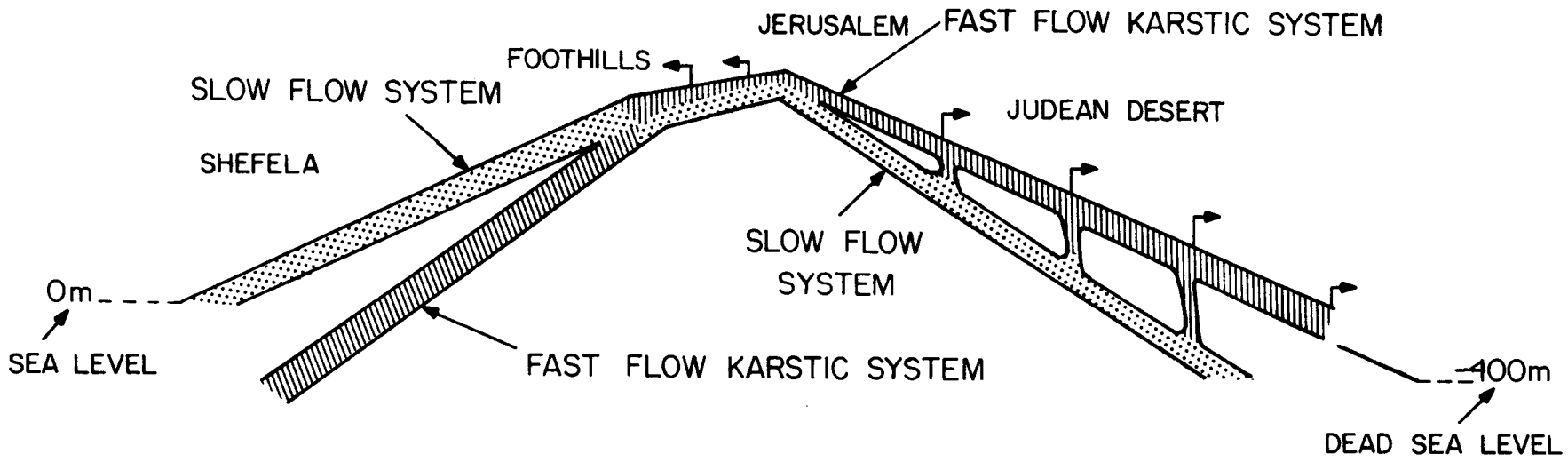

Figure 3. Schematic presentation of flow within the Judean Group groundwater system in central Israel.

Isotopic Indications for a Common Recharge for the Judean Mountains and Judean Desert Groundwaters

The $\delta^{18}O$ (Figure 2) and δD transacts reveal a compositional similarity between the Judean Mountains groundwater and the Judean Desert groundwater, indicating a joint recharge area; that of the Judean Mountains. The isotopic composition of this water is identical to the composition of local precipitation, indicating fast recharge infiltration, leaving no room for evaporation losses.

Isotopic Indications for the Role of Local Rain Additions to the Foothills and Shefela Groundwaters

The Foothills and Shefela groundwaters reveal distinctly heavier δD and $\delta^{18}O$ values, as compared to the Judean Mountains groundwater, indicating that the underground flow of the water from the Judean Mountains is augmented by local rain recharge, through outcrops of the Judean Group rocks.

Boundary Conditions for Groundwater Travel Time Calculations

Geochemical-isotopic mass transfer calculations for the evolution of the Judean Mountain recharge area groundwater (Kroitoru, 1987) indicated a 62% decrease in C-14 concentrations (relative to C-14 of soil CO_2) due to water-rock interaction (Q=0.62). Similar calculations for the Foothills - Shefela area reveal an additional decrease of 10 to 16 pmc due to water-rock interaction (Kroitoru, 1987). In the Judean Desert the observed decrease in the C-14 values is a result of only C-14 decay (as defined by the similarity of the water chemistry and the C-13 values to the Judean Mountains recharge groundwater).

These calculations provide the necessary input for groundwater C-14 age calculations, that can provide boundary conditions for groundwater travel time calculations.

Conclusions: The Conceptual Model

The listed boundary conditions, reached from the various measured parameters, lead to the following conceptual model of the hydrological situation of the Judean Mountains anticlinorium. Recharge at

the mountains infiltrates rapidly (probably of the order of a few months) through the 60 to 260 m deep aerated zone, in a karstic regime. Water-rock interaction is terminated upon arrival of the water in the saturated zone, and includes mainly dissolution of calcite in the aerated zone and incongruent dissolution of dolomite upon arrival in the saturated zone. No further changes occur in the dissolved ion concentrations and carbon isotopic composition of the water along the 15 km westward flow in the phreatic aquifer.

Groundwater flows from the Judean Mountains phreatic system eastward, feeding the Judean Desert springs, but flow is restricted into the Judean Desert deep flow system and the Foothills-Shefela upper flow system. The latter receives recharge additions from local rain. Immediate water-rock interaction decreases the atmospheric C-14 concentration by a factor of Q = 0.62 in the water entering the saturated zone, with no further decrease due to chemical interaction. This Q value was used in groundwater dating and detailed reconstruction of the underground plumbing of the groundwater sub-system (Kroitoru et al., 1987).

Acknowledgements

Financial support by the following agencies is warmly acknowledged: The Minreva Foundation, Germany; Sigram Foundation, Hebrew University, Jerusalem; The Water Commissioner, Ministry of Agriculture, Israel.

Biographical Sketches

Emanuel Mazor holds the F.W. Considine Professorial Chair in Hydrological Rsearch, the Department of Environmental Sciences and Energy Research, the Weizmann Institute of Science. His research interests include terrestrial noble gases, groundwater hydrology, and geology of the Ramon National Geological Park. (Weizmann Institute, D.E.S.E.R., Rehovot 76100, Israel).

Levy Kroitoru is a a senior hydrologist with Weston, Washington D.C. He received his MSc in hydrogeology from the Tel Aviv University in 1980 and a PhD in geochemistry in 1987 from the Weizmann Institute of Science. His research interests include groundwater investigation and resource evaluation by physical, chemical and isotopic methods. (Weston, 955 L'enfant Plaza, S.W, Washington D.C. 20024).

References

Bartov, Y. and A. Bein. 1977. Mediterranean-Dead Sea hydroelectric project. The existence of oil, gas and thermal water. Geolo.. Surv. Israel, Rept. 77/8/MN (in Hebrew).

Carmi, I. and J.R. Gat. 1973. Tritium in precipitation and freshwater sources in Israel. Israel J. Earth Science. v. 22, pp. 71-92.

Kroitoru, L. 1987. The characterization of flow systems in carbonate rocks, defined by the groundwater parameters: Central Israel. PhD. thesis, Weizmann Institute of Science.

Kroitoru, L., I. Carmi and E. Mazor. 1987. Groundwater C-14 activity as affected by initial water-rock interactions in a carbonate terrain with deep water tables: Judean Mountains, Israel. In Isotope Techniques in Water Resources Development, IAEA, Vienna, Proc. pp. 748-750.

Mazor, E. 1986. Chemical, isotopic and physical data used to check basic (commonly assumed) hydrological interrelations. Int. Conf. Groundwater Systems Under Stress, A.W.R.C., Brisbane, Australia, Proc. pp. 1-14.

Mazor, E. and L. Kroitoru. 1987. Phreatic-confined discontinuities and restricted flow in confined groundwater systems. Int. Symp. on the Use of Isotope Techniques in Water Resources Development, IAEA, Vienna, Proc. pp. 427-437.

Hydraulic Evidence of Wisconsinan-aged Open Fractures in a Deep Clayey Till

by David G. Thomson and
John A. Cherry

Abstract

Most investigations of fracturing in clayey glacial till have been limited to shallow weathered deposits. This paper presents the results of an investigation of fracturing in a clay till 60 m below ground level. A detailed vertical profile of hydraulic response in a thick clay till aquitard was recorded with pressure transducers during a 26-day pumping test. The field response was analysed with analytical solutions to determine the bulk hydraulic conductivity. The presence of open fractures was confirmed on the basis that the bulk hydraulic conductivity of fractured clayey till is two orders of magnitude greater than its matrix hydraulic conductivity. A three-dimensional analysis of in situ drawdowns indicates that the spacing between fractures ranges between 1.2 m and 5 m. Geological evidence suggests that the fractures were formed during Wisconsinan time, and have remained open through at least one subsequent glacial advance.

David G. Thomson is a contaminant hydrogeologist in the Environmental Research and Engineering Department at the Alberta Research Council (PO Box 8330, Station F, Edmonton, Alberta T6H 5X2, Canada. He received a BSc in civil engineering from Queen's University, Kingston and a MSc in hydrogeology from the University of Waterloo in 1990. Between 1981 and 1986 he worked in Africa and Canada as a petroleum engineer. Since 1988, his primary research interests have been hydraulic response of fractured tills and numerical analysis of transport in porous media.

John A. Cherry is Director of the Institute for Groundwater Research at the University of Waterloo and a professor in the Department of Earth Sciences. He is coauthor with Allen Freeze of the textbook "Groundwater", published in 1979. Dr. Cherry has been involved in the study of ground water contamination associated with waste disposal since 1968. His research interests have focused on processes of contaminant migration in ground water and field investigations of waste disposal and spill sites across Canada.

LIST OF PARTICIPANTS

5TH CANADIAN/AMERICAN CONFERENCE ON HYDROGEOLOGY: Parameter Identification and Estimation for Aquifer and Reservoir Characterization

September 18-20, 1990

Westin Hotel, Calgary, Alberta, Canada

Dr. Rachid Ababou
Center for Nuclear Waste
Regulatory Analyses
6220 Culebra Road
San Antonio, Texas
78228-0510, USA

Dr. Mary P. Anderson
Department of Geology & Geophysics
University of Wisconsin - Madison
1215 West Dayton
Madison, Wisconsin
53706, USA

Dr. Stefan Bachu
Alberta Geological Survey
Alberta Research Council
PO Box 8330, Station F
Edmonton, Alberta
T6H 5X2, Canada

Professor Jean Bahr
Department of Geology & Geophysics
University of Wisconsin-Madison
1215 West Dayton
Madison, Wisconsin
53706, USA

Mr. Peter S. Baker
ABB Environmental Services, Inc.
261 Commercial Street
PO Box 7050
Portland, Maine
04112, USA

Dr. Fred G. Baker
Woodward-Clyde Consultants
4582 S. Ulster Street Parkway
Denver, Colorado
80237, USA

Dr. P.N. Ballukraya
Department of Applied Geology
University of Madras
Guindy Campus
Madras 600 025, India

Mr. Paul Bauman
Piteau Engineering Ltd.
Suite 100, 4500 - 16th Avenue NW
Calgary, Alberta
T3B 0M6, Canada

Mr. Ron Behrens
Chevron Canada Resources
500 - 5th Avenue SW
Calgary, Alberta
T2P 0L7

Dr. Brian Berkowitz
Water Commission,
Ministry of Agriculture
Hydrological Service
PO Box 6381
Jerusalem 91063, Israel

Mr. R.N. Betcher
Manitoba Water Resources
1577 Dublin Avenue
Winnipeg, Manitoba
R3E 3J5, Canada

Mr. Geoffrey C. Bohling
Advanced Projects Section
Kansas Geological Survey
1930 Constant Avenue, Campus West
University of Kansas
Lawrence, Kansas
66047, USA

Mr. Timothy T.S. Chau
Alberta Environment
14th Floor, Standard Life Centre
10405 Jasper Avenue
Edmonton, Alberta
T5J 3N4, Canada

Mr. Baoren Chen
Earth Sciences Department
Nanjing University
Nanjing 210008, China

Mr. Dennis Coombe
Computer Modelling Group
3512 - 33 Street NW
Calgary, Alberta
T2L 2A6, Canada

Mr. Tom Cronk
Oak Ridge National Laboratory
PO Box 2567
Grand Junction, Colorado
81502, USA

Mr. Terry A. Dash
Agriculture Canada/PFRA
1901 Victoria Avenue
Regina, Saskatchewan
S4P 0R5, Canada

Ms. Janelle Davidson
Canadian Hunter Exploration Ltd.
435 - 4th Avenue SW
Calgary, Alberta
T2P 3A8, Canada

Mr. Tom Davis
Canadian Hunter Exploration Ltd.
435 - 4th Avenue SW
Calgary, Alberta
T2P 3A8, Canada

Mr. Joe O. Davis
Omega Geophysics Ltd.
203 - 888 Burrard Street
Vancouver, British Columbia
V6Z 1X9, Canada

Dr. Alexander J. Desbarats
Geological Survey of Canada
601 Booth Street
Ottawa, Ontario
K1A 0E8, Canada

Mr. John Douglas
Esso Resources Canada Ltd.
3535 Research Road NW
Calgary, Alberta
T2L 2K8, Canada

Ms. Janet Durksen
Canadian Hunter Exploration Ltd.
435 - 4th Avenue SW
Calgary, Alberta
T2P 3A8, Canada

Mr. David C. Elliott
Elliott Development Consulting
6407 Laurentian Way SW
Calgary, Alberta
T3E 5N2, Canada

Professor Iraj Ershaghi
Department of Petroleum Engineering
University of Southern California
University Park, Hedco 316
Los Angeles, California
90089-1211, USA

Mr. James T. Freeman
HCI Hydrologic Consultants, Inc.
12596 W. Bayaud Avenue, Suite 290
Lakewood, Colorado
90228, USA

Mr. Alan Fryar
Department of Geology
University of Alberta
Room 1-26, Earth Sciences Building
Edmonton, Alberta
T6G 2E3, Canada

Dr. Lynn Gelhar
Massachusetts Institute of Technology
Room 48-329
Cambridge, Massachusetts
02139, USA

Mr. Saleem G. Ghori
PRCC,
New Mexico Institute of
Mining and Technology
Socorro, New Mexico
87801, USA

Mr. Lyle Hanna
Vam Premium Connections Ltd.
9815 - 19 Street SW
Calgary, Alberta
T2V 1R5

Mr. Paul Hardisty
Piteau Engineering Ltd.
Suite 100, 4500 - 16th Avenue NW
Calgary, Alberta
T3B 0M6, Canada

Dr. Holger H. Hartmaier
Acres International Ltd.
Suite 500, 10201 Southport Road SW
Calgary, Alberta
T2W 4X9, Canada

Mr. Robert Hawkes
Fekete Associates Inc.
#2000, 540 - 5 Avenue SW
Calgary, Alberta
T2P 0M2, Canada

Mr. John Heller
PRCC,
New Mexico Institute of
Mining and Technology
Socorro, New Mexico
87801, USA

Mr. Joost Herweijer
GeoTrans Inc.,
250 Exchange Place, Suite A
Herndon, Virginia
22070, USA

Dr. Brian Hitchon
Alberta Geological Survey
Alberta Research Council
PO Box 8330, Station F
Edmonton, Alberta
T6H 5X2, Canada

Mr. Ken Hugo
Esso Resources Canada Ltd.
Box 2480, Station M
Calgary, Alberta
T2P 3M9, Canada

Professor Elizabeth Jacobson
Desert Research Institute
University of Nevada
7010 Dandini Blvd.
Reno, Nevada
89506-0220, USA

Mr. Peter Kearl
Martin Marietta
Oak Ridge National Laboratory
PO Box 2567
Grand Junction, Colorado
81503, USA

Ms. Janice Keebler
Canadian Hunter Exploration Ltd.
435 - 4th Avenue SW
Calgary, Alberta
T2P 3A8, Canada

Dr. Peter K. Kitanidis
Water Resources
Department of Civil Engineering
Terman Engineering Center
Stanford University
Stanford, California
94305-4020, USA

Dr. Sait Kocberber
Research and Engineering Consultants
5445 DTC Parkway #640
Englewood, Colorado
80111, USA

Dr. John Kramers
Alberta Geological Survey
Alberta Research Council
PO Box 8330, Station F
Edmonton, Alberta
T6H 5X2, Canada

Dr. Larry Lake
Department of Petroleum Engineering
The University of Texas at Austin
CPE 2.502
Austin, Texas
78712, USA

Mr. Pat Lapcevic
National Water Research Institute
867 Lakeshore Road
Burlington, Ontario
L7R 4A6, Canada

Mr. Eberhard Lorberg
Alberta Environment
11139 - 39A Avenue
Edmonton, Alberta
T6J 0N6, Canada

Mr. Bruce Manchon
International Technology Corporation
4585 Pacheco Blvd.
Martinez, California
94553, USA

Dr. Emanual Mazor
The Weizmann Institute of Science
Isotope Department
76100 Rehovot, Israel

Mr. P.R. McGillivray
Department of Geophysics & Astronomy
University of British Columbia
2219 Main Mall
Vancouver, British Columbia
V6T 1W5, Canada

Mr. G.S. McNab
Esso Petroleum Canada Ltd.
3535 Research Road NW
Calgary, Alberta
T2L 2K8, Canada

Dr. V.A. Mironenko
Mining Institute
Tverskaja 18, ap. 52
Leningrad 19324, USSR

Ms. Gerilynn R. Moline
Department of Geology & Geophysics
University of Wisconsin - Madison
1215 West Dayton
Madison, Wisconsin
53706, USA

*Mr. Lee Nichols
Terracon Geotechnique Ltd.
633 - 6th Avenue SW, Suite 800
Calgary, Alberta
T2P 2Y5, Canada

Dr. Jasper Bruhn Nielsen
Danish Land Development Service
Fabriksvangen 3
Slangerup 3550, Denmark DK

Mr. Manoel Nobre
Department of Civil Engineering
Graduate Office
University of Waterloo
200 University Avenue West
Waterloo, Ontario
N2L 3G1, Canada

Mr. Brent G. Noland
Esso Resources Canada Ltd.
237 - 4th Avenue SW
Calgary, Alberta
T2P 2J2, Canada

Mr. Scott Parker
Hazardous Materials Management
Magazine
12 Salem Avenue, Suite 200
Toronto, Ontario
M6H 3C2, Canada

Dr. Eileen Poeter
Colorado School of Mines
Golden, Colorado
80403, USA

Mr. James C. Redwine
Southern Company Services Inc.
PO Box 2625
Birmingham, Alabama
35202, USA

Dr. Malcolm Reeves
Geological Engineering Department
University of Saskatchewan
Saskatoon, Saskatchewan
S7N 0W0, Canada

Mr. Jeff Riddle
Salt River Project
PO Box 52025
Phoenix, Arizona
85072-2025, USA

Dr. Robert Ritzi
Department of Geological Sciences
Wright State University
Dayton, Ohio
45435, USA

Ms. Carol Rix
Canadian Hunter Exploration Ltd.
435 - 4th Avenue SW
Calgary, Alberta
T2P 3A8, Canada

Mr. Craig Robertson
Monenco
801 - 6 Avenue SW
Calgary, Alberta
T2P 3W3, Canada

Mr. Ben Rostron
Department of Geology
University of Alberta
1-26 Earth Sciences Building
Edmonton, Alberta
T6G 2E3, Canada

Mr. Timothy D. Scheibe
Department of Civil Engineering
Stanford University
Terman Engineering Center
Stanford, California
94305-4020, USA

Dr. Rainer Senger
Bureau of Economic Geology
The University of Texas at Austin
University Station, Box X
Austin, Texas
78713-7508, USA

Ms. Lisa D. Shepherd
Department of Geology & Geophysics
University of Wisconsin - Madison
1215 West Dayton
Madison, Wisconsin
53706, USA

Mr. C. Steve Simmons
Battelle, PNL
MS K6-77
Richland, Washington
99352, USA

Mrs. Kathie Skogg
Alberta Geological Survey
Alberta Research Council
PO Box 8330, Station F
Edmonton, Alberta
T6H 5X2, Canada

Dr. Leslie Smith
Department of Geological Sciences
University of British Columbia
Vancouver, British Columbia
V6T 2B4, Canada

Mr. Richard J. Stebnisky
J.B. Butler and Associates, Inc.
PO Box 23526
Tampa, Florida
33623, USA

Dr. David Thomson
Environmental Engineering
Research Department
Alberta Research Council
PO Box 8330, Station F
Edmonton, Alberta
T6H 5X2, Canada

Mr. Bryan J. Travis
Earth and Environmental
Sciences Division
MS-F665
Los Alamos National Laboratory
Los Alamos, New Mexico
87545, USA

Mr. Mark Trudell
Environmental Engineering
Research Department
Alberta Research Council
PO Box 8330, Station F
Edmonton, Alberta
T6H 5X2, Canada

Mr. Mark Tustian
Amoco Canada
240 - 4 Avenue SW
PO Box 200, Station M
Calgary, Alberta
T2P 2H8, Canada

Mr. Jim Underschultz
Alberta Geological Survey
Alberta Research Council
PO Box 8330, Station F
Edmonton, Alberta
T6H 5X2, Canada

Mr. Cor van Kruysdyk
Shell Canada Ltd.
3655 - 36 Street NW
Calgary, Alberta
T2P 3S6, Canada

Mr. Ian van Staalduinen
Canadian Hunter Exploration Ltd.
435 - 4th Avenue SW
Calgary, Alberta
T2P 3A8, Canada

Mr. Steve Veltman
Esso Resources Canada Ltd.
Box 600
Calgary, Alberta
T2P 2J2, Canada

Mr. Erik K. Webb
Department of Geology and Geophysics
University of Wisconsin at Madison
1215 West Dayton Street, Weeks Hall
Madison, Wisconsin
53706, USA

Dr. John L. Wilson
New Mexico Institute of
Mining and Technology
Socorro, New Mexico
87801, USA

Mr. Glen Winner
Alberta Environment
Groundwater Rights Branch
2nd Floor, 9820 - 106 Street
Edmonton, Alberta
T5K 2J6, Canada

Dr. Kevin K. Wolka
Geraghty and Miller, Inc.
50 West Big Beaver Road, Suite 145
Troy, Michigan
48084, USA

Mr. Jiannan Xiang
Department of Mineral Engineering
104 Mineral Sciences Building
Pennsylvania State University
University Park, Pennsylvania
16802, USA

Mr. E.N. Yearsley
COLOG, Inc.
Borehole Geophysical Services
1019 8th Street, Suite 100
Golden, Colorado
80401, USA

Mr. Steven C. Young
Engineering Laboratory
Tennessee Valley Authority
129 Pine Road
Norris, Tennessee
37828, USA

* - one day participants